Letter of Intent

to build an Off-axis Detector

to study $\nu_\mu \rightarrow \nu_e$ oscillations

with the NuMI Neutrino Beam

Version 4.0

June 3, 2002

D. Ayres, G. Drake, M. Goodman, V. Guarino, T. Joffe-Minor, D Reyna,
R. Talaga, J. Thron
Argonne National Laboratory, IL

B. Choudhary, D. Michael
Caltech, Pasadena, CA

H. Nunokawa
Universidade Astadual de Campinas, Campinas, Brazil

E. Blucher
University of Chicago, Chicago, IL

D. Carey, S. Childress, J. Cooper, S. Geer, R. Hatcher, D. Harris, J. Hylen,
P. Kasper, P. Lucas, V. Makeev, A. Marchionni, N. Mokhov, A. Para,
S. Parke, S. Pordes, P. Shanahan, P. Spentzouris
Fermilab, Batavia, IL

G.J. Feldman, A. Lebedev, R. Lee, M.D. Messier, S.-M. Seun
Harvard University, Cambridge, MA

J. Thomas
University College London, London, UK

R. Imlay, W. Metcalf, R. Svoboda
Louisiana State University, Baton Rouge, LA

K. Scholberg
MIT, Cambridge, MA

C. Bromberg, R. Richards
Michigan State University, East Lansing, MI

P. Border, T. Chase, K. Heller, S. Kasahara, M. Marshak, L. Mualem,
N. Pearson, E. Peterson, K. Ruddick, J. Urheim
University of Minnesota, Minneapolis, MN

P. Huber, M. Lindner, M.Winter
Technische Universitaet München, München, Germany

C. Albright
Northern Illinois University, DeKalb, IL

H. Schellman
Northwestern University, Evanston, IL

C.R. Brune, D.S. Carman, S.M. Grimes, K.H. Hicks, A.K Opper
Ohio University, Athens, OH

V. Paolone
University of Pittsburgh, Pittsburgh, PA

K. T. McDonald
Princeton University, Princeton, NJ

A. Bodek, H. Budd, P. deBarbaro, G. Ginther, S. Manly, K. McFarland, W. Sakumoto, P. Slattery, M. Zielinski
University of Rochester, Rochester, NY

P. Litchfield, G. Pearce, D. Petyt
Rutherford Appleton Laboratory, Chilton, Didcot, UK

S. Wojcicki
Stanford University, Stanford, CA

S. Kopp, K. Lang
University of Texas, Austin, TX

H. Minakata
Tokyo Metropolitan University, Tokyo, Japan

H. Gallagher, T. Kafka, A. Mann, J. Schneps
Tufts University, Boston, MA

D. Cline, K. Lee
UCLA, Los Angeles, CA

C. Hagner, N. Morgan
Virginia Tech, Blacksburg, VT

S. Menary
York University, Toronto, Canada

Contents

Executive summary 5

1 Motivation 1-7

2 The Role of the MINOS Experiment 2-13

3 Possible Evolution of Neutrino Physics 3-18

4 Off-Axis NuMI Neutrino Beam 4-23
- 4.1 NuMI Off-Axis Neutrino Fluxes 4-25
- 4.2 Backgrounds 4-28
- 4.3 Antineutrino Beams 4-28
- 4.4 Proton Economics 4-31

5 $\nu_\mu \rightarrow \nu_e$ Oscillation Appearance Experiment 5-33
- 5.1 Statement of the challenge 5-33
- 5.2 Possible experimental approaches 5-34
- 5.3 Background measurements and estimates; systematics 5-35
- 5.4 Physics Potential of the NuMI Off-axis Beam 5-37
- 5.5 Comparison with JHF Phase I 5-40

6 Future Evolution of the Off-Axis Neutrino Program 6-42

7 Detector 7-45

8 Detector Sites, Physics Considerations 8-47

9 Cost and Schedule, Milestones 9-49
- 9.1 Cost 9-49
- 9.2 Schedule 9-50
- 9.3 Milestones 9-50
- References 9-53

A Possible Detector Technologies **A-1**
A.1 Low Z Tracking Calorimeter A-1
A.1.1 Low energy neutrino interactions in low Z calorimeter . . A-2
A.1.2 Electron identification A-2
A.1.3 Energy resolution A-6
A.1.4 A specific detector example: LoDen - LOw DENsity calorimeter A-7
A.1.5 Glass RPC Chambers A-9
A.1.6 Readout Electronics A-11
A.1.7 Ancillary Systems A-15
A.1.7.1 Gas System A-15
A.1.7.2 HV A-16
A.1.8 Modular Detector Design A-17
A.1.9 Absorber Construction and Composition A-19
A.1.9.1 Containers and Loose Fill Materials A-19
A.1.9.2 Molded Particleboard A-20
A.1.9.3 External Framework and Self Supporting Structures A-20
A.1.10 Liquid Scintillator Option A-22
A.1.10.1 Support Structure A-22
A.1.10.2 Signal Collection A-23
A.1.10.3 Support A-23
A.1.10.4 Readout A-23
A.1.10.5 Cost Estimate A-24
A.1.11 Backgrounds in a surface detector A-25
A.1.11.1 Cosmic ray rates in the detector A-25
A.1.11.2 Tertiary particle production by muons interacting in the environment outside the detector . . . A-25
A.1.11.3 Particle production by unseen muons inside the detector A-26
A.1.11.4 Gamma rays A-26
A.1.11.5 Measurement of cosmic ray backgrounds A-27
A.2 Water Cherenkov option A-28
A.3 Liquid Argon TPC A-33

B Possible Sites for a NuMI Off-Axis Detector **B-40**
B.1 Criteria for Site Selection B-40
B.2 Potential Sites B-41
B.3 LTV sites B-42

I apologize for this letter being so long but I had no time to make it shorter. *Blaise Pascal*

Executive summary

The question of neutrino masses is of fundamental importance. Neutrino oscillations seem to be the only tool available to us to unravel the pattern of neutrino masses and, perhaps, shed some light on the origin of masses in general.

The NuMI neutrino beam line and the MINOS experiment represent a major investment of US High Energy Physics in the area of neutrino physics. The forthcoming results could decisively establish neutrino oscillations as the underlying physics mechanism for the atmospheric ν_μ deficit and provide a precise measurement of the corresponding oscillation parameters, Δm^2_{32} and $\sin^2 2\theta_{23}$.

This, however, is just a beginning of a long journey into uncharted territories. The key to these new territories is the detection of $\nu_\mu \to \nu_e$ oscillations associated with the atmospheric ν_μ deficit, controlled by the little known mixing angle $\sin^2 2\theta_{13}$. A precise measurement of the amplitude of these oscillations will enable a determination of the pattern of the mass hierarchy of neutrinos. If the solar neutrino experiments determine that the value Δm^2_{12} is in the range of $10^{-5} - 10^{-4}\ eV^2$ then the measurement of the CP violation in the neutrino sector may well be within our reach.

The full potential of the NuMI neutrino beam can be exploited by complementing the MINOS detector, under construction, with a new detector(s) placed at some off-axis position and collecting data in parallel with MINOS. The first phase of the proposed program includes a new detector, optimized for ν_e detection, with a fiducial mass of the order of 20 kton and exposed to neutrino and antineutrino beams. In a five year run its sensitivity to the $\nu_\mu \to \nu_e$ oscillations will be at least a factor of ten beyond the current limit.

The future direction of the program will depend on the results of this first phase, but it is very likely that it will be a combination of a significant increase of the neutrino beam intensity via an upgraded proton source and an increase of the detector mass by a factor of five or so. Depending on the circumstances, the goals of Phase II may be a further increase of the sensitivity of a search for $\nu_\mu \to \nu_e$ oscillations, or, perhaps, a measurement of the CP violating phase δ in the lepton sector.

This document is organized as follows:

- Chapter 1 summarizes the physics motivation for the proposed experiment
- Chapter 2 briefly reviews the role of the MINOS experiment in the investigations of neutrino oscillations
- Chapter 3 outlines the possible evolution of the neutrino program in the US and world-wide
- Chapter 4 discusses the properties of the NuMI neutrino beam, especially at the off-axis positions
- Chapter 5 discusses experimental considerations for a $\nu_\mu \rightarrow \nu_e$ oscillation experiment
- Chapter 6 discusses possible detectors. Details of specific detector designs and various technical aspects are described in the Appendix A.
- Chapter 7 addresses the issues of possible sites for the new experiment. Details of a specific site: the LTV mine are described in the Appendix B.
- Chapter 8 discusses possible scenarios of the evolution of the neutrino program at Fermilab
- Chapter 9 outlines a possible schedule and milestones

Chapter 1

Motivation

The SuperKamiokande[1] experiment has recently provided very strong evidence that the muon neutrino undergoes flavor changing transitions. These transitions are seen for neutrinos whose path length divided by energy (L/E) is greater than $\sim 10^2$ km/GeV. SuperK also has some supporting evidence that these muon neutrinos are transformed primarily into tau neutrinos. Although the SuperKamiokande detector has some sensitivity to flavor transitions of electron neutrinos their data provides no evidence that electron neutrinos are involved in these transitions. In fact, the Chooz [2] reactor experiment provides a tighter constraint on the upper limit on the probability of electron neutrino flavor transitions of 5%, at the values of L/E for which SuperKamiokande sees muon neutrino flavor transitions. This leaves open the interesting and important question: What is the role of the electron neutrino in flavor transitions at these values of L/E? A measurement or stringent limit on the probability of $\nu_\mu \rightarrow \nu_e$ for such values of L/E (10^2 to 10^3 km/GeV) is an important step in understand these neutrino flavor transitions in atmospheric neutrinos. As the NuMI beam is primarily a ν_μ beam, the observation of ν_e appearance would address this question directly. This is the primary goal of the experiment described by this letter of intent.

The SNO[3] experiment has recently reported large transitions of solar electron neutrinos to muon and/or tau neutrinos. The onset of these transitions occurs for an L/E which is a least one order of magnitude larger than the L/E for which SuperKamiokande sees flavor transitions in atmospheric muon neutrinos. If these transitions occur near the lower allowed values of L/E then the transition probability $\nu_\mu \rightarrow \nu_e$ measured by an experiment in the NuMI beam can have some sensitivity to the flavor transitions associated with solar neutrinos.

The LSND[4] experiment has reported small muon antineutrino to electron antineutrino transitions for values of L/E which are less than two orders of magnitude smaller than the transitions seen in atmospheric neutrinos. However this transition probability is very small, compared to that observed in atmospheric and solar neutrinos, on the order of 0.3%. If this result is confirmed by the up

coming mini-Boone [5] experiment, this could be an important background for a measurement of $\nu_\mu \rightarrow \nu_e$ transitions at the larger values of L/E associated with atmospheric neutrinos.

To explain the above phenomena, extensions to the Standard Model are required. The simplest and most widely accepted extension is to allow the neutrinos to have masses and mixings such that the above phenomena are explained by neutrino oscillations. The masses and mixing of the neutrinos in these extensions would be the low energy remnant of some yet to be determined high energy physics. Thus, neutrino masses and mixing provide a unique window on physics that is inaccessible to current or near future collider experiments. One popular theory is the so called "seesaw" scenario where the active left handed neutrinos seesaw off their heavier right handed (sterile) partners leaving three very light Majorana neutrinos. It is already clear that the masses and mixings in the neutrino sector are very different than the masses and mixing in the quark sector and that a detailed understanding of the neutrino masses and mixings will be important in differentiating fermion mass theories. Also, they may provide the key to advancing our theoretical understanding of this fundamental question.

If the neutrinos have masses and mixings then the neutrino mass eigenstate $\nu_i = (\nu_1,\ \nu_2,\ \nu_3,\ \ldots)$ with masses $m_i = (m_1,\ m_2,\ m_3, \ldots)$ are related to the flavor eigenstates, $\nu_\alpha = (\nu_e,\ \nu_\mu,\ \nu_\tau,\ \ldots)$ by a unitary MNS matrix,

$$|\nu_\alpha\rangle = \sum_i U_{\alpha i} |\nu_i\rangle \tag{1.1}$$

If we restrict the light neutrino sector to the three known active flavors and set aside the LSND results [1] then the unitary matrix MNS matrix, U, can be written as

$$U_{\alpha i} = \begin{pmatrix} c_{13}c_{12} & c_{13}s_{12} & s_{13}e^{-i\delta} \\ -c_{23}s_{12} - s_{13}s_{23}c_{12}e^{i\delta} & c_{23}c_{12} - s_{13}s_{23}s_{12}e^{i\delta} & c_{13}s_{23} \\ s_{23}s_{12} - s_{13}c_{23}c_{12}e^{i\delta} & -s_{23}c_{12} - s_{13}c_{23}s_{12}e^{i\delta} & c_{13}c_{23} \end{pmatrix} \tag{1.2}$$

where $c_{jk} \equiv \cos\theta_{jk}$ and $s_{jk} \equiv \sin\theta_{jk}$.

With this labeling the atmospheric neutrinos oscillations are primarily determined by θ_{23} and Δm^2_{32} whereas the solar neutrino oscillations depend on θ_{12} and Δm^2_{21}, where $\Delta m^2_{ij} = m^2_i - m^2_j$. From SuperKamiokande we already have some knowledge of $|\Delta m^2_{32}| = (1.4 - 4.0) \times 10^{-3}\text{eV}^2$ and $\theta_{23} \approx \pi/4$. SNO and the other solar neutrino experiments indicate $\Delta m^2_{21} = +(2 - 10) \times 10^{-5}\text{eV}^2$ and $\theta_{12} \approx \pi/6$. Furthermore, Chooz (and SuperK) provide us with *limit* on $\sin\theta_{13} < 0.16$. At present we have no information on the sign of Δm^2_{32} or the CP violating parameter δ.

[1] In the 3+1 neutrino mass hierarchy the LSND result can be accommodated as a perturbation on the pure active 3 neutrino hierarchy. The 2+2 mass hierarchy would require major modifications.

The appearance probability of ν_e in a ν_μ beam in vacuum is given, to leading order, by

$$P_{vac}(\nu_\mu \rightarrow \nu_e) = \sin^2\theta_{23}\ \sin^2 2\theta_{13}\ \sin^2\Delta_{atm} \tag{1.3}$$

where $\Delta_{atm} \approx 1.27\left(\frac{\Delta m^2_{32}L}{E}\right)$. If the experiment is performed at the peak of this probability, that is, when $\Delta_{atm} = \frac{\pi}{2} + n\pi$, then

$$P_{vac}(\nu_\mu \rightarrow \nu_e) \approx \frac{1}{2}\sin^2 2\theta_{13}. \tag{1.4}$$

The first peak occurs at neutrino energy,

$$E = 1.8\ \text{GeV}\left(\frac{\Delta m^2_{32}}{3\times 10^{-3}\text{eV}^2}\right)\left(\frac{L}{732\text{km}}\right). \tag{1.5}$$

Using the constraint from Chooz of $\sin^2 2\theta_{13} < 0.1$ gives a maximum appearance probability of 5%. To be effective any ν_e appearance experiment has to aim to exclude or convincingly see a signal at least an order of magnitude below this 5% limit.

The neutrinos in the NuMI beam propagate through the Earth and matter induced contribution to the propagation amplitude are non-negligible . These matter effects have opposite sign for neutrinos and anti-neutrinos and for the normal versus inverted neutrino mass hierarchies. The matter effects can be thus used to distinguish the two possible three neutrino mass hierarchies, see Fig. 1.1. If the experiment is performed at the first peak in the oscillation, as above, the matter effects are primarily a function of the energy of the neutrino beam and the transition probability in matter can be approximated by

$$P_{mat}(\nu_\mu \rightarrow \nu_e) \approx \left(1 \pm 2\frac{E}{E_R}\right)\ P_{vac}(\nu_\mu \rightarrow \nu_e) \tag{1.6}$$

where E_R is the matter resonance energy associated with the atmospheric Δm^2, that is

$$E_R = \frac{\Delta m^2_{32}}{2\sqrt{2}G_F N_e} = 13\ \text{GeV}\left(\frac{\Delta \text{m}^2_{32}}{3\times 10^{-3}\text{eV}^2}\right)\left(\frac{1.5\ \text{gcm}^{-3}}{\text{Y}_e\rho}\right). \tag{1.7}$$

where N_e is the electron number density in the earth, ρ is the matter density and Y_e is the electron fraction.

For the normal hierarchy, matter effects enhance (suppress) the transition probability for neutrinos (anti-neutrinos) and vice versa for the inverted hierarchy. For a 2 GeV neutrino energy, matter effects give a 30 % enhancement or suppression in the transition probability.

If the solution to the solar neutrino puzzle is determined to be neutrino oscillations with the parameters in the "Large Mixing Angle" (LMA) region then the $\nu_\mu \rightarrow \nu_e$ transition probability is sensitive to sub-leading effects and

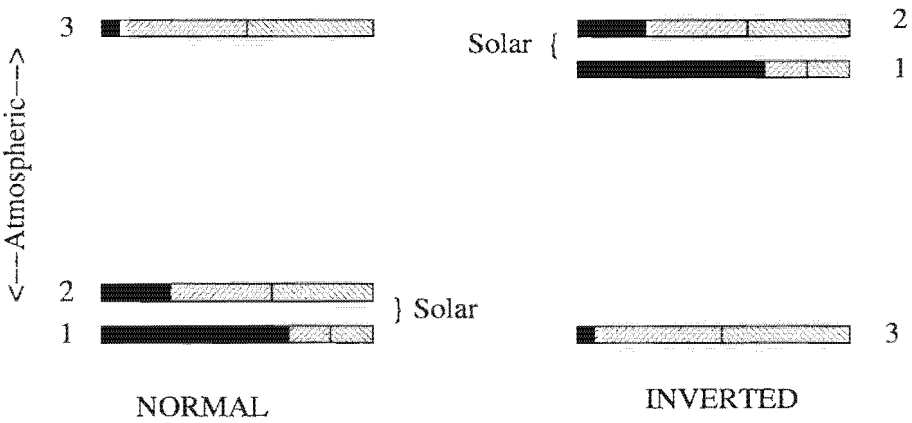

Figure 1.1: The two allowed three-neutrino mass squared spectrums that account for the oscillations of solar and atmospheric neutrinos. The normal spectrum has $\Delta m^2_{32} > 0$ and the inverted has $\Delta m^2_{32} < 0$. The ν_e fraction of each mass eigenstate is indicated by the solid region whereas the ν_μ (ν_τ) fraction is indicated by the right-leaning (left-leaning) hatching. The ν_e fraction in the mass eigenstate labeled, 3, has been enhanced for clarity.

in particular to the CP violating phase δ. In vacuum the shift in the transition probability associated with the CP violating phase is given by

$$\Delta P_\delta(\nu_\mu \to \nu_e) \approx \frac{1}{2} \cos\delta \; J_r \; \Delta_\odot \; \sin 2\Delta_{atm} \pm \sin\delta \; J_r \; \Delta_\odot \; \sin^2 \Delta_{atm} \qquad (1.8)$$

where the plus (minus) sign is for neutrinos (anti-neutrinos),
$J_r = \sin 2\theta_{12} \sin 2\theta_{23} \sin 2\theta_{13} \cos\theta_{13}$ and

$$\Delta_\odot \;\; = \;\; 1.27 \frac{\delta m^2_\odot L}{E} = \frac{\delta m^2_\odot}{\delta m^2_{atm}} \; \Delta_{atm} \approx \frac{1}{60} \; \Delta_{atm}. \qquad (1.9)$$

In the maximum of oscillations at the atmospheric Δm^2 scale the shift in the transition probability dependent on δ is of order

$$|\Delta P_\delta(\nu_\mu \to \nu_e)| \sim 0.5\% \sqrt{\frac{\sin^2 2\theta_{13}}{0.05}} \left(\frac{\delta m^2_\odot \sin 2\theta_{12}}{5 \times 10^{-5} eV^2} \right). \qquad (1.10)$$

This shift is smaller but of similar size to the shift associated with matter effects.

A useful and instructive way to present the combined effects of matter and sub-leading terms is in the bi-probability plots of $P(\nu_\mu \to \nu_e)$ versus $P(\bar{\nu}_\mu \to \bar{\nu}_e)$, invented by Minakata and Nunokawa [6]. Fig. 1.2 shows an example of such a plot for a NuMI case. At the larger values of $\sin^2 2\theta_{13}$ the ellipses associated

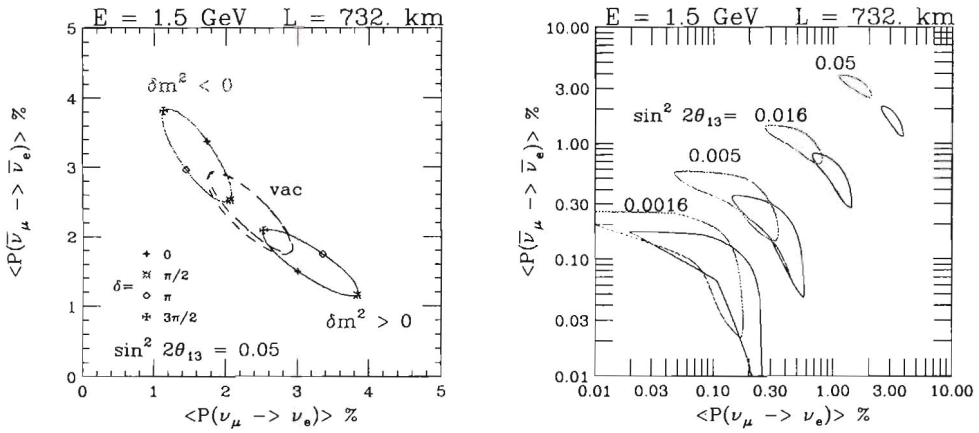

Figure 1.2: The bi-probability plots $P(\nu_\mu \rightarrow \nu_e)$ versus $P(\bar{\nu}_\mu \rightarrow \bar{\nu}_e)$ assuming a constant matter density of $\rho = 3.0 g cm^{-3}$ for an L/E of 500 km/GeV. The mixing parameters are fixed to be $|\Delta m^2_{31}| = 3 \times 10^{-3} eV^2$, $\sin^2 2\theta_{23} = 1.0$, $\Delta m^2_{21} = +5 \times 10^{-5} eV^2$, $\sin^2 2\theta_{12} = 0.8$ with the labeled values of $\sin^2 2\theta_{13}$ and δ.

with the two possible mass hierarchies separate in matter, whereas they are approximately degenerate in vacuum. There is also a significant sensitivity to the CP violating phase, δ. It is the sensitivity to the sign of Δm^2_{32} and the CP violating phase in these plots which allows for the determination of these parameters in a sufficiently accurate experiment. For a single experiment there can be a degeneracy in the determined parameters but this degeneracy can be broken by further experimentation.

A high precision measurement of $\nu_\mu \rightarrow \nu_\mu$ at the atmospheric Δm^2 can also be used to determine the difference from maximal mixing in θ_{23}. This difference is a measure of the breaking of a $\nu_\mu \leftrightarrow \nu_\tau$ symmetry at some high energy scale. Since matter effects are suppressed in the channel $\nu_\mu \rightarrow \nu_\mu$ compared to $\nu_\mu \rightarrow \nu_e$, a comparison of $\nu_\mu \rightarrow \nu_\mu$ to $\bar{\nu}_\mu \rightarrow \bar{\nu}_\mu$ is a sensitive test of CPT in the neutrino sector.

In summary the important measurements that could be made by the proposed experiment are

- Observation of $\nu_\mu \rightarrow \nu_e$ at an L/E of in the range of 10^2 to 10^3 km/GeV which would determine the ν_e role in atmospheric neutrino flavor transitions. In the neutrino oscillation scenario this is a measure of $\sin^2 2\theta_{13}$.
- Matter effects can be used to distinguish the two mass hierarchies and

therefore determine the sign of Δm^2_{32}.

- For the Large Mixing Angle solution to the solar neutrino puzzle there is sensitivity to the CP violating phase in the channel $\nu_\mu \rightarrow \nu_e$.
- Precision measurements in $\nu_\mu \rightarrow \nu_\mu$ channel can measure how close θ_{23} is to $\pi/4$, that is maximal mixing. A comparison of $\nu_\mu \rightarrow \nu_\mu$ to $\bar{\nu}_\mu \rightarrow \bar{\nu}_\mu$ is a sensitive test of CPT violation since matter effects are suppressed in this channel.

Thus, there is a very rich neutrino physics program to be explored in a ν_e appearance experiment using the NuMI beam. Details of experimental and beam possibilities will be explored in subsequent sections.

Chapter 2

The Role of the MINOS Experiment

The zenith angle distribution of atmospheric ν_μ interactions observed in the SuperKamiokande experiment gives a very strong indication of neutrino oscillations. A 50% deficit of upcoming neutrino flux suggests that the mixing angle is very large. A fit to the angular distribution yields the information on the corresponding mass difference Δm^2_{23} in the range $1.4 - 4.0 \times 10^{-3}\ eV^2$. This result is in a good agreement with the initial results of the subsequent accelerator-based long baseline oscillation experiment K2K[7]. Further results from SuperK indicate that the dominant oscillation mode is $\nu_\mu \rightarrow \nu_\tau$, although a significant admixture of the oscillations into a sterile neutrino is not excluded[8].

The Fermilab Main Injector neutrino beam (NuMI)[9] and the long baseline neutrino oscillations experiment MINOS[10] were proposed in early 90's to study the 'atmospheric neutrino anomaly' indicated by the results of the IMB[11] and Kamiokande[12] water Cherenkov experiments. An intense neutrino beam is produced from decays of pions and kaons produced by 120 GeV protons interacting with a carbon target. Two parabolic horns focus the produced mesons into a nearly parallel secondary beam of particles which decay inside a 675 meter long evacuated decay pipe.

The MINOS experiment consists of two functionally identical detectors; magnetized iron and solid scintillator calorimeters. The near detector is located at Fermilab 250 m downstream of the end of the decay pipe. The far detector is located in a Soudan mine at a distance of 735 km from Fermilab.

Charged current ν_μ interactions will be recognized in the MINOS detectors via the presence of a long penetrating muon track. Muon momenta will be measured from range with an accuracy of $\sim$ 6% for stopping tracks and from bending in the toroidal magnetic field with an accuracy of ~12%. The iron-scintillator sandwich provides a calorimetric measurement of the energy of the hadronic final state with the resolution $\Delta E/E \approx 60\%/\sqrt{E}$. The parent neutrino energy is calculated as a sum of the muon and hadronic final state energies. For

a neutrino energy around 5 GeV the typical resolution is of the order of $\sim 20\%$.

Charged current ν_μ interactions observed in the near MINOS detector will provide a basis for the prediction of the neutrino spectrum expected in the far detector. Owing to the finite size of the decay volume the neutrino spectra in these two detectors are not identical, but the difference is small and can be corrected for. The systematic error on the predicted neutrino spectrum in the far detector is expected to be smaller than $4 - 5\%$. An additional systematic cross check of the understanding of the neutrino beam will be provided by precise measurement of the pion and kaon production spectra in the experiment E907, which should enable reliable prediction of the neutrino spectrum in the near detector.

The ratio of the number of charged current ν_μ interactions observed in the far MINOS detector to the number expected from the spectrum observed at the near detector as a function of the neutrino energy will determine the ν_μ survival probability at a distance of $L = 735\ km$ as shown in Fig. 2.1.The functional shape of the observed depletion, if any, will be a direct test of the oscillation hypothesis as an underlying physics mechanism. The energy range available to MINOS is well suited to distinguish the oscillation hypothesis from other ad-hoc models put forward to describe the SuperK atmospheric results.

If the observed survival probability will follow the expected $\sin^2 \Delta m^2 L/E$ behavior then the position of the minimum will yield the information on the Δm^2, whereas a deviation of the minimum from one will measure the mixing angle $\sin^2 2\theta_{23}$. Precise values of the parameters will be determined from a fit to the distribution, after unfolding experimental resolution. Fig. 2.2 shows the expected precision of such a determination.

The MINOS detector is designed for a ν_μ disappearance experiment and the detector design is optimized for the detection, identification and measurement of ν_μ charged current interactions. At the same time, it offers a considerable potential for a search for $\nu_\mu \rightarrow \nu_e$ oscillations. The longitudinal sampling of the MINOS calorimeter, 2.5 cm of iron, represents 1.5 X_0 whereas the transverse granularity of the readout 4 cm, is of the order of the Moliere radius. Electrons produced in ν_e charged current interactions produce a characteristic energy deposition with small spatial extent and high energy density. This pattern is quite different from the pattern produced by charged hadrons, but indistinguishable from the energy deposition of a neutral pion.

Several studies have demonstrated that MINOS detector can identify ν_e charged current interactions[13] with efficiency of the order of 25% while providing a rejection against neutral current background by a factor of 65. This will allow the MINOS experiment to detect $\nu_\mu \rightarrow \nu_e$ oscillations, if they occur at the level of few per cent, or set a limit on $|U_{e3}|^2$ of the order of 0.01. This would represent a factor of 3 improvement over the current limit from the CHOOZ experiment. Table 2.1 shows a composition of the expected background sample in the MINOS detector for an exposure corresponding to 8×10^{20} POT in the low energy beam.

Relatively high background levels, exceeding the unavoidable intrinsic ν_e

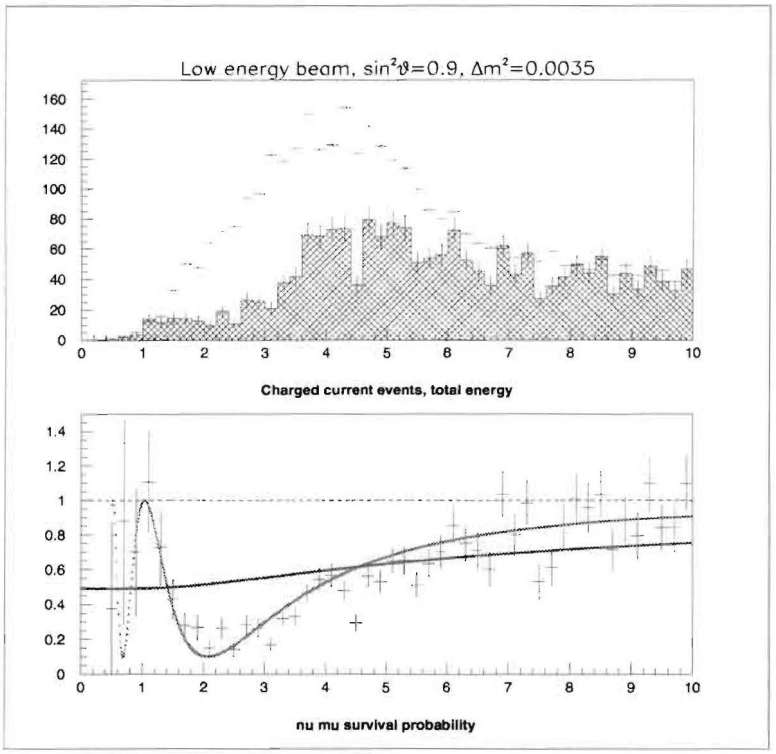

Figure 2.1: Top: expected spectrum of ν_μ charged current events in the far MINOS detector for 8×10^{20} protons and the observed spectrum in case of oscillations with $\Delta m^2_{32} = 0.0035\ eV^2$ and $\sin^2 2\theta_{23} = 0.9$, shaded histogram. Bottom: ratio of the observed and the expected energy distributions, i.e. ν_μ survival probability, as a function of the neutrino energy. Magenta curve is the shape expected for the neutrino oscillations, red curve is the expectation of the neutrino decay model consistent with the SuperK data.

component of the beam are partly related to the relatively poor granularity of the MINOS detector. A significant factor is due to the mismatch between the neutrino spectrum of the NuMI beam and the oscillation probability: a significant fraction of neutrinos present in the beam do not contribute to the signal, whereas it produces background events. Improvement of the $\nu_\mu \rightarrow \nu_e$ oscillations limit with the exposure time will be very slow and it will be limited by the systematic uncertainties in the background estimate.

To attain higher sensitivity to the $\nu_\mu \rightarrow \nu_e$ oscillations the following steps, with respect to the MINOS experiment, are desirable:

- reduce the NC background contribution by a better match of the neutrino

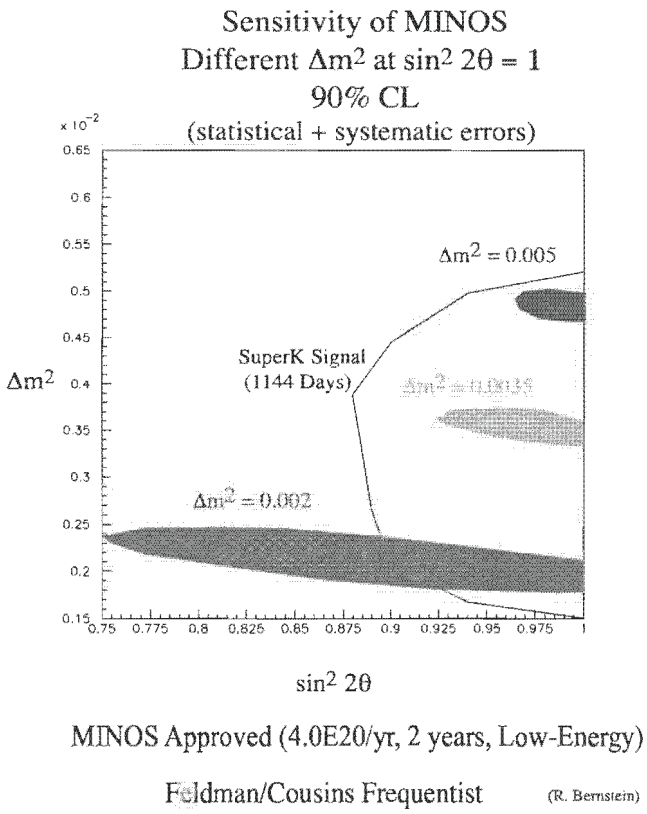

Figure 2.2: Expected precision of the determination of the oscillations parameters, Δm^2_{32} and $\sin^2 2\theta_{23}$ with low energy beam for different values of Δm^2_{32}. Horizontal axis is $\sin^2 2\theta_{23}$, vertical axis is Δm^2_{32} in eV^2.

beam spectrum to the oscillation probability curve

- reduce/eliminate the background due to $\nu_\mu \rightarrow \nu_\tau$ oscillations by reducing the neutrino flux above the τ production threshold
- improve efficiency for the signal detection and reduce the background from NC interaction by an optimization of the detector for the ν_e detection and identification
- improve statistics by an increase of the numbers of protons on the neutrino target and/or an increase of the detector size (preferably both)

signal	beam ν_e	ν_μ CC	$\nu_\mu \rightarrow \nu_\tau$	NC< 10 GeV	NC > 10 GeV
8.5	5.6	3.9	3.0	15.7	11.5

Table 2.1: Number of the expected signal ν_e events, with $|U_{e3}|^2 = 0.01$, and contributions to the background samples for 8×10^{20} POT exposure of the MINOS detector in the low energy beam.

Chapter 3

Possible Evolution of Neutrino Physics

While the preceding chapters gave the motivation for the proposed neutrino oscillation experiment solely from the physics point of view, it may be useful to put this endeavor into the broader context of the research programme of the USA, and even of the world-wide programme.

In the USA, a strong tradition of successful experimentation with accelerator neutrinos exists at Fermilab, which has culminated with the high-precision results from CCFRR and NuTeV on the nucleon structure functions and on the electroweak mixing angle. With the enthusiasm for the prospects offered by the newly discovered neutrino oscillations, MINOS and MiniBooNE will take over and guarantee interesting research and important results in the next five to ten years. Yet, the development in neutrino physics has proven fast, many new initiatives are being discussed also in Europe and Japan. It is important for the USA, and in particular for Fermilab, to plan the future in accelerator neutrino physics beyond MINOS and MiniBooNE now.

With a view to complying with scarce resources the concurrent use of the NuMI beam for a second 'off-axis' detector appears as optimal choice, combining an effective use of existing facilities with both a significant and far-reaching extension of the physics agenda and a relatively modest expenditure. While this program is expected to face some healthy competition from overseas activities, it is fair to say that by and large it fits very well into a largely complementary world-wide effort to advance our understanding of the physics of neutrino oscillations.

The first outstanding issue is pinning down the oscillation parameters of solar neutrinos. The recent spectacular results from SNO[14] (located in the Sudbury mine, Canada) have finally confirmed that the solar neutrino deficit is not of astrophysical origin, but due to the oscillation of electron-neutrinos into other active neutrino flavors. Remaining ambiguities between different domains of oscillation parameters are expected to be resolved within a few months by the KamLAND[15] reactor neutrino experiment (located in the Kamioka mine, Japan), and subsequently confirmed by the BOREXINO[16] experiment (located in the Gran Sasso Laboratory, Italy). From then on, the challenge will be to measure the relevant mixing parameters Δm^2_{12} and $\sin^2 2\theta_{12}$ as precisely as possible, a program to which accelerator neutrinos are not expected to contribute in the foreseeable future.

The main drive to measure the oscillation parameters of atmospheric neutrinos, Δm^2_{23} and $\sin^2 2\theta_{23}$, is expected to come from MINOS. MiniBooNE is expected to rule out the evidence from LSND, or else a new and equally complicated and interesting situation will have to be faced, which is not anticipated here. The second outstanding issue will be to confirm a non-zero value of the third mixing parameter in a scheme with three and only three active neutrino flavors, $\sin^2 2\theta_{13}$, or else reduce its current upper bound of ~ 0.1 to as low a value as possible. In this area, parallel to the ideas put forward in this LoI, several initiatives are currently under discussion also in Europe and Japan, albeit with grossly varying chances of realization.

Table 3 attempts to summarize these initiatives and compare their physics objectives. The table also gives order-of-magnitude prices and an estimate of the earliest time of realization. It should be understood that this assessment constitutes at best an educated guess and can in no way be taken as an commitment of the proponents themselves. The entry 'F2S' of the table refers to the experiment proposed in this letter. The other entries in the table are now discussed in turn:

- An Expression of Interest was recently put forth to look for $\nu_\mu \to \nu_e$ oscillations using the CERN neutrino beam aimed at Gran Sasso Laboratory[18], currently under construction, with an off-axis Cherenkov detector located deep underwater in the Gulf of Taranto, 1200 km from CERN[17]. The off-axis angle of about 2 deg is such that the corresponding neutrino energy of 0.8 GeV would place the second second oscillation maximum at this location. The detector would be movable and would take data at several baselines. This initiative, is listed in the tables as 'C2GT'. The CNGS beam would have to be tuned to a much lower energy than currently being planned for the Gran Sasso program. This would imply either a change in the current plans or a delay till 2011 or later when the OPERA experiment is scheduled to be finished.

- In Japan, a 50 GeV proton accelerator with very high intensity, the Japanese Hadron Facility (JHF)[19], has been approved and is under construction. This facility is due to be completed around 2007 and has a first-stage design beam power of 0.77 MW. There are now rather detailed plans to construct a neutrino beam[19], most likely an off-axis beam at 2 deg with an energy centered around 0.7 GeV, aimed at the Super-K detector 295 km away. Even though the neutrino program at the JHF is not officially approved as yet it is anticipated that the formal approval will be obtained within a year. This proposed experiment is listed as 'JHF2K ' in the table. A more detailed comparison of this program with the proposed NuMI program is given elsewhere in this document. The JHF program envisions also a second phase some time later. The accelerator itself would have its intensity upgraded to 4.0 MW. In addition, plans are being formulated to construct a new water Cherenkov detector in the megaton range, Hyper-K, near the Super-K detector so that the same neutrino beam could be exploited by both detectors. The program based on such a detector with a higher intensity accelerator should be able to address the issues of CP violation if θ_{13} is not too low. This second phase of the Japanese program is termed 'JHF2K II' in the table.

- There has been a discussion at CERN about building a superconducting proton linac re-using the LEP RF cavities. It would deliver a very high flux of protons of 2.2 GeV kinetic energy[20]. Such an accelerator could produce an intense wide-band neutrino beam with an average neutrino energy of 300 MeV. In parallel, the idea was put forth to construct a large water Cherenkov detector of Super-K type in the Fréjus tunnel, utilizing the opportunity of doing that relatively cheaply while other construction was proceeding in that tunnel. The energy of the proposed beam and the CERN Fréjus distance would be a good match to search for the $\nu_\mu \rightarrow \nu_e$ oscillations at the first maximum of oscillations. Both of these efforts are still in the design and discussion stage, they require a considerable financial expenditure and face therefore major hurdles arising from the very tight financial situation at CERN which is imposed by the priority which is given to the LHC program. They are termed 'C2F' in the table.

- The novel idea of a 'Beta-Beam' was recently put forth to create pure ν_e and $\bar{\nu}_e$ beams from decays of radioactive nuclei, ^{18}Ne and ^{6}He[21]. The nuclei would have to be accelerated to a γ around 75 and would give well-collimated wide-band neutrinos in the 300 MeV range. The plan would be to aim this beam at the water Cherenkov detector in the Fréjus tunnel, discussed above. This initiative is indicated as 'C2F+BB' in the table.

  Both a new detector and a new storage ring-accelerator with long straight sections would have to be constructed to make such a program a reality. While interesting in its own right, the realization of such a project appears unrealistic because of the very high expenditure associated with it.

- The ultimate challenge in the physics of neutrino mixing is to determine

the existence and size of leptonic CP-violation. It is universally agreed that the 'neutrino factory[22] based on novel muon storage rings with long straight sections gives the best access to this potentially very important phenomenon. It goes almost without saying that any other aspect of the oscillation $\nu_\mu \rightarrow \nu_e$ which would be left open from earlier experiments, would be easily and decisively addressed by the neutrino factory.

Over the last several years there have been intensive studies of the physics potential of a high energy muon storage ring with energy up to 50 GeV with long straight sections.

The beam of the neutrino factory, for stored μ^+ would consist of ν_e's and $\bar{\nu}_\mu$'s with a well-defined energy spectrum. The $\nu_\mu \rightarrow \nu_e$ oscillations would give a clean and experimentally well accessible signature of "wrong sign" muons.

The technical studies of such a machine identified a number of difficult challenges associated with obtaining the desired high intensity of the stored muon beams. The projected cost appears to be in the range of two billion dollars. Therefore, it is unlikely that there will be a significant movement towards construction of a neutrino factory unless and until θ_{13} is shown to be large enough to allow detailed studies of CP violation. Neutrino factories are entered as 'νF' in the table.

The current best limits on $\nu_\mu \rightarrow \nu_e$ oscillations in the atmospheric Δm^2 range come from reactor experiments, CHOOZ[2] and Palo Verde[23]. They study a related process, i.e. disappearance of ν_e's by measuring flux and energy spectrum of ν_e's some distance away from the reactor and comparing it with the predicted one. Statistical and systematic errors contribute roughly equally in both of these experiments; thus improving the sensitivity will require advances on both of those fronts. Searching for a small effect in a disappearance experiment requires very good control of systematics.

Recently there has been a proposal for a new experiment to search for nue disappearance with a sensitivity roughly a factor of 8 better than the CHOOZ limit. This experiment[24], based on the Krasnoyarsk reactor, would utilize two identical detectors, 50 tons each, at two different locations. The detection method would be similar to the one used by the KamLAND and BOREXINO experiments.

It is not clear whether this proposal will be realized. The proponents plan on performing first a pilot experiment, with smaller detectors at shorter distances, to investigate the LSND effect. There is also a possibility that the Krasnoyarsk reactor will be decommissioned sometimes in the near future.

		F2S	C2GT	JHF2K	JHF2K-II	C2F	C2F+BB	νF
$< E_\nu >$ [GeV]		2	0.8	1	1	0.3	0.3	10
Fiducial mass	Water Cherenkov		1 Mt	22.5 kt	1 Mt	40 kt	1Mt	
	Iron/scintillator	20 kt						40 kt
	Plastic/RPCs	20 kt						
Physics reach	$\sigma(\Delta m^2_{23})$ [eV^2]	1×10^{-1}	3×10^{-5}	1×10^{-4}		1×10^{-4}		
	$\sigma(\sin^2 2\theta_{23})$	0.01	0.01	0.01		0.01		
	$\sin^2 \theta_{13}$ [90% CL]	1.5×10^{-3}		1.5×10^{-3}	2.5×10^{-4}	1.5×10^{-3}		2.5×10^{-5}
	θ_{13} [deg; 90% CL]	2.2		2.2	0.9	2.2		0.3
	sgn Δm^2_{23}	?	No	No	?	No	No	Yes
	CP-violation	No	No	No	?	No	?	Yes
Incremental material cost (facility + detector [10^9 US \$])		0.1	0.1	0.2	1.0	0.7	2.0	2.0
Year of earliest operation		2006	2008		2015		2020	

Chapter 4

Off-Axis NuMI Neutrino Beam

Construction of the NuMI neutrino beam is currently underway at Fermilab. This beam directs 120 GeV protons from the Main Injector towards a 96 cm long graphite target. The secondary pions and kaons produced on this target are captured and focused by two parabolic magnetic horns pulsed at 200 kA. They decay in an evacuated region 675 m in length and 2 m in diameter to yield a very pure beam of muon neutrinos.

The unique feature of the NuMI neutrino beam is its flexibility. The neutrino energy spectrum can be selected as 'low', 'medium' or 'high energy' by adjusting the relative positions of the focusing horns and the target[9]. The neutrino beam energy can be also changed in a continuous fashion by moving the target with respect to the first horn[25]. The expected neutrino spectra at the MINOS far detector site are shown in Figure 4.1 for the NuMI low, medium, and high energy beam tunes.

The NuMI beam line is designed for a proton intensity of 4×10^{13} protons per pulse every 1.9 sec. - roughly 0.4 MW. At the design intensity, NuMI should collect 3.7×10^{20} protons per year, which will produce 470 neutrino interactions, in the absence of oscillations, per year per kt of detector mass at the far MINOS detector location in the low-energy beam configuration.

Excavation of the NuMI beam line is complete. Commissioning of the beam is expected to begin in the first months of 2005.

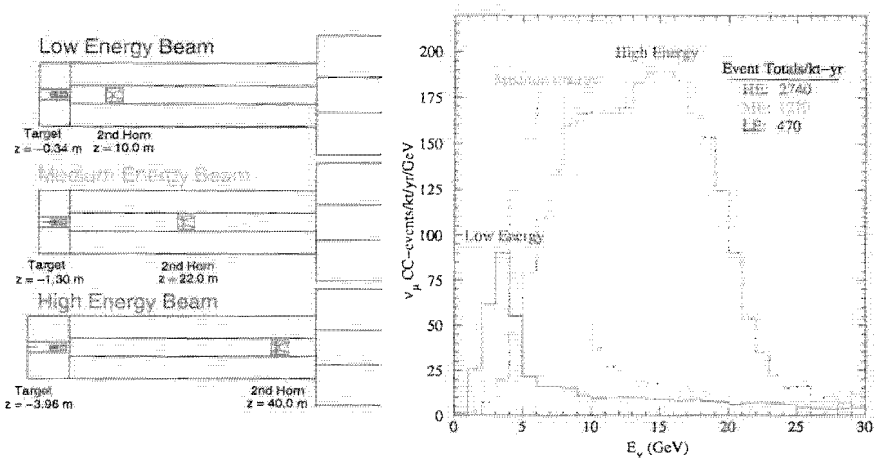

Figure 4.1: Left: The locations of the target and second horn for the NuMI low, medium, and high energy wide-band configurations. Right: Expected neutrino spectra at the MINOS far detector site in each of the NuMI beam tunes.

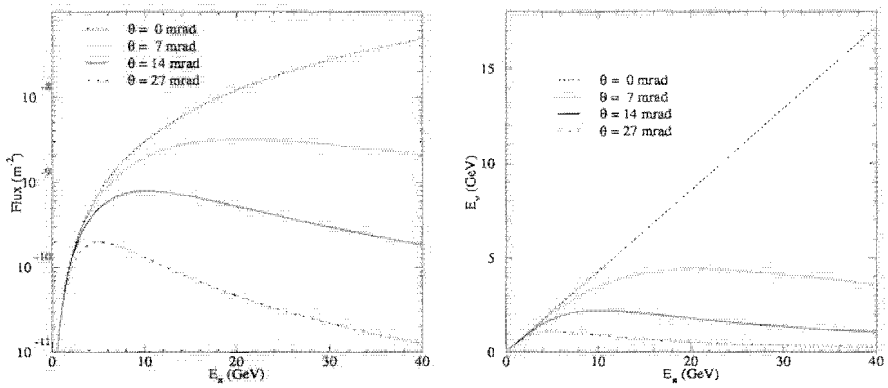

Figure 4.2: Left: The neutrino flux from a pion of energy E_π as viewed from a site located at an angle θ from the beam axis. The flux has been normalized to a distance of z=735 km. Right: The energy of the neutrino produced at angle θ relative to the pion beam direction as a function of the pion energy.

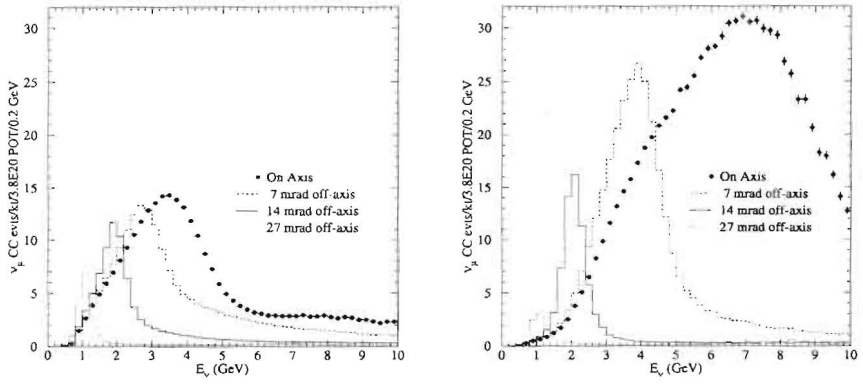

Figure 4.3: CC muon neutrino events rates expected under 'no oscillation' hypothesis at a distance of 735 km from Fermilab and at various transverse locations for the NuMI low-energy beam configuration (left) and medium-energy beam configuration(right).

4.1 NuMI Off-Axis Neutrino Fluxes

Due to the isotropic decays of the focused pions and kaons, the neutrino beam produced at NuMI will have broad angular distribution. For small angles, the flux and energy of a neutrino produced from the two body decay of a pion in flight are given in the lab frame by:

$$\mathcal{F} = (\frac{2\gamma}{1+\gamma^2\theta^2})^2 \frac{A}{4\pi z^2}, \; E_\nu = \frac{0.43E_\pi}{1+\gamma^2\theta^2}, \tag{4.1}$$

where θ is the angle between the pion direction and the neutrino direction, E_π is the energy of the parent pion, and m_π is the mass of the pion and $\gamma = E_\pi/m_\pi$. A and z are the detector cross-sectional area and distance from decay point. As can be seen in the Figure 4.2, the neutrino flux peaks in the forward direction for all values of E_π; this is why the MINOS detectors are placed on axis. As the angle to the beam direction increases, however, the relationship between the pion energy and neutrino energy flattens, with all pions yielding neutrinos of roughly the same energy.

It is possible to construct a nearly mono-energetic neutrino beam by viewing the NuMI beam at a location off the beam axis. This is an implementation of a concept developed for the proposed experiment E-889 at Brookhaven[26]. Because all pions contribute neutrinos of roughly the same energy, it is possible to compensate the reduction in the flux factor. Figure 4.3 shows the neutrino

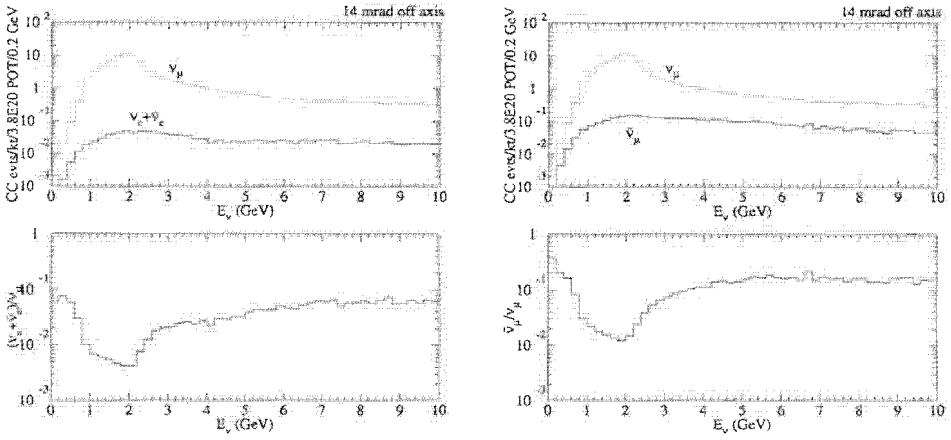

Figure 4.4: The expected energy distribution of the electron neutrino (left) and wrong-sign muon neutrino (right) components of the NuMI off-axis beams, low energy beam.

spectra of the NuMI neutrino beam at locations 5, 10, and 20 km (corresponding to the decay angles of 7, 14, and 21 mrad) off the NuMI beam axis at a distance of 735 km from the target[27]. As can be seen in Fig. 4.3, it is possible to increase the neutrino yield in the 1-2 GeV region by placing the detector off the beam axis, while at the same time reducing the high-energy component of the neutrino beam.

The off-axis beam intensity is higher, the beam energy spread is smaller and the high energy tail is smaller for the medium energy beam tune than for the low energy one. The intensity of the off-axis beam produced in the high energy beam configuration is reduced significantly in comparison with that of the medium energy setting due to the kinematical reduction of the flux.

The low energy peak of the off-axis beam spectrum is produced almost exclusively by decays of pions; hence the prediction of the neutrino flux is quite insensitive to the experimental uncertainties of the ratio of K/π production cross sections. At the typical distance of 10 km from the nominal beam axis the resulting spectrum of the neutrino beam is much narrower than the expected maximum of the oscillation probability. The total number of events in the peak region can be predicted on the basis of the near MINOS detector with an accuracy better than 2%[28].

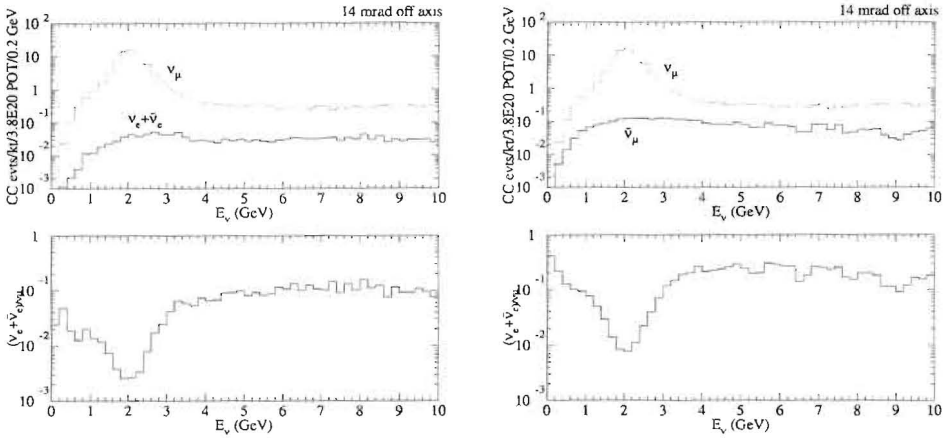

Figure 4.5: The expected energy distribution of the electron neutrino (left) and wrong-sign muon neutrino (right) components of the NuMI off-axis beams, medium energy beam.

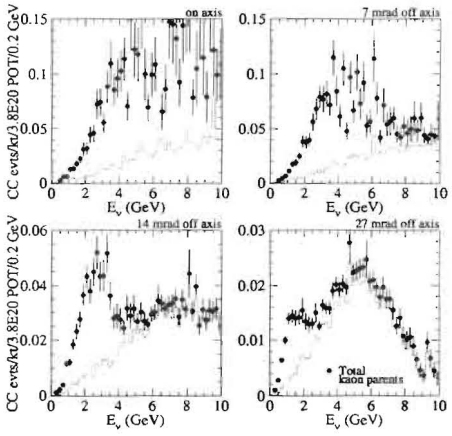

Figure 4.6: Spectra of the electron neutrino component of the beam at different off-axis angles. Points represent the total background and a histogram shows the component due to K_{e3} decays.

4.2 Backgrounds

The neutrino event rates and energy distribution depend on the detector location,its distance from Fermilab, and the distance from the nominal beam axis, but their qualitative features are very similar. As an example, we show the expected composition of the off-axis NuMI neutrino fluxes in Figure 4.4 and 4.5 at a distance of $L = 735\ km$. The $\bar{\nu}_\mu$ component of the beam is due to the decays of high energy π^- traversing the opening of the magnetic horn and not being de-focused by the horn system. This 'wrong' sign beam component contributes roughly 1% of events at the peak of the neutrino flux. More importantly, the component of electron neutrinos is kept to roughly 0.5% in the peak of the neutrino flux. The ν_e component of the beam is due to K_{e3} decays and to the decays of tertiary muons. The ν_e's from the K decays have much higher energies than the main peak of the ν_μ's, whereas the neutrinos from the μ decays populate the low energy part of the spectrum. Fig. 4.6 shows that $\sim 80\%$ of the ν_e background at the peak of the ν_μ flux distribution is due to muon decays. This component of the background should be well constrained by measurements of the muon fluxes and muon neutrino spectra at the Fermilab site. The systematic error of the extrapolation to the off-axis detector is of the order of $5 - 6\%$.

It is worth noting that that the relative contribution of backgrounds is somewhat smaller for the medium energy beam setting than for the low energy one.

4.3 Antineutrino Beams

An antineutrino beam, in addition the neutrino beam, is an important tool for the investigation of the neutrino mass hierarchy and in the search for CP violation in the neutrino sector.

The direction of the current through the NuMI focusing horns can be reversed to produce an anti-neutrino beam rather than a neutrino beam. The expected anti-neutrino event rates are shown in Figures 4.7 and 4.8. The events rates in anti-neutrino mode are $\sim 30\%$ of those expected when running in neutrino mode. Most of the rate reduction is due to the lower anti-neutrino cross-sections, as shown in Fig. 4.11, and the rest is related to the lower production of π^- relative to π^+ in proton-nucleus interactions.

The compositions of the anti-neutrino beams are shown in Figures 4.9 and 4.10. Note that while the wrong-sign muon contamination is worse in anti-neutrino mode, the electron neutrino rates are still roughly $0.3 - 0.5\%$ at the peak of the

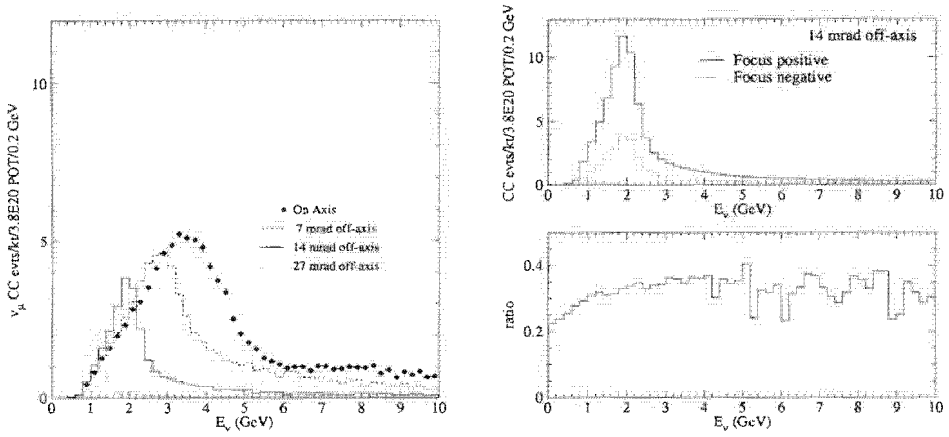

Figure 4.7: Left: The muon anti-neutrino event rates expected at the distance $L = 735\ km$ from Fermilab in the NuMI low energy beam with reversed horn currents at various transverse locations. Right: Comparison of the anti-neutrino event rates to those obtained when running in anti-neutrino mode.

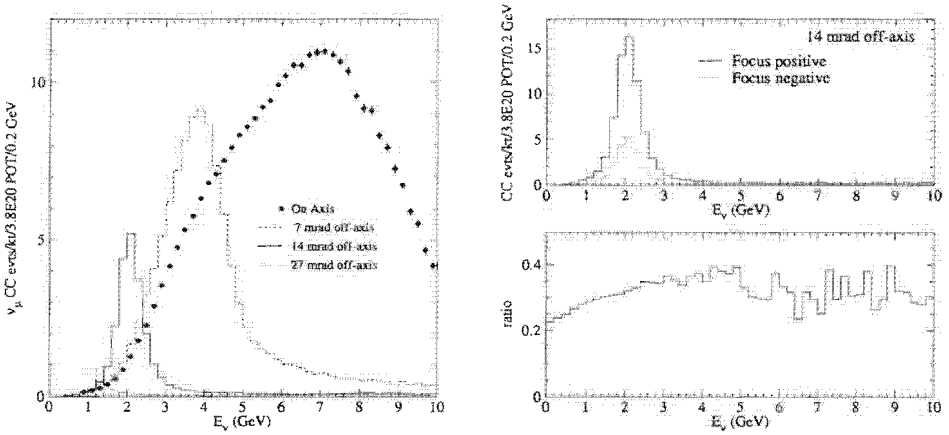

Figure 4.8: Left: The muon anti-neutrino event rates expected at the distance $L = 735\ km$ from Fermilab in the NuMI medium energy beam with reversed horn currents at various transverse locations. Right: Comparison of the anti-neutrino event rates to those obtained when running in anti-neutrino mode.

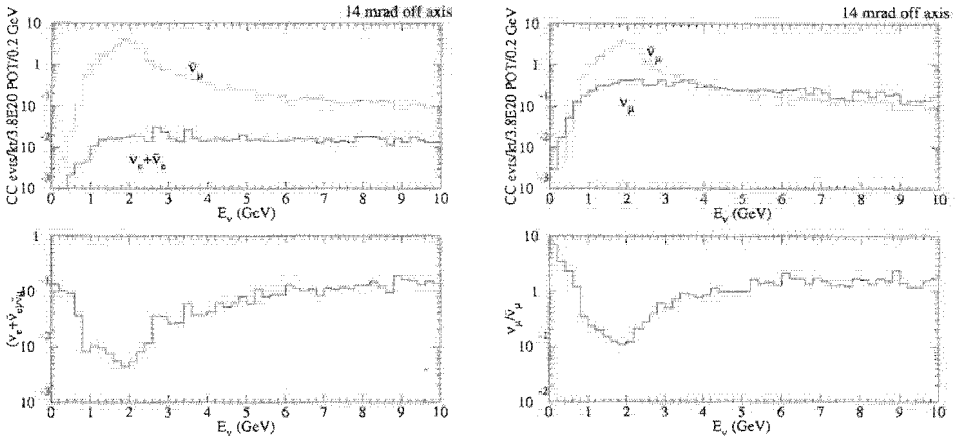

Figure 4.9: Composition of the off-axis antineutrino beam, low energy beam configuration. Left shows the electron neutrino component. Right shows the wrong-sign muon component.

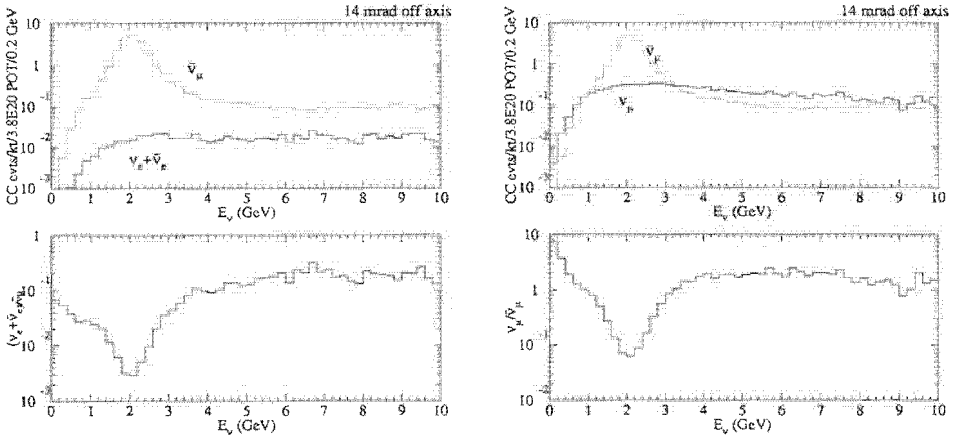

Figure 4.10: Composition of the off-axis antineutrino beam, medium energy beam configuration. Left shows the electron neutrino component. Right shows the wrong-sign muon component.

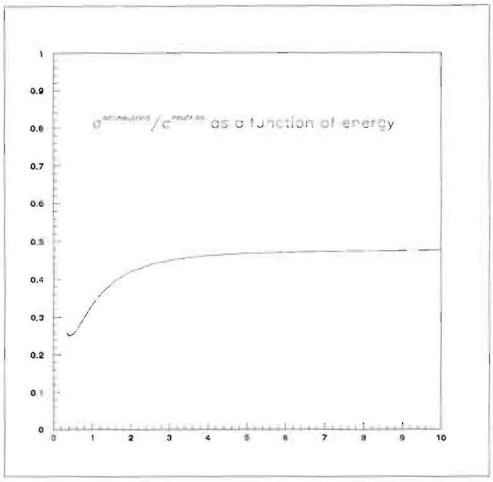

Figure 4.11: Ratio of antineutrino and neutrino CC cross sections as a function the the neutrino energy

neutrino spectrum.

4.4 Proton Economics

In its initial phase of operation NuMI will have to accomodate the $\bar{p}$ production cycle. Six consecutive batches of 8 GeV protons from the Booster will be injected into the Main Injector to be accelerated to 120 GeV, with a cycle time of 1.9 s. One batch will be extracted for $\bar{p}$ production, and the remaining five will be extracted onto the NuMI target in about $8\mu s$.

At present, with the Booster running routinely at 4.5×10^{12} protons/batch, the maximum intensity one can expect is limited to 2.3×10^{13} protons/cycle.This would provide about 2×10^{20} protons/year, assuming 5000 hours/year of operation.

There is no obvious path to increase the total proton flux, but several ideas are being actively investigated. Both the feasibility of Booster upgrades to increase the number of protons/batch and the possible gain provided by proton stacking techniques in the Main Injector (slip-stacking and RF barrier stacking), to increase the number of protons per Main injector cycle, are being currently evaluated. Another path would be an upgrade of the power supplies and the RF system of the Main Injector to allow shorter operation cycles down to 1 s.

A proton intensity working group has been jointly appointed by the Fermilab Directorate and the MINOS experiment to produce a roadmap to help maximize the integrated number of protons to be delivered onto the NuMI target.

Chapter 5

$\nu_\mu \rightarrow \nu_e$ Oscillation Appearance Experiment

5.1 Statement of the challenge

The challenge for future experiments is to observe $\nu_\mu \rightarrow \nu_e$ oscillations in the atmospheric neutrino Δm^2 range down to the level of a few parts per mil. The CHOOZ experiment gives a limit on ν_e disappearance probability of about 0.1. This translates into a limit on the ν_e appearance probability of 0.05. MINOS is expected to improve this by a factor of 2-3, setting the aforementioned scale of few parts per mil. There are no clear theoretical guidelines as to the most likely value of this parameter.

Charged current ν_e interactions can be identified by the presence of an electron in the final state. The experimental backgrounds to the $\nu_\mu \rightarrow \nu_e$ oscillation signals arise from two general sources. There are genuine events with electrons resulting from the intrinsic ν_e component in the beam and from τ decays in the charged current ν_τ interactions from $\nu_\mu \rightarrow \nu_\tau$ oscillations. In addition there are potentially mis-identified NC events or high y ν_μ CC events where one or more π^0's in the final state masquerade as an electron.

The intrinsic ν_e's in the beam come from μ decays and K_{e3} decays (both charged and neutral). They are of the order of $0.5 - 1.0\%$ of ν_μ's, but can be reduced further by an appropriate energy cut. The τ decay contamination has a strong energy dependence; the easiest way to reduce it is to have a significant fraction of the ν_μ flux below the τ production threshold. K_{e3} contamination is typically

of the order of 1/5 of the μ decay contamination in the experiments being considered, as shown in Fig. 4.6.

The experimental challenge can be separated into two parts:

- reducing these two backgrounds as much as possible
- measuring them as accurately as possible so that the principal ultimate uncertainty comes from the statistical fluctuations in the event sample of interest

The background from ν_e's can only be reduced by good energy resolution since the ν_e's from background sources have a broader energy spectrum than the potential signal. The NC background, however, can be reduced by a well designed detector. The challenge is to suppress it to a level comparable or lower than the intrinsic ν_e level without significantly degrading the signal detection efficiency.

5.2 Possible experimental approaches

A traditional challenge in high energy physics experiments has been how to separate out the electromagnetic component in a hadronic jet from the remaining hadrons. In the calorimetric method this was generally achieved by having a high Z electromagnetic calorimeter in front of the hadron section of the calorimeter. Clearly that technique is not suitable for electron/π^0 separation. The latter has been traditionally done in open geometry experiments by using a water Cherenkov , a technique adopted by IMB, Kamiokande and SuperKamiokande. The other technology of choice has been the use of low Z calorimeters (eg CHARM II and BNL oscillation experiment) which allow identification of the electron by tracking.

In principle, at least, in a highly segmented detector electrons can be separated from π^0's by utilizing several experimental characteristics:

- finite separation between the vertex and conversion points of the γ's from the π^0,
- two electromagnetic showers (for π^0) vs one (for electrons),
- double pulse height right after conversion of a γ.

Success of the separation based on these criteria requires fine segmentation: longitudinally, less than a radiation length, X_0; transversely, finer than the

spatial separation of the two γ's from the π^0 decay. The transverse segmentation also has to be such that individual tracks in the final state can be separated from each other.

Besides the need to distinguish electrons from π^0's, one must also distinguish electrons from hadrons. This is harder in a low Z material and relies on the absence of hadronic interactions (for electrons) and a generally broader track from electrons due to accompanying bremsstrahlung.

The other important characteristic of a good ν_e detector is its energy resolution. The way to reduce the intrinsic ν_e background is to utilize the fact that the events from $\nu_\mu \rightarrow \nu_e$ oscillations will have a sharp energy spectrum at a predictable energy in contrast to the backgrounds. This is a key feature of the narrow neutrino beam energy spectrum seen by an off-axis detector. ν_e's from μ decays will be in roughly the same energy range as ν_μ's from π decay (and hence oscillated ν_e's) but have a much broader energy distribution. K_{e3} decay will typically give much higher energy neutrinos whereas the τ decay electrons will peak towards low energies. The shape and the level of backgrounds and possible signal are shown in Fig. 5.1.

5.3 Background measurements and estimates; systematics

The backgrounds discussed above can be both estimated and measured. We discuss each background in turn.

a) ν_e's from μ decay.

   The ν_μ flux at 0^o will be measured in the Near Detector located on axis. Muon flux over all angles can be estimated reliably from those measurements since only kinematics are involved. The ν_e rate and energy distribution from this source can be known with an accuracy of 5%[29]

b) ν_e's from K decay.

   This background is about a factor of 5 lower than the one from muon decays. It can be calculated with the basic limitation coming from uncertainties of π/K production cross section by 120 GeV protons. In principle this uncertainty will be reduced by the measurements of the E907 experiment. Most of this background occurs at high ν_e energies, therefore an extrapolation to the region of interest can be performed.

c) Electrons from τ decays.

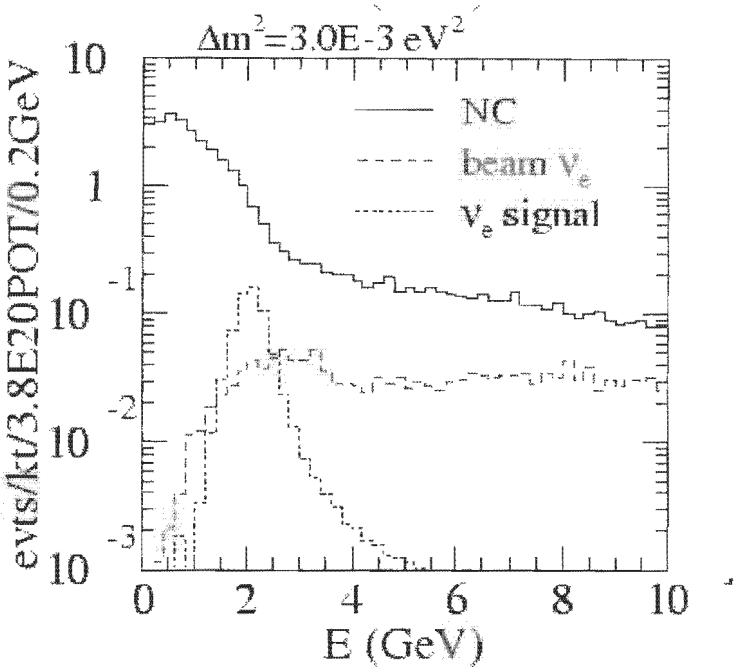

Figure 5.1: Energy distribution of the expected ν_e oscillation signal for $|U_{e3}|^2 = 0.01$ (black histogram), intrinsic beam ν_e events (red histogram), and observed energy distribution of the NC events before rejection (blue histogram)

This background is comparable to but somewhat smaller than the one from K decays in our energy range. The ν_τ rate can be reliably estimated from oscillation parameters and ν_μ flux. There is some uncertainty in the production cross section and angular distributions but, because of the low overall rate, these uncertainties will have a negligible contribution to the overall systematic uncertainty on the total background.

d) NC events misidentified as ν_e interactions.

An a priori estimate of this background is somewhat more difficult than for the cases discussed above and it will need to be measured. Initial Monte Carlo calculations indicate that its contribution can be reduced to a level of the intrinsic ν_e background or better while maintaining the efficiency for ν_e identification at about 30 – 40%. This source of background will probably give the dominant contribution to the systematic error.

A measurement of the NC background can be made using a near off-axis detector located at an angle similar to the one of the far detector. Such a detector is possible in the bypass tunnel downstream of the NuMI absorber

where the neutrino spectrum would be similar to that in the far detector.

e) ν_μ CC events mis-identified as ν_e interactions.

Such a misidentification would require a failure to detect the muon, residual hadronic energy in the range of the expected oscillation signal, and misidentification of a pion as an electron. We note that the rate of the ν_μ CC events is significantly reduced by the oscillations. Initial estimates indicate that this background is significantly lower than the NC background.

f) Hadrons misidentified as electrons.

There is now a significant amount of data on electron-muon (or pion) separation in water Cherenkov detectors with the conclusion that this background is insignificant for energies above few hundred MeV. A low Z detector would have to be exposed to hadrons and electrons in a test beam. Such an exposure will guide the design of the detector and allow one to develop an optimum algorithm for e/hadron separation.

In summary, the Monte Carlo studies to date indicate that for a detector in the tens of kton range the systematics associated with imperfect knowledge of the background levels can be kept sufficiently low so that the dominant uncertainty will be due to statistical fluctuations. More detailed studies with the detector of choice are needed, however, to confirm up this initial impression.

5.4 Physics Potential of the NuMI Off-axis Beam

At the present time there are a large number of unanswered questions in neutrino physics. Some of the most important ones that are relevant to the proposed program are:

- Is the LSND effect related to neutrino oscillations?
- Is the LMA solution to the solar neutrino problem the correct one?
- What is the value of θ_{13}?
- What is the sign of the mass hierarchy?
- Is CP conserved in the neutrino sector?
- Is CPT conserved in the neutrino sector?

It is highly likely that the first two questions will be answered by the time the experimental program described here will begin. The last 4 topics are the focus of the proposed program.

Our discussion below tacitly assumes that the answer to the first question is in the negative. If that assumption is incorrect, the neutrino community will have to rethink seriously the future program.

Regarding the second question, KamLAND should provide a definitive answer here should they see depletion of events. If they do not, and future NC data from SNO reinforce the support for the LMA solution, then very likely new and unexpected physics lurks in the neutrino sector. The argument for new experimental efforts becomes even stronger.

The experimental program being proposed here takes into account the need to maintain maximum flexibility as answers to the last four questions become slowly elucidated. We divide our program into two phases: the second phase will build on the results from Phase I as well as on the information provided by the potential JHF program. We can, however, start planning Phase I now.

At the present time two generic site possibilities appear to be front runners for the Phase I of the proposed experiment. The first one is at 712 km, near the current Soudan experiment. The second site possibility is in the region in Canada between the southern and northern branches of the Trans Canadian Highway, between 850 and 980 km. The near-Soudan site gives good sensitivity to ν_e appearance signal, on the assumption of $\Delta m^2_{32} = 3\times10^{-3}\ eV^2$. The further sites are better if Δm^2 is lower and offer larger matter and CP violation effects and thus a chance to obtain at least the first glance at these two phenomena.

The sensitivity of Phase I to observation of ν_e's is hard to quantify because the size of the expected signal depends not only on the value of θ_{13} but also on the pattern of mass hierarchy (through matter effects) and the value of the CP violation phase as shown in Fig. 5.2. At low values of $\sin^2 2\theta_{13}$ there is an additional potentially important contribution to the uncertainties in the interpretation of the experimental results due to the uncertainty of the value of Δm^2_{12}. We try to give a general estimate by making a rough comparison with the JHF[19] proposal (see below, Tables 5.1 and 5.2). In Table 5.2 we have assumed a 20 kt detector, 5 yr experiment, 85% fiducial volume, NC background equal to the beam ν_e background and 4×10^{20} protons delivered per year and no matter or CP effects. Because the matter effects are much more important at NuMI distances, NuMI sensitivity could increase by up to 30% at 712 km for normal mass hierarchy, or more at 900 km.

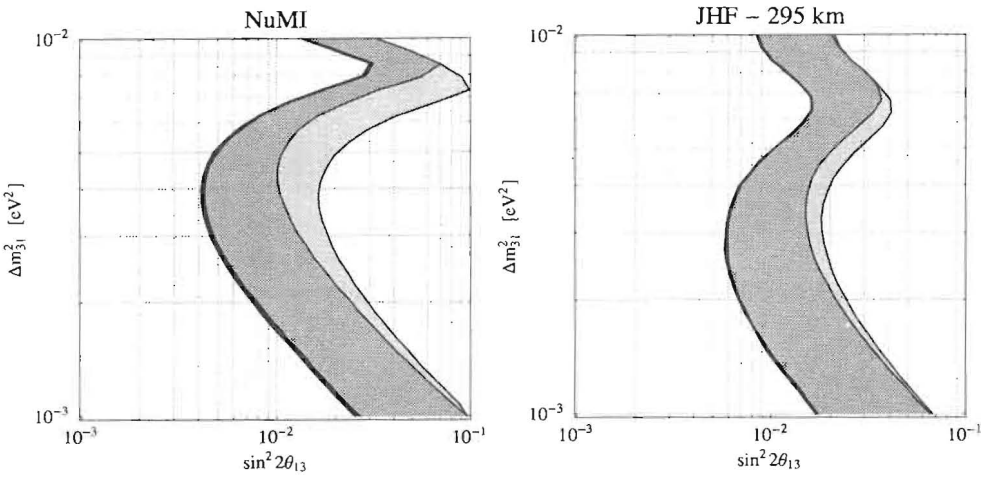

Figure 5.2: Interpretation of the observed $\nu_\mu \rightarrow \nu_e$ transition probability in terms of $\sin^2 2\theta_{13}$ for the NuMI(712 km), left, and the JHF (right). The left edge is the limit implied by the statistical errors. The right edge of the blue region corresponds to a 10% error on the background subtraction. The green band represents uncertainty due to the value of δ. The yellow band shows the impact of degeneracy between $\theta_{23} < \pi/4$ and $\theta_{23} > \pi/4$ solutions.

Fig. 5.3 shows the CP trajectory contours in the bi-probability space for ν_e and $\bar{\nu}_e$ appearance at 712 km and 950 km using optimized energies at those distances. We use the oscillation parameters of the solar neutrinos $\sin^2 2\theta_{12} = 0.8$, $\Delta m^2_{12} = 5 \times 10^{-5}\ eV^2$ and values of $\sin^2 2\theta_{13}$ corresponding to an oscillation probability equal to 1/2 and 1/5 of the current CHOOZ limit. It is clear that given sufficient statistics the proposed experimental program would be very well positioned to identify the sign of the matter effect and obtain some information on CP violation, especially when one combines information from neutrino and antineutrino running. For comparison we show also the same contour plots, for identical oscillation parameters, for the proposed JHF program with $L = 295\ km$ and $E_\nu = 0.8\ GeV$.

Studies of energy dependence of the disappearance of ν_μ CC events can provide information about equivalence of Δm^2_{32} for ν_μ and $\bar{\nu}_\mu$ oscillations and thus validity of CPT in the neutrino sector. This comparative measurement will probably be dominated by systematic effects; no quantitative estimates of how well one can do have been performed to date but 1% accuracy does appear possible.

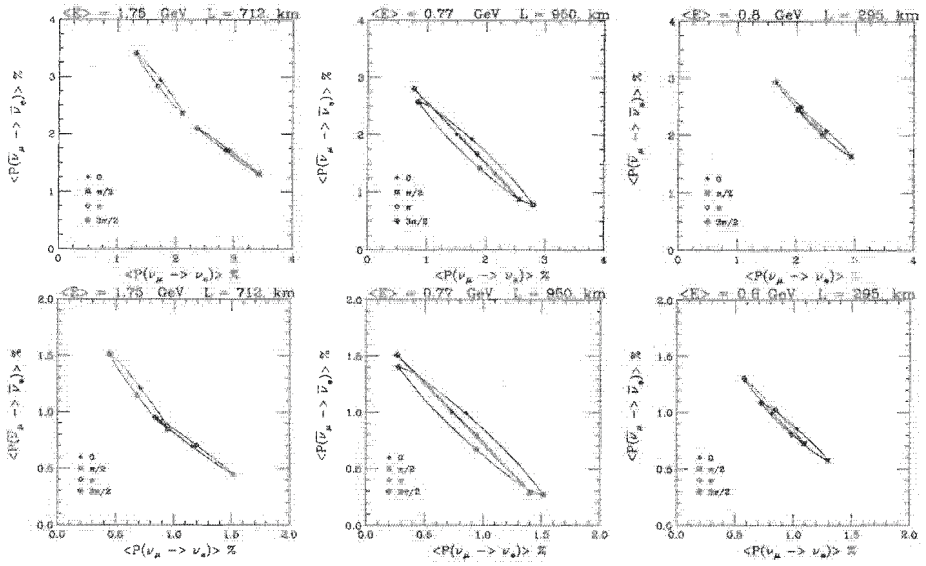

Figure 5.3: CP trajectory contours in the bi-probability space for ν_e and $\bar{\nu}_e$ appearance at 295 km, 712 km and 950 km. Top row is for $\sin^2 2\theta_{13} = 0.05$, bottom row is for $\sin^2 2\theta_{13} = 0.02$. Symbols denote the expected values of probabilities for specific values of the CP phase.

5.5 Comparison with JHF Phase I

The phase I of the contemplated JHF program would utilize the proposed neutrino beam from the JHF accelerator, currently under construction, and the SuperKamiokande detector, to be reconstructed after the end of the K2K experiment. The source to the detector distance would be 295 km and the mean energy for the currently favored 2^o off-axis beam is 0.8 GeV, thus the L/E ratio would be quite comparable to the value in the proposed NuMI program.

Similarly to the NuMI program it plans to achieve better than a factor of 10 improvement in $\sin^2 2\theta_{13}$ over the CHOOZ limit at a value of $\Delta m^2_{32} = 3 \times 10^{-3}$, somewhat better at lower values and somewhat worse at higher values. The matter effects are much smaller than in NuMI case and it probably will not be possible to obtain any significant information on CP violation in this Phase. The most recent proposal does not indicate any plans to run in the $\bar{\nu}_\mu$ mode.

The sensitivity of the proposed JHF PhaseI to matter effects and CP violation is quantified in Fig. 5.3. The relative sensitivity of the two proposed programs to the ν_e appearance signal are compared in Tables 5.1 and 5.2. We use the same

	ν_μ CC	NC	Beam ν_e	Signal ν_e
all	10714	4080	292	302
after cuts	1.8	9.3	11	123

Table 5.1: Anticipated number of signal and background events in JHF OAB 2 deg beam

	ν_μ CC	NC	Beam ν_e	Signal ν_e
all	12104	5696	295.4	293
after cuts		10.2	10.2	85.5

Table 5.2: Anticipated number of signal and background events in the detector located 9 *km* off-axis at a distance of 712 *km* from Fermilab

parameters ($\Delta m^2_{32} = 3 \times 10^{-3}$ and $\sin^2 2\theta_{13} = 0.1$, i.e. at the CHOOZ limit, and a 5 yr exposure for both proposed programs). We assume 4×10^{20} POT/yr for NuMI and a 20 kt detector with 85% fiducial volume. We use numbers from Table 2 of the JHF proposal.

Chapter 6

Future Evolution of the Off-Axis Neutrino Program

In addition to searching for unexpected phenomena, such as CPT violation, the off-axis program strives to measure $\sin^2(2\theta_{13})$, the order of the mass hierarchy, and the CP-violating phase δ. It is rather unlikely that the Phase I program described in this proposal will be able to complete these objectives. In almost all scenarios there will be a strong argument to enhance the program by increasing the flux times detector mass and possibly by moving detectors or building additional detectors to obtain different values of L and E.

There are three reasons for expecting the need to eventually expand the program:

a) The effects, particularly those due to CP violation, are quite likely be small, requiring greatly increased statistics. A reasonable expectation is that one would like to eventually increase the proton flux by a factor of four, as envisioned in the Proton Driver study, and to increase the detector mass by a factor of five.

b) Since the parameters scale differently with L and E, different detector locations will be advantageous to measure them.

c) Different detector locations might be necessary to resolve ambiguities that can occur with a single detector location.

We will give a few examples to illustrate these points. The first goal of the Phase

I program is to detect a positive signal for $\nu_\mu \rightarrow \nu_e$ oscillations. Such a signal should be seen if $\sin^2(2\theta_{13})$ is greater than 0.01. If Phase I is successful in this, then we can proceed to try to determine the parameters. If no significant signal is seen, then increased flux times detector mass will be necessary to continue the search for a non-zero value of $\sin^2(2\theta_{13})$. Systematic errors need to be considered carefully to determine what additional subsidiary experiments are needed to control them.

Detection of a signal for $\nu_\mu \rightarrow \nu_e$ appearance will not in itself provide a measurement of $\sin^2(2\theta_{13})$ since relatively large matter effects introduce a two-fold ambiguity in the measurement of $\sin^2(2\theta_{13})$, in the absence of CP-violating effects. In the presence of CP-violating effects, there will be additional ambiguities caused by the value of δ, unless the value of $\sin^2(2\theta_{13})$ is relatively large, greater than about 0.02.

To understand how we proceed to resolve ambiguities and measure the parameters, it is useful to review how these effects scale with distance, energy, and the small parameters. Since both effects are maximal at the peaks of the $\Delta m^2_{13} \approx \Delta m^2_{23}$ oscillation, we assume that measurements will be done at odd-integer values of the oscillation phase. The practical values of $n\pi/2$ are the first peak, $n = 1$, and the second peak, $n = 3$. This implies the a scaling in E is equivalent to a scaling in L/n. In the NuMI region, the matter effects scale as $\theta^2_{13}E$ or $\theta^2_{13}L/n$. CP violating effects scale as $\theta_{13}\Delta m^2_{12}n$.

Consider the case of relatively large values of θ_{13} first. The matter effects, which scale as θ^2_{13} dominate the CP-violating effects, which scale as θ_{13}. In this regime, the mass hierarchy can be determined without ambiguity by the combination of neutrino and antineutrino runs. (See Fig. 1.2) For NuMI baselines, the matter effects are large. The double ratio

$$\left[\frac{\sigma(\nu_\mu \rightarrow \nu_e)}{\sigma(\bar{\nu}_\mu \rightarrow \bar{\nu}_e)}\right]_{\text{normal}} \Bigg/ \left[\frac{\sigma(\nu_\mu \rightarrow \nu_e)}{\sigma(\bar{\nu}_\mu \rightarrow \bar{\nu}_e)}\right]_{\text{inverted}}$$

is 1.7 for $L = 712$ km, 1.8 for $L = 850$ km, and 2.0 for $L = 985$ km. Thus, once electron appearance has been seen, the value of θ_{13} and the mass hierarchy can be determined simultaneously. However, the necessary antineutrino running requires increased integrated flux times detector mass, since fewer antineutrinos are produced and their cross section is lower.

If $\sin^2(2\theta_{13}) < 0.02$, then there can be ambiguities caused by the CP-violating phase δ. To resolve these ambiguities, and to make a measurement of δ regardless of the value of $\sin^2(2\theta_{13})$, it may be desirable to make measurements at the second oscillation maximum, $n = 3$. The scaling laws indicate that at the second maximum the matter effects decrease by a factor of three and the CP-violating effects increase by a factor of three. (There is however, a decrease in both the flux (see Fig. 4.3 and the cross section, due to the reduced neutrino

energy.) Since, in the off-axis beam, each detector location represents a single L and a single E, this would require an additional far detector site. Water Cherenkov detectors might be more appropriate for the low energies (about 500 MeV) of the second maximum. They have the great advantage that the cost of detectors scales as the area of the detector rather than as the mass.

Finally, it should be noted that there is a high degree of complementarity between a JHF program at 295 km, and NuMI off-axis detectors at 712 km (first maximum) and 985 km (second maximum) as shown in the following table.

Detector	L (km)	E (GeV)	Relative matter effect	Relative CP effect
JHF	295	0.6	1.0	1.0
NuMI Phase I	712	1.4	2.9	1.0
NuMI Phase II	985	0.7	1.1	3.0

Measurements at both a 300 km and a 700 to 1000 km baseline will further aid in resolving ambiguities and checking consistency with the theory.

In summary, we expect that the investigation of the neutrino mass hierarchy and the parameters of the MNS matrix will be an extended and fruitful program. Arguably it is as or more important than the efforts now underway to measure the parameters and check the consistency of the CKM matrix, and should receive, with time, at least a similar level of support. We expect that it will be a major component of the Fermilab program in the LHC era.

Chapter 7

Detector

An off-axis NuMI neutrino beam offers an unique opportunity to study $\nu_\mu \rightarrow \nu_e$ oscillations. There will be a very large number of ν_μ's oscillating away. Most of the resulting ν_τ's will be below the kinematical threshold for τ production hence a small admixture of ν_e's should be detectable with as small background as possible.

To take full advantage of this opportunity it is necessary to construct a new detector capable of the detection and identification of the ν_e charged current interactions. Such a detector must meet several challenges:

- it must have fine granularity in order to identify the final state electrons
- it must have very large mass to provide maximal sensitivity to the oscillation amplitude
- it must have an acceptable cost per unit mass
- it must be able to operate on surface or under a small overburden, as there are no convenient underground locations

The detector should be optimized for the neutrino energy range of $1 - 3\ GeV$.

The ultimate sensitivity of the experiment, at the 90% $C.L.$ will be determined by the condition $S \geq 1.26\sqrt{B}$, where $S = \epsilon \times \#\ of\ signal\ events$ and $B = \epsilon \times \#\ of\ \nu_e + \eta \times NC$ with ϵ being the efficiency for the detection and identification of the ν_e interactions and η being the mis-identification probability for NC interactions. The sensitivity of the experiment improves with the square root

of the exposure time until it becomes limited by the the systematic error of the background. The latter is likely to be dominated by the error on the NC component of the background.

There appear to be three classes of a possible new detector:

- water Cherenkov. It is likely to offer the biggest advantage in terms of the mass of the detector but in the energy regime of interest at NuMI it appears to be dominated by the NC background, i.e. $\eta \times NC \gg \epsilon \times \nu_e$. The efficiency for the signal events is likely to be around 25%.
- fine grained calorimeter. This class of detectors is characterized by the signal detection efficiency of the order of $35 - 40\%$ while maintaining a balance between the intrinsic background and the NC-induced one, i.e. $\eta \times NC \sim \epsilon \times \nu_e$
- Liquid Argon TPC. This is probably the most challenging, but the most powerful detector, offering the highest signal efficiency $\epsilon \sim 90\%$ and background level at the intrinsic ν_e component, $\eta \times NC \ll \epsilon \times \nu_e$

The NuMI neutrino beam will start operations in the early 2005. It is highly desirable that the Phase I of the proposed program is implemented as early as it is practically possible to yield the initial information on the ν_e appearance and to provide guidance for the future phases of the program. Such an accelerated time scale leaves no time for the extensive detector R&D program, but fortunately none is necessary. Forty years of experience in constructing neutrino detectors combined with the impressive progress in the detector technology in the past decade offers several possible implementations for a detector of the 20 kton class.

Phase II of the program may require much large detector, perhaps in the range of 100-200 ktons. It may well be that the the future detector may be required to operate at the energies below 1 GeV, if the second oscillation maximum will offer the best sensitivity. It is not clear, at the present time, if the detector technology for the Phase II will be necessarily the same as the Phase I detector.

Studies of neutrino oscillations, especially in Phase II may require optimization of the detector location. Given the cost of the initial investment it may be advantageous to have a detector design allowing the relocation of the detector from one location to another, or, perhaps, reconfiguration of the detector into two or more smaller detectors located in different positions.

In Appendix A we describe several alternatives for a possible new detector to demonstrate that there are realistic conservative designs of affordable detectors as well as there are possible new alternatives.

Chapter 8

Detector Sites, Physics Considerations

Progress in neutrino physics worldwide will be optimized if the future NuMI program is comparable in quality and as complementary as possible to the planned JHF program. The interpretation of any observation of ν_e's due to oscillations will be difficult because of simultaneous contributions of θ_{13}, matter effects, and CP phase, δ. Several measurements with different conditions will be necessary to unravel the situation.

For a given baseline distance, L, different contributions to the $\nu_\mu \rightarrow \nu_e$ oscillation probability are principally a function of L/E. In our region of parameter space a contribution of matter effects grows with the distance L. The baseline in the JHF program is constrained to be relatively short, i.e. 295 km. Thus the natural choice for NuMI would be to have as long a baseline as is consistent with the energies of Main Injector beams and availability of satisfactory sites.

It is convenient to discuss optimization of the detector position in terms of the oscillation phase $\phi = 1.27L\Delta m^2_{32}/E$. Generally, unless there are strong cancellations from different contributions, the maximum ν_e appearance signal will be obtained when $\phi = \pi/2$. Due to $1/L^2$ dependence of the signal S and the background B, the optimum sensitivity, taken as a ratio of $S/\sqrt{B}$, will correspond to a distance L about 25% shorter. For $\Delta m^2_{32} = 0.3\ eV^2$, this translates to an optimum transverse distance away from the beam axis of about 9 km (independent of L). This distance scales inversely with Δm^2_{32}.

The maximum matter effects occur at a larger value of the phase which trans-

Distance	0.07 - matter	0.07 CPV	0.1 - matter	0.1 CPV
295 km	0.56	2.87	1.14	4.08
712 km	2.45	4.92	4.97	6.99
848 km	3.01	5.08	6.07	7.21
985 km	4.50	5.76	9.12	8.18

Table 8.1: Potential contributions, in parts per thousands, to oscillation probability from matter effects and CP violation

lates into an equivalent transverse distance of $13 - 15$ km. In addition, as mentioned above, they grow with L. CP violation effects also generally increase with increasing ϕ. The NuMI neutrino beam comes to the surface at the distance $L = 747$ km from Fermilab. A transverse displacement from the beam axis can be achieved either by going further or closer, along the nominal beam direction, effectively taking the off-axis beam in the vertical plane or by going sideways at a baseline corresponding to the nominal 0^o distance, or a combination of both.

An important issue is the change in sensitivity as we move away from the optimum distance. This defines how precisely we need to know Δm^2_{32} before choosing the site. This change is relatively small if we try to optimize the size of the total appearance signal, and a transverse displacement from the optimum (at a fixed L) can be as large as ± 2 km.The sensitivity is greater (by roughly a factor of 2) if one tries to maximize a contribution of the matter effects. These comments should be viewed as qualitative statements since due to the coherent nature of all contributions, a more rigorous statement can be made only in the context of specifying values of all the relevant parameters.

Another issue which needs to be considered is the variation of total ν_μ flux as a function of distance L and mean beam energy, controlled by the distance from the beam axis. The flux will fall off with L as $1/L^2$. For 120 GeV proton energy and off-axis angles corresponding to neutrino energy range 1 - 2 GeV, the flux times cross section drops a little faster than E^2. Thus we gain slightly in event rate, for the same phase ϕ, as we go to larger distances, but that effect is sufficiently small so as not to be very important.

To give an idea of the relative magnitude of potential contributions due to matter effects and CP violation in different sites, we present those contributions, in parts per thousand addition to the ν_e appearance probability, in Table 8.1. We show them for two values of θ_{13}, 0.07 and 0.1, corresponding roughly to a factor of 5 and 2.5 below the current CHOOZ limit, and for $\Delta m^2_{32} = 2.5 \times 10^{-3}$ eV^2, the currently best fit to the K2K and SuperKamiokande data.

Chapter 9

Cost and Schedule, Milestones

9.1 Cost

Given the status of the project it is not possible to have a credible cost estimate. It appears, though, that the main cost driver will be the construction of the active detectors. There are several possible detector designs using mature and well understood technologies, thus making a cost of the active detectors reasonably well predictable. These costs are in the range of $\$15 - 20M$ for a 20 kton class detector. Engineering issues associated with construction of a very large and massive detector are very challenging. Costs associated with the construction of the absorber, support structures, experimental halls etc. cannot be very well known before the engineering studies are completed. We aim at the design of the Phase I of the experiment for a cost not exceeding $\$50 - 100M$.

The second phase of the program may involve upgrades to the accelerator complex of Fermilab. These upgrades are subject of a dedicated studies [30]. It is likely that the Phase II detectors will require a significant increase in the fiducial mass (a factor of 5 or so) and, perhaps, in the detector capabilities. It is not possible to give a reliable cost estimate of these detectors, but it appears likely that this phase will require investment of the order of $\$250 - 300M$.

9.2 Schedule

NuMI beam line will start delivering neutrinos, on- and off-axis, at the beginning of the calendar year 2005. While it is not possible to complete a construction of a significant fraction of a large detector in such a short time frame, it is important to point out that a timely construction of a new detector would maximize the scientific output of the NuMI facility. It is important to note that a modular detector design may enable a start of the data taking long before the coentruction is completed.

Proposed Phase I detectors utilize off-the-shelf technology, not requiring time-consuming R&D process. Detailed engineering studies are necessary, though, before the final approval of the experiment. Modular design of the experiment may enable parallel construction at several locations, it may simplify the final assembly as well.

It appears, therefore, that the schedule of a possible experiment will be driven by the approval process and by the availability of the construction funds. We hope for an approval process to proceed efficiently enough to provide construction funds starting in FY2005. We also hope that the construction of the detector may start earlier through forward-funding from universities and/or from foreign sources.

9.3 Milestones

2002 Summer submission of a Letter of Intent

2002 Fall/winter detector design work, measurement of the cosmic ray background

2003 Spring experimental verification of the level of cosmic ray-induced background

2003 Summer Proposal to the Fermilab PAC , NSF

2003-2004 construction of prototypes,

2003 Fall Far site selection

2004 Summer electron and hadron test beam studies of the detector prototypes

2004 Reviews, validation,

2004 Summer final approval

2004 Fall start construction of the far detector building and facility

2005 Construction and installation of the Near Off-Axis detector

2005 Summer Far detector building complete

2005 Fall Near off-axis detector starts taking data

2005-2006-2007 construction of the Far Off-axis detector

2006 Summer start taking data with the initial 5 kton detector

2007-2012 Phase I of the program

We envisage that the Phase II of the program will require an increased useful mass of the neutrino detector by a factor of five or so. It can be achieved through construction of more detector modules of the same design as in the Phase I or by a construction of a diferent detector with much higher detection efficiency (like Liquid Argon TPC) or much larger mass (like water Cherenkov). To be in a position to select the most apropriate strategy for the Phase II it is imperative that adequate funding for the required R&D process is available as early as possible.

Acknowledgments

Many people have contributed to the ideas and concepts presenetd here. Their contributions are gratefully acknowledged.

Special thanks go to Friederich Dydak for his contribution to the chapter on the evolution of neutrino physics.

Achim Geisser, Tommaso Tabarelli de Fatis and Carlo Gustavino were the source of inspiration for the LoDen detector concept.

Dan Marlow was a source of advice on the RPC chambers and has contributed a section on the gas and HV systems.

Marc Mengel made it possible to overcome all annoying problems with forcing Postscript files into a Latex document.

Bibliography

[1] Kamiokande Collaboration, Y. Fukuda *et al.*, Phys. Lett. B**335** (1994) 237; Super-Kamiokande Collaboration, Y. Fukuda *et al.*, Phys. Rev. Lett. **81** (1998) 1562; S. Fukuda *et al.*, *ibid.* **85** (2000) 3999.

[2] CHOOZ collaboration, M. Apollonio *et al.*, Phys. Lett. B **466** 415.

[3] SNO Collaboration, Q. R. Ahmad *et al.*, Phys. Rev. Lett. **87** (2001) 071301.

[4] LSND Collaboration, C. Athanassopoulos *at al.*, Phys. Rev. C **55**, (1997) 2079

[5] E. Church *et al.* [BooNe Collaboration], Booster: BooNE," FERMILAB-P-0898.

[6] H. Minakata and H. Nunokawa, JHEP **0110** (2001) 001 [hep-ph/0108085].

[7] K2K Collaboration, S. H. Ahn *et al.*, Phys. Lett. B **511** (2001) 178

[8] S. Fukuda *et al.* [Super-Kamiokande Collaboration], Phys. Rev. Lett. **85**, 3999 (2000) [arXiv:hep-ex/0009001].

[9] The NuMI Facility, Technical Design Report, Version 1.0, October 1998

[10] The MINOS Detectors, Technical Design Report, NuMI-L-337, October 1998

[11] IMB Collaboration, R. Becker-Szendy *et al* Phys. Rev. Lett. 66 (1991) 2561

[12] Y. Fukuda *et al*, Phys. Lett. B **335** (1994) 237

[13] M. Diwan, M. Messier, B. Viren, L. Wai, A study of $\nu_\mu \rightarrow \nu_e$ sensitivity in MINOS, NuMI-NOTE-SIM-0714
D. Petyt, Nu-mu to Nu-e in MINOS, NuMI-NOTE-SIM-0576
A. Para, Electron ID and transverse granularity, NuMI-NOTE-SIM-0284

[14] Q. R. Ahmad *et al.* [SNO Collaboration], arXiv:nucl-ex/0204008.

[15] L. De Braeckeleer [KamLAND Collaboration], Nucl. Phys. Proc. Suppl. **87**, 312 (2000).

[16] S. Bonetti *et al.* [Borexino Collaboration]. Nucl. Phys. Proc. Suppl. **28A**, 486 (1992).

[17] Expression of Interest in an experiment at the CNGS to measure θ_{13}, http://home.cern.ch/dydak/oscexp.ps

[18] K. Elsener *et al*, The CERN Neutrino beam to Gran Sasso, CERN 98-02, INFN/AE-98/05

[19] Y. Itow *et al*, The JHF-Kamioka Project, hep-ex/0106019

[20] J.J. Gomez Cadenaz *et al* Physics Potential of Very Intense Conventional Neutrino Beams, hep-ph/0105297
M. Vretenar, A high-intensity H^- Linac at CERN based on LEP-2 ccavities, CERN/PS 2000-059 (NUFACT Note 040)

[21] P. Zucchelli, CERN-EP/2001-056, hep-ex/0107221

[22] there is a huge number of papers on neutrino factories covering the machine and experimental aspects as well as the physics potential. A dedicated series of conferences NuFactXX is covering the progress of the project. Proceedings of these conferences and the references cited therein give a good indication of the amount of effort devoted.

[23] F. Boehm *et al.*, Phys. Rev. D **64**, 112001 (2001) [arXiv:hep-ex/0107009].

[24] Y. Kozlov, L. Mikaelyan and V. Sinev, hep-ph/0109277

[25] M. Kostin *et al* Proposal for Continuously-Variable Beam Energy, NuMI-NOTE-BEAM-0783

[26] D. Beavis *et al*, Proposal of BNL AGS E-889 (1995)

[27] A. Para, M. Szleper, Neutrino Oscillation Experiments using Off-axis NuMI Beam, hep-ex/0110032

[28] M. Szleper, A. Para, Neutrino Spectrum at the Far Detector, hep-ex/0110001

[29] M. Szleper, talk at the New Initiatives for the NuMI Neutrino Beam, May 2002,

[30] G. Barenboim *et al*, report in preparation

[31] the BELLE KLM detector group, Nuclear Instruments and Methods in Physics Research A 449 (2000) 112-124
see also Nuclear Instruments and Methods in Physics Research A 456 (2001) 109-112

[32] C. Gustavino et al. A glass resistive plate chambers for large experiments, Nuclear Instruments and Methods in Physics Research A 457 (2001) 558-563

[33] C. Hagner, presentation at the New Initiatives for the NuMI Neutrino Beam workshop.

[34] N. Y. Agafonova *et al.* [MONOLITH Collaboration], LNGS-P26-2000.

[35] Border et al, NIM A 463, 194-204 (2001)

[36] Particle Data Group

[37] W. N. Hess et al., (Phys. Rev 116,445(1959)

[38] D. H. Perkins, Soudan 2 Internal Note; PDK-445 (1990)

[39] K.Ruddick, 25th Int.C.R. Conf, Durban (1997)

[40] M. Messier, talk at the New Initiatives for the NuMI Neutrino Beam workshop, May 2002

[41] C. Mauger presentation at the NuInt2001 workshop, KEK, Dec. 2001 http://neutrino.kek.jp/nuint01/

[42] C. Rubbia, *The Liquid Argon Time Projection Chamber: a New Concept for Neutrino Detector*, CERN-EP/77-08 (1977).

[43] ICARUS home page: http://www.aquila.infn.it/icarus/

[44] The ICARUS Collaboration, *Cloning of T600 Modules to Reach the Design Sensitive Mass*, ICARUS-TM/01-09, http://pcnometh4.cern.ch/Proposals/t2400doc_lowres.pdf

[45] D.B. Cline, F. Sergiampietri, J.G. Learned, K.T. McDonald, *LANNDD, A Massive Liquid Argon Detector for Proton Decay, Supernova and Solar Neutrino Studies, and a Neutrino Factory Detector* (May 24, 2001), astro-ph/0105442

[46] F. Sergiampietri, *On the Possibility to Extrapolate Liquid Argon Technology to a Supermassive Detector for a Future Neutrino Factory*, presented at NuFACT'01 (May 26, 2001), http://www.hep.princeton.edu/mcdonald/nufact/sergiampietri_nufact01.pdf

[47] F. Cavanna, O. Palamara for the ICARUS Collaboration, *Possible Application of the ICARUS technology for Studies of Neutrino Interactions in the Intermediate Energy Range*, ICARUS-TM/02-02, http://www.aquila.infn.it/icarus/icarus_tm/icarus_02_02_NuInt01.pdf

[48] D. Harris, *Comparison of Different Detectors with Same Beam*, (Jan. 18, 2002), http://muonstoragerings.cern.ch/NuWorkshop02/presentations/harris.pdf

[49] A. Bueno *et al.*, *Nucleon decay searches: study of nuclear effects and background*, ICARUS-TM/01-04 (Oct. 9, 2001), http://www.aquila.infn.it/icarus/icarus_tm/icarus_01_04.pdf

[50] Among a vast literature, see, for example, J.C. Pati, *With Grand Unification Signals in, Can Proton Decay be Far Behind?* (June 7, 2001), hep-ph/0106082.

[51] See sec. 6.8 of [44].

[52] S. Ozaki *et al.*, eds., *Feasibility Study-II of a Muon-Based Neutrino Source* (June 14, 2001), http://www.cap.bnl.gov/mumu/studyii/FS2-report.html

[53] A. Bueno, M. Campanelli and A. Rubbia, *Neutrino factories: Detector concepts*, presented at the IX Intl. Workshop on Neutrino Telescopes (Venice, Mar. 6-10, 2001), http://pcicarus7.ethz.ch/Talks_pdfs/venice2001.pdf

[54] M.V. Diwan *et al.*, *Proposal to Measure the Efficiency of Electron Charge Sign Determination up to 10 GeV in a Magnetized Liquid Argon Detector (μLANNDD)*, submitted to BNL (April 12, 2002), http://www.hep.princeton.edu/mcdonald/nufact/bnl_loi/argonprop.pdf

[55] G. Mulholland, *ELAN Detector Vessel Prliminary Study*, (May 17, 2002), http://www.hep.princeton.edu/mcdonald/nufact/mulholland/ELAN_Proposal.pdf

Appendix A

Possible Detector Technologies

A.1 Low Z Tracking Calorimeter

Identification of the final state electron in a calorimetric detector requires that the sampling frequency is high, of the order of $1/4 - 1/3$ of the radiation length X_0. Neutrino detectors must serve as a target and as a detector at the same time, hence their mass must be maximized. These two requirements lead to a conclusion that the absorber should be made out of a low Z material to maximize the mass of the detector while maintaining good sampling frequency. Low Z absorber will lead to a minimal number of the active detector planes, for a given total mass of a detector, hence it will minimize the cost of the detector.

A required transverse granularity of the detector is related to the local particles density on one hand and to the Moliere radius on the other hand. Hadron and electron showers develop over large volumes in a low density detectors, hence the requirements on the transverse granularity of the detector will be relatively modest.

A direct consequence of the large spatial extend of events is a necessity of a fiducial cut of the order of 1 meter away from the edges of the detector. This, in turns requires that the transverse size of the detector is as large as it is practically possible. As an example, with the 1 *meter from edges* fiducial cut only 81% of a total mass of a 20×20 m^2 detector is in the fiducial volume, for the 12×12 m^2 detector it is only 69%.

A.1.1 Low energy neutrino interactions in low Z calorimeter

Neutrino interactions in the region of $1 - 3\ GeV$ involve very low multiplicity reactions: quasi-elastic scattering, resonance production, single pion production. Deep inelastic scattering sets on above 2 GeV although multiplicities of the hadronic final states are still very low. *nue* charged current events are recognizable by the presence of an electron in the final state. The electron, on the other hand, will be characterized by the presence of additional hits, due to the onset of the electromagnetic shower, along its trajectory.

In such a low multiplicity environment a low Z tracking calorimeter will provide a valuable information on the topological properties of the event. This potential is illustrated in Fig. A.1 showing several examples of low energy ν_e CC events are registered in a plastic calorimeter with $1/3\ X_0$ sampling and with the transverse granularity of 3 cm. Black circles denote the hit detector strips. Colored lines are indicating the initial directions of final state particles: red - electron, blue - proton, green - charged pion, yellow - neutron and cyan - gamma.

Typical NC events are not very spectacular - they have just few hits from low energy final state hadrons. More important are the *high y* events as they constitute potential background for the ν_e sample. Some example of such events are shown in Fig. A.2. Most of them do not represent a serious source of background, it is only the small fraction with relatively energetic π^0 which are problematic. To illustrate the qualitative difference between neutrino interactions at very low energies, in 2 GeV region and at higher energies we show examples of ν_e CC event and a typical NC event for neutrino energies of the order of 5 GeV in Fig. A.3.

A.1.2 Electron identification

Charged current ν_e interactions are identified by the presence of an electron among the final state particles. There are several characteristic features of these events which can be used to differentiate them from the NC and ν_μ CC events:

- they do contain a long track
- the track is accompanied by additional hits due to the onset of an electromagnetic shower
- track energy is a significant fraction of the total energy of the event

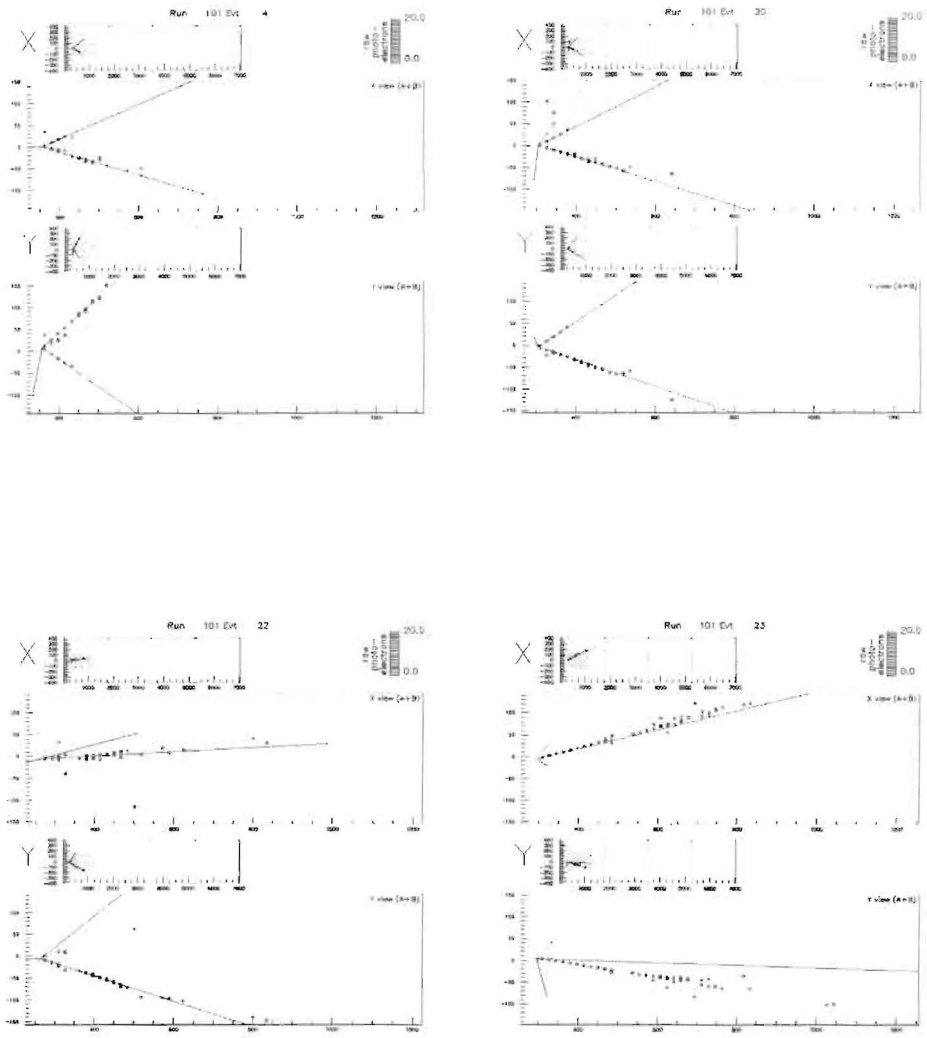

Figure A.1: Typical charged current ν_e interactions with energies $1-3\ GeV$ as detected in a fine grained calorimeter with the longitudinal sampling of $1/3\ X_0$ and the transverse sampling of $3\ cm$.

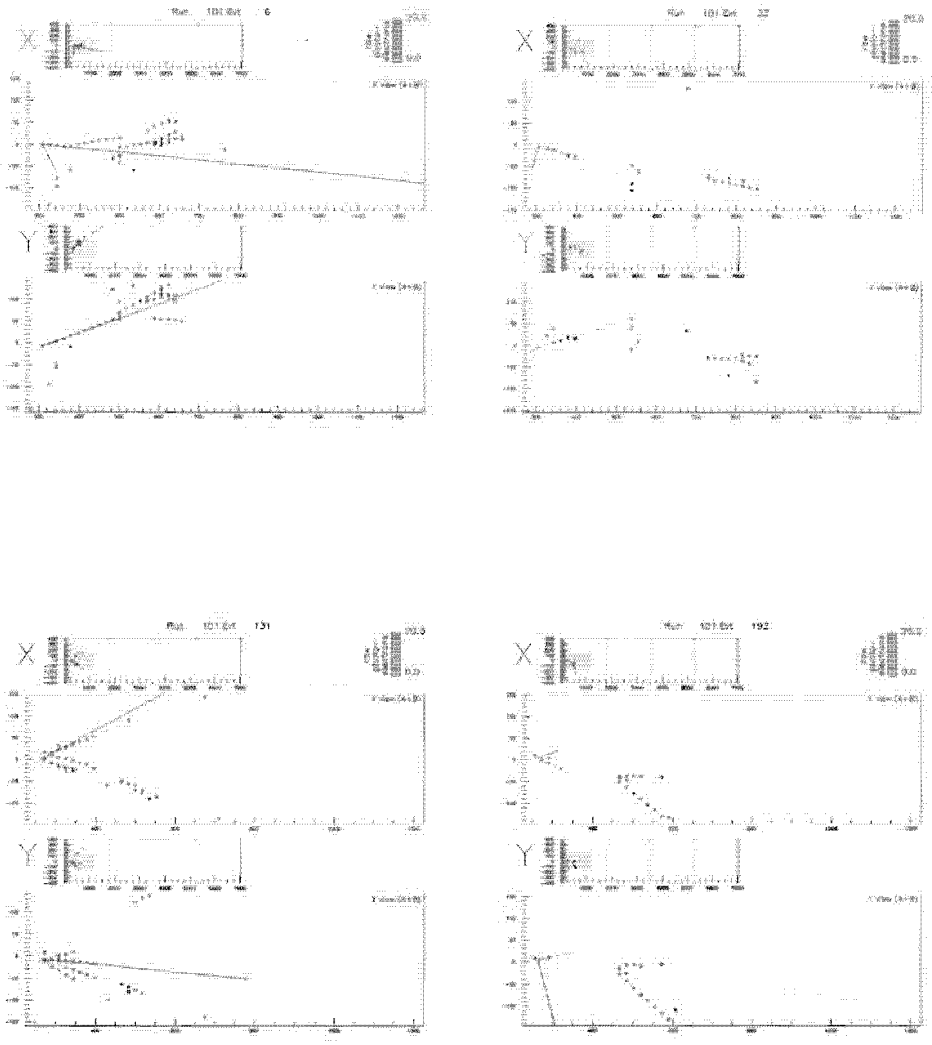

Figure A.2: Typical charged current ν_e interactions with energies $1-3\ GeV$ as detected in a fine grained calorimeter with the longitudinal sampling of $1/3\ X_0$ and the transverse sampling of $3\ cm$.

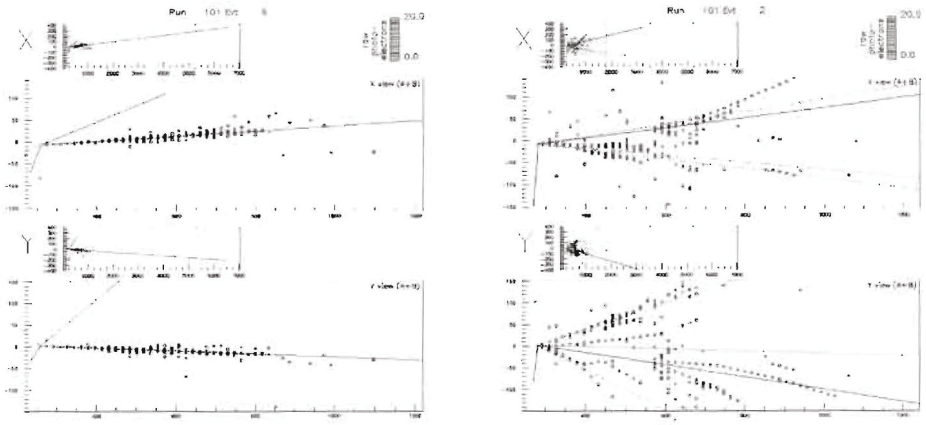

Figure A.3: Typical charged current and neutral current ν_e interactions with energies $\sim 5\ GeV$ as detected in a fine grained calorimeter with the longitudinal sampling of $1/3\ X_0$ and the transverse sampling of $3\ cm$.

- track direction is at a small or moderate angle to the neutrino beam direction
- the energy deposition at the very beginning of the track is consistent with a minimum ionizing particle

Several independent studies involving full GEANT simulation, realistic reconstruction and analysis of events in the fine grained calorimeter indicate that such a detector enables identification of the ν_e CC interactions with a typical efficiency $\epsilon = 0.35 - 0.4$ while keeping the contribution of NC contamination at the level of the intrinsic ν_e component of the beam. An example of the analysis chain is shown in Fig. A.4. These results serve as a basis of the estimates of the physics potential of the off-axis experiment presented in this letter.

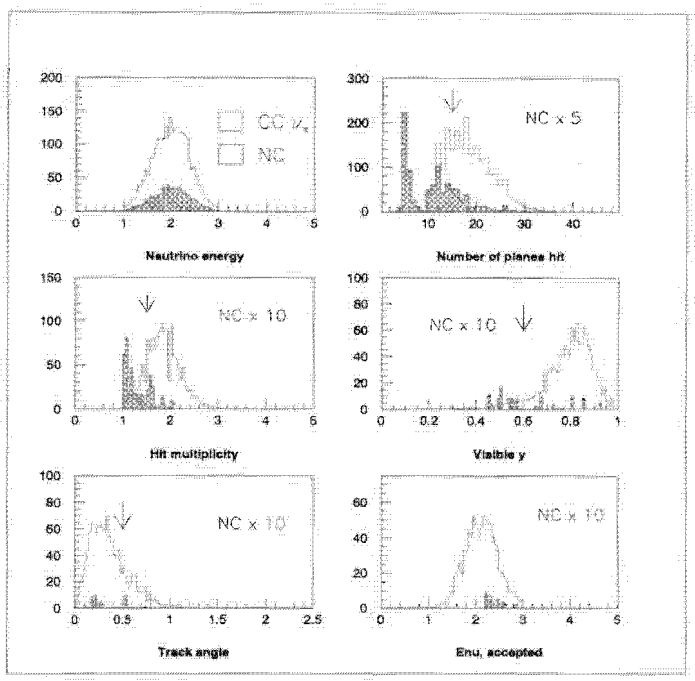

Figure A.4: Typical evolution of the events sample: open histogram for *nue* CC events, shaded histogram is for the NC sample. From top left to bottom right: Neutrino energy, number of planes in the longest track of the event, average number of hits (per plane) in a road around the longest track, fraction of the event energy contained in the longest track, track angle with respect to the beam direction, neutrino energy of the events passing the cuts. Cut values are indicated by arrows.

A.1.3 Energy resolution

Energy resolution of the detector is an important parameter. It provides a significant rejection against the backgrounds, as the oscillation signal events are concentrated in a narrow range determined by the beam spectrum, whereas the backgrounds are characterized by a broad distribution of the observed energy.

Good sampling frequency ensures that the sampling fluctuations will be small, hence the energy resolution will be good. This is true even if the readout is purely digital, i.e. the energy is determined by a number of the hit detectors strips, irrespective of the deposited energy per strip.

The resulting energy resolution, $\Delta E/E \sim 16\%$ is well matched to the off-axis

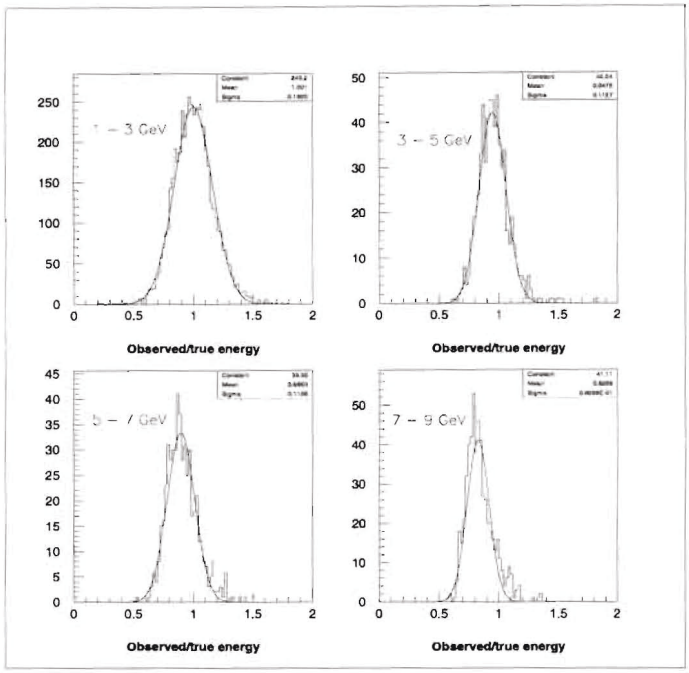

Figure A.5: Total neutrino energy resolution for low y ($y < 0.5$) ν_e CC interactions for different neutrino energies

energy spread. Purely digital readout leads to a non-linearity of the response of the detector, reaching some 18% at $E_\nu = 8\ GeV$. This feature, although irrelevant for the neutrino oscillations experiment, can be avoided by having an analog readout, for example in the liquid scintillator design.

A.1.4 A specific detector example: LoDen - LOw DENsity calorimeter

Neutrino experiments do not present significant challenges to the active detectors. The low cost and long term stability of operations are among the most important characteristics.

The principal challenge of the ν_e detector will be therefore in the engineering area: how to construct as large as possible and as cheap as possible low Z calorimeter.

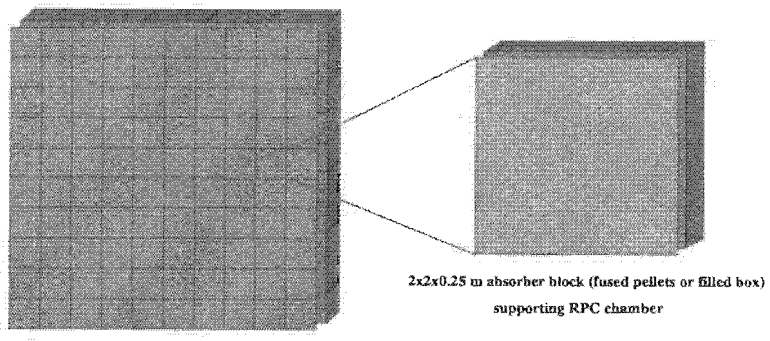

Figure A.6: Modular detector design: $20 \times 20\ m^2$ planes constructed by stacking absorber modules, active detectors supported by the absorber.

The Loden detector consists of the alternating absorber planes, $1/3\ X_0$ in thickness and Glass Resistive Plate Chambers. One detector plane represents a mass of about 70 *tons* hence 300 planes are necessary to attain the mass of 20 *kton*. Total area of the active detectors is $120,000\ m^2$.

The choice of the Glass RPC as a an active detector is primarily dictated by the low unit cost of such detectors. These detectors have several other attractive features: they are robust and reliable. They allow physical decoupling of the active elements (spark gaps) from the readout elements (pick-up strips) making it relatively easy to construct a very large area detector with relatively few redout channels out of a large number of smaller, hence manageable, individual detectors. Glass RPC are read out via pick-up strips providing x and y coordinate in every plane. Optimal transverse granularity of the active detectors needs to be studies in details, but the initial investigations indicate that a strip readout with a strip width of 3 *cm* is adequate. Such a granularity leads to some ~ 1400 readout channels per plane, or $400,000$ channels in total.

Practical design of the detector needs to be validated by the detailed engineering studies. Preliminary calculations indicated that the absorber planes of dimensions approaching $20 \times 20\ m^2$ can be constructed in a self-supporting manner, not requiring external support structures. To prevent potential buckling the absorber planes will be bolted around the periphery and along the center line into modules involving 20 planes.

Practical aspects of constructing very large but relatively thin detector walls must not be underestimated. It would be very desirable to develop a detector design based on a 'human' scale modules, say $2 \times 2\ m^2$ which could be stacked to construct w final large detector plane, as illustrated in Fig. A.6.

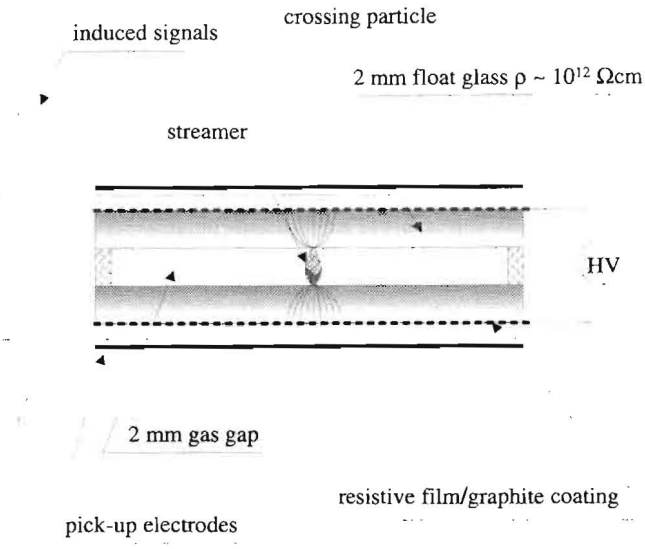

Figure A.7: Glass RPC detector principle

A.1.5 Glass RPC Chambers

Glass RPC chambers belong to a family of the Resistive Plate Chambers, but they utilize inexpensive commercial float glass of high resistivity (10^{12} Ωcm) instead of the traditional bakelite.

The detector, shown in Fig. A.7, is composed of two parallel glass electrodes, 2 mm thick, kept 2 mm apart by appropriate spacers. The gap between electrodes is filled with a suitable inflammable gas mixture. The resistive coating on the outer surfaces of the glass connected to the HV power supply creates a strong electric field $\sim 4 \div 5$ kV/mm across the gap. An ionizing particle initiates a local discharge which induces a signal on external pickup strips. The induced pulses are typically $100 - 300$ $mV/50\Omega$ with $\sim ns$ time resolution. Large signals of $100 - 200$ pC allow for the possibility of a variety of cost saving options in the readout electronics.

This type of detector has been used successfully for muon and K-long detection in the BELLE experiment at KEK [31]. A single detector plane has an efficiency of typically $90 - 95\%$. Double planes in the BELLE experiment were used to provide 99% efficiency. For this experiment we expect single planes to be adequate.

The high resistivity of the glass and the quenching properties of the gas limit the discharge to a small area. This type of detector does not have the rate capability necessary for hadron colliders but, as demonstrated by BELLE, is more than adequate for this neutrino experiment. They are ideal for large area applications since the pickup strips can be configured as transmission lines covering many meters in length.

These detectors are relatively simple and inexpensive to construct. The typical cost of the detectors is in the range of $\$100 - 150/m^2$ of the detector [32, 33]. They have been shown to be stable and reliable in more than four years of operation at KEK.

These low cost detectors which can be configured to cover a large area. As an example, the Monolith [34] group has developed a design for the RPC planes as large as $15 \times 30\ m^2$. This group also developed several possible industrial production techniques whicch may allow further cost savings.

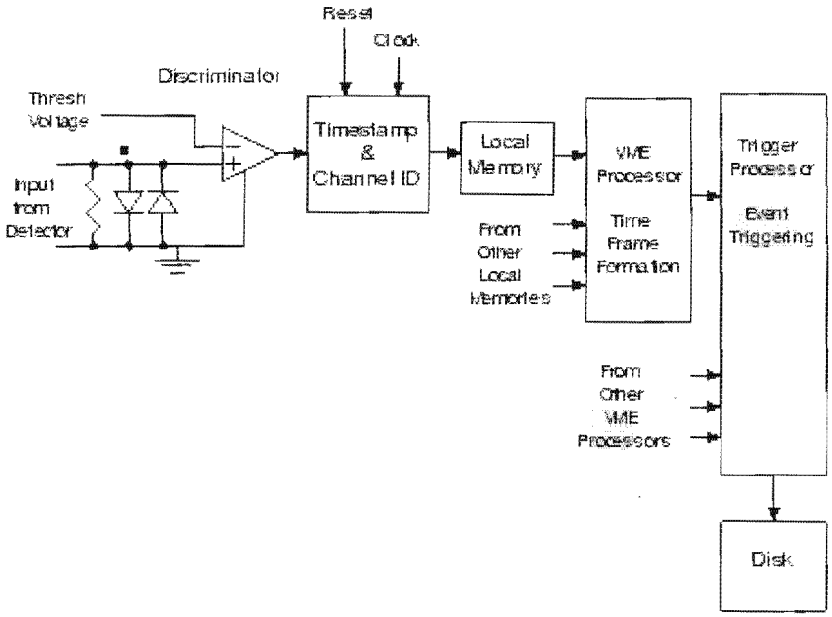

Figure A.8: Block diagram of the readout electronics

A.1.6 Readout Electronics

When operated in streamer mode, RPC detectors produce a large pulse in response to the ionization within the gas. The signals are large so that a significant voltage (100 mV or more) can be developed across a 50 or 100 ohm resistor. Because the measurement of events requires only the observance of hits in the detector, it is sufficient to use a simple discriminator as the front-end electronics, without the need for additional amplification or signal processing.

To facilitate event reconstruction, the output of each discriminator would latch a time-stamp for the event. The time-stamp is formed using local counters, which receive a common clock and counter reset signal from a global timing system. In this way, all time-stamp counters across the detector are synchronized. When an RPC channel is hit, the data that is recorded is the value of the time-stamp counter. The time-stamp hits are stored in a local memory, and read out later. A block diagram is shown in Fig. A.8. The resolution of the time-stamp is determined by the clock speed, which might be 100 ns (10 MHz.) The number of bits in the counter is determined by the frequency of the counter reset, which might be 0.5 Hz, corresponding to frequency of the NuMI beam spill.

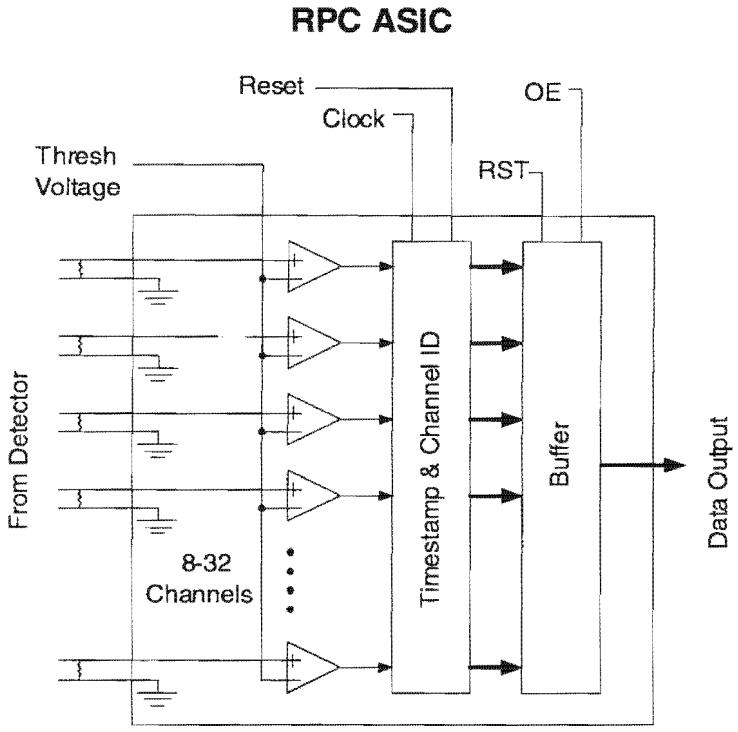

Figure A.9: ASIC for the front-end readout electronics

Because the data rate is low, it is envisaged that no trigger hardware is needed. Instead, the formation of a trigger and the analysis of events are done using a series of processors. This is similar to the data acquisition system of MINOS[10]. The initial sorting of hits by time-stamps is done using a VME-based processor in the front-end crate. The processor would form "time frames" using the time-sorted data. The time frames are then sent to a trigger processor, which receives time frames from the entire detector. The trigger processor runs algorithms that look for tracks and discard noise hits. Those events that pass are either written to disk, or passed to another processor for further analysis.

A goal in the electronics development is to reduce the cost. Given the high channel count and relatively simple front-end configuration, it is practical to implement the functionality in a custom ASIC. The comparator and time-stamp functions are easily realized in silicon. The cost per channel for the ASIC would be \$1.50 for a 16-channel device. A block diagram of the chip is shown in Fig. A.9.

The front end electronics would reside in racks situated close to the detector, as

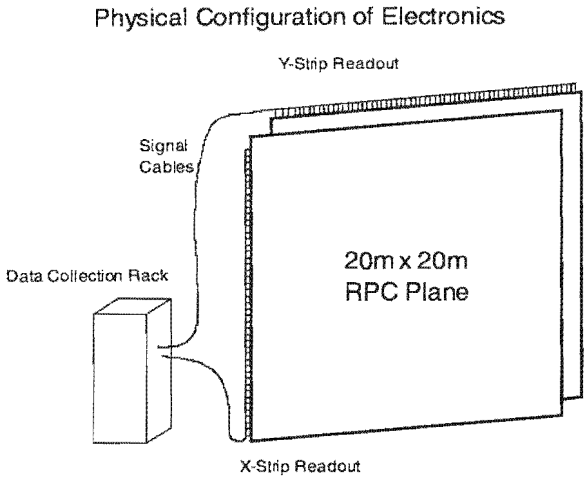

Figure A.10: Physical layout of the readout electronics

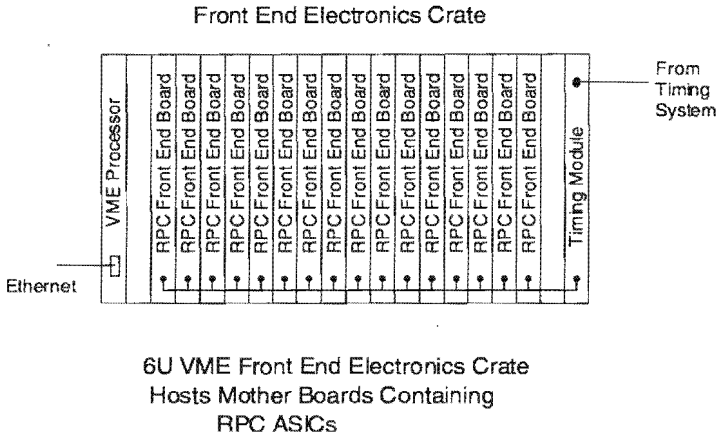

Figure A.11: Front end electronics crate

shown in Fig. A.10. The ASICs would be mounted on VME boards, providing easy access of the data to the front-end processor. Each front-end board would host 16 chips, servicing 256 detector channels. A VME crate would hold 16 such cards, servicing 4096 channels, as shown in Fig. A.11.

A total of 100 front crates would be needed for 400K channels in the detector.

ITEM	Unit Cost	Number Needed	Subotal
16-Ch ASICs	$25	25,000	$625 K
Front End Boards	$700	1,600	$1200 K
VME Crates, Power, & Processors	$5,000	100	$500 K
Trigger Processor	$20,000	1	$20 K
Cables, Misc	$100	1,600	$160 K
Total	$6.25	400,000	$2505 K

Figure A.12: Cost estimate of the front-end electronics

A preliminary cost estimate is shown in Fig. A.12. The total cost of the electronics is estimated to be $\$2.5M$, or $\$6/channel$.

A.1.7 Ancillary Systems

Assuming that the RPC mechanics and electronic readout are engineered to minimize the cost of their fabrication, it will be important to take care in the design of the ancillary systems, namely the gas mixing and distribution system and the HV system.

A.1.7.1 Gas System

The design of the gas system must address a number of challenges:

- the number of distribution channels will be large;
- the gas entering the chambers must be very dry;
- safety;
- cost of operation.

Although it may be possible to feed the gas in series through multiple gas volumes, there will be limits on this since the accumulated effect of the flow resistance of the chambers will eventually result in a pressure that exceeds the limit of the glue joints (the geometry of the RPCs is by its nature very weak with respect to internal overpressure). Moreover, experience with series connection of the Belle RPCs showed that the chambers near the end of the line were slow to achieve stable operation. Thus it will be important to minimize the per-channel cost of the distribution system and to develop a design that provides a balanced flow between channels without the need for extensive adjustment. To solve this problem, Belle used "flow resistors," which are 10 cm stainless-steel tubes drilled down the center with sub-mm bores. These tubes are series inserted in the output of each channel and set the flow impedance of the channel. This provides a simple and economical way to balance the flow from channel to channel without need for tedious adjustment.

Keeping the gas dry (water vapor at the 100 ppm level or less) is very important to avoid formation of hydrofloric acid, which etches the glass, ultimately destroying the RPCs (Belle came very close to having this happen). Achieving the requisite dryness is reasonably simple provided copper tubing is used (plastic tubing is too permeable).

The importance of safety and economy are clear and will no doubt be the subject of extensive design studies.

A.1.7.2 HV

Perhaps the most challenging aspect of the RPC high voltage system is the voltage across the gap must be in the neighborhood of 8 kV. Although it is possible to achieve this with a single ended supply, supplies capable of sourcing more than 5 kV tend to be expensive on a per-channel basis. For that reason the Belle experimented employed a differential scheme, wherein the total bias of 8 kV was achieved by using a pair of supplies operating at opposite polarities. A single 0-6kV supply was used on the positive side. Since these units were somewhat pricey, several RPCS were ganged onto a single supply. For the negative bias, independent (actually only quasi-independent) supplies were used on each channel. This allowed Belle to monitor the current on individual RPCs, which proved to be very important in the operation of the system, as discussed below.

Experience with previous RPC HV distribution systems indicates that it is essential to monitor the current drawn by the RPCs on a per channel basis (the dark current of an RPC is an excellent diagnostic of its overall health). The ability to switch a single chamber on or off is also useful, although perhaps not essential (one could always resort to simply unplugging the cables of misbehaving chambers). Still less important is the ability to adjust the HV on individual chambers.

Once again safety and cost will be important practical considerations.

A.1.8 Modular Detector Design

One possibility for the detector assembly is to use pre-engineered intermodal containers as the basic modular unit and then replicate the unit many times to create a giant structure. Dry Freight containers are used for international exchange of over 90% of the world's manufactured goods and can be transported easily by truck, rail, and sea (therefore termed "intermodal"). These objects are in widespread use throughout the world and the existing mass production infrastructure offers a low cost solution for a low-density neutrino detector.

The basic intermodal container is a steel box 8 ft wide by 8 ft 6 inches high by 20 ft long with an empty weight of about 2,300 kg and a payload capacity of 22,000 - 28,000 kg depending on the manufacturer. These containers have internal volumes of $31 - 36m^3$ and therefore can hold cargo with an average density of about $0.7 - 0.8\ g/cc$. The box has rails around the edges, a set of steel floor supports, a pair of doors at one end, and is typically covered with corrugated steel. Such a container is called a "Twenty-foot Equivalent Unit" or TEU. The International Standards Organization specification calls for the TEU box to be based around 4 corner posts that can each take a load of 86,400 kg. This ISO specification means that the boxes can be stacked 9 high when fully loaded and they are routinely stacked this high in large ocean-going container ships. The cost of a TEU (in quantity) is in the range $\$1500 - \$2500$. Millions of TEUs exist and hundreds of thousands of new ones are built each year.

A modular neutrino detector, 18 m by 20 m by 80 m. could be assembled from about 800 such TEUs at a cost of approximately $\$1.6M$. The resulting structure would be self-supporting and weather-tight. The empty containers by themselves would constitute about 1600 metric tons of steel. Off-the-shelf pre-engineered gantry cranes, lifting fixtures and many other attachments like box-to-box clamps and casters are available.

The small size of the basic TEU would allow construction of detector modules at many institutions around the country. The intermodal feature would allow easy shipment between institutions for different steps in the assembly process and the completed TEUs could easily be shipped to any site along the NuMI beamline. The modular structure allows for mobility of the detector if a different off-axis position becomes desirable part way through data collection, or if a different neutrino beam eventually becomes available from a superbeam or from a muon storage ring.

The concept does have two drawbacks. First, temperature control is not a built in feature of containers, but this can likely be solved using excess load capacity of the stacked TEUs as the supporting structure for an insulating shell. Secondly, when the TEU boxes are stacked, the floor supports carrying the load in each

individual TEU mean that the assembled detector will have an un-instrumented area with an active detector to active detector vertical crack size of about 20 cm. Both of these problems require further study.

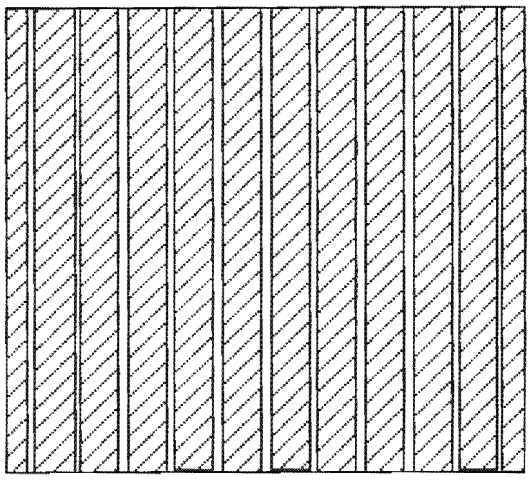

Figure A.13: Container $2.1 \times 2.3\ m^2$ cross section filled with target slabs creating 10 active gaps, 5.4 cm wide.

A.1.9 Absorber Construction and Composition

Typical low Z absorber materials have a density of 0.7 g/cm^3, and a radiation length of about 64 cm (similar to a mixture of 70% polyethylene and 30% air) leading to absorber elements $16 - 20$ cm thick.

Modular construction techniques include: standardized shipping containers filled with alternating layers of target and active detector, layers of target and active detector supported by an external framework, and free-standing structures of the target material with regularly spaced gaps for active detectors.

A.1.9.1 Containers and Loose Fill Materials

Standard shipping containers are inexpensive and strong enough to be stacked at least 9 containers high. The effects of unsampled target and voids in a container array are unlikely to cause serious problems but must be investigated. Using aluminum (instead of steel) containers may reduce the unsampled energy loss, and the inactive volume can used for service and signal connections between containers. The interior of a standard shipping container has the dimensions $(h \times w \times l)$ $2.1 \times 2.3 \times 5.8\ m^3$. The interior 230 cm width can be divided, as shown in Fig. A.13, into 12 layers of target material $(10 \times 16\ cm + 2 \times 8\ cm)$ with

Loose Fill Material	Density (g/cm^3)	Price ($/lbs.$)
Plastics (recycled)	0.6 - 1.0	0.10 - 0.30
Shredded Tires	0.4 - 0.8	0.15
Walnut Shells	0.6 - 0.7	0.1
Cracked Corn	0.7	0.05

Table A.1: Typical Low Z Fill Materials

10×5.4 cm slots for active detectors. Assuming a target density of 0.7 g/cm^3, the container holds 15450 kg of target mass, well below the load limit.

Target layers can use a loose fill if contained in a cavity formed by (wood) walls. To prevent bulging, however, the cavity might require an internal bracing. Low Z, loose fill materials include recycled petroleum based or agricultural products. Some typical loose fill materials are listed in Table A.1.9.1.

Recycled fill materials include plastics that are clean but can obtained only in relatively small batches with large variations in properties, and shredded tires which are quite stable and can be had in various particle sizes. The least expensive loose fill materials are agricultural products that include nutshells and cracked (and dried) corn. However, a polypropylene bag might be required to package these materials. Better yet, loose fill material can be molded into precast blocks, but add significantly to the cost.

A.1.9.2 Molded Particleboard

A standard building material called particleboard, e.g., Georgia Pacific's (GP) MicroFine Novoply, is likely the cheapest (about $\$0.123/lbs.$) commercially available low-Z molded product. Particle board has very good mechanical properties and can produced in 8' x 28' (8.3 m) sheets up to 1.44" thick. The boards can be laminated into slabs of the appropriate thickness, and installed in the containers, as shown in Fig. A.13. This would form smooth and straight gaps for the active elements.

Particle board for a 20 kT detector would cost $5.5M\$$.

A.1.9.3 External Framework and Self Supporting Structures

Particleboard, laminated into target slabs, 8 or 16 cm thick, can be bolted together and then supported by an external framework to generate a large array

of target and active elements. However, particleboard might be strong enough to create a stable (container sized) module ($2.1 \times 2.3 \times 5.8 m^3$) with, as described earlier, gaps for the active elements. Bonding or bolting a steel skin to four sides (top, bottom, and both ends) would stabilize the module against flexing. For active elements that must run the full height of the target, e.g., liquid scintillator filled tubes, internal bracing between the target slabs (instead of an external steel skin) can create continuous vertical slots.

A.1.10 Liquid Scintillator Option

Liquid scintillator makes an ideal active detector for a large inexpensive tracking calorimeter. It is a proven technology that has been used in large quantities in detectors over long periods of time. It gives good energy resolution and charged particle tracking efficiency. Liquid scintillator allows for a flexible geometry and segmentation that can be optimized for the expected events. Because it is a liquid, it can be added to the detector after it is assembled to minimize assembly cost. It can even be removed if repair is necessary or if the detector needs to be disassembled and moved. Modern off-the-shelf photonics can be used to readout the detector so that additional electronics is minimal. Scintillator segmented into cells gives both pulse height information and tracking. Since this type of detector was investigated as a candidate for MINOS, very little additional R&D and engineering is required to construct a 20 kTon detector from this technology.

A.1.10.1 Support Structure

As a specific example, we present a conceptual design of a detector based on liquid scintillator interspersed between planes of water approximately 1/3 of a radiation length thick. Both the liquid scintillator and the water would be contained in modules of extruded PVC plastic colored by titanium dioxide for good reflection. Although this is a conceptual design, its structure has been investigated previously and those investigations documented [35].

The design we consider here is based on modules that contain 6 layers of 30 cells each with the dimensions of each cell 3.3 cm x 3.3 cm x 12 m long. The outer walls are 1 mm thick while the inner webbing of the extrusion is 0.5 mm thick. One of the layers would hold liquid scintillator and the others would hold water. Although the cell sizes are chosen here for ease of calculation and would be optimized by Monte Carlo studies of neutrino events together with structural studies of the plastic, they are close to those required for a final detector and are structurally sound.

For each module, the cells are sealed at one end by a single plug of PVC glued in place. This construction has been tested to be reliable with no leaks to a pressure of over 6.5 atmospheres. If the detector consists of scintillator planes separated by 1/3 radiation length of water as the target mass, a 12m x 12m x 300 m detector will have a 20kT fiducial mass (assuming a 1 m fiducial cut around the edge.) Alternate planes of scintillator/water modules would have perpendicular cells to give an X - Y readout. This geometry would give 1500 planes of liquid scintillator.

A.1.10.2 Signal Collection

Light would be collected using a 1 mm diameter wavelength shifting fiber similar to that used in MINOS. Each cell would have a 12.5 m long fiber placed in it. Our previous studies have shown that the amount of light collected by the fiber is not sensitive to the position of the fiber in the tube. The end of the fiber will dipped in white paint and then in epoxy to provide 30% reflectivity at the end. Tests have shown a minimum ionizing particle this geometry with BC517L scintillator will give 40 photons from the end of the fiber. The fibers from module would be gathered in a manifold to an optical connector similar in design to that of MINOS. The design of the PVC manifold would also include fittings to fill and, if necessary empty the cells of scintillator. Chemical activity tests show [35] there will be no measurable effect of the scintillator on either the fiber or the PVC extrusion over the lifetime of the experiment.

A.1.10.3 Support

The construction of the detector is simplified because the light plastic extrusions would be stacked to form the detector before the liquid was added. Mounting the plastic extrusions with alternating planes at 45^o to the horizontal and 45^o to the vertical would allow the detector to be read out and filled from the top. A possible mounting structure would be a V shaped trench. The sloping walls could be supported by earth in a manner similar to culvert wall construction. The longitudinal direction the trench would be sloped at about 1^o for ease of construction and to allow drainage for water seepage from the ground.

The stacked extrusions would be supported primarily by the sides of the trench and at the ends of the trench by a bookend structure. Most of the weight of the detector is supported by compression on the floor of the trench carried by the entire length of the extrusion. In this configuration, all mechanical stresses are well below the tested strength of the extruded structure. We envision that the detector would be covered with a roof, possibly of Quonset hut design, which would then be covered by about 3 meters of earth. This would ensure a stable operating temperature for the detector and eliminate the soft component of the cosmic ray flux.

A.1.10.4 Readout

Image intensifiers provide a low cost readout well matched to the rates of cosmic rays through the detector. Reading out fibers into a standard 25 mm image intensifier will require one image intensifier for every plane of the detector.

Standard image intensifiers have a quantum efficiency of better than 10% in the green and a gain of at least 10^5. An image intensifier would be read out by a video camera. The CCD in a modern off-the-shelf video camera can be gated to have an exposure of as little as 10 microseconds and can be read out at 30 Hz.

For this experiment we propose an exposure gate of 20 microseconds. Even on the surface, the occupancy rate of a single cell would then be about 1%. The 360 cells of each plane of the detector could be read out by a single image intensifier and video camera. Standard firewire readout would be done into processor for each camera, the processors would be sparsified and read into a PC. If necessary, several PCs would alternate spills to assure adequate readout time.

A.1.10.5 Cost Estimate

The costs of constructing the detector described above is based on quotes and engineering estimates of the liquid scintillation detector proposed for MINOS[35]. It is expected that the cost of the 20 *kton* detector, excluding support structures and building, is of the order of $\$40M$.

A.1.11 Backgrounds in a surface detector

A.1.11.1 Cosmic ray rates in the detector

At the surface of the earth, the products of the extensive air showers initiated by primary cosmic rays high in the atmosphere provide a background flux to any detector. We present some preliminary estimates of these rates.

The principle component is muons with a flux of $110\cos^2\theta/m^2/sr/s$[36]. The net flux on a detector of area 3000 m^2 is then about 7×10^5 muons per second. The average energy of these muons is 4 GeV and about 30% will stop inside a detector of average thickness 1200 g/cm^2.

The live-time of the off-axis detector is given by the product of the 20μs spill length and the 10^7 spills per year = 200 seconds. There are about 1.4×10^8 muons passing through the detector in this time. In any given 20μs spill there are an average of 14 muons distributed throughout the detector.

Accompanying these muons are low energy electrons and photons with net flux about 30% of the muons and with energies in the range ~tens of MeV. In addition, there is a small component of low energy neutrons and protons (the proton flux is ~0.1 the neutron flux) with net vertical flux approximately $3 \times E^{-1.5}/m^2/sr/s$ (E in GeV) [37], i.e. the flux of neutrons with energy above 2 GeV (the onset of inelastic pion production) is about 1.0% of the muon flux. A small overburden is sufficient to effectively remove the soft electromagnetic component but it requires about 3 m of rock or earth (~10 interaction lengths) to attenuate the neutron flux so that there will be ~50 inelastic neutron interactions per year. Pattern recognition plus a moderate fiducial cut will be enough to make this small remnant negligible.

A.1.11.2 Tertiary particle production by muons interacting in the environment outside the detector

There will be a small flux of electrons and photons produced by muon bremsstrahlung in the overburden directly above the detector. This is a very characteristic signal that is trivially accounted for by a small fiducial cut. A neutral hadronic component of such interactions is potentially more serious.

An estimate of the rate of hadronic interactions of the muons passing through the detector can be made by finding the equivalent spectrum of photons using the Weizsacker-Williams formalism coupled with cross-sections for real photons.

This has been done by Perkins with the result $dN/dE \approx (0.61/E) \times 10^{-6}/g/cm^2$ where E is in GeV[38]. Integrating this over the muon energy spectrum we find that the probability of any single muon depositing more than $2GeV$ hadronic energy in one interaction length ($\sim 100 g/cm^2$ of water or other low-Z material) is $\sim 5 \times 10^{-5}$. The fraction of these interactions giving a final state neutron with energy above $2GeV$ is $\sim 10^{-3}$[39]. Estimating the relevant muon flux as 10^8 year and taking the angular acceptance into account, the corresponding flux of energetic neutrons into the detector is $\sim$1/year.

A.1.11.3 Particle production by unseen muons inside the detector

The proposed detectors contain planes of inert material. A cosmic ray muon can pass through one of these regions undetected but might produce a hadronic or electromagnetic shower which is detected. The probability that a muon will pass through one of these spaces is approximately w/L where w is the width of the inert space and L the transverse size of the detector. We will assume that this probability is 1%. Any such interaction will have an energy flow exactly orthogonal to the events of interest. Simple pattern recognition should make any bremsstrahlung-induced background negligible.

Based on the previous discussion, the probability of a hadronic interaction ($> \ 2\ GeV$) in the full $12m$ thickness of the detector is $\sim 6 \times 10^{-4}$. Thus the net background comes from a potential $1.4 \times 10^8 \times .01 \times 6 \times 10^{-4} \approx 1000$ muon hadronic interactions/yr. The highest energy pions in these interactions are produced in the forward direction (vector dominance) which is again exactly orthogonal to the events of interest. Large angle pion production occurs at a rate comparable to the large angle nucleon production and will be accompanied by significant nuclear break-up. Pattern recognition must reduce this background to a negligible level.

A.1.11.4 Gamma rays

There will be a gamma ray flux around the periphery of the detector coming from decay of ^{40}K, and the U and Th decay chains in the rock. These are low energy gammas which will give very small signals in the detectors; the net rate will be similar to that in the MINOS detector, i.e. 1 - 2 kHz/detector plane.

A.1.11.5 Measurement of cosmic ray backgrounds

Very accurate background measurements will be made in a relatively small test setup, as the effective lifetime of the neutrino detector is of the order of 200 s per year of operation. These measurements will validate the correctness of the above estimates.

During the duration of the experiment the background rates will be monitored by triggering the detector during the beam-off time.

A.2 Water Cherenkov option

Large volume water Cherenkov detectors provide a proven technology that must be considered as an off-axis neutrino beam far detector. The Super-Kamiokande detector is already planned as the far detector for the JHF neutrino beam[19]. Whether or not water Cherenkov is appropriate for the NuMI off-axis beam depends critically on the difference between the 0.8 GeV peak neutrino energy planned for JHF and the 2 GeV peak neutrino energy anticipated for the NuMI project. At the low energy of KEK/JHF beams the 22.5 kton Super-Kamiokande has proven capability for separating ν_e CC events from NC π^0 background due to:

- quasi-elastic kinematic constraints,
- good π^0 reconstruction efficiency due to a larger opening angle between the gamma showers,
- low intrinsic NC π^0 background due to the low neutrino energy and small cross section for heavy resonance channels such as the delta.

These advantages can be recovered in the NuMI project by going further off-axis to utilize the 2nd oscillatory maximum; this will be briefly discussed at the end of this section.

The advantages of water Cherenkov for 2 GeV off-axis experiment are:

- it is a mature and proven technology,
- the cost of such a detector can be accurately estimated,
- the cost per kiloton is low, no higher than \$2M/kton [1],
- the energy resolution is good, for example at Super-K one finds for electromagnetic showers that $\sigma/E = 0.5\% + 2.5\%/\sqrt{E}$,

The experimental challenge facing this detector option is accurately counting a small sample of CC ν_e interactions over a background of NC interactions with an associated π^0. In Super-K, the current π^0 analysis is based on ring-finding satisfactory for proton decay signatures (pion momentum 0.5 GeV/c or lower). The efficiency for identifying two separate showers, using the current algorithms, is approximately 10% at 0.8 GeV[41] and nearly zero at higher energies. This is mostly due to events with a small opening angle between the gamma showers,

[1] Estimated in round-numbers from the \$100M cost of the Super-K.

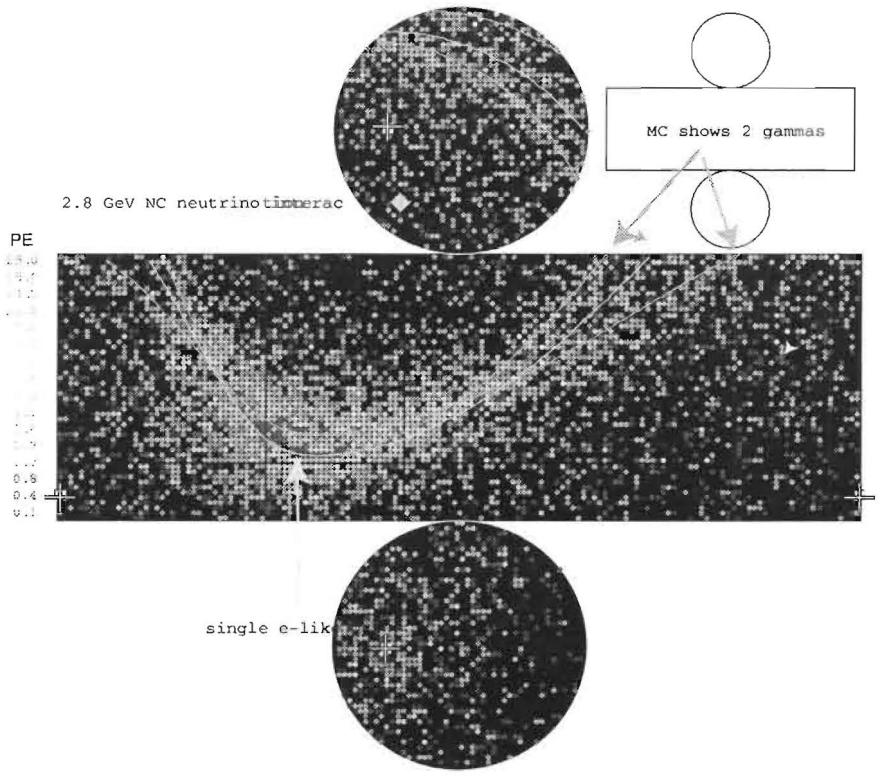

Figure A.14: An event display showing a typical neutral current π^0 event for the NuMI off-axis spectrum. The Super-K reconstruction software finds a single e-like ring.

typically 4 degrees for a 2 GeV π^0. Figure A.14 shows an event display of a simulated event in the Super-K detector. The event is a 2.5 GeV neutral current π^0 where one Cherenkov ring was found. The Monte Carlo simulation shows two gamma rings, as does a reasonably trained human eye scan.

The problem in separating the two showers becomes more difficult up to about 0.8 GeV, but then should not get worse as one goes to higher energies. This is because the vertex separation becomes dominated by the photon attenuation length rather than the angle between the two decay gammas. Firstly, the mean of the angle (θ) between the two gammas is given by:

$$\overline{cos\theta} = 1 - \frac{2}{\beta\gamma^2} ln[\gamma(1+\beta)] \tag{A.1}$$

At higher energies the second term becomes small, so that the mean separation angle goes as:

$$\overline{\theta} \sim \frac{2}{\gamma}\sqrt{2\gamma} = \frac{2m_\pi}{E_\pi}\sqrt{2\gamma} \tag{A.2}$$

When the mean angle becomes less than the intrinsic detector resolution, angular separation becomes less important as a means to recognize π^0's from e's Figure A.15 shows the mean separation angle as a function of pion energy. This becomes equal to the Cherenkov light in water (dashed line) at about 0.6 GeV. At this energy, the rings from the shower begin to overlap and so algorithms must decide which PMT hit goes with which gamma. For a NuMI off-axis experiment, good separation to better than 10 degrees (dotted line) is required.

Until now, experiments have used standard TDC/ADC technology to record PMT data. It is clear that multi-hit waveform digitizers might prove to be very useful in better separating light from individual rings. This is because light from the two rings is likely to be separated in time even though overlapping in postion. Figure refF:gamdist shows the mean distance between the first interaction point of the two gammas. At energies below 1 GeV this is influenced by the opening angle between the gammas so the difference is near a meter. At higher energies, however, the mean distance saturates due to the slow change of the photon attenuation length in water and so even near 3 GeV the average distance is more than half a meter. This might be detectable with reasonably fast PMT's and standard waveform digitizers. Such studies are now in progress.

It is hopeful that improved and specialized reconstruction algorithms may have a significant impact on such high energy π^0 reconstruction. It is already the case that a specialized likelihood fitter has been employed to distinguish between single and double Cherenkov rings. This technique was employed in the studies for section 5.2 of the JHF neutrino proposal [19].

Using a prelimary version of a specialized π^0 fitter developed for Super-K, a study was performed of the hypothetical case of transplanting Super-K into the NuMI off-axis beam[40]. The standard Super-K atmospheric Monte Carlo was

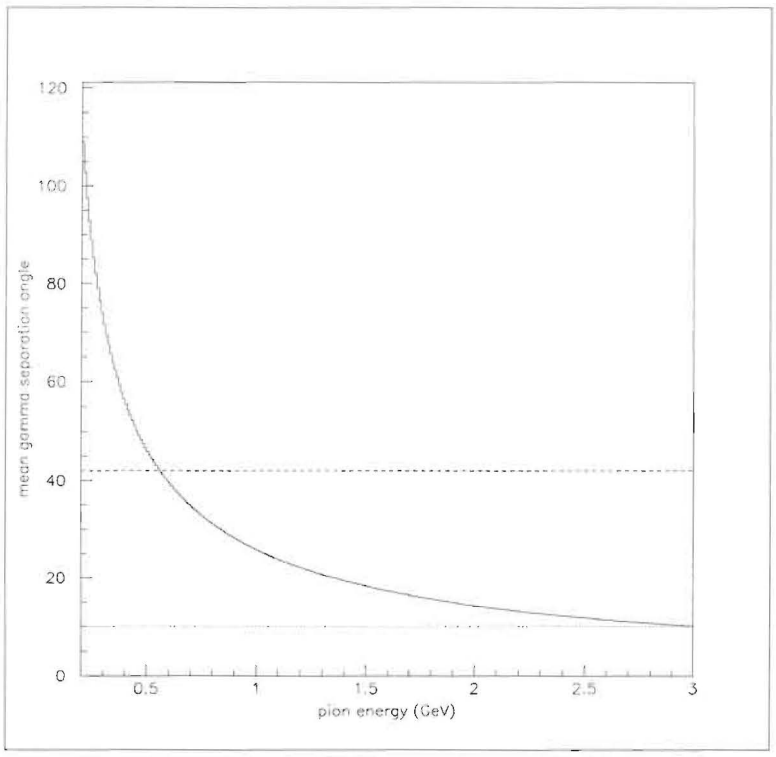

Figure A.15: The cosine of the mean separation angle between γ's from π^0 decay as a function of E_π.

used, reweighting each event to the NuMI beam spectrum using the Monte Carlo truth information. Nine event variables, such as decay electron tag, angle to the beam, the ratio of light in and outside of the single ring fit, and the value of the π^0 fit quality were combined into a likelihood to distinguish NC from ν_e-CC interactions. The analysis was roughly 20-30% efficient for accepting ν_e-CC signal, with a signal-to-background ratio of 0.7-to-1.

There are further possibilities to be explored, including adding new transient recording electronics that can reconstruct multiple close in-time hits on a single PMT, to recover some events where one of the two gammas converts at a significantly displaced vertex.

With further study, the sensitivity of the analysis for ν_e appearance could be clarified using the comparably mature Monte Carlo and reconstruction software used for Super-K and IMB. At this time, it seems like a water Cherenkov is a difficult but but potentially viable detector for the off-axis experiment.

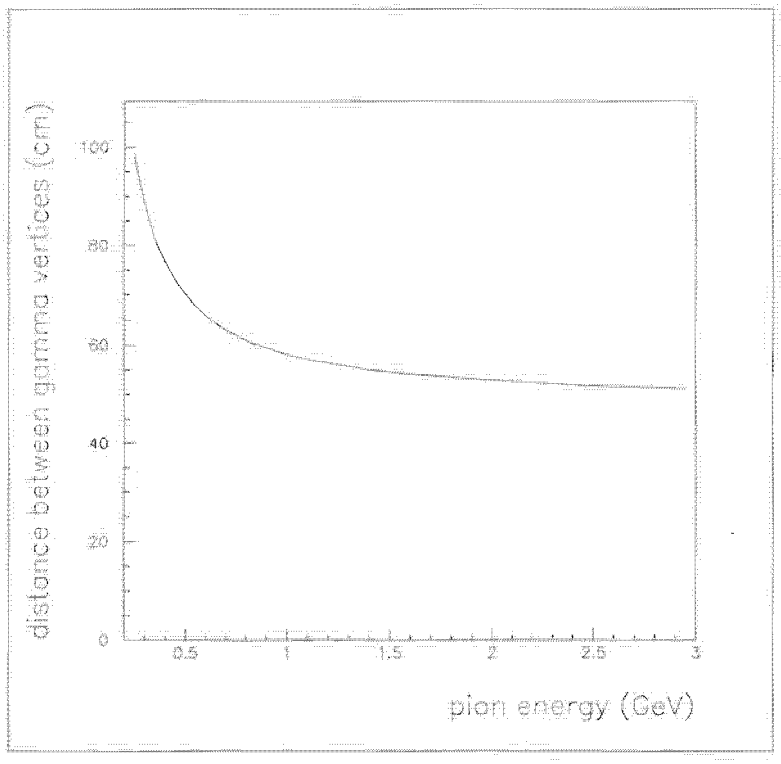

Figure A.16: The mean distance between the initial interaction point of the two γ's as a function of E_π.

There remains an interesting alternative path of inquiry. It is accepted that a Super-K like detector performs very well at lower energies (such as at 0.8 GeV at K2K and eventually the JHF). It may be interesting to consider moving such a detector even further off the NuMI axis, tuning the baseline and angle to second oscillation maximum. This would be at a lower peak energy, more suited to quasi-elastic kinematic reconstruction, and with considerably easier π^0 identification topologies.

A.3 Liquid Argon TPC

The recent successful operation of the ICARUS 300-ton liquid-argon time-projection-chamber prototype [42, 43, 44] indicates that it is timely to review the possibilities for large-scale application of this technology for accelerator-based neutrino physics, neutrino astrophysics, and proton decay [45, 46, 47].

A liquid argon detector for neutrino physics is a total absorption calorimeter with time-projection readout via the signal of drifting electrons collected in crossed planes of wires. The effective pixel size is about $5 \times 5 \times 5$ mm^3, compared to the radiation length of 14 cm and nuclear interaction length of 55 cm. At a drift field strength of 500 V/cm, the drift velocity is about 1 mm/μs, so the drift time over, say, 5 m would be 5 ms. Even if operated at the Earth's surface with no shielding, a liquid argon TPC has only about 1 (localized) cosmic-ray track per m^2 of horizontal surface per drift time, so events appear very clean, as shown in Fig. A.17.

Because a liquid argon TPC is a total absorption detector with fine-grained sampling, it offers superior separation of charged-current and neutral-current neutrino interactions, as we as excellent identification of $e/\mu/\pi/K/p$, included π^0's. Hence, it is the most effective detector per unit mass for $\nu_\mu \to \nu_e$ appearance measurements (of $\sin^2 2\theta_{13}$, the sign of Δm^2_{23}, CP violation, ...), as shown in Fig. A.18.

To obtain economies of scale, a large liquid argon detector should be implemented in a single cryostat, such as those commonly used in the liquefied natural gas industry. Cryogenic volumes of up to 200,000 m^3 (= 280 kton if liquid argon) are now in use, as sketched in Fig. A.19.

An overall concept of a large magnetized liquid argon detector is shown in Fig. A.20. Anticipating the possibility that neutrino beams are eventually sent to it from more than one accelerator, the magnetic field is vertical so the trajectories of secondary particles are generally orthogonal to the magnetic field.

The usable drift distance in a liquid argon detector is limited by oxygen impurities to 2-5 m. The diameter of a large liquid argon detector will be greater than (twice) the maximum drift distance, so the readout must consist of a set of parallel anode and cathode planes that subdivide the detector, as shown in Figs. A.20 and A.21.

A large liquid argon detector has excellent capability to search for nucleon decay [49], particularly because it is almost fully efficient for the decay $p \to K^+\bar{\nu}_\mu$ that is favored in many SO(10) SUSY models [50].

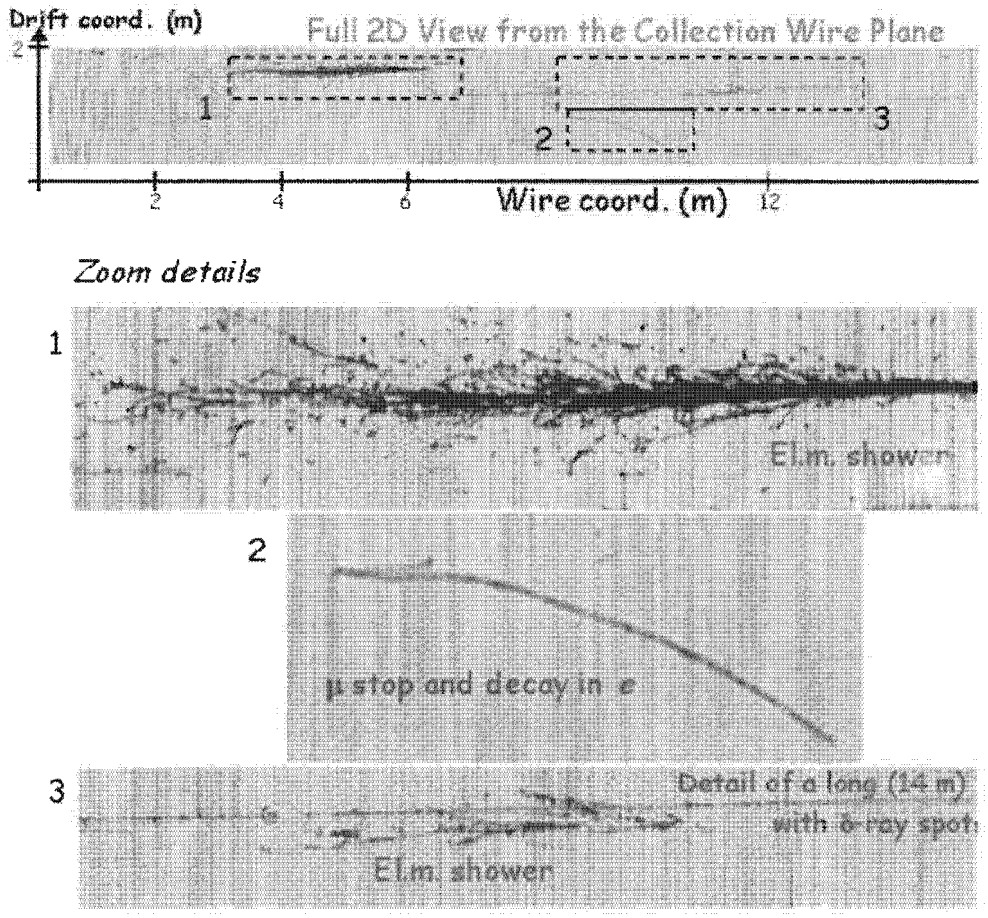

Figure A.17: An event from the recent cosmic-ray test run of ICARUS [43], showing excellent track resolution over long drift distances in zero magnetic field.

The data acquisition for a liquid-argon TPC can operate in a pipelined, dead-timeless mode, with zero-suppression [51]. This could permit fully live operation at the Earth's surface for nucleon decay studies, in addition to triggered data collection of neutrino interactions from a pulsed accelerator beam. The data rate would, of course, be quite high in this case. It may nonetheless be less costly to implement a high rate data-acquisition system than to reduce the un-triggered data rate by siting the detector deep underground.

In the future, neutrino beams from pion decay may be supplanted by those from muon decay [52], in which cases beams of ν_μ and $\bar{\nu}_e$ or $\bar{\nu}_\mu$ and ν_e would be available. To take advantage of such beams for studies of CP violation, the

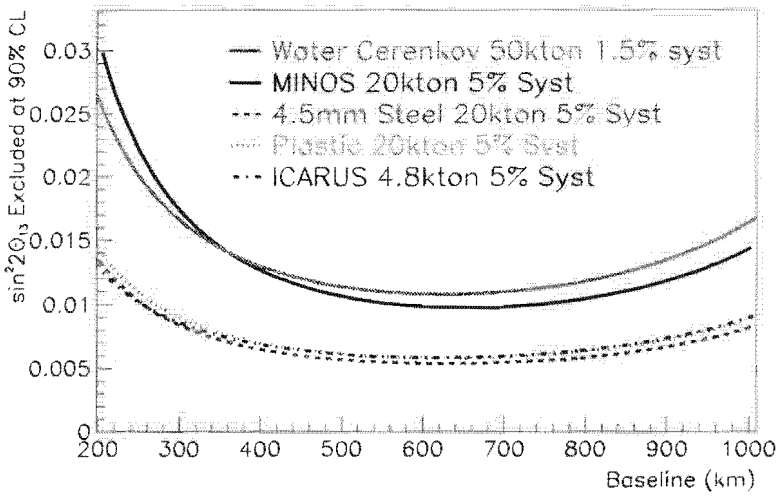

Figure A.18: Comparison of several types of detectors in measuring $\sin^2 2\theta_{13}$ in the presence of backgrounds typical of a pion-decay neutrino beam at intermediate baselines [48]. The detector labeled ICARUS [43] is a liquid argon time projection chamber. With a 25-kton liquid argon detector, and an off-axis NuMI neutrino beam, the sensitivity to $\sin^2 2\theta_{13}$ would be at least 0.002.

sign of the final state lepton much be determined in the detector, which must therefore be immersed in a magnetic field. A liquid argon TPC is compatible with a superimposed magnetic field. The sign of muons could be well determined with a field of only 0.1 T, and the sign of electrons up to a few GeV energy could be determined in a field of 0.5 T by analysis of the curvature of tracks in the electromagnetic shower [53, 54].

As well as being the highest-performance large detector for neutrinos, a liquid argon TPC is also one of the least costly. Liquid argon costs about \$1M per kton, or \$20m for a 20 kton detector. Such a detector would require about 100k readout channels, at a cost of about \$10M. The greatest cost uncertainty at present is in the storage tank and associated cryogenic/purification system. A initial engineering study on this issue is underway [55]. If the cryo system cost proves to be of order the cost of the argon itself, then a 20 kton detector would cost about \$50M – which would make a liquid argon TPC the price/performance leader for large neutrino detectors.

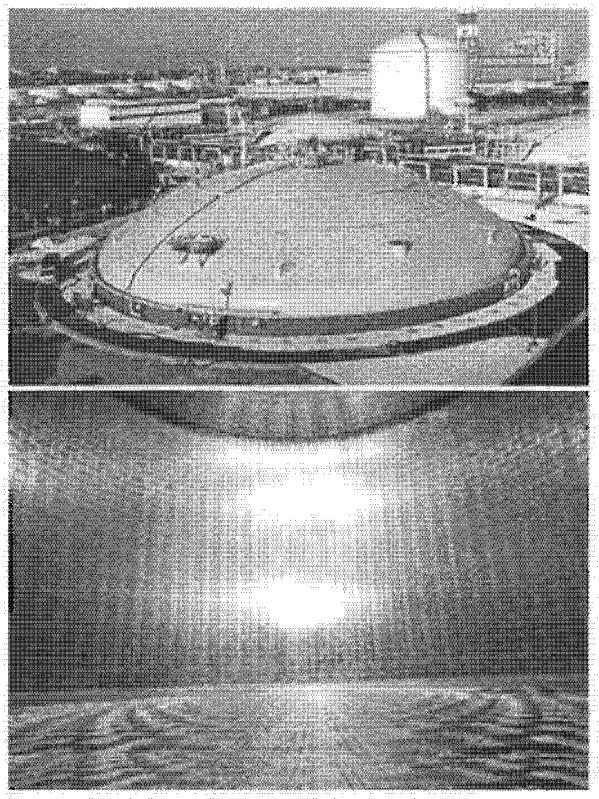

Figure A.19: Photographs of cryogenic storage tanks of volumes $\approx 100,000$ m^3.

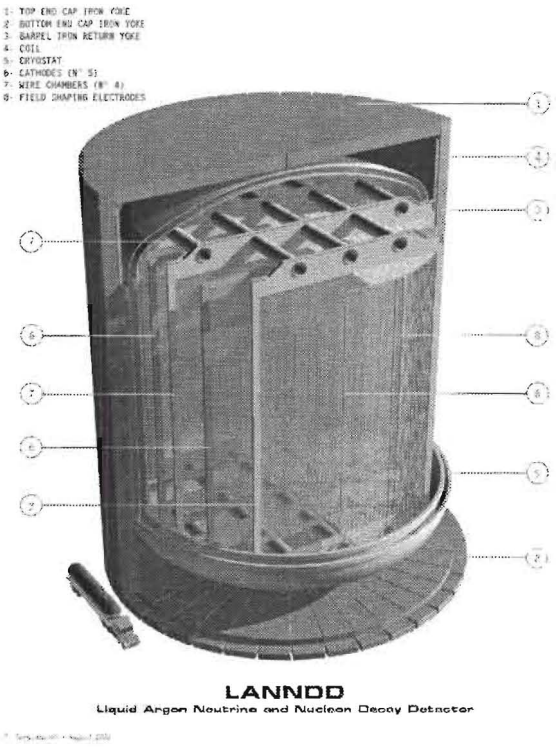

Figure A.20: Concept of a 70-kton Liquid Argon Neutrino and Nucleon Decay Detector (LANNDD) [45, 46].

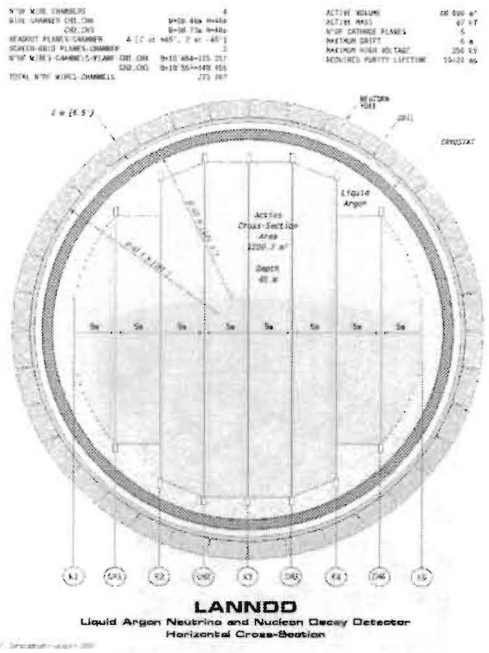

Figure A.21: Top view of the electrode arrangement of a 70-kton Liquid Argon Neutrino and Nucleon Decay Detector (LANNDD) [46].

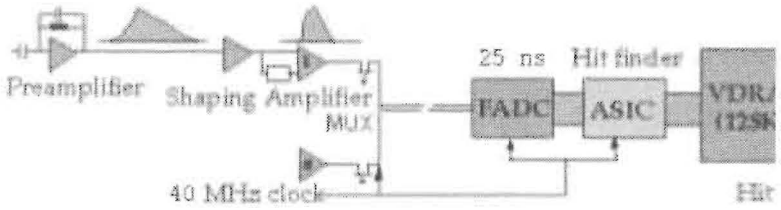

Figure A.22: Scheme of the front-end electronics of the ICARUS detector [51].

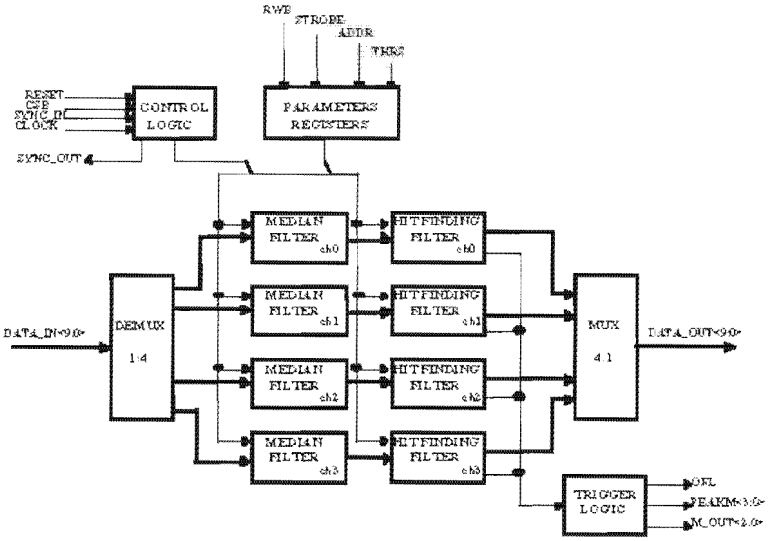

Figure A.23: Scheme of the back-end electronics of the ICARUS detector [51].

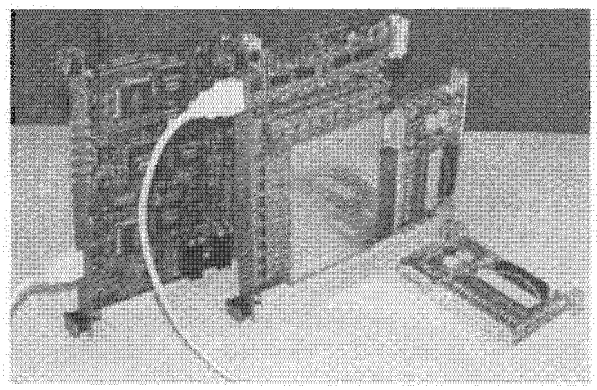

Figure A.24: Readout electronics of the ICARUS detector [51].

Appendix B

Possible Sites for a NuMI Off-Axis Detector

B.1 Criteria for Site Selection

There appears to be general agreement that because of the 10 μs beam spill, a NuMI off-axis detector can be located in a surface or near-surface laboratory. Besides the general physics considerations discussed in the preceeding section there are more specific requirements that determine whether a give site is adequate. The most important ones are listed below.

a) The site should be at least 450 m along an axis pointing towards Fermilab and 100 m along the transverse access. Such a site will accommodate the largest possible detector, earth berms for shielding, if they are required, and space for ancillary facilities. Access to the entire site should be protectable by lease or options, even though only a portion of the site is necessary for the first stage laboratory.

b) The site should permit cost-effective construction of the detector and associated structures, if any. The detector may need shielding and good availability of material for shielding is an advantage.

c) The site should have good highway access. A location close to Soudan is not a requirement. However, a site close enough to Soudan to enable easy staff travel between the laboratories would facilitate laboratory management and result in savings in operating costs.

d) The site should have good access to $\sim$ 1 MW of electrical power and telecommunications, including fiber optic data links. The site needs access to water in quantities that depend on detector design. Existing sewage treatment access would be a plus for any site.

e) An ideal site would have low environmental and political risk, that is, not adjacent to large populations, to conservation or park areas or to areas of natural beauty, such as shorelines or other features. An ideal site would also have soil and rock with low content of sulfur and heavy metals, in order to minimize environmental issues due to leaching.

f) Depending on future information about information about Δm^2, matter effects or CP violation, the detector may be moved at some future time. Although such a relocation might need to be far, in order to substantially change the baseline, another possibility is a short move transverse to the beam. Thus, a site near other ideal sites located at different transverse dimensions from the beam center line would have some advantage.

g) An ideal site would have gravity drainage, even for an underground laboratory location. Such drainage reduces both operating cost and risk of flooding due to electrical or mechanical failure.

B.2 Potential Sites

We have initial examination of possible sites which might satisfy the above requirements. So far, only one has been sufficiently studied. This site, at 712 km from Fermilab is a former mining site owned by LTV. Preliminary discussions with the appropriate parties lead us to believe that there would be a positive response to our potential request to site the detector there. The principal negative factor is that the site is not as far away from Fermilab as one would desire ideally. It is probably adequate if Δm^2_{32} is above 2.5×10^{-3}. The optimal energy for $\Delta m^2_{32} = 2.5 \times 10^{-3}$ would be somewhat below $1.5GeV$. Such a low energy might make the rejection of NC background somewhat easier. The site is described in more detail in the Appendix B.

From examination of the map of Ontario, there are two potential site areas further north, in Canada. The first one lies along the southern Trans Canadian Highway, and is about 850 km away from Fermilab. A somewhat more distant variant in this site area would be along Rt 502 which runs north by north east from the main highway and could offer a site about $20 - 40$ km further. The other site area would be at about 985 km, paralleling the northern branch of the Trans-Canadian Highway. There are also two railroad tracks along the highway, one just south of it and the other one about 20 km north of it. This site would be a little too far if Δm^2_{32} is above $2.5 \times 10^{-3} eV^2$. At this time we do not

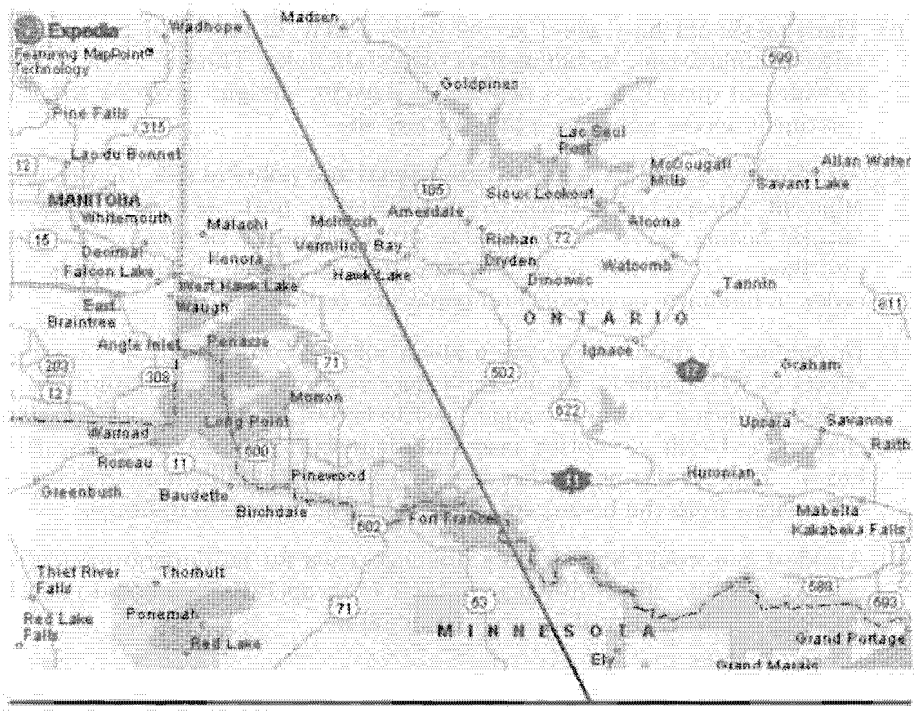

Figure B.1: Map of southern Ontario and the NuMI beam direction

know whether it would be possible to operate a neutrino detector in either one of these areas.

Looking further into the future one might look at possible sites for Phase II, perhaps at the L/E corresponding to the second oscillation maximum. This would involve going further north, to a distance of about 1100 km and energy around 1 GeV. A possible site is in the neighborhood of Red Lake. This is a pretty desolate area and on-site investigation will be required to see if it could be suitable. A map of this area of Canada, with the 0 deg beam line superimposed, is shown in Fig. B.1. A list of the potential sites for an off-axis experiment is shown in Table B.2.

B.3 LTV sites

While the investigation of possible sites continues, the sites for which we have the most information already more than meet the minimum criteria for an ac-

Area	Distance to Fermilab	Depth	Access	Comments
Iron River	612 km	6.5 km	Wisconsin Highway 13	Near mouth of Iron River; rural, forest
Two Harbors (Lake Superior North Shore)	643 km	5.2 km	U.S. Highway 61	Two Harbors MN; mixed urban and rural
Tower-Soudan-Embarass	720 to 735 km	1 km	MN Highway 169	Off-axis locations rural, forest
Buyck	775 km	-1.8 km	Orr-Buyck-Ely Road (Echo Trail)	Off-axis locations rural, forest
Ash River	$\sim$ 800 km	-3.4 km	Ash River Trail, east of U.S. 53	Kabetogama State Forest south side of Voyageur's National Park
Farrington	$\sim$ 850 km	-6.9 km	Ontario Highway 11 east of Fort Frances	
Otukamamoan Lake	$\sim$ 900 km	-10.9 km	Ontario Highway 502 northeast of Fort Frances	
Vermilion Bay	$\sim$ 950 km	-15.3 km	Ontario Highway 17 east of Kenora, west of Dryden	

Table B.1: Possible sites for an off-axis experiment

ceptable site. In particular, we have identified two sites that lie in Minnesota's Iron Range, a mixed hematite, magnetite and taconite deposit several kilometers in width that extends $\sim$ 200 km ENE from Grand Rapids MN to Babbitt MN. These two sites are just north of Erie Pit No. 1 in the former LTV Steel Mine about 10 km north of Aurora MN. Both sites consist of tailings piles, each $\sim 15 - 20$ m in height, 500 m in the beam direction and ¿200 m transverse to the beam direction. The westerly of the two sites is 10.3 km from the beam axis; the easterly site is 9.1 km from the beam axis. Both sites are $\sim$ 712 km from Fermilab. These sites are currently owned by Cliffs-Erie LLC, an iron mining company. There is neither active mining nor plans for mining within several kilometers of either site. Both sites are accessible by a private two-lane paved highway from MN Highway 135. The sites are located $\sim$ 20 miles by state highway from Soudan.

Both LTV sites have good access to mine electrical power. An existing power line connects the two sites. Public utility power is available along Highway 135 and it

may be possible to reconfigure the existing line to provide public utility power to either site. Fiber optic telecommunications exist along Highway 135 and connect to cell phone towers located on the peaks of the Embarrass Mountains less than 2 km north and west of the LTV sites. Erie Pit No. 1, which is about 6 km in length, is a potential source of water for a detector and also provides natural drainage for both sites. The LTV Mine is $\sim$ 20 km transverse to the beam line. It extends past the beam centerline to the east and about 5 km to the west of these two sites. Numerous tailings piles can be found on the LTV site if moving the detector becomes desirable at some later time. Tailings piles also exist further west along Highway 135, both east and west of Biwabik MN. Biwabik is $\sim$ 20 km west of the NuMI beam centerline.

Preliminary information from Michael Johnson, the site manager for Cliffs-Erie indicates low levels of sulfur and heavy metals at these sites. (The other end of the LTV property, east of the beam centerline is believed to have copper-nickel-precious metal deposits in a sulfide ore, with new mining activity possible during the next several years.) Thus, we believe from current information the environmental risk associated with this property is low. Because of previous mining activity, the political risk is also low. Indeed, the IRRRB, the regional state economic development agency, has already indicated positive political and possible financial support for these sites. The positive reputation of the Soudan Lab is also strong in this area, which also minimizes political risk. Mr. Johnson on behalf of Cliffs-Erie has indicated a willingness of the company to discuss various acquisition options any time we are ready.

In summary, the LTV sites located 9.1 and 10.3 km transverse to the beam centerline, 712 km from Fermilab provide high-quality, low-risk areas for an off-axis detector, which could be accessed in a short period of time.

Proposal to Build an Off-Axis Detector to Study $\nu_\mu \rightarrow \nu_e$ Oscillations in the NuMI Beamline

NOνA

NuMI Off-Axis ν_e Appearance Experiment

(P929)

March 15, 2004

The NOνA Collaboration

Argonne, Athens, Caltech, UCLA, Cambridge, Fermilab,
College de France, Harvard, Indiana, ITEP, Lebedev,
Louisiana State, Michigan State, Minnesota/Duluth,
Minnesota/Minneapolis, Munich, Stony Brook,
Northern Illinois, Ohio, Oxford, Rio de Janeiro, Rochester,
Rutherford, South Carolina, Stanford, Texas A&M,
Texas/Austin, Tufts, Virginia, Virginia Tech, Washington,
William & Mary, Wisconsin, York

I. Ambats, D. S. Ayres, J. W. Dawson, G. Drake, M. C. Goodman, J. J. Grudzinski, V. J. Guarino, T. Joffe-Minor, D. E. Reyna, R. L. Talaga, J. L. Thron, R. G. Wagner
Argonne National Laboratory, Argonne, IL

D. Drakoulakos, N. Giokaris, P. Stamoulis, S. Stiliaris, G. Tzanakos, M. Zois
University of Athens, Athens, Greece

B. Barish, J. Hanson, D. G. Michael, H. B. Newman, C. W. Peck, C. Smith, J. Trevor, H. Zheng
California Institute of Technology, Pasadena, CA

D. B. Cline, H. Wang, Y. Chen, K. Lee, Y. Seo, X. Yang
University of California, Los Angeles, CA

M. Thomson
University of Cambridge, Cambridge, United Kingdom

J. Beacom, R. Bernstein, G. Bock, S. Brice, L. Camilleri*, S. Childress, B. Choudhary, J. Cooper**, R. Hatcher, D. Harris, J. Hylen, H. Jostlein, D. Koolbeck, J. Kilmer, P. Lucas, V. Makeev, A. Marchionni, O. Mena, S. Mishra, R. Plunkett, S. Parke, S. Pordes, R. Rameika, R. Ray, R. Schmitt, P. Shanahan, P. Spentzouris, R. Wands, R. Yarema
Fermi National Accelerator Laboratory, Batavia, IL

T. Patzak, R. Piteira
College de France, Paris, France

G. J. Feldman**, N. Felt, A. Lebedev, J. Oliver, M. Sanchez, S.-M. Seun
Harvard University, Cambridge, MA

C. Bower, M. Gebhard, M. D. Messier, S. Mufson, J. Musser, B. J. Rebel, J. Urheim
Indiana University, Bloomington, IN

I. Trostin
Institute For Theoretical And Experimental Physics, Moscow, Russia

V. Ryabov, A. Y. Terekhov
P. N. Lebedev Physical Institute, Moscow, Russia

W. Metcalf
Louisiana State University, Baton Rouge, LA

C. Bromberg, J. Huston, R. Miller, R. Richards
Michigan State University, East Lansing, MI

A. Habig
University of Minnesota, Duluth, MN

T. Chase, K. Heller, P. Litchfield, M. Marshak, W. Miller, L. Mualem, E. Peterson, D. Petyt, K. Ruddick, R. Rusack
University of Minnesota, Minneapolis, MN

P. Huber, M. Lindner, W. Winter
Technische Universität München, Munich, Germany

R. Shrock
State University of New York, Stony Brook, NY

C. Albright
Northern Illinois University, DeKalb, IL

C. R. Brune, D. S. Carman, K. H. Hicks, S. M. Grimes, A. K. Opper
Ohio University, Athens, OH

G. Barr, J. H. Cobb, K. Grzelak, N. Tagg
University of Oxford, Oxford, United Kingdom

H. Nunokawa
Pontifícia Universidade Católica do Rio de Janeiro, Rio de Janeiro, Brazil

A. Bodek, H. Budd, S. Manly, K. McFarland, W. Sakumoto
University of Rochester, Rochester, NY

T. Durkin, R. Halsall, T. Nicholls, G. F. Pearce, A. Weber
Rutherford Appleton Laboratory, Chilton, Didcot, United Kingdom

T. Bergfeld, K. Bhaskaran, A. Godley, S. R. Mishra, C. Rosenfeld, K. Wu
University of South Carolina, Columbia, SC

S. Avvakumov, G. Irwin, S. Murgia, S. Wojcicki, T. Yang
Stanford University, Stanford, CA

E. Tetteh-Lartey, M. Watabe, R. Webb
Texas A&M University, College Station, TX

J. Klein, S. Kopp, K. Lang, M. Proga
University of Texas, Austin, TX

H.R. Gallagher, T. Kafka, W.A. Mann, J. Schneps, A Sousa
Tufts University, Medford, MA

C. Dukes, L. Lu, K. Nelson, A. Norman
University of Virginia, Charlottesville, VA

F. F. Chen, K. Creehan, N. K. Morgan, L. Piilonen, R. H. Sturges, R. B. Vogelaar
Virginia Polytechnic Institute and State University, Blacksburg, VA

J. Rothberg, T. Zhao
University of Washington, Seattle, WA

J. K. Nelson
The College of William and Mary, Williamsburg, VA

A.R. Erwin, C. Velissaris
University of Wisconsin, Madison, WI

S. Menary
York University, Toronto, Ontario, Canada

* On leave from CERN
** Temporary Co-Spokespersons

Table of Contents

1. Executive Summary 1-1
1.1. The Physics of NOvA 1-1
1.2. The NOvA Detectors 1-2

2. Introduction 2-1

3. Physics Motivation 3-1
3.1. Introduction 3-1
3.2. Neutrino Mixing 3-1
3.3. Matter Effects 3-2
3.4. CP Violation 3-3
3.5. Ambiguity Resolution 3-4
3.6. Other NOvA Measurements 3-5
3.7. Neutrino Oscillations in 2010 3-6
3.8. Summary 3-6
Chapter 3 References 3-6

4. Experiment Overview 4-1
4.1. NuMI Beam 4-1
4.2. Off-Axis Concept 4-2
4.3. Detector Design Considerations 4-4
4.3.1. General Goals 4-4
4.3.2. Design Optimization Issues 4-4
4.3.3. Tracking Calorimeter Design Issues 4-5
4.4. Far Detector 4-6
4.5. Backgrounds and the Near Detector 4-6
4.6. Cosmic Ray Backgrounds 4-7
4.7. NOvA Detector R&D Program 4-7
4.8. Collaboration Organization 4-8
Chapter 4 References 4-8

5. Physics Potential of NOvA 5-1
5.1. Introduction 5-1
5.2. Primary NOvA Goal 5-1
5.3. Resolution of the Mass Hierarchy 5-2
5.4. Other Physics 5-4
Chapter 5 References 5-5

6. The Detector Design Process 6-1
6.1. Introduction 6-1
6.2. Calorimeter Absorber Choice 6-1
6.3. Calorimeter Sampling Frequency, Transverse Active Cell Size, and Energy Resolution 6-1
6.4. Calorimeter Active Detector Choice 6-1
6.4.1. Solid Scintillator versus Glass RPCs or Liquid Scintillator 6-2
6.4.2. Glass RPCs versus Liquid Scintillator 6-2
6.5. Next Steps 6-2
6.6. Summary 6-2
Chapter 6 References 6-2

7. The Far Detector 7-1
7.1. Introduction 7-1
7.2. Design Advantages 7-1
7.2.1. Simplicity of Design 7-1
7.2.2. Ease of Construction 7-1
7.2.3. Reliability 7-2
7.2.4. Ease of Shipping and Installation 7-2
7.2.5. Passive Absorber 7-2
7.2.6. Avalanche Photodiodes 7-2
7.3. Passive Absorber 7-2
7.3.1. Overview 7-2
7.3.2. Passive Absorber Details 7-2
7.3.3. Mechanical Integrity 7-4
7.3.4. Longitudinal Design 7-4
7.4. Active Detector Elements 7-4
7.4.1. Overview 7-4
7.4.2. PVC Modules 7-4
7.4.3. Wavelength-Shifting (WLS) Fiber 7-6
7.4.4. Liquid Scintillator 7-7
7.5. Avalanche Photodiodes (APD) 7-8
7.5.1 Overview 7-8
7.5.2. Photodetector Requirements 7-9
7.5.3. Fundamentals of APD Operation 7-9
7.5.4. Experience with the CMS APDs 7-10
7.5.5. APDs for the NOvA Far Detector 7-10
7.5.6. Electronic Readout 7-11
7.5.7. Noise 7-11
7.5.8. Digitizing and Readout Architecture 7-11
7.5.9. APD Housing 7-12
7.6. Data Acquisition 7-12
7.6.1. Data Acquisition Modes 7-12
7.6.2. System Architecture 7-13
7.6.3. Timing System 7-14
7.7. Environmental Safety and Health 7-14
7.7.1. Introduction 7-14
7.7.2. PVC 7-14
7.7.3. Scintillator 7-14
7.7.4. Absorber 7-14
7.8. Installation 7-15
7.9. R&D for the Baseline Design 7-15
7.9.1. Overview 7-15
7.9.2. Overall Design 7-16
7.9.3. Test Beam 7-16
7.9.4. Detector Structure 7-16
7.9.5. Scintillator Mixing and Delivery 7-16
7.9.6. Scintillator Modules 7-16
7.9.7. Photonics 7-16
7.9.8. APD Box and WLS System Design 7-17
7.9.9. Electronics 7-17
Chapter 7 References 7-17

8. Simulations 8-1
8.1. Introduction 8-1
8.2. Detector Definition 8-1
8.2.1. Detector Geometry 8-1
8.2.2. Readout Simulation 8-1
8.3. Event Generation 8-2
8.4. Event Reconstruction 8-2
8.5. Event Weighting 8-3
8.6. Selection of ν_e CC Events 8-4
8.7. Other Simulations 8-8
8.7.1. Alternative Figure of Merit 8-8
8.7.2. Other Off-Axis Positions 8-8
8.7.3. Matter Effects 8-9
8.7.4. Anti-Neutrino Beam 8-9
8.7.5. Lower Δm^2 8-9
8.7.6. Light Level 8-9
8.7.7. RPC Simulation 8-9
8.8. Other Physics 8-9
8.8.1. Measurement of Oscillation Parameters 8-10
8.8.2. Limits on Sterile Neutrinos 8-10
Chapter 8 References 8-10

9. Neutrino Beam Backgrounds, Systematic Studies and the Near Detector 9-1
9.1. Introduction 9-1
9.2. Near Detector Requirements 9-1
9.3. Near Detector Location and Design 9-1
9.3.1. Possible Off-Axis Near Detector Sites 9-2
9.3.2. Near Detector Design 9-3
9.4. Cross-Section Uncertainties 9-4
9.5. The MINOS Near Detector 9-6
9.6. The MINERvA Detector 9-7
9.7. Auxiliary Near Detector Measurements 9-7
9.8. Test Beam Program 9-9
9.9. Conclusions 9-10
Chapter 9 References 9-10

10. Cosmic Ray Backgrounds and Active Shield 10-1
10.1. Introduction 10-1
10.2. Detailed Considerations—Muons 10-1
10.3. Detailed Considerations—Electrons and Photons 10-2
10.4. Detailed Considerations—Neutrons 10-2
10.5. Passive Overburden 10-2
10.6. Need for an Active Shield 10-3
10.7. Active Shield Design 10-3
10.8. Required R&D 10-4
Chapter 10 References 10-5

11. Far Detector Site and Building 11-1
11.1. Detector Site Criteria 11-1
11.2. Most Suitable Sites 11-1

11.2.1. Ash River Trail Site 11-1
11.2.2. Kjostad Lake Site 11-3
11.2.3. Mine Centre Site 11-4
11.3. Other Sites 11-4
11.4. Building 11-4
11.5. Research and Development Topics 11-5
Chapter 11 References 11-5

12. Proton Beam Requirements 12-1
12.1. Introduction 12-1
12.2. Proton Intensity Investment Strategy 12-1
12.3. Current Planning for Proton Intensity 12-1
12.4. Possible Accelerator Investments 12-2
12.5. NOvA and the NuMI Beamline with a Proton Driver 12-3
12.6. Summary on Proton Intensity 12-3
Chapter 12 References 12-4

13. Cost Estimate and Schedule 13-1
13.1. Introduction 13-1
13.2. Cost Estimate Methodology 13-1
13.3. The Baseline Detector Cost Estimate 13-1
13.3.1. Absorber 13-2
13.3.2. Liquid Scintillator Active Detector 13-2
13.3.3. Front End Electronics, Trigger and DAQ 13-2
13.3.4. Shipping 13-3
13.3.5. Installation 13-3
13.4. Other Project Costs 13-3
13.4.1. Far Detector Site, Building and Outfitting 13-3
13.4.2. Active Shield 13-3
13.4.3. Near Detector 13-3
13.4.4. Project Management and ES&H 13-3
13.4.5. Operating Costs 13-3
13.5. Contingency Analysis 13-4
13.6. Schedule 13-4
13.7. Evolution of the Cost Estimate 13-4
13.7.1. Solid Scintillator Active Detector 13-4
13.7.2. RPC Active Detector 13-6

Appendix. RPC Detector Description A-1
A.1. Overview A-1
A.2. Detector Design A-2
A.2.1. Module Geometry A-2
A.2.2. Absorber Planes A-3
A.2.3. Detector Unit A-3
A.2.4. RPC Chambers A-3
A.2.5. Readout Boards A-4
A.2.6. Performance of RPCs A-4
A.3. Readout Electronics A-6
A.3.1. Overview A-6
A.3.2. Front End ASIC A-6
A.3.3. Data Concentrator A-7

A.3.4. Data Collector A-7
A.3.5. VME Crate A-8
A.3.6. Physical Configuration on the Detector A-8
A.4. RPC High Voltage System A-8
A.4.1. Overview A-8
A.4.2. High voltage generation A-9
A.4.3. HV system control A-9
A.4.4. HV system power A-9
A.5. RPC Gas System A-9
A.5.1. Overview A-9
A.5.2. Barometric pressure changes A-10
A.5.3. Gas distribution, storage and circulation A-10
A.5.4. Control of gas contaminants A-11
A.5.5. Instrumentation A-11
A.6. Detector Construction A-11
A.6.1. RPC/Readout Board Assemblies A-11
A.6.2. RPC Construction A-11
A.6.3. Readout Boards A-12
A.6.4. Absorber Boards A-13
A.6.5. RRA Assembly A-14
A.6.5.1. Horizontal Readout Board Units A-14
A.6.5.2. Vertical Readout Boards A-14
A.6.5.3. RPC Layers on HRU A-14
A.6.5.4. HV, Signal and Gas Connections A-14
A.6.6. Detector Installation A-15
A.7. Cosmic Ray Active Shield A-17
A.8. Near Detector A-17
A.9. RPC ES&H Considerations A-17
A.9.1. Fire A-17
A.9.2. Lifting Heavy Loads A-17
A.9.3. Glass Handling Hazards A-17
A.9.4. Oxygen Deficiency Hazard A-17
A.9.5. Fall Protection A-18
A.10. R&D for the RPC Design A-18
A.10.1. RPC Parameters A-18
A.10.2. HV System Simplification A-18
A.10.3. Gas System Simplification A-18
A.10.4. Exploring a Monolithic RPC Design A-19
A.10.5. Exploring a Commercial Modular RPC Design A-19
Appendix References A-19

1. Executive Summary

1.1. The Physics of NOvA

The past two decades have seen great advances in our understanding of neutrinos. Underground experiments detecting neutrinos produced in the sun and in the earth's atmosphere have shown that neutrinos have mass and that they oscillate from one species to another as they travel. These oscillations arise because the neutrino species produced in particle decays (electron, muon, and τ-type neutrinos) do not have specific masses but are combinations of neutrino species (simply called 1, 2, and 3-type neutrinos) that do have specific masses. The average distance a neutrino travels before it oscillates is proportional to its energy and inversely proportional to the difference of the squares of masses of the underlying species of neutrinos. The probability that an oscillation will occur is related to a parameter known as a mixing angle.

The neutrinos that come from the sun are electron-type neutrinos that oscillate to muon and τ-type neutrinos, characterized by the mixing angle θ_{12} and an oscillation length (normalized to an energy of 2 GeV) of approximately 35,000 km. Neutrinos produced by cosmic rays in the earth's atmosphere are primarily muon-type neutrinos that oscillate to τ–type neutrinos, characterized by the mixing angle θ_{23}, and an oscillation length (again normalized to an energy of 2 GeV) of approximately 1,000 km. A third type of neutrino oscillation is possible: the oscillation of muon-type neutrinos to electron-type neutrinos at the atmospheric oscillation length. These neutrino oscillations, which so far have not been observed, would be characterized by the mixing angle θ_{13}. The study of this last category of neutrino oscillations is the main goal of NOvA (**N**uMI **O**ff-Axis ν_e **A**ppearance Experiment)[1].

The significance of the search for these oscillations is that if they exist, i.e., if θ_{13} is not zero, then we will ultimately be able to determine the ordering of the neutrino masses and measure CP violation in neutrino oscillations. There is widespread belief that the very small neutrino masses are related to physics at an extremely high-energy scale, one that cannot be studied directly with accelerator beams. There is also theoretical speculation that CP violation by neutrinos could be one aspect of understanding why the universe is composed solely of matter, rather than equal amounts of matter and antimatter.

MINOS is one of the first generation of long baseline accelerator-based neutrino oscillation experiments.[2] This Fermilab experiment, which has a 730 km baseline, will start taking data in early 2005. The MINOS Far Detector is located in the lowest level of the Soudan mine in northern Minnesota and it sits directly on the center of the Fermilab NuMI neutrino beam line. The physics goals of the MINOS experiment are to verify the atmospheric neutrino oscillations, to improve the measurement of their parameters, and to perform a low-sensitivity measurement of θ_{13}.

We are proposing NOvA to utilize Fermilab's investment in the NuMI beamline by building a second-generation detector, which will have the primary physics goal of measuring θ_{13} with approximately a factor of 10 more sensitivity than MINOS. To accomplish this we make three major improvements on the MINOS detector:

(1) We increase the mass of the detector by a factor of 9, from 5.4 kT for MINOS to 50 kT for

[1] It is also possible that in addition to the three types of neutrinos produced in particle decays and interactions, there could exist additional types of neutrinos that are not produced in these decays and interactions. There is unconfirmed evidence for the existence of this type of neutrino, called a sterile neutrino, from an experiment at Los Alamos National Laboratory. This result is currently being checked by a Fermilab experiment, MiniBooNE. If the existence of sterile neutrinos is confirmed, it will greatly enrich the already rich physics of neutrino oscillations. Searching for evidence of sterile neutrinos will be part of the NOvA physics program.

[2] The other two first-generation experiments are K2K, an experiment in Japan now running over a 250 km baseline, and CNGS, an experiment in Europe over a 730 km baseline, that will start in 2006.

NOvA. At the same time, we decrease the cost per kT by about a factor of 3.

(2) We design a detector that is optimized for the identification of electron-type neutrino events. Specifically, we increase the longitudinal sampling from once every 1.5 radiation lengths[3] in MINOS to once every 0.3 radiation lengths in NOvA.

(3) We position the detector not directly on the NuMI beam, as MINOS is, but 10 to 14 km off the central part of the beam. This provides more neutrino events in the energy range in which the oscillation takes place, and fewer background events.

Once a signal for electron-type neutrino appearance is seen, NOvA can run an antineutrino NuMI beam to attempt to measure the ordering of the neutrino masses. Whether this will be successful will depend on the parameters that nature has chosen. However, the sensitivity of NOvA can be markedly increased by a five-fold increase in the NuMI beam intensity created by the construction of the Fermilab Proton Driver. Smaller, but still quite significant, increases in NOvA sensitivity can be provided much sooner by modest investments in the Fermilab accelerator complex, for example, by reducing the Main Injector cycle time to give more protons per year on the NuMI beamline target.

Since there are three unknown parameters to be measured — θ_{13}, the ordering of the mass states, and the parameter that measures CP violation — a third measurement may eventually be required in addition to neutrino and antineutrino measurements in NOvA to determine all three parameters. The third measurement could be done by moving the NOvA detector, building an additional detector on the NuMI beamline, rebuilding the NuMI beamline to point in a slightly different direction, or combining NOvA measurements with those taken elsewhere on different length baselines. Such experiments are being contemplated in Europe and Japan.[4]

We view NOvA as a second step in a step-by-step Fermilab program to measure all of the unknown parameters of neutrino oscillations. Each step will provide guidance on the optimum direction for the succeeding step.

1.2. The NOvA Detectors

The NOvA Far Detector will be a sandwich detector, like MINOS, with alternating layers of passive absorber and active detector elements. The iron absorber of MINOS will be replaced by particleboard in order to increase the ratio of radiation length to mass. The active absorber in MINOS is solid scintillator strips read out through wavelength-shifting fibers to multi-anode photomultipliers. Our baseline design for NOvA calls for liquid scintillator encased in 14.6 m long 30-cell titanium dioxide-loaded PVC extrusions. The 4 cm wide liquid scintillator cells are read out by U-shaped wavelength-shifting fibers into avalanche photodiodes (APDs). This configuration gives better performance at lower cost than that of MINOS. The liquid scintillator is less expensive than solid scintillator and less costly to assemble. The APDs provide much higher quantum efficiency than photomultipliers and are cheaper. The high quantum efficiency of the APDs allows longer scintillator cells than those in MINOS.

However, this design is not without challenges. The APDs have very low gain requiring very low noise electronics. They must also be cooled to –15 C to reduce the noise level to an acceptable level. As part of our R&D plan for the coming year, we must verify the performance of the full liquid scintillator system.

---

[3] A radiation length is the average distance in which an electron loses 63% of its energy.

[4] T2K, a second-generation experiment being built in Japan, will send an off-axis beam from JPARC to the 50 kT SuperKamiokande detector over a 295 km baseline. It plans to begin operation in 2008. A possible future third-generation experiment on this baseline involves increasing the JPARC intensity by a factor of five and building a new detector with 20 times the mass of SuperKamiokande. There is discussion in Europe on building a third-generation experiment using a proposed CERN proton driver called the SPL. It would provide both a conventional neutrino beam and a beam based on the decay of accelerated ions (called a beta beam) over a 130 km baseline to a new, very massive detector to be built in the Frejus tunnel. It should be noted that neither of these proposed third-generation experiments would have a sufficiently long baseline to resolve the ordering of the neutrino mass states without NOvA data.

We have also developed an alternative technology for the active detectors — resistive plate chambers (RPCs) similar to those used in the BELLE experiment. We plan to review the R&D on both active detectors in December 2004 and come to a final decision on the active detector technology.

We have identified three acceptable sites for the Far Detector, two in Minnesota and one in Ontario. The baseline site is near Ash River, Minnesota, about 810 km from the NuMI target.

Unlike MINOS, the NOvA Far Detector will sit on the earth's surface. With the planned active shield on the top and sides of the detector, our calculations indicate that backgrounds from cosmic radiation will be acceptably low, largely due to the very short beam pulses from Fermilab, one 10 μs pulse every 2 seconds. Part of our R&D program is to verify these calculations with an experimental measurement in a prototype detector.

Like MINOS, NOvA will be a two-detector experiment. A small near detector with, as far as possible, the identical structure of the far detector will be constructed on the Fermilab site. Its function is to predict the expected rates of event types and their energy spectra in the far detector in the absence of oscillations. Differences seen between the events in the two detectors can then be attributed to oscillations.

We have constructed a detailed cost estimate for the full baseline experiment, including a generous contingency for items that have not yet been fully designed. The fully burdened cost in FY2004 dollars is 147.3 M$, of which 44.3 M$ is assigned to contingency.

Our technically driven schedule calls for Fermilab Stage 1 approval in June 2004, and a final active detector technology decision in December 2004, followed by full Fermilab approval in June 2005. Construction funding beginning October 2006 will allow the Near Detector and 15% of the Far Detector to be completed by October 2008, with the full Far Detector to be completed by the end of December 2011. Since the NuMI beam will be available throughout this entire period and the Far Detector is modular, we will be able to begin taking useful data in October 2008.

2. Introduction

In recent years, underground experiments have provided convincing evidence of neutrino oscillations of both solar and atmospheric neutrinos. With these measurements, we have an emerging framework with a rich structure in the lepton sector, which we can compare with a structure in the quark sector that has been studied for more than 25 years. An intriguing possibility is that CP violation exists in the lepton sector and that this asymmetry is somehow related to the fundamental matter-antimatter asymmetry of our Universe.

The flavor-changing transitions observed in atmospheric and solar neutrinos are most naturally described by a simple extension to the Standard Model, in which three types of neutrinos have masses and mix with each other. The three well-known flavor eigenstates, the electron, muon and tau neutrinos, are related to these mass eigenstates by the (3×3) unitary MNS matrix. The model explains the observed flavor-changing transitions as neutrino oscillations, described by mass differences Δm_{ij} and mixing angles θ_{ij} (which are parameters of the MNS matrix). The model also provides for CP violation in a natural way through a phase (δ) in the MNS matrix.

While measurements of atmospheric and solar neutrino oscillations have provided some information about the mass differences and two of the three mixing angles, we have (*e.g.,* from the CHOOZ reactor experiment) only an upper limit on the third mixing angle, θ_{13}. Measuring this parameter is key to obtaining a complete picture of the structure of the lepton sector. In particular, a non-zero value for θ_{13} is a prerequisite to both the ability to probe leptonic CP violation in the leptonic sector and to resolve the ordering of neutrino mass states. The latter can only be determined by matter effects, which occur when electron-type neutrinos propagate long distances through the earth. These measurements are the goal of the NuMI Off-Axis ν_e Appearance experiment (NOvA) described in this proposal.

Chapter 1 of the proposal provides an Executive Summary. Chapter 2 is this introduction. The body of the proposal begins with Chapter 3, which is a concise discussion of the physics motivation. This chapter provides a framework for understanding how the results of this proposed experiment relate to the results of other lepton sector experiments.

An overview of the proposed experiment is provided in Chapter 4. Essentially, we intend to measure electron neutrino appearance in a 50,000 metric ton far detector that will be located about 810 km from Fermilab and 10-14 km off the central axis of the NuMI beam. This off-axis location provides a lower energy, more monoenergetic neutrino beam, which is better suited for this measurement than the on-axis beam. A near detector will measure the electron neutrino content of the beam at Fermilab, characterize the detector response to neutrino events and perform crucial background studies. The NOvA Far Detector will be optimized to separate charged current electron-neutrino events from neutrino events producing neutral pions. The proposed detector is a planar tracking calorimeter with low-density, low-Z, wood absorber and active tracking elements located every 1/3 of a radiation length. In the baseline design, the active elements are ~540,000 cells filled with liquid scintillator. Each cell is 2.5 cm $\times$ 4 cm $\times$ 14.6 m and is grouped together with 29 other cells in a single PVC extrusion. The scintillator will be read out with wavelength-shifting fibers and avalanche photodiodes. We are also developing an alternate design with glass resistive plate chambers (RPCs) as the active tracking elements. This alternate is described in the Appendix.

Chapter 5 presents additional discussion of the possible contribution of this experiment to the ultimate understanding of the mixing parameters in the lepton sector and possible leptonic CP violation. It is likely that multiple experiments, possibly using both neutrino beams and neutrinos from reactors, will be required to fully measure the several leptonic mixing parameters. Chapter 6 provides information about the design methodology for the Far Detector and the several technologies that were considered in the design process. The details of the baseline detector design are described in Chapter 7. The detector consists of three mostly independent systems: the passive absorber, the active scintillator and the photodetectors. It is in many ways similar to the MINOS detector and the active detector design borrows heavily from

MINOS. Simulations of the NOvA Detector also make extensive use of the code developed for MINOS. These simulations have motivated a likelihood analysis algorithm for NOvA events. The details of this algorithm and the results of these simulations are described in Chapter 8. Chapter 9 discusses potential backgrounds to the electron neutrino oscillation signal and the use of the NOvA Near Detector in determining background levels in the Far Detector signal. Chapter 10 estimates the cosmic ray background resulting from the detector's location on the earth's surface and describes the active shield we plan to implement around the detector.

Chapter 11 provides information about three possible sites for the Far Detector, two in Minnesota and one in Ontario. The "baseline" site is close to the northernmost road in the United States near the NuMI beamline, known as the Ash River Trail. We also describe the preliminary design of the building required to house the detector.

The sensitivity of this experiment depends on the product of the detector acceptance—size and sensitivity—and the beam intensity. Chapter 12 discusses beam requirements for this experiment. We also discuss the impact of the proposed Fermilab Proton Driver on this program. Although the Proton Driver is not required for the first phase of the experiment, it provides a natural upgrade path for a Fermilab world-leading program in understanding the physics of the lepton sector. Chapter 13 summarizes our current cost and schedule estimates for the experiment. As already indicated, the Appendix provides additional information about resistive plate chambers (RPCs) as a tracking technology for the Far Detector.

In essence, we lay out in this proposal a major step in a program of experiments to study couplings in the lepton sector, with an eventual goal of measuring leptonic CP violation. NOvA is a natural next step after MINOS. Once this experiment determines the θ_{13}-coupling, it will be possible at Fermilab, likely with the Proton Driver, to go on to the next phase of mass hierarchy and leptonic CP measurements.

When the first neutrinos appear in the NuMI beamline about 9 months from now, they will represent a very significant step forward for particle physics. At a length of more than 800 km, the NOvA baseline will be nearly three times as long as the baseline in T2K (JPARC Phase 1) and somewhat longer than the baseline from CERN to Gran Sasso. Thus, with the NuMI beam, Fermilab has a unique capability to answer some of the most important questions that can be asked in elementary particle physics, both today and in the foreseeable future.

3. Physics Motivation

3.1. Introduction

Recently the SuperKamiokande [1], K2K [2] and Soudan 2 [3] experiments have provided very strong evidence that the muon neutrino undergoes flavor changing transitions. These transitions are seen for neutrinos whose path length divided by energy (L/E) is of order ~500 km/GeV. Super-Kamiokande also has some supporting evidence that muon neutrinos are transformed primarily into tau neutrinos. Although the SuperKamiokande detector has some sensitivity to flavor transitions of electron neutrinos, their data provides no evidence that electron neutrinos are involved in these transitions. In fact, the CHOOZ [4] reactor experiment provides a tighter constraint on the upper limit on the probability of electron neutrino flavor transitions of order 5-10%, at the values of L/E for which SuperKamiokande sees muon neutrino flavor transitions. This leaves open the interesting and important question: What is the role of the electron neutrino in flavor transitions at these values of L/E? A measurement or stringent limit on the probability of $\nu_\mu \rightarrow \nu_e$ for values of L/E of order 500 km/GeV is an important step in understand these neutrino flavor transitions in atmospheric neutrinos. As the NuMI beam is primarily a ν_μ beam, the observation of ν_e appearance would address this question directly. This measurement is the primary goal of the experiment described by this proposal.

The SNO [5] experiment has recently reported large transitions of solar electron neutrinos to muon and/or tau neutrinos both with and without salt added to the heavy water. SuperKamiokande [6] studying solar neutrinos and KamLAND [7] studying reactor neutrinos also see large electron neutrino flavor transitions. From a combined analysis, the L/E for these flavor transitions is a factor of ~30 times larger than the L/E for flavor transitions in atmospheric muon neutrinos. These transitions occur for an L/E such that the transition probability $\nu_\mu \rightarrow \nu_e$ measured by an experiment in the NuMI beam will also have some sensitivity to the flavor transitions associated with solar neutrinos through interference effects.

The LSND [8] experiment has reported small muon anti-neutrino to electron anti-neutrino transitions for values of L/E that are less than two orders of magnitude smaller than the transitions seen in atmospheric neutrinos. However this transition probability is very small, on the order of 0.3% of the one observed for atmospheric and solar neutrinos. If this result is confirmed by the mini-BooNE [9] experiment, this transition could be an important background for a measurement of $\nu_\mu \rightarrow \nu_e$ transitions at the larger values of L/E associated with atmospheric neutrinos.

3.2. Neutrino Mixing

Extensions to the Standard Model are required to explain the phenomena described here. The simplest and most widely accepted extension is to allow the neutrinos to have masses and mixings such that these phenomena are explained by neutrino oscillations. The masses and mixing of the neutrinos in these extensions would be the low energy remnant of some yet to be determined high energy physics. Thus, neutrino masses and mixing provide a unique window on physics that is inaccessible to current or near future collider experiments. One popular theory is the so called "seesaw" scenario where the active left handed neutrinos seesaw off their heavier right handed (sterile) partners leaving three very light Majorana neutrinos. It is already clear that the masses and mixings in the neutrino sector are very different from the masses and mixings in the quark sector and that a detailed understanding of the neutrino masses and mixings will be important in differentiating fermion mass theories. Also, they may provide the key to advancing our theoretical understanding of this fundamental question.

If the neutrinos have masses and mixings then the neutrino mass eigenstates, $\nu_i = (\nu_1, \nu_2, \nu_3, \ldots)$ with masses $m_i = (m_1, m_2, m_3, \ldots)$ are related to the flavor eigenstates $\nu_\alpha = (\nu_e, \nu_\mu, \nu_\tau, \ldots)$ by the equation

$$|\nu_\alpha\rangle = \sum_i U_{\alpha i} |\nu_i\rangle \qquad (1)$$

The charged weak current, for the neutrino flavor states, is given by $J_\lambda = \overline{\nu}_L \gamma_\lambda \ell_L$, where $\ell = (e, \mu, \tau)$ is the vector of charged lepton mass eigenstates. In the absence of light sterile neutrinos, the 3×3 lepton mixing matrix U is unitary. Lepton flavor mixing was first discussed (for the 2×2 case) by Maki, Nakagawa, and Sakata.

If we restrict the light neutrino sector to the three known active flavors and set aside the LSND results[1], then the unitary matrix MNS matrix, U, can be written as

$$U=\begin{pmatrix} c_{13}c_{12} & c_{13}s_{12} & s_{13}e^{-i\delta} \\ -c_{23}s_{12}-s_{13}s_{23}c_{12}e^{i\delta} & c_{23}c_{12}-s_{13}s_{23}s_{12}e^{i\delta} & c_{13}s_{23} \\ s_{23}s_{12}-s_{13}c_{23}c_{12}e^{i\delta} & -s_{23}c_{12}-s_{13}c_{23}s_{12}e^{i\delta} & c_{13}c_{23} \end{pmatrix} \quad (2),$$

where $c_{jk} \equiv \cos\theta_{jk}$ and $s_{jk} \equiv \sin\theta_{jk}$.

With this labeling, the atmospheric neutrinos oscillations are primarily determined by the θ_{23} and Δm^2_{32} parameters, whereas the solar neutrino oscillations depend on θ_{12} and Δm^2_{12}, where $\Delta m^2_{ij} = m^2_i - m^2_j$. From SuperKamiokande we already have some knowledge of $|\Delta m_{32}{}^2| = (1.5 - 3.5)\times10^{-3}$ eV^2 and $0.35 < \sin^2\theta_{23} < 0.65$ (*i.e.*, $\sin^2 2\theta_{23} > 0.91$). Note the substantial uncertainty in these atmospheric measurements. In contrast, the combined analysis of the SNO, SK and KamLAND experiments gives $\Delta m^2_{21} = +7.1 \pm 2.0 \times 10^{-5}$ eV^2 and $\sin^2\theta_{12} = 0.5$ excluded at more than 5σ. This corresponds to $0.71 < \sin^2 2\theta_{12} < 0.91$. For the purposes of this experiment our knowledge of the solar parameters is already in good shape and is expected to improve with time.

CHOOZ (and SuperK) provide us with a limit on $\sin^2 2\theta_{13} < 0.18$. The CHOOZ limit is dependent on the input value used for $|\Delta m_{32}{}^2|$; for the current central value 2.5×10^{-3} eV^2, this limit is $\sin^2 2\theta_{13} < 0.14$, while for $|\Delta m_{32}{}^2| = 2.0\times10^{-3}$ eV^2, it is $\sin^2 2\theta_{13} < 0.18$ [4]. Thus, the proposed long-baseline neutrino oscillation experiment to search for $\nu_\mu \rightarrow \nu_e$ will be sensitive to a substantial range below this upper bound.

The MINOS experiment [10] will provide a 10% measurement of the atmospheric Δm^2_{32} but probably will not improve our knowledge of θ_{23}. This experiment has sensitivity to $\sin^2 2\theta_{13}$ only about a factor of two below the CHOOZ bound. Any future reactor experiment to measure $\sin^2 2\theta_{13}$ could improve our knowledge of this important parameter but such an experiment has no sensitivity to θ_{23}, the sign of Δm^2_{32} or the CP violating phase δ. Therefore, such a reactor experiment is truly complementary to long-baseline experiments to observe $\nu_\mu \rightarrow \nu_e$.

The appearance probability of ν_e in a ν_μ beam in vacuum is given, to leading order, by

$$P_{vac}(\nu_\mu \rightarrow \nu_e) = \sin^2\theta_{23}\sin^2 2\theta_{13}\sin^2\Delta_{atm} \quad (3),$$

where $\Delta_{atm} \approx 1.27\left(\frac{\Delta m^2_{32}L}{E}\right)$. If the experiment is performed at one of the peaks of this probability, that is, when $\Delta_{atm} = \frac{\pi}{2} + n\pi$, then

$$P_{vac}(\nu_\mu \rightarrow \nu_e) = \frac{1}{2}\sin^2 2\theta_{13} = 2.5\%\left(\frac{\sin^2 2\theta_{13}}{0.05}\right) \quad (4)$$

The first peak occurs at neutrino energy,

$$E = 1.7\ \text{GeV}\left(\frac{\Delta m^2_{32}}{2.5\times10^{-3}\text{eV}^2}\right)\left(\frac{L}{820\ \text{km}}\right) \quad (5)$$

The constraint on $\sin^2(2\theta_{13})$ from the CHOOZ experiment varies from 0.14 to 0.18 depending on the atmospheric Δm^2_{32}, therefore the maximum appearance probability ranges from ~7 to 9%. To be effective any ν_e appearance experiment has to aim to exclude or convincingly see a signal at least an order of magnitude below this 7% limit.

3.3. Matter Effects

The neutrinos in the NuMI beam propagate through the Earth and matter induced contributions to the propagation amplitude are non-negligible. These matter effects have opposite sign for neutrinos and anti-neutrinos and for the normal versus inverted neutrino mass hierarchies. The matter effects can be thus used to distinguish the two possible three-neutrino mass hierarchies, see Fig. 3.1. If the experiment is performed at the first peak in the oscillation, as above, the matter effects are primarily a function of the energy of the neutrino beam and the transition probability in matter can be approximated by

$$P_{mat}(\nu_\mu \rightarrow \nu_e) \approx \left(1 \pm 2\frac{E}{E_R}\right)P_{vac}(\nu_\mu \rightarrow \nu_e) \quad (6),$$

where E_R is the matter resonance energy associated with the atmospheric Δm^2, that is

[1] In the 3+1 neutrino mass hierarchy the LSND result can be accommodated as a perturbation on the pure active 3 neutrino hierarchy. The 2+2 mass hierarchy would require major modifications.

$$E_R = \frac{\Delta m^2_{32}}{2\sqrt{2}G_F N_e} =$$
$$12\ \text{GeV}\left(\frac{\Delta m^2_{32}}{2.5\times10^{-3}\ \text{eV}^2}\right)\left(\frac{1.4\ \text{g cm}^{-3}}{Y_e\rho}\right) \quad (7),$$

where N_e is the electron number density in the earth, ρ is the matter density (2.8 g.cm^{-3}) and $Y_e = \frac{1}{2}$ is the electron fraction.

For the normal hierarchy, matter effects enhance (suppress) the transition probability for neutrinos (anti-neutrinos) and vice versa for the inverted hierarchy. For a 2 GeV neutrino energy, matter effects give a 30% enhancement or suppression in the transition probability.

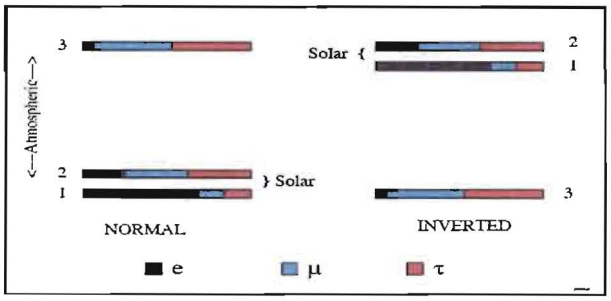

Fig. 3.1: The two allowed three-neutrino mass squared spectra that account for the oscillations of solar and atmospheric neutrinos. The normal spectrum has $\Delta m^2_{32} > 0$ and the inverted has $\Delta m^2_{32} < 0$. The ν_e fraction of each mass eigenstate is indicated by the black solid region, whereas the ν_μ (ν_τ) fraction is indicated by the blue-green right-leaning (red left-leaning) hatching. The ν_e fraction in the mass eigenstate labeled, 3, has been enhanced for clarity.

3.4. CP Violation

Now that the solution to the solar neutrino puzzle consistent with neutrino oscillations is the "Large Mixing Angle" (LMA) region the $\nu_\mu \to \nu_e$ transition probability is sensitive to sub-leading effects and in particular to the CP violating phase δ.

In vacuum the shift in the transition probability associated with the CP violating phase is given by

$$\Delta P_\delta(\nu_\mu \to \nu_e) \approx J_r \sin\Delta_{sol}\sin\Delta_{atm}(\cos\delta\cos\Delta_{atm} \mp \sin\delta\sin\Delta_{atm}) \quad (8),$$

where the minus (plus) sign is for neutrinos (anti-neutrinos),

$$J_r = \sin2\theta_{12}\sin2\theta_{23}\sin2\theta_{13}\cos\theta_{13}$$
$$J_r \approx 0.9\sin2\theta_{13} \quad (9)$$

$$\Delta_{sol} = 1.27\frac{\delta m^2_{21}L}{E} = \frac{\delta m^2_{21}}{\delta m^2_{32}}\Delta_{atm} \approx \frac{1}{36}\Delta_{atm}. \quad (10)$$

At the first oscillation maximum of the atmospheric Δm^2 scale, the shift in the transition probability dependent on δ is of order

$$\left|\Delta P_\delta(\nu_\mu \to \nu_e)\right| \sim 0.6\%\sqrt{\frac{\sin^2 2\theta_{13}}{0.05}} \quad (11)$$

Note that is shift is proportional to $\sqrt{\sin^2 2\theta_{13}}$, while the leading term is proportional to $\sin^2 2\theta_{13}$. Thus, the relative importance of the sub-leading terms grows as $\sin^2 2\theta_{13}$ gets smaller.

The full transition probability, in vacuum, is given by

$$P(\nu_\mu \to \nu_e) = \left|\sum_{j=1}^{3} U^*_{\mu j}U_{ej}e^{-i(m^2_j L/2E)}\right|^2 \quad (12)$$
$$= \left|2U^*_{\mu3}U_{e3}e^{-i\Delta_{32}}\sin\Delta_{31} + 2U^*_{\mu2}U_{e2}\sin\Delta_{21}\right|^2$$

The second form of this probability is especially illuminating as the first term is the amplitude for $\nu_\mu \to \nu_e$ associated with the atmospheric Δm^2 and the second term the amplitude associated with the solar Δm^2. The interference between these two amplitudes differs for neutrinos and anti-neutrinos because for anti-neutrinos the U matrix is replaced with U^*. This difference in the interference term leads to the difference in the transition probability $\nu_\mu \to \nu_e$ between neutrino and anti-neutrinos. Such an effect is an example of CP violation.

Using the MNS mixing matrix given in Eq. 2,

$$2U^*_{\mu3}U_{e3} = e^{-i\delta}\sin2\theta_{13}\sin\theta_{23}$$
$$2U^*_{\mu2}U_{e2} = \sin2\theta_{12}\cos\theta_{23}\cos\theta_{13} + O(\sin\theta_{13}) \quad (13)$$

Since the $O(\sin\theta_{13})$ term is multiplied by $\sin(\Delta_{21})$ in the amplitude, it is quadratic in the small quantities sin θ$_{13}$ and the solar Δm^2 and therefore can be neglected.

$$P(\nu_\mu \to \nu_e) =$$
$$\left|e^{-i(\Delta_{32}+\delta)}\sin2\theta_{13}\sin\theta_{23}\sin\Delta_{31}\right. \quad (14)$$
$$\left.+\sin2\theta_{12}\cos\theta_{23}\cos\theta_{13}\sin\Delta_{21}\right|^2$$

$$P(\nu_\mu \to \nu_e) =$$
$$\sin^2\theta_{23}\sin^2 2\theta_{13}\sin^2\Delta_{31}$$
$$+\cos^2\theta_{13}\cos^2\theta_{23}\sin^2 2\theta_{12}\sin^2\Delta_{21} \quad (15)$$
$$+J_r \sin\Delta_{21}\sin\Delta_{31}$$
$$(\cos\Delta_{32}\cos\delta - \sin\Delta_{32}\sin\delta)$$

The first and second terms are the probability of $\nu_\mu \to \nu_e$ associated with the atmospheric and solar Δm^2 's respectively, whereas the third term is the interference between these two probabilities. The term proportional to sin δ is responsible for CP violation since it changes sign when going from neutrinos to anti-neutrinos[2].

To show the growing importance of the CP violating term as $\sin^2 2\theta_{13}$ gets smaller we have plotted the neutrino anti-neutrino asymmetry, $|P_\nu - P_{\bar\nu}|/(P_\nu + P_{\bar\nu})$ versus $\sin^2 2\theta_{13}$ in Fig. 3.2 at the first oscillation maximum assuming maximum CP violation, *i.e.* $\Delta_{31} = \pi/2$ and $\delta = \pi/2$. The asymmetry grows as $\sin^2 2\theta_{13}$ gets smaller until the amplitude for $\nu_\mu \to \nu_e$ from the atmospheric Δm^2 is equal in magnitude to the amplitude from the solar Δm^2. At this value of $\sin^2 2\theta_{13}$ there is maximum destructive (constructive) interference for neutrinos (anti-neutrinos) and therefore a maximum asymmetry of unity. The value of $\sin^2 2\theta_{13}$ at this peak asymmetry is given by

$$\sin^2 2\theta_{13}\,|_{peak} \approx \frac{\sin^2 2\theta_{12}}{\tan^2\theta_{23}}\left(\frac{\pi}{2}\frac{\Delta m^2_{21}}{\Delta m^2_{31}}\right)^2 \sim 0.002 \quad (16)$$

Even at the CHOOZ bound for $\sin^2 2\theta_{13}$ the asymmetry is greater than 20%. This asymmetry scales as sin δ for values of δ away from π/2.

[2] The inclusion of the $O(\sin\theta_{13})$ terms in $U^*_{\mu 2}U_{e2}$ gives the full expression for $P(\nu_\mu \to \nu_e)$ by multiplying the first term by $\left(1 - 2\sin^2\theta_{12}\sin\Delta_{12}\cos\Delta_{32}/\sin\Delta_{31}\right)$ and the second term by $\left|1 - e^{-i\delta}\sin\theta_{13}\tan\theta_{12}\tan\theta_{23}\right|^2$, while the third term is unchanged. Both of these factors are very close to unity for any reasonable NuMI experimental setup. Equivalent expressions for $P(\nu_\mu \to \nu_e)$ can be found in [11].

3.5. Ambiguity Resolution

The effects of matter can easily be included in our expression for $P(\nu_\mu \to \nu_e)$ by replacing $\sin^n\Delta_{21}$ and $\sin^n\Delta_{31}$ for all n in all three terms using

$$\sin\Delta_{ij} \to \frac{\Delta_{ij}}{(\Delta_{ij} \mp aL)}\sin(\Delta_{ij} \mp aL) \quad (17)$$

where

$$a = \frac{G_F N_e}{\sqrt{2}} \approx (3700\ \text{km})^{-1}\left(\frac{\rho}{2.8\ \text{g cm}^{-3}}\right) \quad (18)$$

The minus (plus) sign is for neutrinos (anti-neutrinos). The factors $\sin\Delta_{32}$ and $\cos\Delta_{32}$ remain unchanged by matter effects. This algorithm comes from the invariance of the product $\Delta m^2_{ij}\sin 2\theta_{ij}$ evaluated in matter and in vacuum.

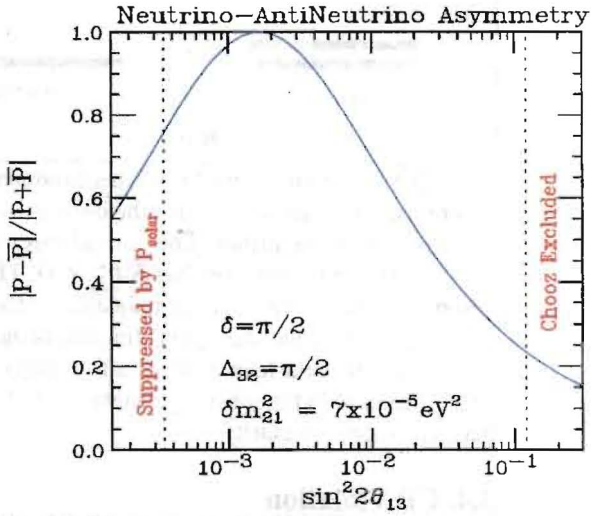

Fig. 3.2: The vacuum asymmetry $\left|P(\nu_\mu \to \nu_e) - P(\bar\nu_\mu \to \bar\nu_e)\right| / \left|P(\nu_\mu \to \nu_e) + P(\bar\nu_\mu \to \bar\nu_e)\right|$ versus $\sin^2 2\theta_{13}$ at oscillation maximum, Δ_{32} assuming that the CP violation is maximal, $\delta = \pi/2$. At the peak of this asymmetry the amplitudes for $\nu_\mu \to \nu_e$ from the atmospheric and solar Δm^2's are equal in magnitude. Above (below) the peak the atmospheric (solar) amplitude dominates.

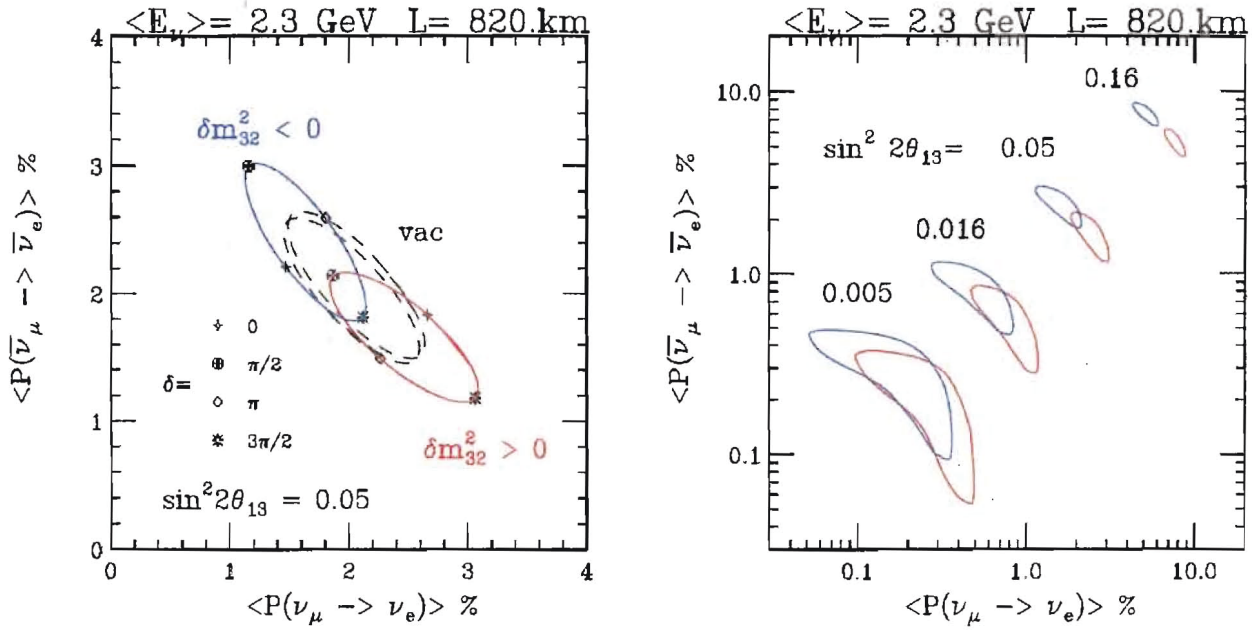

Fig. 3.3: The bi-probability plots $P(\nu_\mu \rightarrow \nu_e)$ versus $P(\overline{\nu}_\mu \rightarrow \overline{\nu}_e)$, assuming a constant matter density of ρ = 2.8 ~g. cm^{-3} at a distance of 820 km and an average energy of 2.3 GeV with a 20% Gaussian spread. The mixing parameters are fixed to be $|\Delta m^2_{31}| = 2.5\times10^{-3}$ eV^2, $\sin^2 2\theta_{23} = 1.0$, $\Delta m^2_{21} = +7\times10^{-5}$ eV^2, $\sin^2 2\theta_{12} = 0.8$ with the labeled values of $\sin^2 2\theta_{13}$ and δ.

A useful and instructive way to present the combined effects of matter and sub-leading terms is in the bi-probability plots of $P(\nu_\mu \rightarrow \nu_e)$ versus $P(\overline{\nu}_\mu \rightarrow \overline{\nu}_e)$, invented by Minakata and Nunokawa [13]. Fig. 3.3 shows an example of such a plot for a NuMI case.

At the larger values of $\sin^2 2\theta_{13}$, the ellipses associated with the two possible mass hierarchies separate in matter, whereas they are approximately degenerate in vacuum. There is also a significant sensitivity to the CP violating phase, δ. It is the sensitivity to the sign of Δm^2_{32} and the CP violating phase in these plots which allows for the determination of these parameters in a sufficiently accurate experiment. For a single experiment there can be a degeneracy in the determined parameters but this degeneracy can be broken by further experimentation.

In particular the normal and inverted hierarchies may also be able to be distinguished by a comparison of the probability of $\nu_\mu \rightarrow \nu_e$ between two different experiments at different baselines, e.g. NuMI and JPARC [12]. If both experiments operated at the first oscillation and both run neutrinos then

$$P^N_{mat}(\nu_\mu \rightarrow \nu_e) \cong \left(1 \pm 2\frac{E^N - E^J}{E_R}\right) P^J_{mat}(\nu_\mu \rightarrow \nu_e) \quad (19)$$

where (P^N, E^N) and (P^J, E^J) are the neutrino transition probabilities and energies for NuMI and JPARC respectively. E_R is the matter resonance energy associated with the atmospheric Δm^2, about 12 GeV, given by eqn. 7. The plus sign is for the normal hierarchy and the minus sign for the inverted hierarchy. For anti-neutrinos these signs are reversed. If either experiment is significantly away from oscillation maximum, the relationship between the two probabilities is more complicated, see [14].

3.6. Other NOvA Measurements

A high precision measurement of $\nu_\mu \rightarrow \nu_\mu$ can be used to determine the atmospheric Δm^2 to the 10^{-4} eV^2 level. Also $\sin^2 2\theta_{23}$ will be determined to 2%. Such a measurement can determine how much θ_{23} differs from maximal mixing, *i.e.*, π/4. This difference is a measure of the breaking of a $\nu_\mu \rightarrow \nu_\tau$ symmetry at some high energy scale. Since matter effects are suppressed in the channel

$\nu_\mu \rightarrow \nu_\mu$ compared to $\nu_\mu \rightarrow \nu_e$, a comparison of $\nu_\mu \rightarrow \nu_\mu$ to $\overline{\nu}_\mu \rightarrow \overline{\nu}_\mu$ is a sensitive test of CPT in the neutrino sector.

3.7. Neutrino Oscillations in 2010

While we have discussed the current status of neutrino oscillations, NOvA will not likely acquire data for a number of years. Thus, although speculative, it is likely worthwhile to attempt to predict the state of knowledge in 5 to 7 years time. There is considerable ongoing activity with respect to solar neutrino oscillations. Thus, by 2010, it is reasonable to expect that the solar Δm^2 and sin $2\theta_{12}$ will be known well enough that they will not be a major source of uncertainty in the interpretation of NOvA results. We also presume that MINOS will have made a 10% measurement of Δm^2_{32}. The JPARC to SuperKamiokande experiment has been delayed to 2008, so it may have only preliminary results by 2010. There has been considerable recent discussion of new reactor-based neutrino oscillation experiments, but the technical and regulatory difficulties of working near a nuclear power plant make prediction of a timescale for those experiments quite uncertain.

3.8. Summary

The important measurements that could be made by NOvA are

- Observation of $\nu_\mu \rightarrow \nu_e$ at an L/E in the range of 10^2 to 10^3 km/GeV, which would determine the ν_e role in atmospheric neutrino flavor transitions. In the neutrino oscillation scenario this is a measure of $\sin^2 2\theta_{13}$.
- Matter effects can be used to distinguish the two mass hierarchies and therefore determine the sign of Δm^2_{32}.
- For the Large Mixing Angle solution to the solar neutrino puzzle there is sensitivity to the CP violating phase in the channel $\nu_\mu \rightarrow \nu_e$.
- Precision measurements in $\nu_\mu \rightarrow \nu_\mu$ channel can measure how close θ_{23} is to $\pi/4$, that is maximal mixing. A comparison of $\nu_\mu \rightarrow \nu_\mu$ to $\overline{\nu}_\mu \rightarrow \overline{\nu}_\mu$ is a sensitive test of CPT violation since matter effects are suppressed in this channel.

Thus, there is a very rich neutrino physics program to be explored in a ν_e appearance experiment using the NuMI beam. Details of experimental and beam possibilities will be explored in subsequent chapters.

Chapter 3 References

[1] Kamiokande Collaboration, Y. Fukuda *et al.*, Phys. Lett. B **335** (1994) 237.
Super-Kamiokande Collaboration, Y. Fukuda *et al.*, Phys. Rev. Lett. **81** (1998) 1562; S. Fukuda *et al.*, *ibid.* **85** (2000) 3999.
[2] K2K Collaboration, M. H. Ahn *et al.*, Phys. Lett. B **511** (2001) 178; Phys. Rev. Lett. **90**, 041801 (2003).
[3] Soudan 2 Collaboration, M. Sanchez *et al.*, Phys. Rev. D **68**, 113004 (2003).
[4] CHOOZ collaboration, M. Apollonio *et al.*, Phys. Lett. B **466** 415.
[5] SNO Collaboration, Q. R. Ahmad *et al.*, Phys. Rev. Lett. **87** (2001) 071301;
S. N. Ahmed *et al.*
[6] S. Fukuda *et al.* [Super-Kamiokande Collaboration], Phys. Lett. B **539**, 179 (2002).
[7] K. Eguchi *et al.* [KamLAND Collaboration], Phys. Rev. Lett. **90**, 021802 (2003).
[8] A. Aguilar *et al.* [LSND Collaboration], Phys. Rev. D **64**, 112007 (2001).
[9] E. Church *et al.* [BooNe Collaboration], FNAL-PROPOSAL-0898.
[10] E. Ables *et al.* [MINOS Collaboration], FERMILAB-PROPOSAL-0875.
[11] V. D. Barger, S. Geer, R. Raja and K. Whisnant, Phys. Rev. D **63**, 113011 (2001), I. Mocioiu and R. Shrock, JHEP **0111**, 050 (2001).
[12] H. Minakata and H. Nunokawa, JHEP **0110** (2001) 001 [hep-ph/0108085].
[13] Y. Itow *et al.*, [The JHF-Kamioka neutrino project], arXiv:hep-ex/0106019.
[14] H. Minakata, H. Nunokawa and S. Parke, Phys. Rev. D **68**, 013010 (2003).

4. Experiment Overview

4.1. NuMI Beam

The NuMI neutrino beam is currently under construction at Fermilab [1]. The beamline begins with 120 GeV protons extracted from the Main Injector accelerator, which are transported downward at a 15.8% slope to the NuMI Target Hall. Before striking the production target the beam is bent upward to a 5.8% downward slope, so that it is aimed at the MINOS far detector in Minnesota. Two parabolic magnetic horns, each about 3 m long and pulsed at 200 kA, focus secondary pions and kaons emitted from the target. The secondary beam subsequently travels with the same downward slope of 5.8% through an evacuated decay pipe, which is 675 m in length and 2 m in diameter. The decay pipe ends in the Hadron Absorber Hall where residual protons and non-decayed secondary mesons are absorbed in the Al-Fe water-cooled beam stop. The muons resulting from pion and kaon decays are absorbed in 240 m of earth shielding, which separates the Absorber Hall from the Near Detector Hall. Three muon alcoves, located within this shielding downstream of the Absorber Hall, contain muon detectors to monitor the beam intensity and shape on a pulse-to-pulse basis. Fig 4.1 shows the plan and elevation views of the NuMI beamline.

A unique feature of the NuMI neutrino beam is the ability to change the focusing optics configuration and hence the neutrino energy band accepted. Specifically, one can change the relative positions of the target and the first horn and the separation between two horns. These configurations are illustrated in Fig. 4.2, together with the spectra for three possible beam element arrangements, referred to as low, medium, or high energy beam tunes. While the movement of the second horn is logistically complex and requires several weeks downtime, the target position can be varied remotely. Accordingly, one also has a method of readily changing the energy spectrum in a continuous fashion by moving just the target at a small sacrifice of the neutrino flux as compared to a fully optimized configuration [2].

Full optimization for a given energy also involves adjusting the target length. The initial beam for the MINOS experiment is the low energy tune, with the front end of the target located 0.34 m upstream of the first horn and a horn separation of 7 m. The target is 0.95 m long and is composed of 47 graphite sections, each 20 mm in length, with 0.3 mm air gaps between sections.

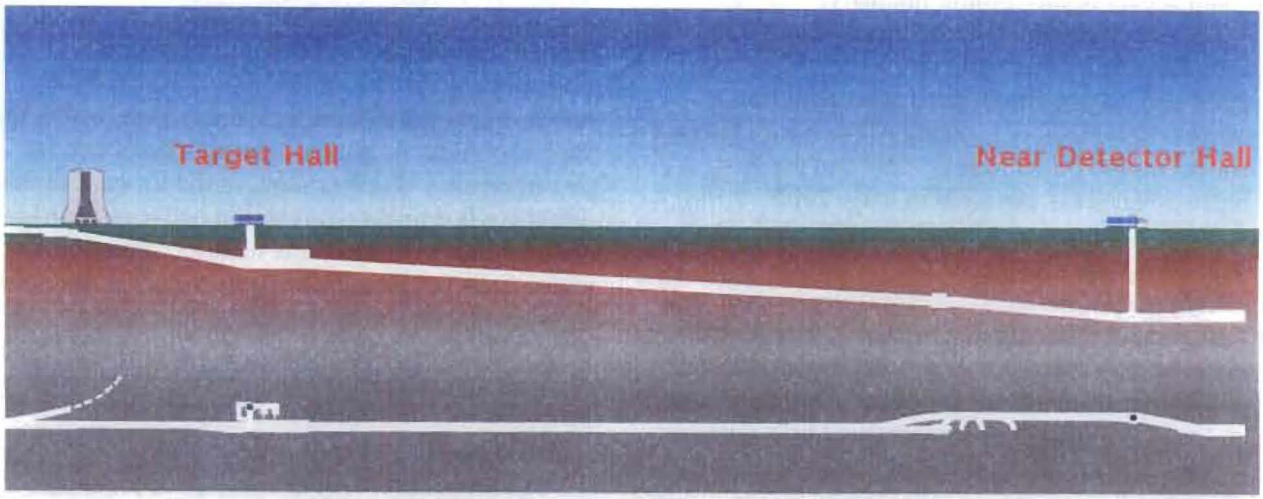

Fig. 4.1: Plan (bottom) and elevation (top) views of the NuMI beam line.

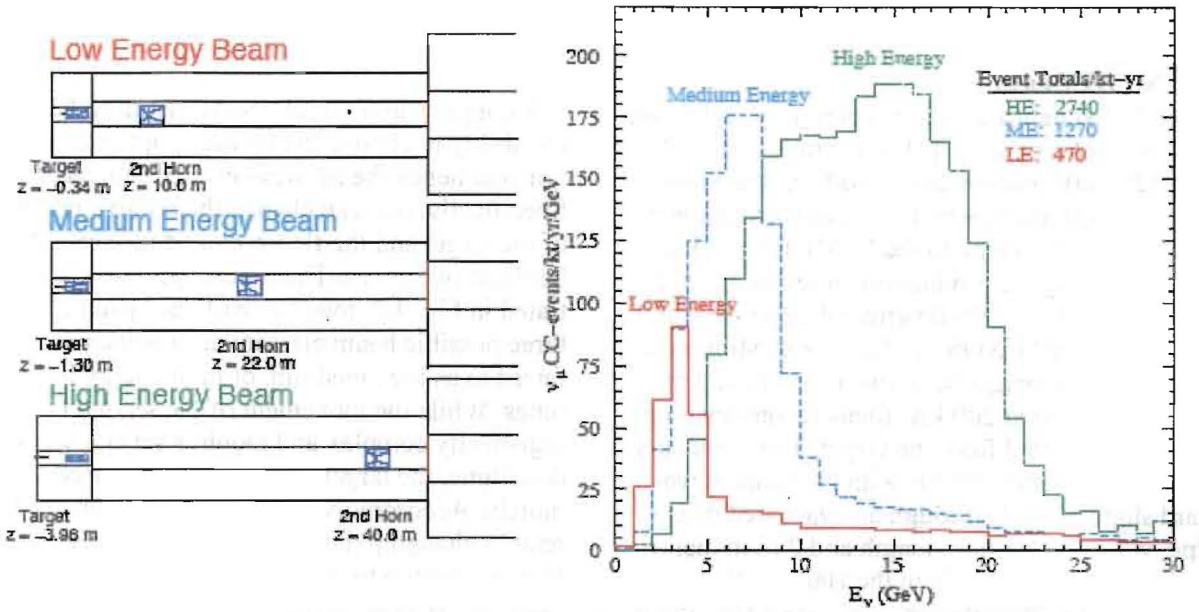

Fig. 4.2: Left: The locations of the target and second horn for the three NuMI beam configurations. Right: The expected neutrino interaction rates at the MINOS far detector site for each of the three beam tunes assuming 3.7 x 10^{20} protons on target per year.

The NuMI beam has been designed for a proton intensity of 4 x 10^{13} protons per pulse every 1.9 sec—roughly 0.4 MW of beam power. Based on previous operating experience of the proton source, this per pulse intensity should produce 3.7 x 10^{20} protons per year. It appears quite likely that the beam line itself, with minor modifications, could accept higher proton intensity.

The outfitting of the NuMI beam tunnels and the associated buildings was completed in October 2003 and installation in the Target Hall has started. Beneficial occupancy of the Near Detector Hall occurred on 10 March 2004 and the first beam on target is expected in early 2005.

4.2. Off-Axis Concept

Pions and kaons decay isotropically in their centers of mass resulting in a relatively broad neutrino beam energy spectrum. For small angles, the flux and energy of neutrinos produced from the decay $\pi \rightarrow \mu + \nu$ in flight and intercepted by a detector of area A and located at distance z are given in the lab frame by:

$$F = \left(\frac{2\gamma}{1+\gamma^2\theta^2}\right)^2 \frac{A}{4\pi z^2} \qquad (1)$$

$$E_\nu = \frac{0.43 E_\pi}{1+\gamma^2\theta^2}, \qquad (2)$$

where θ is the angle between the pion direction and the neutrino direction, E_π the energy of the parent pion, m_π the mass of the pion and $\gamma = E_\pi/m_\pi$. The expressions for the neutrinos from the corresponding charged K decays are identical except that 0.43 is replaced by 0.96 resulting in a more energetic and broader distribution for identical meson energies. The neutrino flux peaks in the forward direction for all meson energies, which is the reason that, in general, neutrino detectors are placed on axis. Furthermore, in the forward direction there is a linear relationship between neutrino and meson energies. As the neutrino direction deviates from the meson direction, however, the relationship between the pion energy and neutrino energy flattens. At some angles, a wide energy band of pions contributes to roughly the same energy neutrinos. Fig. 4.3 illustrates both features.

The angle-energy relationship illustrated in Fig. 4.3 can be utilized to construct a nearly monoenergetic neutrino beam by viewing the NuMI beam with a detector at a location off the beam axis. This concept was first proposed for the experiment E-889 at the Brookhaven National

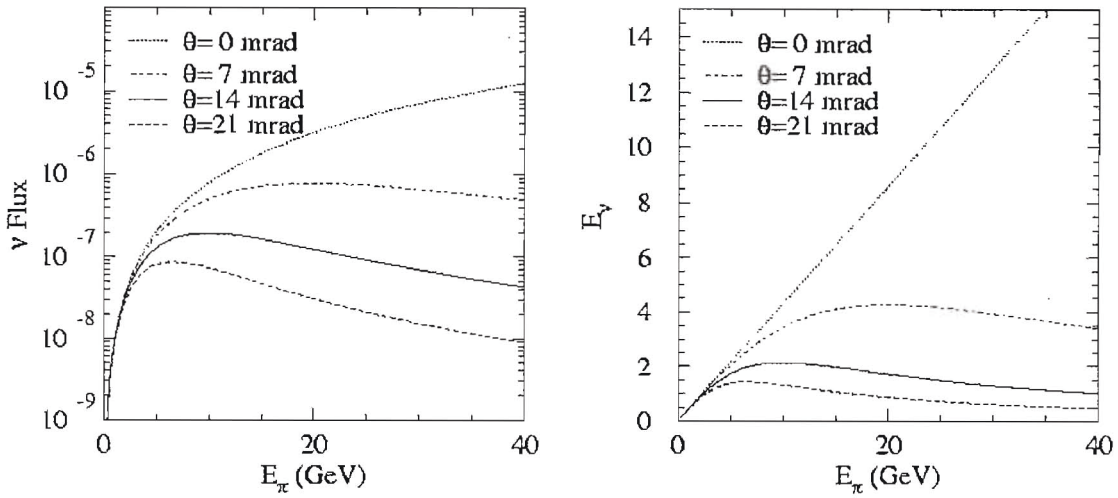

Fig. 4.3: Left: The neutrino flux from a pion of energy E_π as viewed from a site located at an angle θ from the beam axis. The flux has been normalized to a distance of 800 km. Right: The energy of the neutrinos produced at an angle θ relative to the pion direction as a function of the pion energy.

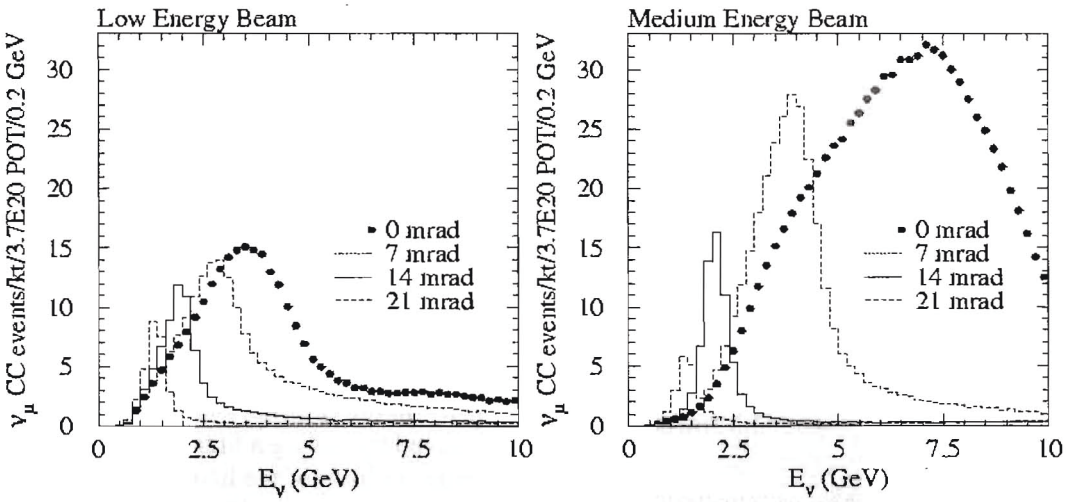

Fig. 4.4: CC ν_μ event rates expected under a no-oscillation hypothesis at a distance of 800 km from Fermilab and at various transverse locations for the NuMI low-energy beam configuration (left) and medium-energy beam configuration (right).

Laboratory [3]. Fig. 4.4 shows the implementation of this scheme at locations of 5, 10, and 20 km (corresponding to the angles of 7, 14, and 21 mr) off the NuMI beam axis at a distance of 800 km from the target.

The off-axis configuration has several important advantages for a $\nu_\mu \rightarrow \nu_e$ oscillation experiment. Among the most important ones are:

- The central energy of the beam can be tuned to the desired energy by selecting an appropriate angle with respect to the beam axis for the location of the detector.
- The spectrum in the peak is quite narrow which helps to reduce the backgrounds, which tend to have much broader energy distributions.

• The high energy tail is considerably reduced with respect to the on-axis beam, which reduces the NC and τ backgrounds

These features are quite apparent from Figs. 4.3 and 4.4.

Finally, we would like to make several additional observations about the properties of the off-axis configuration:

• The energy of the beam is determined primarily by the transverse location of the detector. The dependence on the focusing optics is relatively mild.

• The focusing optics configuration affects primarily the intensity of the beam.

• The main peak is composed almost exclusively of the neutrinos from pion decay; K decays give neutrinos at significantly wider angles. Thus, prediction of the spectrum is very insensitive to knowledge of the K/π production ratio.

For the current range of Δm_{13}^2 values and the three nominal NuMI beam configurations, the medium energy one gives the optimum spectrum for the $\nu_\mu \rightarrow \nu_e$ oscillation experiment. Additional fine tuning of the optics as well of the target geometry around the medium energy configuration should yield some additional optimization.

4.3. Detector Design Considerations

4.3.1. General Goals: The challenge for next generation neutrino experiments is to observe $\nu_\mu \rightarrow \nu_e$ oscillations in the atmospheric neutrino mass squared range down to the level of few parts per thousand. The CHOOZ experiment gives a limit on ν_e disappearance probability in that experiment of about 0.1 – 0.2 [4], the exact limit depending on the value of Δm_{23}^2. This translates into a limit on ν_e appearance probability of 0.05 – 0.1. MINOS is expected to improve this by a factor of 2-3. There are no clear reliable theoretical guidelines as to the most likely value of this parameter.

Charged current ν_e interactions can be identified by the presence of an electron in the final state. The experimental backgrounds to the $\nu_\mu \rightarrow \nu_e$ oscillation signals arise from two general sources. There are genuine events with electrons resulting from the intrinsic ν_e component in the beam and from τ decays produced in the charged current ν_τ interactions from $\nu_\mu \rightarrow \nu_\tau$ oscillations. The latter background is very small for NOvA since most of the ν_μ flux is below τ production threshold. In addition there are potentially misidentified NC events or high y ν_μ CC events where one or more π^0's in the final state masquerades as an electron or, less likely, that a hadron is misidentified as an electron.

The intrinsic ν_e's in the beam come from μ decays and Ke_3 decays (charged and neutral). They are of the order of 0.5-1.0% of ν_μ's, but can be reduced further by an appropriate energy cut. Ke_3 contamination is typically of the order of 1/5 of the μ decay background in NOvA.

The experimental challenge has two parts:

• reducing these two backgrounds as much as possible (discussed below)

• measuring these backgrounds well enough that the principal ultimate uncertainty comes from the statistical fluctuations in the event sample of interest (discussed in Chapter 9).

4.3.2. Design Optimization Issues: The background from ν_e's can only be reduced by good energy resolution since the ν_e's from background sources have a broader energy spectrum than the potential signal, whose width is determined by the spectrum of ν_μ's convoluted with the oscillation probability (see Fig. 4.5). The NC and CC backgrounds can be reduced by a well-designed detector. The challenge is to suppress them to levels comparable or lower than the intrinsic ν_e background level with minimum impact on the signal detection efficiency.

The need to separate out the electromagnetic component in a hadronic jet from the remaining hadrons is common to many high energy experiments. In the calorimetric method, this is generally achieved by having a high Z electromagnetic calorimeter in front of the hadron section. Clearly that technique is not suitable for electron/π^0 separation. The latter has been traditionally done in open geometry experiments by using a Cherenkov counter. In the recent neutrino experiments: IMB, Kamiokande and SuperKamiokande, this general method was implemented by water Cherenkov detectors. The other technology of choice in those experiments (*e.g.* CHARM II and the BNL oscillation experiment) has been use of low Z calorimeters, which facilitate identification of the electron by tracking.

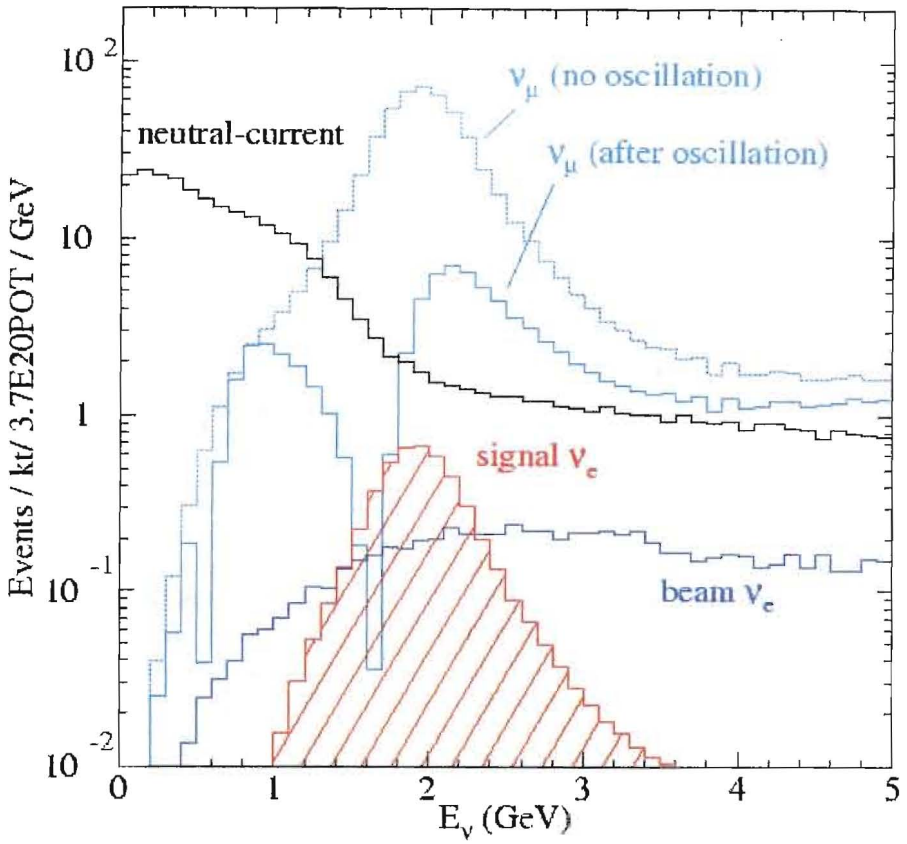

Fig. 4.5: Simulated energy distributions for the ν_e oscillation signal, intrinsic beam ν_e events, NC events and ν_μ CC events with and without oscillations. The simulation used $\Delta m_{23}{}^2 = 2.5 \times 10^{-3}$ eV^2, $\sin^2(2\theta_{23}) = 1.0$ and $|U_{e3}|^2 = 0.01$. An off-axis distance of 12 km at 810 km was assumed.

4.3.3. Tracking calorimeter design issues: In principle, at least, a highly segmented detector can separate electrons from π^0's by utilizing several experimental characteristics:

- finite separation between the vertex and conversion points of the γ's from the π^0,
- two electromagnetic showers (for π^0) *vs* one (for electrons),
- double pulse height right after a γ conversion.

Success of the separation based on these characteristics requires fine segmentation: longitudinally, smaller than a radiation length, X_0; transversely, finer than the typical spatial separation of the two gammas from the π^0 decay. The transverse segmentation also has to be such that individual tracks in the final state can be separated from each other.

Besides the need to distinguish electrons from π^0's, one must also distinguish electrons from hadrons and muons. This is harder in a low Z material and relies on absence of hadronic interactions for electrons and a generally broader pattern of hits along the track for electrons due to the electron shower.

The other important characteristic of a good ν_e detector for $\nu_\mu \rightarrow \nu_e$ oscillations is its energy resolution. One can reduce the intrinsic beam ν_e background utilizing the fact that the events from $\nu_\mu \rightarrow \nu_e$ oscillations will have a sharp energy spectrum at a predictable energy in contrast to the backgrounds that will exhibit a much broader spectrum. This is an important feature of an off-axis experiment, where the detector sees neutrinos in a narrow energy band. Electron-type neutrinos from μ decays will be in roughly the same energy range as the oscillated ν_e's but have a much broader distribution. Ke_3 decays will give higher energy neutrinos covering a broad energy range whereas the τ decay electrons will peak towards low energies. The shape and the level of

backgrounds as well of a possible signal are shown in Fig. 4.5.

4.4. Far Detector

The NOvA Far Detector will be located in a new surface laboratory approximately 810 km from Fermilab and displaced approximately 10 km from the central axis of the NuMI beam. The baseline design for the detector is a low density, low Z, 50,000 metric ton, tracking calorimeter, comprised of 42,000 tons of wood particle board as a passive absorber, 6,900 tons of mineral-oil based liquid scintillator as an active detector and 1,800 tons of polyvinyl chloride (PVC) loaded with 10-15% titanium dioxide extrusions to contain the liquid scintillator.

The liquid scintillator and the passive absorber will be arranged in 750 planes, oriented normal to the axis pointing towards Fermilab. Each plane will be 29.3 m wide by 14.6 m high by 0.229 m thick. The entire detector will therefore extend for a total length of 750 times 0.229 m or 171.5 m along the axis pointing to Fermilab. The liquid will be contained in the PVC extrusions, which will be 1.22 m by 0.029 m by 14.6 m long. Each extrusion will be divided into 30 cells, each cell having a cross-section of 3.96 cm by 2.56 cm, with a total length of 14.6 m. The scintillation light in each cell will be collected by a looped 0.8 mm diameter wavelength-shifting plastic fiber. Light from both ends of the fiber will be directed to a single pixel on an avalanche photodiode (APD). APDs are low cost photodetectors providing high quantum efficiency. Their main difficulties are low amplification and electronic noise. High gain preamplifiers, such as those developed for the LHC CMS detector, can provide the necessary signal output levels. Noise will be reduced to a feasible level by use of Peltier-effect coolers to reduce the operating temperature of the APDs to -15 C.

As described in Chapter 6, the liquid scintillator technology has been selected over several options that have received considerable study during the previous year for reasons of both better event reconstruction and lower cost. The designs that were not selected remain as alternatives, in case of unforeseen difficulties in implementing the baseline design on the required scale. These backups include plastic scintillator as the active detector medium, resistive plate chambers (RPCs) as the active detector and multichannel photomultipliers (PMTs) as high-gain photodetectors.

Chapter 7 describes the NOvA Far Detector in considerable detail and Chapters 5 and 8 discuss its physics capabilities. The Appendix includes information about the alternative RPC detector technology.

4.5. Backgrounds and the Near Detector

The purpose of the NOvA Near Detector is to increase the sensitivity of our search for $\nu_\mu \rightarrow \nu_e$ appearance by improving our knowledge of backgrounds, detector response and the off-axis neutrino beam energy spectrum. The 120-ton near detector would be located about 12 m off the NuMI beam axis, in the access tunnel upstream of the MINOS Near Detector Hall. This site provides a neutrino-beam energy spectrum that is quite similar to that at the far-detector.

Although a primary design requirement is that the near detector be as similar as possible to the far detector, of necessity it will have smaller transverse and longitudinal dimensions and its readout electronics must be able to cope with the high event rates during the 10 microsecond beam spill. We plan to measure the effects of such differences between the near and far detectors in a separate program of test beam measurements.

Chapter 8 describes the simulation and analysis of beam-related backgrounds. The near-detector determination of these backgrounds is described in Chapter 9, along with the test beam program to calibrate detector response. NOvA will also make use of information from the MIPP, MINERvA and MINOS experiments to improve knowledge of the neutrino-beam spectrum and ν_e component.

The beam-related backgrounds to our $\nu_\mu \rightarrow \nu_e$ oscillation search fall into three categories: intrinsic ν_e contamination in the beam, neutral current events, and charged current ν_μ interactions where the outgoing muon is not identified. The levels of the three backgrounds are different at near and far detectors because the beam spectra and compositions are different at the two locations (primarily because of oscillations). The NOvA near detector, along with information about the neutrino beam from the MIPP, MINERvA and MINOS experiments, will

measure these backgrounds and provide information to predict accurately the magnitude of each at the far detector.

We plan to conduct the NOvA test-beam program in two phases. During the first two years a number of small prototype detectors, instrumented with prototype near and far detector electronics, would be used to verify predicted responses. The second stage of the program would make use of larger "calibration detectors," small-scale versions of the near and far detectors, to determine absolute and relative energy calibrations. These data will also be used to tune Monte Carlo simulations and to develop particle identification algorithms. We hope to perform these measurements at a Fermilab test-beam facility.

4.6. Cosmic Ray Background

The atmosphere behaves as a 10-interaction length, 25-radiation length calorimeter for the incident primary cosmic rays. The results of interactions in the atmosphere are extensive air showers, some of whose components persist to the surface: penetrating muons with ~4 GeV average energy, showering electrons and photons with average energies in the range of tens of MeV, and some hadrons (primarily neutrons) with hundreds of MeV. Backgrounds from cosmic rays are substantially suppressed by the fast beam spill of the Main Injector, resulting in a detector live-time of only 100 seconds per year (10^7 spills per year, each 10 μs long). These backgrounds are also reduced by the orthogonality between the horizontal neutrino beam direction and the vertical cosmic ray flux.

In Chapter 10, we show that the detector can easily accommodate the flux of through-passing muons. In addition, we discuss the possibility of further background suppression from a 2-3 m overburden above the detector and also an active shield. We also emphasize that it will be important to measure a large number of cosmic ray induced interactions in the detector during the relatively long intervals between beam spills.

Chapter 10 also discusses the small component of hadrons that survives to ground level. Neutrons are the most significant; they have an interaction length of ~1.5 m in the absorber material and their interactions are therefore a potential source of background. We estimate that 1.0×10^5 neutrons with energies above 2 GeV will interact in the detector per year within the neutrino spill gate; they will be concentrated near the top of the detector.

We conclude in Chapter 10 that the neutron background will not prejudice the quality of our measurements. Although we presently believe that an overburden on the experiment is not needed, we think it is prudent to measure the neutron background with a prototype detector during the coming year.

In addition, the installation of an active shield around the upper portions of the detector appears prudent. Such a shield is significantly less expensive than the support structure required for passive shielding of sufficient thickness to have a significant effect.

4.7. NOvA Detector R&D Program

The conceptual designs of the NOvA Near and Far Detectors described in this proposal require a dedicated R&D program as the next step toward actual construction of the experiment. The goals of the R&D program will be to improve detector performance, optimize and validate choices of critical materials and components, perform engineering studies leading to more accurate cost estimates and, ultimately, to minimize costs. We plan to complete this R&D program over the next two years, culminating in the production of the NOvA Technical Design Report, Fermilab Stage 2 approval and a DOE Project Baseline review.

The last section of Chapter 7 describes the detector technology R&D topics we plan to investigate, including the overall design of the Far Detector and its electronics. This section describes a number of R&D studies that are common to the Near and Far Detectors, as well as some topics that are specific to the Far Detector. The final section of Chapter 9 describes the program of test beam measurements we plan to use to evaluate the performance of prototype detectors and, ultimately, to calibrate the energy responses of the NOvA Near and Far Detectors. The last section of Chapter 10 describes the measurements we plan to make to check the validity of our preliminary conclusion that an overburden is unnecessary to reduce cosmic-ray backgrounds in the far detector. Chapter 11 concludes with a list of engineering topics that need to be investigated to

optimize the design of the Far Detector building, support structure and infrastructure. The final section of the Appendix describes the RPC R&D program, which is focused on reducing the cost of this alternative detector technology for NOvA. Promising areas of study include separate optimization of the detector structure for modular (using commercial shipping containers) and monolithic architectures, investigation of double-gap RPCs, and simplified high-voltage and gas systems.

4.8 Collaboration Organization

At our February 7-8, 2004 collaboration meeting, we took the first steps toward providing governance for the collaboration. Peter Litchfield (Minnesota) was elected temporary Institutional Board chair and John Cooper (Fermilab) and Gary Feldman (Harvard) were elected temporary co-spokespersons. A temporary Executive Council was elected composed of the above officers plus Carl Bromberg (Michigan State), Ken Heller (Minnesota), Mark Messier (Indiana), Doug Michael (Caltech), Ron Ray (Fermilab), Alfons Weber (RAL and Oxford), and Stan Wojcicki (Stanford). These officers will serve approximately six months until the collaboration's August meeting. In the meantime, the Executive Council will appoint a Constitution Committee to draft collaboration bylaws. It is expected that this Committee will report to the August meeting, that a set of bylaws will be adopted at this meeting, and that a new set of officers will be elected in accordance with these bylaws.

Chapter 4 References

[1] The Fermilab NuMI Group, "NuMI Facility Technical Design Report," October 1998, Fermilab Report NuMI-346

[2] M. Kostin *et al.*, "Proposal for a continuously-variable beam energy," October 2001, Fermilab Report NuMI-783.

[3] The E889 Collaboration, "Long Baseline Neutrino Oscillation Experiment at the AGS," Brookhaven National Laboratory Report BNL No. 52459, April 1995.

[4] CHOOZ collaboration, M. Appollonio *et al.*, Phys. Lett. B **466** 415.

5. Physics Potential of NOvA

5.1. Introduction

Assuming that sterile neutrinos either do not exist or do not mix with active neutrinos, there are currently three parameters of neutrino oscillations about which we have no information or only upper limits: $\sin^2(2\theta_{13})$, the sign of Δm_{31}^2 (i.e., whether the solar oscillation doublet has a higher or lower mass than the third state which mixes in the atmospheric oscillations), and the CP-violating phase δ. All three of these parameters significantly affect the rate of $\nu_\mu \rightarrow \nu_e$ oscillations at the atmospheric oscillation length. Thus, a single measurement, for example, an off-axis neutrino run at the first oscillation maximum, will be consistent with more than one set of values for these parameters. An additional measurement, for example an antineutrino run, may or may not be able to resolve all three parameters (in principle). This is illustrated in Fig. 5.1, which shows all of the values of the parameters consistent with a 2% $\nu_\mu \rightarrow \nu_e$ oscillation probability 10 km off-axis at an 820 km baseline. The values of $\sin^2(2\theta_{13})$, are shown on the vertical axis. The solid line represents the normal mass hierarchy (solar doublet low) and the dashed line represents the inverted hierarchy. The values of δ vary around the ellipses as indicated. The horizontal axis shows what the result of an antineutrino run would be.[1] As an example, a sufficiently accurate measurement of a 4% antineutrino oscillation probability would resolve

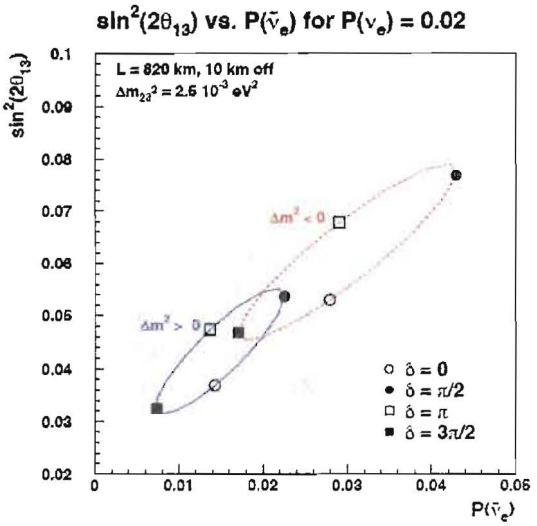

Fig. 5.1: Plot of the possible results of a measurement of a 2% oscillation probability. See text for explanation.

all three parameters with a two-fold ambiguity in δ. However, a measurement of a 2% antineutrino oscillation probability would not be able to resolve the mass hierarchy, regardless of its precision; a third measurement would be required.

5.2. Primary NOvA Goal

The primary goals of the off-axis program will change with time. The first goal will be to measure $\nu_\mu \rightarrow \nu_e$ oscillations with a sensitivity approximately an order of magnitude greater than that of the MINOS experiment.[2] Figure 5.2 shows the calculated three standard deviation discovery limits for $\nu_\mu \rightarrow \nu_e$ oscillations in terms of the three unknown parameters, assuming $\Delta m_{32}^2 = 0.0025$ eV^2. The vertical axis represents the fraction of possible δ values for which a 3-σ discovery could be made. In other words, zero represents the limit for the most favorable value

[1] Figure 5.1 does not include any allowance for either measurement uncertainties or uncertainties in the atmospheric oscillation parameters Δm_{32}^2 and $\sin^2(2\theta_{23})$, and to a much lesser extent, the solar oscillation parameters Δm_{21}^2 and $\sin^2(2\theta_{12})$. The following discussion of sensitivities will include the measurement uncertainties, but not the parameter uncertainties. In this regard it should be mentioned that there is a particularly nasty ambiguity associated with $\sin^2(2\theta_{23})$ if it is not equal to unity. This is because $\nu_\mu \rightarrow \nu_e$ oscillations at the atmospheric mass scale are proportional to $\sin^2(\theta_{23})$. For example, if $\sin^2(2\theta_{23}) = 0.95$, then $\sin^2(\theta_{23}) = 0.39$ or 0.61, depending on whether θ_{23} is less than or greater than $\pi/4$.

[2] With a total of 16×10^{20} pot, MINOS expects to achieve an average three-σ sensitivity to $\sin^2(2\theta_{13})$ of 0.085, assuming a normal mass hierarchy and a typical value of δ. [1] The 90% confidence level upper limit from the CHOOZ experiment at $\Delta m_{32}^2 = 0.0025$ eV^2 is 0.14. [2]

of δ for a given $\sin^2(2\theta_{13})$, one represents the least favorable value of δ, and 0.5 represents a typical value. The lines represent the two possible values of the sign of Δm_{31}^2 and different assumptions on the number of protons on target (pot) that the experiment might see in a five year run. (If the figure is being viewed in gray scale, the line to the right for each number of protons represents the inverted mass hierarchy.) 20×10^{20} pot represents our estimate of what Fermilab might be able to deliver in a five-year run with incremental Booster and Main Injector improvements, while 100×10^{20} pot represents the expectation with the Booster replaced by a new Proton Driver. The three standard deviation sensitivity of the T2K (JPARC Phase 1) proposal [3] is also shown.

This and other calculations in this chapter are based on the baseline detector simulations discussed in Chapter 8.[3] A 5% systematic error on the background determination has been included in this and the other calculations presented in this chapter. However, the statistical errors on the backgrounds always dominate.

The off-axis distance chosen for these calculations is 10 km for $\Delta m_{32}^2 = 0.025$ eV^2. Although results are relatively insensitive to the off-axis transverse distance, there are some trade-offs that need to be considered. For a given set of parameters, the matter effects increase with increasing transverse distance, while the number of signal events tends to decrease. For the primary goal of seeing the $\nu_\mu \rightarrow \nu_e$ oscillations, a 10 km transverse distance is 10 to 20% more sensitive than a 12 km distance. For the resolution of the mass hierarchy, they are almost indistinguishable. We plan to delay the choice of a transverse distance as long as possible to be able to use the most reliable knowledge of the physics parameters and the physics questions of interest.

[3] The results presented here are somewhat less sensitive than those presented in the Progress Report submitted to Fermilab in December 2003[4]. This is due to the use of new beam and physics simulations, as well as a more realistic representation of the detector in the simulations. A major factor was the addition of coherent π^0 production in the backgrounds. A warning was included in the Progress Report stating that the calculations reported there were probably optimistic for the reasons given above.

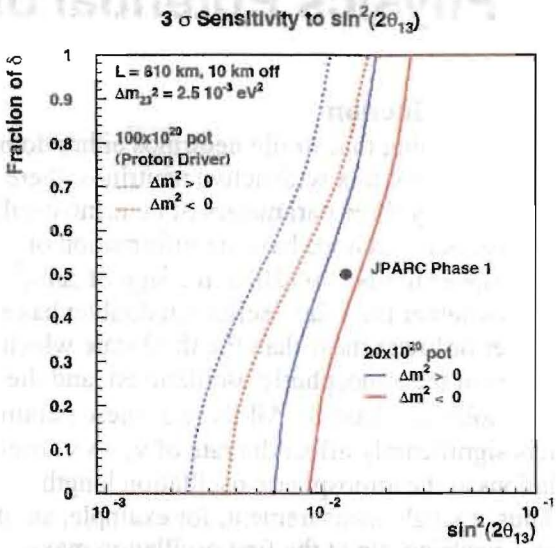

Fig. 5.2: Three standard deviation discovery limits for the observation of $\nu_\mu \rightarrow \nu_e$ oscillations. See text for more details.

5.3. Resolution of the Mass Hierarchy

The issue of the atmospheric mass hierarchy can only be resolved through the observation of matter effects due to the transit of electron-type neutrinos through the earth. As described in Chapter 3, to first order these effects increase linearly with the distance the neutrinos travel through the earth. Since the NuMI beamline provides the longest baseline of currently planned experiments, the resolution of matter effects becomes the primary goal of NOvA once a signal for $\nu_\mu \rightarrow \nu_e$ oscillations is established.

As discussed above, this can be done in some cases with an antineutrino run. Figure 5.3 shows the regions in which a two-standard deviation (i.e., 95% confidence level) resolution of the mass hierarchy is possible with a three-year neutrino run followed by a three-year antineutrino run. The explanations given for Fig. 5.2 apply here as well. The value of a proton driver to extend the reach of the experiment is quite evident.

If nature chooses the parameters such that they cannot be resolved by a single neutrino and a single antineutrino run, then a third measurement will be necessary.

Reactor experiments designed to measure $\sin^2(\theta_{13})$ are generally not useful in this regard. The reason can be seen by examining Fig. 5.1. A

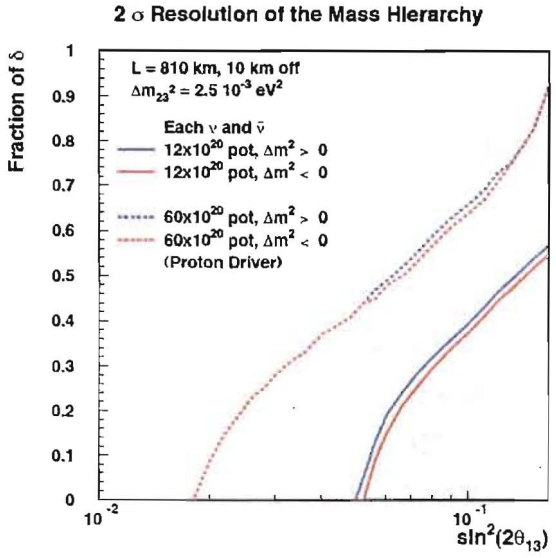

Fig. 5.3: Two standard deviation limits for the resolution of the mass hierarchy with a three-year neutrino and a three-year antineutrino run. See text for more details.

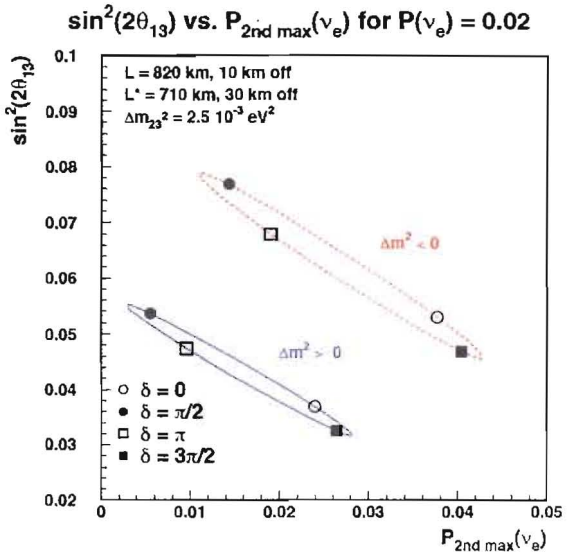

Fig 5.4: Plot of the possible results of a measurement of a 2% neutrino oscillation probability at the first maximum versus the oscillation probability at the second maximum. Compare with Fig. 5.1 to see the how ambiguities there are resolved.

reactor experiment would measure a horizontal band in this plot. Since the ellipses lie along the diagonal, cases for which antineutrino runs do not resolve the mass hierarchy are the same cases in which a reactor experiment does not resolve them. In addition, the θ_{23} ambiguity discussed in Footnote 1 obscures the comparison of the two experiments.

Another possibility for resolving the mass hierarchy is a comparison of NOvA results with T2K (JPARC Phase 1) results [3]. However, the modes in which these two experiments are planning to run combined with their limited statistics does not appreciably increase the parameter space for which the mass hierarchy is resolved.

In general the best way to resolve the mass hierarchy is to run at both the first and second oscillation maxima. The reason is that since the second maximum is at one-third the neutrino energy of the first maximum, matter effects there decrease by a factor of three while CP violating effects increase by a factor of three. (The CP violation comes from an interference term between the atmospheric and solar oscillations; the lower energy increases the solar oscillation part of the interference term.) This is illustrated in the probability plot of Fig. 5.4, which plots the result of a second maximum measurement along the horizontal axis. Points that were ambiguous in Fig. 5.1 are now clearly separated. For example, in Fig. 5.1, the ($\Delta m^2 > 0$, $\delta = \pi/2$) point was close to the ($\Delta m^2 < 0$, $\delta = 3\pi/2$) point. In Fig 5.4, they are separated by approximately an order of magnitude in the neutrino oscillation probability at the second maximum.

In the longer term, one could envision an off-axis measurement at the second maximum in the NuMI beam line. This would involve either moving the detector or building a new detector about 30 km off the center of the beamline, or building a new NuMI beam line to point about 25 mrad away from the present line. Unfortunately, the event rate is proportional to the third power of the energy (two powers from the flux and one from the cross section), so nominally the event rate will be about 27 times smaller. For this reason, the experiment is only possible with the proton intensity increase from a proton driver. Figure 5.5 shows the regions in which a two standard deviation resolution of the mass hierarchy is possible with a three-year neutrino and a three-year antineutrino run into two 50 kT

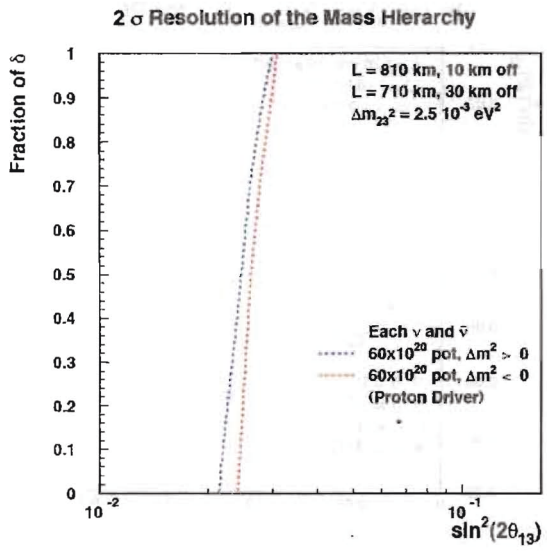

Fig. 5.5: Two standard deviation limits for the resolution of the mass hierarchy with a three-year neutrino and a three-year antineutrino run and two far detectors. See text for more details.

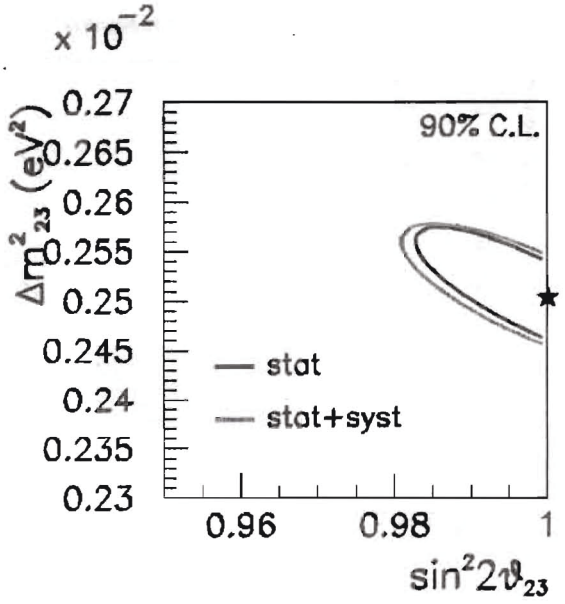

Fig. 5.6: Expected 90% confidence limit allowed region for Δm_{32}^2 and $\sin^2(2\theta_{23})$ for true values shown by the star. The black line represents the results with purely statistical errors; the gray line adds systematic errors.

detectors at different off-axis angles in the NuMI beamline.

An alternative to a second detector in the NuMI beamline would be to combine NOvA measurements taken with a proton driver with results from a high statistics, shorter baseline experiment such as the proposed JPARC phase 2 experiment [3] or proposed beta beams from the CERN SPL [5]. The difference in baselines between NOvA and either of these two proposed experiments could be exploited to provide a resolution of the mass hierarchy with similar sensitivity.

5.4. Other Physics

NOvA will also substantially improve MINOS measurements of oscillation parameters that do not involve ν_e appearance. We will just summarize the results here. Details of the simulation are presented in Chapter 8.

Figure 5.6 shows the expected results of a 20×10^{20} pot neutrino run with true parameters $\sin^2(\theta_{23}) = 1.0$ and $\Delta m_{32}^2 = 0.0025$ eV^2. The sensitivity to $\sin^2(\theta_{23})$ is approximately a factor of four greater than for MINOS with 16×10^{20} pot [1].

Figure 5.7 shows the expected results of a search for sterile neutrinos assuming no true signal.

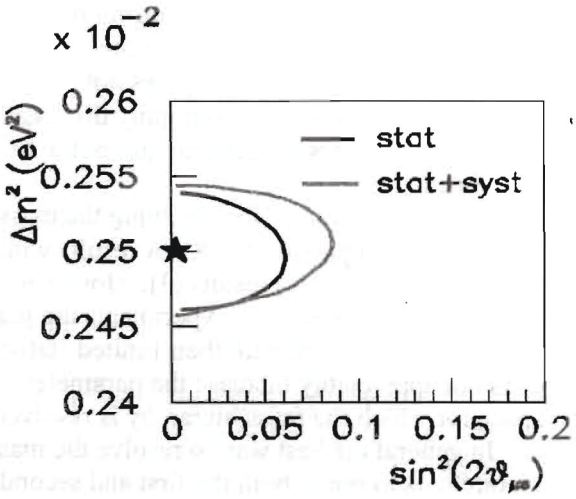

Fig. 5.7: Expected 90% confidence level allowed region for oscillation to a sterile neutrino at the atmospheric Δm^2. The black line represents the results with purely statistical errors; the gray line adds systematic errors.

Chapter 5 References

[1] "Proposal for a Five Year Run Plan for MINOS," Submission to the Fermilab, May 2003. NuMI note 530.

[2] CHOOZ Collaboration, M. Apollonio et al., *Phys. Lett. B* **466**, 415 (1999).

[3] T2K Letter of Intent, January, 2003. http://neutrino.kek.jp/jhfnu/.

[4] "Progress Report on the Proposal to Build an Off-Axis Detector in the NuMI Beamline," Submission to Fermilab, December 2003, Off-Axis note 31.

[5] M. Mezzetto, *J. Phys.* **G29**, 1781 (2003).

6. The Detector Design Process

6.1. Introduction

To reach the physics goals described in the previous chapters, we propose to build a 50,000 metric ton NOvA Far Detector. The size of this detector clearly makes its design and construction a substantial challenge, and the ability to construct a large fiducial mass at low unit cost is key. As described in Chapter 4, additional specific design challenges for the NOvA Far Detector are: (a) good ability to differentiate electrons from other particles, especially π^0 mesons, and (b) ability to measure electron energy as a discriminator between electrons from oscillated neutrinos and electrons from neutrinos initially present in the beam. In addition, since the detector will be operating in a relatively remote location, it should be rugged and robust and capable of operation under a range of environmental conditions with a relatively low level of upkeep and maintenance. In this chapter, we discuss the overall detector concept and the possible designs that continue to be of interest. Our baseline design choice now has liquid scintillator as the active element, and wood particleboard as the absorber. The reasons for these choices are presented here.

6.2. Calorimeter Absorber Choice

In Chapter 4 we discussed the general physics considerations that led us to the need for spatial pattern resolution and a low-Z tracking calorimeter design. After considering several possible materials, we have chosen manufactured wood sheets (particleboard), which is produced in large quantities from low-grade timber and used by the building industry in a variety of sheathing applications. The advantages of these wood board products include low cost (typically $250 - $300 per metric ton [1]) and good structural integrity, which eliminates the need for an extensive detector support design. Particleboard is composed of approximately equal parts of cellulose and urea formaldehyde with about 10% paraffin wax added. The product is therefore mostly carbon, oxygen, hydrogen and nitrogen. Particleboard has a density of about 0.7 g/cc, and we calculate that it will have radiation length of about 55 cm [2].

6.3. Calorimeter Sampling Frequency, Transverse Active Cell Size, and Energy Resolution

Given the choice of particleboard absorber, the specific features of a calorimeter using this material are set by its sampling frequency and by the transverse cell width of its active elements. Our studies [3] compared sampling fractions of 17.5% X_0, 30% X_0 and 60% X_0, concluding that the analysis cuts could be tuned for each case to give very similar signal ν_e event yields. The study aimed at maximizing a figure of merit given by the number of ν_e signal events divided by the square root of the number of background events. The background rejection was worse for 60% X_0, and about the same for 17.5 % X_0 and 30% X_0. Thus we concluded that the increased cost associated with sampling finer than about 30% X_0 was not warranted.

Similar studies [4] on the active detector cell width compared widths of 7 cm, 6 cm, 5 cm, 4 cm, 3 cm, and 2 cm, and tuned the analysis cuts for each individual case. The signal ν_e event yield declined linearly as the strip width was increased, losing about 30% of the oscillated ν_e events between 2 cm and 7 cm. The sum of the background events was minimized at 3 cm and grew larger relative to the signal as the strip width was increased beyond 3 cm. Thus we concluded that a cell size around 3 cm was appropriate and that a smaller cell size was not worth the additional cost.

We examined [5] the energy resolution of a particleboard absorber calorimeter with 30% X_0 sampling and 3 cm wide active cells and find a resolution of $\Delta E/E \sim 16\%$ for low y ν_e CC interactions in the relevant ν_e event energy range of 1 – 3 GeV. This is well matched to the inherent off-axis beam energy width of about 17% at 2 GeV (see Figure 4.5) for our signal ν_e events.

6.4. Calorimeter Active Detector Choice

For more than a year, we have focused on three possible active detector options: solid scintillator, such as the modules used in MINOS [6]; glass resistive plate chambers (RPCs), such as those used in BELLE [7]; and liquid scintillator, such as the

modules used in MACRO [8]. Each of these technologies has advantages and disadvantages.

6.4.1. Solid Scintillator versus Glass RPCs or Liquid Scintillator: Solid scintillator extrusions with multi-anode photomultiplier (PMT) readout represented a starting point for the detector design. Because it is the technology used in the MINOS detector, solid scintillator and phototubes are well understood and have an accurately known cost basis. However, this technology was significantly more expensive than the others that we considered for the detector. Major cost savings can be achieved by the replacement of PMTs with avalanche photodiodes (APDs). This option has the advantage of requiring only one substantial change from the MINOS design. However, its cost is still at the high end of the acceptable range.

Our cost estimates in Chapter 13 clearly demonstrate that a solid scintillator option with APDs is more expensive than either the liquid scintillator or the RPC design. For that reason, while solid scintillator with APD readout remains an option, we are not pursuing this design at this time.

6.4.2. Glass RPCs versus Liquid Scintillator: A major strength of RPCs is the ability to implement two-dimensional readout at each active plane. However, each RPC strip gives only digital information. A major strength of liquid scintillator is the ability to measure dE/dx in addition to position at each active plane. However, liquid scintillator only measures a one-dimensional position at each plane. Our detector simulations to date are described in Chapter 8 and suggest either parity or a slight advantage to liquid scintillator. Our cost estimates in Chapter 13 suggest that liquid scintillator with APD readout has a cost advantage over two-dimensional RPCs. On this basis, we have chosen liquid scintillator with APD readout as the baseline design and RPCs as a design alternate. Details of the liquid scintillator baseline design are described in Chapter 7. The Appendix describes the details of the RPC alternate design.

6.5. Next Steps

Detector simulation studies will continue to evaluate relative advantages of having dE/dx information over knowing two-dimensional coordinates at each plane, since our tracking algorithms and event analysis packages are still in their infancy. Studies on the costs of various detector designs are also continuing with an eye on savings in both the baseline and alternate designs. These studies will focus on liquid scintillator and glass RPCs. The solid scintillator design remains as a second alternate, but this technique is well established and does not require active development at this time, because of the experience gained from the construction and calibration of the MINOS Far Detector.

6.6. Summary

We have chosen a planar tracking calorimeter with alternate planes of manufactured wood particleboard absorber and active liquid scintillator detector elements. Our baseline design has the liquid scintillator contained in cells of PVC with light collected by wavelength-shifting fibers and read out by avalanche photodiodes. This design is different from the proven MINOS technology in three significant ways: use of particleboard rather than iron, use of liquid scintillator rather than solid and use of APDs rather than PMTs. Although we believe that these changes represent a reasonable risk, we will continue to develop the RPC alternative and explore modifications of both designs until the end of 2004, when we expect to choose the final technology for the NOvA Detector.

Chapter 6 References

[1] Off the shelf price at Home Depot™ in Geneva, Illinois, May 2003.

[2] Particle Data Group, Review of Particle Properties, Passage of Particles through Matter.

[3] Off-Axis Note 12, "A Study of Off-Axis Detector Performance as a Function of Sampling Frequency," August 2003.

[4] Off-Axis Note 21, "Resistive Plate Chambers detector for NuMI off-axis experiment," Chapter 2: Analysis and Physics Capabilities, 2003.

[5] "Letter of Intent to build an Off-axis Detector to study $\nu_\mu \rightarrow \nu_e$ oscillations with the NuMI Neutrino Beam," June 2002, page A-6. See also Chapter 8 of this proposal, Figure 8.5b.

[6] The MINOS Collaboration, "The MINOS Detectors Technical Design Report," Fermilab report NuMI-337 (1998).

[7] BELLE KLM detector group, NIM. A 449 (2000) 112-124, and NIM. A 456 (2001) 109-112.

[8] M. Ambrosio *et al.*, Phys. Lett . **B434**, 451 (1998).

7. The Far Detector

7.1. Introduction

The principal physics goals of NOvA are (a) to achieve a significant measurement of θ_{13} for as broad a range of that parameter as possible, and (b) if $\sin^2 2\theta_{13}$ is sufficiently large, to begin a program of measurements of matter effects, mass hierarchy order and CP violation. The requirements placed on the Far Detector by these goals are (a) as large a fiducial mass as is practical and affordable, (b) sufficient instrumentation to distinguish electrons from π^0 background and (c) sufficient energy resolution to distinguish between oscillated ν_e's and ν_e's already present in the NuMI beam when it is produced at Fermilab.

The baseline design described here involves compromises and trade-offs because of the somewhat contradictory design criteria of high resolution and low cost. We have refined this design using the simulations described in Chapter 8. While we believe the baseline design is adequate, it may not yet be optimal. For that reason, we expect to continue to study the effects of changes in granularity, both longitudinal and transverse to the NuMI beam direction, as well as the construction methods for all of the detector components. Section 7.9 describes a research and development program to improve and refine this design, as well as to value-engineer each major system.

The baseline design for the NOvA Far Detector is a nominal 50,000 metric ton tracking calorimeter with alternate vertical planes of active liquid scintillator [1,2] and passive manufactured wood absorber. This design employs multiple repetitions of a few relatively simple elements in order to achieve large mass with low unit costs and high reliability. The detector planes are nearly normal to the NuMI beam direction. (The detector is built level and not along the 58-mrad dip angle of the beam.) The liquid scintillator planes have long, narrow cells that enable one-dimensional measurement of both position and pulse height on each plane using wavelength-shifting (WLS) fiber and avalanche photodiodes (APDs). Pairs of sequential scintillator planes provide x and y coordinates for events. The detector has a scintillator active shield on the top and sides to provide better rejection against cosmic ray background (see Chapter 10), although the short duty cycle of the neutrino beam provides the principal background rejection. The data acquisition system is triggered either by the beam spill, by a random trigger to study cosmic ray background or by optional trigger processors working off short term memories. The design has been initially optimized for efficient installation and for minimizing environmental health and safety (ES&H) costs and risks.

Table 7.1 summarizes the major design parameters for the Far Detector. Throughout this chapter, we use a mixture of US and metric units, reflecting the fact that we plan to purchase some major components as off-the-shelf items in standard US sizes. Some parameters in Table 7.1 have only nominal values because the actual mass, density and thickness of the wood absorber vary with temperature and relative humidity. The density of the mineral-oil-based liquid scintillator also varies with temperature. Details about each of the detector systems are provided in the following sections.

Mass (Nominal)	50,000 metric tons
Width	96 feet
Height	48 feet
Length (nominal)	562.5 feet
Number of Layers	750
Mass of Wood Particleboard (Nominal)	42,000 metric tons
Mass of Scintillator Extrusions	1,800 metric tons
Mass of Liquid Scintillator	6,900 metric tons

Table 7.1: Far Detector Parameters.

7.2. Design Advantages

The strengths of this liquid scintillator baseline design are the following:

7.2.1. Simplicity of Design: The NOvA Far Detector is a challenging project, mostly because of its size. The baseline design specifies many repetitions of a few, mostly low-technology and low-risk elements. The few higher technology elements, such as the wavelength-shifting fiber and the APDs have already received considerable design effort for other experiments.

7.2.2. Ease of construction: The liquid scintillator baseline design derives maximum value from the purchase of large parts of the detector from external vendors with smaller values added by interme-

diate assembly or final installation. The assembly process is mostly gluing together vendor-supplied components.

7.2.3. Reliability: This design facilitates testing of individual components both before and after assembly. Before assembly, WLS fibers will be tested for light transmission. After assembly, a device that connects to the optical connector on a module will provide a final check for fiber continuity. Pressure tests will verify the integrity of the seals at both ends of each PVC module both before shipping and after delivery to the Far Detector Laboratory. APDs will be tested as necessary prior to installation.

7.2.4. Ease of shipping and installation: Extruded PVC liquid scintillator modules will be shipped empty to the detector laboratory, reducing shipping costs because of the low weights of empty modules. The modules will be inserted empty into the particleboard absorber stacks, which are then installed in the detector. The liquid scintillator will be pumped into modules after they are placed in their final positions.

7.2.5. Passive Absorber: Particleboard is a low density, low Z and low cost material. It serves as both a neutrino target and as a structural element. Because this material is commercially manufactured in large quantities in multiple factories, several of which are in the region of the Far Detector Laboratory, shipping costs for the heaviest element of the detector are minimized.

7.2.6. Avalanche Photodiodes: Avalanche photodiodes (APDs) provide photodetectors with both low cost and high quantum efficiency. The need for cooling to minimize noise is a logistical problem, but the advantages of APDs outweigh this disadvantage. We will use development work done for CMS and silicon strip detectors to minimize both cost and risk for these detectors.

7.3. Passive Absorber

7.3.1. Overview: The proposed absorber for the NOvA Detector is wood in the form of sheets of a manufactured wood product, either particleboard or Oriented Strand Board (OSB). Particleboard is manufactured from wood particles ("sawdust"). OSB is manufactured from wood chips. The relative prices of these two materials fluctuate in accordance with supply and demand. The choice between these two products will be based on delivered price at the time of construction.

Density	650 kg/m^3
Plane	12 stacks
Stack Length	48 feet
Stack Width	8 feet
Stack Thickness (nominal)	9 inches
Passive Absorber Mass per Stack (Nominal)	4,650 kg
Particleboard Basic Unit for Stack Construction	24 feet by 8 feet by 1.125 inches thick
Particleboard Basic Unit Mass (Nominal)	330 kg
Number of Basic Units per Stack	14 units + scintillator modules in 8 layers

Table 7.2: Passive Absorber Parameters

Both of these wood products have sufficient structural strength to provide much of the required detector support structure. Quick-set, high-strength adhesives and cartridge-loaded screw guns will be used to assemble the particleboard structure. We expect to coat the exposed surfaces of the assembled blocks with a fire-retardant, to improve the overall safety of the detector.

We will fabricate the passive absorber modules at the laboratory site. The particleboard will be shipped directly from the factory to the Far Detector Laboratory. Sufficient inventory of particleboard will be maintained at the Far Detector site to insure efficient use of available installation labor.

7.3.2. Passive Absorber Details: The basic unit for the passive absorber is a sheet of particleboard 24 feet long by 8 feet wide by 1.125 inches thick. This sheet has a nominal mass of ~330 kg. In addition to the basic unit, the design uses short half units (12 feet long by 8 feet wide by 1.125 inches thick) and narrow half units (24 feet long by 4 feet wide by 1.125 inches thick). All three of these sheets are stock commercial sizes. Using three types of particleboard sheets permits assembly of the absorber without placing butt joints on top of each other.

The next level unit in the passive absorber is the "stack." A stack is 48 feet long by 8 feet wide by a nominal 9 inches thick. It consists of 8 layers—6 layers of particleboard and two layers that are half particleboard and half scintillator module. Fig. 7.1 shows the arrangement of the layers in a stack.

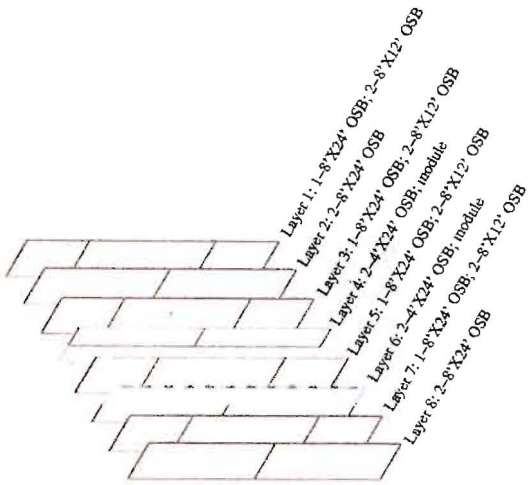

Fig. 7.1: The arrangement of layers in the "stack." (The terms "OSB" and "particleboard" are used interchangeably.)

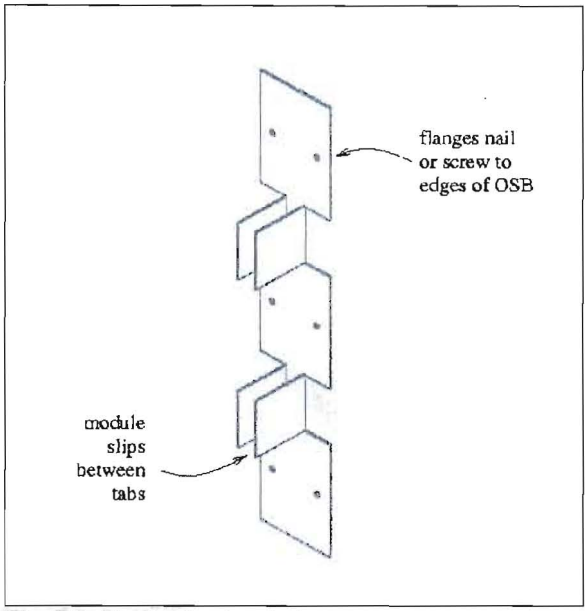

Fig. 7.2: Stack edge bracket.

There are two features built into the stack to facilitate efficient installation and structural stability. The edge bracket positively positions and holds the active detector module and provides structural stability to the stack. A design for this bracket is shown in Fig. 7.2. The other feature is that the outer panels of wood are offset so that their long edges stick out from the stack by 6 inches in opposite directions. This arrangement produces "flanges" that allow for easy installation without exposing the active modules to possible damage.

These flanges can be seen in Fig. 7.3, along with the edge brackets.

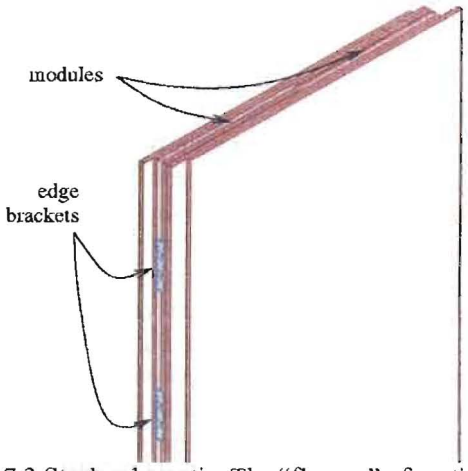

Fig. 7.3 Stack schematic. The "flanges" of particleboard (back left and front right sides) are used to attach each stack to its neighbors.

The highest level unit in the Far Detector design is the plane. As shown in Fig. 7.4, each plane consists of 12 stacks. In the odd-numbered planes, the 12 stacks are arranged side-by-side, providing a readout of the x (horizontal) coordinate. In the even-numbered planes, six stacks are arranged one over another, on both the east and west sides, providing a readout of the y (vertical) coordinate.

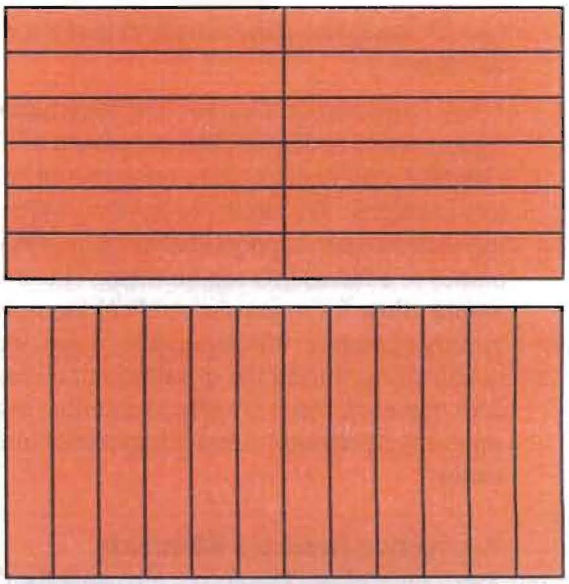

Fig. 7.4: Layout of stacks showing arrangement of alternating layers. Even numbered planes are at the top. Odd numbered planes are at the bottom. Each stack contains two scintillator modules.

7.3.3. Mechanical Integrity: We have evaluated the structural properties of this design. The most recent study used an ANSYS FEA model to determine the structural strength of individual stacks. The model of a stack is shown in Fig. 7.5. To understand the limits of the structure, the strength of the units was tested with point supports in a horizontal orientation. The results (Fig. 7.6) indicate that an extreme case of supporting the units at only the far ends would lead to buckling. However, adding a single additional point in the center of the stack would lead to small enough deflections and stresses to be within the allowed limits for the materials. Thus, due to the low pressures imposed (~15-20 psi) by self-loading, there are no buckling issues associated with the structural elements.

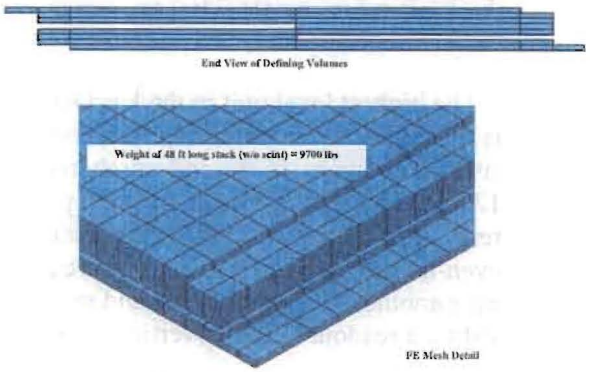

Fig. 7.5: Stack layout and sample of the FEA mesh definition.

7.3.4. Longitudinal Design: The longitudinal design needs to accommodate expansion of the particleboard, due to changes in temperature and relative humidity. We expect to develop a design using intermediate supports between groups of planes to address this requirement. These supports would allow for expansion and contraction of groups of planes. Within a plane group, we will install shims during the installation process to insure that each plane is vertical and thus to minimize any horizontal stress components in the detector.

7.4. Active Detector Elements

7.4.1. Overview: The active elements for the NOvA Far Detector consist of extruded PVC (polyvinyl chloride) cells filled with liquid scintillator and read out by a looped wavelength shifting (WLS) fiber and an avalanche photodiode (APD). The parameters of the active elements are listed in Table 7.3. The APDs are described in Section 7.5.

7.4.2. PVC Modules: The multi-cell PVC modules will be purchased as units from commercial extruders. Extruded panels with nearly the same cell dimensions as those we propose to use for NOvA are off-the-shelf items used to build walls for agricultural buildings. The extruders will ship the modules directly to several assembly sites, likely located at collaborating institutions.

The first step in the assembly process is the insertion of the WLS fiber into each cell of the extrusion. Each fiber will be "looped" at the far end of its cell, providing light collection from two fibers along the full length of the cell. In the next step, the end of the extrusion with the WLS fiber loops will be sealed with a molded plastic end cap glued to the end of the extrusion. The end cap will permit the passage of liquid from one cell to another, in order to facilitate the filling of the cells with liquid scintillator after the extrusions are installed into the detector.

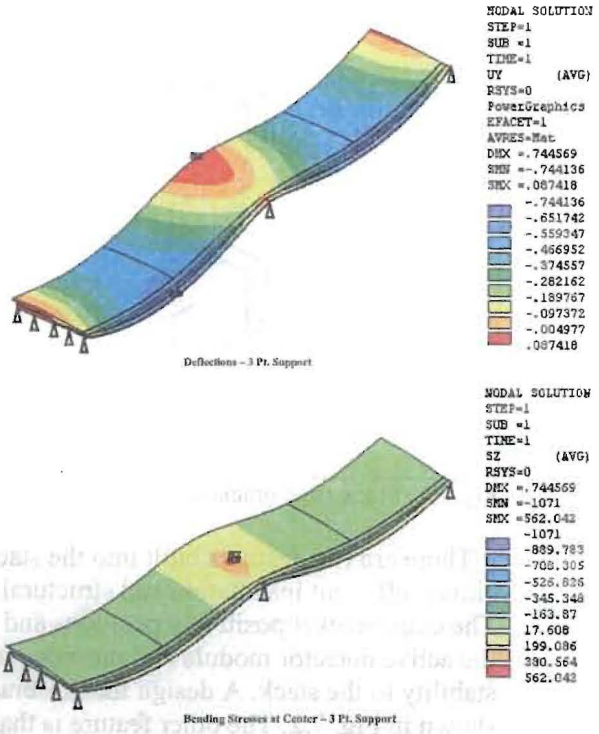

Fig. 7.6: ANSYS calculation of deflections (top; maximum is 0.75 in) and stresses (bottom; maximum is 562 psi) in a horizontal stack with only three support points under self loading.

Extrusions	Polyvinyl Chloride (PVC) with 10%-15% TiO_2 for reflectivity
Extrusion Length	48 feet
Extrusion Width	4 feet
Extrusion Thickness	1.125 inches
Cells per Extrusion	30
Extrusion Outer Wall Thickness	1.5 mm
Extrusion Inter-Cell Wall Thickness	1 mm
Density of PVC	1,400 kg/m^3
Extrusion Mass (Empty)	100 kg
Cell Width (inside dimension)	3.96 cm
Cell Thickness (inside dimension)	2.56 cm
Cell Volume	0.0148 m^3
Extrusions in the Detector	18,000
PVC Mass in the Detector	1,800 metric tons
Liquid Scintillator	Bicron BC517L
Density of Liquid Scintillator	860 kg/m^3
Liquid Scintillator Mass (per cell)	12.7 kg
Liquid Scintillator Mass (per extrusion)	380 kg
Extrusion Mass (Full)	480 kg
Cells Per Plane	720
Number of Cells in the Detector	540,000
Liquid Scintillator Mass in the Detector	6,900 metric tons
Wavelength Shifting Fiber (WLS)	Kuraray
WLS Diameter	0.8 mm
WLS Length Per Cell	32 m
WLS Length for the Detector	17,280 km
WLS Volume in the Detector	8.7 m^3
WLS Mass in the Detector	9 metric tons

Table 7.3: Active Detector Element Parameters

The extrusion assembly is completed by routing the fiber ends through a manifold that both seals the second end of the extrusion and directs the fibers in a specific order to an optical connector. See Fig. 7.7 for a conceptual diagram. The manifold is also glued to the PVC extrusion. In addition to the optical connector, located at the end of the "fiber guide tube", the manifold also provides a filling hole for the liquid scintillator, an air hole for venting the extrusion as the liquid scintillator is filled and a volume for thermal expansion of the liquid scintillator as the ambient temperature changes.

The PVC in the extrusions will be loaded with titanium dioxide for reflectivity. We have tested samples of PVC loaded with various concentrations of TiO_2 and measured their reflectivity at several wavelengths. These measurements indicate that a loading of 10 to 15% TiO_2 will yield a reflectivity greater than 96% at 425 nm. TiO_2 is the additive that gives commercial PVC its white color. Off-the-shelf samples have reflectivities of ~94%. We will monitor the reflectivity of the extrusions as they are manufactured. Fig. 7.8 shows the results of a measurement made on one of the PVC samples that we tested.

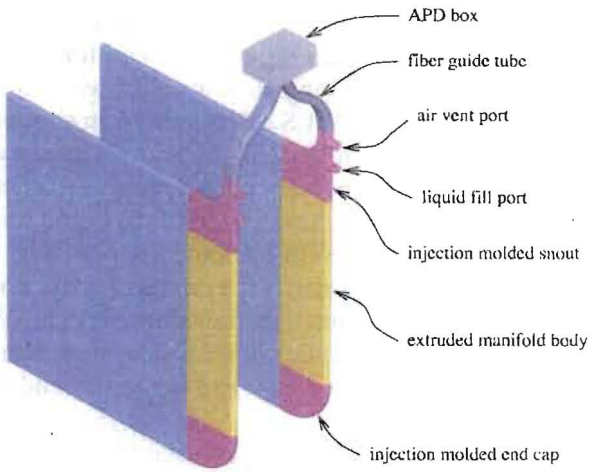

Fig. 7.7: A conceptual diagram of the manifold to lead fibers from the scintillator modules. The ends of 2 horizontal liquid scintillator modules are shown extending off to the left.

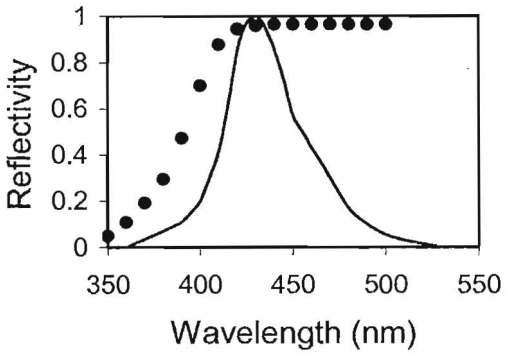

Fig. 7.8: Reflectivity of PVC sample (black circles); the solid line is the emission spectrum of BC517L.

An important aspect of this design is to assure the long-term stability and reliability of the assembled liquid scintillator modules. We have already made a number of both static tests and accelerated lifetime tests for integrity of glue joints, burst resistance, puncture resistance, mechanical "creep" and possible chemical

interactions among glues, PVC, WLS fibers and liquid scintillator. Accelerated lifetime tests involved placing samples in ovens for long-term storage at elevated temperatures. None of these tests has shown significant problems. However, qualification of specific materials and performance of static and accelerated lifetime tests, for both materials and assembled modules, are included in our R&D plan, described in Sec. 7.9.

7.4.3. Wavelength-Shifting (WLS) Fiber: WLS fiber provides an efficient method for collecting light from the long narrow cells used in this detector. The WLS shifts light from shorter wavelengths to green (~550 nm). The use of WLS fiber makes the light output relatively independent of the optical transmission of the liquid scintillator itself. The MINOS Far Detector provides considerable experience on the construction and operation of this light collection design. We expect to purchase multiclad WLS fiber from Kuraray, the same type of fiber and the same vendor used for MINOS.

Essentially the only adjustable design parameter of the fiber is the diameter. Diameters greater than ~1.2 mm are difficult to spool and ship. For fiber diameters around 1 mm, the light collection efficiency depends mostly on the diameter of the fiber while the cost of the fiber depends on the cross-sectional area (volume). Thus, in terms of photons per dollar, two thinner fibers are more efficient than one thicker fiber. Also, the looped fiber design provides a factor of two more light from the far end of each cell, where light output is most important, than two individual fibers with nonreflecting far ends. Using the looped design, as described in Section 7.4.2, we collect ~42 photons for a 1-mip particle from the 48-foot length of the liquid scintillator cell using 0.8 mm diameter fiber. The two ends of the looped fiber will be brought together in the optical connector and presented to one 1.6 mm by 1.6 mm pixel of the APD.

The following figures illustrate some of the characteristics of multiclad WLS fibers. Fig. 7.9 shows that relative light yield, for fiber diameters around 1 mm, is approximately a linear function of diameter.

Fig. 7.10 demonstrates the light collection advantage of a looped fiber design. Note that the ratio of light output for a looped fiber to a single fiber is largest for light from the far end of the liquid scintillator cell.

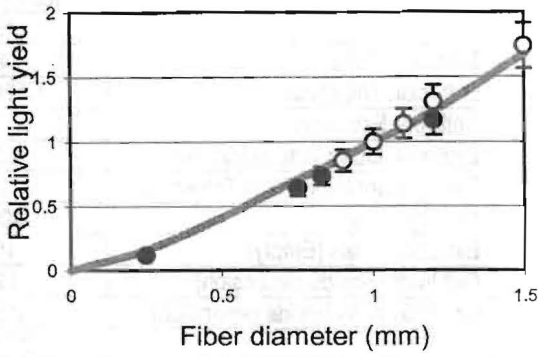

Figure 7.9: Relative light yield as a function of WLS fiber diameter. Open circles - from measurements made for MINOS Detector; closed circles - recent measurements; solid line - Monte Carlo simulation. (Data are normalized to unity at 1 mm diameter.)

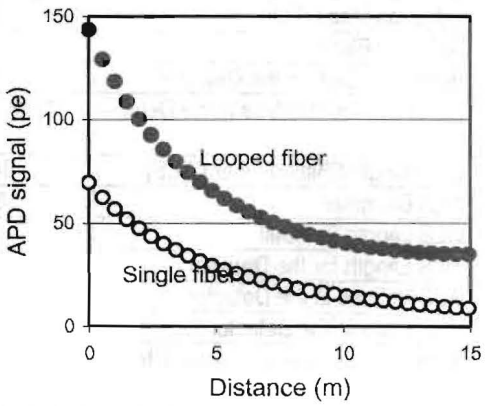

Figure 7.10: Predicted APD signal for looped and single 0.8 mm diameter fibers.

Fig. 7.11 shows our calculation of light output as a function of the location of a single, unmirrored WLS fiber within a liquid scintillator cell. The light output is quite constant over most of the cross-section of the cell but decreases significantly when the fiber is actually touching a cell wall. Our simulations assume realistic fiber locations, with most of the length of a fiber at or near an extrusion cell wall. As part of our R&D program, we intend to explore ways to control the fiber location and to insure that the loop in the fiber is located at the far end.

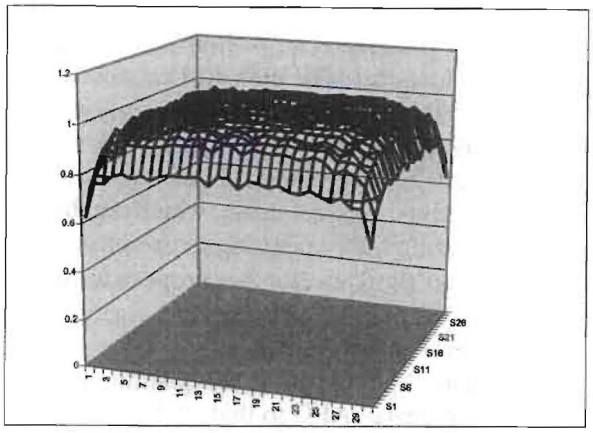

Fig. 7.11: Relative light yield for a single, unmirrored fiber as a function of location within a scintillator cell.

We have performed a number of tests to indicate the validity of a multiplicative light output model, with essentially no correlation among the multiplicative factors. That is, light output is the product of the intrinsic scintillator output times a factor for extrusion reflectivity times a factor for the diameter of the WLS fiber times a factor for the length of the WLS times a factor for the placement of the WLS times a factor for efficiency of the coupling to the photodetector times a factor for the quantum efficiency of the photodetector. The independence of the factors in this model means that tests can be performed for each factor separately, with only occasional end-to-end tests to continue to confirm the accuracy of this approach.

Fig. 7.12 shows a pulse height spectrum of the type we have measured to check the accuracy of our model. This particular spectrum actually results from cosmic ray muons crossing 7.5 m from the readout end of an "off the shelf" extrusion with a 2.1 cm by 2.8 cm channel. The extrusion walls had a 94% reflectivity. The measurements used a hybrid photodiode detector with a quantum efficiency of 12%. The average pulse height is 3.2 photoelectrons. Using our model, and adjusting for differences in detector parameters, we find an expected light yield of 42 photons at the APD face, for a minimum ionizing particle crossing the far end of a scintillator tube.

7.4.4. Liquid Scintillator: The scintillator we propose to use is Bicron BC517L [2] (also sold as Eljen EJ321L), essentially pseudocumene in a mineral oil base. BC517L has a moderate light output, 39% of anthracene, when fresh, and 27% of anthracene, when fully oxygenated. The advantages of BC517L include stability, low cost, availability in large quantities, low toxicity, high flashpoint and low potential as an environmental hazard. Generally, higher light output formulations are less stable and more difficult to use, especially in large quantities.

The oxygenation of BC517L generally proceeds to a stable light output within a few months. Fig. 7.13 shows the results of measurements we have made of pulse-height spectra from solid scintillator, fresh liquid scintillator and oxygenated liquid scintillator. Our simulations use the light yield from fully oxygenated scintillator.

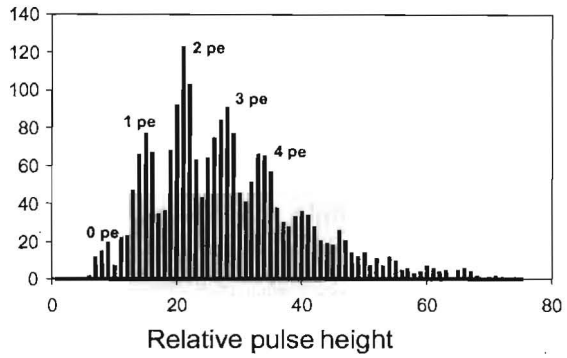

Fig. 7.12: Pulse height spectrum of cosmic ray muons at 7.5 m distance; 2.1 cm x 2.8 cm cell; 1.0 mm WLS fiber; HPD photodetector.

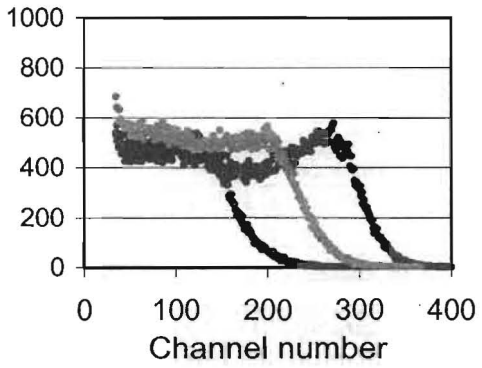

Fig. 7.13: Pulse-height spectra for scintillators showing Compton edge of ^{137}Cs gammas. Black squares (right): MINOS scintillator; gray squares (middle): fresh BC517L; open squares (left): 5-year old BC517L.

The total mass of liquid scintillator in the NOvA Far Detector is 6,900 metric tons or 8.1 million liters or ~2 million gallons. An installation rate of one plane per shift requires a pumping rate of

~300 gallons per hour, about the same rate at which the MACRO detector was filled.

We expect to mix the liquid scintillator in an on-site mixing plant by combining the concentrated fluors shipped from the vendor with the separately purchased mineral oil base. Once mixed, the liquid scintillator would be stored in a holding tank until it is tested for light yield and qualified for use in the detector. A piping system will transfer mixed and tested scintillator from the mixing location to the detector area and then along one of the long sides of the detector to a flexible hose, whose attachment to the fixed piping system would be moved as the detector filling progresses.

Our installation plan assumes on-site storage of mineral oil in five 15,000-gallon tanks and 5500 gallons of storage for scintillator fluors and wave-shifter concentrate. Two 15,000-gallon tanks are used for mixing the mineral oil and concentrate.

7.5. Avalanche Photodiodes (APDs)

7.5.1. Overview: The proposed light detectors for the baseline design are avalanche photodiodes (APDs) [3] manufactured by Hamamatsu and similar to the 5 mm × 5 mm APDs developed for use in the Compact Muon Solenoid (CMS) Detector at the LHC [4]. Table 7.4 summarizes the key parameters of the NOvA APDs.

Manufacturer	Hamamatsu
Pixel Size	1.6 mm by 1.6 mm
Pixel Pitch	2.3 mm
Array Size	16 pixels
Package Size	2 arrays
Quantum Efficiency (>525 nm)	85%
Pixel Capacitance	10 pF
Bulk Dark Current (I_B) at 25 C	10 pA
Bulk Dark Current (I_B) at -15 C	0.15 pA
Peak Sensitivity	600 nm
Operating Voltage	400 ± 50 volts
Gain at Operating Voltage	~100
Operating Temperature (with Peltier Cooler)	-15 C
Expected Signal-to-Noise Ratio (Muon at Far End of Cell)	10:1
APD channels per plane	720
APD pixels per plane (including unused pixels)	768
APD arrays per plane	48
APD channels total	540,000
APD pixels total	576,000

Table 7.4 Avalanche photodiode parameters.

APDs [5] have two substantial advantages over other photodetectors—high quantum efficiency and low cost. The high APD quantum efficiency enables the use of very long scintillator modules, thus significantly reducing the electronics channel count. An operational characteristic of APDs is their high thermal noise, which can be reduced by lowering their operating temperature. For the NOvA Far Detector, we propose to operate the APDs at -15 C, using thermo-electric (Peltier-effect) on-board coolers.

Fig. 7.14 compares the quantum efficiency of a Hamamatsu APD to that of the PMT used in the MINOS Far Detector. In the wavelength region relevant to the output of the WLS fibers, that is 500 to 550 nm, the APD quantum efficiency is 85% *vs.* 10% for the PMT. The figure also shows emission spectra measured at the ends of different lengths of WLS fiber. The quantum efficiency advantage of the APD increases with wavelength. Thus, the APD is even more advantageous for long propagation distances in the WLS fiber, exactly where quantum efficiency is most important because of low light levels. This wavelength dependence leads to a longer effective attenuation length for light in the fiber, as shown in Fig. 7.15, where the attenuation data were obtained using a Hamamatsu APD and a PMT with a bialkali photocathode.

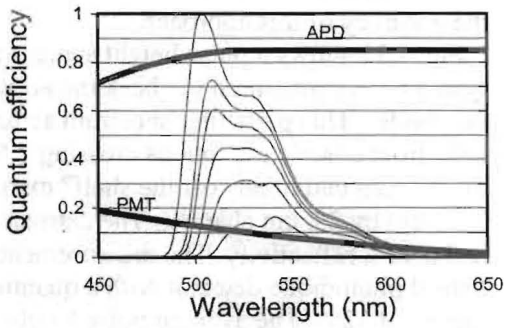

Fig. 7.14: Quantum efficiencies of APD and PMT (bialkali photocathode) as a function of wavelength. The figure also shows WLS fiber emission spectra measured at lengths of 0.5, 1, 2, 4, 8, 16 m, respectively and illustrates the shift of the average detected wavelength as attenuation (fiber length) increases.

The current commercially-available Hamamatsu APD has a pixel size of 1.6 mm by 1.6 mm. A photograph of the 32 pixel APD package is shown in Figure 7.16. We propose to purchase 16-pixel

arrays in the bare die form and mount the chip, cooler, electronics and optical coupler on a single printed circuit board.

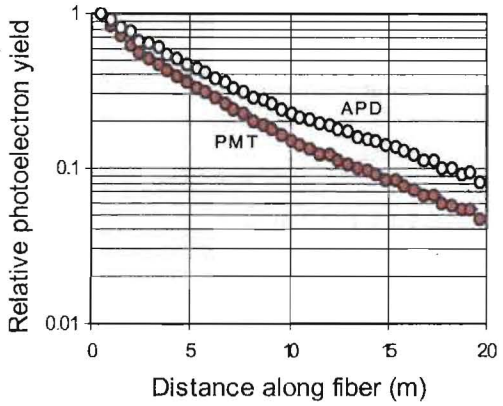

Fig. 7.15: Relative photoelectron yield from 1.2 mm diameter WLS fiber, for APD and PMT. The data have been normalized at 0.5 m to illustrate the effect of the longer wavelength response of the APD.

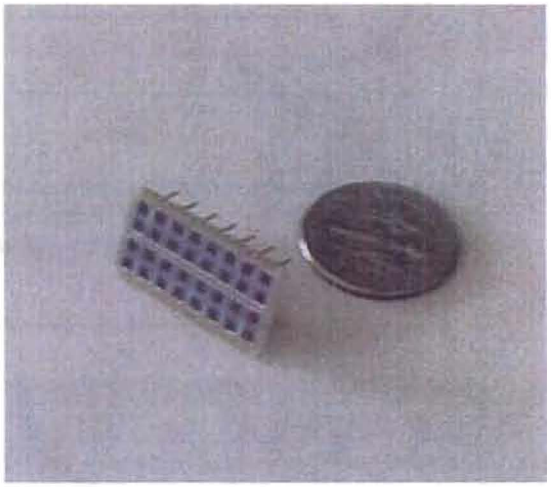

Fig. 7.16: A Hamamatsu APD package shown with a dime. Two 16 pixel arrays are packaged together.

7.5.2. Photodetector Requirements: Photodetectors for the NOvA Far Detector must be able to efficiently detect single minimum ionizing particles traversing the far ends of scintillator strips, ~17 m (of fiber length) away. Each photodetector pixel should be large enough to collect the light from both ends of a 0.8 mm diameter looped fiber.

As described in Sec. 7.4.3, we estimate that a single minimum ionizing particle, normally incident at the far end of a liquid scintillator tube, will produce ~42 photons at the face of the APD. The quantum efficiency for an APD in the region of the spectrum where the light is emitted is 85%, giving a signal for such a particle of ~35 photoelectrons. This signal must be distinguishable from the electronic noise with high efficiency.

7.5.3. Fundamentals of APD operation: The general structure of an APD is shown in Figure 7.17. Light is absorbed in the collection region, electron-hole pairs are generated and, under the influence of the applied electric field, electrons propagate to the *p-n* junction. At the junction, the electric field is sufficiently high that avalanche multiplication of the electrons occurs. The multiplication (M) of the current is determined by the electric field at the junction, and by the mean-free-path of electrons between ionizing collisions, which depends on both the accelerating field and on the temperature. The temperature dependence occurs because of the probability of electron-phonon scattering increases with temperature.

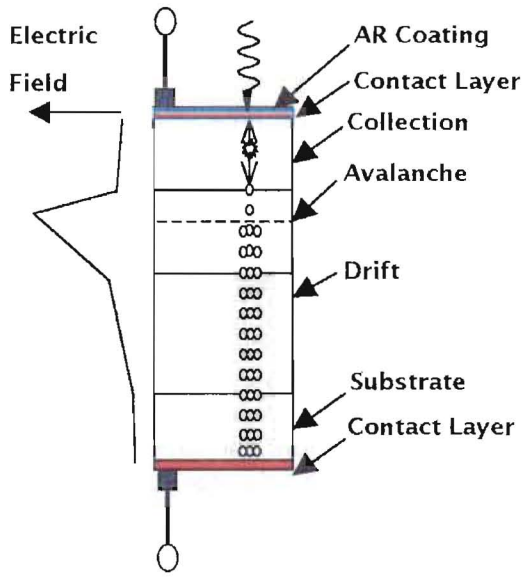

Fig. 7.17: The basic structure of a blue/green sensitive APD. Light crosses the anti-reflection coating at the surface and is absorbed in the collection region. Photoelectrons drift in the electric field to the junction where they undergo avalanche multiplication.

APDs produce intrinsic noise [5] from electron-hole pairs generated thermally in the collection region of the diode. These electrons pass through the junction and are not distinguishable from those

that are photon induced. The thermally generated current of electrons through the junction is called the bulk current (I_B). Other factors such as non-uniformities and other manufacturing imperfections lead to increases in the noise output of the diode.

After APDs have been sorted at the factory, their gains are easily determined by their bias voltages and their operating temperatures. In this detector, we will maintain the operating bias to a precision of ~ 0.2 Volts and control temperature to ~0.5 C. The choice of the -15 C operating temperature for the NOvA Detector application is determined by the need to suppress the bulk-dark current I_B. Roughly, there is a decrease in I_B of a factor of two for every 7 C drop in temperature. Values for I_B of 4.5 pA/mm^2 of sensitive area are typical for the CMS APDs at room temperature.

7.5.4. Experience with the CMS APDs: The CMS experiment will use 124,000 Hamamatsu APDs, with 5 mm × 5 mm pixels, to read out the lead-tungstate calorimeter. To date, more than 100,000 devices have been received from the manufacturer and tested. The quantum efficiency for these devices is consistently at 85% at 550 nm as can be seen in the Fig. 7.18.

7.5.5. APDs for the NOvA Far Detector: We purchased commercially available 32-channel APD arrays from Hamamatsu for possible use in the NOvA Far Detector. The measured dark current, pixel gain and pixel separation for one of the sample arrays are shown in Figs. 7.19, 7.20 and 7.21. The dark current is consistent with expectations from CMS APD measurements. The gain is uniform from pixel to pixel on the same chip. The gain over the sensitive area of an individual pixel is also uniform. The fall-off on the pixel edges in Fig. 7.21 mostly reflects the finite spot size used to illuminate the APD pixels.

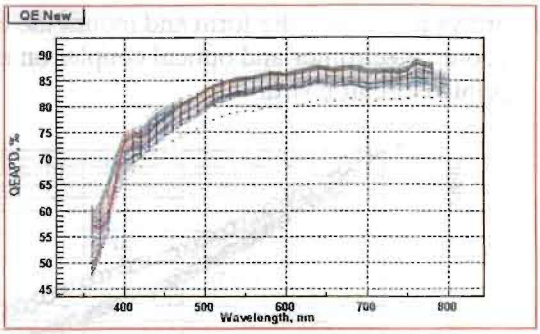

Fig. 7.18: Quantum efficiency of several hundred CMS APDs.

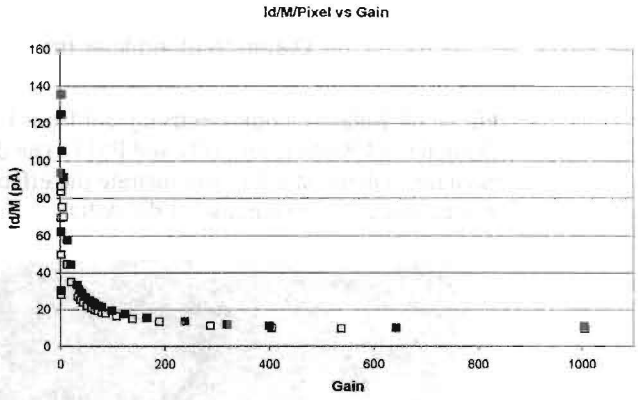

Fig. 7.19: Dark current I_d divided by gain *vs.* gain in a typical NOvA APD at 25 C. The asymptotic value of the current is I_B, which is 10 pA for this sample.

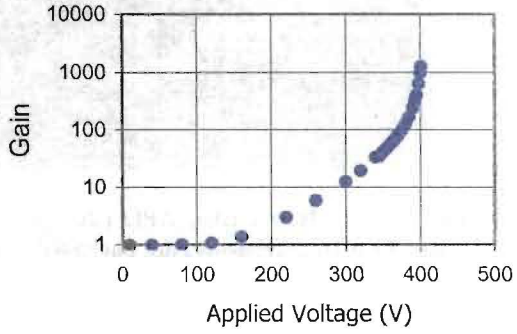

Fig. 7.20: Gain *vs.* applied voltage at 25 C.

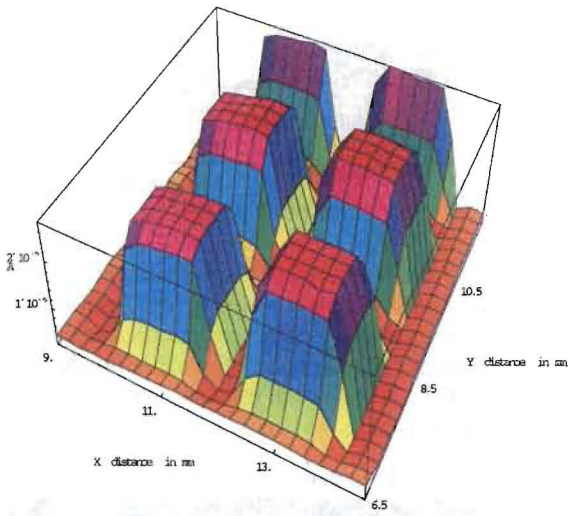

Fig. 7.21: Fine point scan across part of the APD array.

7.5.6. Electronic Readout: Readout of the APDs requires a preamplifier that can sample the signal throughout a 10 μs spill gate. The proposed architecture is based on the Fermilab MASDA (Multi-Element Amorphous Silicon Detector Array) chip [6,7,8] and the SVX4 (a multi-channel amplifying and digitizing chip developed for CDF and D0). In this design, the signal will be amplified by a high gain integrating amplifier with an RC time constant of ~350 ns. The amplifier output will be stored in a switched capacitor array every 500 ns. At the end of beam spill, the signals in each capacitor will be routed via an analog multiplexer to a 40 MHz 10-bit ADC, with one ADC for every 32 APD channels.

7.5.7. Noise: Based on our work with the MASDA chip, we expect a noise level of ~350 electrons is achievable without matching of the input capacitance of the chip to the capacitance of an APD pixel. This should be viewed as an upper limit on the noise level achievable with a practical mass-produced device. We expect to operate the APD at a gain of 100, which reduces the effective equivalent noise charge (ENC) to 3.5 photoelectrons at the photodetector input.

For two 16-pixel APD arrays we measured the average bulk dark current (I_B) per pixel as 10 pA at 23 C. This is consistent with the bulk dark current of the CMS APD: 5 pA/mm^2, corresponding to 12 pA/pixel. A current of 10 pA corresponds to a current of 10 electrons every microsecond. At our operating temperature of -15 C, the APD background rate is ~1 thermally-generated electron in our 1 μs sampling time.

The requirement for the readout is then to detect a signal with an average value of ~35 photoelectrons spread over the short time interval determined by the WLS fluor decay time, with a background rate of 1 thermally-generated electron per microsecond using an amplifier with an effective ENC of 3.5 electrons. Fig 7.22 shows the estimated signals from one and two minimum ionizing particles, considering all noise factors, compared with the thermally generated noise pedestal. The graph shows good discrimination between zero, one and two normally incident muons crossing the far end of the scintillator strip.

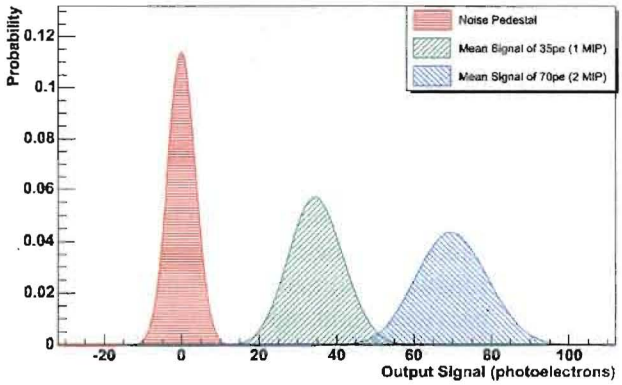

Fig. 7.22: Expected APD signals from noise, 1 and 2 minimum ionizing particles. The calculation uses a total noise of 350 electrons and signal levels of 35 and 70 pe.

7.5.8. Digitizing and Readout Architecture: The proposed digitizing architecture is based on the SVX-4 structure. This configuration consists of an integrating amplifier for each APD pixel, whose output is coupled to an on-board switched capacitor array (SCA). During a 10 μs spill gate, the output of the amplifier is stored on the capacitors in the SCA ASIC at 500 ns intervals.

After the data acquisition interval, the signal on pairs of capacitors will be compared. That is, if the capacitors are labeled C_1, C_2, C_3 etc., then the charge on C_3 is compared with that on C_1 and the difference coupled through an analog multiplexer to a 10-bit ADC where it is digitized and stored. When all the voltage differences for that pixel have been digitized the process is repeated for the SCA associated with the next pixel. A single on-board 40 MHz ADC will be able to digitize the

signals from the 30 pixels that are used to readout a module in ~15 ms.

Adjacent modules will be read out in pairs by a single readout box located between them. We will use four APD arrays with a total of 64 pixels to read out the 60 strips in two modules. The voltage (400 ± 50 V) to bias the four APD arrays (selected to have the same operating voltage) will be supplied from an on-board Cockroft-Walton voltage generator. Each board will have a 64-channel ASIC. Signals are digitized by a pair of 40 MHz 10-bit ADCs. The APD will be cooled with a single-stage thermo-electric (Peltier) cooler. The thermal power generated in the four APD arrays is ~25 μW, so the most significant thermal load will be from local conduction along the fibers and through the electrical interconnects. Temperature monitoring and control, clock regeneration and I/O functions will be controlled with a low-power FPGA. In the design of the readout box the APDs will be mounted on the opposite side of the board from the other electronic components to minimize the thermal load.

7.5.9. APD Housing: The box housing the APDs and their associated electronics must fulfill several functions: (a) match the fibers to the APDs, (b) provide a light tight connection to the scintillator module, (c) house the APDs and the associated electronics, (d) remove heat from the electronics and the Peltier-cooled APDs, (e) protect the cold surfaces from humid air to prevent condensation and (f) provide structural strength. The manifolds are designed such that two scintillator modules can connect into a single APD box. Schematic diagrams of an APD box are shown in Figs. 7.23 and 7.24.

The APD arrays, the PCB, the heat sink, and the electronics are housed in an aluminum sheet-metal box that serves as a Faraday cage. The box also contains connectors that supply the electronics with low voltage, clock signals and electronics readout. The APD box will be designed to be serviceable and light tight.

7.6. Data Acquisition

7.6.1. Data Acquisition Modes: The primary task for the readout and data acquisition system is to concentrate the data from the large number of APD channels into a single stream, which can be analyzed and archived. The complexity of the

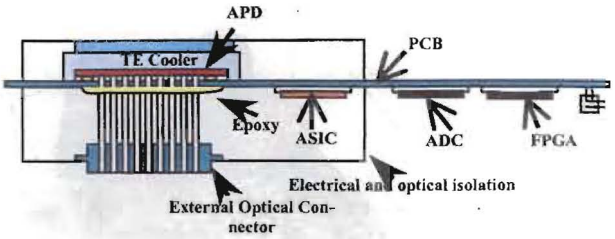

Fig. 7.23: Side view of the components in an APD electronics box. The box receives the signals from two scintillator modules through optical connectors. Peltier-elements (TE cooler) are thermally bonded to the APDs on the PCB and are in thermal contact with the heat sink to remove the heat from the box.

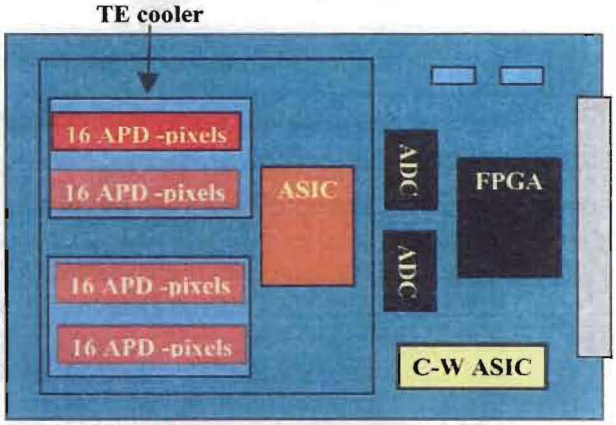

Fig. 7.24: Top view of the component layout in an APD electronics box.

DAQ electronics is dependent on whether the system is externally triggered or self-triggered. An externally triggered system would be "live" for only a short period of time, for example, ~10 μs surrounding the neutrino beam spill. The system could also be randomly triggered at other times in order to measure cosmic ray background. A self-triggered system would be continuously sensitive and would use trigger processors to analyze the data stream looking for hit clusters that might indicate an interesting event. The externally triggered DAQ is clearly easier and cheaper to build and is the system proposed here. We have designed the system so that a continuous readout mode capability could be added at a later time. The parameters of the DAQ system are listed in Table 7.5.

APD boxes per plane	12
APD channels per box	60
APD pixels per box (including unused pixels)	64
Digitization	10 bits every 0.5 μsec
Noise rate per channel	$<10^3$ Hz
Bytes per hit (channel ID, TDC, ADC, status)	≤8

Table 7.5: Specifications for DAQ system.

The data rate per APD box is ~0.5 MB/s, so that an average of 10 bytes is produced per APD box per 20 μs readout, yielding approximately 100 kB per readout for the entire detector. If the readout is triggered at ~100 Hz to measure cosmic ray background, the total data rate is ~10 MB/s. In comparison, the total data rate for the entire detector with a continuous readout mode could be up to 5 GB/s.

The DAQ threshold is set to satisfy two requirements: efficient detection of a minimum ionizing particle and a low noise rate such that the DAQ system is not overwhelmed by spurious hits. Since the system will digitize everything in a spill gate, the threshold can be adjusted to meet these goals. For example, let us assume an electronics noise level of 350 electrons, an APD gain of 100 and a mean signal from a minimum ionizing particle of 35 photoelectrons, or 3500 electrons after the APD. If we set a threshold of 2000 electrons, we expect greater than 99% efficiency for a minimum ionizing particle with a probability for a noise hit of less than 3×10^{-8} in 1 microsecond.

7.6.2. System Architecture: The overall concept of the readout and DAQ system is similar to that of other experiments. Data from each APD is directed to a front-end ASIC, which integrates, pipelines and converts the APD signals to digital values. A Field-Programmable Gate Array (FPGA) receives the data from the front-end ASIC, applies zero suppression and timestamps, and then buffers the digitized values before serialization and transmission to the DAQ. The FPGA can also provide control and monitoring of the APD box. The APD-box FPGA provides an external interface using standard Ethernet protocols. The baseline design specifies less expensive electronic Ethernet interconnections using standard Cat5 cabling. Optical interconnections have the advantages of higher bandwidth and no ground loops at somewhat higher system cost. The final choice will require value engineering.

The overall organization of the DAQ system will be as a collection of local rings readout through Readout Concentrator Nodes (RCN) as shown in Fig. 7.25. The advantage of the ring architecture is that loss of any single ring member disables only that element and not the entire ring. For design simplicity and to reduce requirements for spares, each APD box will have a switchable capability to act as either a ring master or a ring slave. The baseline design is to connect 96 APD boxes from 8 successive planes into each local ring. This gives 750/8 = 94 rings. Since the total detector data rate is 10 MB/s, the rate per ring is ~100kB/s.

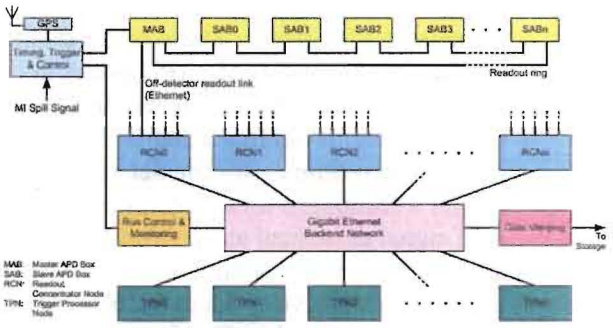

Fig. 7.25: Overview of the entire DAQ system: The data from a number of APD boxes (SAB) will be collected and transmitted by a Master APD Box (MAB) via Ethernet. Data from a number of MAB will be funneled via Ethernet into a Readout Concentrator Node (RCN). The RCNs will transmit this data via Ethernet to trigger processor nodes (TPNs). The TPNs will run trigger algorithms on this data to decide which data to write to the data storage. A timing system will distribute clock signals (locked to the GPS time) to all MAB. These signals would be redistributed by the MABs to the SABs. The timing system also receives the Main Injector spill signal for redistribution.

We expect to use ~10 Readout Concentrator Nodes (RCNs) to collect data from the APD box Ethernet rings. The RCNs will be PC's with multiple Ethernet cards. Each ringmaster APD box will be connected to a dedicated Ethernet interface card on a RCN. The RCNs will direct all data from a specific trigger to one of several Trigger Processor Nodes (TPNs). The TPN that receives all the data from one particular trigger will then determine whether and how the data from that trigger should be archived for later off-line analysis.

Control information will follow an inverse path via the same network. Detector Control System (DCS) computers will send data to the RCNs, which will then distribute control signals to the master APD boxes which will then pass control information around the readout rings.

7.6.3. Timing System: The synchronous readout of data from the detector in the system proposed here requires distribution to the APD boxes of (a) 2 MHz clock, (b) a 1 pulse per second (PPS) signal to reset the hit timestamp counter and (c) a readout trigger ("spill") signal.

These signals are easily modulated onto a 10 MHz carrier frequency, so only a single pair of cables is needed to distribute them. The timing signals are centrally generated and fanned out to the master APD boxes. These boxes distribute the timing signals to all other APD boxes in the ring.

The clock and PPS signals would be locked to a GPS receiver, providing a stable, high-quality absolute time reference for the detector. In order to trigger a readout in time with a beam spill, the spill signal generated at the Main Injection must arrive at the central timing unit around 1 ms before the neutrinos arrive at the detector. A well-defined route for this signal is therefore necessary; either via a reliable, low-latency network connection from FNAL, or possibly via a dedicated radio link.

7.7. Environmental Safety and Health

7.7.1. Introduction: The NOvA Far Detector is an extremely large and massive device. The safe construction and installation of the detector will require a well-planned, well-executed and intensive program of safety, including training, equipment and monitoring. Because of the size of the Detector, the most significant hazards are likely falls and falling objects. We expect that an on-site Environmental Safety and Health (ES&H) staff will be required to insure the necessary level of precautions during the assembly of the detector. The following sections discuss some ES&H considerations for the major detector elements.

7.7.2. PVC: While polyvinyl chloride (PVC) will burn when exposed to an ignition source, it is not particularly flammable. Safety experts at both Fermilab and Argonne have indicated no special problems with our proposed use of PVC. Similarly, the Minnesota Department of Natural Resources believes that our proposed PVC use is in compliance with both OSHA and MSHA regulations, although we believe that only OSHA regulations are actually controlling. Of course, we expect to take suitable precautions to prevent an ignition source coming into contact with the PVC modules. We also expect to install both a smoke detection system and a fire suppression (sprinkler) system. We expect to work with local fire companies to develop and rehearse plans for both personnel rescue and fire suppression in the case of fire.

7.7.3. Scintillator: The material safety data sheet for BC517L (Bicron, 1984) indicates a flashpoint of 102°C and shows that none of the components (mineral oil, pseudocumene ~10%, small amounts of PPO) are highly toxic. Normal precautions with ignition sources will be taken. For example, liquid scintillator or containers used for liquid scintillator, even if empty, will not be exposed to ignition sources. Personnel working with the scintillator or its components will be provided with appropriate personnel protection equipment, since overexposure to BC517L can cause irritation of the eyes. Eating and drinking will not be permitted while working with the liquid scintillator since excessive inhalation or swallowing of material can be dangerous. We will design and install secondary and tertiary containment to limit dispersal of the liquid scintillator in the event of leaks or spillage. Such backup containment measures may include interior walls within the detector and mixing buildings and exterior impermeable berms.

We have investigated the flammability of scintillator-filled extrusions. Test modules have been subjected to temperatures sufficiently high to initiate burning of the PVC. A propane torch required 0.75 to 1.0 minutes to ignite a PVC extrusion. When the flame from the torch was removed, the extrusions self-extinguished within 5 seconds. Modules filled with scintillator were even more difficult to ignite, because of the considerably higher heat capacity. The scintillator-filled PVC modules also self-extinguished when the propane torch was removed.

7.7.4. Absorber: The particleboard absorber is also environmentally benign. The major ES&H concern regarding the absorber is again flammability. We expect to study the utility of coating the exposed absorber surfaces with a fire-retardant. As with the other components, smoke detection and a fire suppression system will address some of these concerns. The detector construction scheme, in which the absorber and the PVC extrusions are

fastened together into a monolithic block reduces the exposure of both the absorber and the PVC extrusions to oxygen, thus reducing the severity of the flammability hazard.

7.8. Installation

The Far Detector installation goal is to achieve a rate of 12 detector stacks or one detector plane installed per day or 4 planes per week (two 10 hour shifts per day for a 4 day week). Including ramp up, the entire installation process will take 4 years to complete, proceeding in parallel with module fabrication. We believe this rate is achievable because (a) there are few different types of parts, (b) the assembly methods require few special skills and (c) the task is large enough to afford some investment in optimal lifting and moving apparatus and fixtures.

To meet this proposed installation rate, an average of 9-10 truckloads of particleboard and two truckloads of scintillator modules must be delivered to the detector site each workweek. We assume that these materials will be delivered to either an attached or separate receiving and preassembly building located at grade on the detector site. A total area of ~700 m^2 will be required for the Far Detector assembly, in addition to the ~7,000 m^2 for the detector and its utilities.

A possible installation plan is as follows: The particleboard arrives by truck pre-cut to size. The scintillator modules arrive in reusable shipping containers. Both of these loads are removed from the truck via Cady-lifting fixture using the bridge crane. Two crewmembers are used to receive materials. A buffer of materials to cover at least 2 weeks of installation work will be stored on site. To minimize construction time the stacks of wood closest to the stack jig will be re-stocked so single sheets are moved less distance.

The stack jig and material storage is as close to the completed detector face as is reasonable. This allows usage of the large building area and minimizes the distance a completed stack is moved. After the stacks are constructed, they are lifted onto the detector face and screwed into place. The completed detector stacks are rigged with a strongback-lifting fixture that has been designed to lift both horizontal and vertical stacks. It uses a vacuum system to hold the stack to the strongback. It then uses a Hillman roller system similar to the MINOS strongback to lift the fixture. Only one fixture is needed for this task.

After the stack is picked up, it is rigged into place with a crane. Once in place, two people (who run tag lines for rigging the stack) use two scissor lifts to move the length of the stack, securing it to the adjacent stack and the previous plane using construction screws delivered by screw driving systems. At the same time, the other member of the team is surveying the unit from one of the scissor lifts. After securing the stack, the crew returns to the location of the next stack. Along the way they will use the surveys from the previous plane to correct it to vertical by attaching wood shims with screws. This operation is repeated 12 times each day to install a plane.

After a plane is installed, some time will elapse before the next steps on that plane, in order to minimize the number of people working in the same physical space. The final installation steps involve two crews of two technicians each. One crew will fill the PVC extrusions with liquid scintillator. The second crew will install the photodetectors and electronics, and cable up the units. Shift physicists then commission the planes.

The construction manpower required for installation (both shifts summed):

2	Receiving team
16	Stack builders (4 crews of 4)
8	Stack installers (2 crews of 4)
4	QA / cablers
4	Scintillator handlers
34	Total installation crew

In addition to the installation staff, an additional 7 support staff (supervision, safety, administration, network, telecommunications and janitorial) are required. Thus, we expect a total staff of 41 full-time people is needed on site for construction of this detector, in addition to the visiting physicists and students, who will do software and systems checkout tasks.

7.9. R&D for the Baseline Design

7.9.1. Overview: The research and development program for the liquid scintillator baseline design is directed towards improving performance, establishing a more precise knowledge of the detector costs and reducing those costs. This plan includes value engineering and prototype testing, in conjunction with an interactive program of simulations. Special attention will given to those ele-

ments of the detector that appear to be cost drivers. We will also seek to identify possible failure modes that cannot easily be remedied. The program will take approximately one year and culminate with the testing of a full scale slice of the detector.

7.9.2: Overall design: As indicated in Section 7.1, we expect to continue to work to optimize the baseline design both in the transverse dimension, that is, the scintillator strip width, and the longitudinal dimension, that is, the amount of passive absorber between active scintillator planes.

As part of this effort, we are investigating an asymptotic longitudinal design with no passive absorber, which we call the Totally Active Scintillator Detector (TASD). Such a detector should have significantly higher efficiency for signal events and better background rejection than the baseline detector. For a cost roughly equal to that of the baseline design, we could build a fully active detector with a total mass of ~25,000 metric tons, that is, half the size of the baseline detector. The two most important research and development questions associated with this design are (a) whether such a detector would better achieve the physics goals of this experiment and (b) how the absence of absorber would affect the mechanical stability of the detector structure. We expect to continue work on both these topics.

7.9.3. Test beam: As described in Chapter 9, we plan to study a very small version of the final detector in a test beam, to experimentally determine its response to GeV electrons and pions. This information will be used to check detector Monte Carlo simulations.

7.9.4. Detector Structure: Full size and part size stacks consisting of wood and plastic scintillator modules will be assembled and tested. Individual stacks will be tested for strength, stability and behavior within the expected ranges of temperatures and humidity. Time and motion studies will determine optimal assembly techniques for each stack. Several stacks will be joined to make a partial plane to investigate the effectiveness of the assembly procedure. Time and motion studies of these partial planes will determine a more precise cost estimate for detector assembly. Also addressed by these studies will be the light tightness of the stacks when assembled, their needs for external support, and removal strategies for the end of the lifetime of the experiment. Safety questions of stability, flammability, and liquid containment will also be addressed with prototypes.

7.9.5. Scintillator mixing and delivery: Functional pieces of the liquid scintillator delivery, mixing, and filling system will be tested and refined. Special attention will be paid to the design necessary to eliminate potential leaks and containment if a leak does occur. We will develop and prototype QA apparatus for determining mineral oil and scintillator quality before filling.

7.9.6. Scintillator modules: Time and motion studies of scintillator module assembly will determine the needs for assembly machines and fixtures and provide the basis for more precise cost estimates. Assembled modules will be tested for structural strength and potential mechanical failure modes including liquid and light leaks. Techniques of filling and emptying the modules will be tested to determine their effectiveness. We will also develop techniques for controlling fiber location within tubes to determine if they are a cost-effective way of improving light yield. WLS fiber positioning and light yield will be determined with modules filled with liquid scintillator. Safety tests will help assess potential flammability or liquid containment issues. In addition, accelerated aging tests will check potential interactions of any of the module components with liquid scintillator or with each other. Modified component designs will be produced as needed to minimize costs. Prototype tests will give more accurate light yield parameters that can be used to determine optimal absorber thickness and scintillator cell size.

7.9.7. Photonics: APDs are low gain devices so that attention to their noise characteristics must be an important part of the detector design. Multipixel APDs marketed by Hamamatsu have the gain and noise characteristics that are needed for the detector. To reduce the cost of the photodetector, we plan to use unpackaged APDs for the experiment. The APD must be cooled by an electronic cooling chip (Peltier) that is coupled directly to the rear of the APD. We will work with Hamamatsu to build prototypes of bare multichannel APDs bonded to the cooling chip and mounted on a circuit board that connects the APD to the amplifier and other electronics. Care must also be taken in the design of the fiber/APD interface that may also be fabricated by Hamamatsu or at one of the collaborating institutions.

Since wavelength shifting fiber is a cost driver for this detector, the cost of the detector is a sensitive function of fiber diameter. The entire photon production chain will be examined to determine if we can reliably increase the photon yield into the APD or decrease the electronics noise. Either modification will allow cost reduction by decreasing the fiber diameter.

7.9.8. APD box and WLS system design: The design of the ~9,000 APD boxes that provide the interface between the fibers, the APD, and the electronics is one of the most complex parts of the detector. Careful design and prototyping is essential to containing detector costs. The box design must be light tight, efficiently remove heat from the Peltier coolers and protect cold surfaces from moist air. Other elements for mechanical design are insertion methods for the WLS fiber, the manifold that aggregates the WLS fibers en route to the APD box, the WLS fiber to APD box optical connector and the APD printed circuit board mounting.

7.9.9. Electronics: The low gain of the APD puts a premium on low noise electronics. We will produce and test modifications of the existing MASDA design to establish a baseline on which to base a custom designed ASIC. Prototypes of the entire circuit board with all components will be tested to optimize layout for the lowest noise. Several noise reduction circuits using multiple sampling will be prototyped and compared.

Chapter 7 References

[1] P. Border, *et al.,* "A large liquid scintillator detector for a long baseline neutrino oscillation experiment," Nucl. Instrum. Meth. A 463 (2001) 194-204; L. Benussi, *et al.*, "Large liquid-scintillator trackers for neutrino experiments," Nucl. Inst. Meth. A 488 (2002) 503-516.

[2] BC517L Material Safety Data Sheet (MSDS), www.bicron.com.

[3] M. Doucet, *et al.*, "Light yield measurements in a liquid scintillator detector with wavelength shifting fibre readout," Nucl. Instrum. Meth. A 459 (2001) 459-468; M. Moszynski, *et al.*, "Avalanche photodiodes in scintillation detection," Nucl. Instrum. Meth. A 497 (2003) 226-233; D. Renker, *et al.*, "Properties of avalanche photodiodes for applications in high energy physics, astrophysics and medical imaging," Nucl. Instrum. Meth. A 486 (2002) 164-169.

[4] K. Deiters, *et al.,* Nucl. Instrum. Meth. A 461 (2001) 574-576; Nucl. Instrum. Meth. A 453 (2000) 223-226; Nucl. Instrum Meth. A442 (2000) 193-197.

[5] A good summary of APD theory, including noise, is given in the CMS ECAL TDR, CERN report CERN/LHCC 97-33.

[6] M. Maolinbay, *et al.*, "Design and performance of a low noise, 128 channel ASIC preamplifier for readout of active matrix flat panel imaging arrays," NIM A 485 (2002) 661-675.

[7] T. Zimmerman, "The MASDA-X chip – a new multi-channel ASIC for readout of pixilated amorphous silicon arrays," Fermilab technical note FERMILAB-TM-2063 (1998).

[8] R. Yarema, *et al.*, "A programmable, low-noise, multi-channel ASIC for readout of pixelated amorphous silicon arrays," presented at the 8th European Symposium of Radiation Detectors, Sloss Elmau, Germany, June 14-17, 1998 (submitted to NIM).

8. Simulations

8.1. Introduction

This chapter describes the simulation methods that have been used to design and verify the performance of the proposed liquid scintillator detector. The main simulation described is for a far detector site 10 km off axis with a beam length of 810 km. This off-axis location is optimal for this beam length and $\Delta m_{32}^2 = 0.0025$ eV^2. However, the performance of the experiment is not strongly dependent on the off-axis position and other considerations may suggest alternative off-axis distances. The simulation assumes $\nu_\mu \rightarrow \nu_e$ oscillations at $\sin^2 2\theta_{13} = 0.1$, somewhat below the CHOOZ limit of $\sin^2 2\theta_{13} = 0.14$ at $\Delta m_{32}^2 = 0.0025$ eV^2.

The code is based on the tested simulation software of the MINOS experiment (GMINOS) using GEANT3 and the NEUGEN3 neutrino interaction generator. This allows the efficient use of some of the tools that have been developed for implementing and analyzing a scintillator detector.

The detailed methodology of the event generation and reconstruction is described below. ν_e events are separated from background by a succession of cuts and by a likelihood analysis. Finally, a figure of merit (FOM1) equal to the number of signal events divided by the square root of the number of background events is calculated.

8.2. Detector Definition

8.2.1. Detector geometry: The simulated detector consisted mainly of passive absorber, modeled as Lucite with a density of 0.7. The active elements were scintillator strips with the dimensions given in Table 7.3. The external and internal walls of the scintillator modules were fully simulated. Half the strips were oriented along the x-axis, and half along the y-axis. The horizontal x-strips were two separate strips with readout at the sides of the detector; the vertical y-strips were single strips with readout at the top. The constraints of the GMINOS system required some minor deviations from the exact form of the detector but the overall outcome was very close to that described in Chapter 7. More details of the geometrical layout actually simulated are given in Reference [1].

8.2.2. Readout simulation: The light collection and transmission in the fiber was simulated using the code for the MINOS light collection. The looped fiber was approximated by assuming MINOS style single-ended readout with an average of 35 photoelectrons collected from a minimum ionizing particle crossing the far end. The attenuation measured for the looped configuration, described in Chapter 7, was used. A WLS fiber tail of length 1 m between the end of the scintillator extrusion and the photodetector was assumed. The photodetector was modeled as an APD with a quantum efficiency of 85%. The parameters of the APD gain and noise given in Chapter 7 were used to smear the APD output. The generated pulse height distribution for minimum ionizing, normally incident, particles as a function of distance along the strip is shown in Fig. 8.1 and the pulse height distribution as a function of the number of particles crossing the strip in Fig. 8.2. A threshold of 20 photoelectrons was imposed in the subsequent analysis.

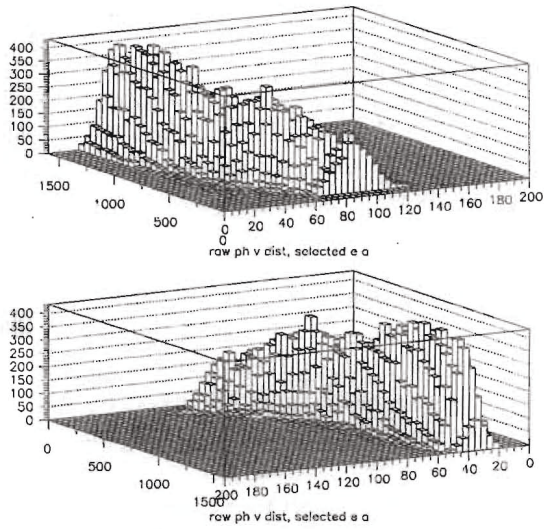

Fig. 8.1: Pulse height as a function of distance along a strip for hits that correspond to the energy deposit of a normally incident minimum ionizing particle, viewed from the APD end (top) and far end (bottom).

8.3. Event Generation

Interactions were simulated spanning the range of energies, neutrino types and interactions. The neutrino interactions were chosen with a 1/E

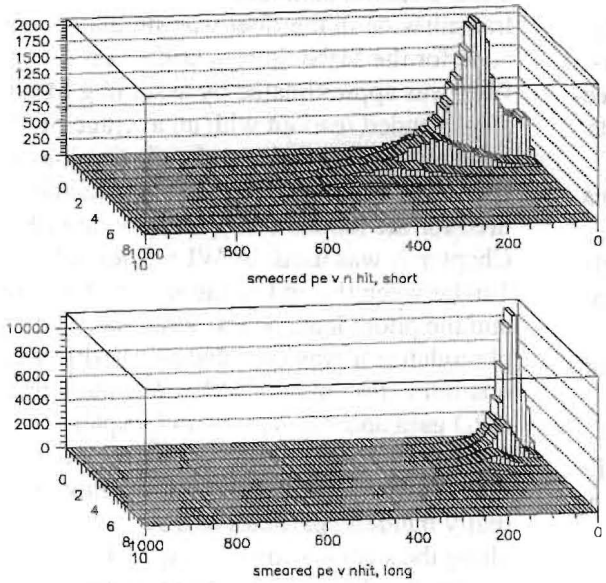

Fig. 8.2: Pulse height distributions as a function of number of particles crossing a strip at the APD end (top) and the far end (bottom). These distributions are for all hits generated by ν_e charged current events.

neutrino energy distribution so that the interacted neutrino spectrum is approximately flat. Initial tests showed that selected ν_μ and ν_e charged current events had incident neutrino energies below 6 GeV. Neutral current events had contributions from beam energies up to 20 GeV. Neutral current events were generated separately from the charged current events to give the required statistics on the predominant background. Two samples of events were generated, one as a training sample for the event cuts and one as a test sample. Approximately 300,000 ν_μ charged current, 100,000 ν_e charged current and 500,000 neutral current events were generated for each sample.

8.4. Event Reconstruction

A loose clustering algorithm was applied to the events, which grouped together hits in each view that occur within a distance of 2 m of each other. Clusters in the two views were matched by the correspondence of their start and end positions in z (along the beam). The matched cluster with the largest number of hits was selected as the event. The large majority of events only produced one matched cluster. Events with no matched clusters were rejected. In addition the event was required to have a minimum of three hits in each view. The clustering removed outlying hits from events and rejected low energy (chiefly neutral current) events.

Events with more than two hits outside the fiducial volume of the detector (closer to an outside face than 50 cm in x or y, or 2 m in z) were rejected at this stage, 86% of reconstructed ν_e events (77% of total events) passed this fiducial requirement.

A straight line was fit to the cluster in each view. The measured pulse height was corrected for attenuation using the information on the position along the strip given by the fit. The hit and pulse height residuals to the straight line and the rms of the hit and pulse height distributions in the beam direction were calculated in each view. These and the other quantities used in the following analyses were summed over both views to apply to the full event.

The event cluster was then passed through a filter, which used the Hough Transform to select the most significant track-like segment of the event. This filter is an iterative procedure where the 2-dimensional hits (x_i,y_i) in each view belonging to the cluster are transformed into trajectories in the parameter space (θ,d) where the relation $x_i \cos\theta + y_i \sin\theta - d = 0$ is asserted. The parameters of the most significant track-like segment of the event were taken to be those where the peak in (θ,d) space occurs, and the hits belonging to the track were those whose trajectories passed within a preset minimum distance to this peak. The procedure was repeated with finer binning in (θ,d) space and more stringent cuts on the minimum distance to the peak. Fig. 8.3 illustrates the effect of the filter for sample ν_μ CC, NC and ν_e CC events. In this implementation, electron showers tend to be sufficiently narrow that most of the shower hits were included in the track-like object, whereas fewer hits were tagged as track-like for NC showers, which are generally more diffuse. A straight line was fit to the hits assigned to the Hough track in each view and again the transverse residual and longitudinal rms calculated. A set of ntuples was produced which was used in the following analysis to select ν_e events.

8.5. Event Weighting

As described above, the events were generated flat in energy. In order to represent the expected event distributions in the detector they were weighted by the following factors:

- The beam neutrino energy distributions for a location 10 km off axis and 810 km from Fermilab, using the medium energy NuMI beam configuration.
- The oscillation probability, for $\nu_\mu \rightarrow \nu_\mu$ with $\sin^2 2\theta_{23} = 1.0$ and $\Delta m_{32}^2 = 2.5 \times 10^{-3}$ (eV/c)^2, and for $\nu_\mu \rightarrow \nu_e$ with $\sin^2 2\theta_{13} = 0.1$.
- For the NC events, the NC/CC ratio as a function of energy.

This calculation does not include any matter effects, which depend on the unknown mass hierarchy, nor any CP violation which depends on the unknown phase parameter, δ. The potential effects of these parameters are discussed in Chapters 3 and 5.

The events were finally normalized to the expected rate of ν_μ CC events in a 5-year exposure of a 50-kiloton detector with 4 x 10^{20} protons on target per year. The numbers of events in the four classes, ν_μ CC, NC, ν_e CC from the beam and ν_e CC oscillated from ν_μ are given in Table 8.1 and shown in Fig. 8.4

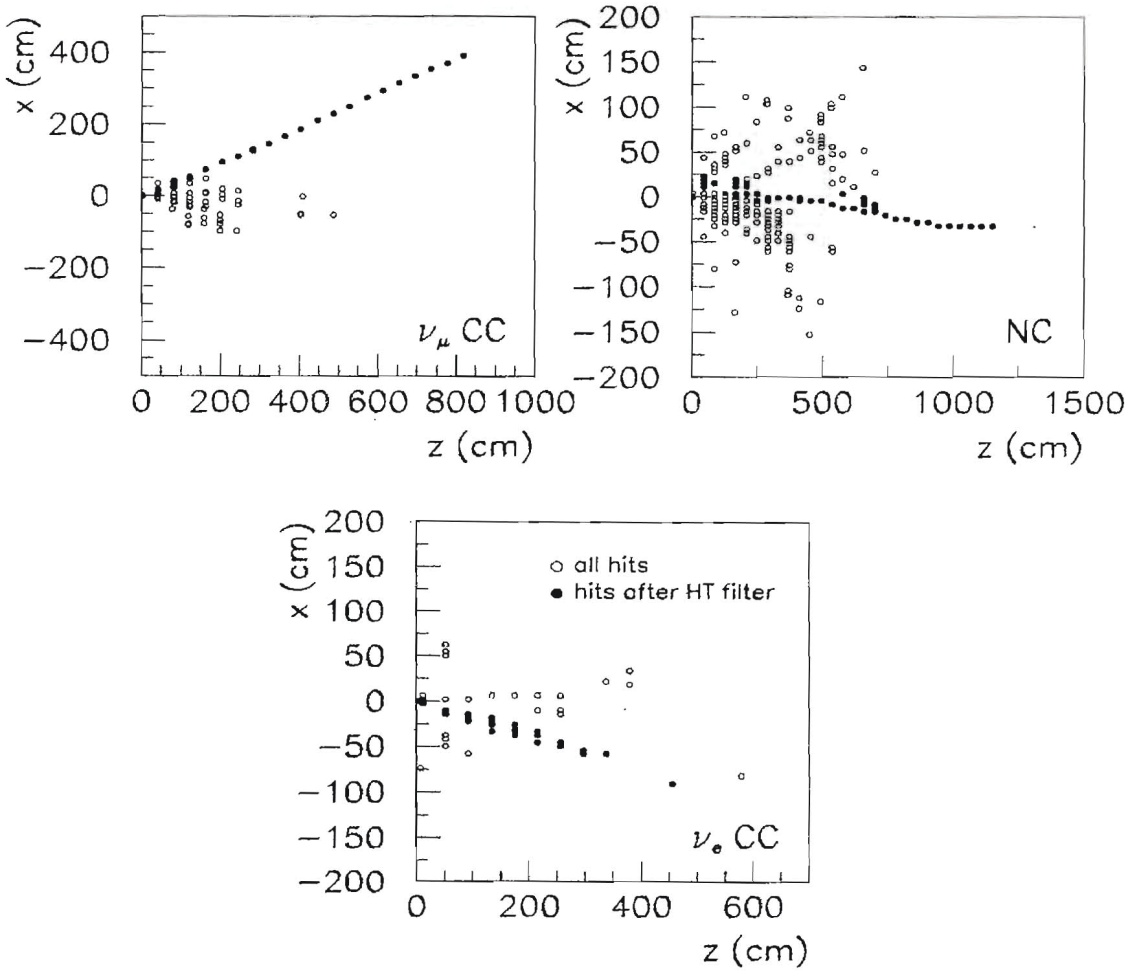

Fig. 8.3: Use of the Hough Transform filter on three example events. The open circles show all the hits in the event and the filled circles show the hits that remain after the filter is applied.

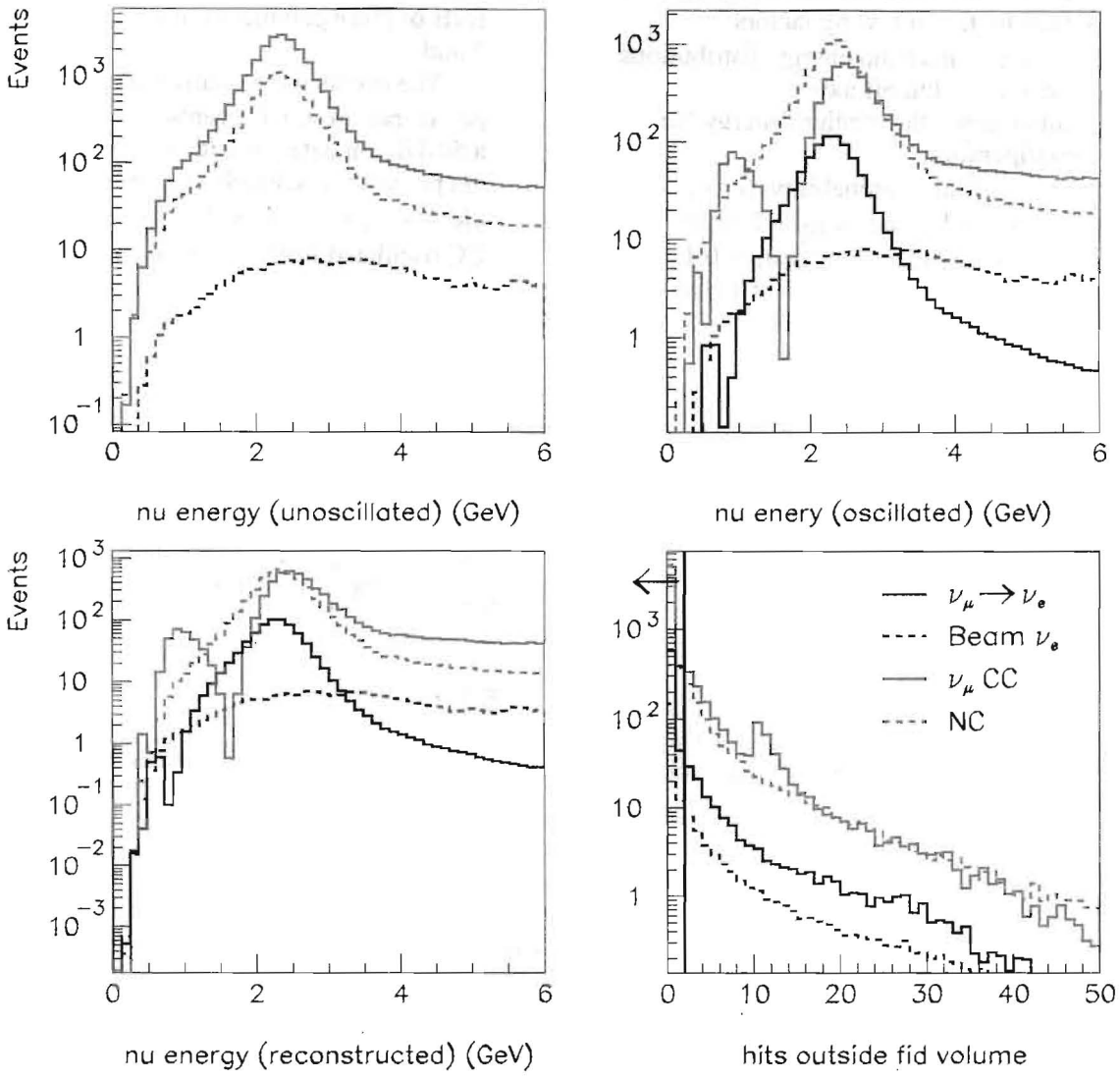

Fig. 8.4: Event samples used in this analysis. Top left: unoscillated true neutrino beam energy distributions for events that leave hits in the detector. Top right: energy distributions after oscillations. Bottom left: energy distributions for events that form a valid cluster. Bottom right: distributions of numbers of hits outside the fiducial volume of the detector. Events with more than 2 hits outside the fiducial volume are rejected.

8.6. Selection of ν_e CC Events

The selection process was in two stages. Firstly a set of cuts was applied which rejected background events with as small as possible effect on the ν_e CC events. The background events remaining after these cuts have a strong overlap with the desired sample. Further separation was obtained by forming a likelihood ratio using a number of variables and cutting on this ratio.

The initial cuts are applied consecutively on the variables shown in Figs. 8.5 and 8.6 and are:

- 200 cm < event length < 800 cm (rejects long muon tracks and short NC events)
- 8000 pe < total pulse height < 18000 pe (rejects low-y NC and high energy ν_e CC events)

- Number of hits in the track found by the Hough transform analysis > 3 (ensures that a Hough track was found)
- fraction of event hits in the Hough track > 0.75 (preferentially selects low-y ν_e CC events)
- hits/plane on the Hough track > 1.5 (selects showering events)
- cosine of the angle between the Hough track and the beam > 0.80 (rejects poorly reconstructed and high-q^2 events)

The weighted number of events remaining after each cut is shown in Table 8.1.

Cut	ν_μ CC	NC	Beam ν_e	$\nu_\mu \rightarrow \nu_e$ Signal
Beam unoscillated	22858	10594	229	
Beam oscillated	5758	10593	229	853
Reconstructed	5501	6681	202	757
Fiducial cut	4410	5950	170	653
Event length	1755	4343	143	593
Pulse height	1226	1327	67.0	508
Hough planes	1120	1043	62.0	474
Hough fraction	150	76.8	27.4	229
Hough hits/plane	20.1	56.0	26.7	223
Beam angle	11.4	50.6	26.0	218
Likelihood cut	3.6	15.4	19.1	175
Efficiency	$6.3\ 10^{-4}$	$1.5\ 10^{-3}$	$8.3\ 10^{-2}$	0.21

Table 8.1: Breakdown of the weighted number of events remaining after the successive cuts.

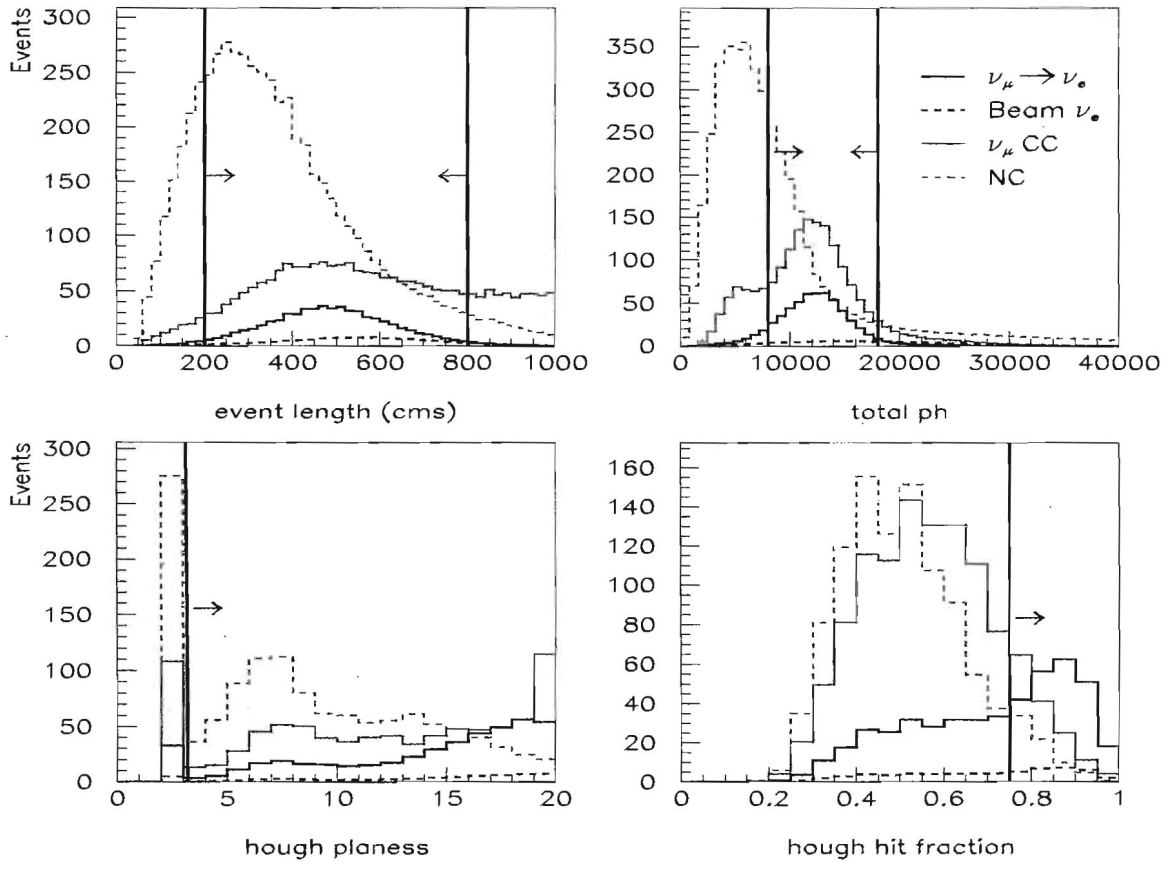

Fig. 8.5: Event distributions used for the cuts. The vertical lines define the cuts The cuts are performed sequentially in the following order. Top left; event length. Top right; summed pulse height. Bottom left; the number of planes in the Hough Transform track. Bottom right; the fraction of hits in the Hough Transform track.

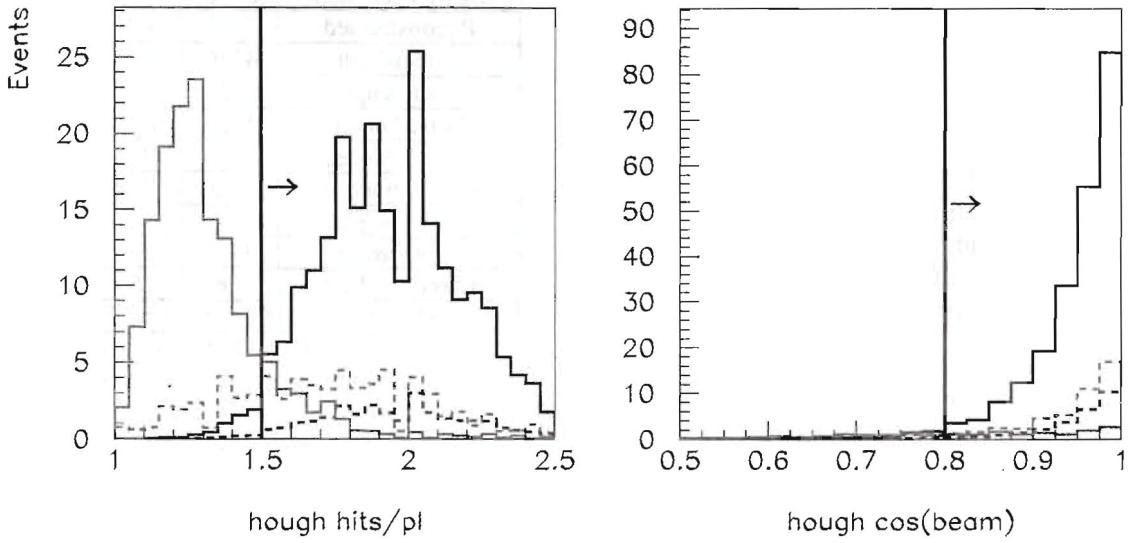

Fig. 8.6: Left; the number of hits per plane in the Hough Transform track. Right; the cosine of the angle between the Hough track direction and the z-axis.

A likelihood analysis was then performed on the remaining events. One or two-dimensional histograms of the variables in the following list were constructed for each of the event types and normalized to a total of 1.0. This then served to define a probability for any given event that it came from any of the samples. A total likelihood for any sample was found by multiplying all of the probabilities. Three log likelihood ratios between the oscillated ν_e hypothesis and the other three hypotheses were formed and plotted. Finally cuts were applied to these ratios to define the final ν_e sample.

The following one dimensional and two dimensional probabilities were used in the likelihood analysis:

- the event length
- the maximum gap (i.e. contiguous planes with no hits) in the event
- the number of detector planes in the event
- the transverse pulse height residual
- the Hough track hit fraction
- the Hough track hits per plane
- the Hough track pulse height
- the cosine of the angle between the Hough track and the beam
- the transverse pulse height weighted residual versus the pulse height in the Hough track
- total pulse height versus pulse height weighted transverse residual
- cosine of the angle between the Hough track and the beam versus total pulse height
- longitudinal rms of the pulse height versus total pulse height

For those parameters that have already been used for the cuts, the events remaining after the cuts were used to define the likelihood function. The log likelihood ratios are shown in Fig. 8.7.

There is quite good discrimination between ν_e signal events and neutral current and charged-current backgrounds. There is less separation between ν_e signal events and beam ν_e background; here the only discrimination is that the beam ν_e events tend to be of higher energy than the $\nu_\mu \rightarrow \nu_e$ signal.

The following cuts on the likelihood ratios define the sample of ν_e events in this analysis:
$\log L_{e/\mu} > -2$,
$\log L_{e/NC} > -2$,
$\log L_{e/ebeam} > -5$

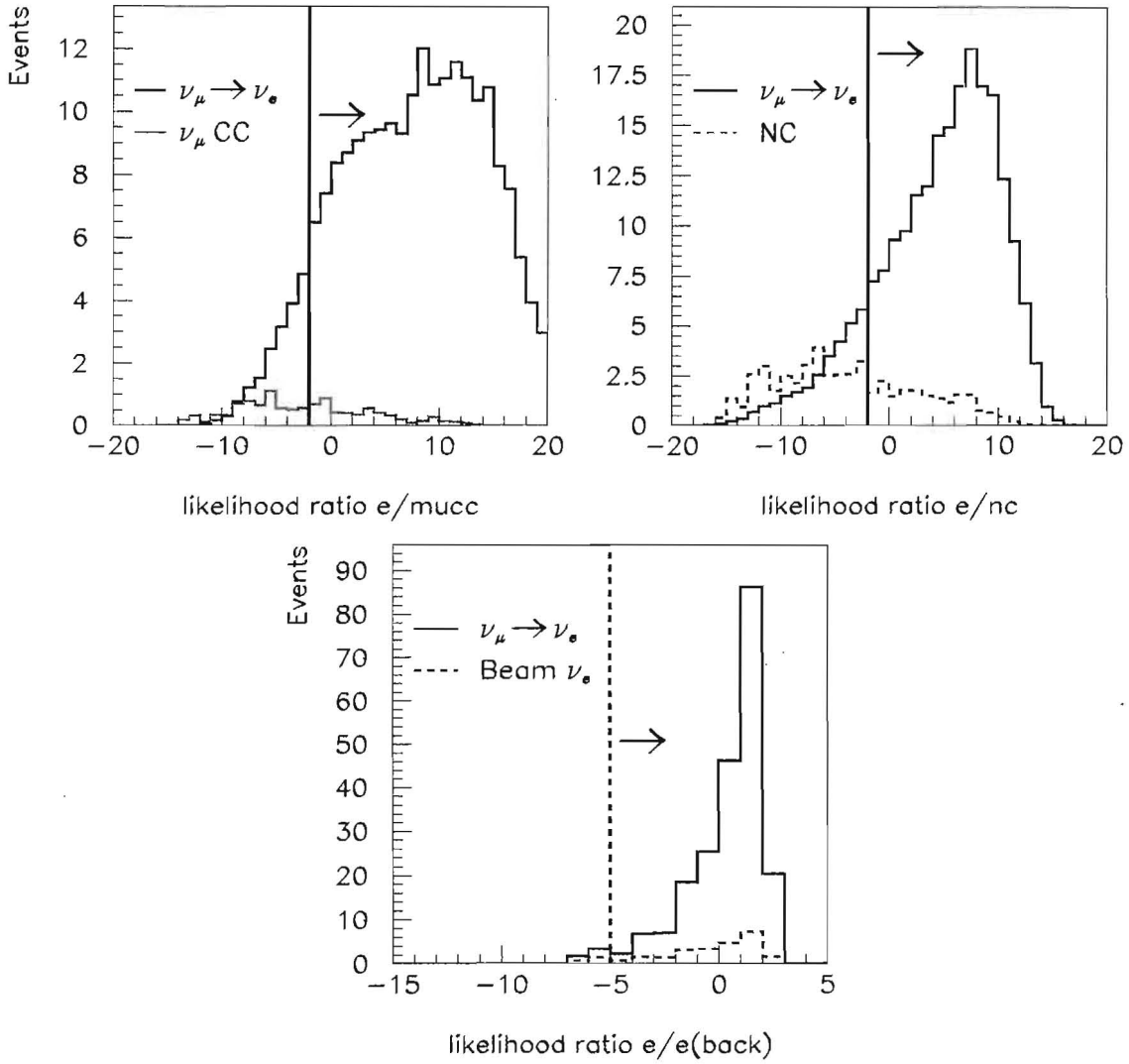

Fig. 8.7: Top left: log of the ratio of the probabilities of the ν_e CC to oscillated ν_μ CC hypotheses. Top right; log of the ratio of the oscillated ν_e CC to the NC likelihood. Bottom; log of the ratio of the oscillated ν_e CC to the beam ν_e CC likelihood.

All the cuts were optimized using the first of the two event samples, and were selected in order to maximize the Figure of Merit (FOM1). The numbers given below and in Table 8.1, show the result of applying the selection cuts to the second, independent, sample of events.

Defining the figure of merit as the number of $\nu_\mu \rightarrow \nu_e$ signal events divided by the square root of the total number of background (ν_μCC, NC and beam ν_e) events, the following results are obtained:

- signal = 175.2±1.8 events
- background = 38.1±1.5 events
- figure of merit = 28.4±0.6
- oscillated ν_e efficiency = 20.5%
- ν_μ CC rejection = 6.3×10^{-4}
- NC rejection = 1.5×10^{-3}
- beam ν_e CC rejection = 8.3×10^{-2}

The quoted errors are the errors on the numbers due to the finite statistics of the Monte Carlo, not the expected errors from any given experiment.

Using these cuts, the background due to misidentified ν_μCC and NC events is reduced to the same level as the intrinsic beam ν_e background. More stringent cuts can further reduce this background at the expense of signal. However it is difficult to reduce the beam background much further, since the only difference between beam ν_e and signal $\nu_\mu \rightarrow \nu_e$ events is the energy distribution, and this is already taken into account by including the total pulse height distributions in the cuts and likelihood analysis. The FOM1 thus does not significantly improve with harder cuts.

We have investigated a large number of alternative cuts and compositions of the likelihood function in attempts to improve the figure of merit. Adding further quantities and combinations of quantities gave little improvement, in fact frequently gave a small reduction, in the FOM1. The cuts were changed to remove more background before the likelihood analysis but after optimization of the likelihood very similar FOM1 were obtained. The changes mostly spread out the likelihood function but do not alter the fraction of background that lies under the signal. Further small reductions in the background with an enhanced signal efficiency may be obtainable by more sophisticated pattern recognition, in particular by identifying more individual tracks in the event. However, it is not expected that this will raise the figure of merit by large amounts.

To first order the effect of the analysis is to select quasi-elastic or low-y ν_e charged current events, which consist mainly of a single showering track. The selection efficiency of such events is high. Scanning the selected background events showed that they closely resembled this topology, either because of the presence of a high-energy gamma or because the superposition of charged and showering tracks resembled a single showering track.

8.7. Other Simulations

8.7.1. Alternative Figure of Merit: The Figure of Merit (FOM1) is quite insensitive to the cuts over a fairly wide range. Harder cuts give fewer events and less background, softer cuts the reverse. Analyses searching for a signal require the maximum value of FOM1. However other analyses, for example those measuring parameter values, may be more sensitive with more events and more background. The relevant function is then an alternative Figure of Merit (FOM2), which is the ratio of the signal to the square root of the signal plus background. In general this has a maximum for softer cuts with larger signal and more background. However, at the maximum of FOM2 the value of FOM1 is only about 1.0 below its maximum value. The above analysis is maximized for a search experiment using FOM1.

8.7.2. Other off-axis positions: The analysis has been repeated for other off-axis positions using the same primary beam. The results are given in Table 8.2. As one goes further from the beam axis the beam flux and the peak energy decrease. The convolution of beam and oscillation function increases and thus the signal increases with decreasing off-axis distance. However the background also increases at smaller distances because of the increase in the higher energy flux and the decrease in the suppression of charged current events by oscillation. 10 km off-axis is an optimum position under the conditions of this simulation but larger off-axis positions could be preferable for the observation of the matter and CP violating effects described in Chapter 3.

Position/Type	Signal	Background	FOM1
8km, ν	228	68	27.5
10km, ν	175	38	28.4
12km, ν	123	24	25.0
14km, ν	89	21	19.5
10km, ν, matter	208	39	33.4
10km, anti-ν	66	22	14.1
10km,ν,Δm^2=0.002	134	42	20.8
10km, ν, RPC	132	27	25.4

Table 8.2: The signal, background and FOM1 of simulations under various different conditions. The first 4 rows are for the main simulation described in this section for different off-axis positions. The fifth row includes matter effects for the normal hierarchy. The sixth row is the simulation for the anti-neutrino beam. The seventh row has a lower value of Δm_{32}^2=0.002 eV^2 and the eighth row is for the RPC simulation. The event selection parameters have been reoptimized for each condition.

8.7.3. Matter effects: Matter effects are significant at these distances and energies and the discussion of this experiment's scientific potential in Chapter 5 includes matter effects and CP violation. If matter effects with a positive Δm_{32}^2 (normal hierarchy) are included in the simulation at 10 km off-axis, the signal rises to 208 events while the background stays essentially constant. This results in a figure of merit (FOM1) of 33.4.

8.7.4. Anti-neutrino beam: A similar analysis has been carried out for the anti-neutrino beam. In this case the contamination of neutrinos in the beam is significant and has been included. The anti-neutrino flux is lower than the neutrino flux but the event selection efficiency is somewhat higher due to the different y distributions of the events. The results for a 250 kT-year exposure, the same as for the neutrino beam, are given in table 8.2

8.7.5. Lower Δm^2: The allowed value of Δm_{32}^2 from the SuperKamiokande analyses still covers a wide range. In general the sensitivity of this experiment decreases as Δm_{32}^2 moves lower, because the peak in the oscillated spectrum moves to lower energies where the beam flux is falling off. To calibrate the changes expected if Δm^2 changes, the simulation has been run for a Δm_{32}^2 of 0.002 eV^2. The results are given in table 8.2. It can be seen that the background remains approximately constant but the signal is reduced by 23%.

8.7.6. Light level: In order to test the sensitivity to the light level a simulation with 25% less light was carried out. The event selection is not expected to be very critical on the light level since the assumed 35 pe collected at the far end of a strip is well above the threshold of 20 pe. Also the event selection is not strongly dependent on the presence or absence of individual hits. In fact the simulation with 25% less light gave no statistically significant change in the signal efficiency, background rejection or figure of merit after reoptimization of the cuts.

8.7.7. RPC simulation: A similar analysis has been carried out for the RPC based detector. A realistic simulation of the 2-dimensional readout detector described in the Appendix has been produced. A similar cut and likelihood analysis to that described in section 8.6 was performed. The results at 10 km off-axis are given in Table 8.2. An RPC detector has the advantage that two-dimensional readout is available in each sensitive gap compared to the one-dimensional readout of the scintillator detector. On the other hand the scintillator detector measures pulse height and is sensitive to the number of particles crossing the sensitive region and their deposited energy, whereas the RPC readout is digital. It is an important goal of the simulations to quantify the relative gain of each case. To do this the simulations must be comparable in all respects other than the ones to be tested. This has not yet been demonstrated with the present simulations but will be done on the time scale of the final technology decision.

8.8. Other Physics

The events generated for the $\nu_\mu \rightarrow \nu_e$ analysis have been used to test this experiment's sensitivity to the quantities, Δm_{32}^2, $\sin^2 2\theta_{23}$ and the possible fraction of sterile neutrinos. The analysis has been carried out at off-axis locations of 12 km and 10 km. The results are better at 12 km off-axis because the oscillation dip is more centered in the beam peak. It is these that are quoted here. The 10 km off-axis results are given in Reference [2]. A likelihood analysis using similar quantities to those of the ν_e analysis was carried out to separate CC and NC events. Figure 8.8 shows the CC/NC likelihood ratio. CC-like and NC-like event samples were selected as shown in the figure. The CC-like sample had a selection efficiency of 82% for true CC events and a 7% contamination of NC events. The NC-like sample had a selection efficiency of 58% and a contamination of 42%.

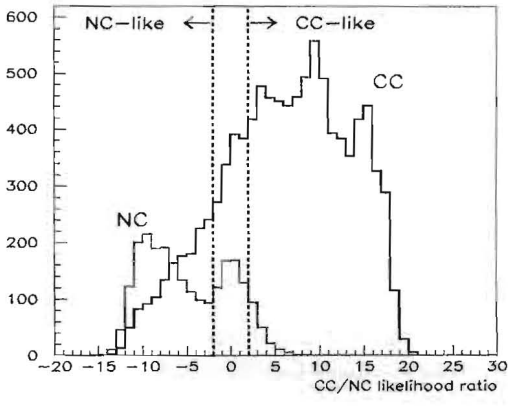

Fig. 8.8: Likelihood ratio distributions for true CC and NC events. The cuts used to define CC-like and NC-like samples are indicated by the two dashed lines.

8.8.1. Measurement of oscillation parameters: The resultant measured energy distribution of CC-like events for oscillation parameters, Δm_{32}^2=0.0025 eV^2 and $\sin^2 2\theta_{23}$=0.95, was fitted to determine the best measured values of the parameters. The same five year exposure as for the ν_e appearance experiment was assumed and systematic errors on the neutrino energy scale, overall flux normalization and the NC cross-section were included. The left hand plot in Figure 8.9 shows the 90% confidence level contour with and without systematic errors and the right hand plot the one dimensional $\Delta\chi^2$ contour for $\sin^2 2\theta_{23}$. It can be seen that if these were the oscillation parameters, it would be possible to exclude maximal mixing ($\sin^2 2\theta_{23}$=1.0) at greater than 99% confidence level and significantly improve the determination of $\sin^2 2\theta_{23}$.

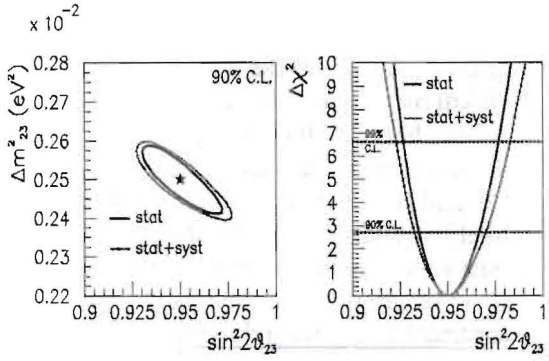

Fig. 8.9: Errors from this analysis on the parameters Δm_{32}^2 and $\sin^2 2\theta_{23}$. The input values are given by the star.

8.8.2. Limits on sterile neutrinos: The signal for $\nu_\mu \rightarrow \nu_s$ oscillations is a depletion in the number of observed neutral current events compared with the expectation if the neutral current events are unaffected by oscillations. A simultaneous fit was performed to the CC-like and NC-like energy distributions with the normal parameters Δm^2 and $\sin^2 2\theta_{23}$ augmented with an additional parameter $\sin^2 2\theta_{\mu s}$, the amplitude for $\nu_\mu \rightarrow \nu_s$ oscillations. It was assumed that the sum of active and sterile oscillations was unity and that the active and sterile neutrinos oscillated with the same value of Δm^2. Figure 8.10 shows the results of a fit assuming Δm^2=0.0025 eV^2 and $\sin^2 2\theta_{\mu s}$=0.0. The left hand plot shows the two-dimensional contours assuming just statistical errors and statistical plus systematic errors. The right hand plot shows the $\Delta\chi^2$ curve for $\sin^2 2\theta_{\mu s}$.

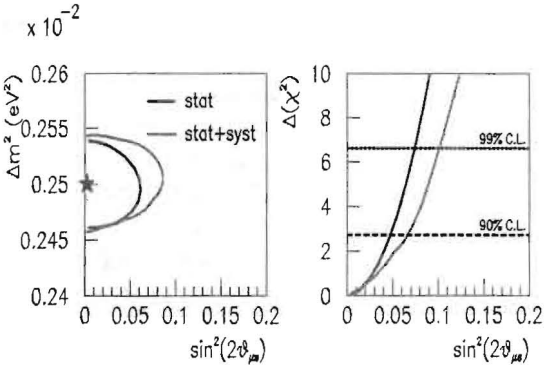

Fig. 8.10: 90% confidence allowed region in the Δm_{32}^2,$\sin^2 2\theta_{\mu s}$ plane. The input values are shown by the star. The right hand plot shows the one dimensional projection of the $\Delta\chi^2$ surface.

It can be seen that 90% confidence limits of 0.07 can be set on the fraction of sterile neutrinos, including both statistical and systematic errors. More details of these analyses can be found in Reference [2].

Chapter 8 References

[1] Peter Litchfield, Leon Mualem, David Petyt, "Simulation of a Solid Scintillator Off-axis Detector," Off-axis-Note-SIM-23 (2003). The liquid scintillator layout was the same apart from the active element dimensions.

[2] David Petyt, "Other oscillation measurements in the off-axis detector," Off-axis-Note-SIM-32 (2004).

9. Neutrino Beam Backgrounds, Systematic Studies and the Near Detector

9.1. Introduction

In this chapter, we discuss the systematic uncertainties related to the NuMI neutrino beam and to detector response. We plan to make use of measurements in the NOvA Near Detector and in test-beam studies with a Calibration Detector to calculate corrections for these systematic effects. We will also use measurements made by the MIPP, MINOS and MINERvA experiments to reduce systematic uncertainties and improve our sensitivity to electron-neutrino appearance. At the end of this chapter, we propose a program of test-beam measurements to determine the absolute and relative responses and energy calibrations of the NOvA Near and Far Detectors.

There are two general categories of backgrounds in NOvA: those that originate from the neutrino beam itself and those that originate from cosmic-ray events that occur within the neutrino-beam time window. Chapter 8 has already described the simulation and analysis of beam-related backgrounds. The current chapter discusses how their levels in the far detector can be determined using measurements in one or more near detectors and what this implies for the near-detector design. Chapter 10 describes the cosmic-ray background sources and their expected magnitudes, which must be well below the beam-induced backgrounds to achieve the best physics sensitivity.

9.2. Near Detector Requirements

The primary near-detector design requirement is that it should be as similar as possible to the far detector in material and segmentation. This requirement ensures that the efficiencies for signal and background events are nearly identical. To predict the backgrounds at the far detector we also need to consider the differences between the neutrino beam spectra at the near and far locations. Differences in background levels will result from the different energy dependence of different neutrino interaction processes. Therefore, errors on the background prediction will come primarily from flux and exclusive-channel cross section uncertainties. If there were only one kind of background, if all neutrino scattering processes had the same cross section as a function of energy, and if their differential distributions did not change with energy, then the far to near ratio for the background would be robust and uncertainties in the absolute flux and cross section would completely cancel. However, this is clearly not the case, although some uncertainties will cancel in the ratios of near and far measurements. To keep the background uncertainties low it is important to optimize both the location and design of the near detector and also to take advantage of measurements by other experiments running in the NuMI beamline.

9.3. Near Detector Location and Design

In this section we compare the neutrino beam spectra at several possible near detector locations with those at the far detector "baseline" site. As described in Chapter 11, this site is assumed to be at Ash River, Minnesota, 810 km from Fermilab and 10 km off the NuMI beam axis. Given the forthcoming hadron production measurements of the MIPP experiment using the NuMI target, the uncertainties on the ratios of the fluxes between the near and far detectors are expected to be at the few percent level. The largest remaining uncertainties will be due to the uncertainties in the total and differential cross sections of channels that produce background events. We consider these processes and the resulting uncertainties on the far detector prediction for different near detector locations.

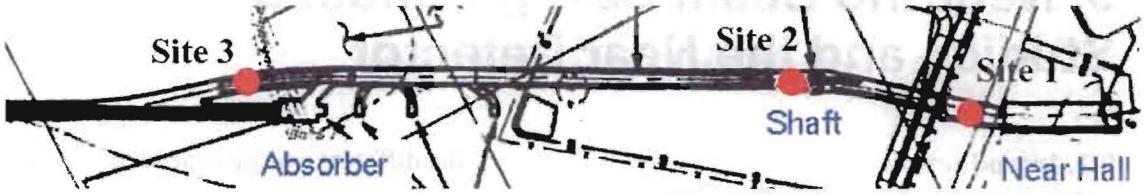

Fig. 9.1: The NuMI access tunnel upstream of the MINOS near detector hall. The beam direction is from left to right. The off-axis angles are: Site 1 - 4 mrad; Site 2 - 21 mrad; Site 3 - 16 mrad. Off-axis angles are measured from the average pion decay location, 200 m downstream of Horn 1.

9.3.1. Possible NOvA Near Detector Sites: The NuMI tunnels have several sites that could accommodate a near detector of similar construction to the far detector. Fig. 9.1 shows the layout of the MINOS near-detector hall access tunnel. Starting at the Absorber Hall, on the left side of the figure, the tunnel makes a sharp turn to the west just downstream of the absorber. It continues parallel to the neutrino beam direction at a distance of ~14 meters from the beam axis for a distance of ~250 meters. Then it bends back east to enter the MINOS near detector hall, which is on the beam axis. This access tunnel geometry makes a wide range of off-axis angles accessible for an off-axis near detector. Fig. 9.1 indicates three possible locations for a near detector: just upstream of the MINOS near detector (Site 1), just upstream of the NuMI access shaft (Site 2), and a third location just down stream of the NuMI hadron absorber (Site 3). The transverse dimensions of the NuMI tunnels in all these locations are similar to those of Site 2, shown in Fig. 9.2. Each location provides ~3.5 meters of useable width (allowing ~1 meter for a walkway), and ~5.0 meters of usable height.

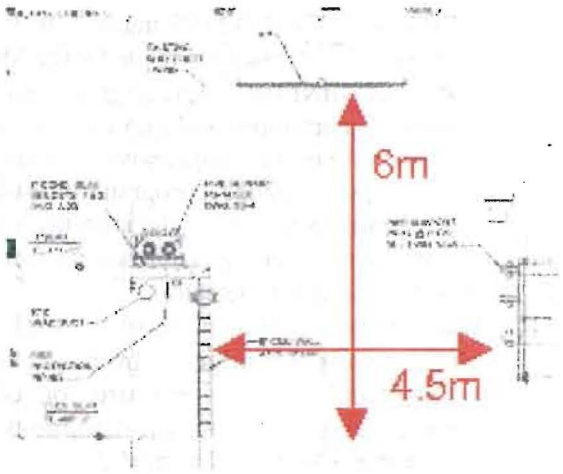

Fig. 9.2: A cross-section view of the access tunnel near Site 2 (see Fig. 9.1).

Downstream locations have the advantage of minimizing the neutron and rock-muon rates. The larger off-axis angles of upstream locations, because of the reduced rates there, minimize the event overlap problem. Given the range of sites available, one can attempt to optimize the near detector location to minimize differences in the neutrino flux at the near and far detector locations.

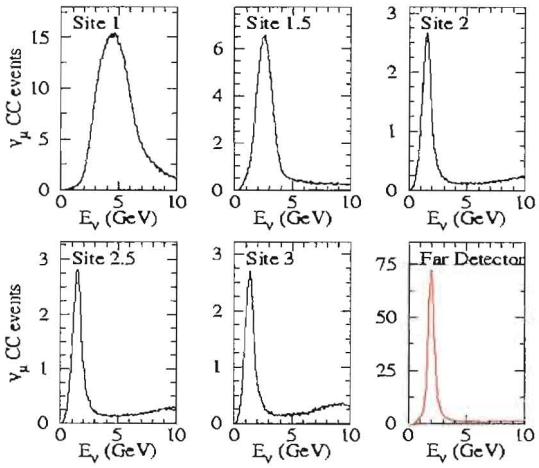

Fig. 9.3: Muon-neutrino event spectra at several different near detector locations (see Fig. 9.1).

Fig. 9.3 shows the muon neutrino event rates for several locations in the NuMI halls, where the sites labeled "1.5" and "2.5" are located midway between the Sites 1, 2, and 3 as shown in Fig. 9.1. There are two main differences between the spectra at these sites and the spectrum at the far detector. The peak is broader at the near site than at the far site, and the "high energy tail" is a larger fraction of the total event sample in the near detector. The energy spectrum is widened at the near detector because there is a broad range of decay positions of the parent pions, so there is no single "off axis angle" that one detector sees. At the far detector, the hundred-meter range of decay locations has a negligible effect on the off-axis angle. At the near detector, the high-energy tail is fractionally higher because these events come from the high-energy pions that decay farthest downstream in the decay pipe. Those decays are significantly closer to the near detector than the decays of the pions that give events in the peak of the distribution. At the far detector these differences are negligible.

Based on this comparison alone, the best near detector location would be midway between the sites labeled "1" and "2," roughly half way between the location of the NuMI shaft and the entrance to the MINOS near detector hall. This site gives electron and total neutrino spectra that are reasonably similar to those at the far-detector site. One cannot optimize for both the electron and total neutrino fluxes at the same time. The electron neutrinos come predominantly from the muon decays farther downstream in the decay pipe while the muon neutrinos, which make up 99% of the total flux, originate from somewhat farther upstream. Although the ν_μ flux is expected to be quite different because of $\nu_\mu \rightarrow \nu_\tau$ oscillations, the total neutrino flux, which gives rise to the neutral current backgrounds, is worth trying to match. At Site 1.5, the expected event rate is 17 events per 4×10^{13} pot/kT (one proton spill at design NuMI intensity per kT). A more detailed comparison between the neutrino fluxes expected at this site and those expected at the far site is shown in Fig. 9.4.

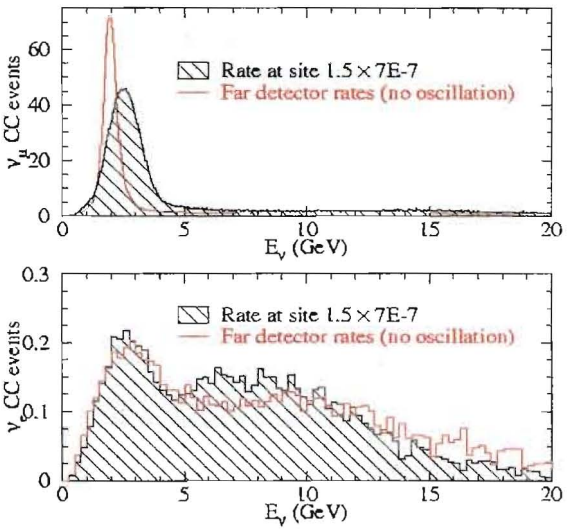

Fig. 9.4: The muon- and electron-neutrino event rates in a detector located at site "1.5."

9.3.2: Near Detector Design: We have designed the NOvA Near Detector to be as similar to the far detector as possible and to fit into the space available at site 1.5 in the access tunnel to the MINOS near detector hall. This detector would be 3.7 m wide by 4.9 m high by 10 m long. With the same transverse (~4 cm) and longitudinal (~23 cm) segmentation as the far detector, it would have 22 planes containing 2,640 horizontal liquid scintillator tubes and 22 planes containing 1,980 vertical tubes. The total number of tubes would then be 4,620, which is also the number of electronics channels. The detector would have a mass of about 120 metric tons.

The 10-m length of the detector provides a 3-m long fiducial region, preceded by a 1-m long upstream "veto" region and followed by a 6-m long downstream region that provides efficient identifi-

cation of muon-neutrino charged current events. The ~1-ton fiducial region is defined by the requirement that neutrino event vertices should be at least 1.5 m from the edges of the detector. A clean sample of ν_μ charged current events is required for the study of ν_e backgrounds arising from this process, described later in this chapter. For reference, overall 10 m depth of the detector is sufficient to range out a 1.5 GeV muon that traverses its entire length.

Approximately two neutrino interactions will occur in the near detector during each 8-microsec beam spill of 4×10^{13} protons on target. The slow response of the high-gain APD electronics used on the far detector will likely prove unsatisfactory for this environment. We expect that the off-axis near detector will be instrumented with photomultiplier tubes and fast electronics similar to that used in the MINOS near detector. Other differences in near and far detector response will result from the shorter tube and WLS fiber lengths. Corrections for these differences will be determined from measurements made with the NOvA Calibration Detector, as described in Section 9.8 below.

Finally, the detector assembly and installation procedures for the near detector will also be different from those used for the far detector. Access shaft limitations may require the particleboard absorber planes and the PVC extrusions for the near detector to be moved underground separately and assembled at the detector site.

Although design optimization for the NOvA near detector is still at an early stage, we believe that the space available in the access tunnel to the MINOS near detector hall will prove adequate for our needs and that additional excavation will not be necessary.

9.4. Cross Section Uncertainties

As was described in Chapter 8, the beam-related backgrounds to a $\nu_\mu \rightarrow \nu_e$ oscillation search fall into three categories: intrinsic ν_e contamination in the beam, neutral current events, and charged current ν_μ events where the outgoing muon is not identified. The challenge is to measure not only the sum of these backgrounds in the near detector, but to predict accurately the total contribution at a far detector.

Assuming the near and far detectors have the same background rejection capabilities, one can also consider these different fluxes to determine the far over near ratio for the three different backgrounds, as a function of near detector off axis angle. Fig. 9.5 shows the far to near ratio for the three different backgrounds, as a function of near detector off axis angle, assuming the far detector is 12 km off axis, 820 km from Fermilab. The simulation assumed a detector of RPCs and particleboard, with 4 cm transverse segmentation and a third of a radiation length longitudinal segmentation. The conclusions would be similar for other choices of readout technology, optimized for the figure of merit (the signal over the square root of the predicted background).

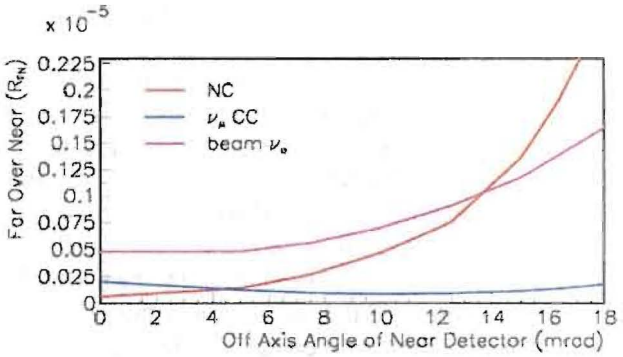

Fig. 9.5: Far-over-near ratios for the three different backgrounds as functions of off-axis angle of a Near Detector. We assume the far detector is 12 km off axis at 820 km from Fermilab (14 mrad), and that $\Delta m^2_{32} = 2.5\times10^{-3}eV^2$ and $\sin^2 2\theta_{23} = 1$.

As an example of what uncertainties would be for the far detector background prediction assuming an identical near detector, consider the effects due to our current imprecise knowledge of cross sections. Neutrino interactions in this energy regime can be classified as four different kinds of processes: (quasi-) elastic, resonance, coherent, and deep inelastic scattering (DIS), where each of these processes can be either neutral current (Z-exchange) or charged current (W-exchange).

In the (quasi-) elastic process, the proton is knocked out of the nucleus and the final state lepton is a (muon) neutrino. In resonant processes a Δ resonance is created, which then decays to a proton or neutron, and a pion. Figure 9.6 shows the current set of measurements of this process in the charged current channel [1]. The neutral current processes are even more poorly constrained.

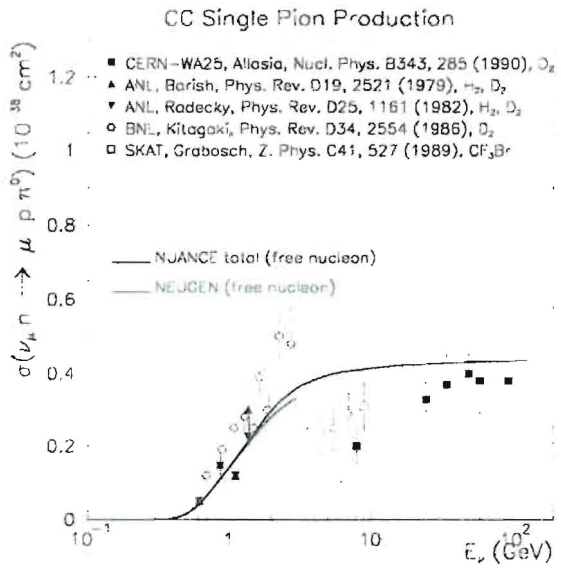

Figure 9.6: Compilation of charged current single pion production cross-section measurements [1].

Coherent processes are where the neutrino scatters off the nucleus as a whole, and the only final state particle produced (besides the lepton) is a single pion—a charged pion for the charged current process, a neutral pion for the neutral current process. Coherent neutral current interactions, while rare, are a significant fraction of the neutral current backgrounds. In these events, most of the final state energy is in an electromagnetic particle. The only ways the detector can distinguish this from the signal is (1) by identifying two incident particles, i.e., two decay photons instead of a single electron, and (2) because the final observed energy is often significantly less than the incoming neutrino energy. Coherent charged current interactions, on the other hand, will not play a significant role and are not included in the simulations. Fig. 9.7 shows a compilation of both charged and neutral current coherent pion production cross-section measurements.

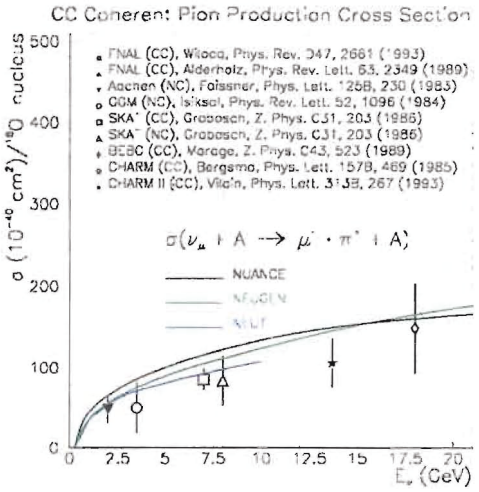

Figure 9.7: Compilation of coherent pion production cross-section measurements. Both charged and neutral pion production are shown [1].

Process	Quasi-elastic	$\Delta\rightarrow$ π^0X	$\nu A\rightarrow$ $\nu A\pi^0$	DIS
$\delta(\sigma)/\sigma$	20%	40%	100%	20%
Signal ν_e	55%	35%	N/I	10%
NC	0%	50%	20%	30%
ν_μ CC	0%	65%	N/I	35%
Beam ν_e	50%	40%	N/I	10%

Table 9.1: Neutrino scattering processes that contribute as either signal or background, the uncertainties on those processes at low energies, and the fraction of each process for each background (±5%). N/I means not included.

Table 9.1 shows the processes, estimates of their associated uncertainties (at the relevant neutrino energy) and their contributions to the background. To evaluate the systematic error in the far detector background prediction due to these uncertainties, we use the simulation to determine by how much the far-to-near ratio would change for shifts of each cross section by its uncertainty. Fig. 9.8 shows how shifts in each of these cross sections would change the total far to near ratio and therefore produce a systematic uncertainty in the background prediction.

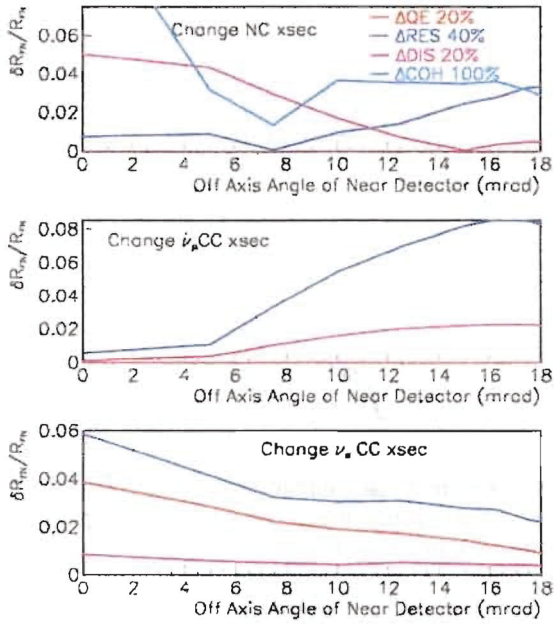

Fig. 9.8: Fractional changes in the far to near ratio (R_{FN}) due to current uncertainties in neutrino cross sections. Uncertainties on the energy dependences of the cross sections are not included.

Fig. 9.8 shows that, the farther off axis one places the near detector, the less the cross section uncertainties will contribute to the ν_e and neutral-current backgrounds. At such locations the $\nu_\mu$and ν_e fluxes have more similar energy distributions to those at the far detector flux, and so the same processes would dominate and there is some cancellation. However, for the ν_μ charged-current backgrounds, the farther off axis one goes, the more likely the events will pass the analysis cuts and so the background level rises.

Fig. 9.9 shows the errors from the above plots added in quadrature. Clearly at all off-axis angles there are significant uncertainties. One way to reduce these uncertainties is to increase the segmentation for sections of the off-axis near detector to better separate the various backgrounds from each other. However, there is currently an experiment proposed to do dedicated cross-section measurements in the NuMI beamline (i.e., MINERνA), and these measurements would reduce several of the cross section uncertainties described above.

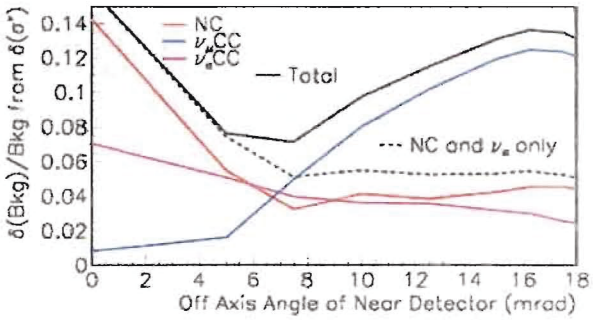

Fig. 9.9: Total cross section errors for a near detector that is identical to the far detector (without auxiliary measurements).

The following three sections describe some auxiliary measurements that could be made to reduce these background uncertainties. First, the charged current cross sections themselves can be better measured (on axis, for example). Second, if one can independently determine the ν_μ charged current backgrounds present in the near detector, the remaining error due to cross-section uncertainties will be reduced to about the 5% level (for a near off-axis detector located at least 8 mr off axis). To minimize the uncertainty due to the imperfect knowledge of the energy dependence of the remaining relevant cross sections, 12 mr would be where the electron neutrino fluxes (and hence the source of the largest background) are best matched to the far detector.

9.5. The MINOS Near Detector

The first question one might ask is whether or not the presence of the MINOS near detector, which is located on the NuMI beam axis, will help in reducing either cross-section or flux uncertainties. Unfortunately, the MINOS near detector will have a limited role to play in NOνA. The MINOS detectors are optimized for muon detection in the few GeV energy range and use 2.54-cm thick steel plates for the absorber material. At this segmentation, the ability of the MINOS detectors to separate electron neutrino events from neutral current events is significantly worse than for the NOνA detector [2]. A direct translation of the "*e*-like" sample measured on the beam axis by the MINOS near detector to a detector optimized for electron neutrino appearance, located off the beam axis,

will rely on detailed models of both detectors and the incident neutrino beam.

The most reliable procedure for estimating the off-axis electron-neutrino flux using the MINOS near detector would start with the measurement of the CC muon-neutrino event rate by the MINOS near detector. From this rate one can infer the ν_e rates using a Monte Carlo prediction of the (far ν_e)/ (near ν_e) ratio. A prediction of this ratio can be made to better than 5% on the beam axis because most uncertainties cancel. The last step is again to rely on a Monte Carlo prediction to translate the on-axis electron-neutrino flux to the off-axis location. Again, since this relies on ratios, many uncertainties cancel. The largest remaining source of uncertainties comes from the ratio of neutrino cross sections at the peak of the off-axis spectrum (2 GeV), to the cross-sections at the peak of the on-axis spectrum (6 GeV).

Using this method, we expect to be able to predict the electron neutrino flux at an off-axis detector with roughly 15% accuracy. Note, however, that this method yields the electron neutrino event rate before corrections for detector efficiencies or cross sections are taken into account. Unfortunately, these corrections will be large, since the ν_μ events that are detected in the MINOS detector are certainly a very different mix of DIS, resonance, and quasi-elastic channels than those events which would pass analysis cuts in a fine-grained near or far detector off the NuMI axis.

9.6. The MINERvA Detector

The proposed MINERvA detector can contribute substantially towards reducing the uncertainties on the backgrounds for NOvA. The MINERvA experiment is designed to measure neutrino-nucleon cross-sections in the few GeV region, and was proposed to Fermilab in late 2003 [3]. The detector has a completely active scintillator target, surrounded by electromagnetic and hadronic calorimetry. The transverse segmentation is 1.65 cm, and the longitudinal segmentation is 1.7 cm. Therefore by summing together two MINERvA planes and ignoring the following nine planes, one can approximately simulate the longitudinal granularity of the NOvA Near Detector, and also measure background rejection as a function of detector granularity. The proposal is to begin the MINERvA running with the detector on the NuMI axis, although the possibility of eventually running at an off-axis location is not precluded.

Even with the detector on axis, MINERvA can make significant contributions to NOvA. Because it is a purely active detector, it can identify ν_e and ν_μ quasi-elastic events with minimum backgrounds from resonant or DIS processes, and provide the cleanest measurement of the ν_e and ν_μ interaction rates as a function of neutrino energy. The fluxes themselves should be predicted to about 5%, from the MIPP experiment [4] combined with NuMI horn B-field measurements. This implies a measurement of the quasi-elastic cross section to about 5%, compared to the current 20% uncertainty. In addition, because of its final state reconstruction capabilities, MINERvA should be able to identify and measure the charged-current resonance processes and reduce the uncertainty on that cross section as well. Therefore, the ν_e flux and estimated background level in the near and far detectors should be predictable with MINERvA to the few percent level.

The MINERvA detector on axis can also provide an important constraint on the ν_μ charged current background. Because the MINERvA detector has very fine segmentation and is totally active, it has better low-energy muon identification than the NOvA detectors. Muons that range out will decay to electrons whose energy can be seen in the pure scintillator detector, while pions will more likely be captured before they decay. In addition, because the MINERvA detector is five times more segmented, low-energy hadronic interactions of pions are more likely to be identified. Although the on-axis and off-axis fluxes are quite different, the study of charged-current processes on-axis is still quite relevant because the total neutrino energy can be reconstructed and the ratio of ν_μ fluxes on and off axis will be well-constrained by MIPP measurements to the few percent level.

9.7. Auxiliary Near Detector Measurements

Besides measuring the sum of all the backgrounds in an identical material, the NOvA Near Detector can also provide an additional handle on the charged current background. In order to do this, it must be made several meters longer than would otherwise be needed to contain the ν_e signal events.

To determine the fraction of ν_μ charged current events that would pass all analysis cuts, one can measure that fraction for events with identified muons, and then predict the number of times that the muon is undetected. This procedure works in the limit that the nature of the hadronic system in a neutrino charged current interaction is dependent only on the hadronic energy of the system, and not on the neutrino energy.

In the analysis described in Chapter 8, in order for the ν_μ CC events to be misidentified as NC events, there has to be a track identified as an electron (most likely an asymmetrically decaying π^0) *and* the muon has to be missed. The cases where a muon is misidentified as an electron, thus fulfilling both conditions, appear to be rare. We define a muon as a non-shower-like track that traverses at least 8 planes, which is approximately 2.7 radiation lengths. Thus, high *y* events (where *y* is defined as the fractional neutrino energy loss) form the majority of the ν_μ CC background.

ν_μ CC events, to a very good approximation, are characterized by a flat *y* distribution near high *y*. Thus, to a good approximation, for a given neutrino energy, the distribution of these events with muon range >8 planes, which satisfy our signal criteria should be flat, when plotted as a function of muon range (equivalent to 1-*y*). The contribution to the background from ν_μ CC events with muon range <8 planes can just be obtained by the integral of this distribution for muon range between 0 and 7 planes, as obtained from the extrapolation of the observed distribution. In reality, the flatness expectation is altered by the fact that our selection criteria for the signal interact at some level with the energy of the muon. Moreover, our energy spectrum is not monochromatic. By allowing a slope in this distribution and its extrapolation, these effects can be incorporated.

The relevant length distributions for the different categories of events are shown in Fig. 9.10. The top figures show the range distribution for NC and beam ν_e events. Here the "muon" is most likely a charged pion (or less likely a proton) that has traveled far enough without interacting visibly to appear like a muon. As expected, there is a sharp increase in such events for short range, and for range >14 planes the contribution is very small. The distribution for the ν_μ CC events, as might be expected, extends to much larger ranges. Furthermore, a linear fit to this distribution not only fits the data with range > 14 well, but also appears to agree well with the predicted number of events with $5 \leq$ range ≤ 14. This vindicates our procedure and gives one confidence that linear extrapolation below range of 8 based on this fit is still valid.

The fourth plot gives the range distribution for all of the above backgrounds summed together. Clearly, this would be the only distribution accessible in the experiment. A fit to those data with range >14 can be used to extrapolate to the number of background events with "muon" range <8 planes. The answer obtained is about 20% ±30% higher than the actual number of ν_μ CC background events.

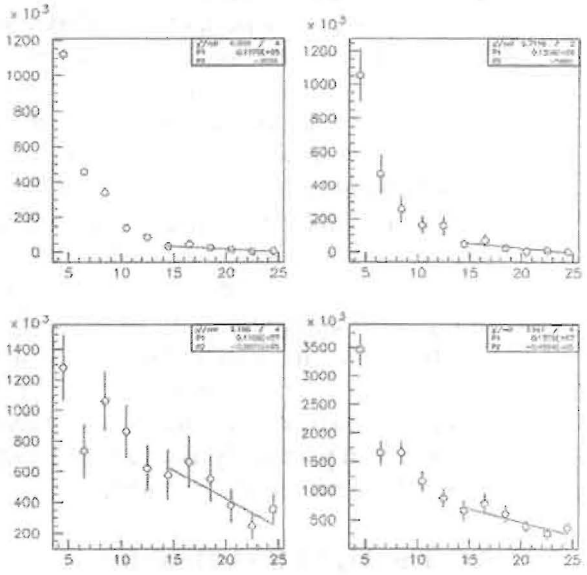

Fig. 9.10: Length distributions (in units of planes, where 1 plane is 0.33 radiation lengths) for the several categories of near detector events. Top left - NC; top right - beam ν_e; bottom left - ν_μ CC; bottom right - total event sample.

To show how much an error on the extrapolation would contribute to an error in the far detector background, we compare the number of background events in the far detector under two different assumptions about ν_μ CC. One is the correct assumption about the fraction of ν_μ CC events in the near detector background and the other when this fraction is either under- or overestimated. Fig. 9.11 shows the difference between the correct far detector prediction and the wrong one, assuming one has the fraction of ν_μ CC events wrong by

10% or 20%. Although the far detector background is small because of oscillations, it must be measured to better than 10% of itself to get a total uncertainty of less than 5% at a near detector location where other uncertainties are minimized.

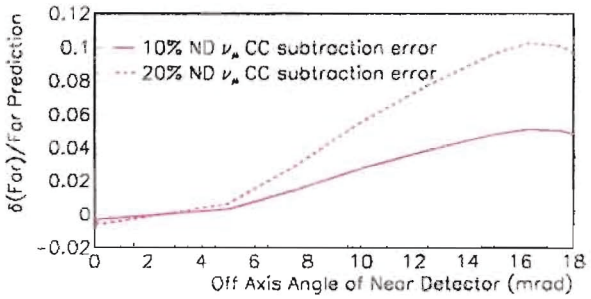

Figure 9.11: Fractional change in the total far detector prediction due to different charged current subtraction errors in the near detector.

9.8. Test Beam Program

The NOvA Near and Far Detectors will have to be calibrated *in situ*, as was the case for the MINOS detectors, and therefore will experience similar limitations to this process. Requirements for the absolute and relative (between the two detectors) energy calibration in the appearance experiment are not as stringent as for MINOS. However, the efficiency of event reconstruction, which is critical for NOvA, generally improves with better calibration. For NOvA disappearance measurements, we assume the same requirements as for MINOS: the energy scales should be determined with 5% absolute and 2% relative uncertainty. More critical for NOvA will be understanding of topological response (a pattern of hits) of electromagnetic interactions. The detailed response function of the low-density detector can be used to tune algorithms to identify an electron signal and to reject backgrounds, mostly from $\pi^0 \rightarrow \gamma\gamma$ followed by the photon conversions in the hadronic cascades.

We assume that the far detector will be located in a surface building with no overburden, while the near detector will be placed in the MINOS near-detector hall access tunnel. There will be a high rate of cosmic ray tracks in both detectors, which will provide a stable source of muons to monitor and calibrate detector response. Although cosmic rays are unlikely to pose a significant background problem, as described in Chapter 10, a detailed understanding of detector response will be essential to maximize the efficiency of event identification and the accuracy of energy determination.

Since neither of the two detectors can be directly exposed to a test beam to enable such calibrations, we plan an extensive test-beam program to expose a special calibration module, a smaller replica of the large detectors, to a charged-particle test beam. Using selectable beam momentum settings and a particle identification system, a full response matrix of the detectors can be measured. The special calibration detector will be constructed with longitudinal and lateral segmentations identical to that of the large detectors. The readout electronics will also replicate the techniques employed by the far and near detectors. The test beam program described here is derived from the MINOS experience and takes advantage of lessons learned there.

We envision several elements of the test beam program that can be executed in stages. Below we present a preliminary outline of the main goals of the program.

FY05 and FY06 (pre-construction period):

- Various prototype versions, consisting of a small number of the far and near detector cells, will be constructed and tested with prototype front-end electronics readout and data acquisition.
- Beam test data will be taken to verify the expected response.
- Response to cosmic ray muons will be studied simultaneously and compared to beam interactions.
- Test beam activities will provide feedback for the improved design and future fabrication and installation effort.

FY07 to FY09 (detector construction period):

- A final version of the calibration detector will be designed and constructed. The overall size of the detector will be large enough to contain electromagnetic and hadronic cascades of energy up to 5 GeV.
- As the first large-scale assembly of the final design components, the construction of the detector will teach lessons about installation of the far and near detectors.
- The calibration detector will be exposed to the test beam in a series of test runs, in both near and far detector configurations.

Collected data will provide a basis to determine a complete response matrix to all particle species at relevant energies and angles.

- A study of response to cosmic ray muons will be conducted simultaneously and compared to beam muons. The energy deposition by cosmic ray muons will provide the energy calibration link between the two detectors.
- Collected data will be analyzed to obtain the maximum information on the response topology of cells hit as a function of particle species and energy.
- The electromagnetic component of hadronic cascades will be studied.
- Collected data will be used to tune Monte Carlo simulations of the detector response and as an aid in developing the most efficient pattern recognition algorithms.

The main requirements for this calibration apparatus are:

- Identical structure and segmentation as the far and near detectors.
- Sufficiently long to contain hadronic cascades with energies up to 5 GeV.
- Sufficiently long to ensure detailed understanding of response to penetrating muons.
- The front-end readout electronics as similar as possible to both near and far detector configurations (probably different).
- Readout electronics capable of handling the higher intensity of interactions expected in the test-beam line.
- The front-end electronic readout that is triggerable by an external trigger (e.g., Cherenkov or TOF counters).

NOvA does not have any unusual demands for the performance of a test beam. However, the beam should have a momentum range of 0.1 to 5 GeV/c, with the absolute momentum known to a few percent, and an integrated particle identification system. It is desirable to have such a test beam at Fermilab, where the entire collaboration could easily contribute to its operation. We would rely on Fermilab support for beamline operation, instrumentation and monitoring, and for integrated data acquisition and processing. During the last three years of our test beam program we would need access to the beam for several months each year.

9.9. Conclusions

We have demonstrated in this chapter that, with a simple detector located around 12 m off the NuMI beam axis, along with the MINERvA detector on axis, each of the beam-related backgrounds can be predicted at the far detector with uncertainties of about 5%. Without the MINERvA detector, and the cross section and ν_e flux measurements it can provide, the NOvA Near Detector design would have to be modified. This would include small regions at the upstream end of the detector with increased longitudinal granularity to provide essential additional information for background determination.

A flexible and versatile test beam facility will significantly improve the sensitivity of our experiment. We would like to work with the Laboratory to plan for the construction or upgrade of a test beam facility that meets NOvA requirements..

Chapter 9 References

[1] G. Zeller, "Low-energy neutrino cross sections: comparison of various Monte Carlo predictions to experimental data," hep-ex/0312061, proceedings of NuInt02, Irvine CA, 12-15 December 2002.

[2] M. Diwan, M. Messier, B.Viren, L. Wai, "A study of $\nu_\mu \rightarrow \nu_e$ sensitivity in MINOS," NuMI-NOTE-SIM-714, February 2001.

[3] D. Drakoulakos *et al.*, "Proposal to perform a high-statistics neutrino scattering experiment using a fine-grained detector in the NuMI beam," February 2004 (http://www.pas.rochester.edu/minerva).

[4] P.D. Barnes Jr. *et al.*, "Proposal to measure particle production in the Meson Area using Main Injector primary and secondary beams," FERMILAB-PROPOSAL-0907, 1998 (http://ppd.fnal.gov/experiments/e907/)

10. Cosmic Ray Backgrounds and Active Shield

10.1. Introduction

The cosmic ray background will be strongly suppressed in NOvA by the very low duty cycle of the accelerator beam (~10 μs spill every 2 seconds), directionality of this incident neutrino beam (pointing from Fermilab) and its relatively high energy (1.5-2 GeV). Our preliminary estimates, described below, indicate that this background should not be a problem. Furthermore, this background can be measured with very high precision during the off-beam time. It is also our intention to test our estimates in a subsidiary experiment on the surface during the next year using a small version of a proposed detector.

The atmosphere behaves as a 10-interaction length, 25-radiation length calorimeter for the incident primary cosmic rays. The results of interactions in the atmosphere are extensive air showers, some of whose components persist to the surface: penetrating muons with ~4 GeV average energy, showering electrons and photons with average energies in the range of tens of MeV, and some hadrons, primarily neutrons, with hundreds of MeV, on average. To estimate the effects of these secondary particles on operation of the NOvA Far Detector we assume: that the detector is 28.8 m wide, 14.4 m high, and 185 m long; that the absorber is a wood product with density 0.65; and that the live-time of the detector is 100 seconds per year (10^7 spills per year, each 10 μs long). We discuss next the manifestation of each component on the detector separately.

10.2. Detailed Considerations—Muons

The muon flux at the surface of the Earth is approximately 120 $\cos^2\theta$ m^{-2} s^{-1} sr^{-1}, where θ is the zenith angle. This flux yields an average of 13 muon trajectories inside the detector per 10 μs spill-gate and a total of 1.3×10^8 muons per year in the Far Detector during the active spill. For the proposed 500 ns electronic gate, each gate will contain an average 0.65 muons over the approximately 5,000 m^2 area of the detector. This flux is a small perturbation on the overall single-element counting rates due to internal and external radioactivity and photodetector noise. Indeed, these muons provide an essential calibration and alignment tool. The muons have a median energy of 4 GeV, and 10 to 20% originate in the same air shower, appearing as in-time multiple tracks. Using an expression for the integral flux as a function of energy and zenith angle [1], we estimate that 51% of the muons will stop in the detector. Muons themselves clearly cannot simulate our signal, which could only happen through their interactions in the detector.

In a segmented detector, it is possible for muons to pass through absorber layers without being detected in the active scintillator. These muons can generate a possible background if they interact hadronicly and produce a charged track along the direction of the neutrino beam from Fermilab. Pion production in hadronic interactions of cosmic ray muons near the earth's surface has been measured; the rate is $(3.5\pm0.7)\times10^{-6}$ π^+/muon/g/cm^2 [2]. A calculation which agrees with these data has been made, and gives the π^+ production rate as a function of the energy of the incident virtual photon [3]. From this calculation, we estimate that the production rate of all pions above 2 GeV photon energy (and assuming that π^+: π^-: π^0 are produced in the ratio 1:1:2 at high energies) is $\sim5.6\times10^{-6}$ /muon/g/cm^2. Fig. 10.1 shows the distribution of these muon-hadronic interaction points projected on to the face of the detector. The calculation assumes that the muon passes through either zero or one active detector plane, corresponding to a 30 cm wide passive absorber plane. Approximately one half of these interactions lie within 1 m of the detector sides. We estimate that 1000 such interactions will lie within the detector's fiducial volume during one year of operation.

The overall energy flow in these interactions is exactly orthogonal to the beam direction. The highest energy pions are therefore produced perpendicular to the neutrino beam (vector meson dominance), but some nucleon isobar production also occurs and isobar decay may produce tracks in the beam direction. In that case, there must also be particle emission in the opposite direction to balance momentum so that the probability that a track should appear electron-like, with the appro-

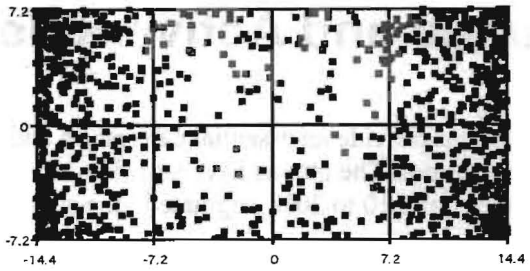

Fig. 10.1: Hadronic interaction points along trajectories of undetected muons. The interaction points are projected on to the face of the detector.

priate energy and interaction topology, makes this an unlikely source of background.

An active shield of scintillator modules around the outside of the detector would be a relatively easy and inexpensive way to efficiently indicate the presence of in-time muon responsible for such events and make the background negligible. The area of shield detector required is only ~ 3% of the total active scintillator planes used in the detector. Assuming that the shield scintillator strips are arranged parallel to detector layers, an interaction in a specific gap would be directly correlated with a corresponding scintillator strip.

10.3. Detailed Considerations—Electrons and Photons

A significant flux of electrons and photons from the extensive air showers survives at ground level. The net flux is about 50% the muon flux, but their average energy is less than 100 MeV [4]. They will generally produce small showers that penetrate short distances (less than 1 m typically) into the top of the detector. Only ~2% have energies above 1 GeV and are capable of producing a significant shower or "splash" at the top of the detector, causing multiple hits in the scintillator strips.

10.4. Detailed Considerations—Neutrons

A small component of hadrons survives to ground level. Neutrons are the most significant; they have an interaction length of ~1.5 m in the absorber material and their interactions are therefore a potential source of background. Their trajectories are much more vertical than the muons, with average angle ~20° from the zenith, and their median energy is ~100 – 200 MeV. Figure 10.2 shows the integral flux of neutrons incident on the top of the detector calculated from the measured

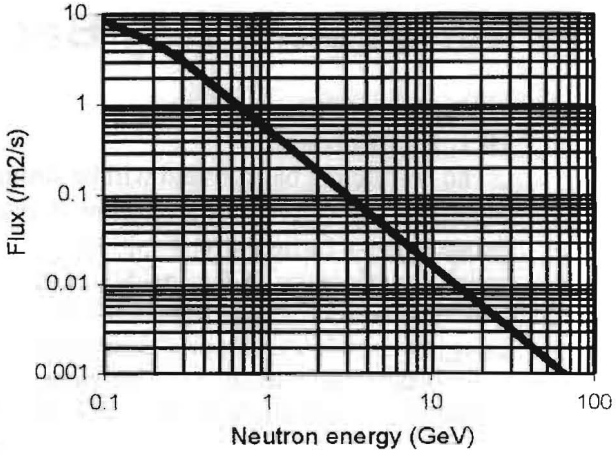

Fig. 10.2: Integral flux of neutrons at ground level

differential flux [5]. We estimate that 1.0×10^5 neutrons with energies above 2 GeV will interact in the detector per year within the neutrino spill gate; they will be concentrated near the top of the detector.

Even though neutrons at ground level are always accompanied by muons or electrons, this fact is not very useful as a veto for neutrons entering the detector because of large typical spatial separation. Using the generic cosmic ray code CORSIKA [6], we found that only 4% (10%) of the neutrons have an accompanying muon within 50 (100) m, providing no satisfactory veto power for the proposed detector dimensions.

In the few GeV energy region, ~20% of the inelastic neutron interactions produce a single pion, which, in principle, might simulate an electron track. 98% of all CC events have a track within 25° of the neutrino beam direction and thus a pion from a neutron interaction must be emitted at an angle at least ~60° to provide a possible background to a beam neutrino event. From kinematics, the maximum possible energy of a pion to be emitted at 60° is 1.5 GeV, just at the edge of possible acceptance. With the addition of a topology requirement that the track should be electron-like, we estimate that background from neutron interactions will be at the level of only ~1 event/year.

10.5. Passive Overburden

One possible method to deal with background effects of cosmic rays, should they turn out to be more serious than the above estimates indicate, is through direct attenuation using a passive absorber

above the detector. While the absorber itself, crushed rock or soil, is cheap, supporting the absorber, both laterally around the detector and especially vertically over the detector, is expensive. It is therefore important to compare a passive absorber with an "active shield" either in the form of a detector fiducial cut or in special, active elements mounted over the upper portions of the detector, as discussed above in connection with muon identification.

Fig. 10.3 shows the relative effect of an overburden on the relative vertical intensities of muons, electrons and photons, and neutrons. The neutron interaction length λ has been taken as 115 g/cm^2 [7] and that for the electron-photon component, 175 g/cm^2, taken from electromagnetic shower attenuation after shower maximum. There is no particular limit to the thickness of an overburden: the neutron flux would be reduced a factor of 100 by a dirt or rock overburden of 500 g/cm^2, ~2 to 2.5 m. This reduction would also reduce the electromagnetic "splash" at the top of the detector. We note that hadronic interactions of the throughgoing muons also produce neutrons. For this thickness of absorber, the production rate of neutrons in the absorber by these muons is approximately equal to the flux of attenuated neutrons from interactions higher up in the atmosphere. The muon-initiated neutrons are typically produced in large hadronic showers. If they are produced in the absorber directly above the detector, they will always be closely associated with the very energetic initiating muon.

10.6. Need for an Active Shield

Possible cosmic ray backgrounds are significantly attenuated by both the short neutrino beam spill and by the orthogonality between the horizontal neutrino beam direction and the vertical maximal direction for cosmic ray flux. Nonetheless, cosmic rays are a potential background source, which will require monitoring effort by recording a large number of off-spill events. To reduce backgrounds from cosmic rays to a minimum, the installation of an active shield around the upper portions of the detector appears prudent. Such a shield is significantly less expensive than the support structure required for passive shielding of sufficient thickness to have a significant effect. We describe a possible shield in the next section.

10.7. Active Shield Design

As discussed above, an active shield may be useful in tagging cosmic rays entering the detector. This can be done by adding active elements on the sides and top of the detector as shown in Figure 10.4. We assume the active shield would be composed of elements similar to the 1.22 m by 14.6 m scintillator modules in the main detector. Since the detector is 29.3 meters wide and 171.3 meters long, it takes 280 modules to cover the top. Similarly since the detector is 14.6 meters high and 171.3 meters long, a set of 140 modules will cover one side as shown in Figure 10.4. The side sections of the shield would be attached to the building walls so that access to the sides of the detector

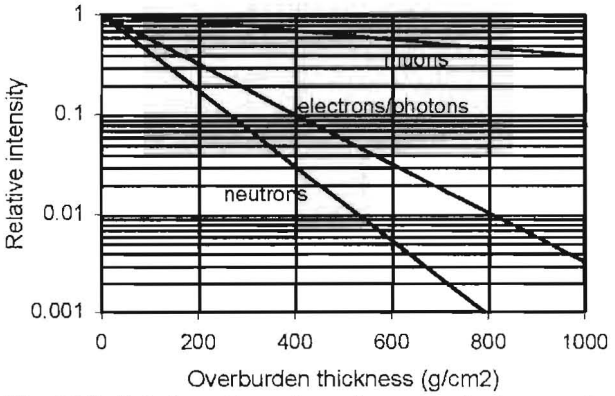

Fig. 10.3: Relative attenuation of muons, electrons and photons, and neutrons as a function of thickness of a dirt overburden.

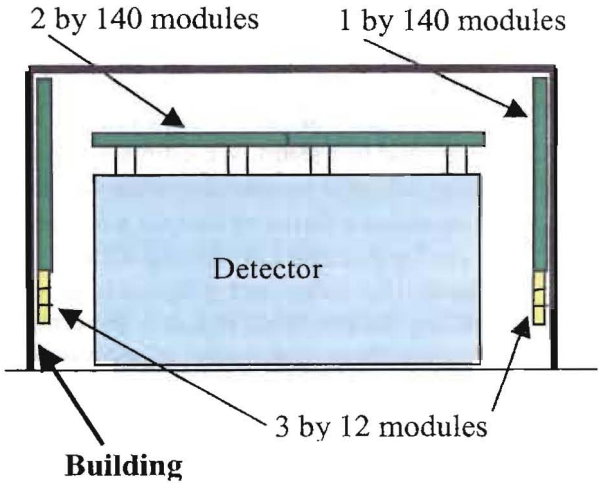

Fig 10.4: Beam's eye view of the detector and Active Shield.

and its electronics would be preserved, therefore an additional 36 modules are required on each side to cover the gap created by this access space. Active elements are not required on the front and back of the detector since the first and last planes in the detector effectively do the same job. The top section of the shield would be supported off the main detector about 2.4 m above the top of the detector so that access to the top of the detector would be preserved.

A single active layer is sufficient. This design requires 632 additional modules for an active shield, 176 to cover one side, 280 modules to cover the top, and with 30 cells per scintillator module, 18,960 APDs and electronics readout channels are also required.

10.8. Required R&D

The Active Shield is part of our cost estimate, but the need for the shield is not yet firmly established. Since the proposed 50 kiloton detector is live for only 100 seconds each year, it is possible to directly measure these cosmic ray rates with a smaller mockup if we run it continuously for a few days or months.

Through our Virginia Tech collaborators we have obtained the loan of 29 BELLE RPCs, each 2.2 meters by 2.7 meters. We are in the process of assembling about 20 of these RPCs into a detector mockup of particleboard absorber interspersed with RPCs to search for cosmic ray induced event candidates which simulate 2 GeV ν_e CC events. Two orthogonal views of the test setup are shown in Figure 10.5. The total mass of the RPCs and particleboard will be about 16 metric tons. For the 100 sec/year of far-detector live-time, (50 kT / 16 tons)×100 sec = about 3.6 days/year in our the background test setup. We estimate that fiducial volume cuts and readout deadtime will increase this by about a factor of four, so a 5-year NOvA run can be simulated in about 2.4 months.

Figure 10.6 shows our progress to date in assembling the test setup in Lab E at Fermilab. The RPCs have been leak tested, a gas system has been built, and we have begun to assemble the RPCs inside particleboard frames. Argonne National Laboratory has contributed a 30-channel Cockroft-Walton HV chassis, and they have designed and built a 64-channel RPC readout board in VME

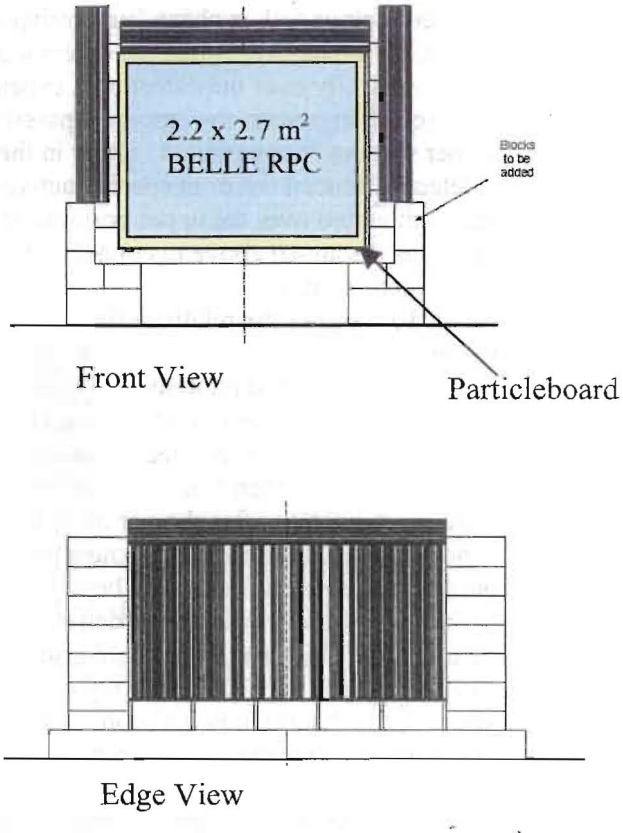

Figure 10.5: RPC front view and edge view of the R&D Cosmic Ray Background Test setup.

Figure 10.6: The beginnings of the Cosmic Ray Background Test setup in Lab E at Fermilab.

format. Our progress is now limited by the funding required to build the complete readout electronics for this test.

We also have another way to make this measurement. The MINOS collaboration recently completed their CalDet calibration run with a MINOS prototype in a CERN test beam. The sixty-five 1 x 1 m^2 arrays of MINOS solid scintillator strips are now available to the NOvA collaboration and could also be used in the Cosmic Ray Background Test setup. Due to this year's MINOS installation, it is not clear if sufficient photomultipliers and electronics will be available for such an test. If not, we are faced with a similar funding problem to acquire the PMTs and electronics to readout a reconfigured CalDet + particleboard mockup.

We believe this Cosmic Ray Background Test effort should have a high priority given its possible impact on the overall detector design and cost.

Chapter 10 References

[1] H. Jokisch et al., Phys. Rev. D19, 1368 (1979).

[2] R. Hertenburger et al., Phys. Rev. C52, 3449 (1995).

[3] J. Delorme et al., Phys. Rev. C52, 2222 (1995).

[4] R. R. Daniel and S. A. Stephens, Revs. Geophys.and Space Sci, 12, 233 (1974).

[5] F. Ashton, "Cosmic Rays at Ground Level', ed. A. Wolfendale (1974); W. N. Hess et al., Phys. Rev.116, 445 (1959).

[6] D. Heck et al., Report KfK6019, Forschungzentrum Karlsruhe (1998).

[7] Particle Data Group, "Review of particle properties," Phys. Rev. **D66**, 010001 (2002), "Atomic and nuclear properties of materials," p.84.

11. Far Detector Site and Building

11.1. Detector Site Criteria

We have examined more than a dozen possible sites for the NOvA Far Detector as well as multiple detector locations within several particular sites. Possible sites begin ~710 km from Fermilab, near the city of Aurora MN, and continue to the north-northwest until a point in Ontario that is about 900 km from Fermilab. Sites more distant than ~900 km are too far off-axis to have desirable beam characteristics because of the beam's upward inclination of 3.3° and the curvature of the Earth. The sites we have examined are all near the half-dozen or so east-west all-weather roads that cross the NuMI beamline.

The principal site selection criteria are:

- Approximately 10-14 km off-axis from the NuMI beam. The beam in this direction has a most probable energy of ~2 GeV. The optimal off-axis distance is not precisely known because of uncertainty in current best value of Δm_{32}^2. An additional issue is the question of strategy. Sites closer to the NuMI beam axis have increased flux and therefore a higher probability of observing the $\nu_\mu \rightarrow \nu_e$ transition. Sites further off-axis provide more sensitivity to matter effects and therefore possibly more accurate measurements of the mass hierarchy and CP violation.
- As far as practical from Fermilab. Beam lengths of ~775 to ~850 km from Fermilab are readily achievable. The dependence on beam length is not strong. A longer beam is more sensitive to matter effects, while a shorter beam and therefore higher flux may yield a better reach in $\sin^2 2\theta_{13}$. One argument for a longer beam is that it is more different from the K2K beam and the CERN-Gran Sasso beam and thus provide a better handle on resolving ambiguities in the neutrino mixing matrix parameters.
- An optimal site will have year-round road access at the maximum trunk highway weight limit, adequate electrical power and T-3 capable communications access. Other geographic criteria include access to workers, road transportation and airports and proximity to support services such as hotels, restaurants, gasoline and other retail outlets.
- An optimal site will have at least 20 and more likely 40 acres of usable land (not wetlands) and permit a layout of a ~200 m by ~40 m footprint for a detector building oriented with its long axis pointing towards Fermilab.
- An optimal site will enjoy strong local support and its selection should be unlikely to result in land use controversies or litigation. The characteristics of the site should also facilitate a straightforward environmental permitting process. Although the University of Minnesota has authority to determine zoning and permitting with respect to its property within Minnesota, minimal land use controversy will facilitate the laboratory construction.

11.2. Most Suitable Sites

While no site is perfect and a number of sites are more than adequate, three particular areas appear to best meet the selection criteria, while also providing considerable flexibility in deciding the actual detector "footprint." From south to north, these sites are: (1) on the Orr-Buyck Road (St. Louis County Highway 23) near the west end of Kjostad Lake, (2) on the Ash River Trail (St. Louis County Highway 129) near the entrance to Voyageur's National Park and (3) on Ontario Highway 11 north of Rainy Lake near Mine Centre ON (about 60 km east of Fort Frances ON). Sites (1) and (2) are west of the beam centerline. Site (3) is east of the beam centerline. Of these sites, the Ash River Trail location has the unique property of being the furthest site from Fermilab in the United States. For this reason, it is the baseline site. The locations of all three sites are shown on the map in Fig. 10.1.

11.2.1. Ash River Trail Site: The Ash River Trail site is located about 15 km east of U.S. Highway 53, about 40 km east south east of International Falls MN. By car, it is about an hour's drive further from the airports at Duluth and Minneapolis than is the laboratory at Soudan. Driving time from Soudan to Ash River is about 1.5 hours.

The access to the Ash River Trail site is via U.S. Highway 53, St. Louis County Highway 129 and then via a private road ~1-3 km in length, depending on the specific site that is chosen. Highway 129 has some spring weight restrictions that will necessitate some load rearrangements for ~45 days

each Spring. There is an existing 7.2 kV, 3 phase power line that runs essentially along the highway. The local power company estimates that 500 kW is readily available with existing facilities; 1 MW or more of power consumption would require an upgrade of the current line. There is an existing fiber optic line along U.S. 53 and along the Ash River Trail.

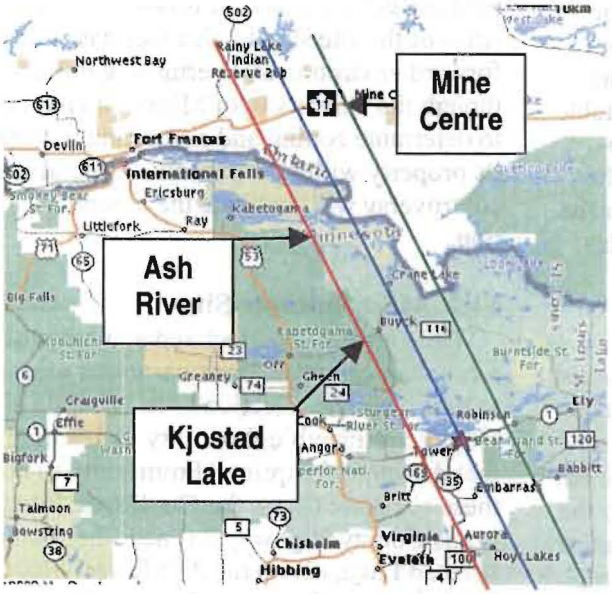

Fig. 11.1 Map showing all three preferred sites. The star indicates the site of the Soudan Underground Laboratory. The beam centerline passes through Soudan; the left line is ~13 km west of the centerline, while the right line is ~13 km east of the centerline.

The settlement of Ash River (U.S. Mail address: Orr MN 55771) is located at the end of the Ash River Trail, about 2 km east of the proposed detector site. This area has several motels and restaurants, although much of the activity is seasonal. (See www.ashriver.com for a listing of hotels and restaurants.) There is a new gas station and convenience store at the intersection of the Ash River Trail and U.S. 53, about 12 km from the laboratory site.

The actual detector laboratory locations at the Ash River Trail site are in Sections 12, 13 and 14 of Township 68 North, Range 15 West, St. Louis County MN. These locations are shown in Fig. 10.2 on the 1:24000 USGS topographic map. All locations would require upgrading of the access road, mostly with an improved gravel base and culverts for drainage (or a new road in the case of Site F). The sites are located near Voyageur's National Park, but GIS studies by the National Park Service suggest that the Detector Laboratory would be essentially invisible from the Park because of intervening high terrain (except for Site F). These sites are all ~810 km from Fermilab. The detailed parameters of all six locations are listed in Table 11.1.

All detector locations shown on the map are on relatively flat land with few, if any, obvious rock outcrops. Thus, it is reasonable to believe that all of these sites have at least a few meters of soil cover over bedrock. Core drilling will be required to more completely characterize a chosen location. Most of the locations are forested with small aspen trees. In forestry terms, they are generally described as areas of aspen regeneration.

All sites would require installation of utilities along the access road. Domestic water would likely come from one or more wells, which would also be used to fill a storage tank for fire protection water. Domestic sewage would require either a septic system or a holding tank with periodic disposal.

At this time, the University of Minnesota is taking preliminary steps towards land acquisition and environmental review of these sites. Our current strategy is to defer a specific selection among the sites for as long as possible, in order to have the best possible understanding of the relevant neutrino oscillation parameters before making a specific site selection.

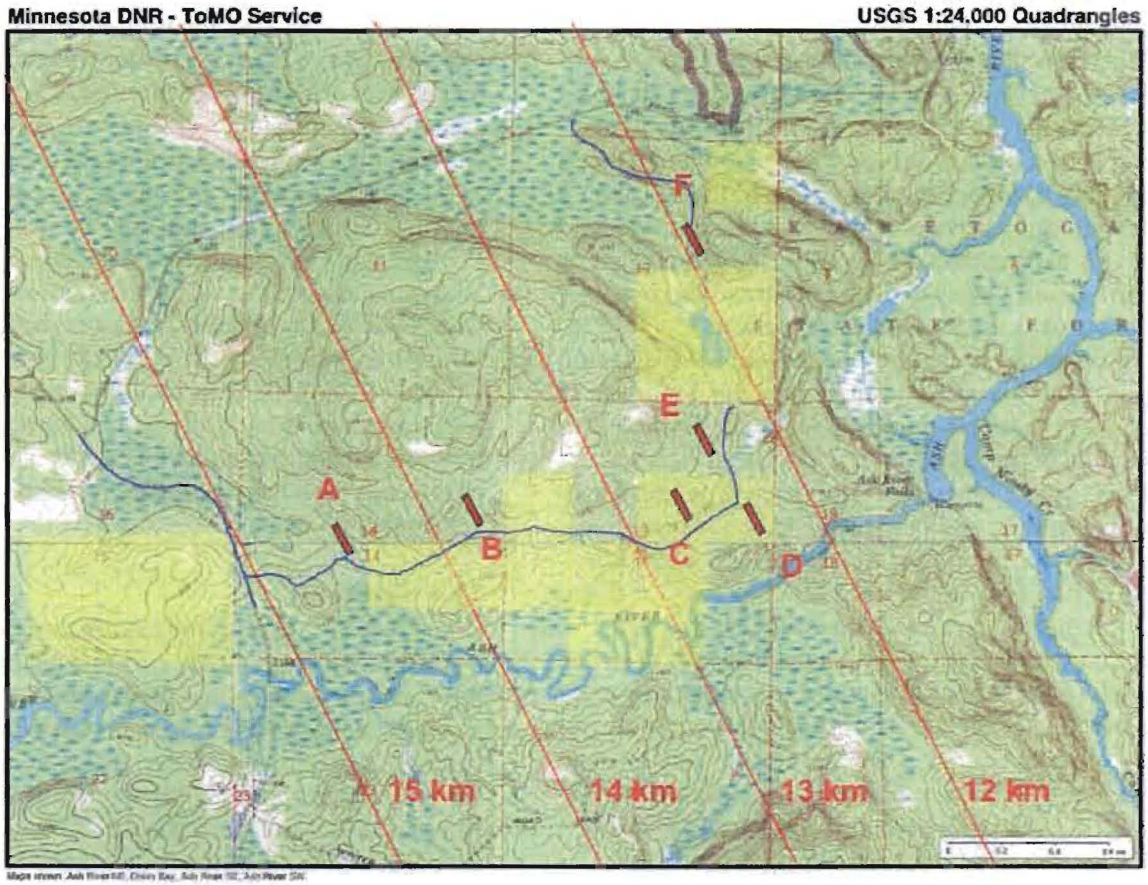

Fig. 11.2: The USGS topographic map for the Ash River Trail sites. The rectangles show a 200 m by 40 m laboratory footprint. The shaded land near the laboratory sites belongs to Boise Cascade. Unshaded land in this area belongs to the State of Minnesota.

Location	Description	Latitude	Longitude	L (km)	T(km)	Angle (mr)	Ownership
A	SENW Sec. 14	48.375°	92.869°	811.4	14.37	17.6	State
B	SENE Sec. 14	48.377°	92.857°	811.2	13.51	16.7	State
C	SWNE Sec. 13	48.378°	92.841°	810.7	12.46	15.4	BCC
D	SENE Sec. 13	48.377°	92.836°	810.5	12.19	15.0	BCC
E	NWNE Sec. 13	48.381°	92.840°	811.0	12.26	15.1	State
F	SWNE Sec. 12	48.391°	92.840°	812.0	11.81	14.5	State

Table 11.1: Parameters of Sites Near the Ash River Trail.

11.2.2. Kjostad Lake Site: The Kjostad Lake sites lie both north and south of St. Louis County Highway 23, approximately 8 km west of Buyck and 15 km east of Orr. Highway 23 is a two-lane, all-weather highway, which intersects U.S. 53 at Orr. North of Buyck, the road ends at Crane Lake, which is a U.S. port of entry for non-vehicular traffic from Canada. East of Buyck, the Echo Trail runs ~100 km to Ely. While the Echo Trail is usable most of the year, only ~15 km near Ely is paved. Orr has several gas stations and cafes, a supermarket, a bank and a few other stores, as well as a new AmericInn motel overlooking Pelican Lake. Buyck has several cafes and a golf course.

Electrical power and fiber optic cable run along Highway 23.

There are numerous possible detector sites in the Kjostad Lake area that lie 13±2 km off the central NuMI beam axis. All sites are ~775 km from Fermilab. Most of the sites are wooded, although often with only small aspen trees. Some of the possible sites belong to private owners, but much of the land belongs to the State of Minnesota, either outright or as tax-forfeit land. The largest private land owner in this area is the Potlatch Corporation.

At this time, we regard the Kjostad Lake detector locations as alternates to the Ash River Trail locations, so we are not currently pursuing detailed site selection in this area.

11.2.3. Mine Centre Site: The furthest practical site from Fermilab, ~845 km away, is on Ontario Highway 11, near Mine Centre ON, about 60 km east of Fort Frances ON. Ontario Highway 11 is an all-weather highway with electrical power, telecommunications and a rail line all running in a parallel corridor between Fort Frances and Thunder Bay ON. This site is east of the beam centerline on Crown (public) land. There are few constraints on land use in this area and it is likely possible to pick a specific detector location essentially adjacent to the highway and utilities at almost any desired distance off-axis by >5 km. We consider a site west of the centerline less practical, because the land in that area is a First Nation reservation.

We have had positive initial discussions with provincial and municipal officials regarding the feasibility of locating the NOvA Far Detector in the Mine Centre area. The disadvantages of a Canadian site are primarily more difficult logistics. Most detector elements and personnel will approach any of the NOvA Detector sites from the south, either on U.S. 53 or the adjacent Canadian National rail line. The Canadian site entails the additional complexity of another hour of driving time and the variable time required for the border crossing. For this reason, a substantial Canadian participation in NOvA would likely be important to managing logistics and facilitating work at Mine Centre or any other Canadian site.

11.3. Other Sites

We have also visited numerous sites close to Soudan. The distance from Fermilab for these sites varies from ~710 km at the Cliffs-Erie Mine site near Aurora to ~745 km for sites near Big Bay on Lake Vermillion, near the Fortune Bay resort complex. While these sites offer somewhat higher operational efficiency because they are in a more populated area than the sites further north, these sites have somewhat reduced matter effects because of the shorter baseline. For those reasons, we are not investigating these sites at this time.

A second Canadian site is available on Crown land on Ontario 502, which runs northeast from Ontario 11 to Dryden ON. This site would be the furthest possible location, ~900 km from Fermilab. However, although Ontario 502 is an all-weather highway, there is currently no electrical power or telecommunications along this route. This stretch of highway also has essentially no support services for about 100 km.

11.4. Building

The NOvA Far Detector requires a detector enclosure ~200 m long by ~35 m wide by ~24 m high. This is a substantial structure, so we commissioned two design studies to get a handle on the costs and cost drivers for such large buildings. The first study was sponsored by the University of Minnesota and was performed by CNA Consulting Engineers with subcontracts to Dunham Associates and to Miller-Dunwiddie Architects [1]. This CNA study focused on a cut and cover approach deep in bedrock with a 10-meter overburden to cover a "worst-case scenario" of a possible required cosmic ray shield.

The second study was done by the Fermilab Facilities Engineering Services Section [2] and focused instead on zero overburden. The Fermilab design is for an above-grade building with a minimal excavation just down to bedrock to ensure the 50 kilotons is sitting on a solid surface. Bedrock at most of the sites considered above is expected to be under only 10 to 15 feet of soil till. At the present time we do not anticipate using earth shielding around or over the detector building. These two design studies indicate that sufficient Earth shielding to have a significant effect (several meters in thickness) would increase the cost of the building by ~50%. Chapter 10 indicates that even this modest overburden is probably not necessary.

While the two building design studies had different goals, they did agree with each other in cost at the 20% level when the Fermilab surface design was compared to a similar subsection of the Minne-

sota design done by Miller-Dunwiddie. In addition, both designs had common assumptions about the general site, for example including modest costs for short roads connecting to existing roads and modest cost to bring in nearby power. Not all sites under consideration satisfy these assumptions, though the Ash River Site is a close match.

For the base detector design in this proposal, we anticipate constructing a 20-year life, metal-sided, metal-roofed building, similar to the usual experimental area buildings located at accelerator laboratories. The building would have an additional 20-meter long staging and assembly area at one end so that semi-trailers delivering either particleboard or PVC modules could be moved inside for unloading. This staging and assembly area would not require the full 20 m height. Another low-roof section would be attached to the middle of one side of the building to handle the scintillator fluor and mineral oil delivery, mixing, and storage. The details of the scintillator preparation and storage requirements are discussed in Chapter 7.

The building meets the horizontal wind stress loads, snow loads, and heating and cooling loads required in northern Minnesota. This area sits on the Canadian Shield and is seismically stable, so no special earthquake design features are required. The building would be insulated, heated and cooled to ~70 ± 10 F year round. The cost of appropriate humidity control (for particleboard) is still under investigation.

The building would be outfitted with a 20-ton building crane on a 35-meter bridge and two mobile gantry cranes for detector assembly. A small control room and a small technician work area would be included inside the main structure. In addition, this "outfitting" of the building would include a robust steel structure underneath the detector to allow access to the bottom. This bottom support would be a simple set of I-beams along the length of the building, each 2-foot high, 1 foot wide, and spaced 3 feet apart. The detector particleboard / PVC structure would sit on top of the I-beams. Another light structure on top of the detector would hold the active shield counters high enough off the top of the detector to allow easy human access. This top structure might be made of scaffolding and catwalk assemblies.

The scintillator oil delivery and storage tank section would require a fully engineered secondary containment. In the main detector building the concrete floors and walls below grade may suffice for secondary containment. For example, the Fermilab MiniBooNE oil tank is a sphere containing 0.8 kilotons of mineral oil and sits in a cylindrical vault of concrete as its secondary containment. In the MiniBooNE case, the only precaution taken in the vault section is that the ground water sump enclosure (for water entering the perimeter of the building and being ejected into the local ground water distribution) has walls high enough to be above the level of the oil even if all of the oil were to leak out of the spherical tank. No special containment pan was required inside of the MiniBooNE vault. In the case of the NOvA Detector, our cellular structure should allow arguments that the worst credible spills are much smaller than those mitigated in the MiniBooNE case. All these secondary containment issues and their associated costs are still under investigation and are of course dependent on possibly different environmental protection regulations in the different states / provinces.

11.5. Research and Development Topics

The constructing and outfitting of the detector building is a high cost element of this project. Since the detector itself can be considered as a structural element, there are potential trade-offs between the building and detector structure. Sufficient civil engineering needs to be available to make a conceptual building design that takes advantage of the detector structure and points out any detector decisions that may significantly increase the building cost. Obvious issues include detector construction speed, safety, and long-term detector stability.

Chapter 11 References

[1] Report for Off-Axis NuMI Neutrino Detector, U of M Project No. 298-03-1113, January, 2003.
[2] Off-Axis Detector Enclosure Design Study Report, Fermi National Accelerator Laboratory, FESS Engineering Project No. 6-2-22, June, 2003. Also available as Off-Axis Note #9.

12. Proton Beam Requirements

12.1. Introduction

This proposal assumes a 5 year run with the 50 kiloton (kT) NOvA far detector and beam intensity in the Main Injector such that the NuMI target receives 4 x 10^{20} protons on target per year (pot/yr). The delivered pot/yr comes from the assumption of 4.3 x 10^{13} protons per pulse (ppp) every 1.9 seconds and a Main Injector annual beam-on fraction of 0.56 (= scheduled beam time x operational efficiency). There are other possible ways of attaining this integrated number of pot/yr, as will be discussed in this chapter. We note that the Main Injector is not yet capable of delivering these protons and that a significant new investment in the accelerator complex will be required in order to achieve this. On the other hand, the NuMI beam has been designed for this ppp intensity which translates into approximately 0.4 MW of beam power.

In this chapter, we discuss some issues regarding the proton intensity, a sensible level of investment in that area for NOvA and the likelihood of achieving the assumed intensity. The most realistic means of delivering the expected protons will require a proton intensity plan, including a reduction of the Main Injector cycle time. We also look ahead to the pot/yr associated with this experiment's long range physics potential as discussed previously in Chapter 5.

12.2. Proton Intensity Investment Strategy

The sensitivity of NOvA depends on the simple product of neutrino flux times far detector mass. To very good approximation the integrated neutrino flux is determined by the number of 120 GeV protons that can be delivered to the NuMI target. Assuming a fixed total cost for the combination of the detector mass and the proton flux, it makes sense for the collaboration and the laboratory together to consider investment in both of these areas in order to optimize sensitivity. We note that, in order to achieve the proton intensity assumed here, the lab must undertake a substantial new investment in this area. Alternately, the lab could simply invest more in additional NOvA detector mass. We believe a joint approach, examining both mass and protons, is likely the most sensible path.

We recognize that investment in proton intensity has much broader usefulness for a variety of future physics programs at Fermilab. Hence, increased proton intensity may be attractive to the laboratory beyond a simple optimization for NOvA.

Viewed from the NOvA side, we believe it is important to assume a detector no smaller than 50 kT. At this time, a well defined plan to deliver the assumed proton intensity does not exist. Relatively risky investments in proton intensity should not be considered as an even trade-off in less risky construction of additional detector mass. The main investments in proton intensity should focus on relatively low risk means of delivering more protons even before a new Proton Driver can be completed. We believe that reduction of the Main Injector cycle time stands out as a unique opportunity that meets these criteria.

12.3. Current Planning for Proton Intensity

Fermilab has an ongoing investment in the accelerator complex to increase the proton intensity for a variety of experiments, including $\bar{p}$ production and Collider luminosity improvement. Recently a study [1] aimed specifically at proton intensity from the Booster and Main Injector was undertaken. The laboratory management directed the study to consider what could be accomplished with an investment of a few times $10M over a several year period. The committee was chaired by Dave Finley with input and participation from laboratory management, experiment collaborators, and Beams Division managers and technical experts. The primary charge to the Finley committee was to study the issue of proton intensity before the anticipated operation of an off-axis experiment. All aspects of the needs in the existing proton source and Main Injector were considered. On the timescale of 2008, the committee anticipated that significant effort and resources will have been invested in the LINAC, Booster and Main Injector.

The Finley Committee report recommends investment in several areas to meet these proton demands:

- Improve control over beam in the Booster to decrease losses and permit more total protons to be accelerated.
- Increase the average acceleration rate capability of the Booster from about 3 Hz to about 7-10 Hz.
- Improve collimation and notch cogging in the Booster to reduce losses and permit lower loss multi-batch stacking into the Main Injector.
- Solve the power tube problem in the LINAC.
- Improve the damping and beam loading compensation systems in the Main Injector to permit higher proton intensities and stacking.
- Develop and implement batch stacking systems in the Main Injector for $\overline{p}$ production and eventually for multi-batch operation.
- Implement a mild reduction in Main Injector cycle time if this can be done easily.

Some of the work recommended by the Finley Committee is already incorporated into Accelerator Division planning and some is underway. The Fermilab Accelerator Division has recently established a new project for increasing proton intensity, with a planned budget over the next several years of roughly $5M per year.

12.4. Possible Accelerator Investments

As discussed above, an important issue for Fermilab to consider in undertaking NOvA is an enhanced level of investment in the existing accelerator complex. The investments relevant to 120 GeV protons for NuMI can roughly be characterized in four categories:

1. Investment in the per-cycle proton intensity capabilities from the 8 GeV proton source. Examples include improvements in various systems to correct/compensate for space charge effects and other instabilities.
2. Investment in techniques to reduce or "hide" the cycle time of the current 8 GeV source from the cycle time of the Main Injector. Such investments would increase the rate of acceleration cycles in the current Booster and also develop techniques to hide the Booster cycle time from the Main Injector cycle time. One approach discussed for the latter is to use the existing Recycler Ring, along with a new transfer line, as a "proton stacker" so the Booster could fill this ring while the Main Injector ramps. Some type of Booster batch stacking into the Main Injector could potentially decrease the Main Injector cycle time by as much as 1 second. This assumes collider running has ended.
3. Investment in the ability of the Main Injector to handle higher proton intensities and techniques for establishing such intensities. This consists of various Booster batch stacking techniques (slip stacking, barrier stacking, and "ramp" stacking have been suggested) along with the RF power and feedback/stability systems necessary to deal with higher intensities.
4. Reduction of the Main Injector cycle time available for providing protons to the NuMI target. Studies suggest that, with adequate magnet and RF power systems, the Main Injector ramp time (not including the time to fill it from the 8 GeV source) could be reduced to as little as 600 ms [2]. The specific medium-term investment required will depend on some of the other parameters of the overall proton demands (protons for $\overline{p}$ production being a major consideration). However, an attractive feature of investment in this area is that the necessary medium-term improvements will be either essential or at the least very useful in the era of an 8 GeV Proton Driver.

We note that the Finley report has called out a faster Main Injector ramp as a likely prime direction for investigation as follows:

> "Increasing the Main Injector ramp rate can obviously increase the number of protons per hour delivered by the MI for the 120 GeV Neutrino Program. An ongoing recent study, if demonstrated to be technically feasible, shows the MI ramp time can be reduced from the current 1.5 sec to 1 sec, or perhaps less. This modification requires both more RF power and more magnet power supplies. This will provide more protons per year to the 120 GeV Neutrino Program as long as antiproton stacking for Run II does not slow the MI cycle time down. It appears to be a relatively low risk approach to getting more protons per year in that it requires engineering development to get more cycles per year rather than the beam physics R&D that is needed to get more protons per cycle. This modification alone is expected to cost a few $10M's. A decision on this must fold in with the recommendations of the Long Range Planning committee, since ideally a new Proton Driver would also make use of this modification."
>
> [reference 1, page 37, our emphasis]

The Proton Driver Study [3] suggests that the cost of the Main Injector cycle time work necessary for the magnet power upgrades is about $9M. The cost of additional RF cavities and power supplies is in the range of $14M. These are "unloaded" costs, so the real totals are more likely $20M and $30M. Hence, a very rough estimate for the total cost of the project is at least $50M. These "loaded" costs should be compared to our "loaded" detector costs outlined in Chapter 13. The cost will also depend on the specific goals of cycle time reduction, since there is a range of assumed intensities and features that one can tune in adding a second, NuMI-only cycle. We believe a directed study on this issue is essential and should be undertaken by the lab immediately.

12.5. NOvA and the NuMI Beamline with a Proton Driver

Over the last year, the idea of building a new 8 GeV Proton Driver has become a centerpiece of the recommendations of the Fermilab Long Range Planning Committee. Both synchrotron and LINAC options have been suggested, and in either case, the nominal design goal is that a total beam power of 2MW will be available from the Main Injector at 120 GeV. This corresponds to $2x10^{21}$ pot/yr delivered to the NuMI target (about 5 times the intensity assumed for this proposal).

The physics case for an enhanced second phase experiment ("SuperNOvA"?) with this beam power has been discussed in Chapter 5. A Proton Driver extends the reach of NOvA for virtually every measurement. Discovery or precision measurement of $\nu_\mu \rightarrow \nu_e$ oscillations is extended. High statistics anti-neutrino running and / or the possibility of running at the second oscillation maximum to resolve the mass hierarchy becomes real. Observing CP violation in the lepton sector may even be possible. A Proton Driver adds yet another exciting feature to an incremental program exploiting the existing MINOS detector, existing NuMI beamline and the NOvA detector. The incremental nature of the NuMI neutrino program is a powerful feature. Each step has a practical cost and we need not proceed unless the science indications warrant going ahead.

In either Proton Driver option, it is anticipated that improvements in the Main Injector are an intrinsic part of the accelerator upgrade effort. We note that the nominal 2 MW of proton beam power from the Main Injector corresponds to $2x10^{14}$ protons per cycle with a 2 second cycle time or 10^{14} protons per cycle with a 1 second cycle time.

Such changes in cycle time also impact the stability of the target and other systems in the NuMI beamline. A target to handle pulses of 10^{14} protons/second may be much easier to build than one to handle twice that number every 2 seconds. The overall issue of removal of the average heat is the same in either case, and will require non-trivial upgrades to the existing NuMI target facility. It is expected that a traditional carbon target like the existing NuMI target can survive 10^{14} protons per pulse but probably will fail with twice that number. The higher number may require the use of something like a liquid mercury target. Again, the shorter cycle time buys additional engineering certainty.

A final issue is whether there will be radiation problems in the NuMI beamline with 2 MW of protons. We do not anticipate any significant differences in this area with a 1 or 2 second cycle time. We anticipate that the NuMI beam design is sufficiently conservative that relatively small modifications should permit operation up to 2 MW. With the current design, it is anticipated that the first possible problems may come in the target hall. If may be possible to address these at relatively low cost, without additional civil construction. It is anticipated that the decay pipe region will be able to accommodate the higher flux, but perhaps will require additional cooling.

12.6 Summary on Proton Intensity

We believe that reduction of the Main Injector cycle time represents an essential investment for Fermilab to undertake as rapidly as possible for NOvA. Cycle time reduction can provide major improvements in the neutrino flux for NOvA in the near term and also match nicely with futures involving a Proton Driver.

We believe that discussions within the laboratory and between our collaboration and the laboratory could lead to a practical intensity vs. time model for the neutrino program. This model would be characterized by a "NuMI base proton level" (meaning likely to occur with a 90% confidence level) and a "NuMI design proton level" (meaning a 50% confidence level which may occur if many of the details go according to plan). This would

reprise the scheme recently used for Run II collider luminosity and would get us all on the same page regarding this issue.

We propose that Fermilab undertake a specific study for this purpose with a goal of completion by the end of 2004. This would mean merging information from the near term proton intensity project with the future Proton Driver possibility. Such a study would be an important next step in establishing a world-class program of neutrino physics with the NuMI beam.

Chapter 12 References

[1] Report to the Fermilab Director by the Proton Committee, October 26, 2003, http://www.fnal.gov/directorate/program_planning/studies/ProtonReport.pdf

[2] Proton Driver Study II, Part 1, Section 20, May 2002. http://www-bd.fnal.gov/pdriver/8GEV/

[3] Proton Driver Study II, Part 1, Appendix 1.

13. Cost Estimate and Schedule

13.1. Introduction

We have constructed a cost estimate for a project that will carry out the physics program described in this proposal. The entire cost estimate is available in an Excel Workbook format upon request. In this chapter we explain briefly the methods used and discuss some of the important features of the estimates for each of the major elements of the proposal. We have also included a brief discussion and summary of the costing that has been done for two alternative active detectors, namely solid scintillator and glass RPC chambers. In addition, we present discussions of our contingency analysis and a model for costing operational expenses, both during and after the completion of the construction project.

Table 13.1 presents a high-level summary of the second-generation cost estimate made for the baseline active-detector technology as well as other costs associated with the project.

Section 13.6 describes the schedule that we envision for the construction of the NOvA detectors, which is shown schematically in Figure 13.1.

Section 13.7 and Table 13.2 present a comparison of the costing for three active detector technologies, which used a preliminary conceptual design for each technology. The results of this exercise, along with evaluation of the detectors' physics capabilities, played an important role in the choice of baseline technology.

13.2. Cost Estimate Methodology

In preparing this cost estimate we have primarily followed the principles used in costing and tracking the MINOS Detector construction project. For each major system we have itemized the materials and services (M&S) that must be procured, fabricated or assembled. Each system is itemized to the lowest level that is realistic for the current state of the system design. For each cost estimate we indicate the source of the estimate as a vendor quote (VQ), engineer's estimate (EE) or physicist estimate (PE). These sources are used to distinguish the confidence level in each estimate and hence are used in the contingency determination.

For each system we also itemize the labor tasks associated with the construction of each system. The cost of each task is determined by identifying the type of labor and duration of time required to carry out the task. Each type of labor is assigned a labor rate. For the purposes of this preliminary estimate we have used labor rates based on Fermilab salaries and fringe (SWF) for technicians, designers, drafters, engineers and project management personnel. For staff and installers at the far detector site we have used the labor rates currently applicable at the Soudan Underground Laboratory. Labor estimates have been made by either engineers or physicists based on time and motion studies or recent experience with similar tasks.

For each detector system we have included costs for engineering, design and engineering oversight (EDIA) throughout the life of the construction project. At this stage we have done this by estimating the person-years required based on experience from similar scale projects. We have also included costs for project management and ES&H oversight through out the life of the construction project.

Our cost summary includes an estimate for institutional overhead based on percentages calculated from the actual costs incurred on the MINOS Detector project, namely 28% for SWF, 9% for M&S procurements under $500k, and 1.5% on the first $500k of procurements of $500k or larger, and 0% on the remaining amount of the procurement. This assumption about reduced overhead on large procurements must be negotiated with the Laboratory. We have included in our contingency funds to cover additional overhead in case such an arrangement is not agreed to.

Contingency is estimated on each item or task based on the confidence level of the estimate, or on an analytical calculation based on a plausible variation of the unit cost or labor estimate.

Table 13.1 summarizes the results of our cost estimate for the construction of this experiment. All costs are presented in FY 2004 dollars.

13.3. The Baseline Detector Cost Estimate

For this proposal we have selected liquid scintillator as the baseline technology for the active detector elements. In this section we briefly discuss each of the major pieces of the estimate.

WBS	Description	Base Cost	Overhead	Contingency	Sub-total
1.0	Near Detector	2,152,582	430,516	2,583,099	5,166,198
2.0	Far Detector				
2.1	Absorber	12,618,525	476,991	3,708,788	16,804,304
2.2	Active Detector	28,324,540	1,468,466	9,230,940	39,023,945
2.3	FEE, Trigger and DAQ	6,375,205	705,098	3,864,988	10,945,290
2.4	Shipping&Customs Charges	5,421,343	1,084,269	1,355,336	7,860,947
2.5	Installation	11,789,067	3,069,957	5,661,376	20,520,401
	Detector Sub-total	64,528,679	6,804,781	23,821,428	95,154,888
3.0	Building and Outfitting				
3.1	Building	16,634,800	499,044	9,971,283	27,105,127
3.2	Outfitting	4,745,748	142,372	4,888,120	9,776,240
	Building and Outfitting Sub-total	21,380,548	641,416	14,859,403	36,881,367
4.0	Active Shield	1,602,882	416,749	2,019,631	4,039,262
5.0	Project Management	3,935,000	1,085,650	1,004,130	6,024,780
TPC	**Total Project Cost**	**93,599,690**	**9,379,113**	**44,287,691**	**147,266,495**

Table 13.1: Work Breakdown Structure and second generation cost estimate for Liquid Scintillator as the Active Detector technology.

13.3.1. Absorber: There are two key elements in the costing of the absorber. The first is the unit cost of the particleboard and the second is the maximum size board available from the vendor. We have obtained quotes from three different vendors. We found that current prices range from $0.10 to $0.12 per pound, not including delivery and that 8-ft by 24-ft by 1.125-in sheets should be available. Quoted Delivery costs by truck to the detector site in northern Minnesota have also been included.

The cost estimate for the absorber system also includes the materials cost of glue, screws and brackets for assembling the absorber sheets into stacks. The cost of the detector support structure is included in the building outfitting

13.3.2. Liquid Scintillator Active Detector: There are three major components to the liquid scintillator active detector. These are the PVC extruded modules, the wavelength shifting fibers and the liquid scintillator, which is a 9:1 mixture of mineral oil and fluor (pseudocumene). The baseline detector requires the assembly of ~18,000 extruded modules with endcaps, fibers and manifolds. It is the simplicity of this assembly process that makes the liquid scintillator "win" as the most cost effective active detector. The time/motion analysis of the module assembly process indicates that a factory staffed with three assemblers and one supervisor can assemble 12 modules in one shift. At this rate, two assembly factories can produce the modules at a rate matched to the stack assembly and installation at the far detector site. Over the four-year production and installation period, the module assembly can be accomplished for under $2M, which is significantly cheaper than can be envisioned for the equivalent process for the alternative active detectors.

13.3.3. Front End Electronics, Trigger and DAQ: The key components in the detector readout are the APD arrays and the custom front-end electronics (FEE) to read out the APDs. The baseline design has just over 540,000 channels to be read out. Our vendor quote is $43 for a sixteen-pixel APD array.

The custom electronics require the development of two custom ASICs incorporating a pre-amplifier, integrating amplifier, Cockroft-Walton voltage generators, multiplexer and ADC. The current estimate for production, fabrication and assembly of the FEE system is ~$4 dollars per channel, bringing the overall production cost of the readout to ~$8/channel.

The FEE, Trigger and DAQ system is the only one where the EDIA estimate has been made based on specific tasks rather than as a top down assessment of the manpower requirements.

13.3.4. Shipping: For the baseline design the shipping estimates include shipping (via truck) the empty modules from the two factories to the installation site, mineral oil (via truck) from Texas to the detector site and absorber boards from a rail site to the far detector site.

13.3.5. Installation: We have developed an installation procedure that enables us to determine the number of people that will be required to install the detector and how long it will take. We have built into the estimate three phases of the installation: ramp-up, steady state and ramp down.

The installation cost estimate also includes the M&S costs of the specialized tools and fixtures required for the installation process.

13.4. Other Project Costs

13.4.1. Far Detector Site, Building and Outfitting: The current cost estimate does not include any land acquisition costs. However, the building cost estimate does include general preparation of the site such as clearing and grading. A one-mile access road is also costed. Additional access roadway costs ~$750k/mile.

The building cost estimate has been based on a simple industrial style building with no overburden. To estimate costs we are using an algorithm developed by Fermilab Engineering Services Section (FESS), which allows us to specify the detector dimensions, the desired depth below grade of the detector, as well as an installation staging area. The building estimate includes basic utilities such as electrical distribution, fire protection and HVAC but does not include any detector specific structures or outfitting.

Outfitting costs have been estimated for the baseline detector based on a model for materials staging and handling. The outfitting cost estimate also includes the cost of a conceptual design for a detector support structure.

13.4.2. Active Shield: We have estimated the cost of an active shield to identify penetrating cosmic ray muons, installed above and on either side of the detector. The front and back of the detector do not have an additional shield since the active planes of the detector serve the same purpose. The veto shield is composed of active detector modules read out by the same electronics as the main detector. Inclusion of this veto shield requires the production of an additional 560 modules and the corresponding 17,000 channels of electronics. We have included the cost of a simple support structure for the veto planes and an estimate of the additional person-hours required for the installation.

13.4.3. Near Detector: The off-axis near detector cost estimate is based on the conceptual design described in Chapter 9. The near detector is structurally similar to the far detector except for its smaller transverse and longitudinal dimensions (3.7 m wide by 4.9 m high by 10 m long). We have scaled the unit costs of the particleboard and the active detector elements from those used in the far detector by the amount of material used, because the components are identical except for the smaller transverse dimensions of the absorber and the shorter extrusions. We have assumed that the near detector is read out with Hamamatsu M64 PMTs, with readout electronics identical to that used for the MINOS Near Detector. The 44 planes of liquid scintillator modules (22 horizontal and 22 vertical planes) contain 4620 tubes, which are read out by the same number of electronics channels.

13.4.4. Project Management and ES&H: We have estimated the manpower needs and corresponding cost of a project office that would oversee the management and administration of this project. This category of project management includes the Project Manager, a deputy, "Level 1" managers for the detector and the conventional construction, a project scheduler, budget officer and administrative assistants. A full time ES&H professional is also included in the project management budget.

13.4.5. Operating Costs: We have used experience from the NuMI-MINOS Project to develop a model that costs those expenses incurred during the construction of a project, but are not appropriate to be funded by capital equipment funds. These are items such as temporary building rental, utilities in the buildings, telephone and network ex-

penses, etc. During the construction of the MINOS far detector these funds were about $350,000 per year. Upon completion of the construction project, a budget was developed for the annual laboratory operating expenses which is currently ~$1.3M per year to support the laboratory with a crew of 8 persons. At this time it is not obvious how the laboratory for the NOvA Far Detector would have to be staffed, but we do not anticipate that such expenses would be in excess of those currently needed at the Soudan Laboratory.

13.5. Contingency Analysis

We are at a very early stage of the design of this experiment. Most designs are only conceptual and still require detailed engineering. Therefore we feel that our overall contingency must be quite large, i.e. approaching 50% or greater on many of the items. Several of our procurements are from foreign countries and the stability of the US dollar against the foreign currency cannot be assured. Technical issues such as the need for an overburden on the building lead to a huge uncertainty in the cost of the civil construction. Finally, given the overall uncertainty in the timescale and funding profile for carrying out this project, we have adjusted our overall contingency accordingly.

13.6. Schedule

Figure 13.1 shows a "technically driven" schedule for the off-axis experiment. In addition to technical considerations, we have assumed that R&D funding will be available (from Fermilab and/or the NSF) in early FY 2005 and that DOE construction funding will be provided at the beginning of FY 2007. If the Laboratory grants final approval in June 2005, the construction project for the experiment could be baselined in time for construction funding to begin in early FY 2007. The near detector and the first 15% of the far detector would then be ready to start recording data from NuMI beam neutrinos two years later, in the fall of 2008. The 50 kT far detector would be completed at the end of CY 2011. We realize that this schedule is aggressive but we believe that it is technically achievable and that the required resources could be made available.

13.7. Evolution of the Cost Estimate

The proposed detector for the NuMI Off-Axis Experiment is a large but uses only a few types of simple components. This simplicity makes the cost estimating exercise straightforward and easy to understand. Most of the mass of the detector is passive absorber and there is only one active detector system, all read out by a single system of electronics. The detector is a monolithic structure assembled from stacks of particleboard interleaved with active detector modules and constructed by carpenter-type skilled labor.

On the other hand, a penny per pound increase in the cost of the particleboard translates into an almost $1M increase in cost.

Likewise, the detector has 540,000 channels of electronics, currently estimated at ~$8/channel. An increase of $2/channel will add another million dollars. Hence, we feel that at this early design stage it is important to allocate contingency in a very conservative manner.

In selecting the liquid scintillator for the active detector technology we have been driven primarily on the basis of a comparison of the cost with two other active detector technologies, namely solid scintillator and glass RPCs, each of which we believe would perform satisfactorily. We are retaining both as possible backup technologies.

Table 13.2 summarizes the cost estimate comparison of the four active detector options that were considered when the baseline technology was chosen for this proposal.

13.7.1. Solid Scintillator Active Detector: The MINOS Far and Near Detectors are tracking calorimeters composed of alternating layers of iron and solid scintillator read out by wavelength shifting fibers and photomultiplier tubes. The far detector has been installed and is currently operating at the Soudan Underground Laboratory and the Near Detector is currently being installed on the Fermilab site. The 5.4-kiloton Far and the one-kiloton Near Detectors were constructed for a total project cost of $42M, including EDIA and overhead, of which $19M was the active detector system. This included the cost of the scintillator strips, module construction, manifolds, fiber, connectors and multi-channel PMTs and bases. The MINOS detectors include 285,000 kg of scintillator, 782,000 m of scintillating fiber and 32,000 channels of PMTs.

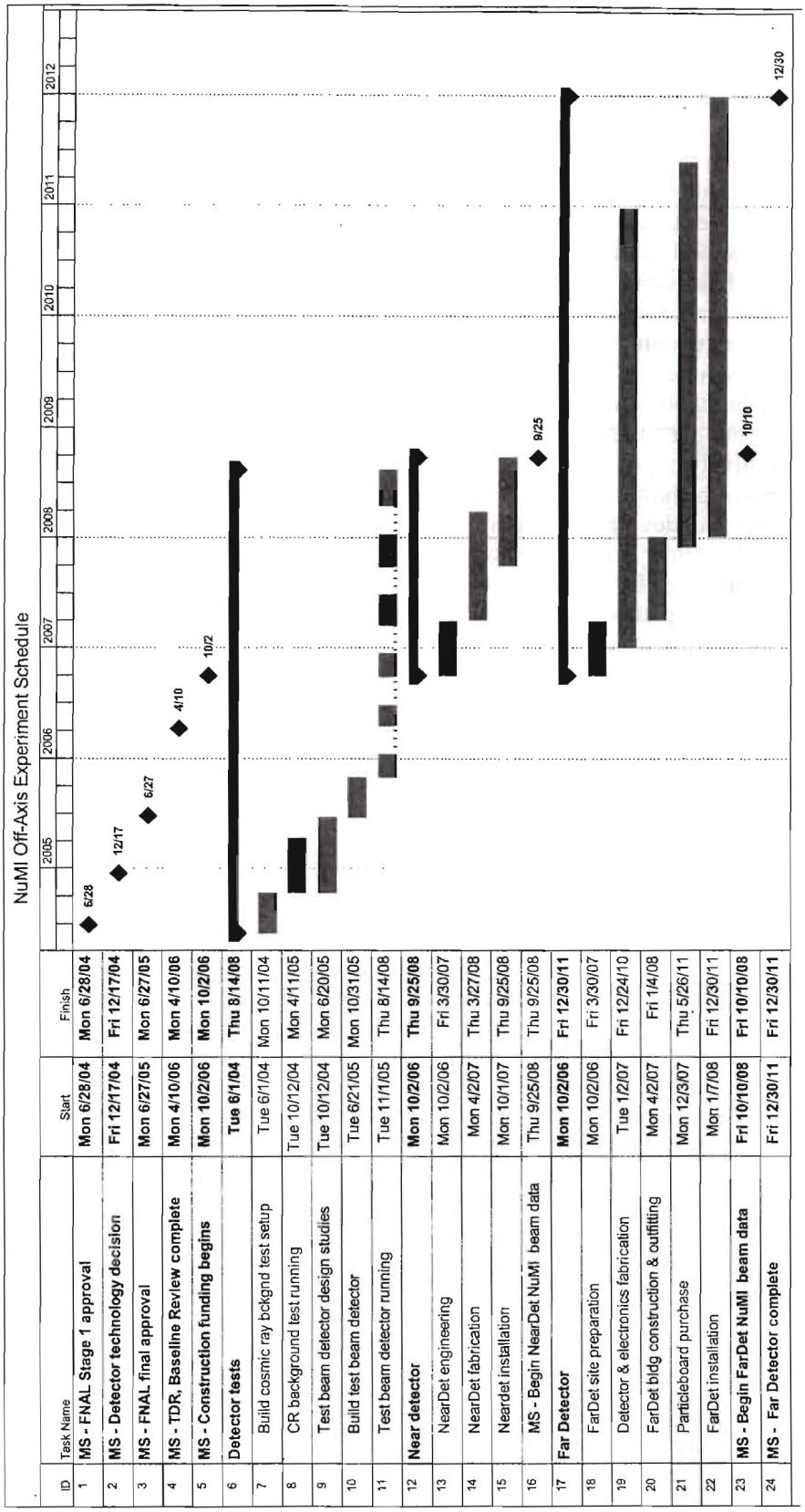

ID	Task Name	Start	Finish
1	**MS - FNAL Stage 1 approval**	**Mon 6/28/04**	**Mon 6/28/04**
2	**MS - Detector technology decision**	**Fri 12/17/04**	**Fri 12/17/04**
3	**MS - FNAL final approval**	**Mon 6/27/05**	**Mon 6/27/05**
4	**MS - TDR, Baseline Review complete**	**Mon 4/10/06**	**Mon 4/10/06**
5	**MS - Construction funding begins**	**Mon 10/2/06**	**Mon 10/2/06**
6	**Detector tests**	**Tue 6/1/04**	**Thu 8/14/08**
7	Build cosmic ray bckgnd test setup	Tue 6/1/04	Mon 10/11/04
8	CR background test running	Tue 10/12/04	Mon 4/11/05
9	Test beam detector design studies	Tue 10/12/04	Mon 6/20/05
10	Build test beam detector	Tue 6/21/05	Mon 10/31/05
11	Test beam detector running	Tue 11/1/05	Thu 8/14/08
12	**Near detector**	**Mon 10/2/06**	**Thu 9/25/08**
13	NearDet engineering	Mon 10/2/06	Fri 3/30/07
14	NearDet fabrication	Mon 4/2/07	Thu 3/27/08
15	Neardet installation	Mon 10/1/07	Thu 9/25/08
16	MS - Begin NearDet NuMI beam data	Thu 9/25/08	Thu 9/25/08
17	**Far Detector**	**Mon 10/2/06**	**Fri 12/30/11**
18	FarDet site preparation	Mon 10/2/06	Fri 3/30/07
19	Detector & electronics fabrication	Tue 1/2/07	Fri 12/24/10
20	FarDet bldg construction & outfitting	Mon 4/2/07	Fri 1/4/08
21	Particleboard purchase	Mon 12/3/07	Thu 5/26/11
22	FarDet installation	Mon 1/7/08	Fri 12/30/11
23	**MS - Begin FarDet NuMI beam data**	**Fri 10/10/08**	**Fri 10/10/08**
24	**MS - Far Detector complete**	**Fri 12/30/11**	**Fri 12/30/11**

Fig. 13.1: Proposed schedule for the NuMI off-axis experiment. This is approximately a technically driven schedule, in that a realistic timetable for the availability of funding has been assumed. The time scale is shown in calendar years.

A cost estimate for using a solid scintillator active detector for NOvA was made and found to be far more expensive than the two other alternatives that were considered, namely the liquid scintillator and the RPCs, mainly because of the cost of the extrusions and the photomultiplier tubes. Replacing the PMTs with APDs reduces the cost accordingly, but to date the cost of the extrusions keeps the solid alternative from being a competitive option. In MINOS the solid extrusions cost ~$10/kg. It is currently thought that this may be able to be reduced to $6-7/kg, but even this rate keeps the solid option prohibitively expensive.

In the cost comparison shown in Table 13.2, $6.4/kg and APD readout devices were used.

13.7.2. RPC Active Detector: A more cost competitive alternate technology for the active detector elements is glass resistive plate chambers (RPCs). A conceptual design for the NOvA Detector using RPCs contained in custom made modules, as described in the Appendix of this proposal, has been costed using the same methodology as for the baseline detector. The results of this costing exercise showed that the RPC active detector was more expensive than the liquid active detector for two main reasons. The first was because of the extra labor involved in the construction of the chambers and the containers. The second was because of the complex gas and high voltage systems. The RPC design incorporates readout of both the x and y coordinates, though it was noted that if an x or y readout scheme were adequate, there could be non-trivial cost savings in the readout board materials and the front end electronics. Proponents of the RPC technology are currently working on design modifications which would address these cost drivers and hence produce a more competitive alternative.

WBS		RPC 2-D (x and y) readout	RPC 1-D (x or y) Readout	Solid Scintillator	Liquid Scintillator
2.0	Far Detector				
2.1	Absorber	12.6	12.6	13.3	12.1
2.2	Active Detector	57.0	50.7	78.2	36.5
2.3	FEE, Trigger and DAQ	8.3	4.5	6.1	5.0
2.4	Shipping & Customs Charges	2.2	2.2	3.0	1.0
2.5	Installation	2.6	2.6	5.8	4.7
	Detector Sub-total	**82.7**	**72.6**	**106.4**	**59.3**

Table 13.2: Work Breakdown Structure and first generation cost estimate for the far detector using three active detector technologies. Note that these are "base costs" only and do not include EDIA, overhead or contingency. These costs were presented in the December 2003 Off-Axis Experiment status report and were the costs used in making the baseline technology choice. Cost estimates for the liquid scintillator technology have now been superceded and are presented in Table 13.1.

Appendix. RPC Detector Description

A.1. Overview

Detailed design studies for an off-axis experiment using both liquid scintillator and Resistive Plate Chamber (RPC) technologies were conducted in parallel during the past two years. Each design study produced a complete, stand-alone plan for constructing, installing and operating detectors for a 50-kiloton off-axis detector, including independent simulations, civil construction plans, cost estimates and schedules.

Chapter 6 describes how the selection of the liquid scintillator technology as the baseline for this proposal was made. This Appendix provides a description of the alternative RPC detector design at the same level as the technical description of the baseline liquid scintillator design in Chapter 7. Descriptions of RPC detector simulations, civil construction plans, cost estimates and schedules are not included here but are documented in detail elsewhere [1,2,3].

The low rate environment of a neutrino experiment makes it possible to utilize glass resistive plate chambers (RPCs) with strip readout as active detectors. Glass RPCs have an excellent track record (BELLE [4], HARP [5]) and should be distinguished from the traditional Bakelite RPC technology.

RPC chambers may be considered as detectors of choice for large area, low maintenance experiments in remote locations. Examples of uses or proposed uses of very large areas of RPC chambers include

- OPERA in Gran Sasso [6],
- ARGO experiment in Tibet [7],
- ATLAS and CMS at LHC [8],
- Indian Neutrino Observatory [9],
- Energy flow calorimeter [10] and muon detectors [11] for the Linear Collider experiment.

Attractive features of the glass RPCs include:

- Two-dimensional position information from every plane of detectors maximizes the topological information about neutrino events,
- Uniform response over the entire detector area,
- Very large induced signals (in streamer mode) require only simple and inexpensive electronics,
- Simplicity of construction leads to low production costs, typically \$100-150/m^2 [12].

An important advantage of the RPC technology is that it allows the detector to be constructed in a modular fashion. This facilitates detector construction and enables distribution of the production effort among a number of collaborating institutions. It could also allow the detector to be moved to another location, at least in principle, should the initial results indicate that moving would enhance the physics reach of the experiment.

The proposed RPC detector consists of 1200 identical 42-metric-ton modules, each 8.534 m (28 ft) long, 2.438 m (8 ft) high and 2.6 m deep. Modules are stacked in an array consisting of 75 planes along the beam direction, each plane being 2 modules wide and 8 high, as shown in Fig. A.1. This design provides a high degree of hermeticity; the gap at the center of the detector between two side-by-side modules is kept to 5 mm. The distance between the modules along the beam axis is chosen to simplify the stacking and unstacking procedure and is of the order of 5 cm. The dimensions of the full detector are 17.1 x 19.5 x 195 m^3.

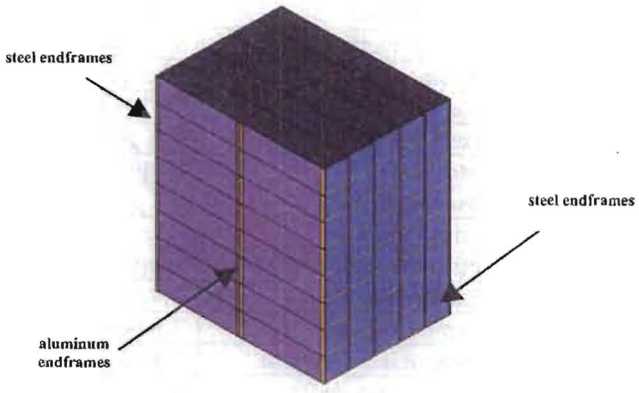

Fig. A.1: Five planes of the stacked modules.

Modules within each plane are interlocked by corner blocks (Fig. A.2), similar to those in commercial shipping containers. Endframes transmit the load of each module to its corner posts and those corner posts bear all the weight of modules stacked above. Readout electronics and gas distribution and recirculation lines are mounted on both sides of the detector and are readily accessible during the operation of the experiment.

Experience with large systems of glass RPCs indicates that there should be no need to replace or repair them. To further minimize any need for replacement, this design provides redundancy by constructing each active detector plane from two independent planes of chambers. Nonetheless, it is worth noting that each vertical column of modules can be unstacked without affecting its neighbors.

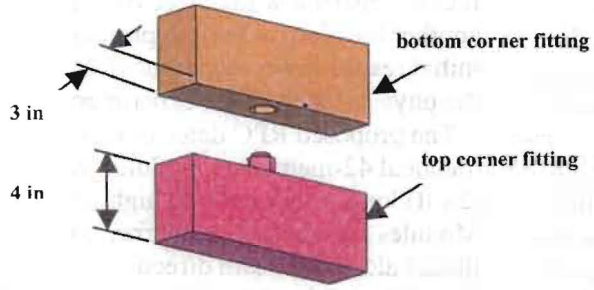

Fig. A.2: Module corner blocks. Aluminum blocks are embedded in the top and bottom of each composite column. The 3.8 cm diameter steel pins in top blocks fit into steel inserts in bottom blocks.

Table A.1 summarizes the parameters of the RPC far detector.

Detector mass	50 kT
Active detector mass	8.9 kT
Detector height	19.5 m
Detector width	17.1 m
Detector length	195 m
Absorber	Particleboard
Absorber density	0.7 g/cc
Active detector	Glass RPC
Active detector module	Single-gap (2 mm) RPC
Chamber height	2.425 m
Chamber width	2.844 m
Horizontal strip width	3.80 cm
Vertical strip width	4.44 cm
Strips per module layer	256
Chambers per module layer	6 = 3 double-gap RPCs
Module layers per module	12
Number of modules/plane	16
Number of module planes	75
Total number of modules	1200
Total number of module layers	900
Total number of chambers	43,200 double-gap RPCs
Total number of strips	3,686,400
Dead area fraction	1.98%

Table A.1: Parameters of the RPC far detector.

A.2. Detector Design

A.2.1. Module geometry: Each module consists of 13 vertical planes of absorber interleaved with double planes of RPCs. Two end plates, Fig. A.3, provide the mechanical rigidity of the module. In order to minimize the amount of dead material in the fiducial volume of the detector, the end plates located in the center of the detector are made of 0.3175 cm thick aluminum. The other end plates, located at the edge of the detector, are made of steel. The weight of the module is supported by two bottom angles, each 1.27 cm thick and 15.24 x 15.24 cm wide, and subsequently transferred to four corner posts. These posts ultimately transfer the load to the floor in a manner analogous to the posts in a standard shipping container.

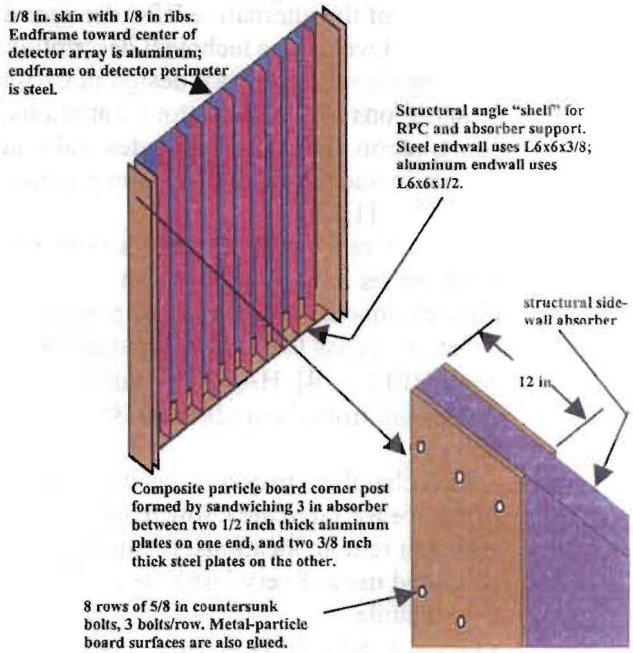

Fig. A.3: End plate and the corner post.

To minimize the dead material in the fiducial volume, the corner posts are composed of two aluminum plates, 1.27 cm x 30.5 cm x 243.8 cm, sandwiched around a 7.62 cm thick particle board. The corner posts are 1.27 cm longer than the vertical absorber height, leaving 6.3 mm vertical clearance between modules.

At the outer edge of the module, the plates are made of steel, which reduces the cost and reinforces the structure. These posts are part of the absorber structure and represent only a small degradation of the sampling of the detector: an addi-

tional 0.25 X_0 over 6% of the area of only 6% of the absorber planes.

To support the module weight, the bottom angles are reinforced by welding 10 ribs (aluminum at the center, steel at the periphery) 0.3175 cm thick and 15.24 cm wide. Absorber/RPC assemblies attached to the corner posts and to the ribs create a toaster-like structure, shown in Fig. A.4.

Module frames, after the proper checkout of the detector elements, will be shipped to the experimental site, where absorber planes are installed, as shown in Fig. A.5.

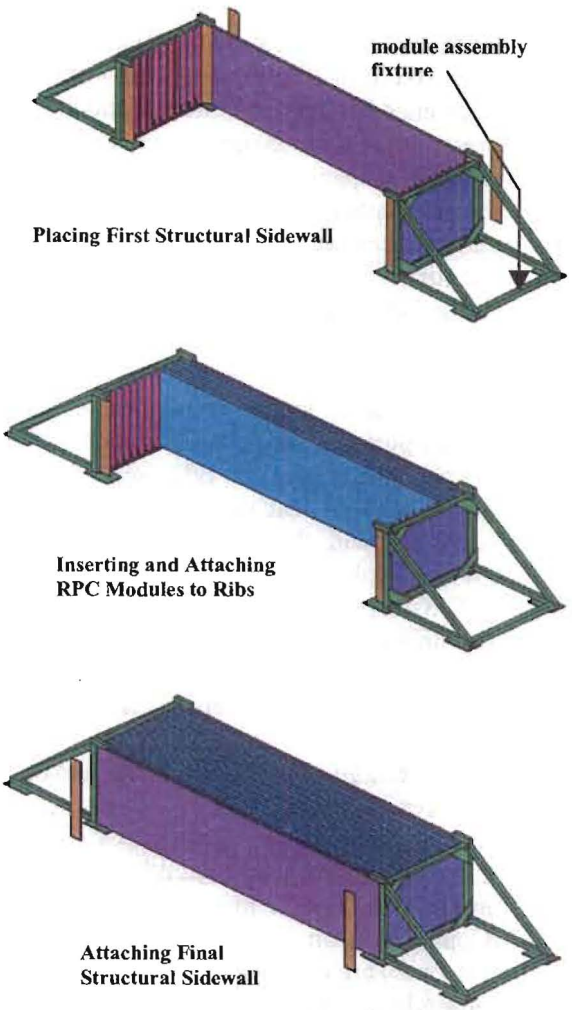

Fig. A.4: "Toaster"construction of a module.

A.2.2. Absorber planes: There are 13 absorber planes in a module. The central eleven are 10.2 cm thick and are assembled out of 4 boards 8.534 m long, 2.438 m wide and 2.54 cm thick, held together by glue and screws. The first and last absorber planes are constructed in a similar manner but are half as thick. Thus, when taken together with the first and last planes of preceding and succeeding modules, they result in a uniform sampling thickness across module boundaries. The absorber planes have 1.27 cm deep and 15.24 cm long notches at the bottom corners to accommodate the weight-supporting angles on which they rest. The support for the two end planes is provided by the corner posts, which are an integral part of them.

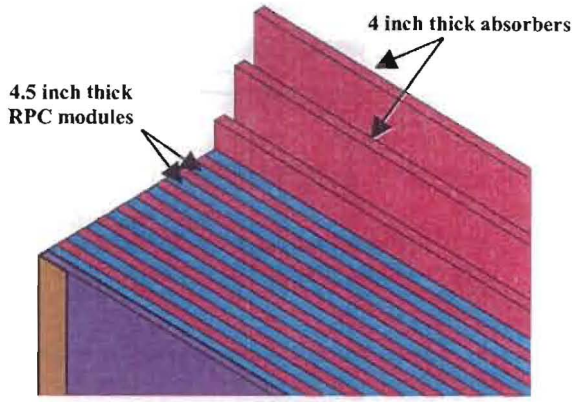

Fig. A.5: Insertion of the absorber planes into a "toaster."

A.2.3. Detector unit: A detector unit consists of two planes of RPCs sandwiched between two particleboards, the readout boards, one carrying the horizontal readout strips and the other the vertical ones. The boards also serve as protection for the glass chambers. A detector unit is 8.534 m long and 2.438 m high. It also has 1.27 cm deep and 15.24 cm long notches at the bottom corners to accommodate the weight-supporting angles on which they rest. The chambers cover an area of 8.534 x 2.425 m^2. Gaps between adjacent chambers and modules result in a total "dead" area fraction of 0.95%.

A.2.4. RPC chambers: Glass RPC chambers utilize inexpensive commercial float glass of high resistivity, 10^{12} Ω cm, instead of the traditional Bakelite used in other RPCs. An RPC, shown in Fig. A.6, is composed of two parallel glass electrodes, kept 2 mm apart by appropriate spacers. The gap between electrodes is filled with a suitable non-flammable gas mixture. The resistive coating on the outer surfaces of the glass connected to the HV power supply creates a strong electric field of about 4.5 kV/mm across the gap. An ionizing par-

ticle initiates a local discharge, which induces a signal on external pickup electrodes strips. The high resistivity of the glass and the quenching properties of the gas limit the discharge to a small area.

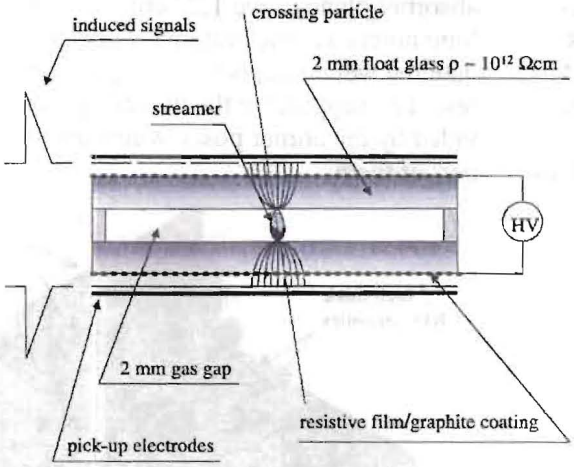

Fig. A.6: Glass RPC detector principle.

The development of an electron avalanche in an RPC gas gap has been simulated by a number of authors [1,13]. In the avalanche, a wave front of electrons moves rapidly (~100 microns/ns) toward the positively charged glass surface. On this time scale, the positive ions are nearly stationary. Simulations indicate that the separation of electrons and positive ions generates a dipole-like electric field extending beyond the gas gap, which induces a signal on the RPC readout strips.

Each pickup electrode is a plane of metallic strips glued to an insulating layer, on the other side of which is glued another metallic plane held at ground. This transforms the pickup strips into transmission lines, allowing the signals to be transported over long strip lengths. The induced pulses are typically 100-300 mV/50Ω with few ns time resolution. These large signals (100-200 pC in streamer mode) allow for the possibility of a variety of cost saving options in the readout electronics. Pickup electrodes are located on both sides of the chamber with strips oriented orthogonal to each other, so that two coordinates can be obtained from a single RPC gap.

Chambers for the NOvA detector are constructed in a manner very similar to the BELLE chambers, which have operated reliably for over four years at KEK. Each RPC plane is made up of three separate chambers with a daisy-chained gas supply and a separate high voltage and current read-back for each chamber. The 2.844 x 2.425 m^2 chambers are built from 3-mm thick float glass. A uniform distance between the glass plates, which defines the electric field in the chamber, is ensured by 2 mm thick Noryl spacers, 20 cm apart and glued to both glass plates. These spacers, glued in a maze-like pattern, serve several purposes:

- Ensure uniform gas flow over chamber area,
- Maintain uniform spacing of the glass plates,
- Protect the chamber from breaking in the event of a sudden change in atmospheric pressure.

The BELLE chambers were built with 2 mm glass. The thicker 3-mm glass in the NOvA detector allows the separation of spacers to be increased from 10 cm to 20 cm, while still withstanding a difference between the internal and atmospheric pressures of up to 20 cm of water. Reducing the number of spacers has two advantages. It reduces the dead space, and therefore the inefficiency, and also reduces the required manpower, and therefore the cost, of gluing the spacers.

The outer perimeter of the glass plates is sealed with a T-shaped extruded Noryl border to provide a gas-tight volume. The corners of the chambers are cut at a 45° angle. Triangular, injection molded plastic pieces glued in the chamber corners contain the gas inlet and outlet. Edge seals and corner cutouts result in a dead area fraction of 1.03% that, combined with the dead area between chambers, gives a total dead area fraction of 1.98%

The outer surfaces of the glass are painted with a resistive paint. High voltage leads are soldered to a copper pad glued to these resistive layers. An insulating plastic sheet covers the entire surface of the chamber.

A.2.5. Readout boards: Two particleboards, 8.534 m long and 2.438 m high, form the covers of the detector unit, with glass RPCs sandwiched between them. Both surfaces of both particleboards are laminated with thin copper foil glued to them. Copper foils on surfaces facing the chambers (inner ones) are cut into strips; the other surface is a ground plane which creates a transmission line.

Horizontal strips are 3.7 cm wide with 3.8 cm pitch, whereas vertical strips are 4.34 cm wide with 4.44 cm pitch. Thus one detector unit has 192 vertical readout strips and 64 horizontal ones.

A.2.6. *Performance of RPCs:* We have studied the performance of RPCs in the laboratory using a cosmic ray telescope and a set of small prototype

chambers. Each prototype is 25 x 25 cm^2 and is built out of two 2-mm thick glass plates. The chamber gas was a mixture of 8% isobutane, 61% R134a (tetrafluoroethane) and 31% argon. A three-fold coincidence of scintillation counters selected particles that traversed a stack of three chambers.

The efficiency of these chambers as a function of high voltage is shown in Fig. A.7. It reaches 92% at 8.3 kV and remains flat for several hundred volts beyond this voltage. The dead space introduced by the spacer can account for about 1-2% of the 8% inefficiency.

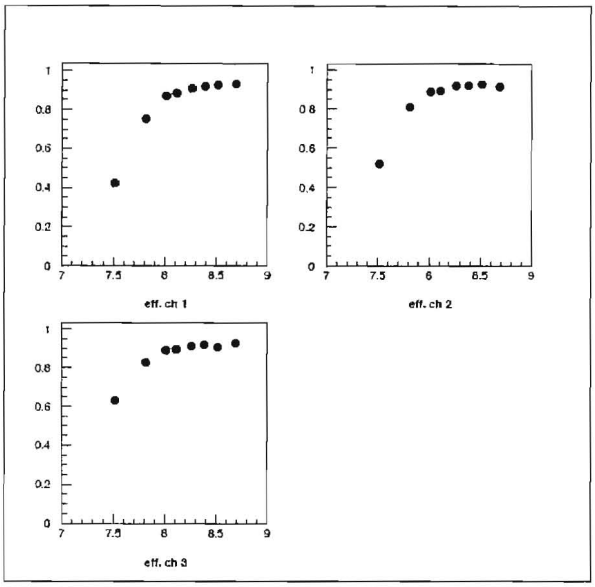

Fig. A.7: Efficiency as a function of high voltage for three chambers.

In BELLE, in order to compensate for the inefficiency of single chambers, two RPCs were sandwiched between a single pair of readout planes. This makes each readout plane sensitive to the sum of the pulse heights generated by the streamers in both RPCs. The positions of the spacers in the two RPCs were staggered so as not to overlap. A similar solution has been adopted for the NOvA detector, with two planes of RPCs positioned between two readout boards.

The pulse height induced by the streamer on the pad increases almost linearly with high voltage as shown in Fig. A.8.

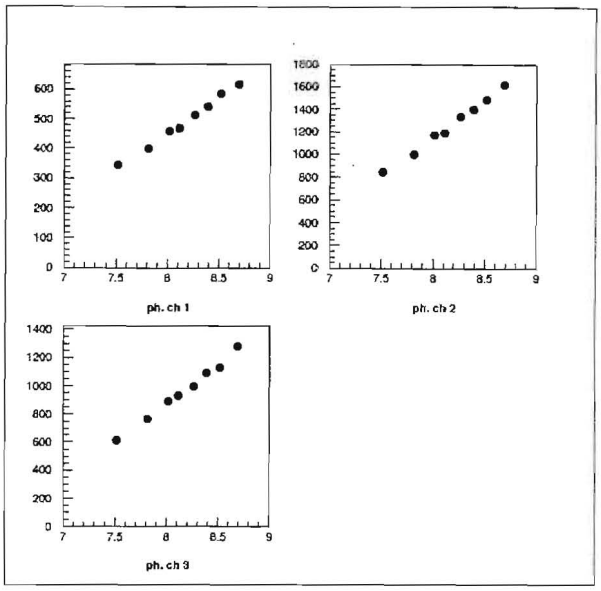

Fig. A.8: Pulse height as a function of high voltage for three chambers.

The dependence of the pulse height on the distance between the readout board and the RPC was measured using the same three chambers and is shown in Fig. A.9. Increasing this distance from 0 to 9 mm results in a factor of two loss in pulse height. Note that in the configuration in which two RPC planes are read out by a single pair of readout boards, each of the two chambers will be at this distance from one of the boards.

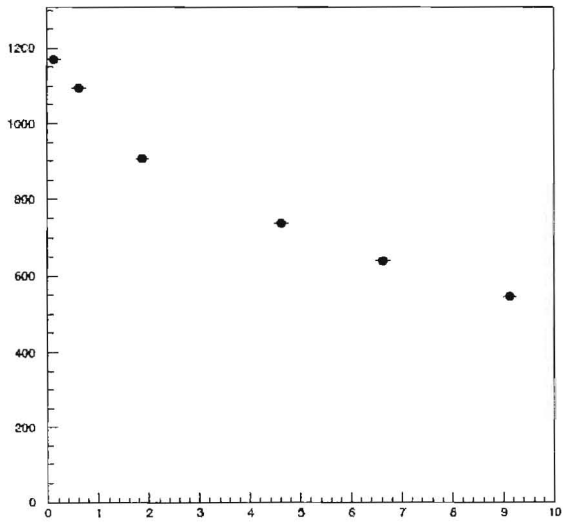

Fig. A.9: Pulse height vs. readout spacer thickness in mm.

The crosstalk, defined in this instance as the number of times a particle gives a signal in two

strips, the one it traverses and an adjacent one, was studied by using a chamber with a 3-cm-pitch strip readout instead of a single pad readout. It goes from 100% when the particle passes just at the edge of the adjacent strip to 3% when the particle is in the center of the neighboring strip.

A.3. Readout Electronics

A.3.1. Overview: When operated in streamer mode, RPC detectors produce a large pulse in response to gas ionization. The signals are large so that a significant voltage (100 mV or more) can be developed across a 50 or 100-ohm resistor. Because the measurement of events requires only recording hits in the detector, it is sufficient to use a simple discriminator as the front-end electronics, without the need for additional amplification or signal processing.

To facilitate event reconstruction, the output of each discriminator latches a timestamp, formed using local counters that receive common clock and counter reset signals from a global timing system. In this way, all timestamp counters across the detector are synchronized. When an RPC channel is hit the value of the timestamp counter is stored in a local memory for later readout. A block diagram of showing the functionality of the system is shown in Fig. A.10. The resolution of the timestamp is determined by the clock speed, which might be 100 ns (10 MHz.) The number of bits in the counter is determined by the frequency of the counter reset, which might be 1 Hz.

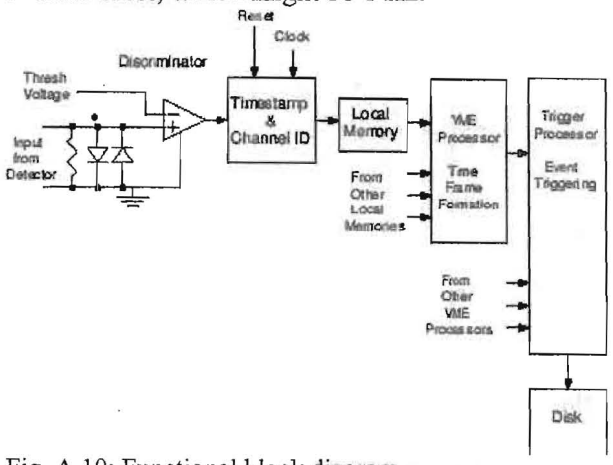

Fig. A.10: Functional block diagram.

Because the data rate is low, it is envisaged that no trigger hardware is needed. Instead, the formation of a trigger and the analysis of events are done using a series of processors. This is similar to the data acquisition system of MINOS. The initial sorting of hits by timestamps is done using a VME-based processor in the front-end crate. The processor would form "time frames" using the time-sorted data. The time frames are then sent to a trigger processor, which receives time frames from the entire detector. The trigger processor runs algorithms that look for tracks and discard noise hits. Those events that pass are either written to disk, or passed to another processor for further analysis.

The functionality of the basic system described above would be configured into the components shown in Fig. A.11 The basic components are: the Front-end ASIC, which processes the detector signals and forms timestamps; the Data Concentrator, which coalesces data streams from the front end ASICs to reduce the number of readout boards; and the Data Collector, which is a VME board that receives the data streams from the front end and makes data available for readout by the front end processor; and the Trigger Farm, which performs the event reconstruction, triggering, and event selection. These components are described below.

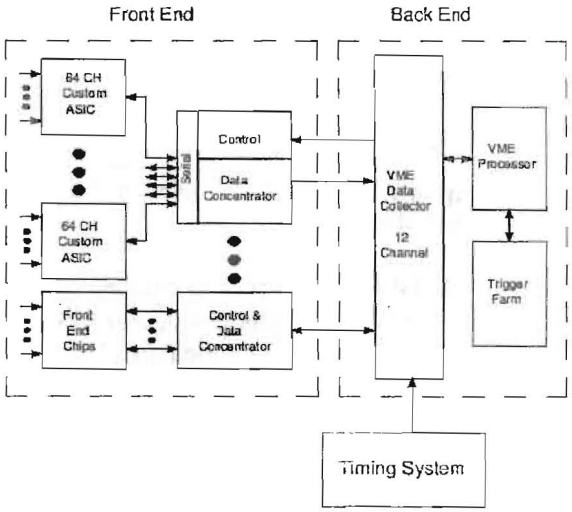

Fig. A.11: RPC electronics system block diagram.

A.3.2. Front-end ASIC: The high channel count and relatively simple front-end configuration make it practical to reduce the cost of the readout system by implementing the functionality in a custom front-end Application Specific Integrated Circuit (ASIC). The discriminator, timestamp counter, and local memory are easily realized in silicon. A block diagram of the ASIC is shown in Fig. A.12.

The ASICs would be mounted directly on the detector.

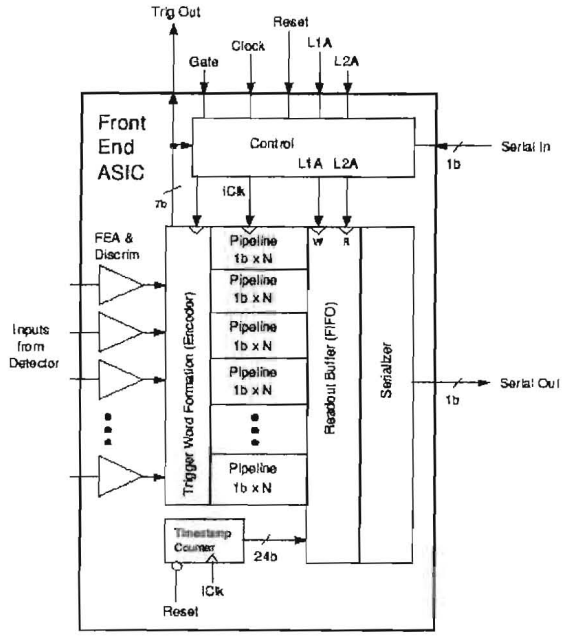

Fig. A.12: ASIC block diagram.

The ASIC would have 64 input channels. Each channel is composed of a fully differential instrumentation amplifier, an optional preamplifier with shaping, and a discriminator, as shown in Fig. A.13. There is a common threshold for all channels on the chip. Since the amplifier is differential, it may be used for either positive or negative input signals.

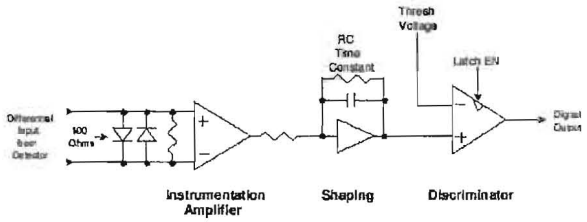

Fig. A.13: Front-end amplifier.

When a discriminator fires, the change in output state is clocked into a shift register at the fundamental clock frequency. The value of the timestamp register is also stored. At the output of the shift register, the decision is made to either write the data to a readout buffer or to reject it. The data are composed of the timestamp and the hit pattern. On-board logic can be configured to auto-accept any nonzero event, or to apply more complicated acceptance criteria.

Once data are stored in the readout buffer, they are serialized, buffered and transmitted out. An on-board UART controls the data transmission whenever the readout buffer is not empty. The readout buffer can store multiple events pending transmission. The output link runs at 100 MHz. An output word consists of 88 bits, which represents the state of the discriminators in one clock period. With control bits, the chip can transmit 1 event in 1 μsec.

A.3.3. Data Concentrator: We expect that the event rate from the NOvA detector will be low. To reduce the cost of back-end electronics, the system would have an intermediate Data Concentrator that coalesces the data streams from the front-end ASICs in an entire plane into one stream. A block diagram is shown in Fig. A.14. The Data Concentrator would reside on the detector, close to the front end ASICs. Essentially, this device is a multiplexer, although it must add an identifier to each data stream. It also must have buffering and flow control. The realization might be achieved using either an FPGA or a custom ASIC.

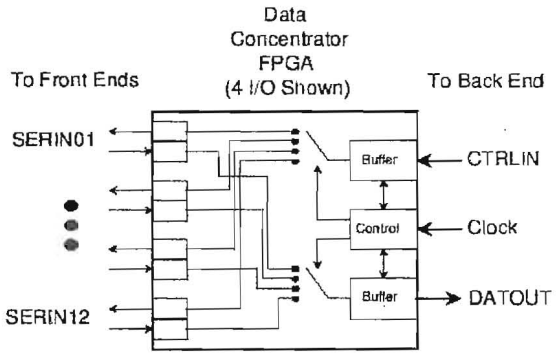

Fig. A.14: Data Concentrator block diagram.

An additional level of data compression may be achieved by concatenating the output data streams from several data concentrators into one "super concentrator." The output would run at 1 GHz and would be serially transmitted over fiber. There would be one super concentrator per module.

A.3.4. Data Collector: The serial data streams from the detector would be received by custom modules that reside in VME Crates, called Data Collectors. A block diagram is shown in Fig. A.15. It is implemented as a 9U by 400 mm card that has

12 inputs for serial data. The data are received, buffered and written into one of two readout buffers. One buffer is made available for reading by the VME processor in the crate while the other is used for writing new data. The state of the buffers changes at a set frequency, synchronized across the system, to facilitate the formation of "timeframes" of data. The Data Collector also provides control for the front ends, including the setting of threshold voltages, the fan-out of clock signals, and diagnostics.

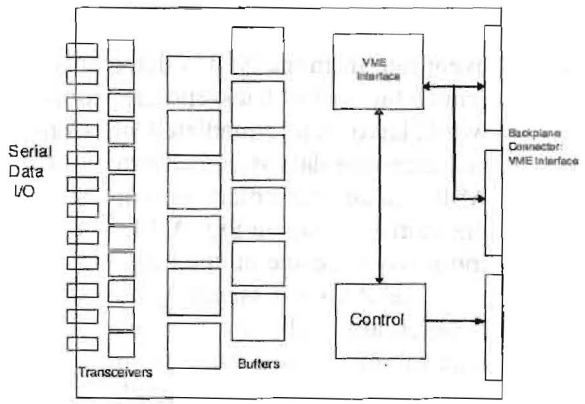

Fig. A.15: Data Collector block diagram.

A.3.5. VME crate: There would be multiple Data Collectors in a VME crate, as shown in Fig. A.16. The crate would also have a Timing Module for synchronizing the formation of timeframes of data. The Timing Module generates Interrupt Service Requests (ISRs) at a predetermined frequency.

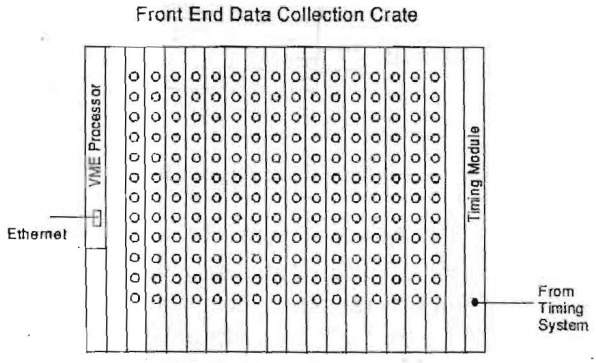

Fig. A.16: VME crate diagram.

When an ISR is received by the VME processor it reads data from the buffers on all of the Data Concentrators associated with that ISR. The next ISR would be generated to read from the other buffer. The VME processor collects blocks of data to form timeframes, which might be nominally 1 second worth of data. At the end of the formation of a timeframe, the VME processor would send the collected data to the Trigger Processor, where event reconstruction and triggering done.

A.3.6. Physical configuration on detector: Each detector module has 12 planes, each with 192 vertical strips and 64 horizontal strips. The horizontal strips come out to the vertical sides of the detector. The front-end ASICs for the horizontal strips reside on a small printed circuit board on the edge of the detector. There is one 64-channel chip per plane for the horizontal strips. The vertical strips have signals brought from the top of the plane over to the side of the detector by flex cables. Thus all of front-end ASICs are located on the side of the detector, providing easy access for servicing. The vertical strips are serviced by three 64-channel ASICs for a total of four chips per plane.

Each plane has one Data Concentrator and each module has one Super Concentrator, producing one serial data stream per module.

Each Data Collector has 12 inputs, requiring 100 Data Collectors to read out the 1200 detector modules. Assuming no limitations due to data rates or data transmission, this could be realized by having six VME crates, three per side.

A.4. RPC High Voltage System

A.4.1. Overview: The high voltage system is composed of distributed HV supplies, with one HV supply per RPC. The NOvA detector then requires approximately 104,000 individually controlled supplies, each with HV reference and current readback. The system is operated via a "slow control" serial network based on the CANbus commercial protocol. CANbus nodes contain multiplexed DAC and ADC modules to set RPC voltage and to read reference voltage and current. Current readback for individual RPCs is an important diagnostic of the operational state of an RPC.

In terms of the detector layout, each of the 1200 detector modules has one CANbus node and 72 Cockroft-Walton (C-W) high voltage supplies, with 6 C-W supplies per HV board. One HV board provides voltage to a full plane of double-layered RPCs, for a total of 12 HV boards per module.

Table A.2 contains the list of HV-system building blocks.

Item	Location	Total Count
C-W Supply	1 of 6 on a C-W board	86,400
C-W Board	1 of 12 on a detector module	14,400
CANbus node	1 per detector module	1,200
24V power supply	1 per 8 detector modules	150
PCI card	On C-W PC	3
PC	Control Room	1

Table A.2: Components of the RPC high-voltage system.

A.4.2. High voltage generation: Six C-W HV supplies are housed on a single 4-inch x 12-inch HV board that powers one plane of RPCs. The board is located on the outside edge of an absorber plane, adjacent to the RPC plane, and feeds HV to the RPCs on 20 kV insulated wires. Wires are soldered to the C-W board and to the RPC. Each wire is routed to an RPC in a groove at the top of the RPC carrier board.

A C-W supply is composed of diodes, capacitors and a transformer. Although the capacitors operate at 200 V the C-W boards use 500V-rated capacitors with a very reliable X7R dielectric (as opposed to the troublesome Z5U dielectric capacitors initially used on the ZEUS experiment).

A.4.3. HV system control: The system is controlled by a PC with three PCI cards (NI PCI-CAN/2). Each PCI card can communicate serially with 500 nodes via two CANbus controllers on the card. The CANbus node sets HV and reads back HV and current for all of the RPCs in a module. The node is a PC board that contains a CANbus processor and other electronics, including a multiplexed DAC and a multiplexed ADC. The processor communicates with the PCI card, executes routines and controls the multiplexed DAC and ADC modules.

Each C-W supply receives a command voltage from the multiplexed DAC to set the HV output. Two reference voltages, proportional to the high voltage and to the current, are read back by the multiplexed ADC. This information is relayed to the PC for monitoring and the possibility of fine-tuning the set point.

Physically, the node board has one connector for the CANbus serial communications bus, one connector for power input and twelve connectors to communicate with all C-W boards on a module.

A.4.4. HV system power: The power consumption per C-W supply is calculated as follows. An RPC draws 1 μA per square meter under good conditions and up to ~5 $\mu A/m^2$ before becoming inefficient. The RPC size is 6.9 m^2, so the current will range from 7 to 35 μA. In addition the no-load current is presently 40 μA (which can be reduced). An average total current of 50 μA is reasonable to expect, with possible surges up to 75 uA. The average power per C-W supply is ~ 400 mW with a maximum of 600 mW. If one includes inefficiencies, the resulting average power consumed is about 1 W per C-W, with surges up to 1.5W.

One module consumes ~72 W for C-W supplies plus ~8 W for the CANbus node, for a total of 80 W. Peak demand if all RPCs draw maximal current is 116 W. A vertical stack of 8 modules draws 640 W average and 928 W peak. Therefore, each vertical stack of 8 modules requires one 1 kW power supply. For a detector 75 modules deep, the number of low voltage power supplies is 150, each using 1 kW at +24V.

A.5. RPC Gas System

A.5.1. Overview: The RPC baseline gas used in our prototype tests and detector design study is a mixture of 8% isobutane, 61% R134a (tetrafluoroethane) and 31% argon. The total gas volume of the RPC detector is approximately 700 m^3, which is recirculated at a rate of one volume change per day. Individual RPC chambers are assumed to have leak rates of less than 10 cc/hr.

Gas will be stored and mixed at a central location from which it will be distributed through manifolds to the 1200 modules. On the supply side, gas within each module is distributed by 24 branch lines supplying 3 RPCs each. On the return side, gas is collected in manifolds, compressed and returned to the central supply.

Table A.3 summarizes the components of the gas system.

The design and fabrication will follow Fermilab PPD practices to ensure gas system reliability [14]. Gas system operation will be largely automatic, with provision for remote monitoring and operation, and gas supplies will be large enough to run for several months at the estimated leak rate.

Item	Features	Total Number
Mixing systems	3 flow meters, pressure control valve	2
Module supply manifolds	W/strainer, flow transmitter	1,200
RPC inlets	W/strainer, flow restriction	28,800
RPC outlets	Large enough for barometric pressure	28,800
Module return manifolds	W/pressure transmitter, relief valves	1,200
Return compressors	Dual compressor stations	10
Gas storage	Mixture storage vessel	1
Mass spec gas analysis	Analyzer with multiple sample points	1
Moisture analyzer	Local analyzers, one sample point	2

Table A.3: Components of the RPC gas system.

The gas system will mix, dry and recirculate the mixture through the RPCs. Flow restrictors will limit variations to less than 15% but flow balancing among RPCs is not critical. The main materials used for gas distribution will be stainless steel, copper or brass, with welded or brazed joints used wherever possible.

Estimates of gas system operating costs and applicable Federal environmental regulations are summarized in Ref. [15]. The gas mixture is non-flammable but precautions will be taken to ensure that the isobutane fraction does not exceed the nominal value. The isobutane storage area will be designed to meet applicable safety regulations.

A.5.2. Barometric pressure changes: Withstanding barometric pressure changes is a fundamental design requirement. The nominal RPC glass thickness of 3 mm is adequate to support the gas system overpressure [16] and pressure-relief valves will be used to ensure that pressure differentials do not exceed acceptable values.

Three criteria were used to specify gas system performance [17]:

- Contain gas for barometric pressure within one inch of mercury of the mean. The gas storage capacity is designed to handle this range so that gas will need to be vented only on rare occasions.
- Contain gas for changes in barometric pressure up to 0.75 inches of mercury/hour. Almost all barometric pressure changes are slower than this. The pumps and tubing will be sized to handle the resulting flow rate.
- Relief capacity for reductions in barometric pressure up to 2.5 inches of mercury/hour. Relief devices will vent directly to the atmosphere.

Pressure-relief devices will be installed on the exhaust of small groups of chambers (e.g., on individual modules) with pressures set to 2 inches of water (based on BELLE experience). Our baseline design uses check valves with the spring removed, a technique which has been shown to work reliably in previous Fermilab experiments.

A.5.3. Gas distribution, storage and circulation: Figure A.17 shows the gas distribution system. Gas from the mixing system, storage and RPC return feeds into a buffer tank, which supplies the detector through 40 branches. Each branch includes a pressure control valve, which allows flow to be varied, and is further split into thirty branches. Each of the 1200 branch lines includes a block valve, strainer and a flow transmitter.

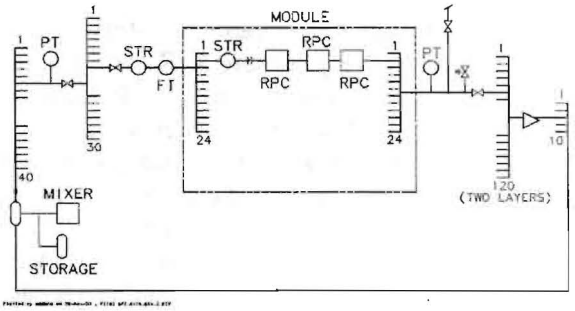

Fig. A.17: RPC gas distribution system.

At the module level the supply is split into 24 branches, each with a strainer and a flow restrictor allowing flows to be balanced to 15%. Each branch supplies 3 RPCs in series. Each module return line has a pressure transmitter, a vent valve, a relief valve and a block valve.

There are 10 return-side compressor stations, each serving 120 module lines. The discharge from the compressor stations is returned to the buffer tank.

The buffer tank is a 500 ft^3 stainless steel vessel used to receive or supply gas during barometric pressure swings. It also provides a buffer to allow brief mixing and purification interruptions. Tank pressure will vary between 0.5 and 35 psig.

The gas mixing system will use mass flow controllers to maintain the desired composition. Similar systems used at Fermilab for two, three and four component mixtures and have proven reliability. Two mixing systems will be used, one sized for filling and purging at 400 SCFH and the second for leakage makeup at 40 SCFH.

The component gases will be delivered and stored in tube trailers. For the estimated leak rate of 5%/day, an isobutane trailer would last 455 days, an R134a trailer would last 75 days and an argon trailer would last 73 days.

A.5.4. Control of gas contaminants: Gas contamination is minimized by material selection, cleaning and leak testing. To keep contaminants from accumulating to unacceptable levels, gas can be vented continuously at a low rate. For example, if a contaminant adds 10 ppm to the gas in one pass, then venting 5% of the circulated gas will limit the contaminant to 200 ppm. When substantial amounts of gas are vented as much of the R134a will be recovered as possible.

Stainless steel pipe, tubing and valves with welded connections would provide the cleanest and most robust distribution system. However we are studying less costly designs using brazed copper tubing for the smaller branches of the system. Connections that must be separated will be either quality compression fittings or O-ring fittings. Neoprene compatible with argon, isobutane and R134a has good long term characteristics and a usable temperature range.

Moisture is known to be detrimental to glass RPCs due to the formation of hydrofluoric acid. Dual molecular sieve driers will remove moisture, with one being regenerated while the other is in operation.

A.5.5. Instrumentation: An ABB IMSQ4 mass spectrometer or equivalent will measure contaminants and the mixture ratio. The mixture ratio data can be used to automatically adjust the mixing system. A single analyzer can be connected to multiple sample points through valves that can sequence automatically through the sample points.

Each module will have pressure and flow transmitters. An industrial programmable logic controller (PLC) will control mixing, circulation, alarms, etc. A commercial human machine interface (HMI) will be used to monitor and control the PLC and gas analyzer. It records historical data and can transmit alarms by Email or telephone. A web interface will be integrated with the HMI to provide remote access.

A.6. Detector Construction

A.6.1. RPC/Readout Board Assemblies: There are twelve RPC/Readout board Assemblies (RRAs) in each module. These are separated by eleven 10.2-cm thick particleboard absorber planes and bounded by two 7.6-cm thick absorber planes at the ends. An RRA is composed of six RPCs, three chambers adjacent in two layers, sandwiched between sheets of particleboard outfitted with readout strips and ground planes. Another 2.5-cm thick particleboard is attached to the outside of each of the two readout boards to protect the flexible circuit cables overlying the ground planes. The layout and assembly of these structures is shown in Fig. A.18 and described below.

The RPC signals are analyzed by discriminators packaged in a 64-channel chip (see Section C). Discriminator chips are mounted on interface boards that are in turn mounted directly on the readout boards. Signals from the readout board strips are collected and transported to connectors on the interface board.

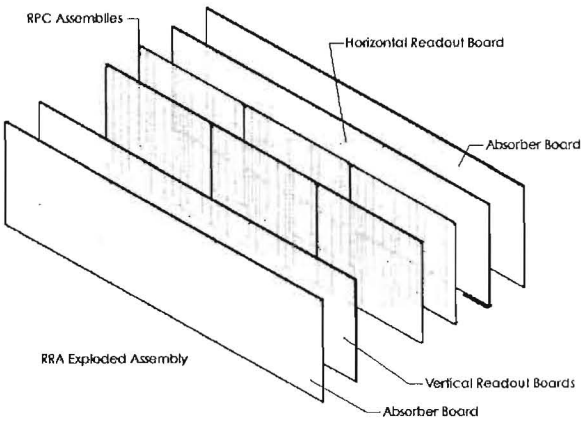

Fig. A.18: Components of an RPC/Readout Assembly (RRA).

A.6.2. RPC construction: Each RPC consists of two glass plates, 3 mm thick held 2 mm apart. The 2 mm separation is ensured by a T-shaped gas seal around the perimeter of the chamber and by a series of 2 mm wide long Noryl spacers positioned 20 cm apart. Each spacer extends from one side of the chamber almost all the way to the opposite side. Alternate spacers start on opposite sides of

the chamber. This maze-like configuration, together with the positioning of the gas inlets and outlets on opposite sides of the chamber, ensures a uniform flow of gas throughout the chamber.

RPCs are produced with a rectangular shape, 284 x 243 cm^2. The corners of each glass plate are cut away, with the resulting discards in the shape of isosceles triangles, 5 cm on shorter sides, as shown in Fig. A.19. The cut out corners are replaced with injection-molded Noryl pieces that act as a gas manifolds and have holes for positioning pins or through-bolts (Fig. A.20).

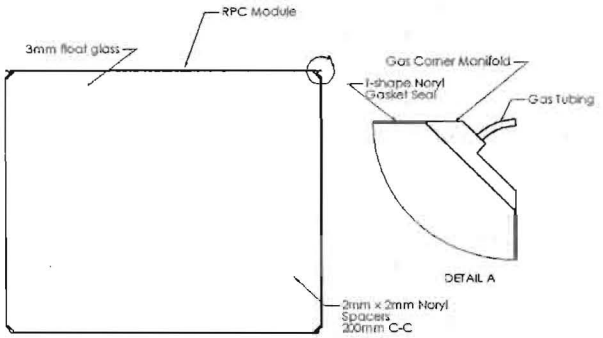

Fig. A.19: Glass RPC design with corner gas manifolds.

The outside faces of RPCs are coated with a conductive acrylic paint [18] resistivity ~1 MΩ/□ (100k-8M Ω/□). Two insulated wire stubs, rated to withstand 20 kV, are attached, one to each side. After installation on the readout board the wires are spliced to a longer harness of 20 kV wires and routed to the outside of the assembly, where a solder connection to the high voltage supply is made.

The injection-molded triangular gas manifolds are installed at the time when RPCs are assembled. Gas connections are made by gluing flexible tubing onto an injection-molded pipe stub. The gas manifolds also have holes for through-bolts and alignment/ retention pins.

A.6.3. Readout boards: Each RPC plane is sandwiched between two readout boards with the copper readout strips facing inward. The readout boards are made of particleboard absorber material with dimensions 243 x 853 x 2.54 cm^3. One board has 64 horizontal strips (3.80 cm pitch) and the other has 192 vertical strips (4.43 cm pitch), as shown in Fig. A.21. To create transmission lines, each board has a solid sheet of copper on the back side.

The horizontal readout boards support the RPCs with a built-in ledge along the bottom of the board. Also, gas tubing and high voltage wires are routed through or behind the top of the horizontal board. In the assembly process, RPCs are attached to the horizontal boards and later covered with vertical readout boards.

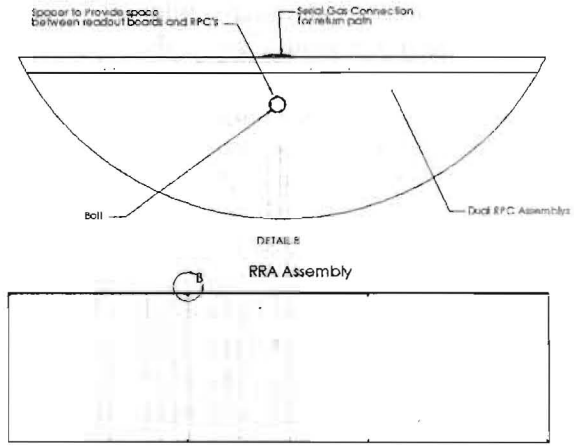

Fig. A.20: Assembly of three RPC chambers bolted to the readout boards.

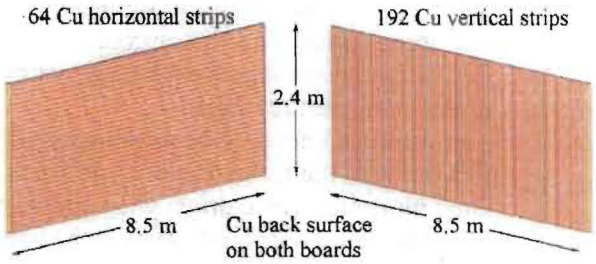

Fig. A.21: The readout boards required for each RPC plane.

The copper-strip side of a readout board is coated with a thin (0.5 mm) plastic sheet to insulate the readout strips from the HV side of the RPCs, to protect the copper strips during the assembly process (when RPCs slide over the strips) and to facilitate the sliding process.

A source for copper foil (1.34 m wide) has been identified. The least expensive unit area cost is obtained if the foil is purchased in a 17-micron thickness (1/2 oz/sq ft). We have contacted several firms who can laminate this foil to the 2.4 m wide

particleboard surfaces and cut the strips. One company gave us a budgetary cost estimate based on a custom-built production line. Strips would be cut with roller cutters specifically designed to prevent bulging on sides of the wedge blades, as shown in Fig. A.22. The company would set up the line and operate it for 2.5 years to produce a total of 28,800 boards plus spares.

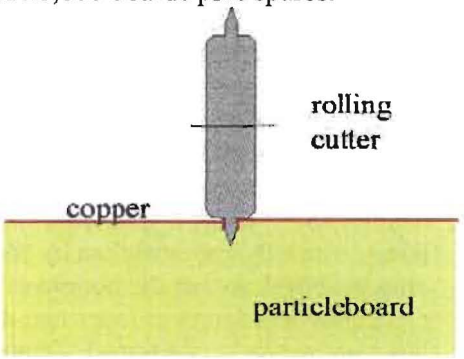

Fig. A.22: Detail of roller cutter shape.

We will use flexible (flex) circuit boards and flat conductor cables as the collection and transportation path, which will maintain the transmission line impedance of the readout strips (~100 Ohms).

A single-sided flex circuit board has been designed with 32 pads on the same pitch as the readout strips, as shown in Fig. A.23. The pads are glued face down on the end of the readout strips with an adhesive (3M z-phase) that makes connections through the glue, but does not conduct between pads. The circuit has a 32-channel fan-in to a neck 6.5 cm wide. Mating to the conductors at the neck of the flex circuit, and permanently attached by the manufacturer, is a 32-channel flat conductor cable with 1 mm wide conductors on a 2 mm pitch. The flat conductor cable will be made in seven different lengths; six for the vertical strips and one for the horizontal strips. The flex circuits bend over the edge of the readout board, lie flat and are taped against its back side, as is shown in Fig. A.24.

A dielectric sheet separates the flex circuit from the back conductor. The thickness of the dielectric is chosen to match the fan-in and cable impedance to the impedance of the strips. The cables must make 90° folds to reach the outer edge of the boards. In each fold it may be necessary to insert a conductor and (or) the proper thickness of dielectric to prevent an impedance mismatch. At the outer edge of the readout boards the flexible flat conductor cables will insert and lock into mating connectors on the discriminator interface cards. The flat conductor cable will extend beyond the end of the readout boards but will fold back into a 2.5 cm wide slot, created by attaching a another particleboard "spacer" on the back side of each readout board, as shown in Fig. A.25.

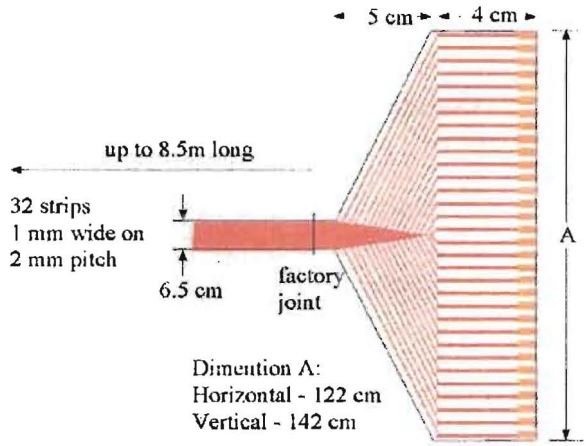

Fig. A.23: Signal collection flex-circuit and flat conductor cable (not to scale).

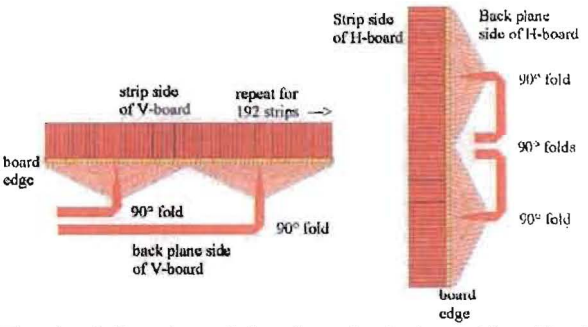

Fig. A.24: Routing of signals on backplane side of horizontal and vertical readout boards.

This arrangement is designed so that electronics can be mounted and tested on the RPC detector package. The package can then be inserted into an absorber module without modification.

A.6.4. Absorber boards: The absorber boards are made of particleboard with similar dimensions to readout boards, except that the absorber board attached to the horizontal readout board is 1.27 cm shorter (241.7 cm). The bottoms of the readout and absorber boards overlap exactly, but the top of the absorber board is 1.27 cm shorter than the readout board. This forms a slight depression that is used

to route gas tubing and high voltage wires to the RPCs.

The absorber boards are connected to readout boards with screws that penetrate about halfway into the readout boards through the ground plane. Care will be taken to avoid using screws in areas where flexible cable is routed.

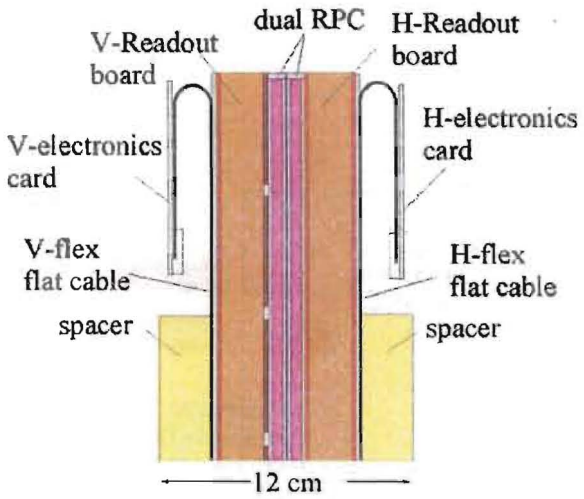

Fig. A.25: Routing of flat conductor cables to allow connection to discriminator interface cards.

A.6.5. RRA Assembly: The RRA assembly process starts with the following preassembled components:

- Horizontal readout boards,
- Vertical readout boards,
- RPCs,
- Gas tubing harness,
- High voltage harness.

A.6.5.1. Horizontal readout board units: To assemble a horizontal readout board unit (HRU), a horizontal readout board is first attached to an absorber board with screws. Recall that the absorber is 1.27 cm shorter on the top side and 2.54 cm longer on the "outside" to protect the front-end electronics connections. RPC support ledges are attached to the lower portion of the absorber board, with the requirement that the attachment is flush with the backside of the absorber (counterbored surface). The ledge supports the readout board and the eventual RPC layers and vertical readout board unit. Finally, the through-holes and alignment holes are drilled into the strip-side for eventual insertion of pins to align the RPCs via the injection-molded manifolds.

The HV and gas harnesses are attached to the HRU and, where appropriate, routed through the HRU to the inside surface for attachment to RPCs.

A.6.5.2. Vertical readout boards: To assemble a vertical readout board unit (VRU), a vertical readout board is first attached to an absorber board with screws. Recall that the absorber is 2.54 cm longer on the "outside" to protect the front-end electronic connections. Care is taken to avoid screwing through any flexible cables.

A.6.5.3. RPC layers on HRU: The next step in the assembly process is to attach RPCs to the HRUs. To facilitate this process a moveable table, equipped with height and tilt adjustment, is placed next to, and at equal height with, the supply of RPCs. The RPCs are installed by sliding them onto the HRU, so that the bottom of the RPC is in contact with the support ledge and the alignment holes are properly positioned. Temporary alignment pins are placed in the holes, gas connections between adjacent RPCs are made and high voltage wires are spliced to the harness. Conductivity is verified and gas connections are checked for leaks.

The table is lowered to facilitate sliding of the next layer of RPCs in a similar fashion. Temporary alignment pins are replaced with the longer, permanent pins. Gas and HV connections are made and tested. Note that the gas connections, although serial in one plane, are totally independent between layers.

Next, the VRU is lowered onto the RPC-HRU assembly on the table. The VRU is supported on the bottom with the HRU ledges. It is tied to the HRU using through-bolts in the clear areas provided at the corners of the RPCs.

The RRA assembly is ready to be rotated to a vertical orientation for insertion into the preformed absorber module.

The RPC chambers are supported from the bottom by support shelf attached to the readout boards, as shown in Fig. A.26.

A.6.5.4. HV, signal and gas connections: After the assembly of the RRA structure is completed, C-W supplies are mounted to absorber planes and the HV harness is soldered to the supplies. Readout front-end chips are attached at this point, along with the gas connections to the supply and vent manifolds.

Gas supply lines are routed inside a cutout in the HRU, as shown in Fig. A.27.

Front-end electronics chips are mounted on the sides of the readout boards and the signal cables are attached. The readout boards are 1.27 cm shorter than the backing absorber boards, so the absorber protects the electronics from accidental damage.

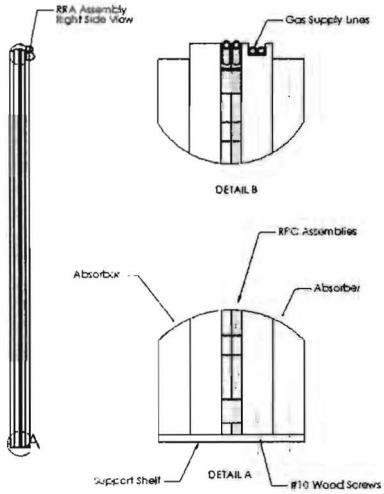

Fig. A.26: Side view of the RRA assembly showing the chamber support shelf in detail.

A.6.6. Detector Installation: To complete the installation of the far detector in 4 years we must construct and test 88 RPC chambers per day. Our construction plan assumes 4 RPC fabrication facilities with large floor space and highly automated equipment. Appropriate lifting fixtures for safe handling of large sheets of glass will require special attention. The completed RPCs will be assembled into RRAs at a rate of 16 per day, probably at two facilities that may be located away from the RPC fabrication sites. Separate fabrication facilities will provide a total of 30 readout boards and 16 Cockroft-Walton HV supply boards to RRA assembly facilities each day.

The far detector contains a total of 1200 modules, requiring 1.2 modules to be produced per day. Finished modules weigh about 42 tons, which is too heavy to transport over most roads and would require special equipment at the module assembly sites. We plan to assemble the module "toaster" structures at the two RRA assembly facilities. These facilities would build the toasters, attach the RRAs and electronics and perform final module quality control tests. The gas manifolds and wiring for electronics and high voltage power supplies are also installed. Substantial floor space and a 20 ton crane will be required to assemble the modules and load them onto trucks for shipping to the final site. The absorber boards would be installed in the modules at the detector site. Figure A.28 summarizes the flow of detector components during module construction.

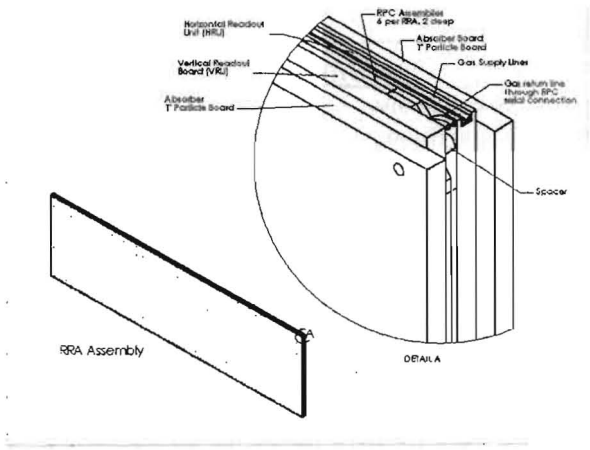

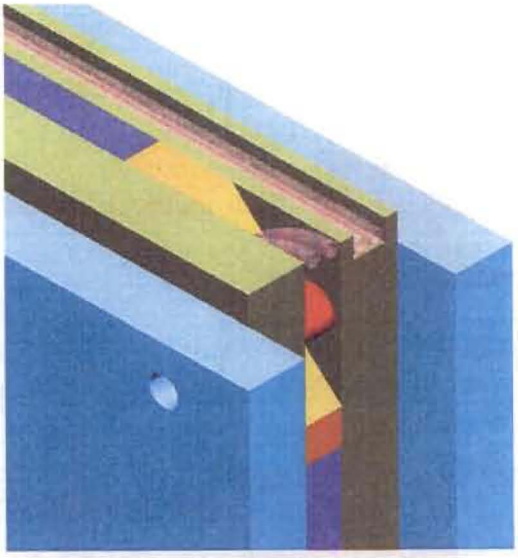

Fig. A.27: Corner of the RRA assembly showing the routing of the gas lines.

Final module testing includes the following:

- The RPCs will be tested for leaks and gas flow will be checked to ensure that the tubing to each set of chambers is clear.
- A high voltage test will ensure that the RPCs are functioning properly.

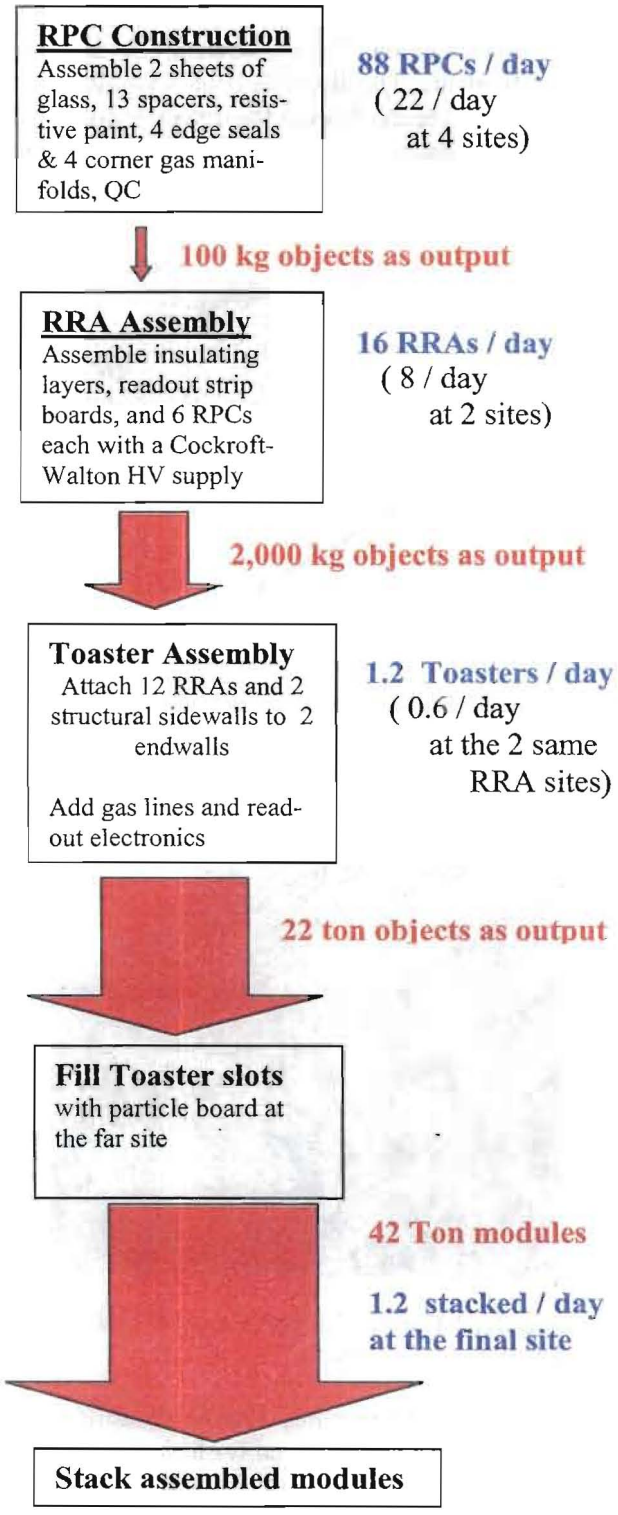

Fig. A.28: Flowchart of detector construction.

• The final test will use cosmic rays to measure performance after a module has been installed in the detector. Each module will be installed in such a manner that it remains accessible until this test is complete, allowing it to be removed for repairs before it is buried under other modules.

The detector is assembled as stacks of modules, 2 wide by 8 high by 75 deep, occupying a total area 17.1 m wide x 19.5 m high x 195 m long. In the initial stacking the modules will be installed to form a working face of the detector that is stepped like stairs. This will allow the final testing to proceed without burying untested modules.

Columns along each side of the detector footprint will support the gas manifolds and signal and power cables. These will be installed before the detector stacking begins. Each side of the detector will also have an aisle way just outside of the columns, wide enough to allow a man lift to make electrical and gas connections as detector modules are added.

Modules will be rigged by a 50-ton overhead crane using a spreader bar and four swivel hoist rings. This will require a total detector building height of about 33 m. Each module has corner blocks at the top drilled and tapped for the hoist rings. After a module is placed in position the hoist rings are removed and tapered pins are screwed in the same holes. These pins match the holes in the bottom corner blocks of the modules and are used for alignment as the modules are stacked up.

During and after assembly the detector will require access to the long (195 m) sides of the detector parallel to the neutrino beam. There will be two lanes on each side of the detector. The outside lane would be about 1 meter wide and primarily for personnel access. The inside lane next to the detector would be reserved for scissor-lifts, boom-and-bucket devices or a warehouse distribution system on rails (see Fig. A.29), allowing a person to reach the entire outside surface for installation, debugging, and maintenance of electronics, high voltage and gas systems. This lane would be approximately 3 meters wide. The access lanes add about 8 meters to the width of the building, giving a total width of 25 m.

The RPC detector building will need to be about 25 m longer than the 195 m length of the detector itself in order to provide room for final module assembly, component storage, the gas system and

office space. The overall building dimensions are then 220 m long x 33 m high x 25 m wide.

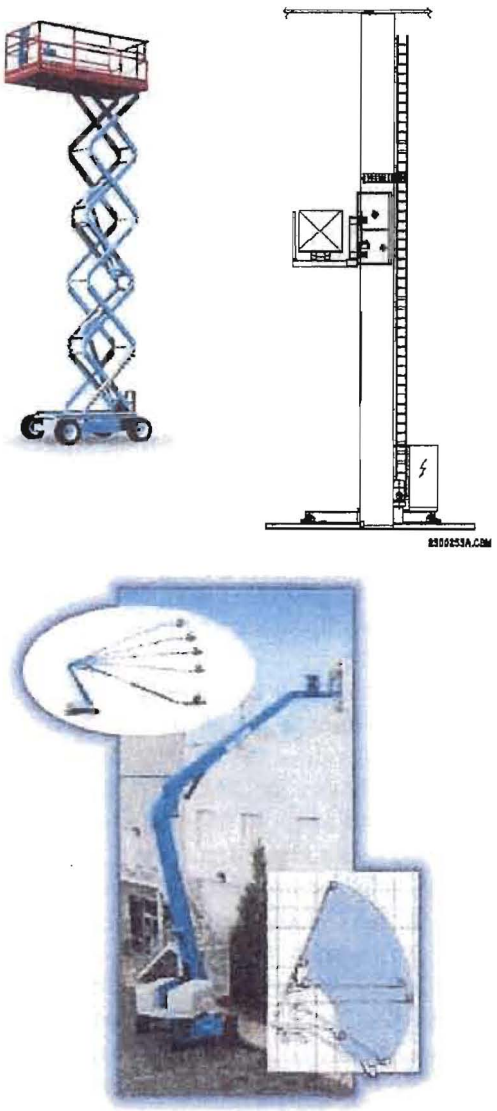

Fig. A.29: Possible access vehicles.

A.7. Cosmic Ray Active Shield

Just as in the Liquid Scintillator design, the RPC design would have a layer of counters on the top and the two long sides of the 75 rows of stacked modules. The side counters would be attached to the building walls, and the top counters would just be set on top of the stack of 8 modules, since there are no signals to access on the top of the detector. Each counter would be a RRA-like object with a double layer of single-gap RPCs. This would require an additional 3,000 RPCs of the type used in the RRAs.

A.8. Near Detector

The near detector could be constructed as a stack of 6 or 8 modules, of the same construction as the far detector modules, arranged in 3 or 4 walls, 2 modules high. Due to space limitations of the existing near-detector hall access tunnel, the modules would have to be shorter than far detector modules: about 4 m wide x 2.438 m high x 2.6 m deep.

Limitations of the access shaft to the Near NuMI hall will require the absorber planes and RRAs to be lowered separately and installed in modules underground. The upstream modules could have improved sampling at twice the frequency of standard RRAs.

A.9. RPC ES&H Considerations

Several ES&H issues must be considered during construction and operation of the RPC detector.

A.9.1. *Fire:* The detector's principal component is wood and represents a substantial fuel load at any module fabrication site as well as at the final location. Assembly methods chosen must ensure that module construction areas meet fire safety codes. It may be necessary to paint the completed assemblies with fire retardant paint to limit their flammability. Housekeeping will also be important because sawdust is more flammable than particleboard planes.

A.9.2. Lifting heavy loads: Every stage of construction will require commercial or specially designed lifting fixtures to handle the wood panels, glass plates and the finished modules. All fixturing must meet the requirements of the OSHA standards. These fixtures will include vacuum fixtures for handling glass plates and container-style lifting fixtures for the modules. Rigging procedures will be reviewed in advance of construction and operators will be trained in the proper use of hoisting equipment.

A.9.3. Glass handling hazards: Handling thousands of square meters of glass is potentially hazardous and procedures must be worked out to protect workers from the occasional broken pane. We will investigate the procedures and equipment used by large glass making companies to protect their employees.

A.9.4. *Oxygen deficiency hazard:* For such a large detector the inventory of gas is significant. Standard Fermilab ES&H rules will be followed to

minimize this hazard at every location, including all gas storage and mixing areas.

A.9.5. Fall protection: Because of the height of the detector fall protection must be provided for work on the detector stack. This might include railings and certainly will require harnesses and lanyards compliant with OSHA regulations. Crane cages, if used to lift personnel to the top of the detector, must be certified for that service. The present design does not include any need for working on top of the detector stack for operations or maintenance.

A.10. R&D for the RPC Design

As noted in Chapter 7, the RPC Design performance is essentially equal to the Liquid Scintillator Design performance and therefore our choice of Liquid Scintillator as the baseline is determined mostly on the issue of price (see Chapter 6). It follows that all our R&D efforts on the RPC Design will be aimed at reducing the price of this option. The object of the collaboration is to explore the parameter space of these options to find the best cost-performance solution.

A.10.1. RPC parameters: One simple change to the RPC design would be to construct "double gap" chambers using three pieces of glass instead of the four required for the two RPCs in each plane. This scheme has been used elsewhere and we will explore some prototypes for the NOvA detector. In this scheme the center glass plate polarizes so that each gap has the appropriate HV gap, requiring a higher voltage across the outside two glass plates.

The double layer of RPCs in each plane was motivated by our desire to have high efficiency in each plane and the efficiency reached in streamer mode is limited to 93 – 95%. However it is possible to operate RPCs in avalanche mode with very high efficiency, 98 – 99%. The signals become 100 times smaller, so this change would require amplification in the electronics. We are exploring this option in collaboration with the Linear Collider Hadron Calorimeter group and in fact are working with them to produce an ASIC which can handle either streamer or avalanche mode.

The readout strips in our basic RRA unit are made of copper laminated to particleboard. The cost of doing the lamination ourselves is high, estimated at about $ 0.30 per square foot of material and we need 6.5 million square feet. One possibility to reduce this cost would be to use a standard building material composed of polyisocyanurate foam faced with aluminum on both sides. The idea is to take advantage of existing large scale industrial output of a pre-laminated product. In this case we would be confronted with making grooves in the aluminum facing to form strips, but we think this can be done cheaply. The real R&D in this effort involves understanding how to make robust electrical connections to aluminum: the solution may be to capacitively couple our signals. Small prototypes will answer these questions.

A.10.2. HV System Simplification: The Cockroft-Walton HV system was designed so that each individual RPC chamber had its own HV and its own current readout. This count of 86,400 HV channels could be reduced by ganging the three or more RPCs in one Toaster module layer together.

A.10.3. Gas System Simplification: Our gas system design is based on copper tubing and we continue to search for a cheaper alternative. Any solution has to be impervious to water vapor.

In our base design described above, only 3 RPCs are in series in the gas flow. We could combine the gas path so that one set of six RPCs in a layer had only one gas path. The total pressure drop of the system would need additional study.

We could also simplify our gas system manifold on each Toaster module. The base design has expensive sintered metal filters and small diameter flow restrictors in front of each set of 3 RPCs. This was done to ensure balanced flow. We will do R&D on different schemes and understand just how balanced the gas flow has to be.

Our gas system design is a recirculating system with one volume change per day. BELLE operates with only 0.5 volume changes per day. If we could lower our gas flow a bit further than BELLE, say to 0.1 or 0.2 volume changes per day, we could eliminate the recirculation and just pass the gas once through each set of chamber, venting to the outside. This actually could be viewed as a less risky design since recirculation entails the possibility of contamination of the total detector if something goes wrong in just one small part. Our R&D here has to focus on how the pressure in the chambers can then track the outside atmospheric pressure without introducing oxygen and water vapor back through the outlet line (we contemplate

a long exhaust line with no bubbler, as was done 30 years ago on large spark chambers).

A.10.4. Exploring a Monolithic RPC Design: Our base RPC design is modular but there seems to be a cost advantage to construction of a monolithic device as is outlined for the liquid scintillator in Chapter 7. We will investigate if the assembly could be done at the far site using single RPCs and particleboard sheets as the basic units to be shipped.

A monolithic design should have a clear advantage in the number of electronics channels required for our RPCs. The modular design breaks the vertical strips into 8 parts, since we stack up 8 modules to make the detector. Reducing the number of vertical strips by 8 would result in a large cost savings.

A.10.5. Exploring a Commercial Modular RPC Design: Our design described in this Appendix relies on a custom container-like structure which is rather expensive to build. In addition, each of the modules is so large that we can't transport them on US Interstate highways unless they are only half-full. Thus this design suffers from having assembly labor at both ends of a transportation pipeline. This custom "container" was motivated by a desire to keep the dead space in each module at a minimum and our design did achieve a dead space of only 1.98 %.

Our "container-like" modules were in fact inspired by standard ISO Intermodal Shipping Containers. One avenue of R&D is to see if these existing cheap containers can be used in the NOvA detector. Standard ISO Containers come in a 20 foot long, 8.5 foot high, 8 foot wide version and can be purchased for about on-third the cost of our custom designed module. The one drawback of ISO Containers is that they have dead space at the bottom of the container where there are open pockets for forklifts and a steel grid structure which supports a plywood floor on the interior of the container. Use of these containers with such a dead area (about 7.5 %) between vertically stacked modules will require investigation of more sophisticated event tracking algorithms than those we have studied to date. The R&D here focuses on the tracking algorithms and simulations. We have to see if we can follow a track across a dead area and yet not label the track interruption as a real gap, which might be indicative of a π^0.

ISO Containers do have additional advantages other than the purchase price vs. custom-built price. One is that the steel gridwork and plywood floor support the load directly, allowing different building materials to be considered for the absorber. One such attractive alternate is gypsum in the form of sheetrock or drywall, which has the same density as particleboard. This material works well at supporting itself inside an 8 foot high container and appears to be available at about one-third the price of particleboard. This would give a very substantial cost savings. The radiation length of gypsum is about 37 cm vs. 53 cm for particleboard, but we will have to understand that effect on the detector performance.

A second additional advantage is that ISO Containers can be stacked quite high. They are routinely stacked 10 high on container ships and we have calculated they can be stacked 13 high on land when loaded at our projected density. This could make the profile of the NOvA detector higher and narrower. Our studies indicate that the detector enclosure building will be substantially cheaper (at equal volume) if the building is higher with a smaller footprint area.

We believe we can bring all these R&D ideas together into a few new RPC based re-designs during the next year. In each case, we have to develop a full model of detector construction and understand the attendant transportation costs and labor costs for assembly. We need the complete picture in hand to judge one scheme relative to another.

Appendix References

[1] A. Para, "RPC detector simulation using GMINOS," NuMI Off-axis Note 10, August 2003.

[2] A. Para, "Fiducial volume of the RPC detector," NuMI Off-axis Note 16, September 2003.

[3]A. Para, "Resistive Plate Chamber detector for NuMI off-axis experiment - collective work," NuMI Off-axis Note 21, September 2003.

[4] BELLE KLM detector group, Nucl. Instrum. and Meth. A 449 (2000) 112-124, and Nucl. Instrum. and Meth. A 456 (2001) 109-112.

[5] L. Linssen, HARP detector talk at the 7th Workshop on RPCs and Related Detectors, Claremont-Ferrand, France, Oct. 2003 (to be published in NIM A).

[6] A. Paolini, OPERA detector talk at the 7th Workshop on RPCs and Related Detectors, Claremont-Ferrand, France, Oct. 2003 (to be published in NIM A).
[7] C. Bacci et al. (ARGO experiment), Nucl. Instrum. and Meth. A 508 (2003) 110-115.
[8] P. Iengo (ATLAS) and B. Pavlov (CMS), talks at the 7th Workshop on RPCs and Related Detectors, Claremont-Ferrand, France, Oct. 2003 (to be published in NIM A).
[9] The Indian Neutrino Observatory design study is described by M. Goodman in "New Projects in Underground Physics," proceedings of the Tenth International Symposium on Neutrino Telescopes, Venice, Italy, March 2003.
[10] J. Repond, "A Digital Hadron Calorimeter for the Linear Collider," to appear in the proceedings of the 9th Pisa Meeting on Advanced Detectors, La Biodola, Isola d'Elba, Italy, May 2003.
[11] M. Piccolo, "Report on Muon Activities," ECFA Study of Physics and Detectors for a Linear Collider, Montpellier, France, Nov. 2003.
[12] C. Gustavino et al., "A glass resistive plate chambers for large experiments," Nucl. Instrum. and Meth. A 457 (2001) 558-563.
[13]W. Riegler, C. Lippmann, R. Vennhof, "Detector Physics and Simulation of Resistive Plate Chambers," Nucl. Instrum. and Meth. A 500 (2003) 144-162, and references therein.
[14] T. Gasteyer, "Fixed Target Gas Systems," Fermilab PPD Internal Note, March 1995.
[15] I. Ambats and R. Schmitt, "RPC Gas System Operation," talks given at the 2nd NuMI Off-axis Detector Workshop, April 2003. (http://neutrinooscillation.org/offaxisworkshop.htm)
[16] R. Schmitt, "Study of RPC Glass and Spacer Parameters," NuMI Off-axis Note 14, Aug. 2003.
[17] Data to determine these specifications were obtained from the National Climatic Data Center, International Falls (2002) and the Soudan 2 experiment, 80,200 measurements (1989 to 2001).
[18] G.C. Trinchero *et al.*, Nucl. Instrum. and Meth. A 508 (2003) 102; M. Ambrosio *et al.*, Nucl. Instrum. and Meth. A 508 (2003) 98.

Proposal to Build a 30 Kiloton Off-Axis Detector to Study $\nu_\mu \rightarrow \nu_e$ Oscillations in the NuMI Beamline

NOνA

NuMI Off-Axis ν_e Appearance Experiment

March 21, 2005

The NOνA Collaboration

Argonne, Athens, Caltech, UCLA, Fermilab, College de France,
Harvard, Indiana, ITEP, Lebedev, Michigan State,
Minnesota/Duluth, Minnesota/Minneapolis, Munich,
Stony Brook, Northern Illinois, Ohio, Ohio State, Oxford,
Rio de Janeiro, Rutherford, South Carolina, Stanford, Texas A&M,
Texas/Austin, Tufts, Virginia, Washington, William & Mary

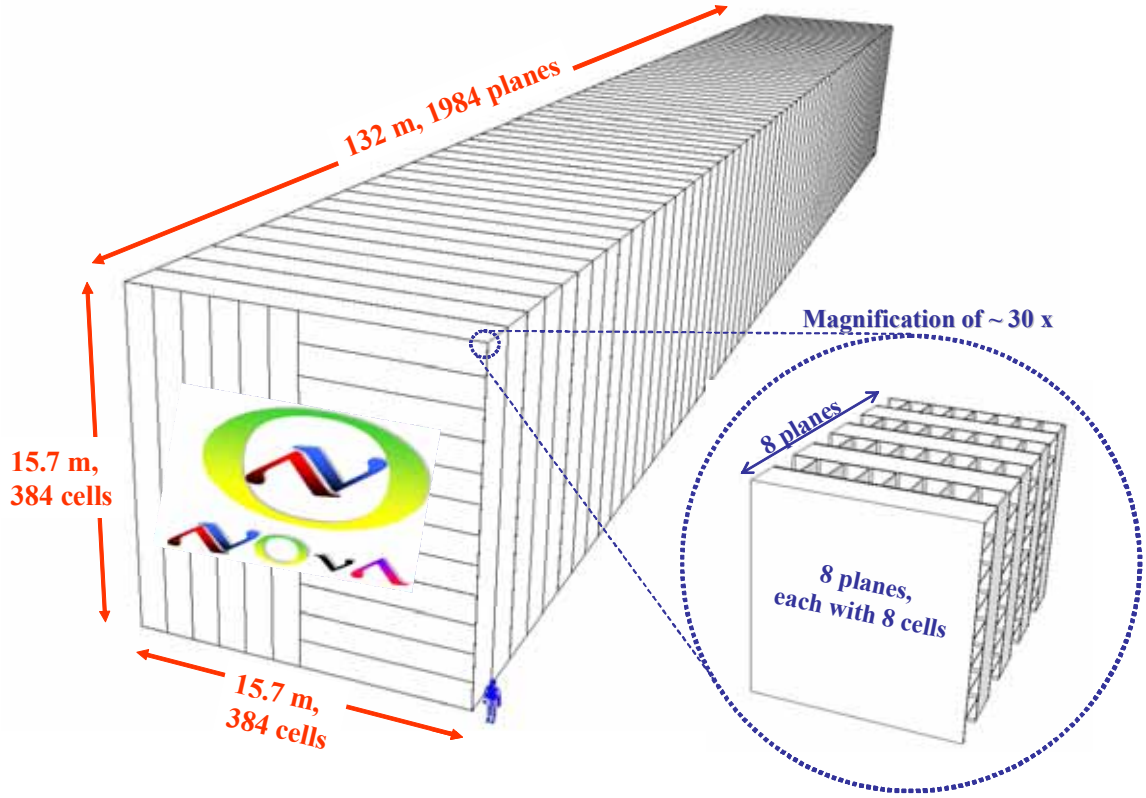

D. S. Ayres, J. W. Dawson, G. Drake, M. C. Goodman, J. J. Grudzinski,
V. J. Guarino, T. Joffe-Minor, D. E. Reyna, R. L. Talaga, J. L. Thron, R. G. Wagner
Argonne National Laboratory, Argonne, IL

D. Drakoulakos, N. Giokaris, P. Stamoulis, S. Stiliaris, G. Tzanakos, M. Zois
University of Athens, Athens, Greece

J. Hanson, C. Howcroft, D. G. Michael, H. B. Newman, C. W. Peck, J. Trevor, H. Zheng
California Institute of Technology, Pasadena, CA

D. B. Cline, K. Lee
University of California, Los Angeles, CA

R. Bernstein, G. Bock, S. Brice, L. Camilleri*, S. Childress, B. Choudhary, J. Cooper**,
D. Harris, R. Hatcher, J. Hylen, H. Jostlein, J. Kilmer, D. Koolbeck, P. Lucas,
V. Makeev, O. Mena, S. Mishra, S. Parke, R. Plunkett, R. Rameika, R. Ray, B.J. Rebel, R.
Schmitt, P. Shanahan, P. Spentzouris, R. Wands, R. Yarema
Fermi National Accelerator Laboratory, Batavia, IL

T. Patzak
College de France, Paris, France

J. Boehm, G. J. Feldman**, N. Felt, A. Lebedev, J. Oliver, M. Sanchez, S.-M. Seun
Harvard University, Cambridge, MA

C. Bower, M. D. Messier, S. Mufson, J. Musser, J. Urheim, A. Waldron
Indiana University, Bloomington, IN

I. Trostin
Institute For Theoretical And Experimental Physics, Moscow, Russia

V. Ryabov
P. N. Lebedev Physical Institute, Moscow, Russia

C. Bromberg, J. Huston, R. Miller, R. Richards
Michigan State University, East Lansing, MI

A. Habig
University of Minnesota, Duluth, MN

T.R. Chase, D. Cronin-Hennessy, K. Heller, P.J. Litchfield, M.L. Marshak,
W.H. Miller, L. Mualem, E.A. Peterson, D.A. Petyt, K. Ruddick, R. Rusack
University of Minnesota, Minneapolis, MN

M. Lindner
Technische Universität München, Munich, Germany

R. Shrock
State University of New York, Stony Brook, NY

C. Albright
Northern Illinois University, DeKalb, IL

J. Beacom
Ohio State University, Columbus, OH

C. R. Brune, S. M. Grimes, A. K. Opper
Ohio University, Athens, OH

G. Barr, J. H. Cobb, K. Grzelak, N. Tagg
University of Oxford, Oxford, United Kingdom

H. Nunokawa
Pontifícia Universidade Católica do Rio de Janeiro, Rio de Janeiro, Brazil

A. Belias, T. Durkin, T. Nicholls, G. F. Pearce, A. Weber
Rutherford Appleton Laboratory, Chilton, Didcot, United Kingdom

T. Bergfeld, A. Godley, J. Ling, S. R. Mishra, C. Rosenfeld
University of South Carolina, Columbia, SC

S. Avvakumov, G. Irwin, S. Murgia, S. Wojcicki, T. Yang
Stanford University, Stanford, CA

E. Tetteh-Lartey, R. Webb
Texas A&M University, College Station, TX

S. Kopp, K. Lang
University of Texas, Austin, TX

H.R. Gallagher, T. Kafka, W.A. Mann, J. Schneps, A. Sousa
Tufts University, Medford, MA

C. Dukes, K. Nelson
University of Virginia, Charlottesville, VA

J. Rothberg, T. Zhao
University of Washington, Seattle, WA

J. K. Nelson, F.X. Yumiceva
The College of William and Mary, Williamsburg, VA

* On leave from CERN
** Co-Spokespersons

Table of Contents

1. Executive Summary 7

1.1. The Physics of NOνA 7
1.2. The NOνA Detectors 8

2. Introduction 10

3. Physics Motivation 12

3.1. Introduction 12
3.2. Neutrino Mixing 12
3.3. Matter Effects 13
3.4. CP Violation 14
3.5. Ambiguity Resolution 15
3.6. Other NOνA Measurements 16
3.7. Neutrino Oscillations in 2010 17
3.8. Summary 17
Chapter 3 References 17

4. Experiment Overview 18

4.1. NuMI Beam 18
4.2. Off-Axis Concept 19
4.3. Detector Design Considerations 21
4.4. Evolution of the Detector Design 23
4.5. Far Detector 24
4.6. Near Detector 24
Chapter 4 References 24

5. The NOνA Far Detector 26

5.1. Overview 26
5.2. Extrusion Module Fabrication 28
5.3. Detector installation at the Far Site 29
5.4. Filling the Detector with Liquid Scintillator 30
5.5. Structural Considerations 31
5.6. Summary 34
Chapter 5 References 35

6. Light Collection 36

6.1. Introduction 36
6.2. Liquid Scintillator 36
6.3. Wavelength-Shifting (WLS) Fiber 36
6.4. Cell Structure – Reflectivity and Geometry 38
6.5. Light Yield 39
Chapter 6 References 40

7. The Photodetector and Readout 41

7.1. Introduction 41
7.2. Avalanche Photodiodes (APDs) 41
7.3. The Readout Electronics. 44
7.4. Mechanics 46
7.5. Data Acquisition 47
Chapter 7 References 48

8. Far Detector Site, Building, and ES&H Issues 50

8.1. Detector Site Criteria 50
8.2. The Ash River Site Characteristics 50
8.3. ES&H Issues 52
8.4. Building 52
Chapter 8 References 54

9. The NOνA Near Detector 55

9.1. Introduction 55
9.2. Near Detector Location 55
9.3. Near Detector Design 56
9.3. Near Detector Event Rates 58
9.4. Test Beam Program 58
9.5. Tests of the Near Detector in the MINOS Surface Building at Fermilab 59
Chapter 9 References 61

10. Backgrounds and Systematics 62

10.1. Introduction 62
10.2. Energy Calibration of the NOνA Detectors 63
10.3. Particle Production at 120 GeV and the Neutrino Beam Spectra 64
10.4. Near Detector Location and the Neutrino Beam Spectra 64
10.5. The Effect of a Possible MiniBooNE Confirmation of LSND 67
10.6. Backgrounds from ν_μ Charged Currents 68
10.7. Neutrino Cross Section Uncertainties 69
10.8. Summary of Beam Backgrounds 70
10.9. Cosmic Ray Backgrounds 71
Chapter 10 References 73

11. Proton Beam 74

11.1. Introduction 74
11.2. The Proton Plan 74
11.3. Proton Plan in the Post-Collider Era 74
11.4. Possible Limitations to the NOνA assumption of 6.5×10^{20} pot per year 75
11.5. Possible Limitations from the NuMI Beamline 76
11.6. NOνA and the NuMI Beam Line with a Proton Driver 77
Chapter 11 References 77

12. Simulations of NOνA Performance 78

12.1. Introduction 78
12.2. Detector Optimization 78
12.3. Detector Performance 79
12.4. Typical Events 83
12.5 Prospects 85

13. Physics Potential of NOνA 86

13.1. Introduction 86
13.2 The Optimization Problem 87
13.3. Sensitivity to Observing $\nu_\mu \rightarrow \nu_e$ Oscillations 88
13.4. Sensitivity to the Mass Hierarchy 90
13.5. Sensitivity to CP Violation 94
13.6. Measurement of the Dominant Mode Oscillation Parameters 95
13.7. Short Baseline Neutrino Oscillation Measurements with the NOνA Near Detector 97
13.8. Neutrino Cross Section Measurements with the NOνA Near Detector 99
13.9. Supernova Detection 100
Chapter 13 References 102

14. Cost Estimate and Schedule 104

14.1. Introduction 104
14.2. Cost Estimate Methodology 104
14.3. The Detector Cost Estimate 105
14.4. Other Costs 106
14.5. Operating Costs 107
14.6. Offline Computing 107
14.7. Schedule 108

15. NOνA R&D Request 110

15.1. Introduction 110
15.2. Specific R&D tasks 110
15.3. R&D Cost Estimate 111
Chapter 15 References 112

1. Executive Summary

1.1. The Physics of NOνA

The past two decades have seen great advances in our understanding of neutrinos. Underground experiments detecting neutrinos produced in the sun and in the earth's atmosphere have shown that neutrinos have mass and that they oscillate from one species to another as they travel. These oscillations arise because the neutrino species produced in particle decays (electron, muon, and τ-type neutrinos) do not have specific masses but are combinations of neutrino species (simply called 1, 2, and 3-type neutrinos) that do have specific masses. The average distance a neutrino travels before it oscillates is proportional to its energy and inversely proportional to the difference of the squares of masses of the underlying species of neutrinos. The probability that an oscillation will occur is related to a parameter known as a mixing angle.

The neutrinos that come from the sun are electron-type neutrinos that oscillate to muon and τ-type neutrinos, characterized by the mixing angle θ_{12} and an oscillation length (normalized to an energy of 2 GeV) of approximately 35,000 km. Muon-type neutrinos produced by cosmic rays in the earth's atmosphere oscillate to τ–type neutrinos, characterized by the mixing angle θ_{23}, and an oscillation length (again normalized to an energy of 2 GeV) of approximately 1,000 km. A third type of neutrino oscillation is possible: the oscillation of muon-type neutrinos to electron-type neutrinos at the atmospheric oscillation length. These neutrino oscillations, which so far have not been observed, would be characterized by the mixing angle θ_{13}. The study of this last category of neutrino oscillations is the main goal of NOνA (**N**uMI **O**ff-Axis ν_e **A**ppearance Experiment)[1].

The significance of the search for these oscillations is that if they exist, i.e., if θ_{13} is not zero, then we will ultimately be able to determine the ordering of the neutrino masses and measure CP violation in neutrino oscillations. There is widespread belief that the very small neutrino masses are related to physics at an extremely high-energy scale, one that cannot be studied directly with accelerator beams. There is also theoretical speculation that CP violation by neutrinos could be one aspect of understanding why the universe is composed solely of matter, rather than equal amounts of matter and antimatter.

MINOS is one of the first generation of long baseline accelerator-based neutrino oscillation experiments.[2] This Fermilab experiment, which has a 735 km baseline, will start taking data next month, April 2005. The MINOS Far Detector is located in the lowest level of the Soudan mine in northern Minnesota and it sits directly on the center of the Fermilab NuMI neutrino beam line. The physics goals of the MINOS experiment are to verify the atmospheric neutrino oscillations, to improve the measurement of their parameters, and to perform a low-sensitivity measurement of θ_{13}.

We are proposing NOνA to utilize Fermilab's investment in the NuMI beamline by building a second-generation detector, which will have the primary physics goal of measuring $\nu_\mu \rightarrow \nu_e$ with approximately a factor of 10 more sensitivity than MINOS. To accomplish this we make three major improvements on the MINOS detector design to optimize it for the detection of electron neutrinos:

[1] It is also possible that in addition to the three types of neutrinos produced in particle decays and interactions, there could exist additional types of neutrinos that are not produced in these decays and interactions. There is unconfirmed evidence for the existence of this type of neutrino, called a sterile neutrino, from an experiment at Los Alamos National Laboratory. This result is currently being checked by a Fermilab experiment, MiniBooNE. If the existence of sterile neutrinos is confirmed, it will greatly enrich the already rich physics of neutrino oscillations. Searching for evidence of sterile neutrinos will be part of the NOνA physics program.

[2] The other two first-generation experiments are K2K, an experiment in Japan over a 250 km baseline, now completed, and CNGS, an experiment in Europe over a 730 km baseline, that will start in 2006.

(1) We increase the mass of the far detector by a factor of 5.5, from 5.4 kT for MINOS to 30 kT for NOνA. At the same time, we decrease the cost per kT by about a factor of two.

(2) We design a detector that is optimized for the identification of electron-type neutrino events. Specifically, we increase the longitudinal sampling by an order of magnitude from once every 1.5 radiation lengths[3] in MINOS to once every 0.15 radiation lengths in NOνA. Further, 80% of the NOνA detector mass will be active detector, compared to about 5% for MINOS.

(3) We position the detector not directly on the NuMI beam, as MINOS is located, but 12 km off the axis of the beam. This provides more neutrino events in the energy range in which the oscillation takes place, and fewer background events.

Once a signal for electron-type neutrino appearance is seen, NOνA can run an antineutrino NuMI beam to attempt to measure the ordering of the neutrino masses. Whether this will be successful will depend on the parameters that nature has chosen. However, the sensitivity of NOνA can be markedly increased by a four-fold increase in the NuMI beam intensity created by the construction of the Fermilab Proton Driver. In the absence of a Proton Driver, smaller, but still quite significant, increases in NOνA sensitivity can be provided by less expensive investments in the Fermilab accelerator complex, for example, by reducing the Main Injector cycle time to give more protons per year on the NuMI beamline target.

Since there are three unknown parameters to be measured — θ_{13}, the ordering of the mass states, and the parameter that measures CP violation — a third measurement may eventually be required in addition to neutrino and antineutrino measurements in NOνA to determine all three parameters. The third measurement could be done by building an additional detector on the NuMI beamline but further off-axis to measure the second oscillation maximum, or by combining NOνA measurements with those taken elsewhere on different length baselines. Such experiments are being contemplated in Europe and Japan.[4]

We view NOνA as a second step in a step-by-step Fermilab program to measure all of the unknown parameters of neutrino oscillations. Each step will provide guidance on the optimum direction for the succeeding step.

1.2. The NOνA Detectors

Like MINOS, NOνA will be a two-detector experiment. A small Near Detector, as identical in structure to the far detector as possible, will be constructed on the Fermilab site. Its function is to predict the expected rate of event types and their energy spectra in the Far Detector in the absence of oscillations. Differences seen between the events in the two detectors can then be attributed to oscillations.

The MINOS detectors are sandwich detectors with alternating layers of iron absorber and active detector made from solid scintillator strips. By contrast, the NOνA detectors will be of a "totally active" design.

The NOνA Far Detector will be composed solely of liquid scintillator encased in 15.7 m long 32-cell titanium dioxide-loaded PVC extrusions. The 3.9-cm wide, 6-cm deep liquid scintillator cells are read out by U-shaped wavelength-shifting fibers into avalanche photodiodes (APDs). This configuration gives better performance at lower cost than that of MINOS. The liquid scintillator is less expensive than solid scintillator and less costly to assemble.

[3] A radiation length is the average distance in which an electron loses 63% of its energy.

[4] T2K, a second-generation experiment being built in Japan, will send an off-axis beam from JPARC to the 50 kT SuperKamiokande detector over a 295 km baseline. It plans to begin operation in 2008. A possible future third-generation experiment on this baseline involves increasing the JPARC intensity by a factor of five and building a new detector with 20 times the mass of SuperKamiokande. There is discussion in Europe on building a third-generation experiment using a proposed CERN proton driver called the SPL. It would provide both a conventional neutrino beam and a beam based on the decay of accelerated ions (called a beta beam) over a 130 km baseline to a new, very massive detector to be built in the Frejus tunnel. It should be noted that neither of these proposed third-generation experiments would have a sufficiently long baseline to resolve the ordering of the neutrino mass states without NOνA data.

The APDs provide much higher quantum efficiency than photomultipliers and are cheaper. The high quantum efficiency of the APDs allows longer scintillator cells than those in MINOS.

However, this design is not without challenges. The APDs have low gain requiring low noise electronics. They must also be cooled to –15 C to reduce the dark noise to an acceptable level. Recently, we have verified that we can obtain adequate signals from prototype liquid scintillator-filled extrusions read out into APDs. Our ongoing R&D program will verify the performance of the full liquid scintillator system.

We have selected a site for the NOνA Far Detector near Ash River, Minnesota, about 810 km from the NuMI target. This site is the furthest site from Fermilab along the NuMI beam line in the United States.

Unlike MINOS, the NOνA Far Detector will sit on the earth's surface. Our calculations indicate that backgrounds from cosmic radiation will be acceptably low, largely due to the very short beam pulses from Fermilab, one 10 μs pulse every 1.5 seconds. Part of our R&D program is to verify these calculations with an experimental measurement in a prototype detector.

We have constructed a detailed cost estimate for the full experiment, including a generous contingency for items that have not yet been fully designed. The fully burdened cost in FY2004 dollars is 165 M$, of which 55 M$ is assigned to contingency.

Assuming a project start in October 2006, our technically driven schedule calls for 5 kT of the Far Detector to be constructed by February 2010 and the full detector by July 2011. Since the NuMI beam will be available throughout this entire period and the Far Detector is modular, we will be able to begin taking useful data in February 2010.

To meet this schedule NOνA needs a prompt approval and approximately $ 2–3M in R&D funds before the project start in October 2006. Our R&D request is detailed in the final chapter of this proposal.

2. Introduction

In recent years, underground experiments have provided convincing evidence of oscillations of both solar and atmospheric neutrinos. With these measurements, we have an emerging framework with a rich structure in the lepton sector, which we can compare with a structure in the quark sector that has been studied for more than 25 years. An intriguing possibility is that CP violation exists in the lepton sector and that this asymmetry is somehow related to the fundamental matter-antimatter asymmetry of our universe.

The flavor-changing transitions observed in atmospheric and solar neutrinos are most naturally described by a simple extension to the Standard Model, in which three types of neutrinos have masses and mix with each other. The three well-known flavor eigenstates, the electron, muon and tau neutrinos, are related to these mass eigenstates by the (3×3) unitary MNS matrix. The model explains the observed flavor-changing transitions as neutrino oscillations, described by mass differences Δm^2_{ij} and mixing angles θ_{ij} (which are parameters of the MNS matrix). The model also provides for CP violation in a natural way through a phase (δ) in the MNS matrix.

While measurements of atmospheric and solar neutrino oscillations have provided some information about the mass differences and two of the three mixing angles, we have (*e.g.,* from the CHOOZ reactor experiment) only an upper limit on the third mixing angle, θ_{13}. Measuring this parameter is key to obtaining a complete picture of the structure of the lepton sector. In particular, a non-zero value for θ_{13} is a prerequisite to both the ability to probe CP violation in the leptonic sector and to resolve the ordering of neutrino mass states. The latter can only be determined by matter effects, which occur when electron-type neutrinos propagate long distances through the earth. These measurements are the goal of the NuMI Off-Axis ν_e Appearance experiment (NOνA) described in this proposal.

Chapter 1 of the proposal provides an Executive Summary. Chapter 2 is this introduction. The body of the proposal begins with Chapter 3, which is a concise discussion of the physics motivation. This chapter provides a framework for understanding how the results of this proposed experiment relate to the results of other lepton sector experiments.

An overview of the proposed experiment is provided in Chapter 4. Essentially, we intend to measure electron neutrino appearance in a 30,000 metric ton Far Detector that will be located about 810 km from Fermilab and 12 km off the central axis of the NuMI beam. This off-axis location provides a lower energy, more monoenergetic neutrino beam, which is better suited for this measurement than the on-axis beam.

A Near Detector will measure the electron neutrino content of the beam at Fermilab, characterize the detector response to neutrino events and perform crucial background studies. The NOνA detectors will be optimized to separate charged current electron-neutrino events from neutrino events producing neutral pions. The proposed detectors are "totally active" planar tracking calorimeters with 0.15 radiation length longitudinal segmentation.

Chapter 5 describes the Far Detector structure and its fabrication and assembly. A five-story structure constructed from plastic is not conventional. The detailed engineering studies we have done to assure ourselves of its stability are described in this chapter.

The process of collecting light from the scintillator is discussed in Chapter 6. Chapter 7 follows with a description of the photodetector, the electronics for its readout, and the data acquisition system.

The preferred site for the Far Detector is Ash River, Minnesota, close to the northernmost road in the United States near the NuMI beamline. Chapter 8 describes this site and the design of the building required to house the detector, as well as ES&H considerations.

The Near Detector design and the test beam program are covered in Chapter 9. The purpose of the Near Detector is to measure the process that will be the backgrounds to the signal in the Far Detector. These backgrounds and systematic uncertainties will be the subject of Chapter 10.

The termination of Tevatron Collider operations prior to the start of NOνA running allows higher NuMI beam intensity and repetition rate than had been earlier anticipated. Chapter 11 details how this improvement can be obtained and also discusses the improvement that would be possible with the construction of a Proton Driver to replace the Booster. Although the Proton Driver is not required for the first phase of the experiment, it provides a natural upgrade path for a Fermilab world-leading program in understanding the physics of the lepton sector.

Chapter 12 describes simulations of the NOνA detector performance and their results. Chapter 13 uses these results to assess the physics potential of the NOνA experiment. It outlines a step-by-step program through which NOνA can contribute to the determination of the mass ordering and the measurement of CP violation, if θ_{13} is in the range accessible to conventional neutrino beams. Chapter 13 also discusses the use of NOνA's high-resolution to make highly precise measurements of Δm^2_{32} and $\sin^2(2\theta_{23})$. Finally, it discusses measurements that can be made with the near detector and the detection of galactic supernovae in the far detector.

Chapter 14 presents the cost and schedule of NOνA, and Chapter 15 presents our R&D request. Prompt approval and a FY 2007 construction start will allow NOνA to start data taking in February 2010, with the completion of the full Far Detector by July 2011. Substantial R&D funds will be needed prior to the start of construction and into the first year of construction. A prototype Near Detector will focus our efforts to address many detailed design issues.

In essence, we lay out in this proposal a major step in a program of experiments to study co uplings in the lepton sector, with an eventual goal of measuring leptonic CP violation. NOνA is a natural next step after MINOS. Once NOνA determines the θ_{13}-coupling, it will be possible at Fermilab, likely with the Proton Driver, to go on to the next phase of mass hierarchy and leptonic CP measurements.

The recent commissioning of the NuMI beamline represents a very significant step forward for particle physics. At a length of more than 800 km, the NOνA baseline will be nearly three times as long as the baseline in T2K and somewhat longer than the baseline from CERN to Gran Sasso. Thus, with the NuMI beam, Fermilab has a unique capability to answer some of the most important questions that can be asked in elementary particle physics, both today and in the foreseeable future.

3. Physics Motivation

3.1. Introduction

Recently the SuperKamiokande [1], K2K [2], and Soudan 2 [3] experiments have provided very strong evidence that the muon neutrino undergoes flavor changing transitions. These transitions are seen for neutrinos whose path length divided by energy (*L/E*) is of order ~500 km/GeV. SuperKamiokande also has some supporting evidence that muon neutrinos are transformed primarily into tau neutrinos. Although the SuperKamiokande detector has some sensitivity to flavor transitions of electron neutrinos, their data provides no evidence that electron neutrinos are involved in these transitions. In fact, the CHOOZ [4] reactor experiment provides a tighter constraint on the upper limit on the probability of electron neutrino flavor transitions of order 5-10% at the values of *L/E* for which SuperKamiokande sees muon neutrino flavor transitions. This leaves open the interesting and important question: What is the role of the electron neutrino in flavor transitions at these values of *L/E*? A measurement or stringent limit on the probability of $\nu_\mu \rightarrow \nu_e$ for values of *L/E* of order 500 km/GeV is an important step in understand these neutrino flavor transitions in atmospheric neutrinos. As the NuMI beam is primarily a ν_μ beam, the observation of ν_e appearance would address this question directly. This measurement is the primary goal of the experiment described by this proposal.

The SNO [5] experiment has recently reported large transitions of solar electron neutrinos to muon and/or tau neutrinos both with and without salt added to the heavy water. SuperKamiokande [6], studying solar neutrinos, and KamLAND [7], studying reactor neutrinos, also see large electron neutrino flavor transitions. From a combined analysis, the *L/E* for these flavor transitions is a factor of ~30 times larger than the *L/E* for flavor transitions in atmospheric muon neutrinos. These transitions occur for an *L/E* such that the transition probability $\nu_\mu \rightarrow \nu_e$ measured by an experiment in the NuMI beam will also have some sensitivity to the flavor transitions associated with solar neutrinos through interference effects.

The LSND [8] experiment has reported small muon antineutrino to electron antineutrino transitions for values of *L/E* that are more than two orders of magnitude smaller than the transitions seen in atmospheric neutrinos. However this transition probability is very small, on the order of 0.3% of the one observed for atmospheric and solar neutrinos. If this result is confirmed by the MiniBooNE [9] experiment, this transition could be an important background for a measurement of $\nu_\mu \rightarrow \nu_e$ transitions at the larger values of *L/E* associated with atmospheric neutrinos.

3.2. Neutrino Mixing

Extensions to the Standard Model are required to explain the phenomena described here. The simplest and most widely accepted extension is to allow the neutrinos to have masses and mixings such that these phenomena are explained by neutrino oscillations. The masses and mixing of the neutrinos in these extensions would be the low energy remnant of some yet to be determined high energy physics. Thus, neutrino masses and mixing provide a unique window on physics that is inaccessible to current or near future collider experiments. One popular theory is the so called "seesaw" scenario, where the active left handed neutrinos seesaw off their heavier right handed (sterile) partners, leaving three very light Majorana neutrinos. It is already clear that the masses and mixings in the neutrino sector are very different from the masses and mixings in the quark sector and that a detailed understanding of the neutrino masses and mixings will be important in differentiating fermion mass theories. Also, they may provide a key to advancing our theoretical understanding of this fundamental question.

If the neutrinos have masses and mixings then the neutrino mass eigenstates, $\nu_i = (\nu_1, \nu_2, \nu_3, \ldots)$ with masses $m_i = (m_1, m_2, m_3, \ldots)$ are related to the flavor eigenstates $\nu_\alpha = (\nu_e, \nu_\mu, \nu_\tau, \ldots)$ by the equation

$$|\nu_\alpha\rangle = \sum_i U_{\alpha i} |\nu_i\rangle \qquad (1)$$

The charged weak current for the neutrino flavor states is given by $J_\lambda = \bar{\nu}_L \gamma_\lambda \ell_L$, where $\ell = (e, \mu, \tau)$ is the vector of charged lepton eigenstates. In the absence of light sterile neutrinos, the 3×3 lepton mixing matrix *U* is unitary. Lepton flavor mixing was first discussed (for the 2×2 case) by Maki, Nakagawa, and Sakata.

If we restrict the light neutrino sector to the three known active flavors and set aside the LSND results[1], then the unitary MNS lepton mixing matrix, U, can be written as

$$U = \begin{pmatrix} c_{13}c_{12} & c_{13}s_{12} & s_{13}e^{-i\delta} \\ -c_{23}s_{12} - s_{13}s_{23}c_{12}e^{i\delta} & c_{23}c_{12} - s_{13}s_{23}s_{12}e^{i\delta} & c_{13}s_{23} \\ s_{23}s_{12} - s_{13}c_{23}c_{12}e^{i\delta} & -s_{23}c_{12} - s_{13}c_{23}s_{12}e^{i\delta} & c_{13}c_{23} \end{pmatrix} \quad (2),$$

where $c_{jk} \equiv \cos\theta_{jk}$ and $s_{jk} \equiv \sin\theta_{jk}$.

With this labeling, the atmospheric neutrino oscillations are primarily determined by the θ_{23} and Δm^2_{32} parameters, whereas the solar neutrino oscillations depend on θ_{12} and Δm^2_{12}, where $\Delta m^2_{ij} = m^2_i - m^2_j$. From SuperKamiokande[1] we already have some knowledge of $|\Delta m^2_{32}| = (1.5 - 3.4) \times 10^{-3}$ eV^2 and $\sin^2 2\theta_{23} > 0.92$ at the 90% confidence level. A SuperKamiokande analysis which concentrates on events with high resolution in L/E yields $|\Delta m^2_{32}| = (1.9 - 3.0) \times 10^{-3}$ eV^2 and $\sin^2 2\theta_{23} > 0.90$ at the 90% confidence limit. The K2K experiment[2] results give $|\Delta m^2_{32}| = (1.9 - 3.6) \times 10^{-3}$ eV^2 for $\sin^2(2\theta_{23}) = 1$, at the 90% confidence level. The K2K lower limit on $\sin^2(2\theta_{23})$ is considerably less constraining than those from SuperKamiokande.

Note the substantial uncertainty in these atmospheric measurements. In contrast, the combined analysis of the SNO, SuperKamiokande and KamLAND experiments gives $\Delta m^2_{21} = +7.9 \pm 0.6 \times 10^{-5}$ eV^2 and $\sin^2 2\theta_{12} = 0.82 \pm 0.07$. For the purposes of this experiment our knowledge of the solar parameters is already in good shape and is expected to improve with time.

CHOOZ (and SuperKamiokande) provide us with a limit on $\sin^2 2\theta_{13} < 0.18$. The CHOOZ limit is dependent on the input value used for $|\Delta m_{32}{}^2|$; for the current central value 2.5×10^{-3} eV^2, this limit is $\sin^2 2\theta_{13} < 0.14$, while for $|\Delta m_{32}{}^2| = 2.0\times10^{-3}$ eV^2, it is $\sin^2 2\theta_{13} < 0.18$ [4]. Thus, the proposed long-baseline neutrino oscillation experiment to search for $\nu_\mu \to \nu_e$ should be sensitive to a substantial range below this upper bound.

The MINOS experiment [10] will provide a 10% measurement of the atmospheric $|\Delta m^2_{32}|$ but probably will not improve our knowledge of θ_{23}. This experiment has sensitivity to $\sin^2 2\theta_{13}$ only about a factor of two below the CHOOZ bound. Any future reactor experiment to measure $\sin^2 2\theta_{13}$ could improve our knowledge of this important parameter but such an experiment has no sensitivity to θ_{23}, the sign of Δm^2_{32} or the CP violating phase δ. Therefore, such a reactor experiment is complementary to long-baseline experiments to observe $\nu_\mu \to \nu_e$.

The appearance probability of ν_e in a ν_μ beam in vacuum is given, to leading order, by

$$P_{vac}(\nu_\mu \to \nu_e) = \sin^2\theta_{23} \sin^2 2\theta_{13} \sin^2 \Delta_{atm} \quad (3),$$

where $\Delta_{atm} \approx 1.27\left(\frac{\Delta m^2_{32} L}{E}\right)$, where Δm^2_{32} is measured in eV^2, L is measured in km, and E is measured in GeV. If the experiment is performed at one of the peaks of this probability, that is, when $\Delta_{atm} = \frac{\pi}{2} + n\pi$, and $\sin^2(\theta_{23}) = \frac{1}{2}$ then

$$P_{vac}(\nu_\mu \to \nu_e) = \frac{1}{2}\sin^2 2\theta_{13} = 2.5\%\left(\frac{\sin^2 2\theta_{13}}{0.05}\right) \quad (4)$$

The first peak occurs at neutrino energy,

$$E = 1.64 \text{ GeV}\left(\frac{\Delta m^2_{32}}{2.5\times10^{-3}\text{eV}^2}\right)\left(\frac{L}{810 \text{ km}}\right) \quad (5)$$

The constraint on $\sin^2(2\theta_{13})$ from the CHOOZ experiment varies from 0.14 to 0.18 depending on the atmospheric Δm^2_{32}, therefore the maximum appearance probability ranges from ~7 to 9%. To be effective any ν_e appearance experiment has to aim to exclude or convincingly see a signal at least an order of magnitude below this 7% limit.

3.3. Matter Effects

The neutrinos in the NuMI beam propagate through the Earth and matter induced contributions

[1] In the 3+1 neutrino mass hierarchy the LSND result can be accommodated as a perturbation on the pure active 3 neutrino hierarchy. The 2+2 mass hierarchy would require major modifications.

to the propagation amplitude are non-negligible. These matter effects have opposite sign for neutrinos and antineutrinos and for the normal versus inverted neutrino mass hierarchies. The matter effects can be thus used to distinguish the two possible three-neutrino mass hierarchies, see Fig. 3.1. If the experiment is performed at the first peak in the oscillation, as above, the matter effects are primarily a function of the energy of the neutrino beam and the transition probability in matter can be approximated by

$$P_{mat}\left(\nu_\mu \to \nu_e\right) \approx \left(1 \pm 2\frac{E}{E_R}\right) P_{vac}\left(\nu_\mu \to \nu_e\right) \quad (6),$$

where E_R is the matter resonance energy associated with the atmospheric Δm^2, that is

$$E_R = \frac{\Delta m^2_{32}}{2\sqrt{2} G_F N_e} = 12\ \text{GeV}\left(\frac{\Delta m^2_{32}}{2.5\times10^{-3}\ \text{eV}^2}\right)\left(\frac{1.4\ \text{g cm}^{-3}}{Y_e \rho}\right) \quad (7),$$

where N_e is the electron number density in the earth, ρ is the matter density (2.8 g.cm^{-3}) and Y_e is the average Z/A.

For the normal hierarchy, matter effects enhance (suppress) the transition probability for neutrinos (antineutrinos) and vice versa for the inverted hierarchy. For a 2 GeV neutrino energy, matter effects give a 30% enhancement or suppression in the transition probability.

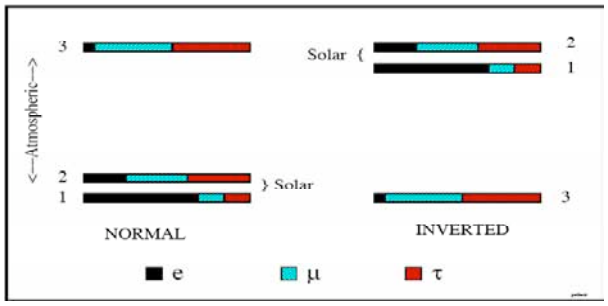

Fig. 3.1: The two allowed three-neutrino mass squared spectra that account for the oscillations of solar and atmospheric neutrinos. The normal spectrum has $\Delta m^2_{32} > 0$ and the inverted has $\Delta m^2_{32} < 0$. The ν_e fraction of each mass eigenstate is indicated by the black solid region, whereas the ν_μ (ν_τ) fraction is indicated by the blue-green right-leaning (red left-leaning) hatching. The ν_e fraction in the mass eigenstate labeled, 3, has been enhanced for clarity.

3.4. CP Violation

The "Large Mixing Angle" (LMA) solution for solar neutrino oscillations, now the only viable solution, has the property that the $\nu_\mu \to \nu_e$ transition probability is sensitive to sub-leading effects and in particular to the CP violating phase δ.

In vacuum, the shift in the transition probability associated with the CP violating phase is given by

$$\Delta P_\delta\left(\nu_\mu \to \nu_e\right) \approx J_r \sin\Delta_{sol} \sin\Delta_{atm}\left(\cos\delta\cos\Delta_{atm} \mp \sin\delta\sin\Delta_{atm}\right) \quad (8),$$

where the minus (plus) sign is for neutrinos (antineutrinos),

$$J_r = \sin 2\theta_{12}\sin 2\theta_{23}\sin 2\theta_{13}\cos\theta_{13} \approx 0.9\sin 2\theta_{13} \quad (9)$$

$$\Delta_{sol} = 1.27\frac{\Delta m^2_{21} L}{E} = \frac{\Delta m^2_{21}}{\Delta m^2_{32}}\Delta_{atm} \approx \frac{1}{36}\Delta_{atm}\,. \quad (10)$$

At the first oscillation maximum of the atmospheric Δm^2 scale, the shift in the transition probability dependent on δ is of order

$$\left|\Delta P_\delta\left(\nu_\mu \to \nu_e\right)\right| \sim 0.6\%\sqrt{\frac{\sin^2 2\theta_{13}}{0.05}} \quad (11)$$

Note that the shift is proportional to $\sqrt{\sin^2 2\theta_{13}}$, while the leading term is proportional to $\sin^2 2\theta_{13}$. Thus, the relative importance of the sub-leading terms grows as $\sin^2 2\theta_{13}$ gets smaller.

The full transition probability, in vacuum, is given by

$$P(\nu_\mu \to \nu_e) = \left|\sum_{j=1}^{3} U^*_{\mu j} U_{ej} e^{-i\left(m_j^2 L/2E\right)}\right|^2 = \left|2U^*_{\mu 3}U_{e3}e^{-i\Delta_{32}}\sin\Delta_{31} + 2U^*_{\mu 2}U_{e2}\sin\Delta_{21}\right|^2 \quad (12)$$

The second form of this probability is especially illuminating as the first term is the amplitude for $\nu_\mu \to \nu_e$ associated with the atmospheric Δm^2 and the second term the amplitude associated with the solar Δm^2. The interference between these two amplitudes differs for neutrinos and antineutrinos because for antineutrinos the U matrix is replaced with U^*. This difference in the interference term leads to the difference in the transition probability $\nu_\mu \to \nu_e$ between neutrino and antineutrinos. Such an effect is an example of CP violation.

Using the MNS mixing matrix given in Eq. 2,

$$2U^*_{\mu 3}U_{e3} = e^{-i\delta}\sin 2\theta_{13}\sin\theta_{23}$$
$$2U^*_{\mu 2}U_{e2} = \sin 2\theta_{12}\cos\theta_{23}\cos\theta_{13} + O(\sin\theta_{13}) \quad (13)$$

Since the $O(\sin\theta_{13})$ term is multiplied by $\sin(\Delta_{21})$ in the amplitude, it is quadratic in the small quantities sin θ_{13} and the solar Δm^2 and therefore can be neglected.

$$P(\nu_\mu \to \nu_e) =$$
$$|\, e^{-i(\Delta_{32}+\delta)}\sin 2\theta_{13}\sin\theta_{23}\sin\Delta_{31} \quad (14)$$
$$+\sin 2\theta_{12}\cos\theta_{23}\cos\theta_{13}\sin\Delta_{21}\,|^2$$
$$P(\nu_\mu \to \nu_e) =$$
$$\sin^2\theta_{23}\sin^2 2\theta_{13}\sin^2\Delta_{31}$$
$$+\cos^2\theta_{13}\cos^2\theta_{23}\sin^2 2\theta_{12}\sin^2\Delta_{21} \quad (15)$$
$$+J_r\sin\Delta_{21}\sin\Delta_{31}$$
$$(\cos\Delta_{32}\cos\delta - \sin\Delta_{32}\sin\delta)$$

The first and second terms are the probability of $\nu_\mu \to \nu_e$ associated with the atmospheric and solar Δm^2 's respectively, whereas the third term is the interference between these two corresponding amplitudes. The term proportional to sin δ is responsible for CP violation since it changes sign when going from neutrinos to antineutrinos[2].

To show the growing importance of the CP violating term as $\sin^2 2\theta_{13}$ gets smaller we have plotted the neutrino antineutrino asymmetry, $|P_\nu - P_{\bar\nu}|/(P_\nu + P_{\bar\nu})$ versus $\sin^2 2\theta_{13}$ in Fig. 3.2 at the first oscillation maximum assuming maximum CP violation, *i.e.* $\Delta_{31} = \pi/2$ and $\delta = \pi/2$. The asymmetry grows as $\sin^2 2\theta_{13}$ gets smaller until the amplitude for $\nu_\mu \to \nu_e$ from the atmospheric Δm^2 is equal in magnitude to the amplitude from the solar Δm^2. At this value of $\sin^2 2\theta_{13}$ there is maximum destructive (constructive) interference for neutrinos (antineutrinos) and therefore a maximum asymmetry of unity. The value of $\sin^2 2\theta_{13}$ at this peak asymmetry is given by

$$\sin^2 2\theta_{13}\,|_{peak} \approx \frac{\sin^2 2\theta_{12}}{\tan^2\theta_{23}}\left(\frac{\pi}{2}\frac{\Delta m^2_{21}}{\Delta m^2_{31}}\right)^2 \sim 0.002 \quad (16)$$

Even at the CHOOZ bound for $\sin^2 2\theta_{13}$ the asymmetry is greater than 20%. This asymmetry scales as sin δ for values of δ away from $\pi/2$.

3.5. Ambiguity Resolution

The effects of matter can easily be included in our expression for $P(\nu_\mu \to \nu_e)$ by replacing $\sin^n\Delta_{21}$ $\sin^n\Delta_{21}$ and $\sin^n\Delta_{31}$ for all n in all three terms using

$$\sin\Delta_{ij} \to \frac{\Delta_{ij}}{(\Delta_{ij} \mp aL)}\sin(\Delta_{ij} \mp aL) \quad (17)$$

where

$$a = \frac{G_F N_e}{\sqrt{2}} \approx (3700\ \text{km})^{-1}\left(\frac{\rho}{2.8\ \text{g cm}^{-3}}\right) \quad (18)$$

The minus (plus) sign is for neutrinos

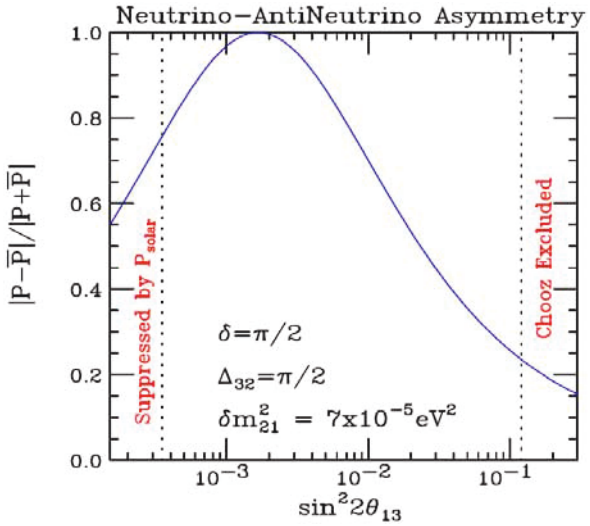

Fig. 3.2: The vacuum asymmetry $\left|P(\nu_\mu \to \nu_e) - P(\bar\nu_\mu \to \bar\nu_e)\right| / \left|P(\nu_\mu \to \nu_e) + P(\bar\nu_\mu \to \bar\nu_e)\right|$ versus $\sin^2 2\theta_{13}$ at oscillation maximum, Δ_{32} assuming that the CP violation is maximal, $\delta = \pi/2$. At the peak of this asymmetry the amplitudes for $\nu_\mu \to \nu_e$ from the atmospheric and solar Δm^2's are equal in magnitude. Above (below) the peak the atmospheric (solar) amplitude dominates.

[2] The inclusion of the $O(\sin\theta_{13})$ terms in $U^*_{\mu 2}U_{e2}$ gives the full expression for $P(\nu_\mu \to \nu_e)$ by multiplying the first term by $(1 - 2\sin^2\theta_{12}\sin\Delta_{12}\cos\Delta_{32}/\sin\Delta_{31})$ and the second term by $\left|1 - e^{-i\delta}\sin\theta_{13}\tan\theta_{12}\tan\theta_{23}\right|^*$, while the third term is unchanged. Both of these factors are very close to unity for any reasonable NuMI experimental setup. Equivalent expressions for $P(\nu_\mu \to \nu_e)$ can be found in [11].

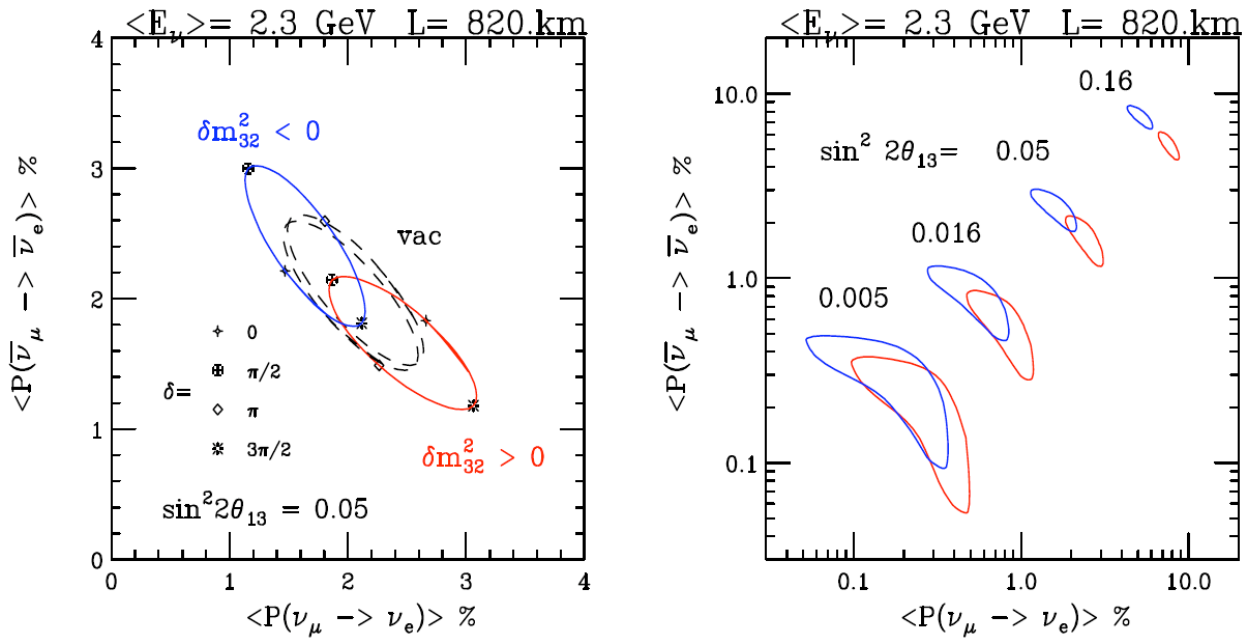

Fig. 3.3: The bi-probability plots $P(\nu_\mu \to \nu_e)$ versus $P(\bar{\nu}_\mu \to \bar{\nu}_e)$, assuming a constant matter density of $\rho = 2.8$ g. cm^{-3} at a distance of 820 km and an average energy of 2.3 GeV with a 20% Gaussian spread. The mixing parameters are fixed to be $|\Delta m^2_{31}| = 2.5\times10^{-3}$ eV^2, $\sin^2 2\theta_{23} = 1.0$, $\Delta m^2_{21} = +7\times10^{-5}$ eV^2, $\sin^2 2\theta_{12} = 0.8$ with the labeled values of $\sin^2 2\theta_{13}$ and δ.

(antineutrinos). The factors $\sin\Delta_{32}$ and $\cos\Delta_{32}$ remain unchanged by matter effects. This algorithm comes from the invariance of the product $\Delta m^2_{ij}\sin 2\theta_{ij}$ evaluated in matter and in vacuum.

A useful and instructive way to present the combined effects of matter and sub-leading terms is in the bi-probability plots of $P(\nu_\mu \to \nu_e)$ versus $P(\nu_\mu \to \nu_e)$, invented by Minakata and Nunokawa [13]. Fig. 3.3 shows an example of such a plot for a NuMI case.

At the larger values of $\sin^2 2\theta_{13}$, the ellipses associated with the two possible mass hierarchies separate in matter, whereas they are approximately degenerate in vacuum. There is also a significant sensitivity to the CP violating phase, δ. It is the sensitivity to the sign of Δm^2_{32} and the CP violating phase in these plots which allows for the determination of these parameters in a sufficiently accurate experiment. For a single experiment there can be a degeneracy in the determined parameters but this degeneracy can be broken by further experimentation.

In particular the normal and inverted hierarchies may also be able to be distinguished by a comparison of the probability of $\nu_\mu \to \nu_e$ between two different experiments at different baselines, e.g. NuMI and JPARC [12]. If both experiments operated at the first oscillation maximum and both run neutrinos then

$$P^N_{mat}(\nu_\mu \to \nu_e) \cong \left(1 \pm 2\frac{E^N - E^J}{E_R}\right) P^J_{mat}(\nu_\mu \to \nu_e) \qquad (19)$$

where (P^N, E^N) and (P^J, E^J) are the neutrino transition probabilities and energies for NuMI and JPARC respectively. E_R is the matter resonance energy associated with the atmospheric Δm^2, about 12 GeV, given by Eq. 7. The plus sign is for the normal hierarchy and the minus sign for the inverted hierarchy. For antineutrinos these signs are reversed. If either experiment is significantly away from oscillation maximum, the relationship between the two probabilities is more complicated, see [14].

3.6. Other NOvA Measurements

A high precision measurement of $\nu_\mu \to \nu_\mu$ can be used to determine the atmospheric Δm^2 to the 10^{-4} eV^2 level. Also $\sin^2 2\theta_{23}$ will be determined

from 1 to 2%. Such a measurement can determine how much θ_{23} differs from maximal mixing, *i.e.,* $\pi/4$. This difference is a measure of the breaking of a $\nu_\mu \rightarrow \nu_\tau$ symmetry at some high-energy scale. Since matter effects are suppressed in the channel $\nu_\mu \rightarrow \nu_\mu$ compared to $\nu_\mu \rightarrow \nu_e$, a comparison of $\nu_\mu \rightarrow \nu_\mu$ to $\bar{\nu}_\mu \rightarrow \bar{\nu}_\mu$ is a sensitive test of CPT in the neutrino sector.

3.7. Neutrino Oscillations in 2010

While we have discussed the current status of neutrino oscillations, NOνA will not likely acquire data for a number of years. Thus, although speculative, it is likely worthwhile to attempt to predict the state of knowledge in 5 to 7 years time. There is considerable ongoing activity with respect to solar neutrino oscillations. Thus, by 2010, it is reasonable to expect that the solar Δm^2 and $\sin^2 2\theta_{12}$ will be known well enough that they will not be a major source of uncertainty in the interpretation of NOνA results. We also presume that MINOS will have made a 10% measurement of Δm^2_{32}. The T2K experiment has been delayed to 2008, so it may have only preliminary results by 2010. There has been considerable recent discussion of new reactor-based neutrino oscillation experiments, but in the absence of an approved experiment, it is difficult to predict a time scale for the results of such an experiment.

3.8. Summary

The important measurements that could be made by NOνA are

• Observation of $\nu_\mu \rightarrow \nu_e$ at an *L/E* in the range of 10^2 to 10^3 km/GeV, which would determine the ν_e role in atmospheric neutrino flavor transitions. In the neutrino oscillation scenario this is a measure of $\sin^2 2\theta_{13}$.

• Matter effects can be used to distinguish the two mass hierarchies and therefore determine the sign of Δm^2_{32}.

• For the Large Mixing Angle solution to the solar neutrino puzzle there is sensitivity to the CP violating phase in the channel $\nu_\mu \rightarrow \nu_e$.

• Precision measurements in the $\nu_\mu \rightarrow \nu_\mu$ channel can measure how close θ_{23} is to $\pi/4$, that is maximal mixing. A comparison of $\nu_\mu \rightarrow \nu_\mu$ to $\bar{\nu}_\mu \rightarrow \bar{\nu}_\mu$ is a sensitive test of CPT violation since matter effects are suppressed in this channel.

Thus, there is a very rich neutrino physics program to be explored in a ν_e appearance experiment using the NuMI beam. Details of experimental and beam possibilities will be explored in subsequent chapters.

Chapter 3 References

[1] Kamiokande Collaboration, Y. Fukuda *et al.*, Phys. Lett. B **335** (1994) 237.
Super-Kamiokande Collaboration, Y. Fukuda *et al.*, Phys. Rev. Lett. **81** (1998) 1562; S. Fukuda *et al.*, *ibid.* **85** (2000) 3999; Y. Ashie *et al., ibid*, **93** (2004) 101801; hep-ex/0501064 (2005).
[2] K2K Collaboration, M. H. Ahn *et al.*, Phys. Lett. B **511** (2001) 178; Phys. Rev. Lett. **90**, 041801 (2003); E. Aliu *et al*., hep-ex/0411038 (2004).
[3] Soudan 2 Collaboration, M. Sanchez *et al.*, Phys. Rev. D **68**, 113004 (2003).
[4] CHOOZ collaboration, M. Apollonio *et al.*, Phys. Lett. B **466** 415.
[5] SNO Collaboration, Q. R. Ahmad *et al.*, Phys. Rev. Lett. **87** (2001) 071301;
S. N. Ahmed *et al.*
[6] S. Fukuda *et al.* [Super-Kamiokande Collaboration], Phys. Lett. B **539**, 179 (2002).
[7] K. Eguchi *et al.* [KamLAND Collaboration], Phys. Rev. Lett. **90**, 021802 (2003); T. Araki *et al*., hep-ex/0406035 (2004).
[8] A. Aguilar *et al.* [LSND Collaboration], Phys. Rev. D **64**, 112007 (2001).
[9] E. Church *et al.* [BooNe Collaboration], FNAL-PROPOSAL-0898.
[10] E. Ables *et al.* [MINOS Collaboration], FERMILAB-PROPOSAL-0875.
[11] V. D. Barger, S. Geer, R. Raja and K. Whisnant, Phys. Rev. D **63**, 113011 (2001), I. Mocioiu and R. Shrock, JHEP **0111**, 050 (2001).
[12] H. Minakata and H. Nunokawa, JHEP **0110** (2001) 001 [hep-ph/0108085].
[13] Y. Itow *et al.*, [The JHF-Kamioka neutrino project], arXiv:hep-ex/0106019.
[14] H. Minakata, H. Nunokawa and S. Parke, Phys. Rev. D **68**, 013010 (2003).

4. Experiment Overview

4.1. NuMI Beam

As of this writing, the NuMI neutrino beam [1] is currently being commissioned. The beamline begins with 120 GeV protons extracted from the Main Injector accelerator, which are transported downward at a 158 mrad angle to the NuMI Target Hall. Before striking the production target the beam is bent upward to a 58 mrad downward angle, so that it is aimed at the MINOS far detector in Minnesota. Two parabolic magnetic horns, each about 3 m long and pulsed at 200 kA, focus secondary pions and kaons emitted from the target. The secondary beam subsequently travels with the same downward 58 mrad angle through an evacuated decay pipe, which is 675 m in length and 2 m in diameter. The decay pipe ends in the Hadron Absorber Hall where residual protons and non-decayed secondary mesons are absorbed in the Al-Fe water-cooled beam stop. The muons resulting from pion and kaon decays are absorbed in 240 m of earth shielding, which separates the Absorber Hall from the Near Detector Hall. Three muon alcoves, located within this shielding downstream of the Absorber Hall, contain muon detectors to monitor the beam intensity and shape on a pulse-to-pulse basis. Fig 4.1 shows the plan and elevation views of the NuMI beamline.

A unique feature of the NuMI neutrino beam is the ability to change the focusing optics configuration and hence the neutrino energy band accepted. Specifically, one can change the relative positions of the target and the first horn and the separation between two horns. These configurations are illustrated in Fig. 4.2, together with the spectra for three possible beam element arrangements, referred to as low, medium, or high energy beam tunes. While the movement of the second horn is logistically complex and requires several weeks downtime, the target position can be varied remotely. Accordingly, one also has a method of readily changing the energy spectrum in a continuous fashion by moving just the target at a small sacrifice of the neutrino flux as compared to a fully optimized configuration [2].

Full optimization for a given energy also involves adjusting the target length. The initial beam for the MINOS experiment is the low energy tune, with the front end of the target located 0.34 m upstream of the first horn and a horn separation of 7 m. The target is 0.95 m long and is composed of 47 graphite sections, each 20 mm in length, with 0.3 mm air gaps between sections.

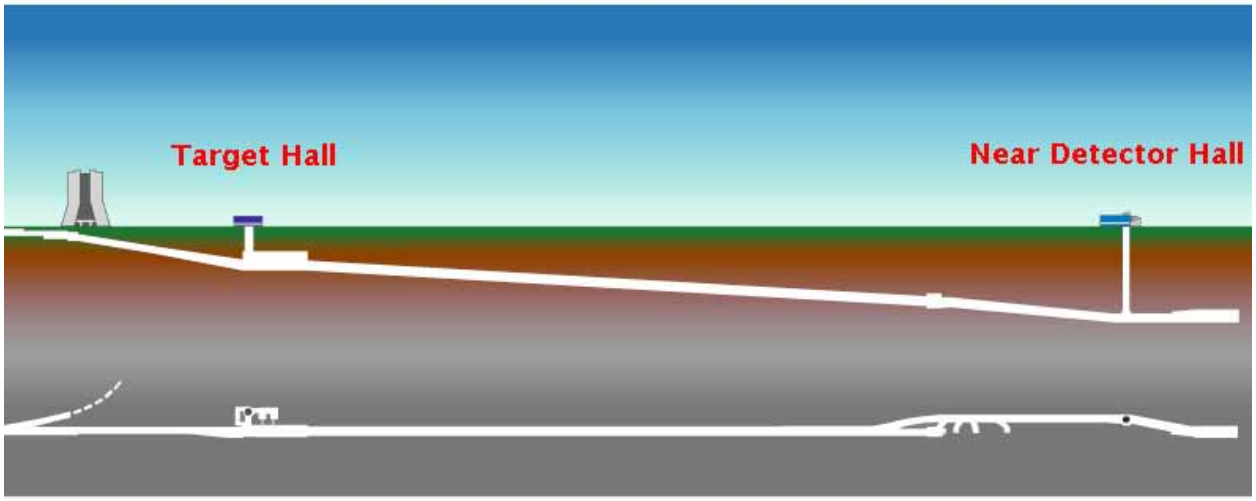

Fig. 4.1: Plan (bottom) and elevation (top) views of the NuMI beam line.

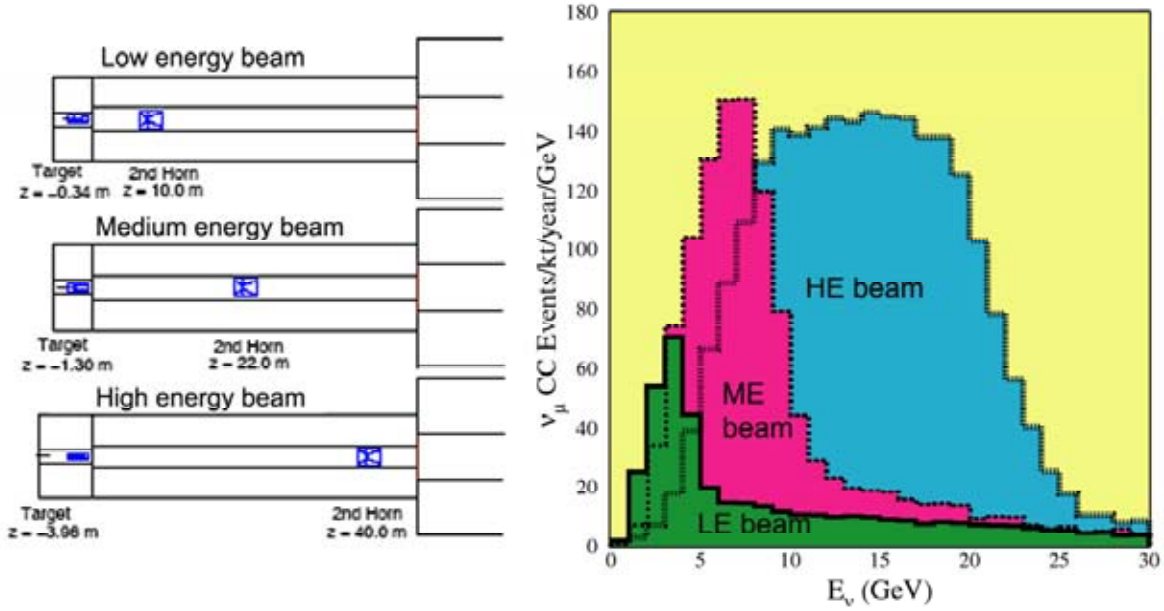

Fig. 4.2: Left: The locations of the target and second horn for the three NuMI beam configurations. Right: The expected neutrino interaction rates at the MINOS far detector site for each of the three beam tunes assuming 2.5×10^{13} protons on target per year.

Under the assumption that it would run compatibly with Tevatron Collider, the NuMI beam was designed for a proton intensity of 4 x 10^{13} protons per pulse every 1.9 sec, roughly 0.4 MW of beam power. Since Tevatron Collider operations will cease prior to the start of NOνA, more protons will be available and the Recycler can be used to hide the filling time from the Booster. As is explained in Chapter 11, this should allow 6×10^{13} protons per pulse every 1.467 sec, or 0.8 MW.

This intensity will stress the present target and beam components. However, Section 11.5 discusses these issues in detail and concludes that with some additional cooling, NuMI will be able to handle this power level.

4.2. Off-Axis Concept

Pions and kaons decay isotropically in their centers of mass resulting in a relatively broad neutrino beam energy spectrum. For small angles, the flux and energy of neutrinos produced from the decay $\pi \rightarrow \mu + \nu$ in flight and intercepted by a detector of area A and located at distance z are given in the lab frame by:

$$F = \left(\frac{2\gamma}{1+\gamma^2\theta^2} \right)^2 \frac{A}{4\pi z^2} \qquad (1)$$

$$E_\nu = \frac{0.43 E_\pi}{1+\gamma^2\theta^2}, \qquad (2)$$

where θ is the angle between the pion direction and the neutrino direction, E_π the energy of the parent pion, m_π the mass of the pion and $\gamma = E_\pi / m_\pi$. The expressions for the neutrinos from the corresponding charged K decays are identical except that 0.43 is replaced by 0.96 resulting in a more energetic and broader distribution for identical meson energies. The neutrino flux peaks in the forward direction for all meson energies, which is the reason that, in general, neutrino detectors are placed on axis. Furthermore, in the forward direction there is a linear relationship between neutrino and meson energies. As the neutrino direction deviates from the meson direction, however, the relationship between the pion energy and neutrino energy flattens. At some angles, a wide energy band of pions contributes to roughly the same energy neutrinos. Fig. 4.3 illustrates both features.

The angle-energy relationship illustrated in Fig. 4.3 can be utilized to construct a nearly monoenergetic neutrino beam by viewing the NuMI

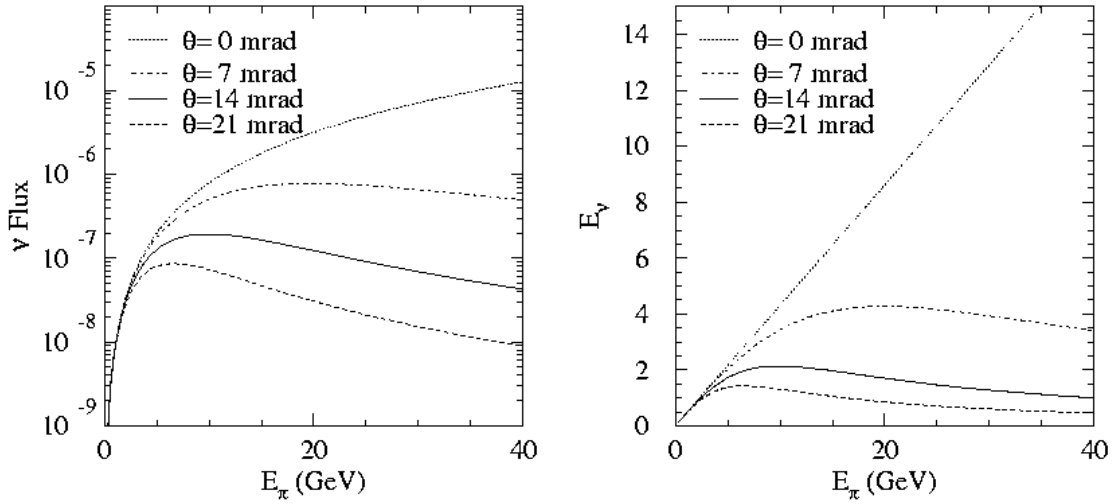

Fig. 4.3: Left: The neutrino flux from a pion of energy E_π as viewed from a site located at an angle θ from the beam axis. The flux has been normalized to a distance of 800 km. Right: The energy of the neutrinos produced at an angle θ relative to the pion direction as a function of the pion energy.

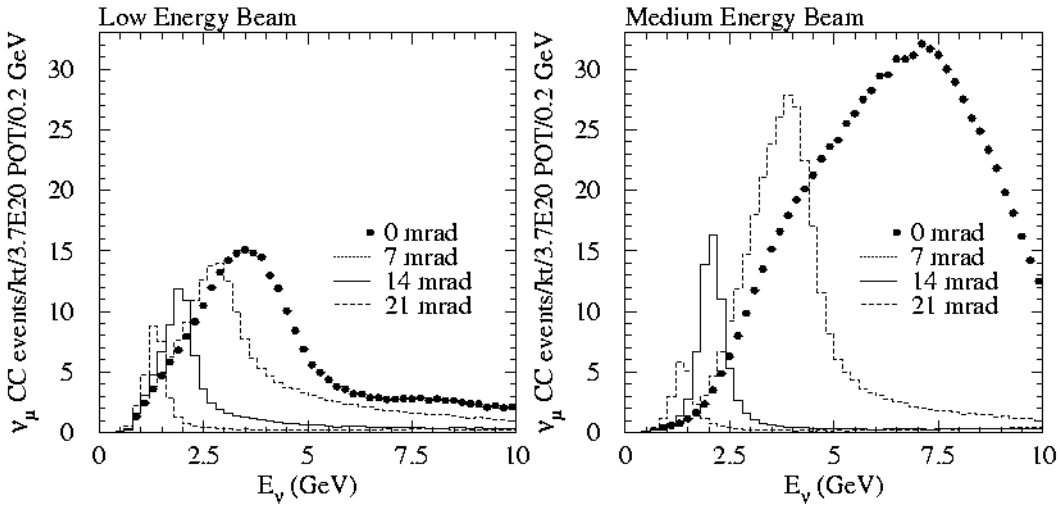

Fig. 4.4: CC ν_μ event rates expected under a no-oscillation hypothesis at a distance of 800 km from Fermilab and at various transverse locations for the NuMI low-energy beam configuration (left) and medium-energy beam configuration (right).

beam with a detector at a location off the beam axis. This concept was first proposed for the experiment E-889 at the Brookhaven National Laboratory [3]. Fig. 4.4 shows the implementation of this scheme at locations of 5, 10, and 20 km (corresponding to the angles of 7, 14, and 21 mrad) off the NuMI beam axis at a distance of 800 km from the target.

The off-axis configuration has several important advantages for a $\nu_\mu \rightarrow \nu_e$ oscillation experiment. Among the most important ones are:

• The central energy of the beam can be tuned to the desired energy by selecting an appropriate angle with respect to the beam axis for the location of the detector.

• The spectrum in the peak is quite narrow which helps to reduce the backgrounds, which tend to have much broader energy distributions.
• The high energy tail is considerably reduced with respect to the on-axis beam, which reduces the neutral current and τ backgrounds

These features are quite apparent from Figs. 4.3 and 4.4.

Finally, we would like to make several additional observations about the properties of the off-axis configuration:
• The energy of the beam is determined primarily by the transverse location of the detector. The dependence on the focusing optics is relatively mild.
• The focusing optics configuration affects primarily the intensity of the beam.
• The main peak is composed almost exclusively of the neutrinos from pion decay; K decays give neutrinos at significantly wider angles. Thus, prediction of the spectrum is very insensitive to knowledge of the K/π production ratio.

For the current range of Δm^2_{32} values and the three nominal NuMI beam configurations, the medium energy one gives the optimum spectrum for the $\nu_\mu \rightarrow \nu_e$ oscillation experiment. Additional fine tuning of the optics as well as the target geometry around the medium energy configuration should yield some additional optimization.

4.3. Detector Design Considerations

4.3.1. General Goals: The challenge for next generation neutrino experiments is to observe $\nu_\mu \rightarrow \nu_e$ oscillations in the atmospheric neutrino mass squared range down to the level of few parts per thousand. The CHOOZ experiment gives a limit on ν_e disappearance probability in that experiment of about 0.1 – 0.2 [4], the exact limit depending on the value of Δm^2_{32}. That translates into a limit on ν_e appearance probability of 0.05 – 0.1. MINOS is expected to improve this by a factor of two to three. There are no clear reliable theoretical guidelines as to the most likely value of this parameter.

Charged current ν_e interactions can be identified by the presence of an electron in the final state. The experimental backgrounds to the $\nu_\mu \rightarrow \nu_e$ oscillation signals arise from two general sources. There are genuine events with electrons resulting from the intrinsic ν_e component in the beam and from τ decays produced in the charged current ν_τ interactions from $\nu_\mu \rightarrow \nu_\tau$ oscillations. The latter background is very small for NOνA since most of the ν_μ flux is below τ production threshold. In addition there are potentially misidentified neutral-current events or high y ν_μ charged-current events where one or more π^0's in the final state masquerades as an electron or, less likely, that a hadron is misidentified as an electron.

The intrinsic ν_e's in the beam come from μ decays and K_{e3} decays (charged and neutral). They are of the order of 0.5-1.0% of ν_μ's, but can be reduced further by an appropriate energy cut. K_{e3} contamination is typically of the order of 20% of the μ decay background in NOνA.

The experimental challenge has two parts:
• reducing these two backgrounds as much as possible (discussed below)
• measuring these backgrounds well enough that the principal ultimate uncertainty comes from the statistical fluctuations in the event sample of interest (discussed in Chapter 10).

4.3.2. Design Optimization Issues: Background and signal ν_e events are identical except for their energy spectrum. The background events have a broader energy spectrum than that of the potential signal events, whose width is determined by the spectrum of ν_μ's convoluted with the oscillation probability (see Fig. 4.5). Thus, the background from ν_e's can only be reduced by good energy resolution.

The ν_μ neutral and charged-current backgrounds can be reduced by a well-designed detector. The challenge is to suppress them to levels comparable or lower than the intrinsic ν_e background level with minimum impact on the signal detection efficiency.

The need to separate out the electromagnetic component in a hadronic jet from the remaining hadrons is common to many high-energy experiments. In the calorimetric method, this is generally achieved by having a high Z electromagnetic calorimeter in front of the hadron section. Clearly that technique is not suitable for electron/π^0 separation. The latter has been traditionally done in open geometry experiments by using a Cherenkov

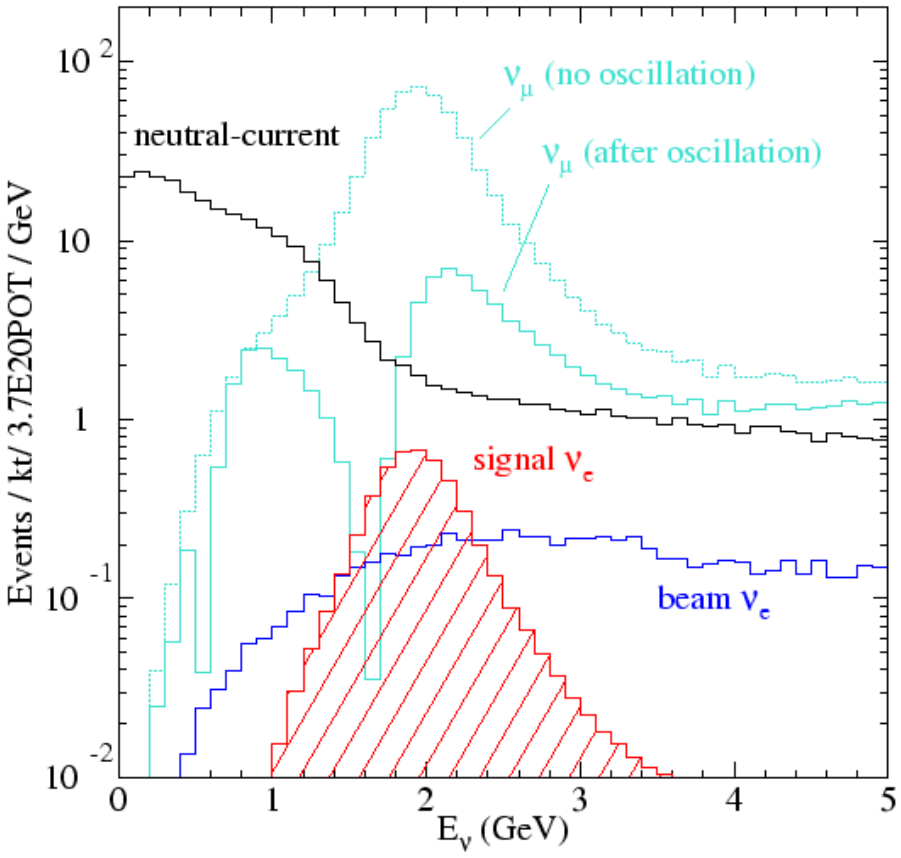

Fig. 4.5: Simulated energy distributions for the ν_e oscillation signal, intrinsic beam ν_e events, neutral-current events and ν_μ charged-current events with and without oscillations. The simulation used $\Delta m^2_{32} = 2.5 \times 10^{-3}$ eV^2, $\sin^2(2\theta_{23}) = 1.0$, and $\sin^2(2\theta_{13}) = 0.04$. An off-axis distance of 12 km at 810 km was assumed.

counter. In the recent neutrino experiments: IMB, Kamiokande and SuperKamiokande, this general method was implemented by water Cherenkov detectors. The other technology of choice in those experiments (*e.g.* CHARM II and the BNL oscillation experiment) has been use of low Z calorimeters, which facilitate identification of the electron by tracking.

4.3.3. Tracking calorimeter design issues: In principle, at least, a highly segmented detector can separate electrons from π^0's by utilizing several experimental characteristics:

• finite separation between the vertex and conversion points of the γ's from the π^0,

• two electromagnetic showers (for π^0) *vs* one (for electrons),

• double pulse height right after a γ conversion.

Success of the separation based on these characteristics requires fine segmentation: longitudinally, a fraction of a radiation length, and transversely, finer than the typical spatial separation of the two gammas from the π^0 decay. The transverse segmentation also has to be such that individual tracks in the final state can be separated from each other.

Besides the need to distinguish electrons from π^0's, one must also distinguish electrons from hadrons and muons. This is harder in a low Z material and relies on absence of hadronic interactions for electrons and a generally broader pattern of hits along the track for electrons due to the electron shower.

The other important characteristic of a good ν_e detector for $\nu_\mu \rightarrow \nu_e$ oscillations is its energy resolution. One can reduce the intrinsic beam ν_e background utilizing the fact that the events from $\nu_\mu \rightarrow \nu_e$ oscillations will have a sharp energy spectrum at a predictable energy in contrast to the backgrounds that will exhibit a much broader spectrum. This is an important feature of

an off-axis experiment, where the detector sees neutrinos in a narrow energy band. Electron-type neutrinos from μ decays will be in roughly the same energy range as the oscillated ν_e's but have a much broader distribution. K_{e3} decays will give higher energy neutrinos covering a broad energy range whereas the τ decay electrons will peak towards low energies. The shape and the level of backgrounds as well of a possible signal are shown in Fig. 4.5.

4.4. Evolution of the Detector Design

The first NOνA proposal [5], submitted in March 2004, called for a 50 kT sandwich far detector. The detector in that proposal had alternating planes of absorber and active elements. The absorber consisted of eight inches of either particleboard or oriented strand board. In the baseline design, the active element was a plane of 30-cell PVC extrusions containing liquid scintillator. The cell size was 3.96 cm wide, 2.56 cm deep, and 14.6 m long. An appendix to the proposal described an alternative design in which the active elements were resistive plate chambers.

At around the time that the proposal was submitted, Stan Wojcicki suggested an alternative design in which the passive absorber was removed and the liquid scintillator cell dimensions were reoptimized [6]. The rationale for this suggestion was that in this "totally active" design, the higher resolution of the detector would lead to a higher efficiency for detection of $\nu_\mu \rightarrow \nu_e$ oscillation events along with a greater rejection of background events. This, in turn, would allow a detector with a smaller total mass to have as good or better performance for the same cost.

The reoptimization of the liquid scintillator cells consisted of making the cells deeper. The deeper cells produced more light per track, allowing longer cells with corresponding longer attenuation factors. However, the cell length was limited to 15.7 m, since 53 feet is the longest length that can be transported in the United States without substantial extra cost.

Preliminary investigations of this design showed that it was promising and Appendix B [5] to the proposal was submitted to the PAC for its June 2004 meeting.[7] At that meeting the PAC was told that more detailed simulations and engineering studies were needed before the collaboration could decide on whether to substitute the totally active design for the baseline design.

The decision to propose the totally active design was made at the January 2005 NOνA collaboration meeting. The reasons for this decision were

(1) The sensitivity for measuring $\nu_\mu \rightarrow \nu_e$ oscillations was the same for a 30 kT totally active detector and a 50 kt detector sandwich detector and the costs were comparable.

(2) It was anticipated that the ability to see almost all of the energy deposition, the finer longitudinal segmentation, the higher resolution, and the increased signal to background ratio[8] would yield a number of advantages, including
   (a) eventual improvement in the figure of merit as more sophisticated analyses use more aspects of the finer segmentation and higher resolution,
   (b) better understanding of the backgrounds and confidence in their subtraction,
   (c) increased precision in measuring $\sin^2(2\theta_{23})$, measuring neutrino cross sections in the Near Detector, and galactic supernovae in the Far Detector (see Sections 13.6, 13.8, and 13.9, respectively), and
   (d) reduction in backgrounds due to cosmic rays to a negligible level (see Section 10.7).

(3) Faster detector assembly time at the Far Site.

[7] The detector described in Appendix B was a 25 kT detector with 17.5 m long and 4.5 cm wide cells. The shipping limitation was ignored at the time of writing Appendix B. In this proposal, the mass has been increased to 30 kT and the cells deepened to 6 cm as a result of the simulations described in Chapter 12.

[8] For $\sin^2(2\theta_{13}) = 0.1$, the typical signal to background increases from 4.8 to 7.3 in going from the sandwich design to the totally active design.

4.5. Far Detector

The NOνA Far Detector will be located in a new surface laboratory approximately 810 km from Fermilab and displaced approximately 12 km from the central axis of the NuMI beam. The detector will be a low density, low Z, 30,000 metric ton, tracking calorimeter, comprised of approximately 24,000 metric tons of mineral-oil based liquid scintillator as an active detector and 6,000 tons of rigid polyvinyl chloride (PVC) extrusions, loaded with 15% titanium dioxide, to contain the liquid scintillator.

The liquid-scintillator filled extrusions will be arranged in 1984 planes, oriented normal to the axis pointing towards Fermilab. Each plane will be 15.7 m wide by 15.7 m high by 6.6 cm thick. The planes alternate horizontal and vertical alignments. Thirty-two planes are glued together into a block with a one-cm gap between blocks for structural reasons. The total length of the detector is 132 m.

The liquid will be contained in the PVC extrusions, which will be 1.3 m by 6.6 cm by 15.7m long. Each extrusion will be divided into 32 cells, each cell having an inner cross-section of 3.87 cm by 6.00 cm, with a total length of 15.7 m. The scintillation light in each cell will be collected by a looped 0.8 mm diameter wavelength-shifting plastic fiber. Light from both ends of the fiber will be directed to a single pixel on an avalanche photodiode (APD).

APDs are low cost photodetectors providing high quantum efficiency. Their main difficulties are low amplification and electronic noise. High gain preamplifiers, such as those developed for the LHC CMS detector, can provide the necessary signal output levels. Noise will be reduced to a feasible level by use of Peltier-effect coolers to reduce the operating temperature of the APDs to -15 C.

4.6. Near Detector

The purpose of the NOνA Near Detector is to increase the sensitivity of our search for $\nu_\mu \rightarrow \nu_e$ appearance by improving our knowledge of backgrounds, detector response and the off-axis neutrino beam energy spectrum. The Near Detector would be located about 12 m off the NuMI beam axis, in the access tunnel upstream of the MINOS Near Detector Hall. This site provides a neutrino-beam energy spectrum that is quite similar to that at the far-detector.

Although a primary design requirement is that the near detector be as similar as possible to the far detector, of necessity it will have smaller transverse and longitudinal dimensions. As described in Chapter 9, the active area of the detector will be 3.25 m wide and 4.57 m high. The first eight meters of the detector will be composed of the exact same extrusion cells as in the Far Detector. It will be logically be divided into three sections: the first 0.53 m will be a veto region, the second 2.64 m will be the target region, and the final 4.75 m will be a shower containment region. The fiducial volume of the target region will be the central 2.5 m horizontally and 3.25 m vertically. The final section of the detector will be a muon catcher with 10 10-cm plates of iron interspersed with additional planes of liquid scintillator cells. The total mass of the Near Detector will be 262 tons, of which 145 tons are in the totally active region. The fiducial region will have a mass of 20.4 tons.

As discussed in Chapter 10, the Near Detector will be modular, so that it can be placed in the MINOS Surface Building prior to NOνA running, where it will be illuminated by the 75-mrad off-axis NuMI beam. There it will see a ν_μ beam peaked at 2.8 GeV and a ν_e beam peaked at 1.8 GeV, both from kaon decay. Running the Near Detector on the surface will also allow us to verify our calculation of the level of cosmic ray backgrounds.

Chapter 4 References

[1] The Fermilab NuMI Group, "NuMI Facility Technical Design Report," October 1998, Fermilab Report NuMI-346.

[2] M. Kostin *et al*., "Proposal for a continuously-variable beam energy," October 2001, Fermilab Report NuMI-783.

[3] The E889 Collaboration, "Long Baseline Neutrino Oscillation Experiment at the AGS," Brookhaven National Laboratory Report BNL No. 52459, April 1995.

[4] CHOOZ collaboration, M. Appollonio *et al*., Phys. Lett. B **466** 415.

[5]http://www.nova.fnal.gov/NOvA%20Proposal/Revised_NOvA_Proposal.html

[6] S. Wojcicki, NOνA Note 28, http://www-nova.fnal.gov/notes/notes.html

5. The NOνA Far Detector

5.1. Overview

The NOνA Far Detector is optimized for detecting low-energy (~2 GeV) electron showers while rejecting background events. High signal efficiency and good background rejection require frequent sampling in low-Z materials. The NOνA detector has 80% active material and fine segmentation, providing good discrimination between signal and background.

The detector is a 30 kton tracking calorimeter, 15.7 m by 15.7 m by 132 m long, with alternating horizontal and vertical rectangular cells of liquid scintillator contained in rigid polyvinyl chloride (RPVC) extrusion modules. One plane of the detector is constructed from 12 extrusion modules as shown in Figure 5.1. Each extrusion module contains 32 cells and is sealed with a closure block on one end and a readout manifold on the other end. Individual cells in each extrusion have an interior cross section of 3.87 cm by 6.0 cm along the beam direction as shown in Figure 5.2. Each cell is 15.7 m long.

Extrusion modules will be made in three factories, operated by NOνA collaborators, and trucked to the Far Detector site. The factories

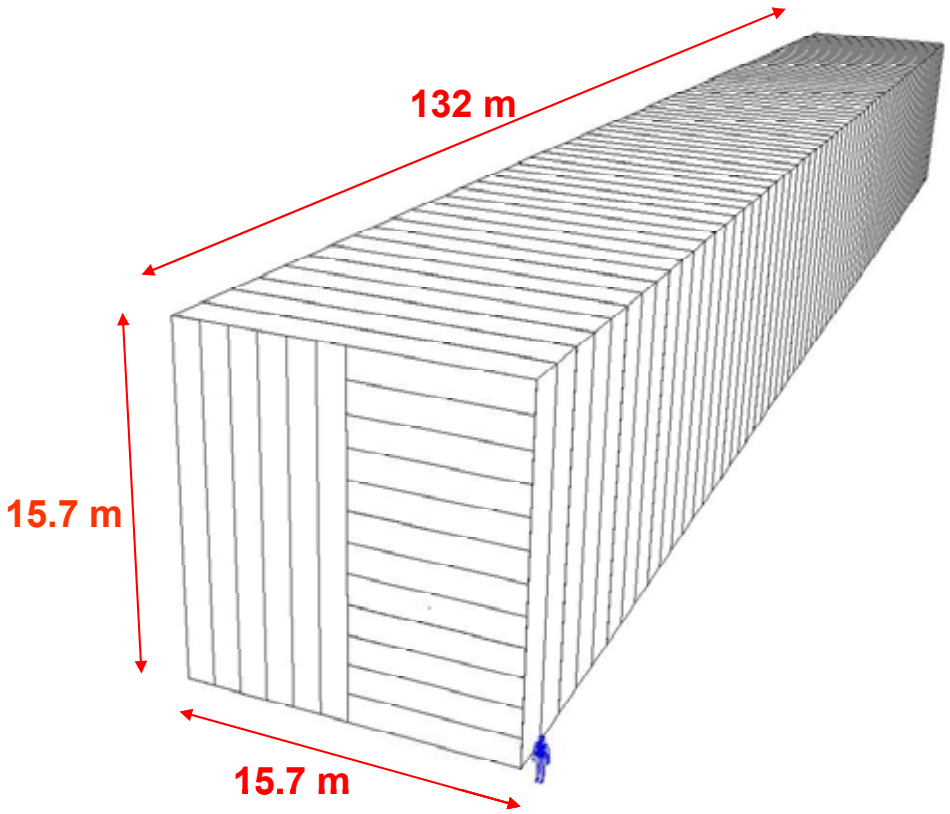

Fig. 5.1: Overview of the NOνA detector structure, showing the 132 meter length of the detector separated into blocks of 32 planes. The cut-away view of the front plane shows the alternating layers of horizontal and vertical extrusion modules.

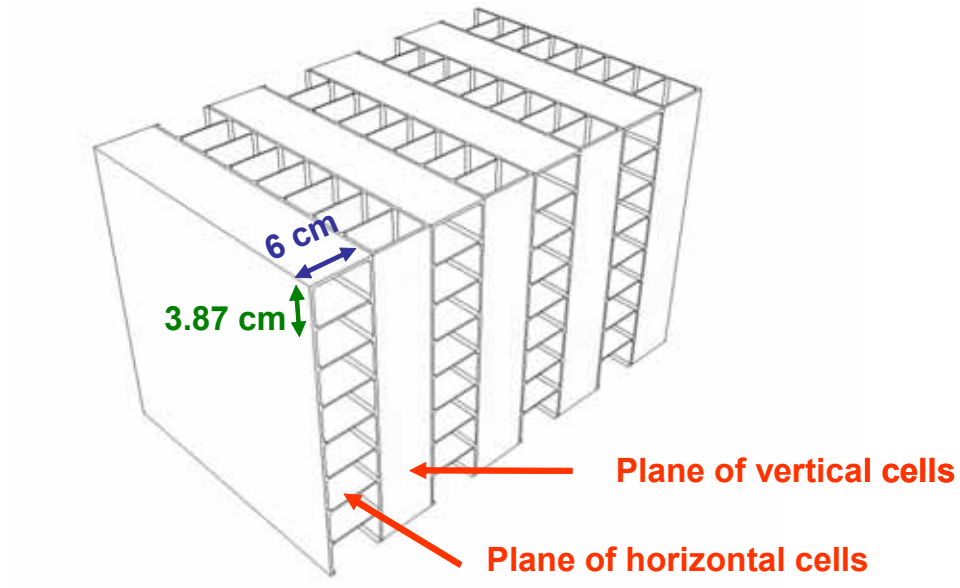

Fig. 5.2: Close-up of the detector structure, showing the cell structure of alternating horizontal and vertical extrusion modules.

assemble a rigid PVC module complete with a looped 0.8 mm diameter wavelength shifting (WLS) fiber in each cell to collect scintillation light and route it to a single photodetector pixel. The details of the light collection by the WLS fibers are discussed in Chapter 6.

The empty extrusion modules are assembled into planes and the planes are assembled into larger blocks at the far site. The photodetectors and readout electronics are mounted on each extrusion module, on the top and on one side of the detector. Details of the readout electronics are discussed in Chapter 7.

The extrusion module assembly process takes 44 months. The Far Detector installation can be completed in 26 months. Chapter 14 discusses how these schedules are interleaved, while the details of the assembly times are discussed here. The Far Detector gets filled with liquid scintillator as the last step of the assembly process, with liquid filling following the plane construction by about one month.

The Far Detector parameters are summarized in Table 5.1.

Total mass	30,090 tons
Mass of RPVC extrusions	5,970 tons
Mass of liquid scintillator	23,885 tons
Liquid scintillator	Bicron BC517L (or equivalent)
Active mass fraction	80%
Active height × width	15.7 m × 15.7 m
Active length	132 m
Number of layers	1984
Radiation length per layer	0.15
Mass of epoxy between layers	222 tons
Extrusions per layer	12
Extrusion outer wall thickness	3 mm
Extrusion inner web thickness	2 mm
Extrusion width	1.3 m
Extrusion length	15.7 m
Maximum pressure in vertical cells	19.2 psi
Cells per extrusion	32
Cell width × depth	3.87 cm × 6.00 cm
Total number of cells	761,856
Total number of extrusions	23,808
Wavelength-shifting fiber	Kuraray, Y-11 fluor, S-type (or equivalent)
WLS fiber diameter	0.8 mm
Total WLS fiber length	25,629 km
Total WLS fiber mass	13.5 tons

Table 5.1: Summary of Far Detector parameters.

5.2. Extrusion Module Fabrication

A 32-cell extrusion forms the body of each module, which has a WLS fiber manifold and photodetector assembly at one end and is sealed with a closure plate on the other end. The closure plate is a grooved RPVC block that is glued across the extrusion end, as shown in Figure 5.3. Before installing the closure plate a series of small circular holes are made in the interior webs so that the extrusion consists of a single liquid volume.

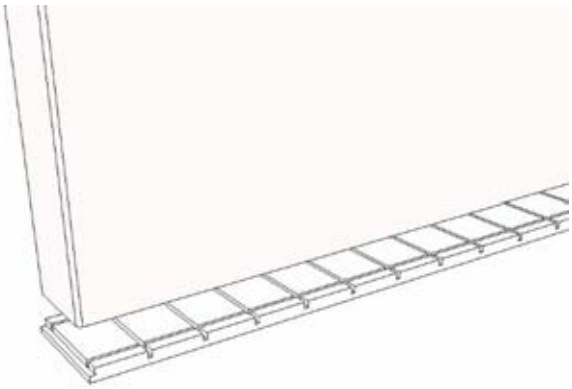

Fig. 5.3: Closure plate (bottom piece) for the "closed" end of an RPVC extrusion module.

Identical WLS manifolds, shown in Figures 5.4 and 5.5, are used on both the vertical and horizontal modules. The vertical extrusion manifolds have room for thermal expansion of the liquid scintillator. The horizontal extrusions have external overflow canisters for that purpose. Clips are used to position the fibers at the top of each extrusion and routing grooves align the fibers on the connector, control the fiber bend radii and facilitate assembly. The manifolds provide filling and venting ports, seal the extrusions, and guide the fibers to the photodetector connector [1].

Extrusions for modules arrive at three assembly factories, cut to length, from the commercial extruder. The factories perform the following tasks:

1. Inspect the incoming extrusions,
2. Install the looped WLS fiber in all cells,
3. Install end closures and manifolds,
4. Pot fibers in connectors and fly-cut faces,
5. Check fiber loops for continuity,
6. Leak test modules,
7. Pack modules and ship to detector site.

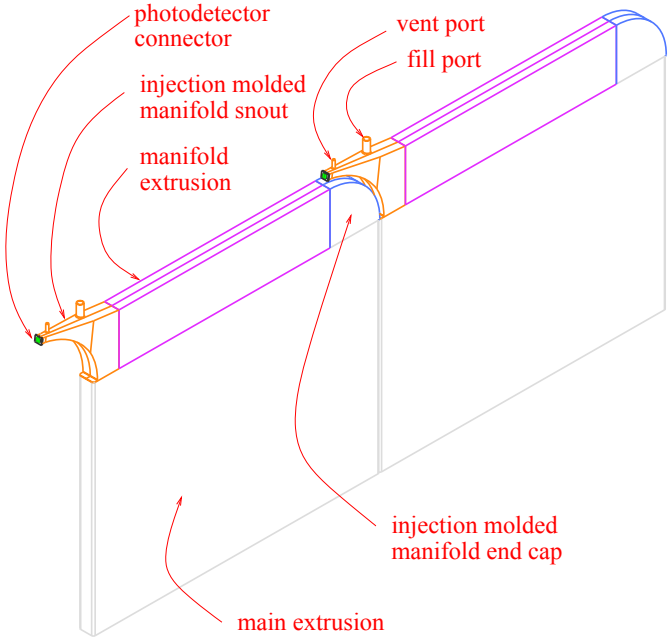

Fig. 5.4: WLS fiber manifolds mounted on adjacent RPVC extrusion modules.

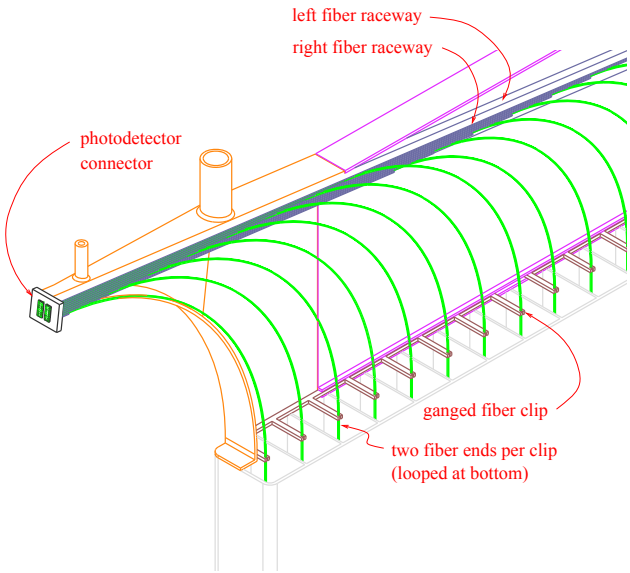

Fig. 5.5: WLS fiber routing within a manifold.

To complete the 23,808 modules during 4 years with 200 working days per year of construction, each of the three factories will complete 10 modules per day with a crew of 4. This schedule is derived from a time and motion study [2] based on the assembly of MINOS modules.

5.3. Detector installation at the Far Site

Detector installation starts with a steel frame bookend. Eight planes of 12 (empty) modules each are glued together on a horizontal assembly tables to form a sub-block. Each 26-ton sub-block is raised and glued to the previously installed sub-block. Four sub-blocks are glued together to form a 32-plane block. Small (~1 cm) expansion gaps are left between the 32-plane blocks to accommodate expansion of the RPVC when the modules are filled with liquid scintillator. PVC spacers (1 cm thick by 30 cm wide by 15.7 m long) are glued in place to maintain the gaps. Figure 5.6 shows the geometry of blocks and sub-blocks. Figure 5.7 shows the assembly tables and the "Block Raiser" lifting fixture.

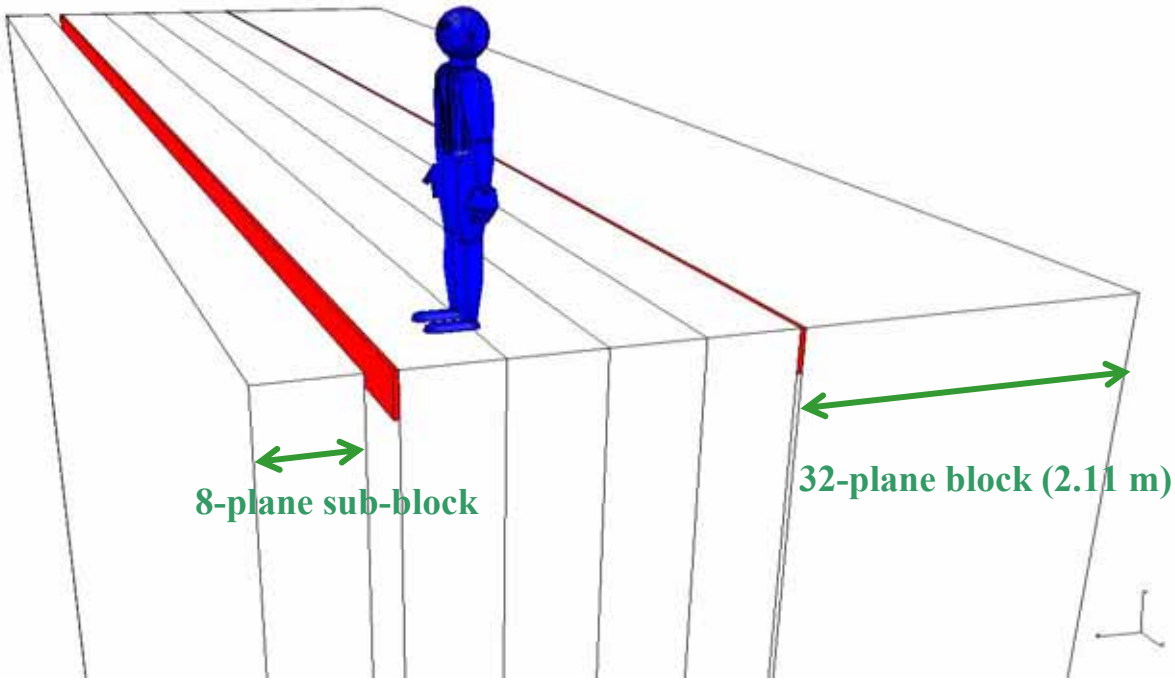

Fig. 5.6: Geometry of the NOνA detector structure. The 32-plane-blocks are made up of four 8-plane sub-blocks and are separated by 1 cm by 30 cm PVC spacers (shown in red) to create expansion gaps.

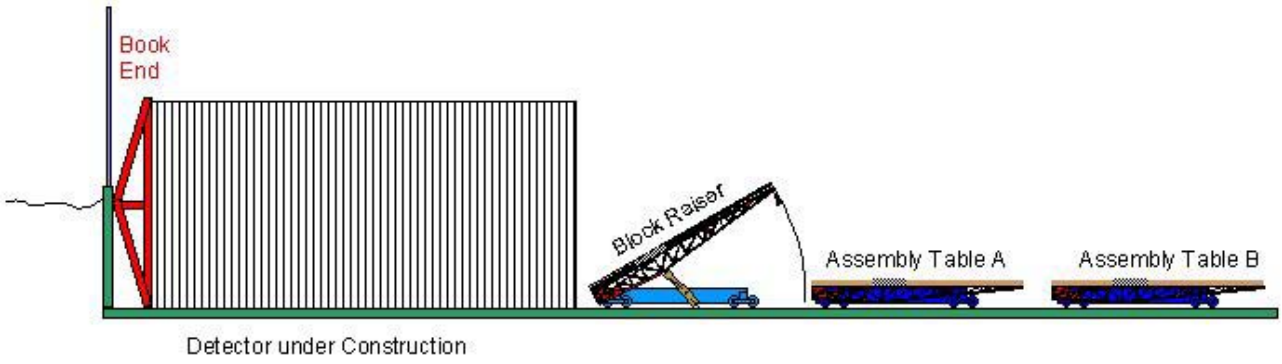

Fig. 5.7: Side elevation view of the detector during assembly, showing the bookend, the Block Raiser and two assembly tables. The Block Raiser and the two assembly tables operate on rails installed on the floor of the detector building.

In Figure 5.7 both assembly tables and the Block Raiser ride on rails installed in the floor along the length of the detector. The assembly tables are stationed near the receiving dock, while the Block Raiser shuttles completed blocks to the end of the detector, raises them up, aligns them, and holds them while the glue sets. After a startup period, crews of three technicians will be able to install one 8-plane sub-block in two shifts.

To illustrate the details of the assembly procedure, let us start with the first four planes of an 8-plane sub-block already completed on Table A (nearest to the detector) and an empty Table B (nearest to the receiving dock). Two operations now occur in parallel: The crew brings the next extrusion module to Table A using the crane and a vacuum lifting fixture, and a semi-automatic machine dispenses glue dots over the area where this module will be placed. The glue dispensing takes 4 minutes and moving the module into place takes 8 minutes. Stops on the table are used to align the module. The lifting fixture (one of 13) will be left on top of the module as a weight until the glue is sufficiently cured. Built-in arms push the module against its neighbor to straighten out the extrusion if necessary. This operation is repeated for the remaining 11 modules. To complete a plane takes a little under 2 hours.

A crew of outfitting technicians works on the newly completed plane on Table A while the glue cures. They install a signal concentrator box on the plane, install an electronics box on each module and plug in the power and readout cables. A test fixture is used to check all modules and cables for correct performance. The crew also installs the liquid scintillator fill panels and routes the liquid fill lines and air return lines to them (This is discussed in more detail in section 5.4).

Meanwhile, the assembly crew begins installing modules on Table B. The first layer gets set down without glue. The second layer is installed and glued in place as described above. Vacuum fixtures are retrieved from Table A as needed. Each fixture will have served as a glue-curing weight for about 2 hours before it is removed.

After completion of the glued layer on Table B, the crew resumes work on Table A, and so on. Eight layers will be stacked in a two-shift, 16-hour day.

By the next morning the epoxy has cured to sufficient strength for safe handling. A separate block installation crew comes in 4 hours before the day shift starts and retrieves the Block Raiser from the end of the detector where it has been holding the last completed block while the glue cured. The crew parks the block raiser next to Table A and transfers the 8-layer block from Table A onto the Block Raiser table. This is done on an air cushion, by pressurizing a plastic pipe system in the table to 0.1 psi to "float" the block. A set of wheels, inset into both tables, pushes and controls the block during the transfer.

Next the 4-plane half-block from the previous day's work is transferred from Table B to Table A and the block assembly cycle starts over when the day crew arrives.

The block installation crew uses a laser system to check alignment of the block that was installed the day before. Based on the results, they select spacers of appropriate thickness to keep the next block exactly vertical. Then they drive the Block Raiser with the completed block on its rails to the end of the detector. They glue the selected spacers to the block using a fast setting epoxy. They mix and spread grout on the floor and dispense epoxy on the spacer board. Now they are ready to raise the next block and align it, using the laser system and the control cylinders embedded in the Block Raiser. The Block Raiser holds the block in position overnight, pressed firmly against the existing detector stack, until the epoxy has cured.

5.4. Filling the Detector with Liquid Scintillator

The detector holds 23,885 tons (about 7.5 million gallons) of liquid scintillator. To match the overall assembly time at the far site, the detector will be filled in 20 months (333 8-hour shifts), requiring a fill rate of 46 gallons (174 liters) per minute. Time must be allowed for the liquid level to equalize between module cells through the 0.5-inch diameter holes in the internal webs. This requires the fill rate to be 3 liters/minute or less for a single module, so 48 modules must be filled simultaneously.

We will use an automated filling machine to fill 12 modules at once, metering the liquid mass output and fill rate in each module. The system will shut off the flow when the desired liquid level is reached or if any unusual situation occurs. To simplify the procedure, the fill and air return lines from each module will be routed to common fill panels located on the 8-plane sub-blocks near the building catwalks (see Chapter 8). The filling machine receives liquid scintillator from a pipeline installed along each catwalk.

Each filling machines takes 6.5 hours to fill 12 modules and 5 machines will be required to fill the entire detector in 333 shifts. One machine needs to be moved every 75 minutes, so one worker can handle the whole filling job.

Vendors will deliver pre-mixed liquid scintillator to the detector site in standard tanker trucks. We will use 88,000 gallons of scintillator mix a week, requiring 3.3 trucks per workday. In-line quality assurance will be used at both the mixing plant and the receiving site. Some intermediate storage, possibly in the form of leased tanker trailers, will be used as buffers while we verify product quality before injecting the scintillator into the distribution system. These also provide a steady supply of liquid for distribution.

5.5. Structural Considerations

The following sections describe our analyses of the composite detector structure. The structure is designed to be mechanically stable for the lifetime of the experiment and allows the completed planes of the detector to be filled with liquid scintillator and operated while the remaining planes are being installed. The design process includes testing sample portions of the structure to validate the engineering calculations.

5.5.1. Rigid Polyvinyl Chloride (RPVC): RPVC is an inexpensive, high-strength, readily available material. It has a high glass transition temperature (making it less prone to creep) and industrial extruders find it easy to work with. NOνA will use 5970 tons of RPVC, which represents less than one day of U.S. production capacity.

The ASTM D1784 "Standard Specification for Rigid PVC Compounds" defines six grades, with allowable design stresses ranging from 1000 psi to 2000 psi [3]. The Plastic Pipe Institute defines the design stress as the hoop stress in a pipe that, when applied continuously, will cause failure of the pipe at 100,000 hours (11.43 years) due to long-term creep. We have chosen a grade of RPVC with a design stress of 2000 psi for NOνA. Figure 5.8 shows a yield stress measurement of approximately 6000 psi in the kind of RPVC that we expect to use.

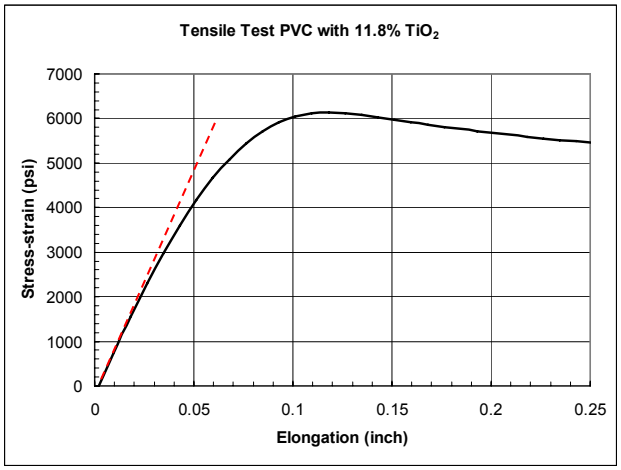

Fig. 5.8: Measured tensile test of RPVC with 11.8% TiO_2.

In RPVC, the elastic range extends to approximately 2000 psi, beyond which the material creeps [4]. RPVC is a tough material with low brittleness that limits crack propagation. For this reason, the choice of an allowable stress depends on the stress pattern. For NOνA, our Finite Element Analyses (FEAs) show that the high stress areas are limited to small, isolated regions [5]. If creep occurs, it will re-distribute the forces over a larger area, relaxing the stresses without a failure occurring. We use a design stress of 1500 psi, without any additional safety factors. Preliminary results from our long-term creep tests [4] indicate the choice of 1500 psi to be acceptable.

5.5.2. Extrusion cell parameters: The cell dimensions used for the NOνA RPVC extrusions have been optimized for signal efficiency and background rejection using the simulation studies described in Chapter 12. We used FEA calculations to determine the extrusion wall thicknesses that would provide mechanical stability of the far-detector structure at all stages of the

detector construction and during filling with liquid scintillator. The effects of long-term creep in the RPVC material were also taken into account. The 6-cm extrusion cell depth we have chosen is the maximum allowed for the 3-mm extrusion wall thickness and 2-mm web thickness used [6], [7].

5.5.3. Hydraulic forces: The weight of the liquid scintillator in the vertical extrusion modules is transferred to the floor by the hydraulic pressure on their base plates.

Within one extrusion module, all 32 cells are hydraulically connected to allow the flow of liquid scintillator and displaced air during filling. Adjacent extrusion modules are not hydraulically connected to one another. The15.7-m high vertical extrusions have a hydrostatic pressure of 19.2 psi at the bottom. The horizontal extrusions are only 1.3 m high and have maximum pressures of only 1.6 psi. The greatest forces are exerted by the hydraulic pressure on the outer cell walls of the vertical extrusions.

Each vertical extrusion will swell during filling by 2 to 5 mil near the bottom, where the hydrostatic pressure is highest, due to bowing of the outer walls and stretching of the webs. Our FEA calculations show that friction will prevent the bottom plates of the vertical extrusions from sliding on the floor [8], so stresses will build up during filling. Fig. 5.9 shows how this affects a stack of planes.

Our FEA analysis has determined that local stresses in the RPVC will exceed our design stress if more than 80 planes are assembled in one block [9]. We therefore plan to use 32-plane blocks separated by expansion gaps to limit the buildup of hydraulic stress during filling.

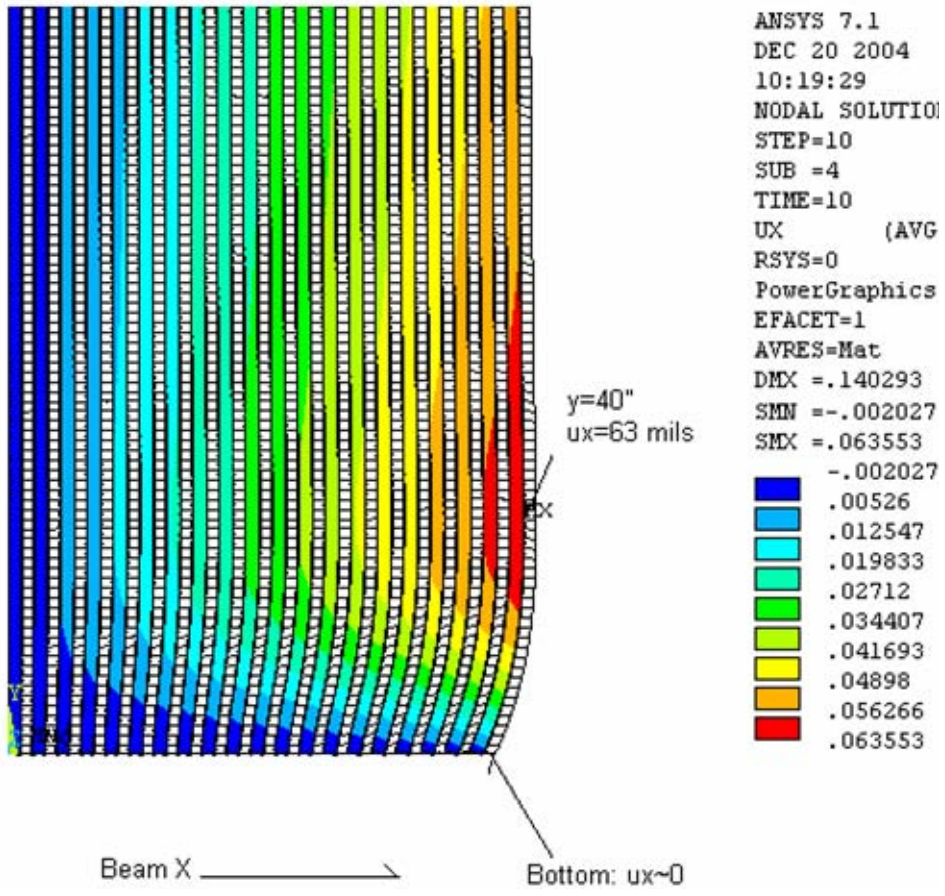

Fig. 5.9: The displacement along the beam direction after 40 planes are filled (80 planes total due to symmetry condition). Only the bottom 3 m out of the 15.7 m height is shown, and that the deformation is highly exaggerated. The deformation and stress is concentrated at the bottom of the detector.

5.5.4. Vertical extrusions: Each vertical extrusion is filled with liquid scintillator to a height of 15.7 m, subjecting the bottom of the extrusion to 19.2 psi. The pressure creates a downward force on the bottom closure plate that is transmitted to the floor. This force also bows out the outer walls and stretches the webs between adjacent cells.

For an outer extrusion wall thickness of 3 mm and a web thickness of 2 mm, the FEA gives a maximum stress of 1400 psi for the interior cell, as shown in Fig 5.10.

5.5.5. Horizontal extrusions: Although the maximum hydrostatic pressure in each horizontal cell is only 1.6 psi, the lower extrusions cannot support the load of the filled extrusions above them. For this reason the horizontal extrusions are glued to the adjacent vertical extrusions, which support their weight and prevent it from being transferred to the horizontal extrusions below [7], [10]. Table 5.2 shows that gluing horizontal and vertical extrusions together further reduces the stresses from hydrostatic pressure.

	Fully glued	No glue
Deflection (mils)	1.5	5.7
Maximum Stress (psi)	560	1,400
Maximum shear stress in the mid plane (psi)	70	Not applicable

Table 5.2: Deflections and forces calculated for planes of vertical and horizontal extrusions, with and without glue. The deflections at the outer edge of the horizontal extrusion are given. The pressures shown are conservative in that they do not take this deflection into account.

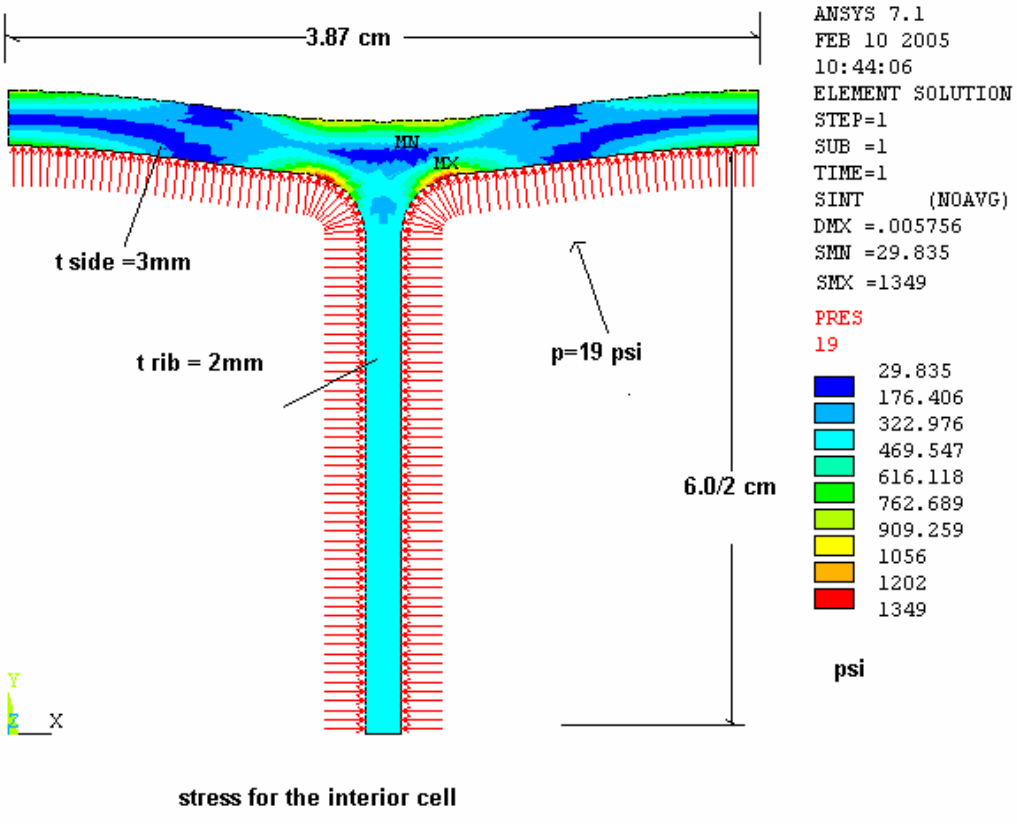

stress for the interior cell

Fig. 5.10: FEA results for interior cell stresses.

5.5.6. Buckling stability: FEA calculations show that the 32-plane blocks do not buckle under their own weight [10]. Figure 5.11 shows that a 32-plane block, when free standing, has a safety factor of 2.3 against buckling. This safety factor applies to each block and demonstrates that a collective failure, where all blocks would buckle together, is extremely unlikely.

For additional stability, successive 32-plane blocks will be connected along their top edges using the PVC spacer blocks described earlier. This increases the buckling safety factor for each block to 2.9, as shown in Fig. 5.12 [9].

5.5.7. Thermal expansion: RPVC has a thermal expansion coefficient of 67 ppm per ^{0}C. If we take a design temperature range of 20 ± 10 ^{0}C, then the complete detector RPVC stack will try to expand or contract by 9 cm. The bottom plates of each extrusion module are held in place by friction and will not move. The top spacer plates are glued to the adjacent blocks and hence the whole top moves as a unit as the temperature changes. Thermal expansion will tilt the planes slightly, starting with an exactly vertical plane at the first bookend, and ending with a 9 cm tilt at top of the far end of the complete detector (for a 10 C change). The tilt creates a force parallel to the detector axis proportional to the angle. Summing over all planes, the force is ±15 tons at the extremes of the design temperature range. The bookend will be designed to resist that force. The top spacer board is 30 cm by 15.7 m in area, and will see a stress of just ± 4.3 psi, which is small compared to typical epoxy yield strength of 2000 psi.

5.6. Summary

Our initial detector engineering studies have led to a design that meets conservative structural safety standards while providing the excellent performance of a highly segmented, totally active liquid scintillator detector. Chapter 15 outlines our plan and funding request for extending this work to develop a complete conceptual design of the NOνA detector.

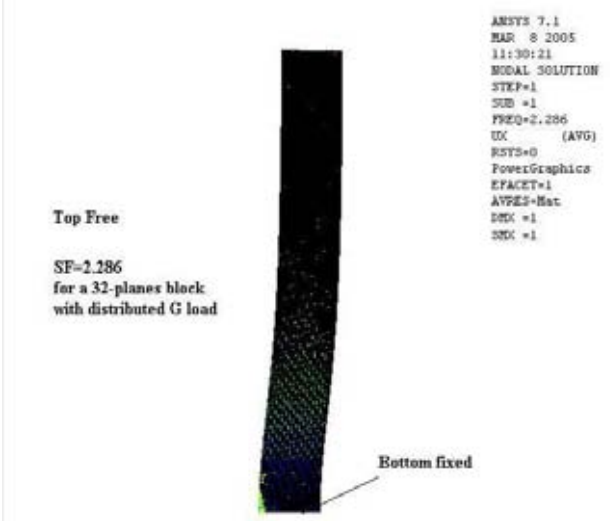

Fig. 5.11: Buckling calculation for a 32-plane free-standing block.

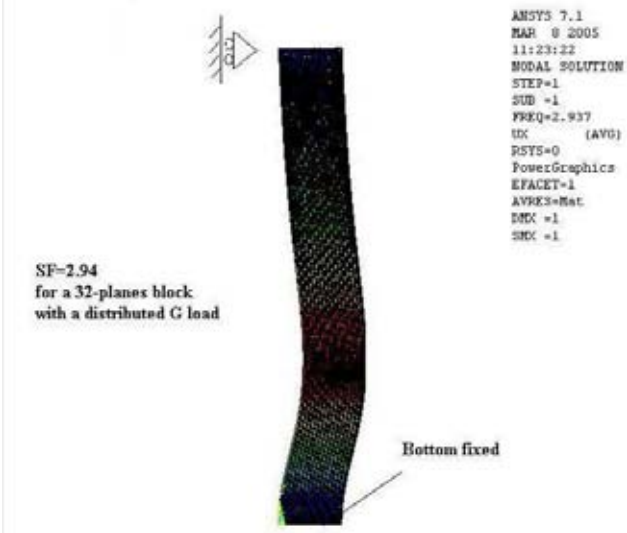

Fig. 5.12. Buckling calculation for a 32-plane block that is constrained at the top. Beginning with the first block, the tops of all blocks are connected together and also tied to the bookend, to increase the safety factor against collective buckling.

Chapter 5 References

[1] T.R. Chase, "Conceptual design of module manifolds for the NOνA detector," NOνA-NOTE-SCINT-74, March 2005.

[2] J. Nelson, "Time and Motion Study for Liquid Scintillator Module Assembly", NOνA-NOTE-DET-75, Feb 2004.

[3] V. Guarino, "PVC Pipe Design Stress," NOνA-NOTE-DET-60, October 2004.

[4] H. Jostlein, "First results from creep test on commercial PVC," NOνA-NOTE-SCINT-49, September 2004.

[5] A. Lee, NOνA-NOTE-DET-70, "Results for a mini-3D model for both vertical and horizontal," October 2004; A. Lee, NOνA-NOTE-DET-71, "Results based on the criteria of maximum working stress at or below 1800 psi for PVC," October 2004.

[6] A. Lee, NOνA-NOTE-DET-61, "A preliminary result for several different sizes of cell," February 2004; A. Lee, NOνA-NOTE-DET-62, "A preliminary stress calculation for cell structure using liquid scintillator," February 2004.

[7] A. Lee, J. Kilmer, J. Cooper, "A recent stress and stability study for the RPVC structure used in a liquid scintillator detector," NOνA-NOTE-GEN-51, July 2004; A. Lee, NOνA-NOTE-DET-65, "Stress and stability calculation for the cell size 6 cm x 3.87 cm," February 2005; A. Lee, NOνA-NOTE-DET-66, "Results of a revised mini-3D for different sizes of cells," October 2004.

[8] A. Lee, NOνA-NOTE-DET-67, "The effect of friction force for a 40-plane block - 1," November 2004; A. Lee, NOνA-NOTE-DET-68, "The effect of friction force for a 40-plane block - 2," November 2004; A. Lee, NOνA-NOTE-DET-69, "The effect of friction force for a 40-plane block - 3," December 2004.

[9] A. Lee, NOνA-NOTE-DET-72, "A buckling calculation for a 32-plane block with a cell size of 6 cm x 3.8 cm," February 2005.

[10] A. Lee, NOνA-NOTE-DET-64, "Comparison between the test data and FEA calculation for buckling of a single PVC panel," July 2004.

6. Light Collection

6.1. Introduction

The signal resulting from the passage of a charged particle through a cell of the detector depends on the type of scintillator used, the wavelength shifting fiber, the size of the cell, the cell wall reflectivity, and the photodetector response.

6.2. Liquid Scintillator

The scintillator we propose to use is a mixture equivalent to Bicron BC517L [1] (also sold as Eljen EJ321L), essentially pseudocumene in a mineral oil base. BC517L has a moderate light output, 39% of anthracene, when fresh, and 27% of anthracene, when fully oxygenated. The advantages of this mixture include stability, low cost, availability in large quantities, low toxicity, high flashpoint and low potential as an environmental hazard. Previous work has shown that this scintillator attacks neither wavelength shifting fiber nor PVC over lifetimes exceeding this experiment [2]. Formulations with significantly higher light output are less stable and do interact with the WLS fiber.

Oxygen will pass through the PVC cell walls so that the scintillator will become oxygenated. The oxygenation of BC517L generally proceeds to a stable light output within a few months. Fig. 6.1 shows the results of measurements we have made of pulse-height spectra from solid scintillator, fresh liquid scintillator and oxygenated liquid scintillator. Our light yield calculations and measurements are with fully oxygenated scintillator.

We have tested BC517L to determine how its light yield changes with temperature. Over temperature ranges between 15 ^{0}F and 110 ^{0}F degrees F (-10 ^{0}C to 48 ^{0}C), there was no measurable change in light yield (less than 1%). At the low end of the temperature range, mineral oils experience a rapid increase in viscosity as the temperature is reduced below their pour point, which is typically around 10 ^{0}F (-12 ^{0}C). This is due to gelling of the oil as crystalline wax is precipitated. Below 15 ^{0}F (-9 ^{0}C) our measurements showed the scintillator begins to get cloudy. At -22 ^{0}F (-30 ^{0}C) wax balls precipitated out of the scintillator. These wax balls do not dissolve when the liquid is warmed to room temperature. On the high end of the temperature range, the light yield of the scintillator decreased when the pseudocumene began to vaporize, above its flashpoint of 118 ^{0}F (48 ^{0}C). Although the performance of liquid scintillator is very robust to temperature changes, extremes need to be avoided both in its transportation and storage. The scintillator is likely to be permanently damaged at temperatures below about -20 ^{0}F and above 110 ^{0}F. Both extremes are possible in a building without climate control in Northern Minnesota. We discuss the building for this detector in Chapter 8.

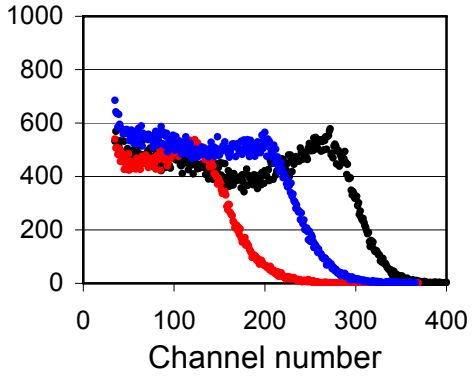

Fig. 6.1: Pulse-height spectra for scintillators showing Compton edge of ^{137}Cs gammas. Black (right): MINOS scintillator; blue (middle): fresh BC517L; red (left): 5-year old BC517L.

6.3. Wavelength-Shifting (WLS) Fiber

WLS fiber provides an efficient method for collecting light from the long narrow cells used in this detector. The WLS shifts light from shorter wavelengths to green (~525 nm) and traps it within the fiber. The MINOS Far Detector provides considerable experience on the construction and operation of this light collection design. Suitable multiclad WLS fiber is available from Kuraray, the same type of fiber and the same vendor used for MINOS.

One adjustable design parameter of the fiber is its diameter. Diameters greater than ~1.5 mm are difficult to spool and ship. For fiber diameters around 1 mm, the light collection efficiency depends approximately linearly on the radius of the fiber as shown in Figure 6.2, while the cost of the fiber depends on its volume (r^2). Thus, in terms of photons per dollar, two thinner fibers are more efficient than one thicker fiber.

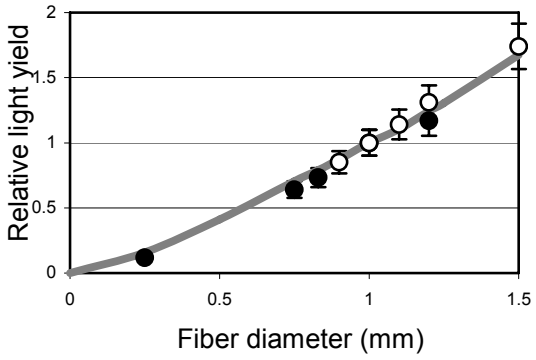

Fig. 6.2: Relative light yield as a function of WLS fiber diameter. Open circles - from measurements made for MINOS Detector; closed circles - recent measurements; solid line - Monte Carlo simulation. (Data are normalized to unity at 1 mm diameter.)

The looped fiber design shown in Figure 6.3 effectively provides two fibers with a no cost, perfect mirror at one end. This gives a factor of two more light from the far end of each cell, where light output is most important, than from the far end of two individual fibers with nonreflecting far ends. The two ends of the looped fiber will be brought together in an optical connector and connected to one pixel of an avalanche photodiode (APD). Our current design uses 0.8 mm diameter looped fiber, which satisfies our requirements for cost, light yield, and handling. During the proto-typing phase we will examine these parameters to determine the optimal fiber diameter.

Figure 6.4 shows the attenuation of light in a 0.8 mm diameter Kuraray multiclad fiber. It demonstrates the light collection advantage of a looped fiber design. Note that the ratio of light output for a looped fiber to a single fiber is largest at the far end of the liquid scintillator cell where light collection is at a premium.

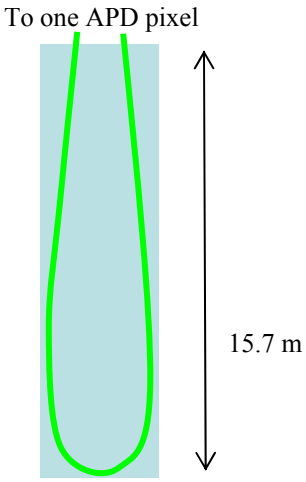

Fig. 6.3: A single liquid scintillator filled PVC cell with a 0.8 mm diameter looped WLS fiber shown in green.

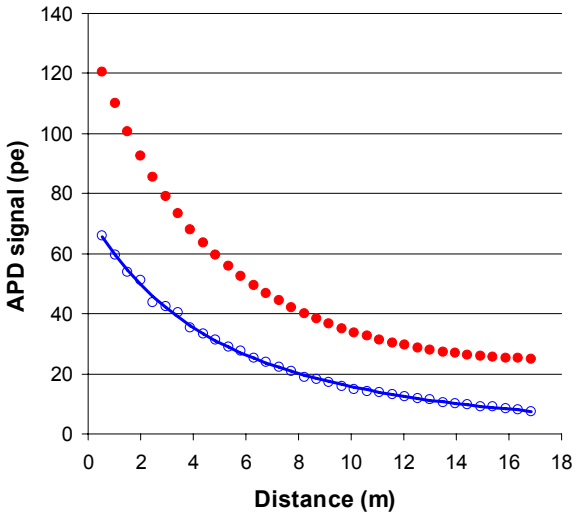

Fig. 6.4: APD signal for looped (red) and single (blue) 0.8 mm diameter fibers. The red curve is scaled from the measured blue curve using the measured shadowing factor of 1.8 for two fibers. At the end near the APD the ratio of the single fiber signal to that of the looped fiber is 1.8 while at the far end it is 3.3.

The attenuation of light in a fiber is a function of its wavelength since short wavelengths are attenuated more strongly than long wavelengths. Figure 6.5 shows the spectrum of light transported through a fiber as a function of the fiber length. Also shown is the

quantum efficiency of an APD and, for comparison, a bialkali photocathode photomultiplier tube. The high quantum efficiency of the APD and its flat response over the wavelengths transmitted from the far end of the fiber, where the signal is smallest, make it the ideal for this detector.

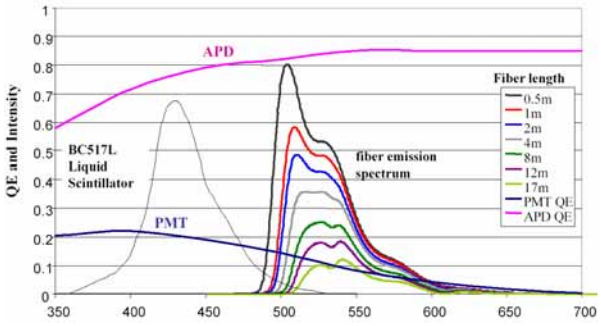

Fig. 6.5: WLS fiber emission spectra measured at lengths of 0.5, 1, 2, 4, 8, 16 m, respectively illustrating the shift of the average detected wavelength as attenuation (fiber length) increases. Also shown are the quantum efficiencies of APD and PMT (bialkali photocathode) as a function of wavelength. The emmission spectrum of the liquid scincillator is also shown..

6.4. Cell Structure – Reflectivity and Geometry

The PVC in the extrusions will be loaded with titanium dioxide for reflectivity. TiO_2 is the additive that gives commercial PVC its white color. We have tested prototypes of a multi-cell extrusion with a 12% content of TiO_2 and measured their reflectivity as a function of wavelength. Pictures of these prototypes are shown in Figures 6.6 and 6.7. The reflectivity measurements are shown in Figure 6.8. This figure also shows the reflectance is reasonably matched to the spectrum of light being reflected, the liquid scintillator emission spectrum. Since photons are, on the average, reflected over 10 times before hitting the fiber, good reflectance is an important component of light yield. For reference, we remeasured the reflecting layer of the MINOS plastic scintillator and the prototype PVC extrusion discussed in ref. [2], and these data are also shown in Figure 6.8.

Within a cell, the light captured by a fiber is fairly independent of its position in a cell but

Fig. 6.6: Cell structure of the three cell prototype of extruded PVC with 12% TiO_2.

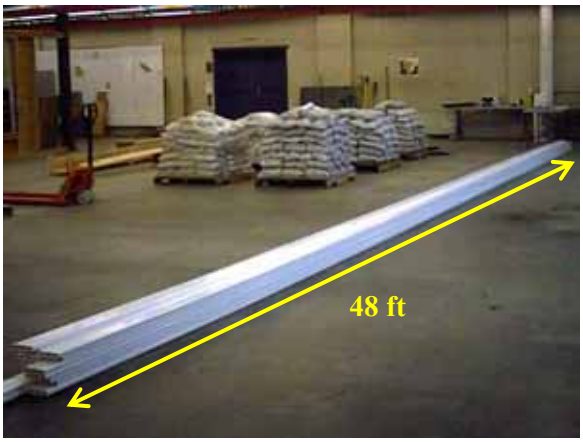

Fig. 6.7: 48 foot long three cell prototype of extruded PVC with 12% TiO_2 delivered for testing.

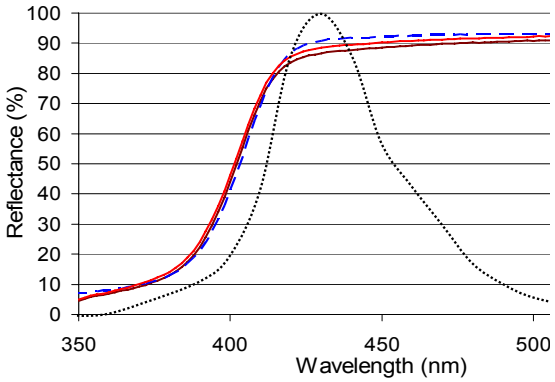

Figure 6.8: Reflectance of the prototype multicell PVC extrusion with 12% TiO2 (red) together with the liquid scintillator emission spectrum (black dots). Also shown is the reflectance of the MINOS plastic scintillator cap (blue dashes) and the MINOS liquid scintillator prototype extrusion (purple) from ref. [1].

decreases significantly when it is actually touching a cell wall. Figure 6.9 shows a simulation of light capture as a function of the location of a single, unmirrored WLS fiber within a liquid scintillator cell. Our test setup does not constrain the fiber position, so over most of its length the fiber will be at or near an extrusion cell wall. As part of our R&D program, we intend to explore economical ways to control the fiber location.

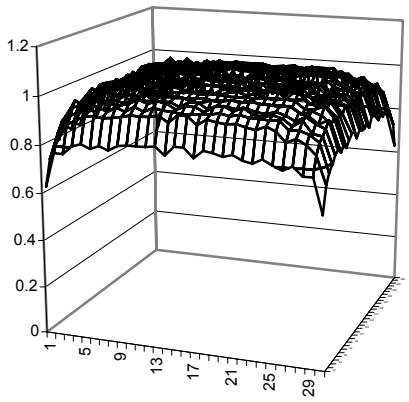

Fig. 6.9: Relative light yield for a single fiber as a function of location within a scintillator cell.

6.5. Light Yield

We have measured the light from minimum ionizing cosmic rays passing through 2.2 cm of BC517L liquid scintillator in a prototype multicell extrusion (12% TiO_2) shown in Figure 6.6. The cell size is 2.2 cm deep by 4.2 cm wide. The light was captured by a looped 0.8 mm WLS fiber and transported 16.4 m to an APD operated at a temperature of -15^0C. This prototype setup tests the basic NOνA detector cell using cosmic ray muons. The average signal for muons traversing the cell perpendicular to its walls was 13 photoelectrons (pe). Previous short sample measurements using a photomultiplier tube had predicted 15 pe. Based on the measured attenuation curve shown in Figure 6.4, the signal from the very end of the 16.7 m length would be 12.5 pe.

For the NOνA detectors proposed here, the cell size is modified from the prototype 2.2 cm (along the beam) by 4.2 cm (wide) to 6.0 cm (along the beam) by 3.9 cm (wide). The increase cell size will increase the energy deposited since the charged particle traverses almost three times more scintillator. In the larger cell, however, the fiber is typically farther from the reflecting walls, decreasing the light collected. Since we do not yet have an extrusion of this size, we have used our light collection simulation to determine a relative light yield from the two geometries. The simulation program includes the emission spectrum of the liquid scintillator, defuse reflection from the cell walls, and the absorption and reflection characteristics of the fiber. The simulation program predicts a ratio of 1.75 for the two cell geometries. Thus we expect that a minimum ionizing particle traveling in the beam direction and traversing a NOνA cell perpendicular to its walls 16.7 m from the photodetector will give a signal of 22 pe.

Event simulations show that 22 pe is sufficient for event discrimination. However we expect several simple improvements will increase the light yield by 20 to 30%. For example, increasing the reflectance by 1%, increases the light yield by about 10%. We expect at least this increase when the TiO_2 content of the PVC is increased from the 12% in our prototype extrusion to the design value of 15%. Figure 6.8 shows the reflectance measurement of the MINOS plastic scintillator cap, which has a TiO_2 content of 15% in polystyrene. This TiO_2 content is 3% higher than our current prototype extrusion in the relevant part of the spectrum but in a different plastic. Another light yield increase of greater than 10% can be achieved by controlling the position of the fiber in the cell as predicted by simulations shown in Figure 6.9 and verified by our measurements. With these changes, we expect at least 25 pe from the far end of the detector. Using the electronics described in Chapter 7 would then give a signal to noise ratio in excess of 10 to 1.

The prototype electronics used in our test setup have a noise level of about 350 electrons. Figure 6.10 shows the measured photoelectron distribution for a light yield of 25 pe with the prototype cell, fiber, APD, and electronics. The peak at 0 shows the pedestal caused by random coincidence triggers. The pedestal is separated from the single minimum ionizing signal.

A 10 to 1 signal to noise ratio is illustrated by Figure 6.11. In this case the cosmic ray muon signal was measured at 8.4 meters which gives a signal of about 35 pe and a noise of about 350 electrons. The ASIC proposed in Chapter 7, which is matched to the APD capacitance, has a noise of 250 electrons thus achieving the 10 to 1 signal to noise ratio with a signal of 25 pe.

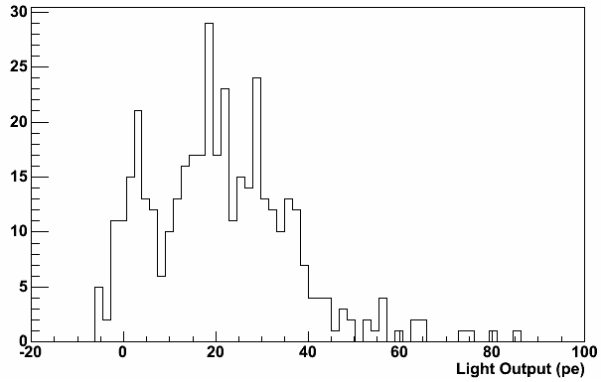

Fig. 6.10: Histogram of the cosmic ray muon signal from an 0.8 mm fiber with an average signal of 25 pe with a noise of about 350 electrons. The peak at 0 is the pedestal from random triggers.

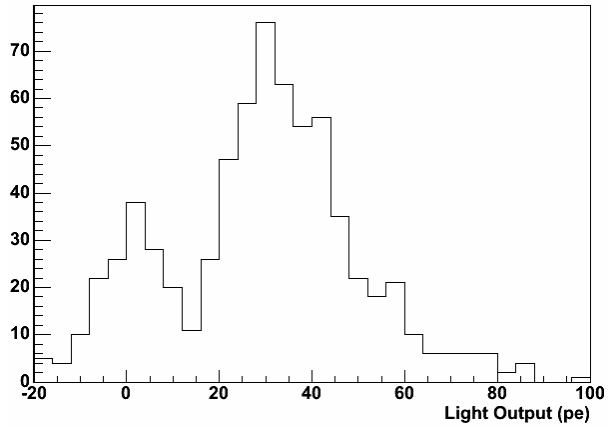

Fig. 6.11: Histogram of the cosmic ray muon signal from 8.4 m along a looped 0.8 mm fiber with the prototype cell, fiber, APD, and electronics. The average signal of 36 pe shows a 10 to 1 signal to noise with the existing electronics (350 electrons). The peak at 0 is the pedestal.

Chapter 6 References

[1] BC517L Material Safety Data Sheet (MSDS), www.bicron.com.

[2] P. Border, *et al.,* "A large liquid scintillator detector for a long baseline neutrino oscillation experiment," Nucl. Instrum. Meth. A 463 (2001) 194-204; L. Benussi, *et al.*, "Large liquid-scintillator trackers for neutrino experiments," Nucl. Inst. Meth. A 488 (2002) 503-516.

7. The Photodetector and Readout

7.1. Introduction

The function of the readout is to convert the optical signal from the wavelength shifting fibers into an electrical signal. The readout of the NOvA detector has two distinct tasks: (1) read out events caused by neutrinos from Fermilab and (2) operate between spills in a triggerless mode to collect cosmic ray events for calibration and supernova events if they occur. A trigger generated from the early stages of the Main Injector cycle can be used to form the gate for the in-spill events, while the other mode requires fast signal processing.

In our design the phototransducer is an avalanche photodiode (APD), one per detector channel, readout though a low-noise preamplifier. The APDs are in 32-channel arrays, with one array being coupled to all the fibers from a 32-channel detector module. The signal processing behind the preamplifier allows for two data acquisition modes to be operated alternatively: one on-spill and another between the spills.

7.2. Avalanche Photodiodes (APDs)

7.2.1. Overview: The proposed light detectors for the baseline design are avalanche photodiodes (APDs) [1] manufactured by Hamamatsu. They are similar to the 5 mm × 5 mm APDs developed for use in the Compact Muon Solenoid (CMS) detector at the CERN Large Hadron Collider [2]. Table 7.1 summarizes the key parameters of the NOvA APDs.

APDs have two substantial advantages over other photodetectors: high quantum efficiency and low cost. The high APD quantum efficiency enables the use of very long scintillator modules, thus significantly reducing the electronics channel count, while the per channel cost is about a factor of four less than that of a multi-channel photomultiplier tube (PMT). Figure 6.5 compares the quantum efficiency of a Hamamatsu APD to that of the PMT used in the MINOS Far Detector. In the wavelength region relevant to the output of the wavelength shifting (WLS) fibers described in Chapter 6, 500 to 550 nm, the APD quantum efficiency is 85% *vs.* 10% for the PMT. As shown in that figure, the quantum efficiency advantage of the APD increases with wavelength and thus the length of the fiber. This gives the APD an even greater advantage over a PMT for long fibers as shown in Figure 7.1.

Manufacturer	Hamamatsu
Pixel Active Area	1.8 mm × 1.05 mm
Pixel Pitch	2.3 mm
Array Size	32 pixels
Die Size	15 × 15 mm^2
Quantum Efficiency (>525 nm)	85%
Pixel Capacitance	10 pF
Bulk Dark Current (I_B) at 25 C	10 pA
Bulk Dark Current (I_B) at -15 C	0.15 pA
Peak Sensitivity	600 nm
Operating Voltage	400 ± 50 volts
Gain at Operating Voltage	100
Operating Temperature (with Thermo-Electric Cooler)	-15°C
Expected Signal-to-Noise Ratio (Muon at Far End of Cell)	10:1
APD channels per plane	384
APD arrays per plane	12
Total number of planes	1,984
APD pixels total	761,856

Table 7.1 Avalanche Photodiode Parameters.

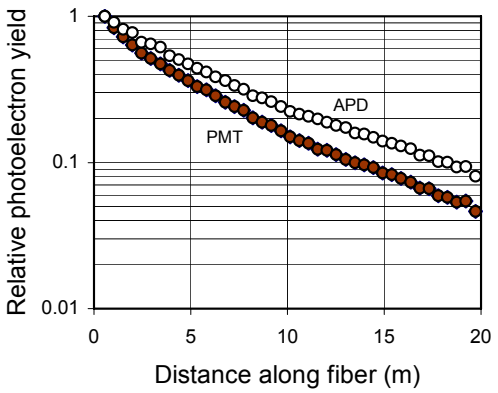

Fig. 7.1: Relative photoelectron yield from 1.2 mm diameter WLS fiber, for APD and a PMT with a bialkali photocathode. The data have been normalized at 0.5 m to illustrate the effect of the longer wavelength response of the APD.

The commercially-available Hamamatsu APD has a pixel size of 1.6 mm by 1.6 mm. A photograph of the 32 pixel APD package is shown in Figure 7.2. We will use a 32 pixel array of APD's in the bare die form and mount the chip, cooler, electronics and optical coupler on a printed circuit board.

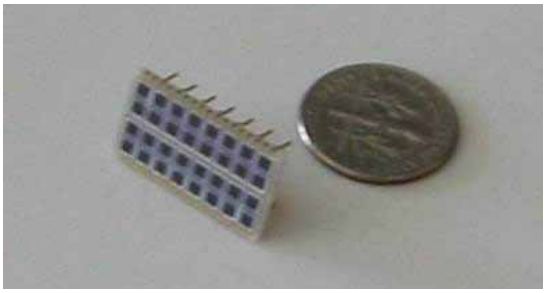

Fig. 7.2: A commercially available Hamamatsu APD package shown with a dime. Two 16 pixel arrays are packaged together.

7.2.2. Photodetector Requirements: Photodetectors for the NOνA Far Detector must be able to efficiently detect single minimum ionizing particles traversing the far ends of scintillator strips, ~16.7 m (of fiber length) away. Each photodetector pixel should be large enough to collect the light from both ends of a 0.8 mm diameter looped fiber.

Based on the measurements described in Section 6, we estimate that a single minimum ionizing particle, normally incident at the far end of a liquid scintillator tube, will produce ~30 photons at the face of the APD. The quantum efficiency for an APD in the region of the spectrum where the light is emitted is 85%, giving a signal for such a particle of ~25 photoelectrons. This signal must be distinguishable from the noise with high efficiency. One of the operational characteristic of APDs, and, in fact, all silicon devices, is the thermal generation of electron hole pairs which mimic the signal. The thermally generated electrons are amplified at the diode junction and appear at the input to the pre-amplifier and thus contribute directly to the noise. To reduce this generation rate to a manageable level we will lower the operating temperature to -15^{o} C using thermo-electric (TE or Peltier-effect) coolers. These are very common commercially available devices.

7.2.3. Fundamentals of APD operation: The general structure of an APD is shown in Figure 7.3. Light is absorbed in the collection region, electron-hole pairs are generated and, under the influence of the applied electric field, electrons propagate to the p-n junction. At the junction, the electric field is sufficiently high that avalanche multiplication of the electrons occurs. The multiplication (M) of the current is determined by the electric field at the junction, and by the mean-free-path of electrons between ionizing collisions, which depends on both the accelerating field and on the temperature. This temperature dependence occurs because the probability of electron-phonon scattering increases with temperature.

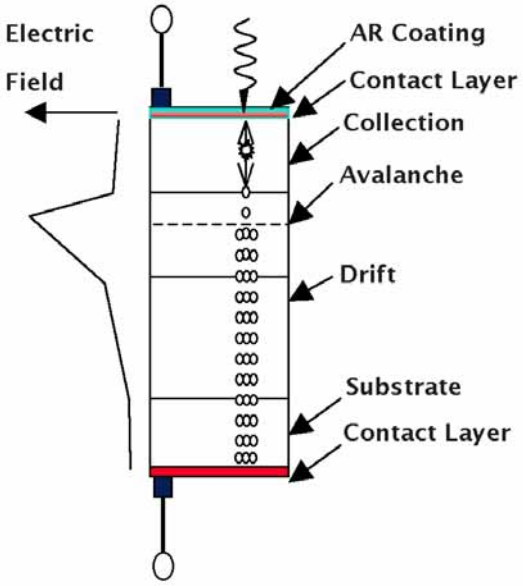

Fig. 7.3: The basic structure of a blue/green sensitive APD. Light crosses the anti-reflection coating at the surface and is absorbed in the collection region. Photoelectrons drift in the electric field to the junction where they undergo avalanche multiplication.

APDs, like PIN diodes, have an intrinsic noise that comes from the electron-hole pairs generated thermally in the depletion region of the diode. Since the current from the positive carriers is amplified about fifty times less than the negative carrier current at the junction, only the current from electrons generated in the photo-conversion region (I_B), or the bulk current, needs to be considered in the noise current estimation. As it is a thermally generated cuurent, it can be reduced by lowering the operating temperature of the APD. We will operate the APDs in the NOνA detector at

-15° C to keep the noise contribution from I_B small in comparison to the front-end noise. This choice is based on measurements obtained with the prototype readouts.

Besides this source of noise, the amplification mechanism is itself subject to noise, characterized by the excess noise factor F, with such factors as device non-uniformities and the ratio of the positive to negative impact ionization coefficients contributing. This factor is well modelled and has been included in our signal to noise calculations.

One of the attractive features of APDs is that once they have been calibrated, the gain can be easily determined from the applied bias voltage and the operating temperature. In the NOνA detector, we will maintain the operating bias to a precision of 0.2 Volts and control the temperature to 0.5° C and thus hold the gain stability to about 3%.

7.2.4. Experience with the CMS APDs: The CMS experiment is using 124,000 Hamamatsu APDs, with 5 mm × 5 mm pixels, to read out the lead-tungstate calorimeter. The full order has been delivered to the experiment and tested. The quantum efficiency for these devices is consistently at 85% at 550 nm as can be seen in the Figure 7.4.

7.2.5. APDs for the NOvA Detector: We have purchased Hamamatsu's of-the-shelf APDs for our measurements. The measured dark current, pixel gain and pixel separation for one of the sample arrays are shown in Figures 7.5, 7.6 and 7.7. The dark current is consistent with expectations from CMS APD measurements, and the gain is uniform from pixel to pixel on the same chip and within an individual pixel. The fall-off on the pixel edges in Figure 7.8 mostly reflects the finite spot size used to illuminate the APD pixels.

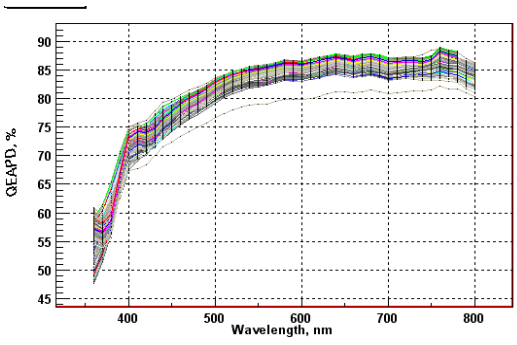

Fig. 7.4: Quantum efficiency of several hundred CMS APDs.

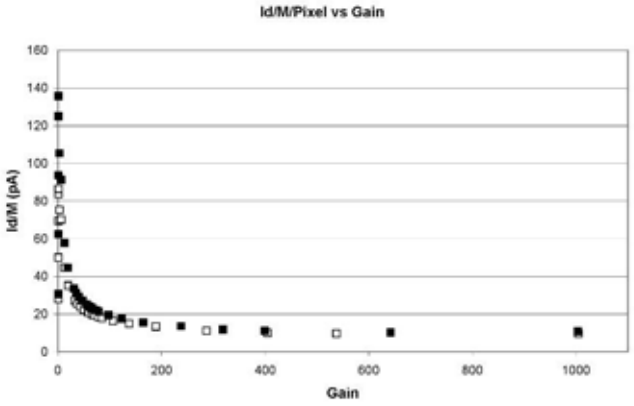

Fig. 7.5: Dark current I_d divided by gain *vs.* gain in a commercial Hammatsu APD at 25 C. The asymptotic value of the current is I_B , which is 10 pA for this sample.

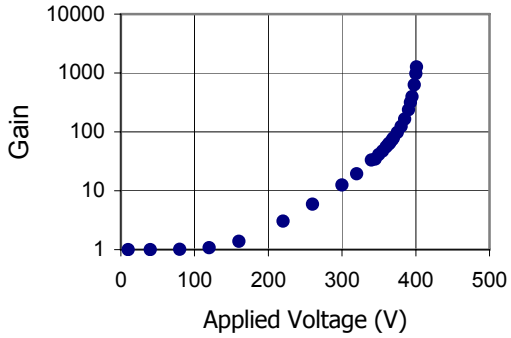

Fig. 7.6: Gain *vs*. applied voltage at 25 C.

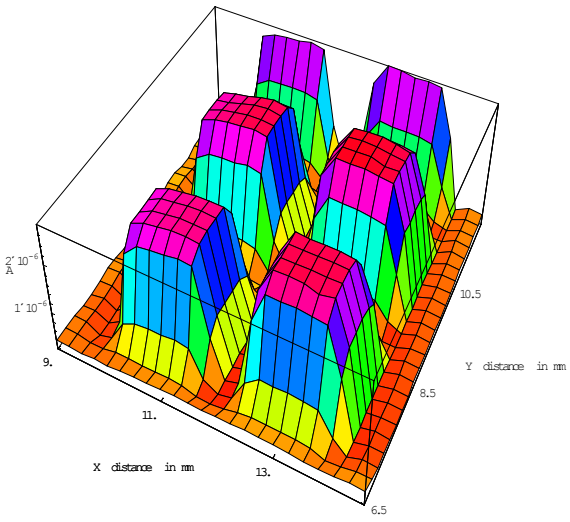

Fig. 7.7: Fine point scan across part of the APD array.

7.3. The Readout Electronics.

The readout of the APDs requires a preamplifier that can sample the signal throughout a 10 μs spill gate. The proposed architecture is based on the Fermilab MASDA (Multi-Element Amorphous Silicon Detector Array) chip [4,5,6] and the SVX4 (a multi-channel amplifying and digitizing chip developed for CDF and D0). An ASIC has been designed and simulated specifically for this readout. It has two operating modes which can be selected electronically, one for gated in-spill collection and another for the triggerless mode. In the design the dual correlated sampling (DCS) method or a multiple correlated sample method is used to remove the common mode noise.

7.3.1. Signal-to-Noise: We have investigated the performance of the APD coupled with the MASDA ASIC, which uses the dual correlated sampling (DCS) technique, to investigate the noise performance that can be achieved with a cooled APD. The MASDA is optimized for 70 pF input capacitance, rather then the 10 pF of the APD, so these measurements are upper limits. Figure 7.8 shows the measured noise of several APD's operating at a gain of 100. At about -10° C the noise plateaus at around 300 electrons, indicating that the contribution from the dark current has become negligible.

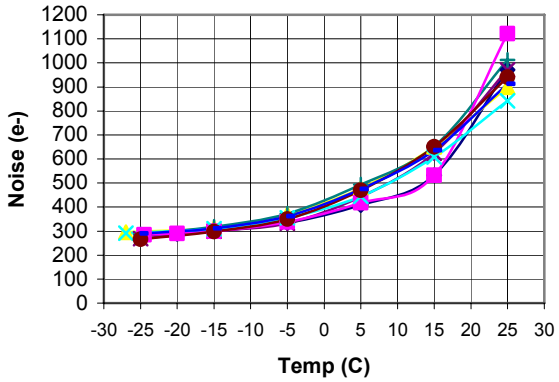

Fig. 7.8: Noise measurements of the readout of an APD operating at a gain of 100, as a function of temperature. The readout used in this test was the MASDA ASIC which was optimized for 70 pF input capacitance.

The computed noise level for the chip that we have designed specifically for this application operating with an APD at a gain of 100 and cooled to -15° C is 150 electrons. From this we estimate that the real noise levels for production devices will be ~ 200 electrons. This is much lower than normally associated with readout electronics because we are using the DCS method, which eliminates much of the correlated noise.

For our discussion we will always refer to the noise level at the photo-electron level, thus with the APD at a gain of 100, the 200 equivalent noise charge (ENC) reduces to 2.0 photoelectrons at the photodetector input. This is to be compared with the 25 photoelectron signal we expect from a muon at the far end of the channel.

We have measured the bulk dark current (I_B) for several APDs and the average value per pixel as 10 pA at 23°C. This is consistent with the bulk dark current of the CMS APD: 5 pA/mm^2, corresponding to 12 pA/pixel. A current of 10 pA corresponds to a current of 62 electrons every microsecond. At our operating temperature of -15 C, the APD background rate is then 2 thermally-generated electrons in our 1 μs sampling time with a rms noise of 1.4.

The requirement for the readout is then to detect a signal with an average value of 25 photoelectrons spread over a short time interval, with a background rate of 2 thermally-generated electrons per microsecond using an amplifier with an effective ENC of 2.0 electrons. Figure 7.9 shows the estimated signals from one and two minimum ionizing particles, considering all noise factors, including amplification noise, compared with the noise. In making this graph we have assumed that the ENC of the amplifier is 2.5. The graph shows good discrimination between zero, one and two normally incident muons crossing the far end of the scintillator strip. For comparison, Figure 7.10 shows the actual signal measured using the current prototype described in Chapter 6 using light injection to generate a signal corresponding to one and two minimum ionizing particles at the end of the proposed detector (25 and 50 pe).

7.3.2. Digitizing and Readout Architecture: We have examined several different readout architectures and have settled on a baseline design based on the SVX4 structure that makes use of the DCS method of the MASDA chip. The ASIC has several modes of operation. In one mode – the

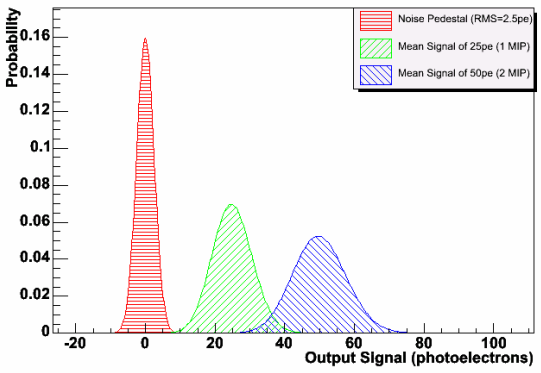

Fig. 7.9: Expected APD signals from noise, 1 and 2 minimum ionizing particles. The calculation uses a total noise of 250 electrons and signal levels of 25 and 50 photoelectrons.

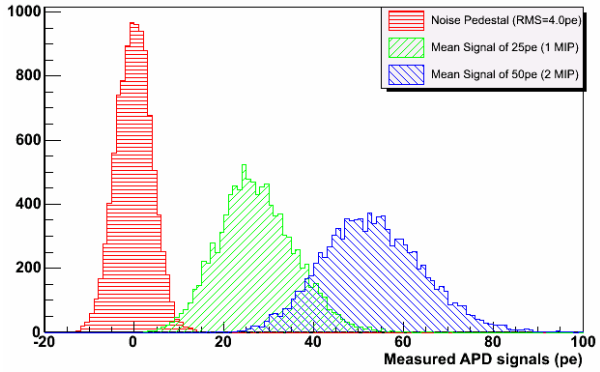

Fig. 7.10: Measured APD signals from noise, 1 and 2 minimum ionizing particles using the current prototype electronics. This measurement has a total noise of about 400 electrons and signal levels of 25 and 50 photoelectrons generated by light injection.

high precision mode - the data are stored in a 32-channel wide 64 deep switched capacitor array (SCA) during the spill and digitized afterwards. This minimizes any risk of noise from the conversion appearing at the signal inputs. The signal from each APD is amplified by a high gain integrating amplifier with a shaping time of ~350 ns and the output is stored in the SCA every 500 ns. After the beam spill, the SCA contains 64 samples taken 500 ns apart for the 32 APD channels. The difference in the stored signals, taken 1 μs apart for all 32 channels, are compared in parallel with a linear ramp and the crossover times stored, as in a Wilkinson ADC. When this digitization is complete, the difference between the next pair of stored signals is converted. At the end of the conversion every digitized difference is stored in an field programmable gate array (FPGA) for transmission to the data acquisition (DAQ) system. The chip's architecture is shown in Figure 7.11. In this design the gate width can be up to 30 μs; this is wide enough to accommodate uncertainties in the foreknowledge of the beam arrival time.

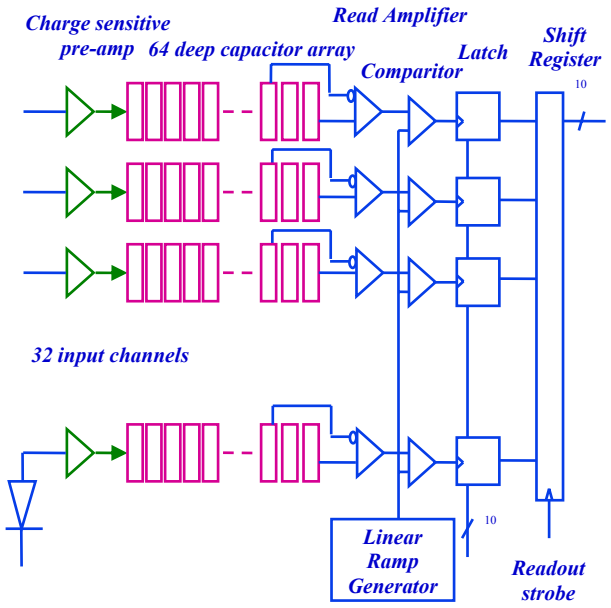

Fig. 7.11: Proposed architecture of the front-end electronics ASIC. Shown here is the configuration that would be used for data collection during the spill and digitization after the spill.

In addition to the in-spill data taking mode we have designed the possibility of taking data in a triggerless mode so that the detector can be used to search for supernova events and to collect cosmic ray data. A supernova signal would be a large number of small energy depositions spread over an interval of several seconds. To collect data in this mode the linear ramp is stopped earlier, reducing the dynamic range from 100 to 8 MIP's, or a pseudo-logarithmic ramp is used which achieves the full dynamic range at the expense of resolution of large signals. Here one MIP is defined as the signal of a minimum ionizing particle crossing a liquid scintillator cell at the far end of that cell, a 25 photoelectron signal.

7.3.3.Further improvements: We have been investigating a method to further reduce the noise levels by using multiple, rather than just two, correlated samples. Since the data rate in the NOνA detector is low, we can use considerably more signal information than would be available with DCS and by using many consecutive samples we can further reduce the noise. The degree to which the signal to noise ratio (SNR) can be improved will depend on the detailed noise spectrum of the front end integrator and APD combination. If the noise is dominated by APD leakage currents then any gains will be small, but if the noise is completely dominated by the integrator front end and the APD capacitance, then the signal to noise ration would improve by $\sqrt{N}$, where N is the number of pairs of data points used. As discussed above, both noise components will be present. Tests performed on a prototype system have achieved a 25% improvement in the signal to noise ratio over dual correlated sampling and we anticipate an improvement of this order could be achieved if we implement this method. This would entail converting the individual samples stored in a SCA rather than the differences. The most significant difference would be in the complexity of the FPGA firmware.

In addition to improving the noise performance, time resolution can also be improved. To study this we have conducted tests to establish the limits of the timing resolution that can be achieved. In our baseline with 500ns sampling of the integrator waveform, a timing resolution of no better than the sampling interval divided by $\sqrt{12}$, or about 145 ns can be achieved. We have examined various digital signal processing techniques for timing resolution improvement. The most promising of these is a combination of "matched filtering" and "interpolation" filters. The matched filter output is the cross-correlation between the incoming signal and an ideal version taking by averaging over many signals. This yields a fairly symmetric output, upon which a low-pass interpolation filter is applied. This filter supplies a 10:1 interpolation between the 500ns data points, providing computed points every 50ns. These calculations, while currently done off-line, can be easily done in firmware on the FPGA. As one might expect, the resulting timing resolution depends on pulse height. For very small signals, the timing resolution is about the same as DCS, while for larger pulse height, it is up to five times better.

In summary, in our baseline design there is a FPGA on each front end board to handle control and data transmission. Digital signal processing algorithms could be encoded in the FPGA firmware to improve both SNR and timing resolution. This would require that data collected during the beam spill are the stored as signals instead of differences. We will continue to evaluate the possibility of employing these advanced signal processing methods as needed.

7.4. Mechanics

Each module will have a single readout box mounted on it, with a single 32-channel amplifier reading out a 32 pixel APD which will be connected to the 32 channels in the detector module. The operating voltage (400 ± 50 V) to bias the APD array will be supplied from an on-board high voltage generator designed for this purpose, an integrated circuit based on the Cockroft-Walton technique. The APD array will be cooled by a single-stage TE cooler. The thermal power generated in the APD array is ~25 μW, so the most significant thermal load will be from local conduction along the fibers and through the electrical interconnects. The TE cooler will produce less than 2W of heat for each 32 channel liquid scintillator module. Temperature monitoring and control, clock regeneration and I/O functions will be controlled with a low-power FPGA. The APD array will be mounted on the opposite side of the board from the other electronic components to minimize the thermal load. The mounting will be done with flip-chip technology, so the active area will be facing a hole cut out in the electronics board (PCB) where the fiber ends will be located. The flip-chip method provides an accurate way to align of the APD to the PCB, to which the fiber connector will also be aligned.

A box housing the APD and the associated electronics will be connected to the end of each scintillator manifold. The APD box has several functions: (a) align the fibers to the APD array, (b) provide a light tight connection to the scintillator module, (c) house the APD and the associated electronics, (d) remove heat from the electronics and the TE-cooler, (e) protect the cold surfaces from humid air to prevent condensation and (f) provide structural strength. The manifolds are designed such that a module can be connected into a

single APD box. This modularity allows for testing of the complete system prior to installation.

The APD arrays, the PCB, the heat sink, and the electronics are housed in an aluminum sheet-metal box that serves as a Faraday cage. The box also contains connectors for the low voltage, clock signals and electronics readout. The APD box will also be light tight. A schematic of our concept of the APD housing showing is shown in Figure 7.12.

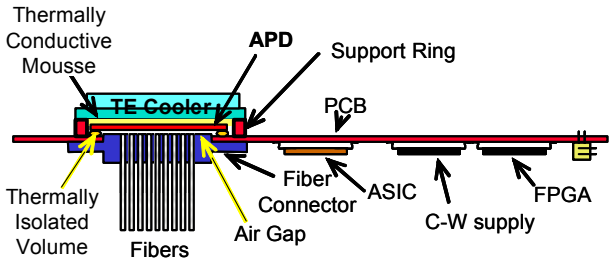

Fig. 7.12: Side view of the components in an APD electronics box. The box receives the signals from a scintillator module through an optical connector. A TE cooler is connected to the APD through an electrically insulating, thermally conducting material. The hot side of the TE cooler is in thermal contact with a heat sink to remove the heat from the box. The APD is mounted on the PCB using the flip-chip method.

7.5. Data Acquisition

7.5.1 Data Acquisition Modes: The primary task for the readout and data acquisition system is to concentrate the data from the large number of APD channels into a single stream, which can be analyzed and archived. The specifications of the (DAQ are given in Table 7.2. The complexity of the DAQ electronics comes from the requirement that system is both externally triggered, for in-spill events, and triggerless for cosmic ray and supernovae events. We will discuss both these modes of operation in turn.

APD boxes per plane	12
APD channels per box	32
Digitization	10 bits every 0.5 μsec
Digitization in triggerless mode	7 bits every 0.5 μsec
Noise rate per channel	$<10^3$ Hz
Bytes per hit (channel ID, TDC, ADC, status)	≤8

Table 7.2: Specifications for DAQ system.

The externally triggered system is "live" for only a short period of time, ~30 μs surrounding the neutrino beam spill. The actual beam spill will be 10 μs allowing a large margin for predicting the arrival time of the neutrino pulse. The upper limit is determined by the depth of the SCA memory. We plan to use the $23 and $A5 signals from the Main Injector which occur 1.4 s before the spill and predict the beam arrival time to within ± 5 μs.

For triggerless operation, the data will be input continuously to an FPGA where it will be sparsified and stored. We would use trigger processors to analyze the data stream looking for hit clusters that might indicate an interesting event.

The data rate per APD box is ~0.5 MB/s, so that an average of 10 bytes is produced per APD box per 20 μs readout, yielding approximately 100 kB per readout for the entire detector. If the readout is triggered randomly at ~100 Hz to measure cosmic ray background, the total data rate is ~10 MB/s. In comparison, the total data rate for the entire detector with a continuous readout mode is estimated to be 5 GB/s.

The DAQ threshold is set to satisfy two requirements: efficient detection of a minimum ionizing particles and a low noise rate so that the DAQ system is not overwhelmed by spurious hits. Since the system will digitize everything in a spill gate, the threshold can be adjusted to meet these goals. For example, assume an electronics noise level of 250 electrons, an APD gain of 100 and a mean signal from a minimum ionizing particle of 25 photoelectrons, or 2500 electrons after the APD. If we set a threshold of 1200 electrons, we expect greater than 99% efficiency for a minimum ionizing particle with a probability for a noise hit of less than 3×10^{-6} in 1 microsecond.

7.5.2. System Architecture: The overall concept of the readout and DAQ system is similar to that of other experiments. Digitized signals from each ASIC are input into a FPGA. This applies zero suppression and timestamps, and then buffers the digitized values before serialization and transmission to the DAQ. The FPGA can also provide control and monitoring of the APD box. The APD-box FPGA provides an external interface using standard Ethernet protocols. The baseline design specifies less expensive electronic Ethernet interconnections using standard Cat5 cabling. Optical interconnections have the advantages of higher bandwidth and no ground loops at somewhat

higher system cost. The final choice will require value engineering.

The overall organization of the DAQ system will be as a collection of local rings readout through Readout Concentrator Nodes (RCN) as shown in Figure 7.13. The advantage of the ring architecture is that the loss of any single ring member disables only that element and not the entire ring. For design simplicity and to reduce requirements for spares, each APD box will have a switchable capability to act as either a ring master or a ring slave. The baseline design is to connect 96 APD boxes from 8 successive planes into each local ring. This gives 1994/8 = 250 rings. Since the total detector data rate is 10 MB/s, the rate per ring is ~100kB/s.

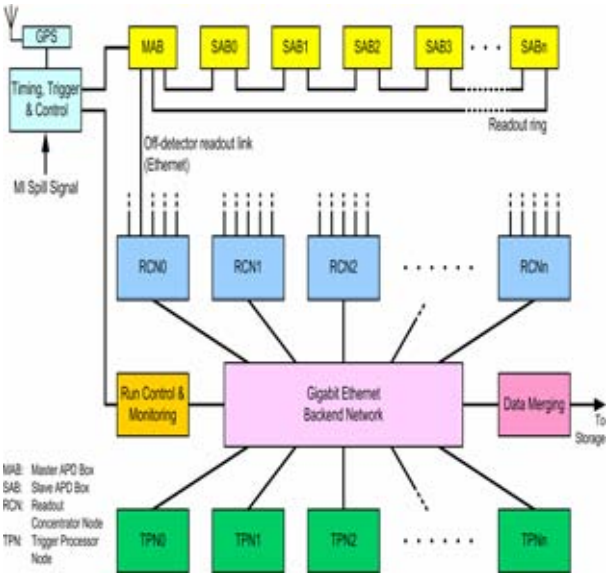

Fig. 7.13: Overview of the entire DAQ system: The data from a number of Slave APD Boxes (SAB) will be collected and transmitted by a Master APD Box (MAB) via Ethernet. Data from a number of MAB will be funneled via Ethernet into a Readout Concentrator Node (RCN). The RCNs will transmit this data via Ethernet to trigger processor nodes (TPNs). The TPNs will run trigger algorithms on this data to decide which data to write to the data storage. A timing system will distribute clock signals (locked to the GPS time) to all MAB. These signals would be redistributed by the MABs to the SABs. The timing system also receives the Main Injector spill signal for redistribution.

We expect to use ~25 Readout Concentrator Nodes (RCNs) to collect data from the APD box Ethernet rings. The RCNs will be PC's with multiple Ethernet cards. Each ringmaster APD box will be connected to a dedicated Ethernet interface card on a RCN. The RCNs will direct all data from a specific trigger to one of several Trigger Processor Nodes (TPNs). The TPN that receives all the data from one particular trigger will then determine whether and how the data from that trigger should be archived for later off-line analysis.

Control information will follow an inverse path via the same network. Detector Control System (DCS) computers will send data to the RCNs, which will then distribute control signals to the master APD boxes which will then pass control information around the readout rings.

7.5.3. Timing System: The synchronous readout of data from the detector in the system proposed here requires distribution to the APD boxes of (a) 2 MHz clock, (b) a 1 pulse per second (PPS) signal to reset the hit timestamp counter and (c) a readout trigger ("spill") signal.

These signals are easily modulated onto a 10 MHz carrier frequency, so only a single pair of cables is needed to distribute them. The timing signals are centrally generated and fanned out to the master APD boxes. These boxes distribute the timing signals to all other APD boxes in the ring.

The clock and PPS signals would be locked to a GPS receiver, providing a stable, high-quality absolute time reference for the detector. In order to trigger a readout in time with a beam spill, the spill signal generated at the Main Injection must arrive at the central timing unit around 1 ms before the neutrinos arrive at the detector. A well-defined route for this signal is therefore necessary; either via a reliable, low-latency network connection from FNAL, or possibly via a dedicated radio link.

Chapter 7 References

[1] "Avalanche photodiodes in scintillation detection," Nucl. Instrum. Meth. A 497 (2003) 226-233; D. Renker, *et al*., "Properties of avalanche photodiodes for applications in high energy physics, astrophysics and medical imaging," Nucl. Instrum. Meth. A 486 (2002) 164-169.

[2] K. Deiters, *et al.,* Nucl. Instrum. Meth. A 461 (2001) 574-576; Nucl. Instrum. Meth. A 453 (2000) 223-226; Nucl. Instrum Meth. A442 (2000) 193-197.

[3] A good summary of APD theory, including noise, is given in the CMS ECAL TDR, CERN report CERN/LHCC 97-33.
[4] M. Maolinbay, *et al*., "Design and performance of a low noise, 128 channel ASIC preamplifier for readout of active matrix flat panel imaging arrays," NIM A 485 (2002) 661-675.
[5] T. Zimmerman, "The MASDA-X chip – a new multi-channel ASIC for readout of pixilated amorphous silicon arrays," Fermilab technical note FERMILAB-TM-2063 (1998).
[6] R. Yarema, *et al*., "A programmable, low-noise, multi-channel ASIC for readout of pixelated amorphous silicon arrays," presented at the 8th European Symposium of Radiation Detectors, Sloss Elmau, Germany, June 14-17, 1998 (submitted to NIM).

8. Far Detector Site, Building, and ES&H Issues

8.1. Detector Site Criteria

We have chosen a location near Ash River, Minnesota as the NOνA Far Detector site. Ash River is about 810 km from Fermilab. We examined more than a dozen possible sites for the NOνA Far Detector as well as multiple detector locations within several particular sites. Possible sites begin ~710 km from Fermilab, near the city of Aurora MN, and continue to the north-northwest until a point in Ontario that is about 900 km from Fermilab. Sites more distant than ~900 km are too far off-axis to have desirable beam characteristics because of the beam's upward inclination of 3.3° and the curvature of the Earth. The sites we examined were all near the half-dozen or so east-west all-weather roads that cross the NuMI beamline.

Our principal site selection criteria were:

- Availability of land approximately 10-14 km (12 – 17 mrad) off-axis from the NuMI beam.
- As far as practical from Fermilab. A longer baseline is more sensitive to resolution of the mass hierarchy.
- A site with year-round road access at the maximum trunk highway weight limit, adequate electrical power and T-3 capable communications access. Other geographic criteria included access to workers, road transportation and airports and proximity to support services such as hotels, restaurants, gasoline and other retail outlets.
- A site with at least 20 and more likely 40 acres of usable land (not wetlands) which would permit a layout of a ~200 m by ~40 m footprint for a detector building oriented with its long axis pointing towards Fermilab.
- A site which would likely enjoy strong local support. The selection should not result in land use controversies or litigation. The characteristics of the site must also facilitate a straightforward environmental permitting process.

8.2. The Ash River Site Characteristics

The Ash River site is on the Ash River Trail (St. Louis County Highway 129) near the entrance to Voyageur's National Park. The site is west of the NuMI beam centerline and has the unique property of being the furthest site from Fermilab in the United States. See Figure 8.1.

Ash River is located about 15 km east of U.S. Highway 53, about 40 km east south east of International Falls MN. By car, it is about an hour drive from International Falls which is served by a Northwest Airlines affiliate from Minneapolis with four flights per day. By car, the site is about a 2 hour drive from the airport at Duluth and about a 4 hour drive from the Minneapolis airport. Driving time from Soudan to Ash River is about 1.5 hours.

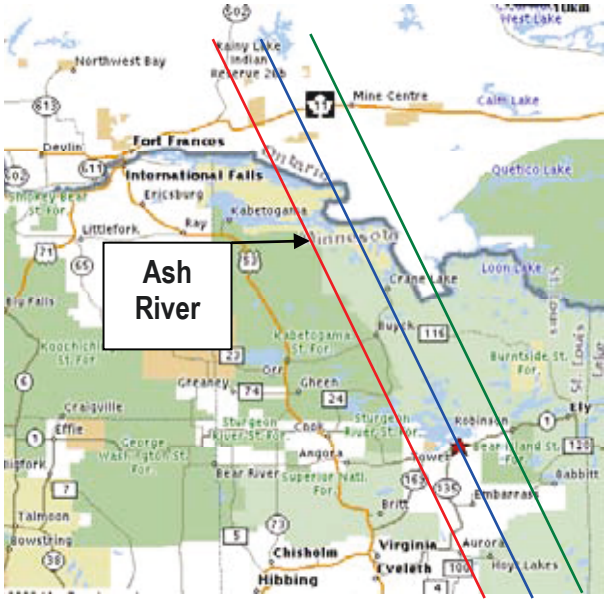

Fig. 8.1: Map showing our preferred site. The red star indicates the site of the Soudan Underground Laboratory. The beam centerline passes through Soudan; the left line is ~13 km (~ 16 mrad) west of the centerline, while the right line is ~13 km east of the centerline.

The actual detector laboratory locations at the Ash River Trail site are in Sections 12, 13 and 14 of Township 68 North, Range 15 West, St. Louis County MN. These locations are shown in Fig. 8.2 on the 1:24000 USGS topographic map. All locations would require upgrading of the access road, mostly with an improved gravel base and culverts for drainage (or a new road in the case of Site F).

The sites are located near Voyageur's National Park, but GIS studies by the National Park Service

suggest that the Detector Laboratory would be essentially invisible from the Park because of intervening high terrain (except for Site F). These sites are all ~810 km from Fermilab. The detailed parameters of all six locations are listed in Table 8.1.

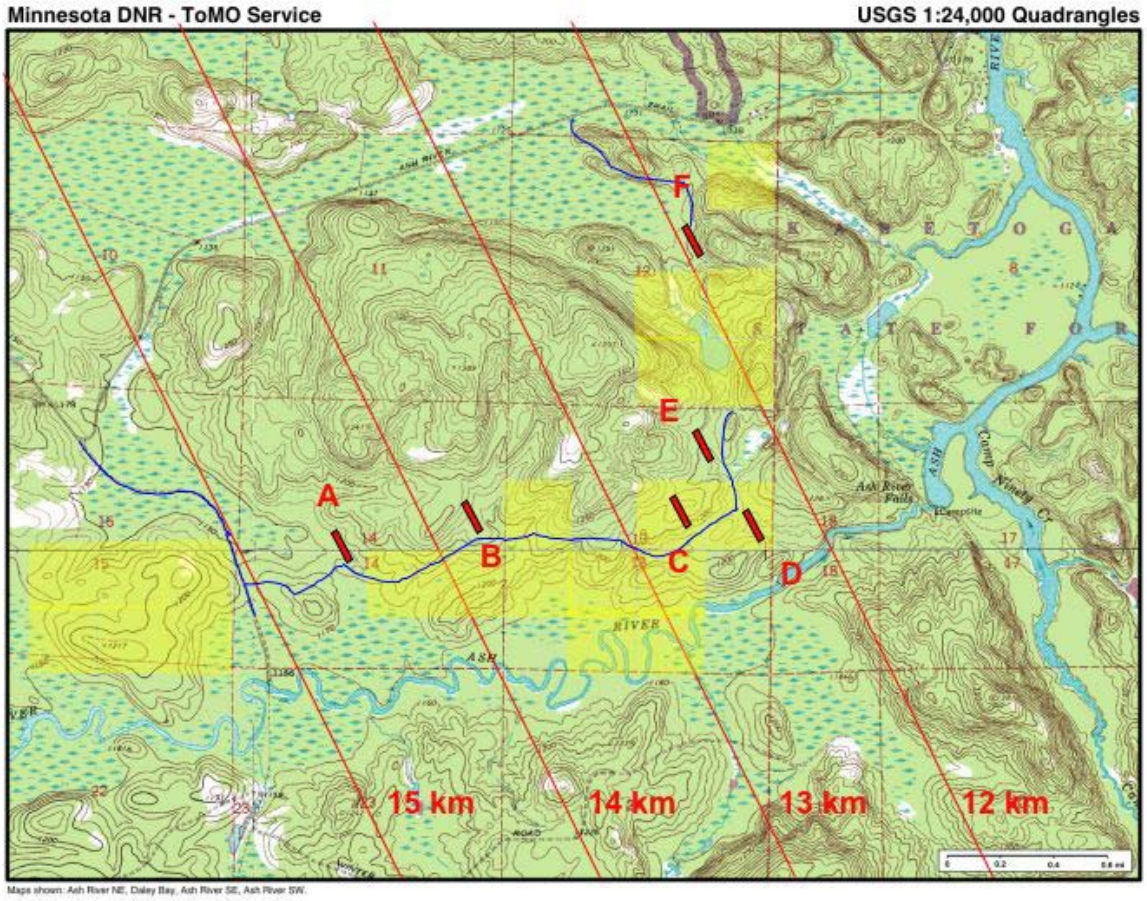

Fig. 8.2: The USGS topographic map for the Ash River Trail sites. The rectangles show a 200 m by 40 m laboratory footprint. The yellow shaded land near the laboratory sites belongs to Boise Cascade. Other land in this area belongs to the State of Minnesota.

Location	Description	Latitude	Longitude	L (km)	T(km)	Angle (mr)	Ownership
A	SENW Sec. 14	48.375°	92.869°	811.4	14.37	17.6	State
B	SENE Sec. 14	48.377°	92.857°	811.2	13.51	16.7	State
C	SWNE Sec. 13	48.378°	92.841°	810.7	12.46	15.4	BCC
D	SENE Sec. 13	48.377°	92.836°	810.5	12.19	15.0	BCC
E	NWNE Sec. 13	48.381°	92.840°	811.0	12.26	15.1	State
F	SWNE Sec. 12	48.391°	92.840°	812.0	11.81	14.5	State

Table 8.1: Parameters of Sites Near the Ash River Trail. The angles in the table are the full space angle relative to the beam which is about 4.2 km above ground at Ash River.

All detector locations shown in Figure 8.2 are on relatively flat land with few, if any, obvious rock outcrops. Thus, it is reasonable to believe that all of these sites have at least a few meters of soil cover over bedrock. Core drilling will be required to more completely characterize a chosen location. Most of the locations are forested with small aspen trees. In forestry terms, they are generally described as areas of aspen regeneration.

The access to the Ash River Trail site is via U.S. Highway 53, St. Louis County Highway 129 and then via a private road ~ 1-3 km in length, depending on the specific site that is chosen. Highway 129 has some weight restrictions that will necessitate some load rearrangements for ~ 45 days each Spring. There is an existing 7.2 kV, 3 phase power line that runs essentially along the highway. The local power company estimates that 500 kW is readily available with existing facilities; 1 MW or more of power consumption would require an upgrade of the current line. There is an existing fiber optic line along U.S. 53 and along the Ash River Trail.

The site would require installation of utilities along the access road. Domestic water would likely come from one or more wells, which might also be used to fill a storage tank for fire protection water if required (foam fire suppression systems are probably preferred for PVC and liquid scintillator). Domestic sewage would require either a septic system or a holding tank with periodic disposal.

The settlement of Ash River (U.S. Mail address: Orr MN 55771) is located at the end of the Ash River Trail, about 2 km east of the proposed detector site. This area has several motels and restaurants, although much of the activity is seasonal. (See www.ashriver.com for a listing of hotels and restaurants.) There is a new gas station and convenience store at the intersection of the Ash River Trail and U.S. 53, about 12 km from the laboratory site.

At this time, the University of Minnesota is taking preliminary steps towards land acquisition and environmental review of the Ash River sites. Although the University of Minnesota has authority to determine zoning and permitting with respect to its property within Minnesota, minimal land use controversy will facilitate the laboratory construction.

8.3. ES&H Issues

Recent exchanges [1] with the Fermilab Environment, Safety and Health Section have indicated that NOνA will need a DOE Environmental Assessment much like the one [2] done for NuMI and MINOS, and that three NOνA components will require special consideration. The first of these is the impact of a major discharge of liquid scintillator to the environment. While a credible scenario resulting in the discharge of the full 23,885 tons of liquid scintillator is difficult to imagine, the Fermilab ES&H Section advises that we design for containment of the full inventory. This will impact our building design in the next section.

The other two special ES&H issues for NOνA are the flammability of liquid scintillator and rigid PVC and the implied fire protection requirements. The Fermilab Fire Protection engineer has studied both liquid scintillator and PVC [3, 4]. The PVC was found not to ignite or become flammable or drip material when it was subjected to various ignition sources, even when it was covered with the liquid scintillator. The BC-517L tested could be ignited with a torch but was difficult to ignite with a low energy flame even when the liquid was pre-heated to 150 ^{0}F. Additional testing will be done with the liquid scintillator under pressure to simulate the conditions of melting PVC forming pinholes and spraying the liquid scintillator onto surrounding surfaces.

The Fermilab Fire Protection Engineer advises that we plan a zoned fire suppression system of either dry chemical or non-alcohol foam. Fire fighting with normal water sprinklers is ineffective since the liquid scintillator has a density of 0.86 g/cc. In addition the runoff from fire fighting with water would have to be held in containment due to environmental concerns.

8.4. Building

The 30 kiloton NOνA Far Detector requires a detector enclosure ~170 m long by ~22 m wide by ~22 m high. This is a substan-

tial structure, so we commissioned two design studies to get a handle on the costs and cost drivers for such large buildings. The first study was sponsored by the University of Minnesota and was performed by CNA Consulting Engineers with subcontracts to Dunham Associates and to Miller-Dunwiddie Architects [4]. This CNA study focused on a cut and cover approach deep in bedrock with a 10-meter overburden to cover a "worst-case scenario" of a possible required cosmic ray shield. As outlined in Chapter 10, we do not believe such an overburden is required.

The second study was done by the Fermilab Facilities Engineering Services Section [5] and focused instead on zero overburden. The Fermilab design was for buildings at any depth but with an above ground portion similar to experimental laboratory buildings at Fermilab. The minimum case has an excavation just down to bedrock to ensure the 30 kilotons is sitting on a solid surface. Bedrock at most of the sites considered above is expected to be under only 10 to 15 feet of soil till.

While the two building design studies had different goals, they did agree with each other in cost at the 20% level when the Fermilab design at the surface was compared to a similar surface design subsection of the Minnesota design done by Miller-Dunwiddie. In addition, both designs had common assumptions about the general site, for example including modest costs for short roads connecting to existing roads and modest cost to bring in nearby power. The Ash River Sites are a close match to these assumptions.

The secondary containment issue discussed in Section 8.4 led us to a building design with the floor level ~ 9 meters below grade. The building is ~ 5 meters wider than the detector and ~ 25 meters longer than the detector as shown in Figures 8.3 and 8.4. The detector therefore sits in a concrete bathtub which is sized to hold the entire inventory of liquid scintillator. This containment design is similar to that used for MiniBooNE at Fermilab. In addition we would paint the inside of the bathtub with epoxy-based paint to ensure the liquid scintillator cannot leave the building. This copies the recent retrofit efforts at the Gran Sasso laboratory. Interior grating covered gutters will direct small scintillator spills to a special sump. All floors and walkways would slope gently towards the gutters which in turn

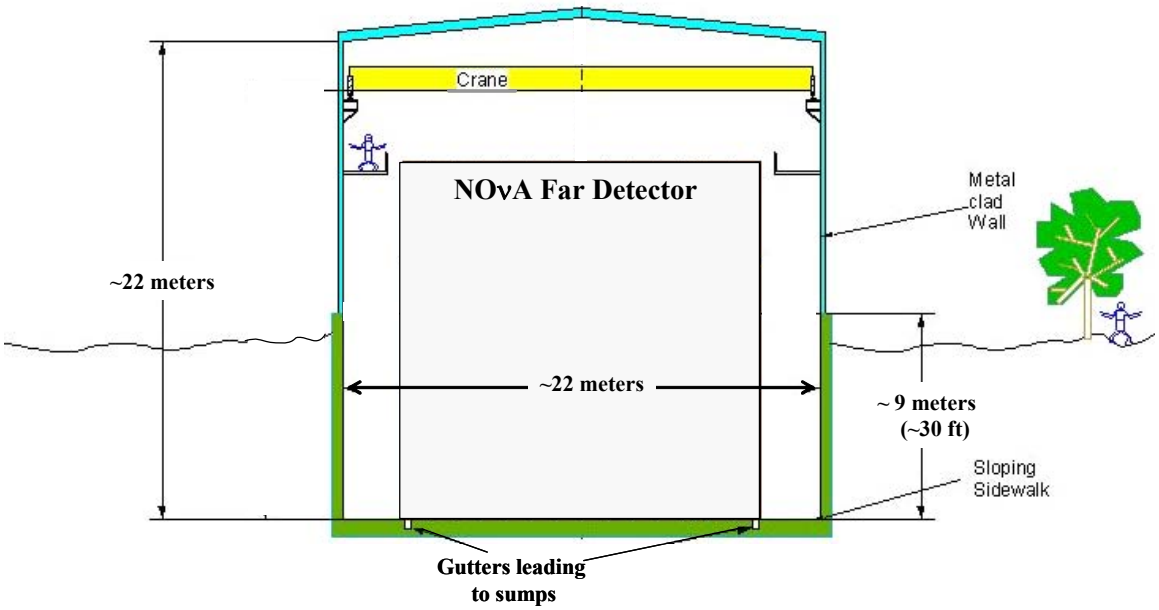

Fig. 8.3: Neutrino beam view of the NOvA Far Detector building. The green shaded portion is the concrete bathtub.

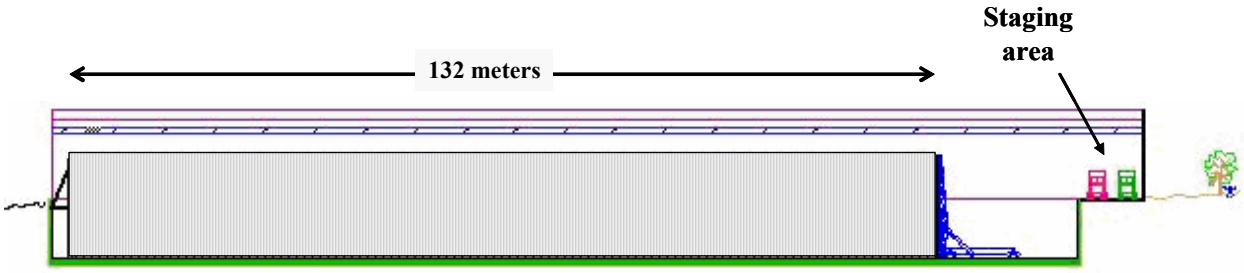

Fig. 8.4: Longitudinal cross section of the Far Detector building. The neutrino beam comes from the left. The green shaded area is the concrete bathtub. The staging area at grade level is shown. The block raiser described in Chapter 5 is shown in its position after the detector is completed.

slope towards the sump. The sump(s) would have ejector pumps that transfer the spilled liquid into a separate holding tank.

For the detector design in this proposal, we anticipate constructing a 20-year life, metal-sided, metal-roofed building, similar to the usual experimental area buildings located at accelerator laboratories. The interior building walls would be sheet metal clad to deflect any potential scintillator leaks into the concrete bathtub. The building would have an additional 10-meter long staging and assembly area at grade at one end so that semi-trailers delivering PVC modules could be moved inside for unloading. This staging and assembly area does not require the full 22 m height. Premixed liquid scintillator delivery and storage could be handled in the main building or in another low-roof section attached to the middle of one side of the main building with additional appropriate secondary containment.

The building meets the horizontal wind stress loads, snow loads, and heating and cooling loads required in northern Minnesota. This area sits on the Canadian Shield and is seismically stable, so no special earthquake design features are required.

The building would be insulated, heated and cooled to ~20 ± 10 ^{0}C year round. This level of temperature control ensures that we avoid liquid scintillator oil temperature damage discussed in Chapter 6. A backup emergency heating source will be immune from electrical power failures (e.g., propane with a pilot light instead of electronic thermostat controls and electronic ignition systems). The building would be outfitted with a 5-ton building crane on a ~22-meter bridge. Catwalks below the crane would allow access to the top of the detector along its full length and could double as fall protection. The building would have several mobile scissor-lifts for access along the sides of the detector. Other custom assembly fixtures are described in Chapter 5. A small control room and a small technician work area would be included inside the main structure.

Chapter 8 References

[1] D. Coissart, P. Kesich, D. Pushka, E. McHugh, NOνA-NOTE-DET-57, NOνA Safety Considerations, February 2005.

[2] Environmental Assessment and Finding of No Significant Impact for the Proposed Neutrino Beams at the Main Injector Project, http://www-esh.fnal.gov:8001/Env/Documents/EAFONSI.pdf

[3] J. Priest, NOνA-NOTE-DET-58, NOνA Rigid PVC Flammability Tests and Other Fire Related Issues, February 2005.

[4] J. Priest, NOνA-NOTE-DET-59, Liquid Scintillator Flammabiltiy Testing, February 2005.

[5] Report for Off-Axis NuMI Neutrino Detector, U of M Project No. 298-03-1113, January, 2003.

[6] Off-Axis Detector Enclosure Design Study Report, Fermi National Accelerator Laboratory, FESS Engineering Project No. 6-2-22, June, 2003. Also available as NOνA Note #9.

9. The NOνA Near Detector

9.1. Introduction

NOνA proposes to construct a Near Detector on the Fermilab site at a distance of about 1 km from the NuMI target in the NuMI access tunnel upstream of the MINOS access shaft. The primary Near Detector design requirement is that it should be as similar as possible to the Far Detector in material and segmentation. This requirement ensures that the efficiencies for signal and background events are identical and ideally will allow us to understand the ν_e charged current and ν neutral current beam spectra seen in the Near Detector as a measure of the expected backgrounds to $\nu_\mu \rightarrow \nu_e$ oscillation signals in the Far Detector.

This chapter describes a design based on the same PVC extrusions, the same PVC cell size, the same liquid scintillator, the same wavelength shifting fiber, and the same electronics readout as the Far Detector. Our design is influenced by the physical limitations at the Near site. The space restrictions in appropriate underground Near sites in the NuMI tunnels dictate a small Near Detector and the access to these underground sites through the MINOS shaft dictate a modular design.

A modular Near Detector has other advantages, and in particular, we propose to operate it in a Fermilab test beam and also in the MINOS Surface Building as venues to understand our detector response before the NOνA Far Detector is completed. The test beam can determine the absolute and relative response and energy calibration of the NOνA design. Running the Near Detector in the MINOS Surface Building at Fermilab allows us to easily study low energy neutrino interactions without the overhead of underground access and space restrictions.

9.2. Near Detector Location

The NuMI tunnels have several sites that could accommodate a Near Detector of similar construction to the Far Detector. Figure 9.1 shows the layout of the MINOS near-detector hall access tunnel. Starting at the Absorber Hall, on the left side of the figure, the tunnel makes a sharp turn to the west just downstream of the absorber. It continues parallel to the neutrino beam direction at a distance of ~14 meters from the beam axis for a distance of ~250 meters. Then it bends back east to enter the MINOS near detector hall, which is on the beam axis. This access tunnel geometry makes a wide range of off-axis angles accessible for a NOνA Near Detector. The range of sites is shown by three possible near detector locations in Figure 9.1 and in Table 9.1: just upstream of the MINOS near detector, just upstream of the vertical MINOS access shaft, and a third location just downstream of the NuMI hadron absorber. Chapter 10 discusses possible sites and concludes that it may be advantageous to move the Near Detector among several sites approximately midway between Site 1 and Site 2 (at ~ 12-17 mrad off-axis). Underground mobility of the detector will be a design requirement.

Site	Number of milliradians off-axis
1	~ 4
2	~21
3	~26

Table 9.1: Off-axis angles of the three underground sites in Figure 9.1 as measured from the average pion decay location in the medium energy NuMI configuration, ~ 200 m downstream of NuMI Horn 1.

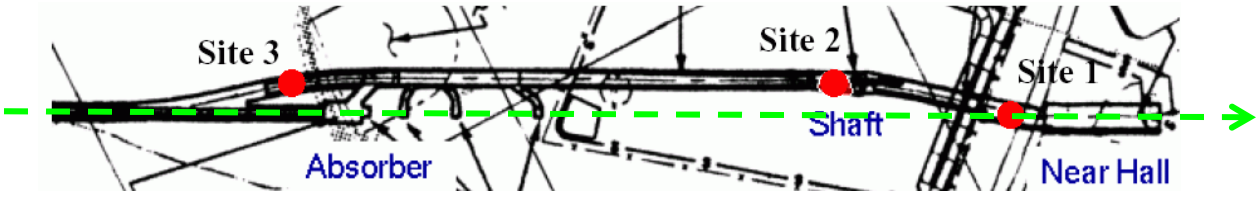

Fig. 9.1: Plan view of the NuMI access tunnel upstream of the MINOS near detector hall. The projection of the beam axis is from left to right along the dotted green line. The beam heads down at 58 mrad relative to the surface.

To reach these NuMI access tunnel sites, a near detector will have to be lowered underground via the MINOS shaft. Figure 9.2 shows a picture from the bottom of the shaft. The Shaft has a D-shaped cross section that is roughly a semicircle with a radius of about 3.3 meters. A 15 ton crane at the top of the shaft provides an additional constraint.

Fig. 9.2: View from the bottom of the MINOS shaft as a MINOS near detector plane comes down the shaft. The D-shaped shaft cross section is evident. The MINOS module shown is ~4.5 m wide by ~3.5 m high by ~0.2 m thick (including the red strong-back frame).

The transverse dimensions of the NuMI tunnels in all these locations are similar to those of Site 2, shown in Fig. 9.3. Each location has approximately 3.5 meters of useable width and about 5.0 meters of usable height. This width leaves about 1 meter for an access walkway around any object placed in the tunnel.

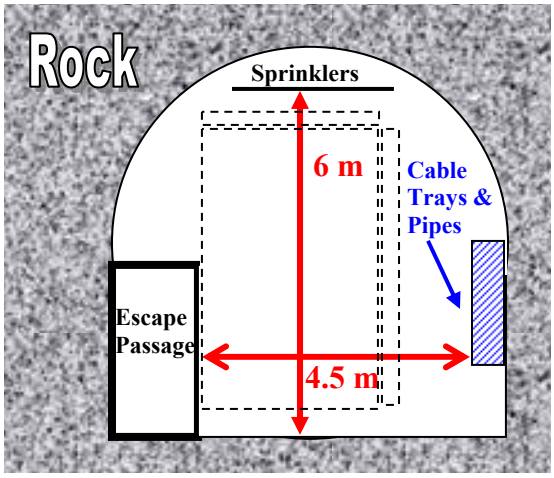

Fig. 9.3: A cross-section view of the access tunnel near Site 2 (see Fig. 9.1). The dotted outline shows the NOνA Near Detector cross section with the fiber manifolds sticking out the top and right side of the device.

9.3. Near Detector Design

With these space restrictions we have designed a NOνA Near Detector that is 3.5 m wide and 5.0 m high, indicated as the dotted outline in Figure 9.3. The active area is 3.25 m wide by 4.57 m high and the fiber manifolds plus electronics take up the additional space on the top and on one side of the detector.

The first 8 meters of the detector is composed of the exact same extrusion cells as in the Far Detector design. It is split into three logical parts: an upstream veto region, a fiducial event region, and a shower containment region. Figure 9.4 displays this longitudinal detector structure. The 4.75 m long shower containment length is chosen to fully contain electron showers from charged current ν_e interactions of a few GeV. The 8 meters of active detector sections are followed by a muon catcher composed of 1.0 meter of steel interspersed with additional planes of liquid scintillator cells. The length of the muon catcher is chosen to so that it plus the shower containment region will contain muons from charged current ν_μ interactions of a few GeV.

The fiducial region is further divided transverse to the beam direction with a central 2.5 m by 3.25 m area designated as the fiducial area. This is

illustrated in Figure 9.5. The border area is designed to contain the transverse size of electron showers in the few GeV region. The border is further subdivided with the outer 19 cm logically designated as an area where less than 5% of the total energy deposition will be allowed. Our simulations indicate that 96% of good ν_e events pass these criteria.

Altogether there are 130 planes of liquid scintillator cells, 65 planes with horizontal cells and 65 planes with vertical cells. The total mass of the detector is 262 tons with 145 tons totally active. The fiducial volume has a mass of 20.4 tons.

The detector would be constructed in modular packages 8 planes thick. Each module will be 10.6 tons when full of liquid and about 1.6 tons

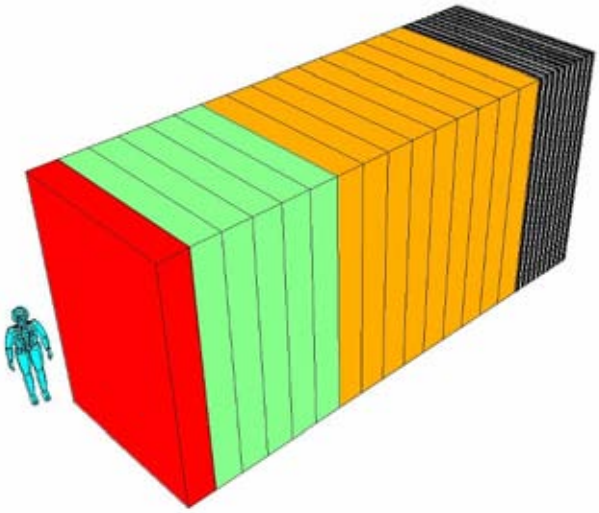

Fig. 9.4: The NOνA Near Detector. The beam comes from the lower left in this diagram. Each modular piece consists of 8 planes of extrusions, 4 vertical interleaved with 4 horizontal planes. The upstream module is a veto region (red), the next 5 modules are the fiducial region (green), and these are followed by a 9 module shower containment region (orange). All parts of these three sections are fully active liquid scintillator cells identical to the Far Detector and the colored areas just represent a logical assignment. Downstream of this active region is a 1.7 m muon catcher region of steel interspersed with 10 active planes of liquid scintillator (black and white).

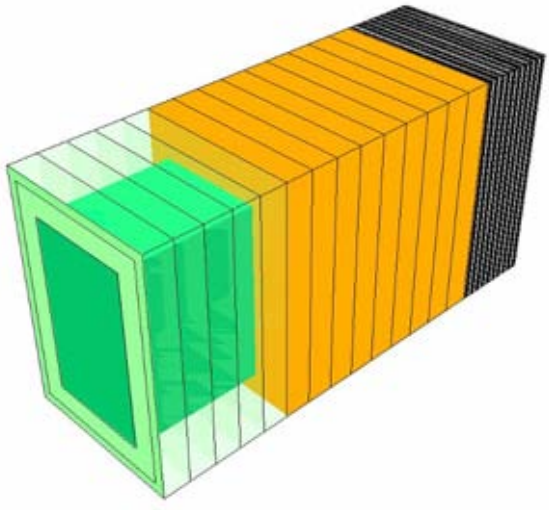

Fig. 9.5: The NOνA Near Detector with the front veto region removed, showing the detector fiducial region (dark green). The fiducial region is surrounded by a border area (lighter shades of green) to contain the transverse size of electron showers in the few GeV region. We would veto events with more than 5% of total energy in the outermost border region (lightest green).

empty. The modules reasonably fit the MINOS access shaft constraints and could be moved full or empty. The Near Detector parameters are summarized in Table 9.2.

Near Detector Parameter	**Parameter Value**
Total mass	262 metric tons
Active detector mass	145 metric tons
Fiducial mass	**20.4 metric tons**
Extrusion cells, liquid scintillator, waveshifting fiber, APD readout	Identical to the NOνA Far Detector
Number of channels	12,480
total Liquid Scintillator	41,000 gallons
Detector Width (m and # of cells), Height (m and # of cells, length (m)	 3.5 m, 80 cells 4.8 m, 112 cells 9.58 m
Total active planes	130 planes 65 horizontal & 65 vertical
Basic modular piece in the active section # planes Thickness of module Empty weight Full weight	 8 planes 52.8 cm 1,417 kg 9,600 kg
Veto region, # of active planes	 8 planes
Fiducial region, # of active planes	 40 planes
Shower Containment region, # of active planes	 72 planes
Muon catcher Steel (m/section, # of sections) # of active planes	 0.1 m, 10 sections 10 planes
Muon catcher mass Steel Scintillator planes	 117.5 metric tons 11.1 metric tons

Table 9.2: NOνA Near Detector Parameters.

9.3. Near Detector Event Rates

At a site midway between Sites 1 and 2 in Figure 9.1, the event rates in the 20.4 ton fiducial mass will be about 0.09 event per 10^{13} protons on the NuMI target. The rate drops about a factor of three near Site 3 and increases about a factor of three near Site 1. The maximum beam from a single Main Injector (MI) pulse is expected [1] to be 6×10^{13} protons, so we would get about 0.5 events per MI spill. As we will see in Chapter 10, about two-thirds of these events would be from neutrinos with energies below 5 GeV. We would collect about 6.5 million such events in one year with 6.5×10^{20} p.o.t (see Chapter 11).

The rate of events in the whole active detector is larger. Since the total active mass in 145 tons, we would see a rate of 3.8 events per MI pulse of 6×10^{13} protons. Assuming a 500 ns time bin in our electronics and a 10 microsecond spill [2], that would imply 9% of our events would have two or more overlapping events in the active detector. We therefore expect to include an additional 6 planes interspersed throughout the 120 active planes, each with ganged fast MINOS-style Near Detector electronics to identify the presence of more than one event in a spill. Such spills could then be cleanly rejected in an unbiased manner.

9.4. Test Beam Program

Given the modular form of the Near Detector, it can be moved to various sites relatively easily. We plan a program to expose the detector to a charged-particle test beam. Using selectable beam momentum settings and a particle identification system, a full response matrix can be measured. Response to cosmic ray muons will be studied simultaneously and compared to these beam interactions. Both the Far Detector and the Near Detector will always see a high rate of out-of-time cosmic ray tracks, which will provide a stable source of muons to monitor the detector response. The collected test beam data will also be used to tune Monte Carlo simulations of the detector response and to aid in developing the most efficient pattern recognition algorithms.

NOνA does not have any unusual demands for the performance of a test beam. However, the beam should have a momentum range from well below 1 GeV up to 5 GeV/c, with the absolute momentum known to a few percent, and an integrated particle identification system. The Fermilab Meson Test Beam Facility in MTest could be used even though it has rather low beam rates at these low energies [3]. Initially we imagine testing prototype Near Detector modules in MTest, but eventually we could put the entire NOνA Near Detector in MTest as shown in Figure 9.5. Since the shower containment and muon catcher regions

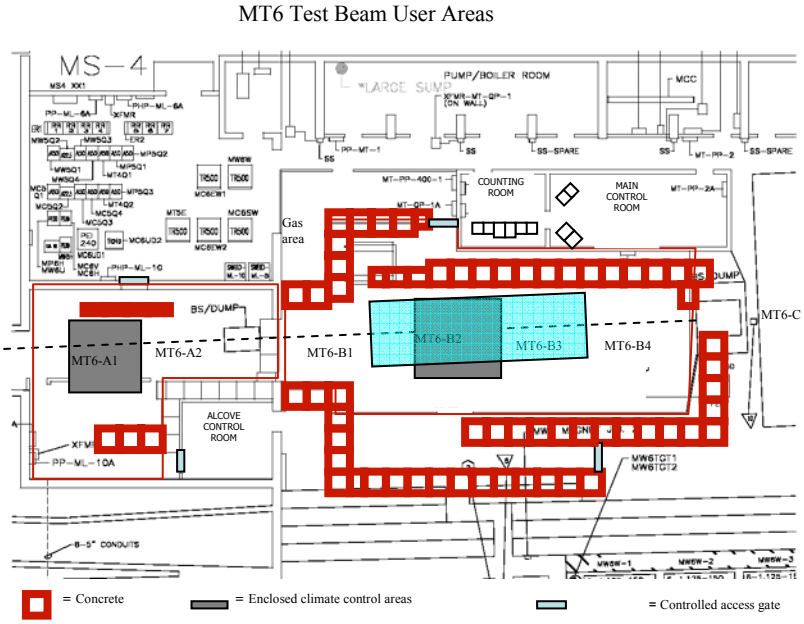

Fig. 9.5: The Fermilab MTest experimental area with the NOνA Near Detector (in blue) superimposed.

would be a little thin at higher energies, we would add modules from the prototype Near Detector discussed in Chapter 15 for these measurements.

Over the life of the experiment we may need access to the test beam for several periods of a few months each. We would rely on Fermilab support for MTest beam line operation, instrumentation, and monitoring.

The Near Detector described here is essentially sampling the Far Detector in the upper right corner as seen by the neutrino beam as shown in Figure 9.6. We could replace the fibers in the Near Detector with 15.7 meter long fibers (coiled up outside the liquid cells) and calibrate / study a different part of our Far Detector. Other positions could be calibrated in the same manner.

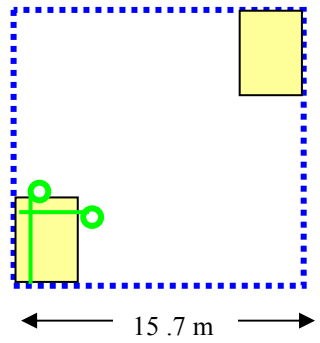

Fig. 9.6: The Far Detector front face (dotted blue line) with two configurations of the Near Detector superimposed. For the lower left version, the extra wavelength shifting fiber gets coiled up outside the Near Detector as represented by the green circles.

9.5. Tests of the Near Detector in the MINOS Surface Building at Fermilab

We also plan to put the NOνA Near Detector in the MINOS Surface Building and look at extremely off-axis neutrinos from the NuMI beam. The surface building is about 75 mrad off-axis and the NuMI beam runs parallel to the axis of the building's highbay. The NOνA Near Detector fits easily in the highbay area but would not block access to the MINOS shaft for other users. This is shown in Figure 9.6.

The predicted ν_μ spectrum in the MINOS Surface Building is shown in Figure 9.7. The main feature is a ν_μ beam strongly peaked near 2.8 GeV. These neutrinos are from kaon decays in the NuMI beam [4]. In addition there is a nice ν_e spectrum which peaks at 1.8 GeV as shown in Figure 9.8.

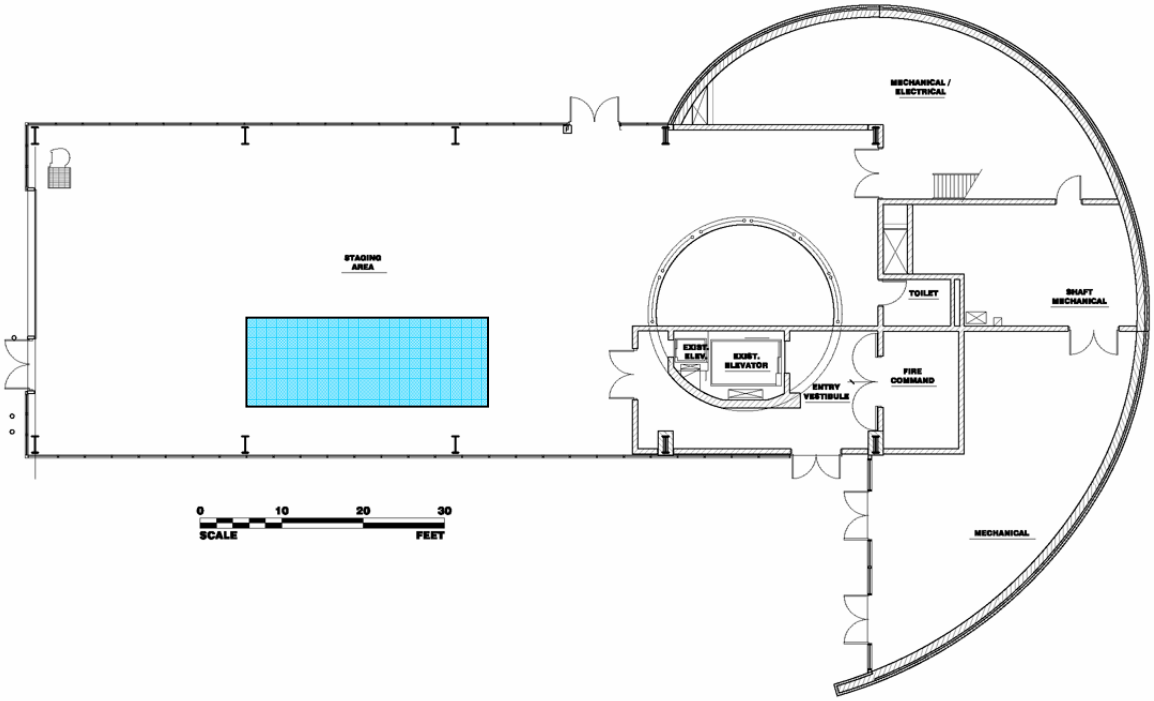

Fig. 9.6: The 9.2 m long NOνA Near Detector (in blue) shown to scale inside the MINOS Surface Building. The NuMI beam runs parallel to the main axis of the building from left to right (but ~105m below the building and ~14m towards the bottom of the figure as shown). The beam is also heading down at 58 mrad relative to the surface.

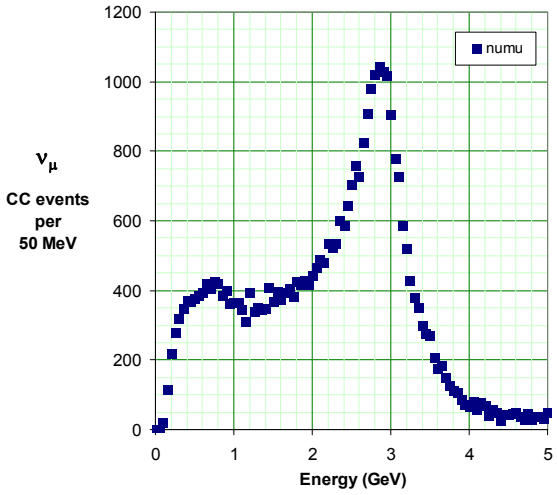

Fig. 9.7: Charged Current ν_μ event spectra vs. energy for neutrino events in the 20.4 ton fiducial mass of the NOνA Near Detector placed the MINOS Surface Building for 6.5 x 10^{20} p.o.t.

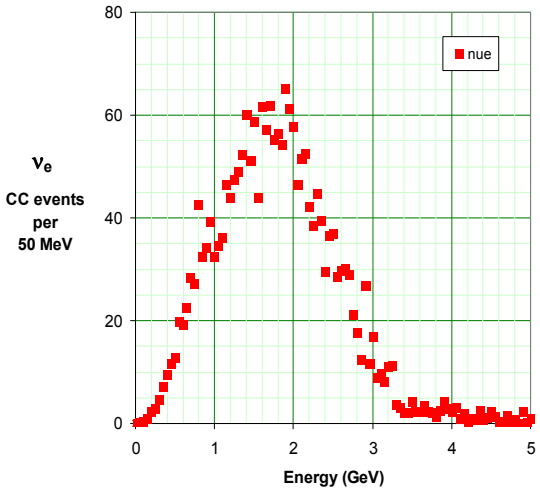

Fig. 9.8: Charged Current ν_e event spectra vs. energy for neutrino events in the 20.4 ton fiducial mass of the NOνA Near Detector placed the MINOS Surface Building for 6.5 x 10^{20} p.o.t.

The ν_e over ν_μ ratio is 10 - 15% in the 1 – 2 GeV range of Figures 9.7 and 9.8., making the target population of ν_e rather accessible in any event sample.

The event rates at 75 mrad off-axis are down by a factor of 150 relative to the underground off-axis sites in the NuMI tunnels of Figure 9.1. The total event rate in our 20.4 ton fiducial volume will The be only about 1 event every 5 minutes with the Main Injector operating at 6 x 10^{13} p.o.t. per pulse. Still, integrated over a year with 6.5 x 10^{20} p.o.t. delivered to NuMI, we would see about 45,000 charged current neutrino events. The event rates are summarized in Table 9.3.

Event Type	Event Rates
Total CC events per MI pulse	0.0044
MI pulses between CC events	~ 230
Average time between events	5 - 6 minutes
	Event Samples
CC neutrino events per year	~45,000
ν_μ charged current events per year in the kaon peak between 2.4 and 3.2 GeV	~ 13,000
ν_e charged current events per year	~ 2,200

Table 9.3: Event rates for 6 x 10^{13} p.o.t. per MI pulse and Event samples for 6.5 x 10^{20} integrated p.o.t. delivered to NuMI. These rates and samples are those expected in the 20.4 ton fiducial volume of the NOνA Near Detector at the MINOS Surface Building.

There are clear advantages to starting with the NOνA Near Detector in this position.

- The building already exists and can easily hold the detector as shown in Figure 9.6.
- We can initially avoid the complications of underground access.
- The event rates are low enough that initially we would not need special fast electronics to reject multiple events in a single MI spill.
- The event rates are high enough that substantial numbers can be collected in a year of running.
- In particular, reasonably large samples of ν_e charged current events will be available to aid in developing more efficient pattern recognition algorithms.
- We can gain experience with a fully active detector running on the surface.

We propose to start immediately with an R&D prototype NOνA Near Detector taking data as soon as possible in the MINOS Surface Building. This is discussed in Chapter 15. During the construction project we would build the final Near Detector from identical objects to those in the NOνA Far Detector.

Chapter 9 References

[1] draft Fermilab Proton Plan, November 2004, see http://www.fnal.gov/directorate/program_planning/Nov2004PACPublic/PACagendaNov2004OPEN.htm

[2] The spill length is 9.78 microseconds for the case of no anti-proton operation discussed in Chapter 11. See the NuMI Technical Design Handbook, Chapter 3, "Design Parameters" at http://www-numi.fnal.gov/numwork/tdh/tdh_index.html

[3] The Fermilab Meson Test Beam Facility is described at http://www-ppd.fnal.gov/MTBF-w , the beam has recently been tuned as low as 4 GeV and the yields were about 100 particles per MI spill with 50% of the particles being electrons, E. Ramberg, private communication.

[4] We thank the MiniBooNE collaboration for pointing out this far off-axis effect. Janet Conrad, private communication.

10. Backgrounds and Systematics

10.1. Introduction

In Chapter 9 we describe a NOνA Near Detector that is virtually identical to our proposed Far Detector. This ensures that the efficiencies for signal and background events are nearly identical in the two detectors. If there were no other effects, then understanding the un-oscillated beam spectra seen in the Near Detector would be a perfect measure of the expected background to $\nu_\mu \rightarrow \nu_e$ oscillation signals in the Far Detector. Unfortunately this simple relation can break down in several ways, leading to incorrect conclusions about the background in the Far Detector and therefore leading to systematic effects in our search for $\nu_\mu \rightarrow \nu_e$ oscillations.

In this chapter we examine several effects which can alter the Near to Far extrapolation and affect our primary measurement. We have not yet fully simulated these effects, but it is important to recognize each one at this proposal stage and indicate our strategies for dealing with each. We find that moving our Near Detector around to different positions in the NuMI tunnel should allow us to understand all these effects sufficiently well such that the total error on the background in our $\nu_\mu \rightarrow \nu_e$ search will be below 10%. The modular nature of the NOνA Near Detector described in Chapter 9 is therefore an important design aspect of the device, since it will be moved several times during the experiment.

NOνA aims to detect excess ν_e events in the Far Detector. Our principle backgrounds are beam ν_e , beam ν_μ , neutral current (NC) ν events, and cosmic rays, each of which can masquerade as ν_e oscillations. We use the off-axis beam to obtain a nearly monochromatic neutrino energy spectrum and then one of our principle analysis weapons in the Far Detector is an energy cut to eliminate backgrounds. Systematics influencing our result can therefore be tied to energy-dependent effects.

In this chapter we will consider the following list of effects:

- Energy-dependent backgrounds require that we understand the energy calibration of our Near and Far Detectors. The inherent energy resolution of our detectors sets a scale for the precision of this calibration. We will use test beam and other data to set the absolute energy scale to a few percent.
- Predictions of the neutrino beam spectra at the Near and Far sites involve rather simple kinematics in a Monte Carlo simulation, but the input particle production spectra for this Monte Carlo are only known to about the 20% level. We expect Fermilab E-907 MIPP (Main Injector Particle Production) [1] to improve this knowledge before NOνA takes data. Several members of the NOνA Collaboration are also members of the MIPP Collaboration and will have first-hand experience with these improved data.
- The neutrino beam spectra at the Near and Far Detectors cannot be identical because the Near Detector sees a line source from decays only a few hundred meters away while the Far Detector sees a point source from 810 km. The off-axis angle of our detectors makes this situation different from that in MINOS. We will optimize the location of our Near Detector to minimize this effect. The optimization requires moving the Near Detector to different positions for each background.
- A potential MiniBooNE confirmation of the LSND result for short baselines may mean that our Near Detector will see a distorted ν_e component to the NuMI beam. The NOνA Far Detector would not see the same effect due to its long baseline. If the LSND signal were confirmed, we would have to respond by moving our Near Detector around to different off-axis angles so that we could disentangle the NuMI beam spectra effects from the short baseline oscillation effects.
- The Far Detector ν_e background from ν_μ CC events masquerading as ν_e comes from the oscillated ν_μ spectrum. Therefore any measurement of this background with the un-oscillated beam in the Near Detector will not be quite correct. We can estimate this effect by studying ν_μ events with an identified muon as a

function of the observed event energy. Different ν_μ CC spectra can be seen by the NOνA Near Detector at different off-axis positions.

- To first order the present rather poor knowledge of low energy neutrino cross sections [2] does not matter to NOνA since the same unknown cross section is seen in both the Near and Far Detectors.

  However, since the neutrino beam spectra are not identical at the NOνA near and far sites, some differences in background levels can result from different energy dependences and from different NOνA efficiencies for detection of the different neutrino interaction processes. To second order we can minimize these effects by selecting the best Near site to measure each background.

  Knowledge of the low energy neutrino cross sections will be much improved before the bulk of NOνA data is collected, since Fermilab E-938 MINERνA [3] is designed to attack this very problem. Several members of the NOνA Collaboration are also members of the MINERνA Collaboration and will have direct knowledge of these improved cross section data at a detailed level. Benchmarking our Near Detector measurements against these improved cross section data will help us understand our detector response to neutrinos.
- Our Near Detector will be underground and shielded from cosmic rays, while our Far Detector will be on the surface and unshielded from cosmic ray events that occur within the neutrino beam time window (about 100 seconds per year of running). Monte Carlo calculations indicate this should not be a problem, but we will run our Near Detector on the surface to check this Monte Carlo simulation.

10.2. Energy Calibration of the NOνA Detectors

In Chapter 9 we described our plans to calibrate the NOνA Near Detector in a test beam to determine the absolute response and energy calibration of both the Near and Far detectors. As described in Chapter 12, we expect our detector energy resolution to be $\Delta E/E$ (sigma) ~ $0.10 / \sqrt{E}$ for ν_e CC events. For a 2 GeV ν_e event at the peak energy of our oscillation signal, we expect to measure the event energy to about 7%. This 7% resolution does set a rough practical scale to our requirements for understanding shapes of the neutrino energy spectra in both detectors.

Momentum tagged electrons in a test beam will allow us to measure our energy resolution and absolute energy scale directly. With a detector electromagnetic resolution of order $0.10 / \sqrt{E}$, the absolute scale can be determined to a few percent providing the test beam momentum resolution is not the dominant effect. The Fermilab MTest test beam has a momentum bite of a few percent, and the last string of dipoles is instrumented with a tracking system which allows momentum tagging at the $\Delta p/p = 0.25\%$ level. In practice multiple scattering off material in the beam at low energies will limit this tagging ability. Understanding the absolute momentum scale in MTest requires a field map of the final 5 dipoles and a precision shunt resistor on the magnet power supply to monitor that field. Overall, a 1 - 2% absolute calibration of the beam should be attainable, and in turn we should establish the absolute energy scale of our Near Detector to 2 – 3%.

Since high *y* ν_e events can contain multiple charged pions with a substantial fraction of the energy, we will also want to use the MTest charged pion beam to understand our detector response. For ν_μ events, the NOνA detector energy resolution comes from the total pulse height of the muon track, since the muon range is subject to straggling at the 2-3% level. Running with muons in MTest will allow us to study this resolution directly.

We intend to carry the absolute test beam calibration of the NOνA Near Detector to the Far Detector and through the life of the experiment by constantly monitoring each detector's pulse height response to cosmic ray muons in individual cells. Cross calibration with cosmic ray muons in the test beam will initiate this energy scale tracking.

The extreme off-axis neutrino flux in the MINOS Surface Building provides another calibration path. Figures 9.7 and 9.8 in Chapter 9 illustrate the neutrino CC flux at ~75 mrad off-axis. The ν_μ CC peak at 3 GeV is dominated by neutrinos from K decays, and the kinematics of $K \rightarrow \mu\ \nu_\mu$ vs. K_{e3} decays will allow us to cross correlate the ν_μ and ν_e energy distributions. The 3 GeV peak energy measurement is dominated by muon energy and that provides an absolute calibration of the

electron energy scale near 2 GeV. The relative branching ratios for the two decays provide another cross check on the spectra. This measurement will require a longer Near Detector than the one described in Chapter 9 and we would supplement the detector with parts of the prototype Near Detector described in Chapter 15.

10.3. Particle Production at 120 GeV and the Neutrino Beam Spectra

Existing particle production data have errors of order 20% and this translates into a ~20% uncertainty [1] in the neutrino flux produced in NuMI with the Medium Energy configuration NOνA proposes to use. The MIPP experiment intends [4] to run with 120 GeV protons to directly measure the flux from the MINOS target. These data should reduce the particle production uncertainties to the level of a few percent. With these data the NOνA neutrino fluxes should then be predicted to about 5% when combined with NuMI horn magnetic field measurements.

The MIPP measurements are clearly important to NOνA since an improved beam Monte Carlo will help us understand any Near to Far differences in the neutrino spectra. We hope that MIPP can get the appropriate MINOS target data as planned during 2005.

10.4. Near Detector Location and the Neutrino Beam Spectra

NOνA plans to use the NuMI beam in the medium energy configuration. In this section we compare the neutrino beam spectra at several possible Near Detector locations with the spectra at the Far Detector site. Figure 10.1 reproduces Figure 9.1 to again show the possible Near Detector locations. Figures 10.2 and 10.3 show the charged current (CC) ν_μ event rates for several locations in the NuMI halls along with the unoscillated ν_μ CC rate expected in the Far Detector. The actual Far Detector ν_μ flux will be quite different from Figure 10.2 due to $\nu_\mu \rightarrow \nu_\tau$ oscillations, but the figure does show the shape of the <u>total</u> neutrino flux and particularly the flux of the neutral currents (NC) which are a background source for NOνA. Matching the un-oscillated Far Detector ν_μ CC spectrum shape in the Near Detector will be important for our understanding of the NC backgrounds.

There are two main differences between the muon neutrino spectra at these sites and the spectrum at the far detector. The peak is broader at the near site than at the far site, and the "high energy tail" is a larger fraction of the total event sample in the near detector. The energy spectrum is widened at the near detector because there is a broad range of decay positions of the parent pions, so there is no single "off axis angle" seen at one position. At the Far Detector, the range of decay locations has a negligible effect on the off-axis angle. At the Near Detector, the high-energy tail is fractionally higher because these events come from the high-energy pions that decay farthest downstream in the decay pipe. Those high-energy decays are significantly closer to the Near Detector than the decays of the pions that give events in the peak of the distribution and they are at a larger off-axis angle. The prominent kaon decay peak seen in Chapter 9 for the MINOS Surface Building site is also beginning to be visible at Sites 2 and 3 around 8 – 10 GeV.

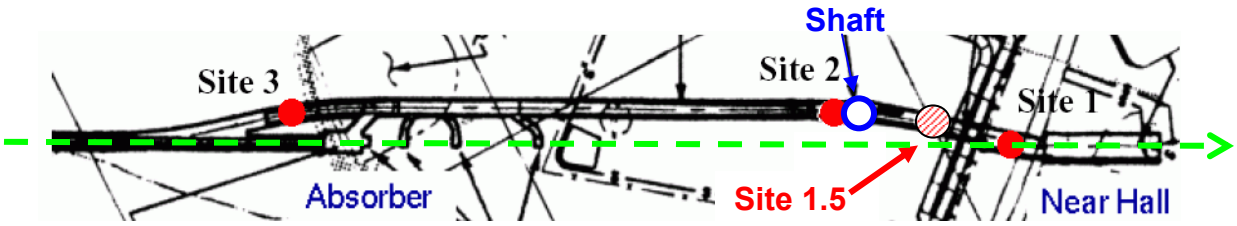

Fig. 10.1: The NuMI access tunnel upstream of the MINOS near detector hall. The beam direction is from left to right as shown by the dashed green line. Our preferred Near Detector sites are in the range between Site 1.5 and Site 2. Site 1.5 is at an off-axis angle of ~ 12 mrad as measured from the average pion decay location in the medium energy NuMI configuration, ~ 200 m downstream of NuMI Horn 1. Site 2 is at ~ 21 mrad.

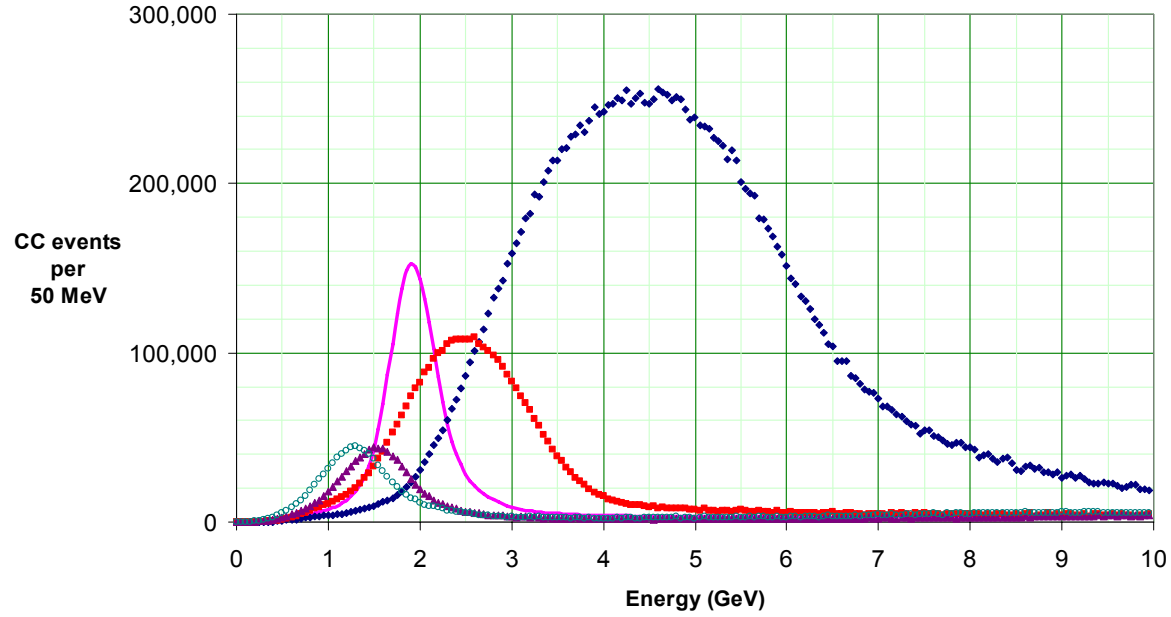

Fig. 10.2: ν_μ CC spectra for the various Near Sites [Site 1(blue diamonds), Site 1.5(red squares), Site 2 (purple triangles), Site 3 (open green circles)] for one year of running at 6.5 10^{20} pot. The un-oscillated Far Detector ν_μ spectrum for one year of running (times an arbitrary scale factor of 800) is shown as the solid pink line. These spectra are for the NuMI medium energy configuration.

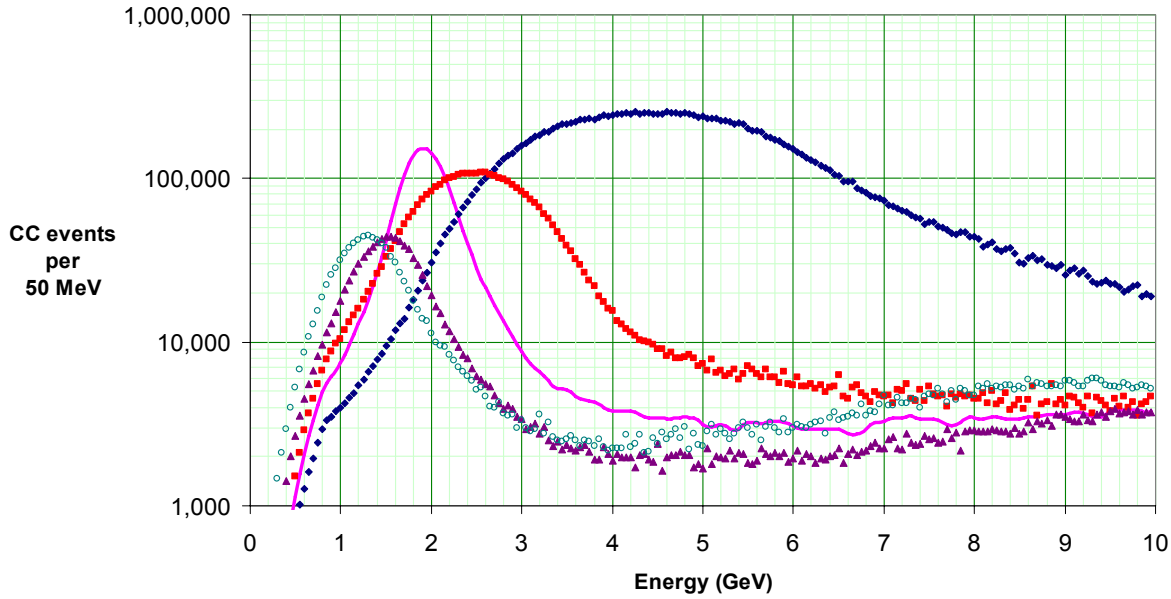

Fig. 10.3: Same ν_μ CC spectra as shown in Figure 10.2 but with a logarithmic vertical scale to better display the high energy tails of the distributions.

Based on the total ν flux spectrum comparison alone, the preferred Near Detector location would be approximately midway between Site 1.5 and Site 2, where the best match is made to the NC background seen at the Far Detector.

Figures 10.4 through 10.7 show the beam ν_e spectra for these same sites, again for the NuMI medium energy configuration. In each figure the beam ν_e spectrum for the Far Detector is superimposed with an arbitrary normalization so that the two distributions agree at ~2 GeV. Based on these beam ν_e spectra comparison alone, the preferred Near Detector location would be Site 1.5. Over the 1.5 – 2.5 GeV energy range, the Near and Far distributions agree to within ~7% in every bin.

One cannot optimize for both the electron and total neutrino fluxes at the same time. The electron neutrinos come predominantly from the muon decays farther downstream in the decay pipe while the muon neutrinos, which make up 99% of the total flux, originate from somewhat farther upstream. Site 1.5 gives electron neutrino spectra reasonably similar to those at the Far Detector. A site midway between Site 1.5 and Site 2 would be a better match to the total neutrino spectrum at the Far Detector site. The solution is to move our Near Detector to the appropriate site for each background study.

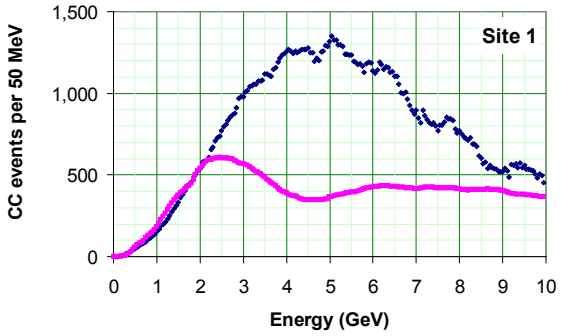

Fig. 10.4: The beam ν_e event rates for one year of data in the Near Detector located at Site 1(solid blue diamonds). The Far Detector beam ν_e distribution is also shown (solid pink line) assuming no oscillation, but has been normalized so that the distributions have the same value at ~2 GeV. Both distributions assume the NuMI medium energy configuration.

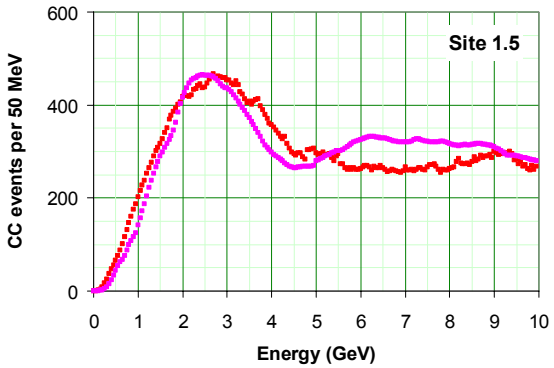

Fig. 10.5: The beam ν_e event rates for one year of data in the Near Detector located at Site 1.5 (red squares). The Far Detector beam ν_e distribution (pink line) is also shown assuming no oscillation, but has been normalized to have the same value at ~2 GeV.

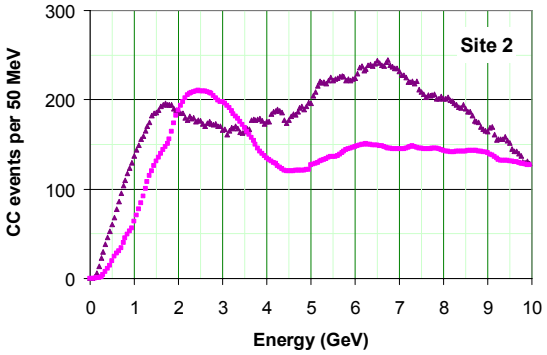

Fig. 10.6: The beam ν_e event rates for one year of data in the Near Detector located at Site 2 (purple triangles). The Far Detector beam ν_e distribution (pink line) is also shown assuming no oscillation, but has been normalized to have the same value at ~2 GeV.

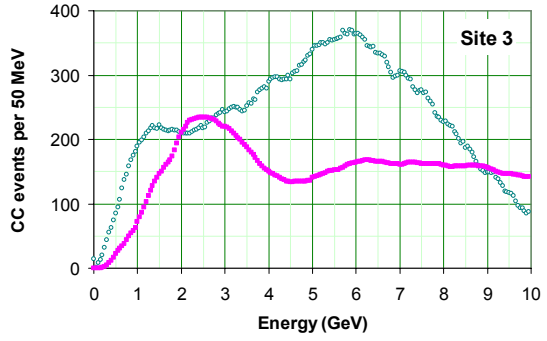

Fig. 10.7: The beam ν_e event rates for one year of data in the Near Detector located at Site 3 (open green circles). The Far Detector beam ν_e distribution (pink line) is also shown assuming no oscillation, but has been normalized to have the same value at ~2 GeV.

10.5. The Effect of a Possible MiniBooNE Confirmation of LSND

A MiniBooNE confirmation of the LSND result for short baselines would mean that our Near Detector will see a distorted ν_e component to the NuMI beam. LSND reported [5] an anti-$\nu_\mu \rightarrow$ anti-ν_e oscillation probability of 2.6×10^{-3}. In the naive oscillation framework given by

$$P_{ab} = \sin^2(2\theta_{ab}) \sin^2[1.27\,(\Delta m^2)\,(L/E)], \qquad (1)$$

the allowed LSND parameter space is shown in Figure 10.8.

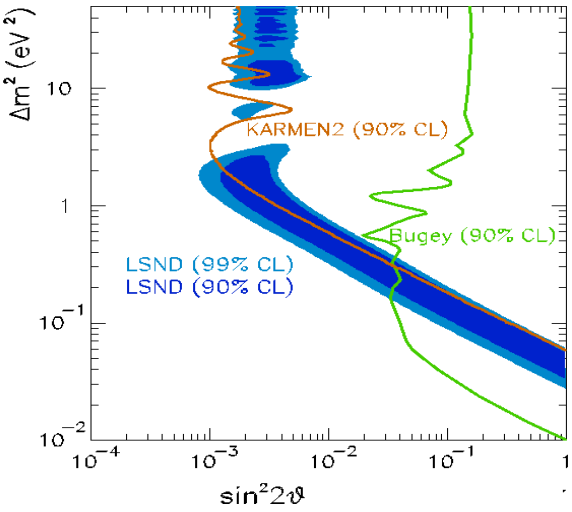

Fig. 10.8: The final LSND allowed region (90, 99%CL), together with the final KARMEN2 90%CL excluded region (Feldman-Cousins approach), and the 90%CL Bugey excluded region. This image comes from the MiniBooNE Public Plots web area.

Figure 10.9 shows a 60% effect in the Near Detector ν_e spectrum for the case of an LSND signal at 2.5 eV^2 and $\sin^2(2\theta_{\mu e}) = 2.6 \times 10^{-3}$ (center of the LSND range, but excluded by KARMEN2 at 90% confidence level). Figure 10.9 shows an extreme case, but Figure 10.10 shows the effect persists for all values of Δm^2 and $\sin^2(2\theta_{\mu e})$ consistent with the LSND, KARMEN2, and Bugey results. There is always an effect at the level of 20% or more in the measured "beam ν_e" spectrum amounting to ~100 events per 50 MeV bin over a wide energy range.

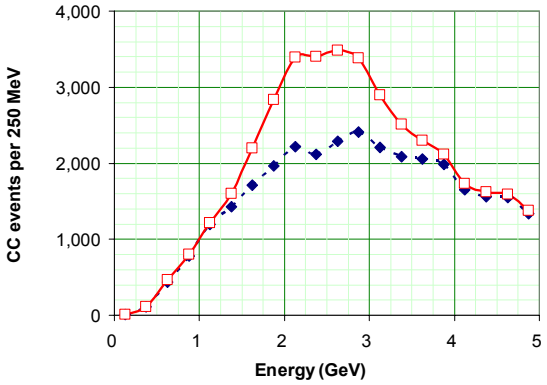

Fig. 10.9: The NOνA Near Detector ν_e charged current spectrum with (open red squares) and without (solid blue diamonds) the effect of an LSND short baseline oscillation with $\Delta m^2 = 2.5$ eV^2 and $\sin^2(2\theta_{\mu e}) = 2.6 \times 10^{-3}$. These spectra are for one year of running at 6.5×10^{20} pot in the NuMI medium energy beam. No detector resolution effects, ν_e CC efficiencies, or NC backgrounds are included here.

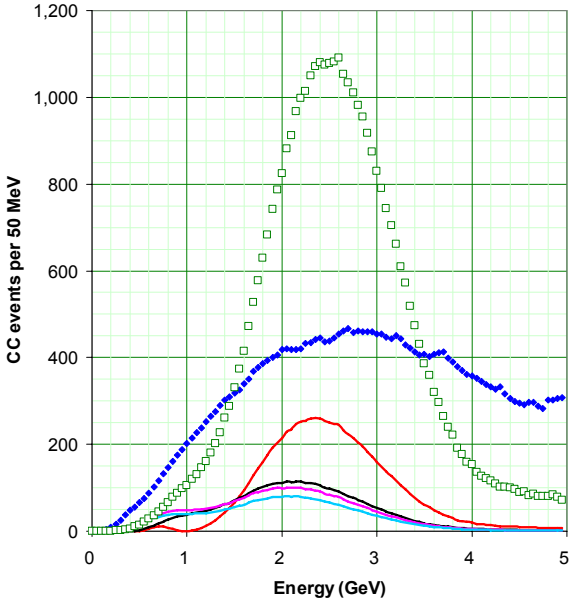

Fig. 10.10: The NOνA Near Detector ν_e CC spectrum (solid blue diamonds) at Site 1.5 compared with a short baseline oscillation effect at different values of Δm^2 (four solid lines for 2.5, 1.0, 0.4, and 0.25 eV^2) consistent with the allowed LSND parameter space in Figure 10.8. The four lines have (Δm^2, $\sin^2(2\theta_{\mu e})$) parameters of (2.5, 2.6×10^{-3}, red line), (1.0, 4×10^{-3}, black line), (0.4, 2×10^{-2} , pink line), and (0.25, 4×10^{-2}, light blue line). The parent ν_μ CC spectrum for the oscillation is shown at 1% of its value (open green squares). No detector resolution effects, ν_e CC efficiencies, or NC misidentification backgrounds are included here.

The effect in the NOνA Near Detector depends on Δm^2 and L/E, but it is also a strong function of the parent ν_μ spectrum in the off-axis near beam. The Near and Far NOνA detectors would see different effects from this short baseline oscillation. For a large $\Delta m^2 = 2.5\ eV^2$, the Far Detector sees a small effect as the second factor in Equation (1) just averages to 0.5 and the overall value for P_{ab} goes to 0.0013. For small $\Delta m^2 \sim 0.3\ eV^2$, the Far Detector sees an order of magnitude larger effect since the first factor in Equation (1) approaches 0.04 and so P_{ab} approaches 0.02. Meanwhile the effect seen in the Near Detector is dominated by the second factor in the equation and the particular values of Δm^2 and L/ E. In general, we would always see a substantial effect in the Near Detector and incorrectly extrapolate the beam ν_e spectrum to the Far Detector. Depending on the oscillation parameters we could extrapolate too high a background or too low a background as summarized in Table 10.1.

LSND parameters		Near Detector excess at 2 GeV	Far Detector excess at 2 GeV
Δm^2 (eV^2)	$\sin^2(2\theta_{\mu e})$		
2.5	2.6×10^{-3}	52%	46%
1.0	4.0×10^{-3}	26%	70%
0.4	20.0×10^{-3}	24%	350%
0.25	40.0×10^{-3}	19%	700%

Table 10.1: Expected excess beam ν_e events for both the Near and Far NOνA Detectors for several LSND parameters consistent with Figure10.8 as a percentage of the beam ν_e's observed in the absence of an LSND effect. The Near percentages are from Figure 10.10. The Far percentages are relative to the beam Monte Carlo prediction (in the absence of an LSND effect) of 2.85×10^{-3} for the ν_e to ν_μ ratio at the far site.

If the LSND signal were confirmed, we would likely have to respond by moving our Near Detector around to a wide variety of different off-axis angles (Sites 1 -3) to exploit the different parent ν_μ spectra and different L/E distributions. These data sets would allow us to disentangle the NuMI beam spectra effects from the short baseline oscillation effects. In Chapter 13 we turn this LSND "background" argument around and ask what NO˜A could contribute to measurements in this sector if MiniBooNE confirms the LSND effect.

10.6. Backgrounds from ν_μ Charged Currents

In the analysis described in Chapter 12, in order for the ν_μ CC events to be misidentified as NC events, there has to be a track identified as an electron (most likely an asymmetrically decaying π^0) *and* the muon has to be missed. The cases where a muon itself is misidentified as an electron are rare due to the good μ-e separation in our detector. High *y* events (where *y* is defined as the fractional neutrino energy loss) form the majority of the ν_μ CC background.

To determine the fraction of ν_μ charged current events that would pass all analysis cuts, one can measure that fraction for events with identified muons, and then predict the number of times that the muon is undetected. This procedure works in the limit that the nature of the hadronic system in a neutrino charged current interaction is dependent only on the hadronic energy of the system, and not on the neutrino energy.

ν_μ CC events, to a very good approximation, are characterized by a flat *y* distribution near high *y*. Thus, for a specific neutrino energy, the distribution of these events with longer muon range which satisfy our ν_e signal criteria should be flat when plotted as a function of muon range (= 1-*y*). The contribution to the background from ν_μ CC events with shorter muon range (dominated by unidentified muons) can then be obtained by integrating the extrapolation of the observed distribution. In reality, the *y* flatness expectation is altered by the fact that our selection criteria for the ν_e signal interacts somewhat with the energy of the muon. By allowing a slope in this distribution and its extrapolation, these effects can be incorporated. We have tried this procedure in simulations and find that we can extract the actual number of Near Detector ν_μ CC background events to about ±30%. The simulation indicates that this Near Detector background extraction procedure will translate into about a 15% error in our prediction of the Far Detector background.

In addition, our energy spectrum is not monochromatic. This background from ν_μ CC events masquerading as ν_e comes from the oscillated ν_μ spectrum (see Figure 4.5). Therefore a measurement of this background with the un-oscillated beam in the Near Detector will not be quite correct. We can get a handle on this effect by repeat-

ing the described extrapolation procedure for the different ν_μ energy spectra available at different near sites as illustrated in Figure 10.2. Again, this means moving the NOνA Near Detector around to different underground sites.

10.7. Neutrino Cross Section Uncertainties

Assuming identical Near and Far Detectors, the present imprecise knowledge of low energy neutrino cross sections [2] does not matter to first order to NOνA since the same unknown cross section is seen in both the Near and Far Detectors. The predictions for the Far Detector background could still have second order effects due neutrino cross sections if we do not choose our Near site(s) carefully. Measuring these neutrino cross sections with the NOνA Near Detector will be an excellent benchmark of our understanding of both the Far and Near Detectors.

Neutrino interactions in this energy regime are classified as four different kinds of processes: Quasi-elastic (QE), Resonance, Coherent, and Deep Inelastic Scattering (DIS). Each process can be either neutral current (NC) via Z-exchange or charged current (CC) via W-exchange.

In the QE process, a nucleon is knocked out of the nucleus and the final state lepton is a muon or electron for CC events and a ν_μ or ν_e for NC events. In Resonant processes a Δ resonance is created, which then decays to a proton + pion, or a neutron + pion. The DIS process produces multiple pions.
Figure 10.11 shows the current status of measurements for these processes in the CC channels [2]. At NOνA neutrino energies, these CC processes are all about equal in magnitude and each known only to about 20 - 30%. These CC cross sections are changing within our narrow off-axis energy band as indicated in Figure 10.11.

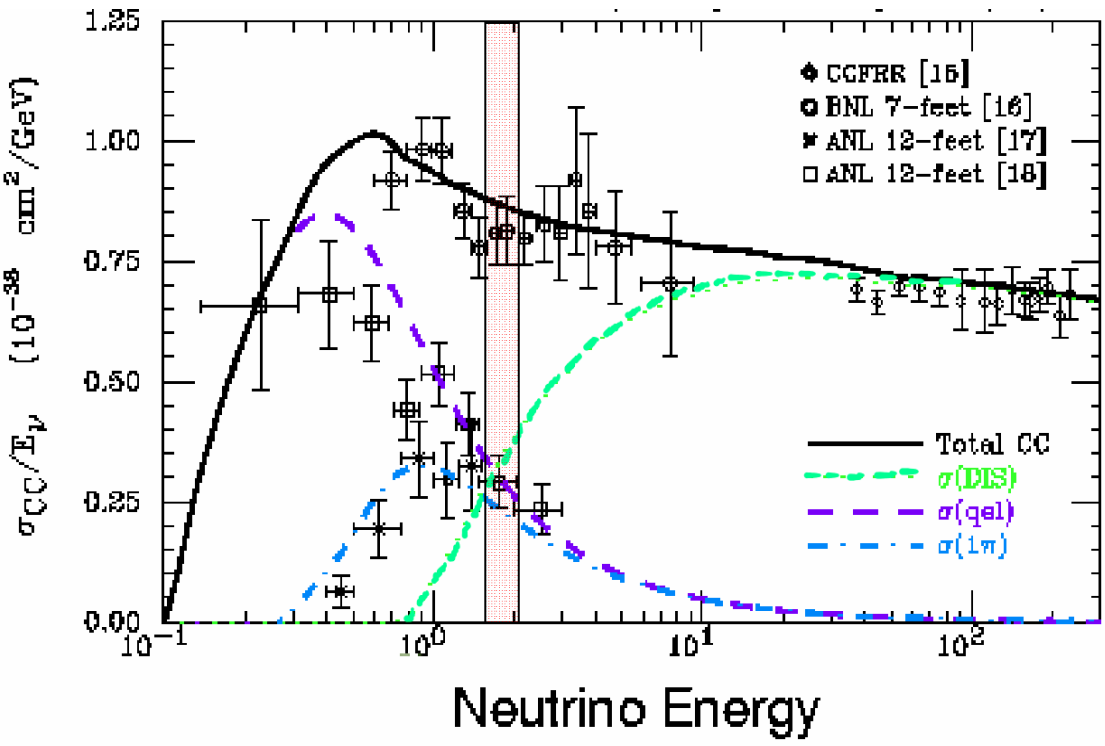

Fig. 10.11: A compilation of low energy charged current neutrino cross sections from G. Zeller [2]. The transparent red band indicates the peak energy of NOνA oscillated ν_e events.

The NC cross sections are even more poorly constrained by existing data, often with only one experiment contributing any data at all, so that a figure like Figure 10.11 is not even possible. Based on the few existing data, it appears that the NC cross sections are known to about 50% at best. NC Resonance and NC DIS events in the NOνA detector can fake ν_e CC events if a higher energy NC neutrino interaction creates a π^0 which gets misidentified as a 2 GeV electron. This feed-down from higher energies means we are interested in the NC cross sections well above 2 GeV. The parent neutrino energy spectrum for NC π^0 events which fake a beam ν_e at 2 GeV is roughly flat in energy.

In Coherent processes the neutrino scatters off the nucleus as a whole, and the only final state particle produced (besides the lepton) is a single charged pion for the CC process, or a single neutral pion for the NC process. Coherent CC events are not a problem for NOνA since they should not fake our ν_e oscillation signal. Coherent NC interactions have the same properties as the more familiar NC processes discussed above in that the observed energy is typically significantly less than the energy of the parent neutrino energy initiating the interaction. Figure 10.12 shows a compilation of both CC and NC coherent pion production cross-section measurements. These cross sections are known only to about 50% and their absolute values are roughly 20% of the NC Resonance plus DIS processes.

All these data will be substantially improved during the next few years. K2K, with 1.3 GeV neutrino data, and MiniBooNE, with 0.8 GeV neutrino data, each have high statistics samples and will contribute improved low energy cross section data. MINOS is optimized for ν_μ detection [6] and can probably only add to the ν_μ CC data. The MINERνA experiment [3] aims to measure all of the relevant CC cross sections to the 5% level and the NC cross sections to the 20% level before NOνA begins taking data. MINERνA will make the greatest difference to NOνA, particularly because MINERνA will run in the NuMI low energy beam and collect data on neutrino cross sections in the 1.5 – 5 GeV range.

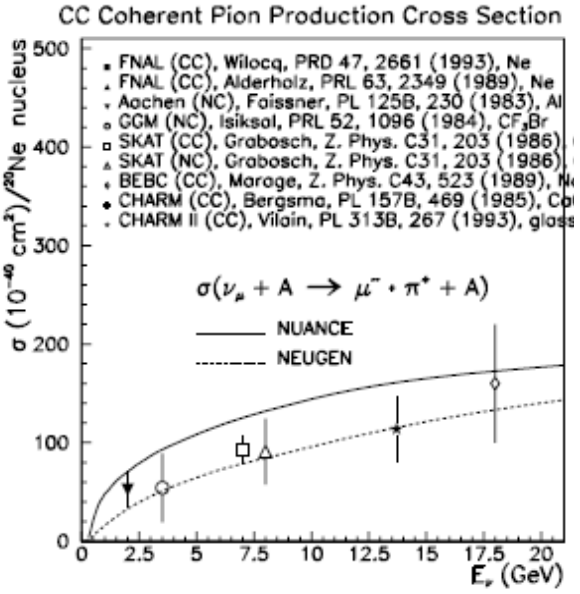

Fig. 10.12: Compilation of coherent pion production cross-section measurements from G. Zeller [2]. Both CC and NC pion production data are shown. NUANCE and NEUGEN are Monte Carlos which model these cross sections in different ways.

MINERνA data on NC above 2 GeV will be invaluable to NOνA simulations. In addition, we will be able to compare NOνA measurements of CC and NC QE, Resonance, Coherent, and DIS interactions to the precise MINERνA results and understand the NOνA detector response to each process.

In Chapter 13 we discuss measurements NOνA should be able to contribute to the low energy neutrino cross section picture.

10.8. Summary of Beam Backgrounds

Many of the uncertainties discussed in this chapter will be greatly reduced by the time NOνA runs: MIPP data will constrain the beam flux calculations, MiniBooNE will illuminate the LSND question, and MINERνA will measure the basic neutrino cross sections. We will calibrate our Near Detector and study its properties in a test beam and in the MINOS Surface Building. Still, the NOνA Collaboration and the laboratory need to be aware of these various effects and that has been the motivation for this discussion.

Ignoring NC effects, the NOνA Near Detector at Site 1.5 sees a "real" beam ν_e distribution ("real" defined as ν_e from decays in the secondary beam off the NuMI target) that can be ~ 7% different from the Far Detector as shown in Figure 10.5. The Near and Far Detectors both see additional "fake" beam ν_e distributions from contamination by NC and Coherent NC events with π^0s, and in fact the two detectors will see somewhat different NC effects since they see somewhat different parent energy spectra. All these effects can conspire to introduce systematics into our determination of the ν_e background for any ν_e appearance signal in the Far Detector.

A NOνA Far Detector ν_e appearance signal energy distribution will have a very different shape from the beam ν_e energy distribution ("real" or "fake"), peaking near 2 GeV as shown in Figure 4.5. We exploit that difference in our analysis to obtain large rejection factors for the various backgrounds, and this is discussed in Chapter 12. Our simulations indicate we will see a 19.5 event background to a NOνA ν_e appearance signal measurement. This background is composed of 61% from "real" beam ν_e events (11.9 events), of 2.5% from ν_μ CC backgrounds (0.5 events), and of 36.5% from NC backgrounds (7.1 events).

From a simulation point of view, the first of these backgrounds ("real" beam ν_e) will be known to ~ 7% from our matching of the Near Detector at Site 1.5 to the far site. This implies an uncertainty of 0.8 event on the 11.9 events. The second (ν_μ CC) background will be known to ~ 15% from our extrapolation procedure described in section 10.6. This implies an uncertainty of 0.08 events on the 0.5 events. The last background (NC) will be known to ~ 5% from the kinematics of the flux prediction for the unoscillated neutrino spectrum in the Far Detector. This implies an uncertainty of about 0.4 events on the 7.1 events. Assuming uncorrelated errors for these three processes would indicate an overall uncertainty at the level of about 0.9 events (5%) for the 19.2 event background discussed in Chapter 12.

Measurements and understanding of these backgrounds with our Near Detector will require careful work and data taking in several off-axis positions.

10.9. Cosmic Ray Backgrounds

The cosmic ray background will be strongly suppressed in NOνA by the very low duty cycle of the accelerator beam (~10 μs spill every ~2 seconds), directionality of this incident neutrino beam (pointing from Fermilab) and its relatively high energy (1.5-2 GeV).

Our preliminary estimates and simulations, described below, indicate that this background should not be a problem. Furthermore, this background can be measured with very high precision during the off-beam time. It is also our intention to test our estimates during prototype testing.

The atmosphere behaves as a 10-interaction length, 25-radiation length calorimeter for the incident primary cosmic rays. The results of interactions in the atmosphere are extensive air showers, with the following components persisting to the surface: penetrating muons with average energy ~ 4 GeV, showering electrons and photons with average energies in the range of tens of MeV, and some hadrons, primarily neutrons, with average energies of hundreds of MeV. To estimate the effects of these secondary particles on operation of the NOνA Far Detector we assume the detector as described in Chapter 5 and a live-time of the detector of 100 seconds per year (~10^7 spills per year, each 10 μs long). We discuss next the manifestation of each component on the detector separately.

10.9.1. Cosmic Ray Muons: The muon flux at the surface of the Earth is approximately 120 $\cos^2\theta$ m^{-2} s^{-1} sr^{-1}, where θ is the zenith angle. This flux yields an average of 8 muon trajectories inside the detector per 10 μs spill-gate and a total of 8×10^7 muons per year in the Far Detector during the active spill. Each of our 500 ns electronic time slices (described in Chapter 7) will contain an average 0.4 muons over the ~ 2000 m^2 area of the detector. These muons provide an essential calibration and alignment tool. The muons have a median energy of 4 GeV, and 10% to 20% originate in the same air shower, appearing as in-time multiple tracks. Using an expression for the integral flux as a function of energy and zenith angle [7], we estimate that 50% of the muons will stop in the detector. Muons themselves clearly cannot simulate our

signal, which could only happen through their interactions in the detector.

10.9.2. Cosmic Ray Electrons and Photons: A significant flux of electrons and photons from the extensive air showers survives at ground level. The net flux is about 50% the muon flux, but their average energy is less than 100 MeV [8] as shown in Figure 10.13. The electrons and photons will generally produce small showers that penetrate short distances (less than 1 m typically) into the top of the detector. Only ~2% have energies above 1 GeV and are capable of producing a significant shower or "splash" at the top of the detector, causing multiple hits in the scintillator strips.

10.9.3. Cosmic Ray Hadrons: A small component of hadrons survives to ground level. Neutrons and protons are nearly equal components. Protons, having an electric charge, will be detected as background events with high efficiency. The neutrons have an interaction length of ~1.5 m and their interactions are therefore a potential source of background. Their trajectories are much more vertical than the muons, with average angle ~20° from the zenith, and their median energy is ~100 – 200 MeV. Figure 10.14 shows the integral flux of neutrons incident on the top of the detector calculated from the measured differential flux [9]. We estimate that 1.0×10^5 neutrons with energies above 2 GeV will interact in the detector per year within the neutrino spill gate; they will be concentrated near the top of the detector.

Even though neutrons at ground level are always accompanied by muons or electrons, this fact is not very useful as a veto for neutrons entering the detector because of large typical spatial separation. Using the standard cosmic ray code CORSIKA [10], we found that only 4% (10%) of the neutrons have an accompanying muon within 50 (100) m, providing no satisfactory veto power for the proposed detector dimensions.

In the few GeV energy region, ~20% of the inelastic neutron interactions produce a single pion, which, in principle, might simulate an electron track. 98% of all CC events have a track within 25^o of the neutrino beam direction and thus a pion from a neutron interaction must be emitted at an angle at least ~60° to provide a possible background to a beam neutrino event. From kinematics, the maximum possible energy of a pion to be emitted at 60° is 1.5 GeV, just at the edge of possible acceptance. With the addition of a topology requirement that the track should be electron-like, we estimate that background from neutron interactions will be at the level of <1 event/year.

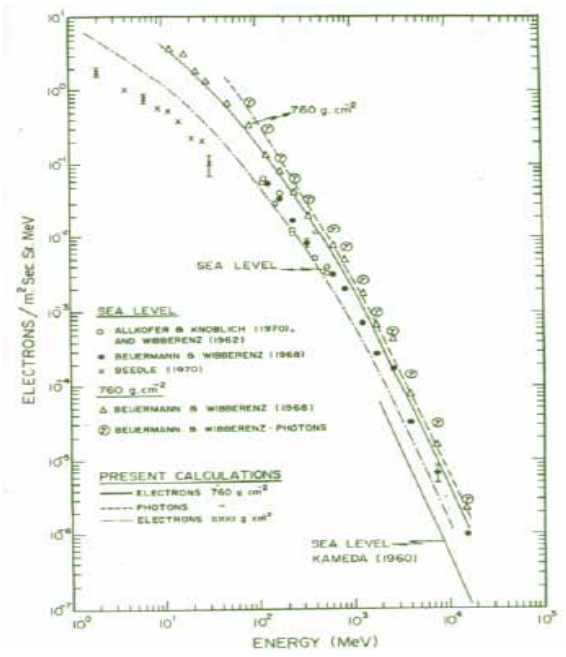

Fig. 10.13: Observed and calculated differential energy spectra of electrons and photons from ground based measurements. This figure comes from reference [8].

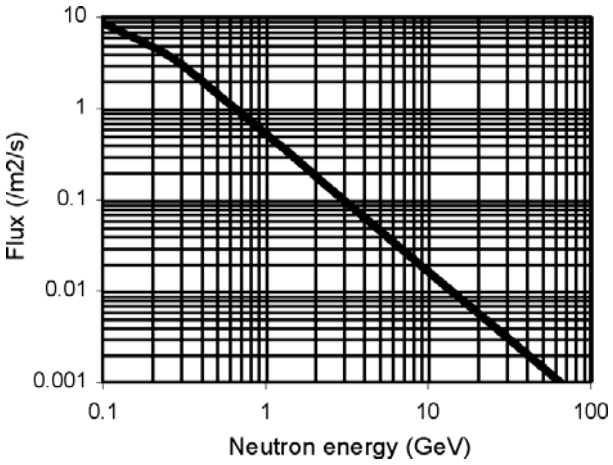

Fig. 10.14: Integral flux of neutrons at ground level

A GEANT simulation of neutrons incident on the detector was performed to determine this number more precisely. In the simulation, neutrons with energies ranging from 1-5 GeV, uniform in azimuth, and fixed zenith angles were incident on the detector. The results were analyzed against the standard selection criteria that are used for signal selection to determine the probability of selecting a cosmic ray neutron event as a signal. Figure 10.15 shows how the selection probability increases as zenith angle increases, as expected, and is still small, even at horizontal incident angles.

Convoluting this result with the measured flux [9], which is steeply falling with both energy and zenith angle, and the detector geometric acceptance, gives an expected number of events shown in figure 10.16. The total number of events selected in a 5 year exposure is 0.44 events.

Off-spill cosmic ray data in NOvA will precisely measure the cosmic ray backgrounds.

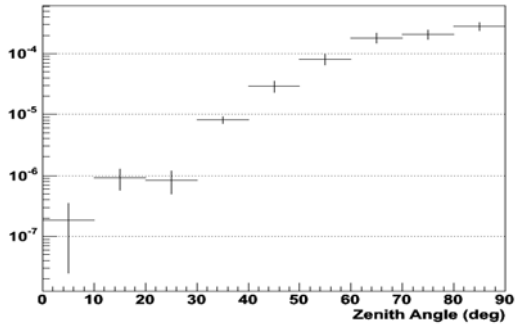

Fig. 10.15: Selection probability for neutrons with energy in the range of 1-5 GeV as a function of zenith angle.

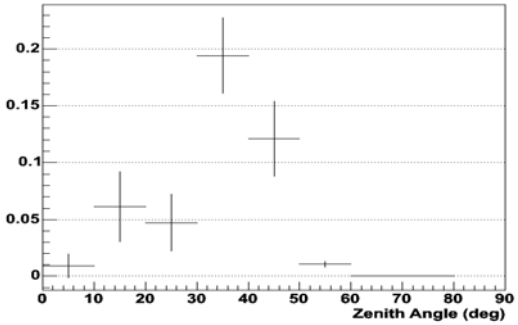

Fig. 10.16: Number of selected events in a 5 year exposure due to cosmic ray neutrons as a function of zenith angle.

Chapter 10 References

[1] Y. Fisyak *et al*., "P-907: Proposal to Measure Particle Production in the Meson Area Using Main Injector Primary and Secondary beams," May, 2000. See Figure 5 in this proposal. http://ppd.fnal.gov/experiments/e907/Proposal/E907_Proposal.html

[2] G. Zeller, "Low-energy neutrino cross sections: comparison of various Monte Carlo predictions to experimental data," hep-ex/0312061, proceedings of NuInt02, Irvine CA, 12-15 December 2002.

[3] D. Drakoulakos et al., "Proposal to perform a high-statistics neutrino scattering experiment using a fine-grained detector in the NuMI beam," February 2004, see http://www.pas.rochester.edu/minerva

[4] Director's Review of MIPP, November 12, 2004, see http://www.fnal.gov/directorate/program_planning/Nov2004PACPublic/Raja_PAC_Nov2004.pdf

[5] A. Aguilar et al., Phys. Rev. D **64**, 112007 (2001).

[6] M. Diwan, M. Messier, B.Viren, L. Wai, "A study of $\nu_\mu \rightarrow \nu_e$ sensitivity in MINOS," NuMI-NOTE-SIM-714, February 2001.

[7] H. Jokisch et al., Phys. Rev. D19, 1368 (1979).

[8] R. R. Daniel and S. A. Stephens, Revs. Geophys.and Space Sci, 12, 233 (1974).

[9] F. Ashton, "Cosmic Rays at Ground Level', ed. A. Wolfendale (1974); W. N. Hess et al., Phys. Rev.116, 445 (1959).

[10] D. Heck et al., Report KfK6019, Forschungzentrum Karlsruhe (1998).

11. Proton Beam

11.1. Introduction

This proposal assumes a 5 year run with the 30 kiloton (kT) NOνA Far Detector and beam intensity in the Main Injector such that the NuMI target receives 6.5 x 10^{20} protons on target per year (pot/yr). The laboratory and the NOνA Collaboration have mutually agreed [1] that NOνA should use this number to illustrate the reach of the experiment in a pre-Proton Driver era. The laboratory and the NOνA Collaboration also have agreed that this number of pot/yr should not be viewed as a promise of delivered beam. We will review the details of this pot/yr calculation in this chapter and assess the probability of not reaching the full beam intensity.

With a Proton Driver at Fermilab the beam intensity expected in the NOνA experiment would increase and we have mutually agreed that 25.0 x 10^{20} pot/yr on the NuMI target should be used to illustrate the reach of the experiment in a Proton Driver era. We also discuss the details of this assumption here.

11.2. The Proton Plan

Following the work of a "Proton Committee" [2], the laboratory is assembling a "Proton Plan" for the years 2005-2008. The November 9, 2004 draft Proton Plan [3] indicates the laboratory would be in Phase III of that program beginning in 2008, about one year before NOνA begins data taking. Table 6 of the November 2004 Proton Plan shows the following parameters:

- Booster Batch Size of 5.5 x 10^{12} protons.
- Main Injector (MI) loading with 2 Antiproton Source + 9 NuMI batches. This means slip-stacking is implemented for both programs. (Barrier bucket stacking has also been discussed recently).
- MI Cycle Time of 2.2 seconds.
- MI Intensity of 6.0 x 10^{13} protons.
- Booster maximum rate of 8.3 Hz limited by radiation levels.
- NuMI annual rate of 3.4 x 10^{20} protons on the NuMI target.
- Booster Neutrino Beam annual rate of 2.2 x 10^{20} protons.

Phase III includes 10% down time for NuMI for collider shot setup and a 5% reduction to NuMI to allow for antiproton transfers from the Accumulator to the Recycler. Phase III also includes a 90% operational efficiency factor for NuMI and another 90% efficiency applied to slip stacking for NuMI.

11.3. Proton Plan in the Post-Collider Era

Recent direction from the Department of Energy indicates that the Fermilab Proton Plan can be updated to show the end of the Fermilab Collider Program in 2009, about the same time as NOνA would begin operating. We envision several changes to the parameters listed in Section 11.2 above in this post-collider era.

Without a collider program, there is no need for anti-proton production batches in the Main Injector, so 11/9 (a factor of 1.22) more beam could be available to NuMI. Without a collider program, the 10% downtime for NuMI for collider shot setup and the 5% reduction to NuMI for antiproton transfers from the accumulator to the Recycler can be recovered (in total this is another factor of 1.176).

Without a collider program, the Recycler is also available as a proton accumulator. The 2.2 second MI cycle time in Section 11.2 comes from the time to load 11 Booster batches during 12 Booster cycles at 15 Hz (0.8 seconds) plus the MI ramp up and down time of 1.4 seconds. The time to load the Booster batches into the MI can be hidden under the MI cycle time by loading these Booster batches into the Recycler and then taking only one Booster cycle (0.067 seconds) to inject from the Recycler to the MI. This would reduce the effective MI cycle time from 2.2 seconds to 1.467 seconds and give a factor of 1.50 more beam to NuMI.

These three factors imply the NuMI annual rate could be increased by (1.22)(1.176)(1.50)(3.4 x 10^{20} protons) = 7.3 x 10^{20} protons. We have agreed with the laboratory to use ~90% of this value (6.5 x 10^{20} protons per year) in this proposal to illustrate the reach of the NOνA experiment.

As a crosscheck, the total Booster rate in this scenario is now 11 batches in 1.467 seconds or 7.5 Hz. This is comfortably below the Phase III

maximum Booster rate of 8.3 Hz limit due to Booster radiation limits anticipated in 2008.

Another required crosscheck is for the number of seconds the MI would operate in one year. The total annual NuMI rate of 7.3×10^{20} protons divided by the Phase III MI intensity of 6.0×10^{13} per pulse gives 1.22×10^{7} MI pulses in a year. At a cycle time of 1.467 seconds, this means 2.0×10^{7} seconds of MI operations per year or 63% of the available seconds in a year. This can be compared to typical laboratory assumptions of 40 weeks of operations per year with each week averaging 120 hours of beam time yielding 1.73×10^{7} seconds of operations per year. 46 weeks of operations would be required for 7.3×10^{20} protons, or 41 weeks for 6.5×10^{20}.

11.4. Possible Limitations to the NOνA assumption of 6.5×10^{20} pot per year

The Proton Plan [3] and the factors multiplied together in Section 11.3 could be overly optimistic, so we examine these assumptions in this section. Main Injector proton losses in the acceleration cycle may be a limiting factor as operations approach 6×10^{13} protons per cycle. Part of the Proton Plan includes increasing aperture restrictions, reducing beam tails, and adding a collimation system to the MI. MI slip stacking or barrier bucket stacking may not succeed completely when extended from 2 booster batches in pbar production to 11 batches for NuMI. As noted in Section 11.2, the Proton Plan already assumes a 90% efficiency for NuMI operations and another 90% efficiency applied to slip stacking for NuMI.

In Section 11.3 we have assumed that the Recycler can be used as a proton accumulator including slip stacking in the Recycler as was originally assumed to occur in the MI. The laboratory [4] believes this use of the Recycler is a reasonable assumption since the Recycler looks almost identical (same aperture, same energy, …) to the MI at 8 GeV. Using the Recycler would involve some expense. Protons from the Booster currently cannot be injected directly into the Recycler, so the transfer line from the Booster to the MI would have to be redirected. This would not involve civil construction. The Recycler would also require additional RF to handle the increased beam and slip stacking.

So in both of the above cases, the tricky part is the slip stacking of many Booster batches. The Proton Plan does note [5] that

> "slip stacking has been successfully developed for antiproton production, and development for NuMI will be demonstrated by early 2006."

As a measure of the risk that NuMI slip / barrier stacking does not materialize, one could assume only Phase II of the Proton Plan is realized. The parameters of Phase II are as follows:

- Booster Batch Size of 5.3×10^{12} protons.
- Main Injector (MI) Loading with 2 Antiproton Source + 5 NuMI batches. This means slip-stacking is implemented only for antiproton production.
- MI Cycle Time of 2.0 seconds.
- MI Intensity of 3.7×10^{13} protons.
- Booster maximum rate of 7.5 Hz limited by radiation levels.
- NuMI annual rate of 2.2×10^{20} protons on the NuMI target.
- Booster Neutrino Beam annual rate of 2.8×10^{20} protons.

Without a collider program, we next apply similar scaling factors to the Phase II NuMI protons following the arguments made in Section 11.2 for Phase III:

- Now it's a factor of 7/5 = 1.40 since the 2 Booster batches destined for the antiproton source can be redirected to NuMI.
- The same factor of 1.176 applies for recovering collider shot setup time and Accumulator to Recycler transfer time.
- The Recycler could still be used as a proton accumulator. The 2.0 second MI cycle time comes partially from the time to load 7 Booster batches during 8 Booster cycles at 15 Hz (0.467 seconds). Of this time, 0.400 seconds can be hidden under the MI cycle time by loading these Booster batches into the Recycler and then taking perhaps only one Booster cycle (0.067 seconds) to inject from the Recycler to the MI. This would reduce the effective MI cycle time from 2.0 seconds to 1.467 seconds, giving a factor of 1.36 more beam to NuMI.

The net result is $(1.4)(1.176)(1.36)(2.2 \times 10^{20}$ protons$) = 4.9 \times 10^{20}$ protons to NuMI. This is 67% of the annual rate calculated in Section 11.3. We

believe this represents the most conservative assumption for NOνA in a pre-Proton Driver era.

We note that a contingency to this 67% assumption exists in a possible upgrade to the MI RF system to shorten the MI ramp rate to as little as 1.0 seconds. This scheme will be discussed below in section 11.6.

11.5. Possible Limitations from the NuMI Beamline

The NuMI components were designed for 4 x 10^{13} protons per MI pulse and the discussion in Section 11.3 would increase that instantaneous rate by a factor of 1.50. The NuMI components were designed for a 1.87 second cycle time and the discussion in Section 11.3 would decrease the cycle time to 1.467 seconds, a factor of 1.27. For some components the two factors get multiplied together to give an overall increase of 1.90. In this section we examine these components to see if any of them will limit our assumption of 6.5 x 10^{20} pot per year. These issues are under study and this section gives a first look at the situation.

The beam windows in the system would not be over stressed by these higher intensity and cycle time numbers.

The NuMI target was designed with a safety factor of 1.8 against stress from instantaneous beam, so we would push nearer to the limit with a factor 1.5 more instantaneous beam. However, NOνA proposes to use the medium energy configuration of the NuMI beam and in this case the target is outside of the horn (vs. inside Horn 1 for MINOS in the low energy configuration). This makes solutions somewhat simpler if there is need to reduce target stress or deal with radiation damage. For example it would be possible to replace the target more often or possible to make a moving target so that no one section accumulated too much radiation damage.

The horns themselves would see additional heating from the factor of 1.50 in instantaneous rate, but they can take this load as long as the heat is removed by the water cooling system. The air cooled stripline to the horn would be right on the edge of needing water cooling in the last ten-foot section. Such water cooling is possible and might cost of order $300K.

The Target Pile Air System also would be pushed hard since the capacity of the water chiller is only ~15% oversized. The minimum upgrade would be to add an additional chiller to the existing Air System, gaining about a factor of two.

The Decay Pipe cooling would have to be looked at in more detail. For the Proton Driver case (next section), studies so far have not been able to prove or to disprove that the water cooling piping is adequate. There are cooling lines every 30^0 around the circumference of the pipe, so stress can increase due to differential heating between the hot spots and the cooling lines 15^0 away. This Decay Pipe is a vacuum vessel, so one simple fallback here would be to remove the vacuum vessel stress (and attendant heightened design requirements) by filling the pipe with helium at atmospheric pressure. This would reduce the neutrino flux by a few percent.

The absorber could handle the increased instantaneous rate since the aluminum components can easily remove the heat. The current aluminum design allows cooling to one of three modules to fail and the absorber is still adequately cooled by air convection to the adjacent modules. However, the absorber water system cooling capacity would probably have to be upgraded. The absorber was designed with redundant cooling lines, so one solution is to use the original lines plus the redundant ones.

For NuMI running at 4 x 10^{20} pot per year, conservative designs were adopted to ensure that the groundwater radiation concentrations would be well below the regulatory limits[6]. Beginning in 2005, measurements of radiation levels from NuMI running will be available and allow extrapolation to the case of 1.63 (= 6.5 x 10^{20} pot / 4 x 10^{20} pot) times as many pot/year being discussed here. Measurable levels of ^{3}H or ^{22}Na in the groundwater monitoring wells around NuMI are not expected at 4 x 10^{20} pot/year and extrapolations by a factor of 1.63 after initial NuMI running should indicate negligible levels relative to the regulatory limit in these wells. Similarly, measurements during the initial years of NuMI running will be made of the levels of radionuclides in the water pumped from the NuMI tunnel and released to the surface waters. These levels are expected to be at least a factor of 20 (twenty) below the surface water limits, so that a factor of 1.63 increase should not be a problem.

Overall the conclusion is that the NuMI components with additional cooling could handle the 6 x

10^{13} protons in MI pulses and the shortened cycle time of 1.467 seconds as outlined in Section 11.3 for the post-collider era. There are work-arounds for each component in case further study indicates some need further help.

The more conservative beam assumption discussed in Section 11.4 with 70% of 6.5 x 10^{20} pot per year delivered to NOνA is handled more easily by NuMI components. This reduced beam scenario has the same cycle time of 1.467 seconds but with only 3.7 x 10^{13} protons per MI pulse. The instantaneous rates are down by 40% and within the original design envelope for the components.

11.6. NOνA and the NuMI Beam Line with a Proton Driver

Over the last year, the idea of building a new 8 GeV Proton Driver has become a centerpiece of the recommendations of the Fermilab Long Range Planning Committee [7]. The 8 GeV proton linac plan under discussion would increase the MI intensity and shorten the MI ramp time, realizing a 2 MW proton source. This would benefit NOνA as discussed below:

- The MI intensity per pulse would be increased to 15 x 10^{13} protons. In this era, slip stacking is not part of the plan and the linac's small beam emittance is used to increase the MI intensity. Compared to the NuMI annual rates calculated in Section 11.3, the Proton Driver would increase the NuMI proton beam by a factor of (15 x 10^{13} / 6 x 10^{13}) = 2.5.
- The MI cycle time would be reduced to 1.37 seconds for the MI ramp (now free of the Booster clock cycle that meant the minimum was 21/15 sec) plus 0.1 seconds to fill the MI from the Proton Driver. Compared to the rates calculated in Section 11.3, the shorter cycle time would increase the NuMI proton beam by a factor of (1.467 / 1.470) = no effect.
- The laboratory is considering adding a MI RF and MI power supply upgrade to the Proton Driver scheme to decrease the MI cycle + fill time further to as little as 1.00 seconds. This would increase the NuMI proton beam by a factor of (1.467 / 1.00) = 1.467. Decreasing the MI cycle time in this way would carry a substantial additional cost of 10-20% to a Proton Driver project.

Overall the Proton Driver could increase the annual NuMI beam intensity to (2.5)(1.0)(1.47)(6.86 x 10^{20} protons) = 25.2 x 10^{20} protons.

As a conservative fall-back position, we think of an annualized NuMI intensity using only the Proton Driver itself and realizing (2.5)(6.86 x 10^{20} protons) = 17.2 x 10^{20} protons. This is 68% of the annual rate calculated above. We believe this represents the most conservative assumption for NOνA in the Proton Driver era. We note that in the event a Proton Driver is not approved, decreasing the MI cycle time is still an option and still provides additional reach to a Fermilab neutrino program.

All changes discussed in this section impact the stability and lifetime of the target, horns and other systems in the NuMI beam line. These issues are still under study and upgrades to the target and beam line are anticipated.

Chapter 11 References

[1] February 21, 2005 meeting with Mike Witherell, Ken Stanfield, Steve Holmes, Hugh Montgomery, Jeff Appel, John Cooper, and Gary Feldman. We note here that the post-collider / pre-Proton Driver numbers agreed upon are 90% of the maximum MI beam available at Fermilab. Fermilab could elect to send more than 10% of available beam (or MI cycles) to other laboratory programs instead of sending this fraction to NuMI.

[2] Report to the Fermilab Director by the Proton Committee, October 26, 2003, http://www.fnal.gov/directorate/program_planning/studies/ProtonReport.pdf

[3] draft Proton Plan, November 9,2004, http://www.fnal.gov/directorate/program_planning/Nov2004PACPublic/Draft_Proton_Plan_v2.pdf

[4] Steve Holmes, private communication.

[5] draft Proton Plan, page 30.

[6] The applicable standards are based on DOE Order 5400.5, USEPA regulations 40 CFR 141, and 35 IAC 620.410 (e) Groundwater Quality Standards for Class I: Potable Resource Groundwater, P. Kesich and N. Grossman, private communication.

[7] Report of the Long Range Planning Committee, May 2004, www.fnal.gov/directorate/Longrange/Long_range_planning.html

12. Simulations of NOνA Performance

12.1. Introduction

We have simulated the signals and backgrounds for $\nu_\mu \rightarrow \nu_e$ oscillations using relevant parts of the MINOS experiment software, the NEUGEN3 neutrino interaction generator and the GEANT3 detector simulation. The steps in the simulation were

1) Generation of the event interaction.
2) Calculation of the detector response to the generated particles.
3) Reconstruction, i.e. track finding and fitting. A quadratic fit is made to each track using the pulse height-weighted cell positions in each plane.
4) Calculation of various parameters associated with each track.
5) Assignment of particle identity to each track (e, μ, p, γ, or hadron).
6) Calculation of the interaction vertex.
7) Preliminary identification of events with
   a) A measured energy within 25% of the nominal off-axis energy.
   b) No significant energy deposition near the detector boundaries.
   c) An electron candidate, which starts near the vertex and has no gaps near the vertex.
   d) No μ or γ in the event.
8) Separation of signal and background events using a maximum likelihood analysis with the following variables
   a) Total measured energy
   b) Fraction of total energy carried by the electron
   c) Mean pulse height near the origin of the electron
   d) Pulse height per plane for the electron
   e) Number of hits per plane for the electron
   f) Energy upstream of the vertex
   g) Curvature of the electron
   h) Missing transverse momentum
   i) Fraction of total electron energy contained in the first half of the electron track
   j) rms deviation of electron hits from the fitted track
   k) number of tracks identified as hadrons in the event

The maximum likelihood optimization was done by maximizing a figure of merit (FoM) defined as the signal divided by the square root of the background, assuming that the oscillation is given by the formula

$$P\left(\nu_\mu \rightarrow \nu_e\right) = 0.5\sin^2(2\theta_{13})\sin^2\left(\frac{1.27\Delta m^2_{32} L}{E}\right), \quad (1)$$

where Δm^2_{32} =0.0025 eV^2, L = 810 km, and the energy spectrum is given by the NuMI medium energy beam. The matter, solar, and CP effects are not included in Eq. 1, but are incorporated in the discussion of the physics potential of NOνA in Chapter 13.

12.2. Detector Optimization

12.2.1. Cell Dimensions: Results for a few combinations of cell widths and depths are shown in Table 12.1. It appears that widening the transverse dimension of the cell from 3.8 cm to 5.4 cm causes a significant decrease in the FoM. However lengthening the longitudinal dimension of the cell from 4.5 cm to 6 cm appears to have little effect. A slightly different set of simulations indicate a reduction in the FoM for cells longer than 6 cm. Such cells would also require a thickening of the cell walls for structural reasons. Since lengthening the cell reduces the cost per unit mass of the detector, we have chosen 6 cm long cells rather than the 4.5 cm long cells described in Appendix B of the previous version of the proposal. The cell width of 3.8 cm has been retained.

Cell width	Cell depth	Relative FoM	Electron energy resolution
3.8 cm	4.5 cm	1.00	10.0%
3.8 cm	6.0 cm	1.02	10.7%
5.4 cm	4.5 cm	0.90	9.9%

Table 12.1. Simulation results for various cell dimensions.

12.2.2. Detector Off-Axis Transverse Location: Table 12.2 shows results for various transverse detector locations for both neutrinos and antineutrinos. The choice of transverse location depends

on the physics goals of the experiment and this topic is discussed in detail in Chapter 13.

Off-axis distance	ν or $\bar{\nu}$	Number of signal events	Number of background events	Figure of merit
8 km	ν	284.5	61.2	36.4
10 km	ν	227.4	39.0	36.4
12 km	ν	142.4	19.5	32.2
14 km	ν	90.5	12.9	25.2
8 km	$\bar{\nu}$	147.2	32.2	25.9
10 km	$\bar{\nu}$	109.0	18.5	25.3
12 km	$\bar{\nu}$	71.8	12.1	20.6
14 km	$\bar{\nu}$	49.3	8.4	17.0

Table 12.2: Number of $\nu_\mu \rightarrow \nu_e$ oscillation signal and background events and FoM for different off-axis detector locations. The numbers are for a 5-year run at 6.5×10^{20} pot/year and do not include matter, solar, and CP effects, which are included in the discussion of physics potential in Chapter 13. They assume that $\sin^2(2\theta_{13}) = 0.10$, $\sin^2(2\theta_{23}) = 1.0$, and $\Delta m^2_{32} = 0.0025$ eV^2. The number of signal events is proportional to $\sin^2(2\theta_{13})$, but the number of background events is essentially independent of it. The variation with Δm^2_{32} is discussed in Chapter 13.

The background listed in Table 12.2 is typically about two-thirds from beam ν_e's produced from muon and kaon decay and one-third from neutral-current events. The background from ν_μ charged-current events is quite small, less than one event. This is shown in the bottom half of Fig. 12.1, which plots the number of each class of background events as a function of the number of accepted signal events generated by changing the cut on the likelihood function. The numbers in Fig. 12.1 are for a 5-year neutrino run with NOνA situated at 12 km off axis and the other conditions as in Table 12.2. The top half of Fig. 12.1 shows the resulting FoM as a function of the number of accepted signal events.

The accepted fraction of ν_μ charged-current events is approximately 4×10^{-4} and the accepted fraction of neutral-current events is approximately 2×10^{-3}. The efficiency for accepting a ν_e event from $\nu_\mu \rightarrow \nu_e$ oscillations is approximately 24%.

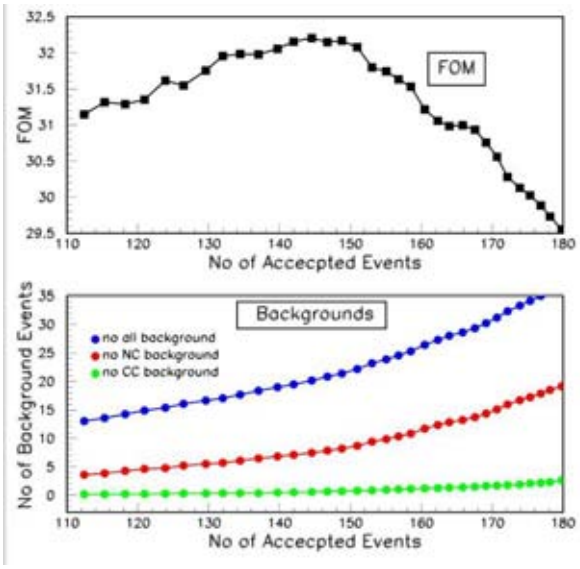

Fig. 12.1: The numbers of $\nu_\mu \rightarrow \nu_e$ oscillation background events and the FoM as a function of the number of accepted signal events generated by varying the cut on the likelihood function. The top half of the figure shows the FoM. The bottom half shows the number of background events. The green (bottom) curve shows the number of misidentified ν_μ charged-current events; the red (middle) curve shows the number of misidentified neutral-current events; and the blue (top) curve shows the total number of background events including the number of beam ν_e events.

12.3. Detector Performance

The simulations described in the preceding sections allow us to study the NOνA detector performance. We discuss here those features that are most relevant for the physics of highest current interest.

12.3.1. Energy resolution: There are several areas where energy resolution helps in improving quality of physics. In brief, they are:

a) In reducing the intrinsic beam ν_e background for the $\nu_\mu \rightarrow \nu_e$ appearance analysis. This is the only handle one has on that background.

b) In reducing the neutral-current and ν_μ charged-current backgrounds for this analysis; the energy distributions from these two sources generally will not peak at the oscillation maximum and be much broader.

c) In measuring the dominant oscillation mode parameters. This will be discussed in Section 13.6

For the first two, it is sufficient that the energy resolution should be good enough so that there is no appreciable broadening in the measured energy spread of the convolution of the beam energy distribution and the oscillation function. Then, the eventual energy cuts are determined by the natural energy spread of the beam. For the last, the energy resolution should be as good as possible.

The true and measured energy distributions for all $\nu_\mu \rightarrow \nu_e$ events are shown in Fig. 12.2. The additional spread in measured energy distribution due to the resolution is hardly perceptible – the rms width of the distribution changes only from 19.2% to 21.4%.

Another useful way of looking at the energy resolution is to look for correlations with the fraction of the total energy that goes into the electron, effectively the (1-*y*) parameter of the interaction. This is shown in Figure 12.3 where the energy information, represented as σE and defined as the difference between the true and measured energies divided by square root of true energy in GeV. The scatter plot of the left shows σE as a function of (1-*y*). Clearly as *y* approaches zero the number of events increases and the energy resolution improves. The middle plot shows the mean σE as function of (1-*y*) indicating adequate weighing of hadronic and electromagnetic energy deposition. Finally, the plot on the right shows the σE distribution; the rms width of the fitted curve is 8.7%. Restricting that sample to events passing all cuts for ν_e identification reduces this width to 6.7%.

12.3.2. Electron / muon separation: The electrons and muons look quite different in the NOνA detector. The electrons tend to deposit more energy per plane and are more "fuzzy", i.e. have more hits per plane. In addition, electrons, because of their showering nature tend to have a larger rms spread of the accepted hits and also have more gaps, whereas the muon tracks are rather continuous.

These are the principal parameters that distinguish muons from electrons and the separation is excellent. This is illustrated in Fig. 12.4, which

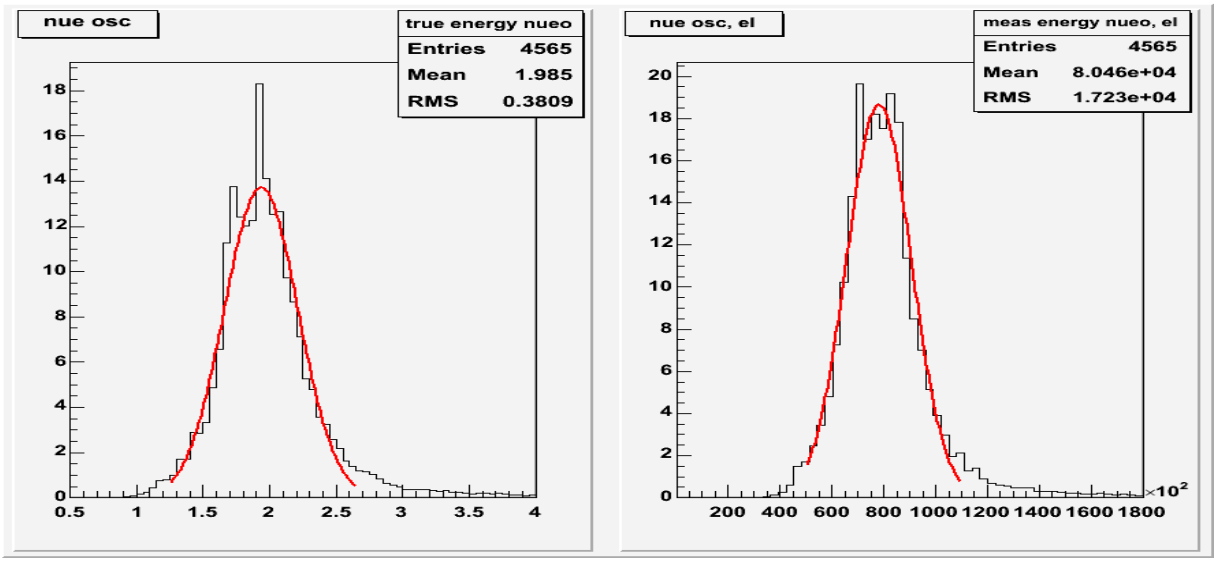

Fig. 12.2: True (left) and measured (right) energy distributions for all events with a reconstructed electron track. The units are GeV for the true energy and attenuation-corrected photoelectrons for the measured energy.

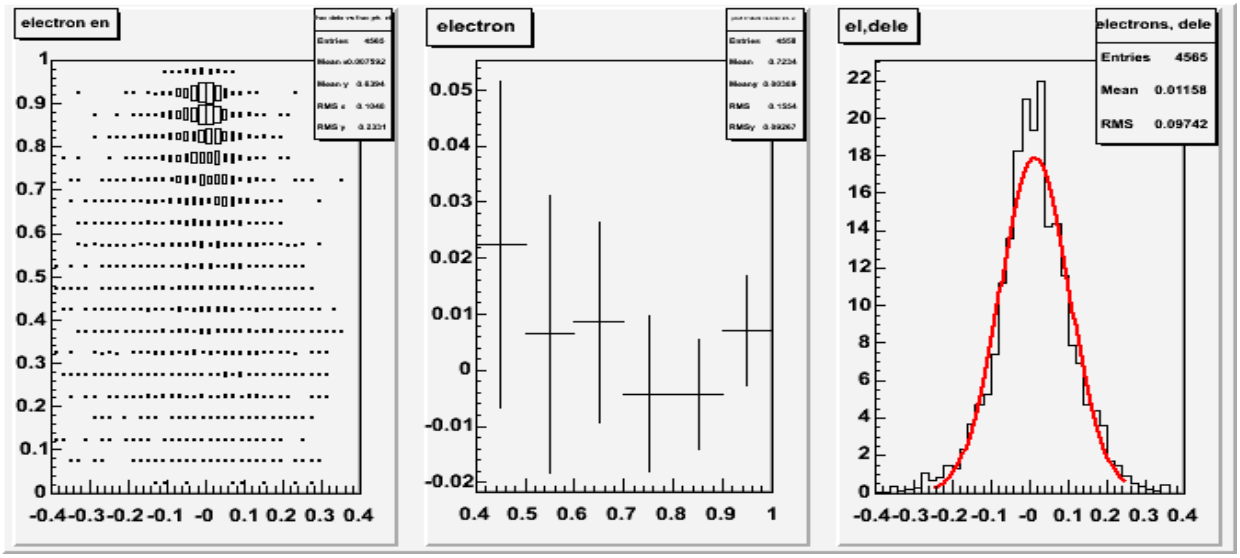

Fig. 12.3: Left: Measured minus true energy difference divided by square root of true energy in GeV, σE, on the horizontal axis as function of (1-y) on the vertical axis. Middle: average σE on the vertical axis as a function of (1-y) on the horizontal axis. Right: Distribution of σE.

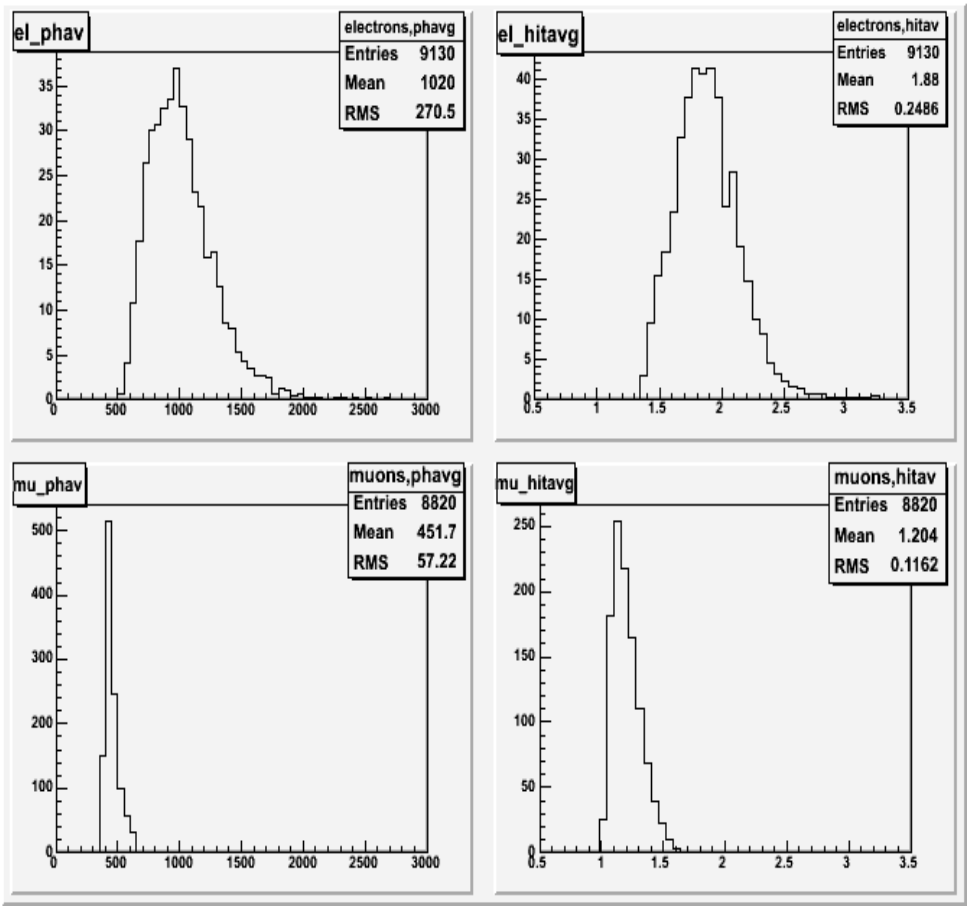

Fig. 12.4: Distributions of average pulse height/plane (left) and average number of hits per plane (right) for electrons in electron charged-current events (top) and muons in muon charged-current events (bottom).

shows the first two of these parameters, i.e. average pulse height per plane and the average number of hits per plane, both for electrons and muons. The muon hits per plane distribution is significantly broadened by the finite angle of the muon with respect to the beam direction, i.e. crossing of two cells in one plane. Once that is corrected the distribution will be even narrower.

Figure 12.5 further illustrates NOνA performance in separating electrons and muons. Forty thousand ν_μ charged-current events and 40,000 ν_e charged-current events were generated. Events outside the fiducial volume, events with energies clearly too high or too low to be of interest, and events in which no tracks were found were eliminated. The ν_e events were required to have a found electron with an average number of hits per plane greater than 1.4, and the ν_μ events were required to have a found muon with an average pulse height per plane less than 550. The remaining events are separated into two bins by event total energy, and for each energy band the average pulse height per plane is plotted versus the average number of hits per plane in Fig. 12.5.

These distributions indicate that the electron/muon separation is very clean. Thus the main mechanism for muon charged-current events looking like electron charged-current events would be production of π^0's, which then simulate electrons.

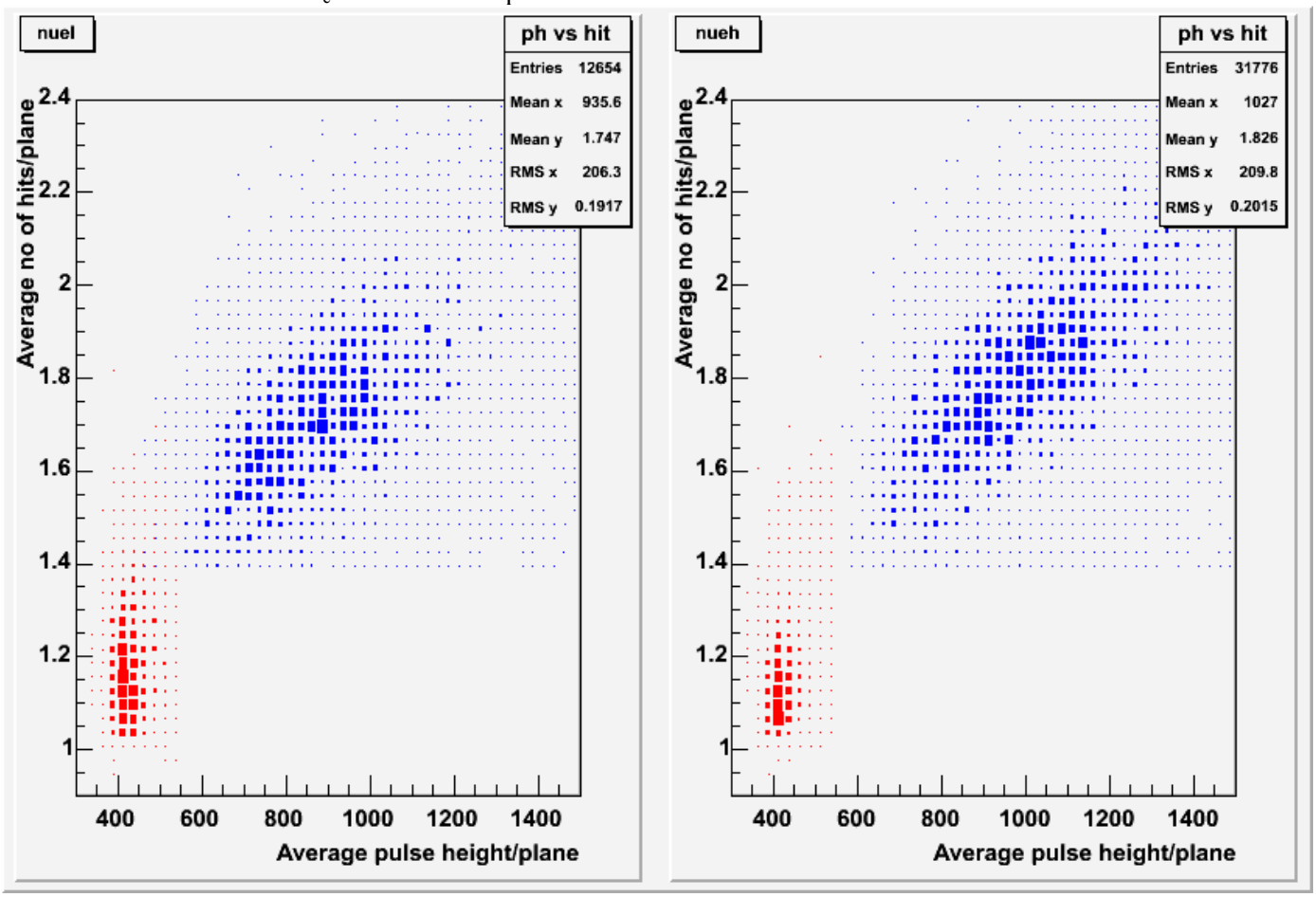

Fig. 12.5: Average pulse height per plane versus average number of hits per plane plotted for low energy events (left) and high energy events (right). Electrons are in blue; muons are in red. See text for additional details.

12.4. Typical Events

Figures 12.6-12.9 present a few typical events that illustrate the performance of the detector, using one example of each category of events: passing ν_e charged-current, failing ν_e charged-current, passing neutral current background and passing ν_μ charged-current background. These events are typical in so far that no special effort has been made to select them. They illustrate the most important characteristics of the different categories of events: the passing ν_e events tend to be rather clean without much extraneous pulse height and with most of the energy in the electron. On the other hand the failing ν_e events have most often a low energy electron. Both NC and ν_μ CC background events tend to have an energetic π^0 that is called an electron and the muon from the ν_μ CC background events has rather low energy. In addition these background events tend to be somewhat "messier".

Each figure has the *x*-*y* view on top and the *y*-*z* view on the bottom. The indicated color code represents the relative pulse height of the hits. The lines represent the trajectories of the final state particles with the following color code: charged leptons in red, charged pions in blue, protons in black, and π^0 in green. The length of the colored trajectory is proportional to the energy of the particle but is not its expected length in the detector.

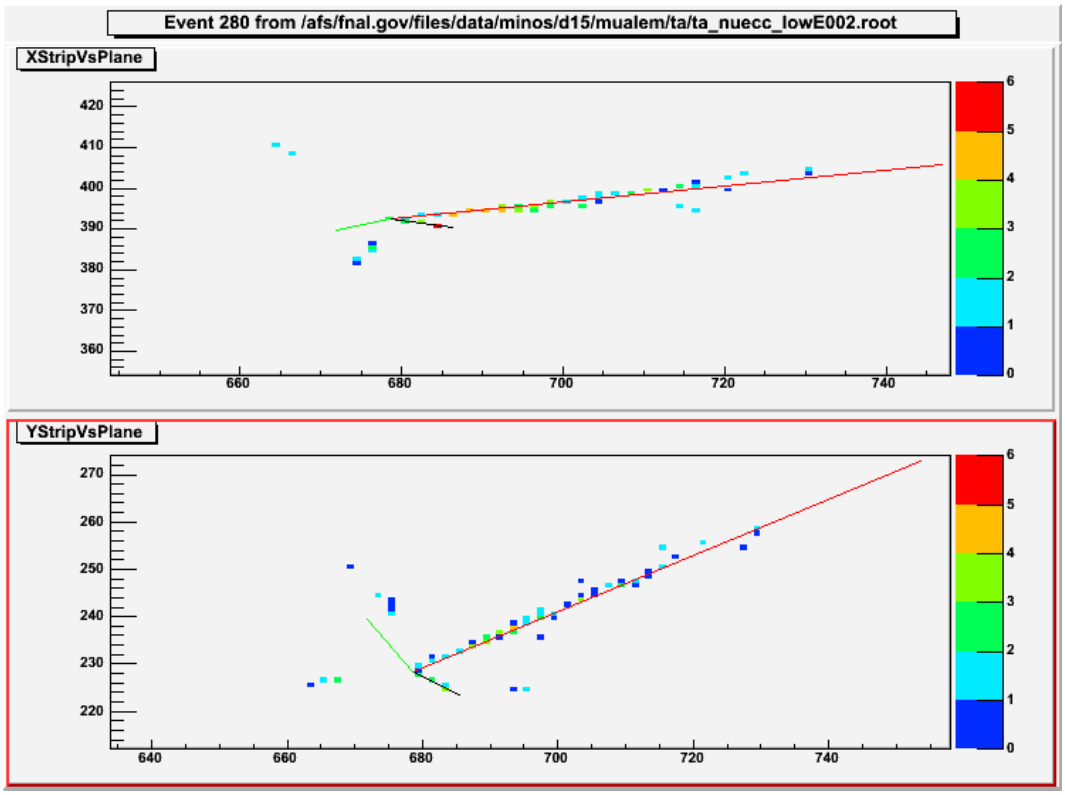

Fig. 12.6: An accepted ν_e charged-current event : $\nu_e A \to pe\pi^0$, E_ν = 1.65 GeV. See text for explanation of the codes.

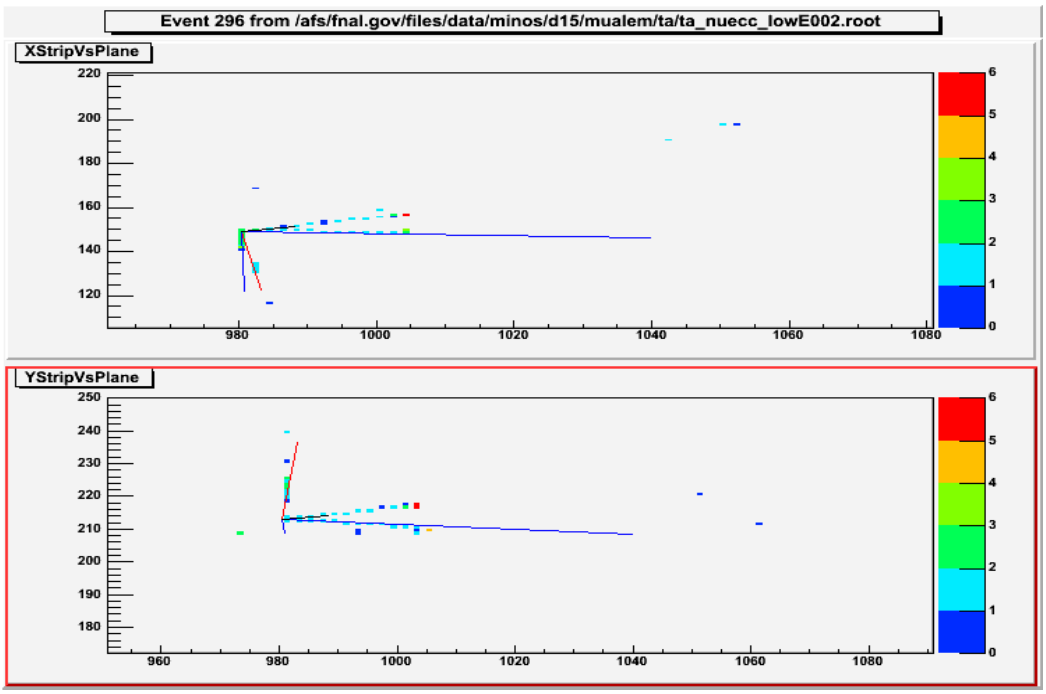

Fig. 12.7: A failing ν_e charged-current event : $\nu_e A \rightarrow pe\pi^+\pi^-$, E_ν = 1.87 GeV. See text for explanation of the codes.

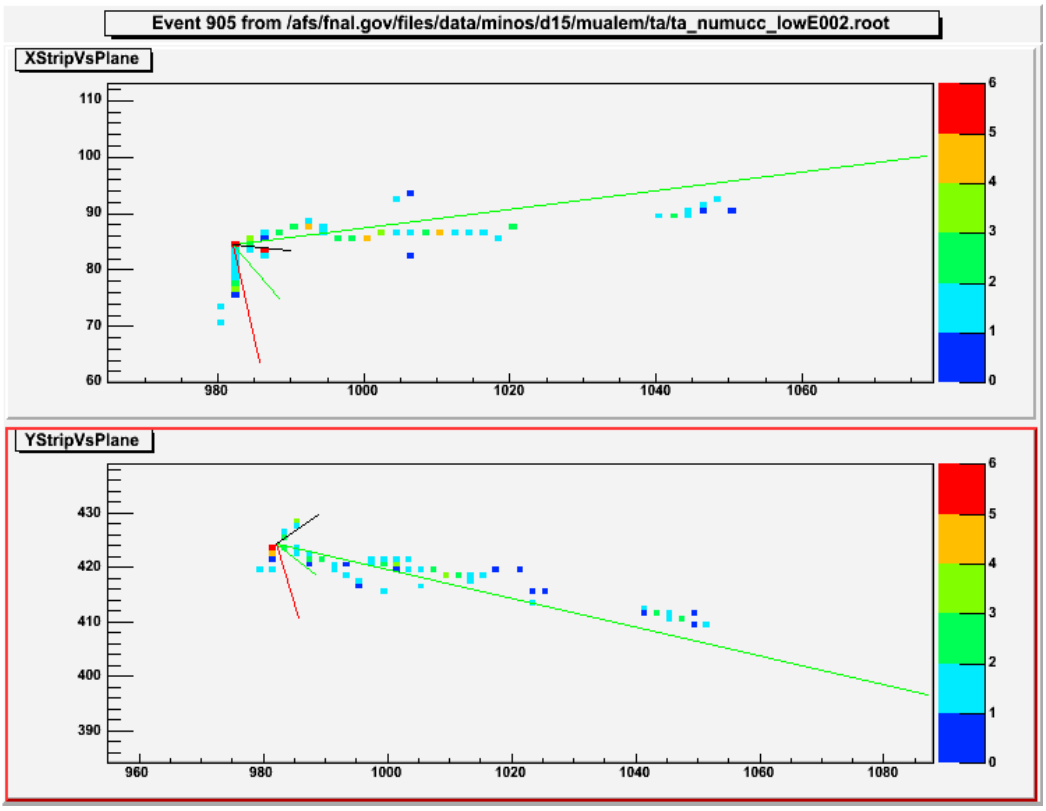

Fig. 12.8: A background ν_μ charged current event: $\nu_\mu A \rightarrow p\mu\pi^0\pi^0$, E_ν = 1.70 GeV. See text for explanation of the codes.

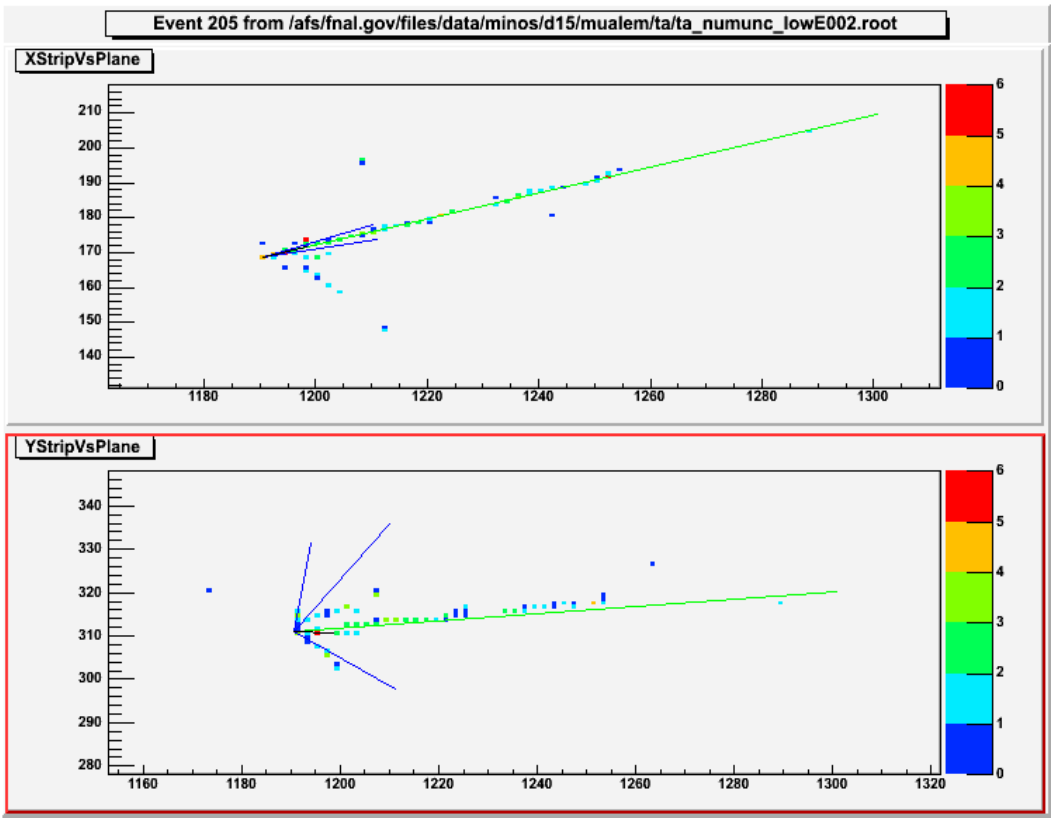

Fig. 12.9: A background neutral-current event: $\nu A \rightarrow p\nu\pi^{+}\pi^{-}\pi^{-}\pi^{0}$, $E_{\nu} = 4.95$ GeV. See text for explanation of the codes.

12.5 Prospects

The combination of the high level of segmentation and the "totally active" nature of NOνA yields a large amount of information for each event. While the simulations described here have attempted to use most of that information, it is unlikely that we have already found the optimum ways of increasing the efficiency for signal and the rejection of background. Thus, the results presented here should be considered as a lower bound on the ultimate performance of the detector

13. Physics Potential of NOνA

13.1. Introduction

Assuming that light sterile neutrinos either do not exist or do not mix with active neutrinos, there are currently three parameters of neutrino oscillations about which we have no information or only upper limits: $\sin^2(2\theta_{13})$, the sign of Δm^2_{32} (i.e., whether the solar oscillation doublet has a higher or lower mass than the third state which mixes in the atmospheric oscillations), and the CP-violating phase δ.

The goal of NOνA will be to acquire information on all three of these parameters. However, provided that θ_{13} is in the range accessible to conventional neutrino beams, the unique contribution of the NuMI neutrino program will be the resolution of the mass hierarchy. This can only be done by experiments that measure the matter effect due to ν_e's traveling long distances through the earth. Planned future experiments in both Japan [1] and Europe [2] are concentrating on baselines that are too short for this purpose.

The determination of whether the solar neutrino doublet is at a higher or lower mass than the third neutrino mass state is important in its own right, for interpreting neutrinoless double beta decay experiments, and for the eventual measurement of CP violation in the lepton sector. As an example of the last, consider Fig. 13.1, which is taken from the T2K LoI [1]. The T2K collaboration is proposing a very ambitious long-term program to make precision measurements of CP violation by increasing the JPARC proton intensity by a factor of 5 (to 4 MW) and by building a new detector, HyperKamiokande, which will have twenty times the mass of SuperKamiokande. Fig. 13.1. shows the numbers of ν_e and $\bar{\nu}_e$ appearance events with two years of neutrino and six years of antineutrino running for $\sin^2(2\theta_{13}) = 0.1$. It is clear that without a resolution of the mass hierarchy, there are large areas of the parameter space in which the CP phase cannot be determined with any precision. The JPARC program is relying on the NuMI program for this information. This will be made quantitative in Section 13.5.

Given this unique role for the NOνA experiment, we believe it should be designed and sited to optimize this role.

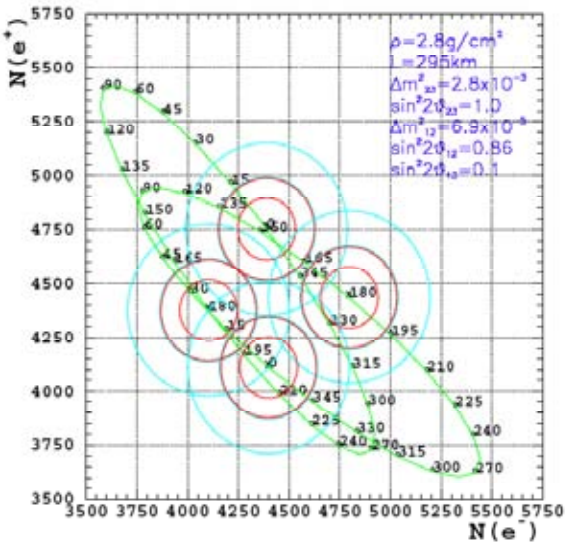

Fig. 13.1: The numbers of ν_e and $\bar{\nu}_e$ appearance events with two years of neutrino and six years of antineutrino running for $\sin^2(2\theta_{13}) = 0.1$ in an anticipated experiment utilizing an upgraded JPARC proton beam and the HyperKamiokande detector. Each of the two green contours corresponds to the different mass hierarchy and the numbers on the contours are the CP phase in degrees. The red circles correspond to the 90% confidence level contours and the blue circles correspond to three standard deviation contours. The outer circles include errors due to a 2% systematic uncertainty. From the T2K LoI [1].

The next section will introduce the problem of optimizing the siting of NOνA. Section 13.3 will discuss the sensitivity of NOνA to the observation of a signal in $\nu_\mu \rightarrow \nu_e$ oscillations, which is related to the sensitivity to $\sin^2(2\theta_{13})$. Section 13.4 and 13.5 will explore the sensitivity of NOνA to the neutrino mass ordering and the CP-violating phase δ, respectively. These sections will also show how NOνA fits into a long-range step-by-step program for the measurement of these parameters.

We will conclude this chapter with a discussion of other physics that NOνA can do. Section 13.6

will discuss how NOνA can improve on MINOS's measurements of $\sin^2(2\theta_{23})$ and Δm^2_{32}. Sections 13.7 and 13.8 will discuss measurements that could be made with the NOνA Near Detector, and Section 13.9 will discuss the NOνA sensitivity to galactic supernova explosions.

13.2 The Optimization Problem

There are two aspects to the optimization problem. The first is illustrated in Fig. 13.2, which shows all of the values of the parameters consistent with a (perfectly measured) 2% $\nu_\mu \rightarrow \nu_e$ oscillation probability 12 km off axis at an 810 km baseline. There are three parameters, $\sin^2(2\theta_{13})$, shown on the vertical axis, the two possible mass orderings, the normal hierarchy, shown by the solid blue curve and the inverted hierarchy, shown by the dashed red curve, and the CP phase δ, shown as values around the ellipses. The horizontal axis shows the result of a (perfect) measurement of the $\bar{\nu}_\mu \rightarrow \bar{\nu}_e$ oscillation probability.[9]

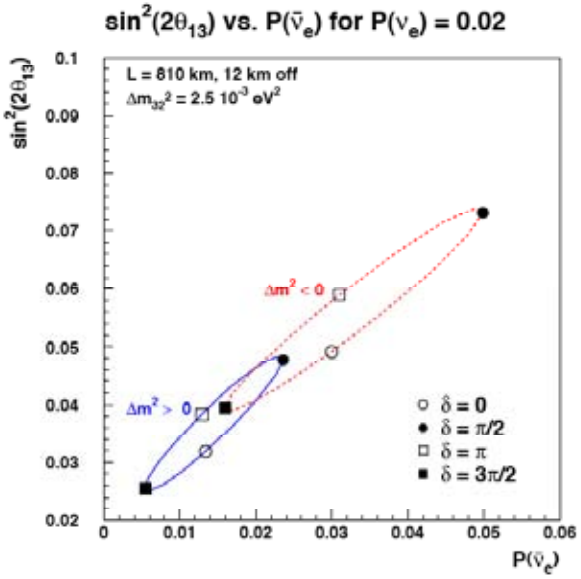

Fig. 13.2: Plot of the possible results of a measurement of a 2% neutrino oscillation probability. See text for an explanation.

NOνA is capable of making two measurements, the neutrino and the antineutrino oscillation probabilities near the first oscillation maximum. In some cases, these two measurements are capable, in principle, of measuring all three parameters, up to a two-fold ambiguity in the CP phase. For example a neutrino oscillation probability of 2% and an antineutrino oscillation probability of 4% or 1%, determine the mass hierarchy unambiguously. However, a neutrino oscillation probability of 2% and an antineutrino oscillation probability of 2% cannot resolve the inherent ambiguity shown in Fig. 13.2. A third measurement is needed in this case, either from an experiment done elsewhere at a different baseline, or from an additional measurement on the NuMI beamline, for example, on the second oscillation maximum.

Figure 13.3 shows the same information as Fig. 13.2, except for neutrino oscillation probabilities of 0.5%, 1%, 2% (again), and 5%. This figure illustrates that the fraction of possible δ values for which there is an ambiguity increases with decreasing values of θ_{13}.

The second aspect of the optimization problem is illustrated in Fig. 13.4. The figure of merit (FoM) squared and the neutrino asymmetry are plotted as a function of the off-axis transverse angle for $\Delta m^2_{32} = 0.0025$ eV^2. The FoM is defined as the signal divided by the square root of the background. It is proportional to the sensitivity (in standard deviations) for seeing an oscillation signal, and the inverse of its square is proportional to amount of detector mass times beam flux required to obtain a given result. The neutrino asymmetry is defined as the neutrino oscillation probability minus the antineutrino probability divided by their sum, due to the matter effect. Thus, it is a measure of how far the two ellipses separate in Figs. 13.2 and 13.3. The ability to resolve the mass hierarchy will depend on both the rate of events as given

[9] Figs. 13.2 and 13.3 are drawn assuming that $\sin^2(2\theta_{23}) = 1.0$. If it is less than unity, then there will be a two-fold ambiguity in the value of $\sin^2(2\theta_{13})$ derived from $\nu_\mu \rightarrow \nu_e$ oscillations since the "atmospheric scale" oscillation probability is largely proportional to $\sin^2(\theta_{23})$. Since this factor is the almost the same for all $\nu_\mu \rightarrow \nu_e$ oscillation experiments, it will not affect the resolution of the mass hierarchy or the determinations of the CP-violating phase δ by these experiments. It will, however, affect the comparison of these experiments to reactor experiments, and may eventually be resolved by the comparison of precise reactor and accelerator oscillation experiments.

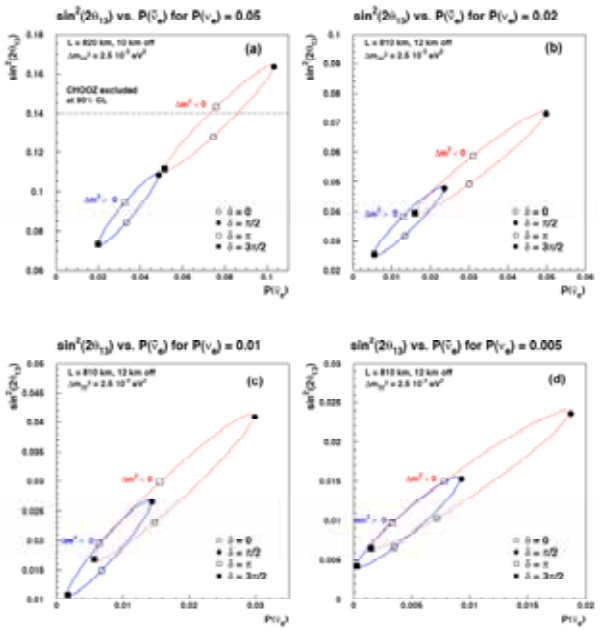

Fig. 13.3: Plots of the possible results of a measurement of a (a) 5%, (b) 2%, (c) 1%, and (d) 0.5% neutrino oscillation probability. See text for an explanation.

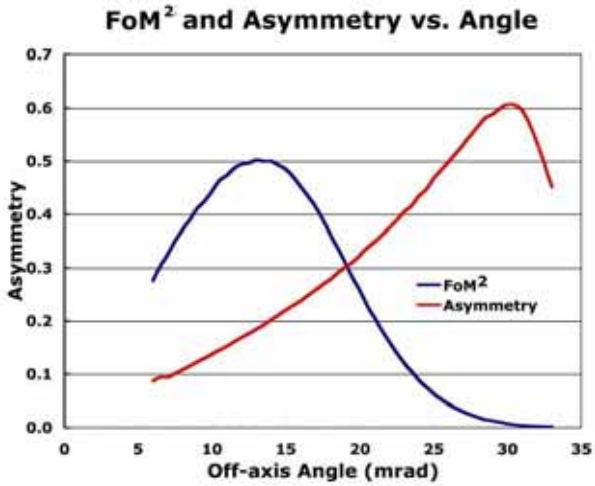

Fig. 13.4: Figure of merit squared (arbitrary units) and neutrino oscillation asymmetry due to the matter effect for $\Delta m^2 = 0.0025$ eV^2 versus off-axis angle. See text for an explanation. This figure is for illustrative purposes. It is based on a toy model and may not agree precisely with the simulation data presented in this chapter.

by the FoM and separation given by neutrino asymmetry.

Figure 13.4 shows that the sensitivity to observing the oscillation will not optimize at the same place as the sensitivity to the mass hierarchy. In Section 13.4, we will see that siting NOνA at 12 km off-axis is optimum for resolving the mass hierarchy, and this is what we propose. However, in the next section we will show that optimizing for resolving the mass hierarchy results in only a small loss of sensitivity for seeing the oscillation. Further, this optimization will be approximately correct for each possible future stage of the evolution of the NOνA program, and it is largely insensitive to the value of Δm^2_{32} within the range suggested by the latest SuperKamiokande and K2K analyses.[10]

The conclusion of this chapter will be that NOνA is optimized for a long-range program that is capable of resolving the mass hierarchy over most of the range accessible to conventional neutrino beams. In addition, we will show that with the construction of a Proton Driver at Fermilab, NOνA will have a substantial capability to measure CP violation, both alone and in combination with other experiments.

13.3. Sensitivity to Observing $\nu_\mu \rightarrow \nu_e$ Oscillations

Figures 13.5 and 13.6 show the calculated three standard deviation discovery limit for $\nu_\mu \rightarrow \nu_e$ oscillations in terms of the three unknown parameters, assuming $\Delta m^2_{32} = 0.0025$ eV^2. The vertical axis represents the fraction of possible δ values for which a 3-σ discovery could be made. At a fraction of 1.0, a 3-σ discovery can be made for all values of δ. This sets the $\sin^2(2\theta_{13})$ limit for a certain discovery. At lower values of $\sin^2(2\theta_{13})$, a 3-σ discovery is only possible for a range of delta. When there is no value of δ that gives a 3-σ discovery, the fraction is 0.0, and this sets the lower limit for $\sin^2(2\theta_{13})$ at which a discovery is possible. A fraction of 0.5 may be taken as the typical value.

[10] See Section 3.2 for a summary of results. Both the SuperKamiokande analysis of high-resolution events and the K2K analysis give a 90% confidence level lower limit for Δm^2_{32} of 0.0019 eV^2.[3]

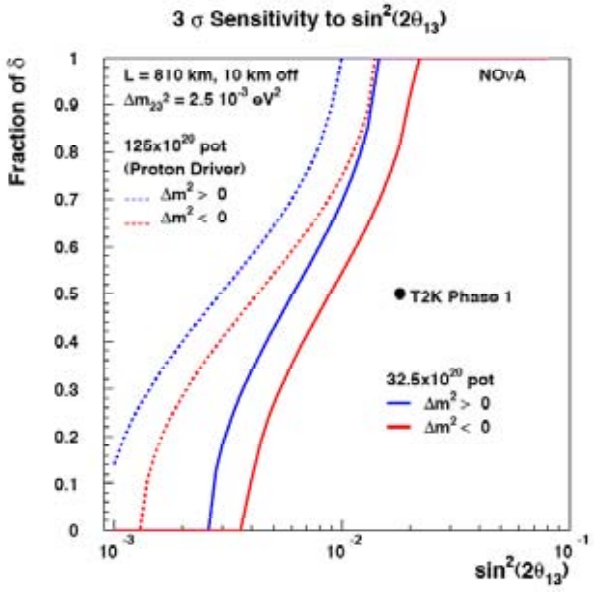

Fig. 13.5: Three standard deviation discovery limits for the observation of $\nu_\mu \rightarrow \nu_e$ oscillations for the NOνA detector situated 10 km off the NuMI beamline. See the text for more details.

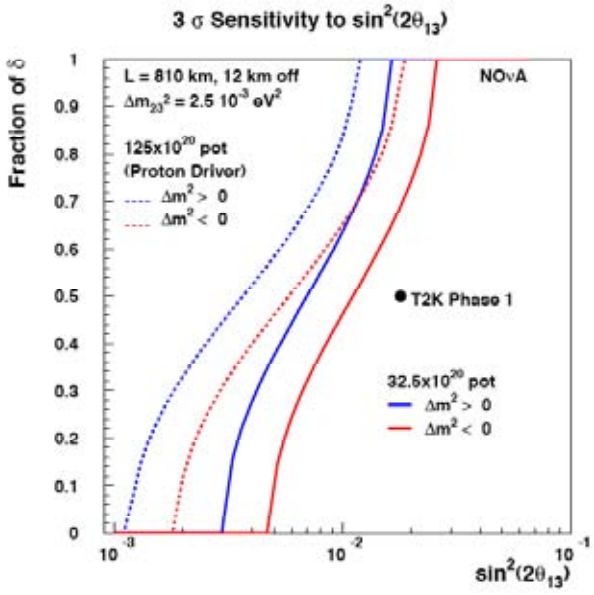

Fig. 13.6: Three standard deviation discovery limits for the observation of $\nu_\mu \rightarrow \nu_e$ oscillations for the NOνA detector situated 12 km off the NuMI beamline. See the text for more details.

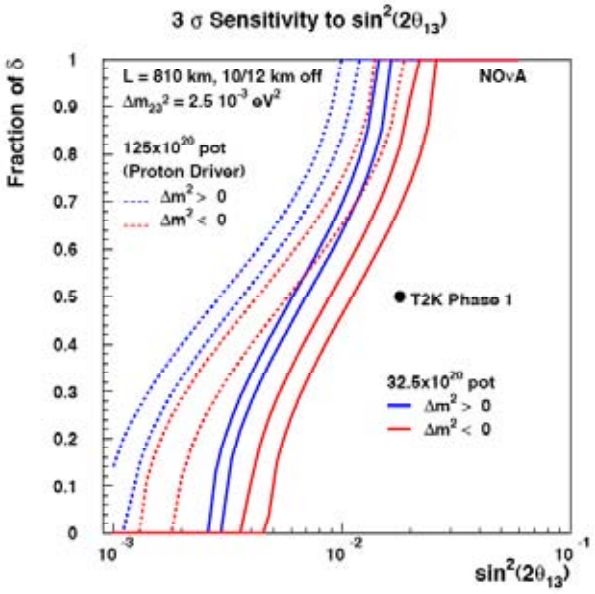

Fig. 13.7: Data from Figs. 13.5 and 13.6 superimposed for comparison purposes.

The curves represent the two possible values of the sign of Δm^2_{32} and different assumptions on the number of protons on target (pot) that the experiment might see in a five-year run. (If these figures are being viewed in gray scale, the line to the right for each number of protons represents the inverted mass hierarchy.)

The value of 35.2×10^{20} pot represents our estimate of what Fermilab might be able to deliver in a five-year run as discussed in Chapter 11, while 125×10^{20} pot represents the expectation with the Booster replaced by a new Proton Driver. A 5% systematic error on the background determination has been included in these and the other calculations presented in this chapter, but as can be seen from Table 12.2, the statistical errors on the backgrounds always dominate. The three standard deviation sensitivity of the T2K phase 1 proposal [1] is also shown in these figures.

Figures 13.5 and 13.6 differ in that the former displays data for the NOνA detector situated 10 km off-axis, while the latter is for 12 km off-axis. There is some loss of sensitivity in going from 10 to 12 km. This is best seen in Fig. 13.7, which superimposes the data from the previous two figures. There is only a minor loss of sensitivity for the normal mass hierarchy, because the larger matter effects at 12 km enhance the neutrino

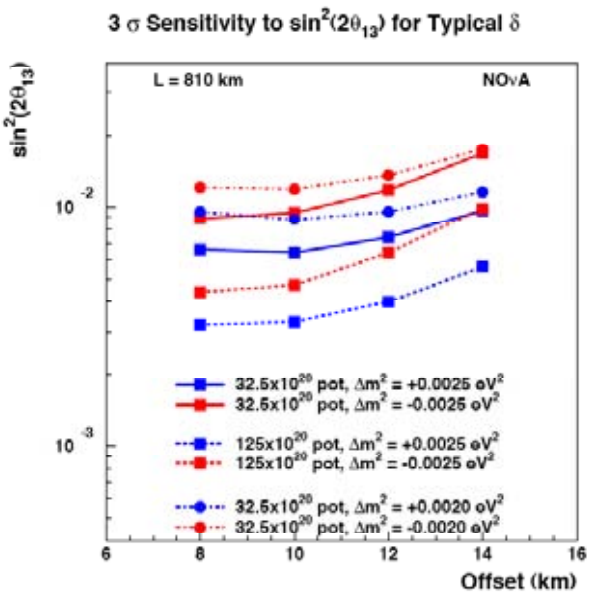

Fig. 13.8: Three standard deviation discovery limits for the observation of $\nu_\mu \rightarrow \nu_e$ oscillations for the typical CP phase δ versus the NOνA detector off-axis distance for the integrated fluxes and Δm^2 values shown.

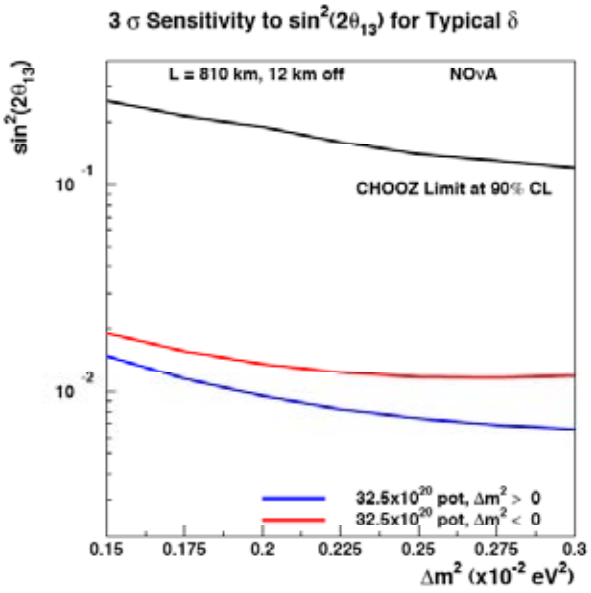

Fig. 13.9: Three standard deviation discovery limits for the observation of $\nu_\mu \rightarrow \nu_e$ oscillations for the typical CP phase δ versus Δm^2_{32} for the NOνA detector sited 12 km off axis

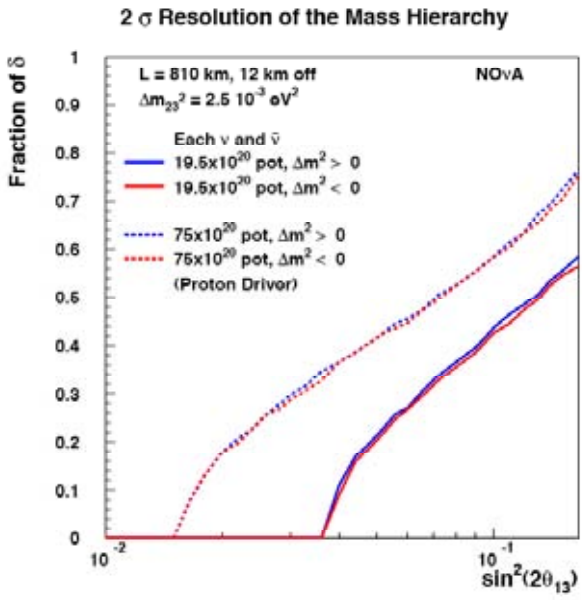

Fig. 13.10: The 95% confidence level resolution of the mass hierarchy versus $\sin^2(2\theta_{13})$ for three years of running each neutrinos and antineutrinos, with and without a proton driver.

oscillation probability. The loss is somewhat larger, but still relatively small, for the inverted mass hierarchy, where the matter effects suppress the neutrino oscillation probability.

Figure 13.8 shows the three standard deviation discovery limits for the typical δ for both $\Delta m^2_{32} = 0.0025$ eV^2 and $\Delta m^2_{32} = 0.0020$ eV^2 as a function of the off-axis distance. For all cases, the sensitivity maximizes around 8 to 10 km off-axis. Figure 13.8 also shows the loss of sensitivity going from $\Delta m^2_{32} = 0.0025$ eV^2 to $\Delta m^2_{32} = 0.0020$ eV^2. However, it should be noted that this is not a loss in range, since the CHOOZ limit [4] is correspondingly weaker at 0.0020 eV^2. This is further illustrated in Fig. 13.9, which shows the three standard deviation discovery limits for the typical δ for NOνA sited at 12 km off axis as a function of Δm^2_{32}.

13.4. Sensitivity to the Mass Hierarchy

13.4.1. NOνA Alone: Figure 13.10 shows the 95% confidence level resolution of the mass hierarchy as a function of $\sin^2(2\theta_{13})$ for the NOνA detector sited at 12 km off-axis. The 95% confidence level has been chosen since the mass hierar-

chy is binary, so 20:1 odds should be reasonably convincing. The assumed scenario is that within three years of neutrino running, a three-σ signal is observed for ν_e appearance, after which the running is switched to antineutrinos for studying the mass hierarchy. Thus, Fig. 13.10 assumes three years of each neutrino and antineutrino running, both with and without a proton driver.

The shapes of the curves are easily understood from Fig. 13.3. There is a limited range of δ values for which two measurements can resolve the mass hierarchy, and this range decreases with decreasing values of $\sin^2(2\theta_{13})$. There is a reasonable region of parameter space in which NOνA could resolve the mass hierarchy before a Proton Driver is available, and a larger region after.

To emphasize the point that only a long baseline experiment can resolve the mass hierarchy, we have calculated the sensitivity of T2K phase 1, if it were to run for three years each on neutrinos and antineutrinos. This is shown in Fig. 13.11. The horizontal scale has been expanded in order to show the T2K sensitivity, which otherwise would be off-scale to the right. The CHOOZ limit for $\Delta m^2_{32} = 0.0025$ eV^2 is also indicated [4]. Points substantially to the right of this limit are largely irrelevant. We emphasize that the results for T2K are our calculations, since the T2K collaboration, quite sensibly, has not proposed this measurement.

Figure 13.12 shows the mass hierarchy resolution sensitivity for all of the simulations in Table 12.2. This figure displays the value of $\sin^2(2\theta_{13})$ for which the δ value is at the limit of first quartile, i.e., the δ value such that 25% of δ values give a lower value of $\sin^2(2\theta_{13})$ and 75% give a higher value. This δ was chosen because the typical δ is in the region of the CHOOZ limit for running before the Proton Driver, and thus less relevant. However, the siting optimization does not depend significantly on which δ value is chosen.

Fig. 13.12 shows that the mass hierarchy resolution optimizes around 12 km off-axis for both $\Delta m^2_{32} = 0.0025$ and 0.0020 eV^2. It appears to optimize between 10 and 12 km for $\Delta m^2_{32} = 0.0025$ eV^2 and between 12 and 14 km for $\Delta m^2_{32} = 0.0020$ eV^2.

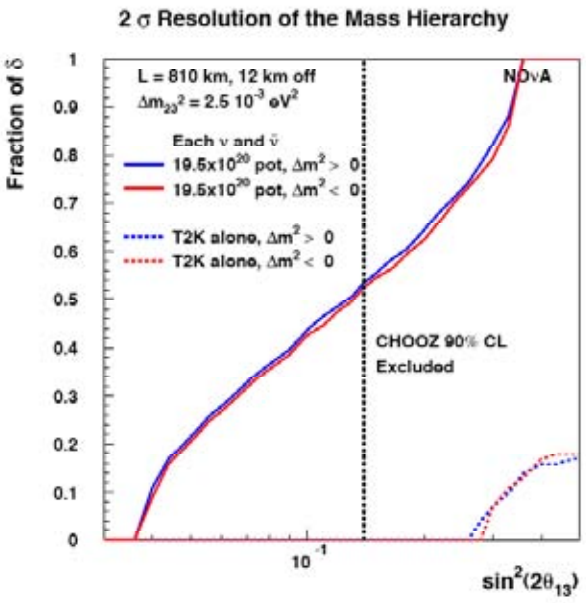

Fig. 13.11: A comparison of NOνA's and T2K's abilities to resolve the mass hierarchy alone.

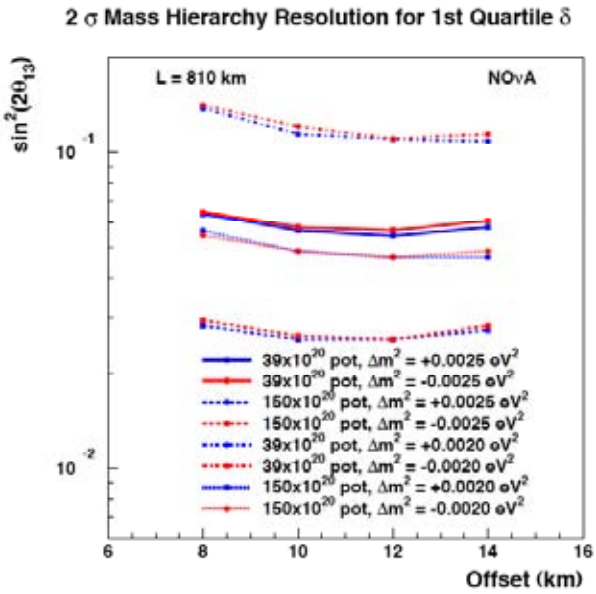

Fig. 13.12: 95% confidence level for resolution of the mass hierarchy for the 1st quartile δ. See the text for additional explanation.

13.4.2: NOνA in Combination with Another Measurement: If the neutrino oscillation parameters are such that the mass hierarchy cannot be resolved by NOνA alone, then combining NOνA measurements with the measurement of another detector will be necessary. The most obvious candidate is T2K. Figures 13.13 and 13.14 show

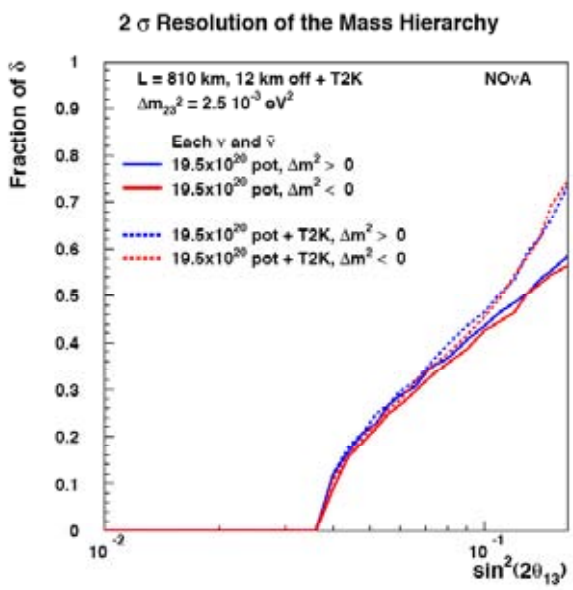

Fig. 13.13: A comparison of the 95% confidence level resolution of the mass hierarchy with NOνA alone (solid curves) and the combination of NOνA and T2K phase 1 data (dashed curves). It is assumed that both NOνA and T2K run three years each on neutrinos and antineutrinos.

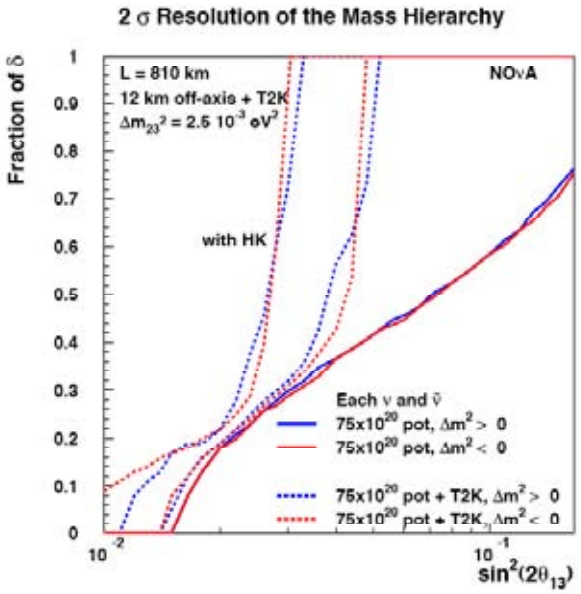

Fig. 13.14: A comparison of the 95% confidence level resolution of the mass hierarchy with NOνA alone with the Proton Driver (solid curves) and the combination of NOνA and T2K data with an upgraded proton source (dashed curves). The curves labeled "HK" assume that the T2K detector is HyperKamiokande; the other set of dashed curves assume that it is SuperKamiokande. It is assumed that both NOνA and T2K run three years each on neutrinos and antineutrinos.

these results. Figure 13.13 is for NOνA without the Proton Driver combined with T2K phase 1. Figure 13.14 is for a later time in which NOνA with the Proton Driver can be combined with T2K with an upgraded proton source. For this later case, we have calculated the results assuming either that the T2K detector is SuperKamiokande or HyperKamiokande.

The structure of these plots is that the combination with T2K does not have much effect until a critical value of $\sin^2(2\theta_{13})$, after which the mass hierarchy is resolved for all values of δ. The reason for this is fairly easy to understand. We are comparing two distributions that have approximately the same structure due to the CP phase, and differ primarily by a factor of 2.3 in the matter effect. Thus, sufficient statistics to pass the 95% confidence level threshold happens for all values of δ at approximately the same point.

The difference between the critical value of $\sin^2(2\theta_{13})$ for HyperKamiokande is only about 30 to 40% lower than that for SuperKamiokande, even though the former has twenty times the mass of the latter. This is because the statistical precision is limited by the number of events in NOνA.

If comparisons with T2K are insufficient to resolve the mass hierarchy, then an attractive approach would be to do a measurement with an additional detector on the NuMI beamline to measure events at the second oscillation maximum. At the second maximum the matter effect is smaller by a factor of three and the CP violating effects are larger by a factor of three, both for the same reason – the energy is smaller by a factor of three.

There will be sufficient information available at that time that it will be known whether this technique will work and how much detector mass will be required. For the purpose of our calculation, we have adopted the following scenario. After two years of running with the Proton Driver, it is realized that a second off-axis detector will be needed and it is constructed in four years and then runs for an additional six years. Thus, there will be twelve years of NOνA data with a Proton Driver and six years of data with the second detector, both split equally between neutrinos and

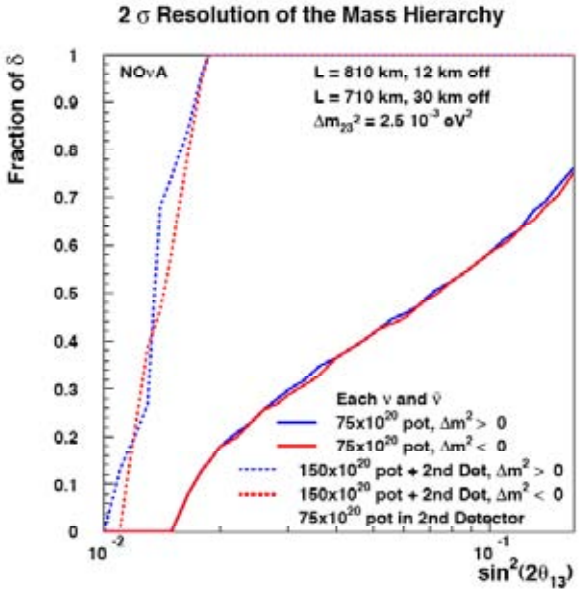

Fig. 13.15: A comparison of the 95% confidence level resolution of the mass hierarchy with NOνA alone (solid curves) and the combination of NOνA and an additional NuMI detector sited to measure the second oscillation maximum (dashed curves). See the text for details of the scenario.

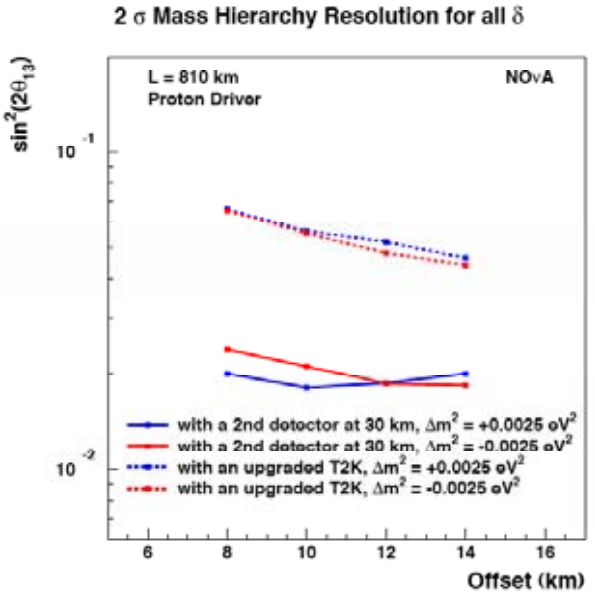

Fig. 13.16: 95% confidence level for resolution of the mass hierarchy for all values of δ for various NOνA off-axis distances. The dashed lines are for a combination of NOνA data with the Proton Driver and T2K data with an upgraded proton source and SuperKamiokande as the T2K detector. The solid lines are for a combination of NOνA data with an additional NuMI detector as discussed in the text.

antineutrinos. It is not clear at this time what technology would be best for the second detector. Liquid scintillator, water Cerenkov, and liquid argon detectors are all reasonable candidates. For the purpose of this calculation, we have just assumed a 50 kT detector with efficiencies equal to those of T2K. The detector is assumed to be sited 30 km off axis at a baseline of 710 km. Since we want to minimize the matter effects in this detector, there is no reason to place it at a longer baseline. The results are shown in Fig. 13.15. The mass hierarchy is resolved for all values of δ for values of $\sin^2(2\theta_{13})$ greater than 0.01 to 0.02.

Figure 13.16 addresses the siting optimization for combinations of NOνA data with T2K data or with that of an additional NuMI detector. It displays the value of $\sin^2(2\theta_{13})$ at which the mass hierarchy is resolved at the 95% confidence level for all values of δ. For the comparison of NOνA data with that fromT2K, the optimum off-axis distance appears to be near 14 km. For the comparison of NOνA data with a second off-axis detector, the optimum is shallow and different for the two mass orderings. For the normal ordering, it optimizes at 10 km, while for the inverted ordering, it optimizes at 14 km.

Thus, based on our present knowledge of Δm^2_{32}, it appears siting NOνA 12 km off axis is reasonable for all stages of the NuMI program. As we get more information on Δm^2_{32} from MINOS, we can refine the optimization.

13.4.3: Summary of the Evolution of the NOνA Program to Resolve the Mass Hierarchy: Figure 13.17 summarizes the possible evolution of the NOνA program by combining the results shown in Figs. 13.9, 13.13, 13.14, and 13.15. The NOνA program allows the resolution of the mass hierarchy over most of the range in θ_{13} accessible to conventional neutrino beams. The program is flexible; each stage can be guided by the information obtained in prior stages, and the NOνA detector that we are proposing here remains a key and well-optimized participant throughout the program.

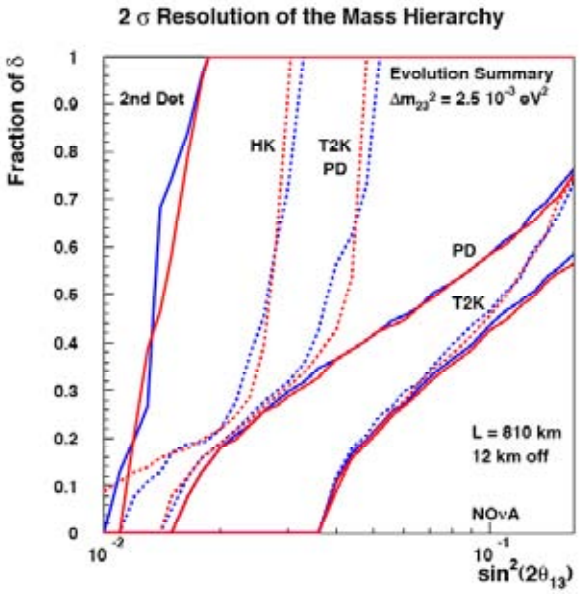

Fig. 13.17: A summary of the data presented in Figs 13.9, 13.13, 13.14, and 13.15.

13.5. Sensitivity to CP Violation

13.5.1: Introduction: The relationship between the resolution of the mass hierarchy and the observation of CP violation varies from experiment to experiment. Very short baseline experiments, such as the beta beam experiments being planned in Europe [2] have very small matter effects and can measure CP violation phase δ without regard to the determination of the mass hierarchy. Long baseline experiments such as NOνA generally require a resolution of the mass hierarchy to measure the CP phase because maximal CP violation for one mass ordering can have the same or similar neutrino and antineutrino oscillation probabilities as no CP violation for the other mass ordering. An example of this is shown in Fig. 13.3(c). Shorter baseline experiments such as T2K are intermediate between these extremes. This section will explore the capability of NOνA to measure the CP violating phase δ and the power of combinations of NOνA measurements with those of other experiments.

One should keep in mind that CP-violating effects are proportional to the first power of θ_{13}, while CP-conserving effects are, for the most part, proportional to the square of θ_{13}, as can be seen in Fig. 13.3. This has led some to argue that the ability to measure δ is independent, to some extent, of the value of $\sin^2(2\theta_{13})$. We will see that there are regions of $\sin^2(2\theta_{13})$ in which the probability of measurement is flat. We will also see that there can be peaks and dips in the probability as a function of $\sin^2(2\theta_{13})$ due to the complex relationship between CP-violating effects and matter effects.

In order to take this relationship into account, we use the following measure of our ability to measure CP violation: the fraction of possible δ values for which there is a three standard deviation demonstration of CP violation, that is, that δ is neither zero nor π for both mass orderings. Of course, this fraction can never be 100%, since there will always be some range of δ values very close to zero or π. A rough way to convert this measure into a one standard deviation measure of δ is that a small, but non-zero fraction corresponds to 30 degrees, a 25% fraction to 22.5 degrees, a 50% fraction to 15 degrees, and so on.

13.5.2: Simulation Results: Neither NOνA nor T2K can demonstrate CP violation even at the two standard deviation level with six years of running without an enhanced proton source. However, both experiments gain some ability with their proposed proton drivers. This is shown in Fig. 13.18, in which both experiments are assumed to have run three years each on neutrinos and antineutrinos and the T2K detector is assumed to be Super-Kamiokande. T2K and NOνA have a similar reach in $\sin^2(2\theta_{13})$, but T2K saturates at a lower fraction of δ due to its inability to resolve the mass hierarchy. Combining measurements from both experiments gives a large gain in both the breadth and precision of the measurement. The sharp rise around $\sin^2(2\theta_{13}) = 0.05$ is due to the resolution of the mass hierarchy, as discussed in Section 13.4.3 and seen in Fig. 13.14.

Fig. 13.19 shows the same information as Fig. 13.18, except that HyperKamiokande is assumed to be the T2K detector. The twenty-fold increase in mass gives it high statistical precision. The role of NOνA is to resolve the mass hierarchy so that the precision can be used, as was discussed in the opening section of this chapter.

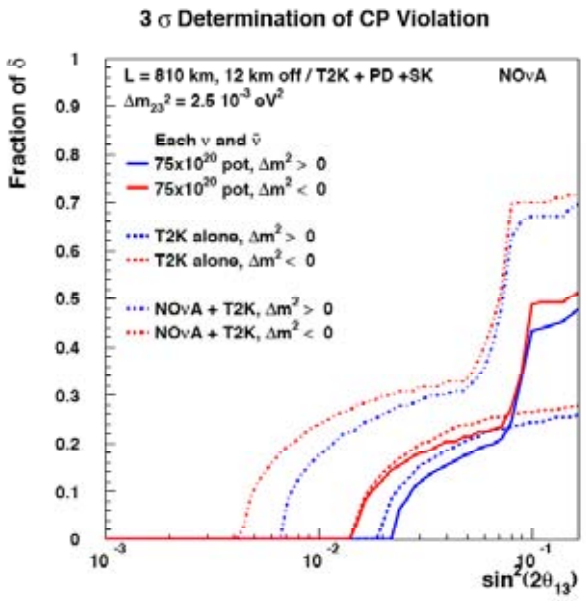

Fig. 13.18: The fraction of δ values for which CP violation can be demonstrated at three standard deviations. A three year run on each of neutrinos and antineutrinos is assumed for NOνA with the Proton Driver and for T2K with an enhanced proton source and SuperKamiokande as the detector.

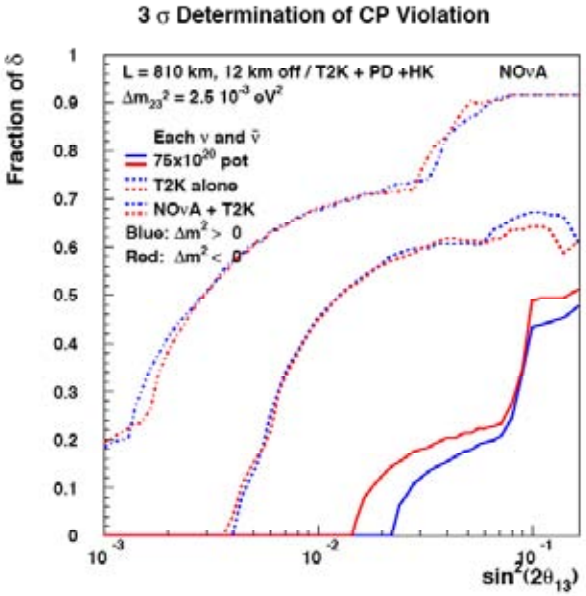

Fig. 13.19: The same as Fig 13.18 except that Hyper-Kamiokande is assumed to be the T2K detector.

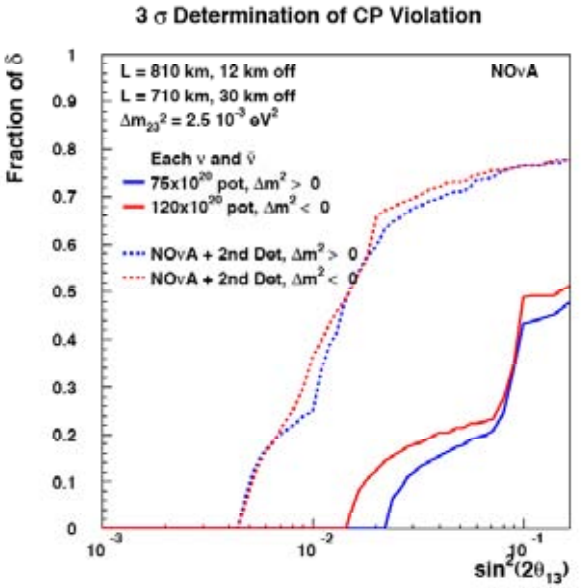

Fig. 13.20: The fraction of δ values for which CP violation can be demonstrated at three standard deviations for NOνA with the Proton Driver and combined with an additional detector on the NuMI beam line, as discussed in the text.

Finally, Fig. 13.20 addresses the CP violation measurements that could be made by a combination of NOνA and the additional detector on the NuMI beamline, running at the second oscillation maximum, which was suggested in Section 13.4.3 to resolve the mass hierarchy in the case of small values of $\sin^2(2\theta_{13})$. This figure shows that there is also a good capability for measuring CP violation at these $\sin^2(2\theta_{13})$ values.

13.6. Measurement of the Dominant Mode Oscillation Parameters

One of the most important measurements in neutrino physics today is the precise determination of $\sin(\theta_{23})$. The best current measurement comes from the SuperKamiokande study of atmospherically produced neutrinos [3,5]. This measurement is consistent with maximal mixing, $\sin^2(2\theta_{23}) = 1$, but with a considerable uncertainty. At the 90% confidence level, $\sin^2(2\theta_{23}) > 0.92$, which translates into a rather large range of possible values of $\sin^2(\theta_{23})$, namely $0.36 < \sin^2(\theta_{23}) < 0.64$.

There are three reasons why determining $\sin(\theta_{23})$ is of high interest:

(1) If the mixing is maximal, it might be due to some currently unknown symmetry.

(2) The $\nu_\mu \rightarrow \nu_e$ oscillation is mostly proportional to $\sin^2(\theta_{23})\sin^2(2\theta_{13})$ while $\bar{\nu}_e$ disappearance, measured by reactor experiments is proportional to $\sin^2(2\theta_{13})$. Thus, if the mixing is not maximal, there is an ambiguity in comparing accelerator and reactor experiments, or conversely

(3) whether θ_{13} is greater than or less than $\pi/4$, which measures whether ν_e's couple more strongly to ν_μ's or ν_τ's, can probably best be measured by comparing precise accelerator and reactor measurements.

The deviation of $\sin^2(2\theta_{23})$ from unity is measured by the depth of the oscillation dip in the ν_μ disappearance spectrum. Thus, precision in this quantity requires good statistics in this region, excellent neutrino energy resolution, and good control of systematics. NOνA offers the possibility of satisfying all of these requirements.

It appears that the best way to meet these requirements is to limit the analysis to totally contained quasielastic events, i.e., those events in which the geometrical pattern of energy deposition is consistent with the presence of only an energetic muon and a possible recoil proton.

We have performed a preliminary study of how well NOνA can use these events to measure $\sin^2(2\theta_{23})$ and Δm^2_{32} using a parametric representation of the energy. This procedure is justified by the nature of these events, which are extremely clean as is demonstrated by a typical quasielastic event displayed in Fig. 13.21.

With the exception of energy deposited in the PVC walls, which can be estimated from the trajectories, all of the final state energy should be visible in NOνA. The overall scale of unknown missing energy will be from the boiloff neutrons from the struck nucleon. The typical Fermi momentum is about 250 MeV/*c*, corresponding to a kinetic energy of the nucleon of about 33 MeV, or about 2% of the neutrino energy. Considering the various sources that contribute to the energy resolution, including photoelectron statistics,

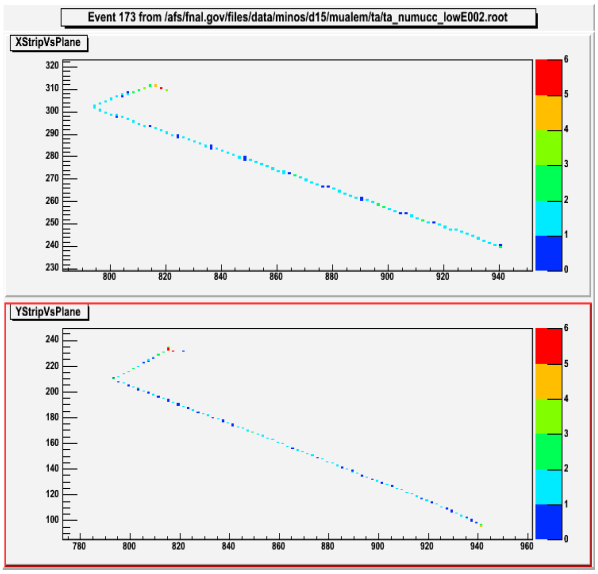

Fig. 13.21: An example of a quasielastic ν_μ CC interaction in the NOνA detector. Note the proton scatter near the end of its range. The color of the hits indicates the relative pulse height.

straggling fluctuations[11], saturation effects in the scintillator, undetected neutron emission, nuclear excitation, and reabsorption and rescattering in the nucleus, we conclude that the energy resolution should be in the 2 to 4% range [6]. The absolute energy scale can be determined from stopping cosmic ray muons and should be understood to better than 2%.

The calculated one and two standard deviation contours are displayed in Figs. 13.22 and 13.23 for assumed values of $\sin^2(2\theta_{23})$ of 0.95, 0.98, and 1.00. Figure 13.22 is for a five-year neutrino run without a Proton Driver and Fig. 13.23 is for the same length run with a Proton Driver. The energy resolution has been assumed to be 2%, but the contours do not change markedly as one increases the resolution to 4%.

Note that the precision of the $\sin^2(2\theta_{23})$ measurement increases as the value of $\sin^2(2\theta_{23})$ approaches unity. For maximal mixing, the error on

[11] The main source of straggling fluctuations are the Landau fluctuations in the energy loss along the muon path. Since we measure all of the energy loss, this effect is relevant only for the straggling fluctuations in the PVC walls.

the measurement of $\sin^2(2\theta_{23})$ is about 0.004 without a Proton Driver and about 0.002 with.

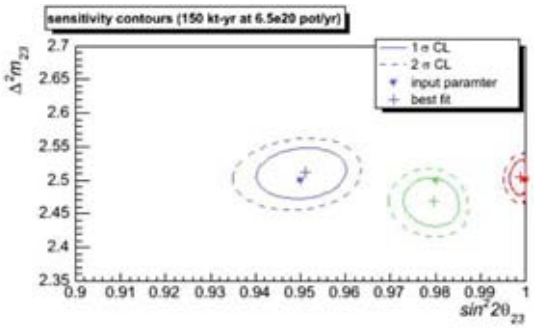

Fig. 13.22: One and two standard deviation contours for the simultaneous measurements of Δm^2_{32} and $\sin^2(2\theta_{23})$ for a five-year neutrino run without a Proton Driver.

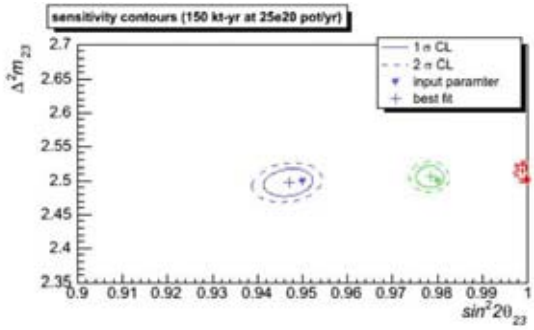

Fig. 13.23: One and two standard deviation contours for the simultaneous measurements of Δm^2_{32} and $\sin^2(2\theta_{23})$ for a five-year neutrino run with a Proton Driver.

13.7. Short Baseline Neutrino Oscillation Measurements with the NOνA Near Detector

In Chapter 10 we noted that an LSND[7] oscillation would distort our beam ν_e spectrum. While a short baseline oscillation will complicate our background subtraction process at the Far Site, it also presents an opportunity. If MiniBooNE confirms the LSND signal, NOνA can expect to see hundreds of excess ν_e events in the Near Detector, providing additional confirmation for a result of immense importance.

At Site 1.5 (see Chapter 10), the ν_μ spectrum peaks at about 2.5 GeV and has a width of about 1.5 GeV FWHM. In the extreme case of Δm^2 = 2.5 eV^2, 0.26% of the copious ν_μ spectrum would oscillate into ν_e's. Our "beam ν_e" measurement would be off by about 60% at the peak of the short baseline oscillation and we would overestimate our beam ν_e background at the far site. For other values of Δm^2, the effect is less pronounced but still significant, as shown in Fig. 13.24.

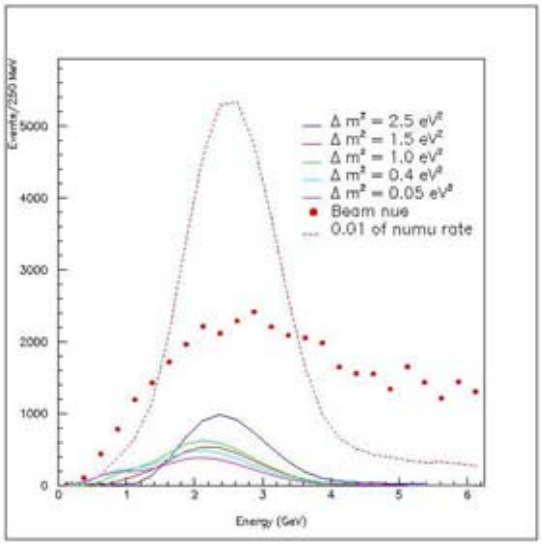

Fig. 13.24: The NOνA Near Detector (at Site 1.5) ν_e CC spectrum (red dots) compared with a short baseline oscillation effect at different values of Δm^2 consistent with the allowed LSND parameter space. The parent ν_μ CC spectrum for the oscillation is shown at 1/100 of its value. No detector resolution effects or backgrounds are included here. The plot corresponds to 6.5 x 10^{20} pot (about one year) on a near detector with 20.4 tons of fiducial mass.

NOνA is sensitive to effects over a large range of Δm^2, but can it differentiate one Δm^2 from another? Figure 13.25 shows the number of events at Site 1.5, after subtraction of the expected beam ν_e spectrum, for a number of different short baseline oscillation scenarios. We assume an oscillation with parameters of (Δm^2, $\sin^2 2\theta$) = (1.0 eV^2, 0.004) for a data run with 6.5 x 10^{20} pot (about one year) on a near detector with 20.4 tons of fiducial mass and compare it to curves for oscillations with different Δm^2's. The error bars are dominated by

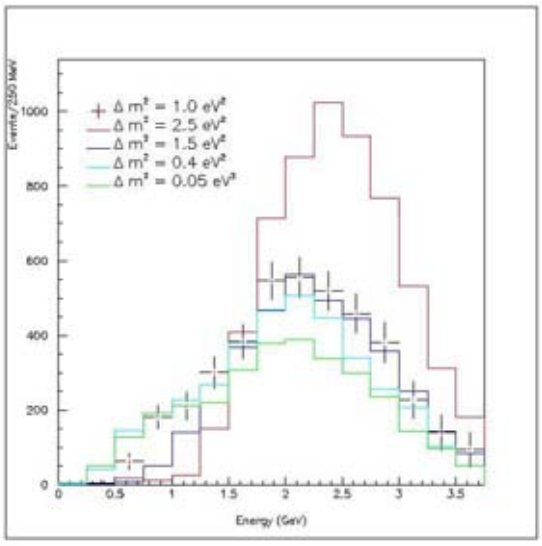

Fig. 13.25: Events after subtraction of the expected beam ν_e spectrum at Site 1.5 for a oscillation with parameters of (Δm^2 , $\sin^2 2\theta$) = (1.0 eV^2, 0.004) for a data run with 6.5 x 10^{20} pot (about one year) on a near detector with 20.4 tons of fiducial mass compared to histograms for other Δm^2's. The error bars are dominated by the statistical error on the expected beam ν_e events per bin. Systematic errors, neutral current background and detector resolutions are not included.

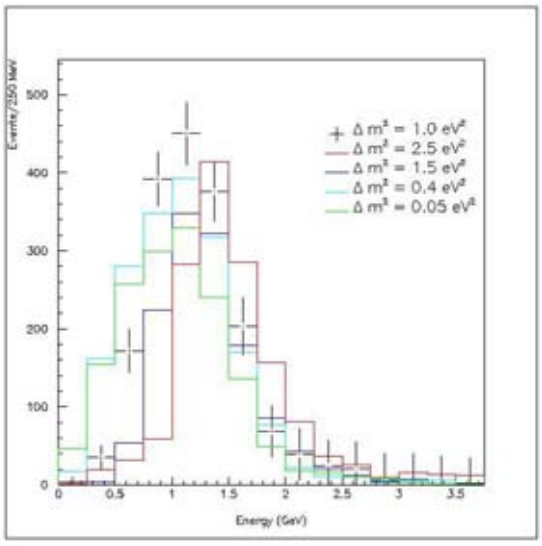

Fig. 13.26: The same as Fig. 13.25, except for a near detector located at Site 3.

the statistical error on the expected beam ν_e events per bin. Systematic errors, backgrounds and detector resolutions are not included, though given the size of the signal we do not expect background to be an issue. It is apparent that some curves can be easily differentiated from others. Our ultimate sensitivity on Δm^2 and $\sin^2 2\theta$ will depend on how well we can control systematic errors.

Near detectors in different locations could allow for better discrimination of the oscillation parameters. Figure 13.26 repeats the exercise illustrated in Fig. 13.25, but at Site 3 where the energy spectrum peaks at lower energy. Again it is apparent that some curves can easily be discriminated from others. The relative characteristics of the curves change from Fig. 13.25 to Fig. 13.26 due to the different neutrino energy spectra. This could allow for simultaneous fits to the spectra from both locations and result in a more accurate extraction of the oscillation parameters. Again, the ultimate accuracy that can be achieved will depend on systematic errors.

Even if MiniBooNE definitively rules out the LSND oscillation in $\nu_\mu \to \nu_e$, it is still possible that the oscillation occurs in $\bar{\nu}_\mu \to \bar{\nu}_e$ where LSND observed their most significant excess. MiniBooNE would now want to run in antineutrino mode, and the APS Joint Study on the Future of Neutrino Physics [8] has strongly recommended that the LSND result be tested with both neutrinos and antineutrinos.

MiniBooNE has recently noted [9] that there are new CP violation models in which the oscillation probability for $\bar{\nu}_\mu \to \bar{\nu}_e$ s can be three times as large as $\nu_\mu \to \nu_e$. However, the antineutrino production and interaction cross sections make this test more challenging than for the case of neutrino running. It seems clear that the NOνA Near Detector could also contribute to this antineutrino effort using the off-axis beam in antineutrino mode.

MiniBooNE also notes [9] that they have a large ~30% "wrong sign" background of neutrinos in their antineutrino event samples (to be compared to only about a 2% wrong sign antineutrino background in their neutrino samples). This is presumably due to the difficulty in defocusing the leading positively charged particles produced in their target. This is of course important for non-magnetic detectors like MiniBooNE and NOνA.

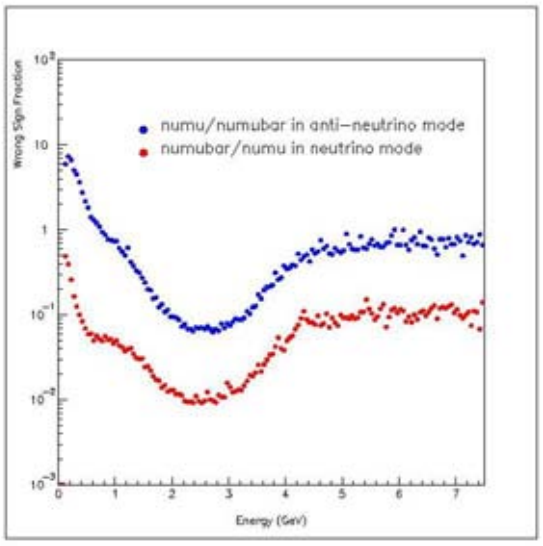

Fig. 13.27: Wrong sign fractions in the neutrino (red) and antineutrino (blue) beams for the NO˜A Near Detector at Site 1.5.

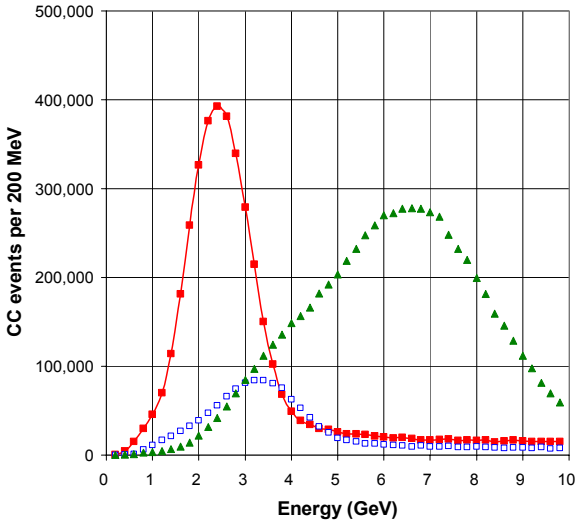

Fig. 13.28: Charged Current ν_μ events seen in the NOνA Near Detector at Site 1.5 for 6.5 x 10^{20} pot (~1 year of data) in the NuMI medium energy beam (red squares with red line). The CC ν_μ events seen by MINERνA in their 4 ton "active target" are shown for 7 x 10^{20} pot (~ 3 years of data) in the NuMI low energy beam (open blue squares). The CC ν_μ events are also shown for MINERνA for 6.5 x 10^{20} pot (~ 1 year of data) in the NuMI medium energy beam (solid green triangles).

The NuMI off-axis beam has different properties than the MiniBooNE beam, as shown in Figure 13.27. Away from the off-axis energy peak, the wrong sign fraction in the antineutrino beam is about 100%, but at the peak it is only about 7%. This lower level of neutrino contamination could allow NOνA to make a clean confirmation of a possible observation by MiniBooNE using anti-neutrinos.

13.8. Neutrino Cross Section Measurements with the NOνA Near Detector

The large samples of neutrino events collected in the NOνA Near Detector should allow some "bread and butter" measurements of basic neutrino cross sections much as planned by MiniBooNE and MINERνA. The narrow energy spectrum in the off-axis beam would make these NOνA measurements unique.

Figure 13.28 illustrates the charged current (CC) neutrino energy spectrum that will be seen by NOνA in the Near Detector running for one year in the NuMI medium energy beam at the off-axis Site 1.5 (see Chapter 9). At that time MINERνA [10] could collect an on-axis data sample in the same medium energy beam and will have already collected a large data sample with ~ 7 x 10^{20} pot on-axis in the NuMI low energy beam. These three potential data samples are shown together in Fig. 13.28 as a function of neutrino energy.

It is clear from Figure 13.81 that NOνA would see a high statistics data sample with a narrow energy spectrum peaked at ~2.4 GeV, to be compared with MINERνA's expected data samples peaked at ~3.3 GeV and ~6.5 GeV. The MiniBooNE data [11] peaks at lower energy (~0.7GeV). The K2K SciFi and SciBar data [12] also peak at lower energy (~1.3 GeV).

MINERνA aims to measure CC cross sections to 5% and NC cross sections to 20% with the data illustrated with the dashed curve in Figure 13.28. Both NOνA and MINERνA have totally active detectors. The NOνA Near Detector is less well suited to measuring cross sections since NOνA has a larger granularity and does not have the MINERνA additions designed for complete containment of events.

We have not yet studied the NOνA capabilities in detail, but several strategies are obvious. We could cut harder on the defined fiducial volume to reduce systematic effects from events with

energy escaping out the sides or end of the NOνA Near Detector. Since NOνA sees multiple events in each 500 nsec window within the 10 microsecond MI spill (see Chapter 9), we would limit any analysis to events with only one event per 500 nsec window and the NOνA curve in Figure 13.28 already has this efficiency factor included.

Studying neutral current (NC) cross sections with the samples in Figure 13.28 is particularly interesting for the NOνA ν_e appearance analysis since NC events with π^0s can fake a ν_e event. These NC backgrounds feed down from higher neutrino energies, so measuring the NC cross sections above our oscillation ν_e peak at 2 GeV is most interesting. The NC/CC ratio is about 0.2, so NOνA would have over 700,000 NC events with the "true energy" distribution shown. Like MINERνA, NOνA could study NC π^0 production cross sections producing by looking for two photon conversions in the detector. We have not yet studied the NOνA efficiency for these specific event types.

13.9. Supernova Detection

13.9.1 Supernova Physics: At 7:35 AM on February 23, 1987, the first of about 20 neutrinos from a supernova explosion in the Large Magellanic Cloud (LMC) were detected by the IMB, Kamiokande II, and Baksan detectors [13]. Optical observations of the LMC taken at 9:30 AM showed no evidence of the blast, but it was present in observations taken one hour later at 10:30 AM indicating the neutrino signal led the optical signal by at least two hours [14].

Though the number of events was small, these neutrinos generated a great deal of interest in both the astrophysics community by confirming the core-collapse model of supernova explosions, and in the particle physic community by limiting various neutrino properties such as their mass and magnetic moment [15].

During a supernova event, the star radiates 98% of its energy in the form of neutrinos of all flavors. The neutrinos are emitted over a period of roughly 10 seconds with a time constant of roughly 3 seconds. The initial burst contains half the total neutrino signal in the first second. Before they escape the exploding star, neutrinos are trapped and reach thermal equilibrium. The neutrinos from a supernova which are detected by experiments on the earth, have an energy spectrum which peaks at roughly 20 MeV and extends out to roughly 60 MeV. Neutrino detectors capable of detecting neutrinos in this range expect to see roughly 400 events per kiloton of detector mass via the inverse beta decay reaction $\nu_e p \rightarrow e^+ n$ from a supernova located at a distance of 10 kiloparsecs (roughly the distance to the galactic center). The galactic supernova rate has been estimated to be roughly 3 ± 1 per 100 years [16].

Currently there are several neutrino experiments that are sensitive to supernovas. These include, SuperKamiokande, SNO, KamLAND, MiniBooNE, LVD, and AMANDA. However, several of these (SNO, KamLAND, MiniBooNE, AMANDA) are planning to complete their running over the next several years. In the time period in which NOνA expects to run, there may only be SuperKamiokande, Borexino, and ICECUBE in operation. In this case, NOνA would serve as an important backup to the SuperKamiokande detector as a detector of comparable size that is capable of supernova detection. NOνA would also serve as an important input to the supernova early warning network (SNEWS [17]), which provides astronomers an automatically generated supernova alert. In the case where both SuperKamiokande and NOνA detect a supernova signal, the neutrino flight paths through the earth to the detectors will be different, allowing the matter effect on neutrino oscillations in the earth to be studied [18].

13.9.2 Detection of Supernova neutrinos: A supernova explosion at a distance of 10 kpc will produce a total of 9000 neutrino interactions via inverse beta decay in the NOνA detector. Electrons at these energies produce roughly one hit strip per 15 MeV of energy, so that the majority of events between 20 and 40 MeV will have coincident hits in adjacent strips of the detector which exceed 0.5 mip (energy deposited by a minimally ionizing particle). Figure 13.29 shows the number of signal events selected by cuts on the minimum pulse height per hit and the minimum number of hit strips in the detector. Selecting hits with more than two hits which have a pulse height more than 0.5 mip yields an 80% efficiency for detection of

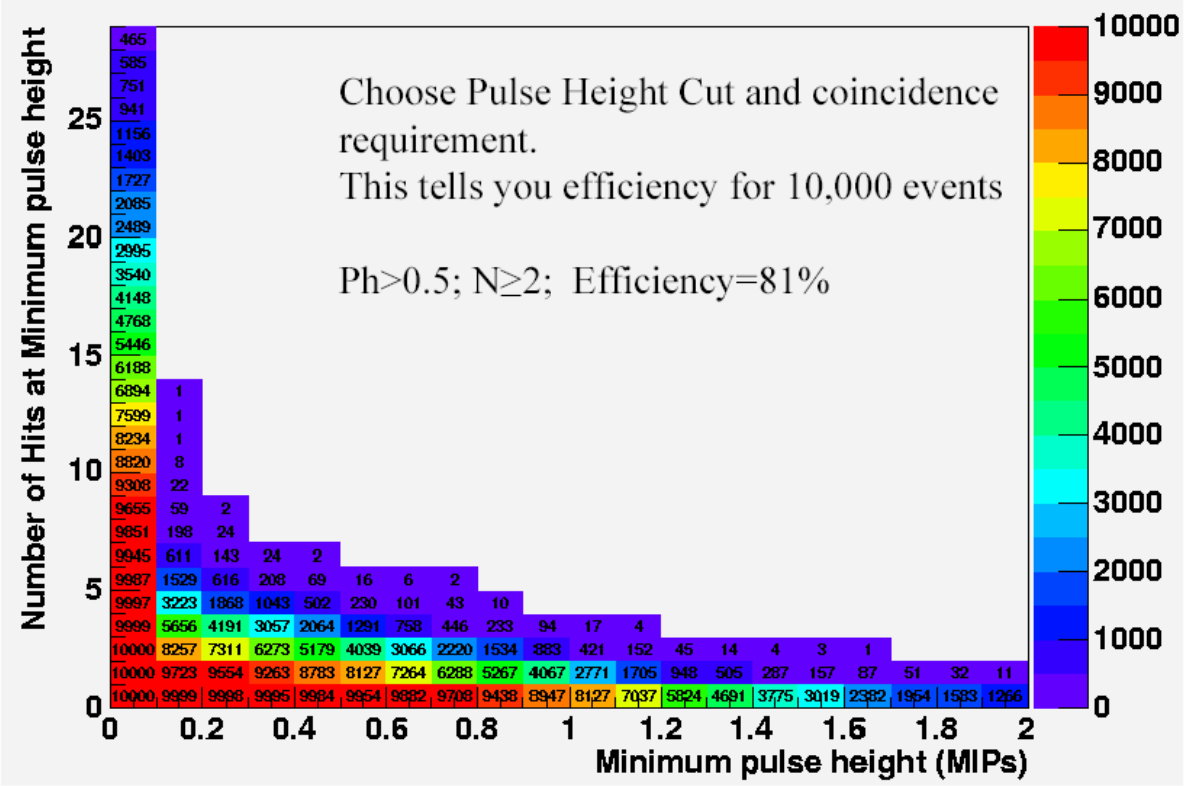

Fig. 13.29: Fraction of supernova neutrino interactions accepted as a function of minimum pulse height seen in a single cell of the detector (horizontal axis) and the minimum number of hits cells (vertical axis). Cuts on >0.5 and >2 accept 80% of the signal events.

supernova neutrinos. Folded with an estimated 50% reconstruction efficiency would yield an estimated signal of 1800 events in the first second of the neutrino burst.

Backgrounds to this neutrino signal have several sources from cosmic rays and neutrons. Detailed calculations have yet to be done, but it is possible to estimate the backgrounds based on experience with other surface detectors.

- Backgrounds from natural radioactivity will be small as the maximum energy for these decays is 2 MeV which is well outside the signal region of 20-60 MeV.
- The electromagnetic component of the cosmic ray backgrounds expected in NOνA is roughly 300 kHz at 10 MeV dropping to 150 kHz at 100 MeV. We expect roughly half of these particles to have energies in the 20-60 MeV signal region, and of those, 90% of them can be removed by placing the fiducial boundary for the detector 1.5 m from the detector edge. This reduces the rate from this source to roughly 10-20 kHz.
- The rate of neutrons entering the detector is roughly 30 kHz above 100 MeV. Of these, only 10% survive a 1.5 m fiducial boundary cut, yielding a background rate of roughly 3 kHz.
- The cosmic ray muon rate in the NOνA detector will be roughly 500 kHz. The muons themselves should be very easily vetoed using a 1.5 m veto region around the central part of the detector. Roughly half of the cosmic ray muons will stop in the detector and will eventually produce Michel electrons with energies up to 52 MeV – right in the heart of the supernova neutrino signal region. Assuming that muons can be tracked, one can place a time-dependent veto region around the muon track. Assuming this region is vetoed for 15 μs, the rate of Michel electrons would be reduced by 99.9%, to roughly 0.25 kHz. Likewise, the beta decay of ^{12}B, which produces positrons below 15 MeV, can be vetoed.

Taking all sources together, we estimate that the background trigger rate will be between 15 and 25 kHz. A supernova signal would appear as an upward fluctuation of this trigger rate of roughly 3.6.

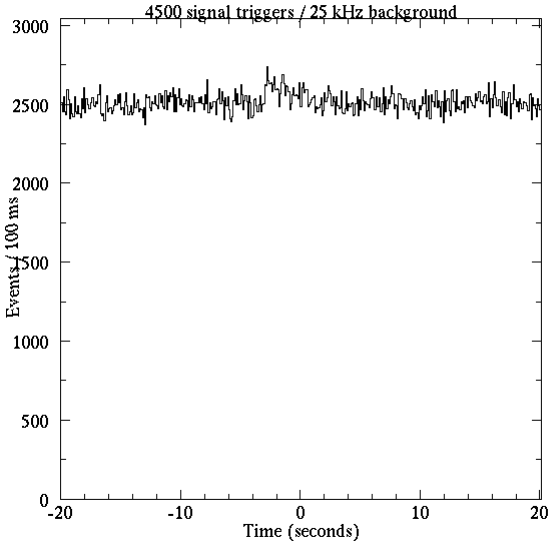

Fig. 13.30: The expected trigger rate as a function of time for a supernova explosion at a distance of 10 kpc. The supernova signal appears at time t=-3 s over a background of 25 kHz.

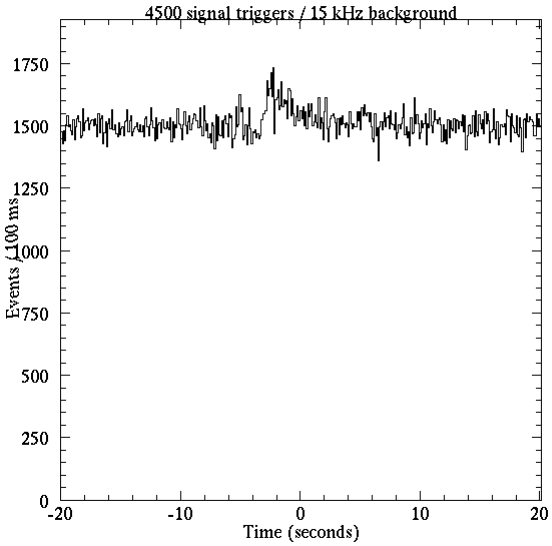

Fig. 13.31: As figure 13.30, but assuming a supernova signal at t=-2 s over a 15 kHz background.

kHz in the first second. Figures 13.31 and 13.31 shows the expected time signature for a supernova signal in the NOνA detector. Assuming 25 kHz of background, the supernova signal is at the edge of detection; at 15 kHz the signal is very clear.

13.9.3 DAQ Requirements: Supernova detection would place significant demands on the DAQ. First, the front end electronics would have to operate with very low dead time and the DAQ would be required to operate in a "free running" mode, and not rely solely on a beam trigger signal from Fermilab. The readout system proposed in Chapter 7 meets these requirements. Second, as the search for a supernova signal would have to be done off-line in real time, the DAQ would have to be able to handle very large data rates – roughly 3 Gb/sec. This is also possible by dividing the detector into sections that are read out and analyzed independently.

Chapter 13 References

[1]T2K Letter of Intent, January, 2003. http://neutrino.kek.jp/jhfnu/.
[2] See, for example, M. Mezzetto, http://axpd24.pd.infn.it/NO-VE/index-of-transparencies.html
[3] Y. Ashie *et al., Phys. Rev. Lett.* **93** (2004) 101801; E. Aliu *et al*., hep-ex/0411038 (2004).
[4] CHOOZ Collaboration, M. Apollonio et al., *Phys. Lett B* **466**, 415 (1999).
[5] Y. Ashie *et al.,* hep-ex/0501064 (2005).
[6] T. Yang and S. Wojcicki, NOνA Note 30, http://www-nova.fnal.gov/notes/notes.html.
[7] A. Aguilar et al., *Phys. Rev. D* **64**, 112007 (2001); C. Athanassopoulos et al., Phys. Rev. Letters 81, 1774 (1998).
[8] The DNP / DPF / DAP / DPB Joint Study on the Future of Neutrino Physics: The Neutrino Matrix, see http://www.aps.org/neutrino/
[9] W. Lewis and J. Conrad, MiniBooNE talks at the November 11, 2004 Fermilab PAC meeting, see http://www.fnal.gov/directorate/program_planning/Nov2004PACPublic/PACagendaNov2004OPEN.htm.
[10] D. Drakoulakos *et al*., "Proposal to perform a high-statistics neutrino scattering experiment using a fine-grained detector in the NuMI beam," February 2004 (http://www.pas.rochester.edu/minerva).
[11] see the MiniBooNE website and Beam TDR (http://www-boone.fnal.gov/publicpages/index.html)
[12] E. Aliu et al., *Phys. Rev. Letters* **94**, 081802 (2005)
[13] K. Hirata et al., *Phys. Rev. Lett*. **58**, 1490 (1987); K.S. Hirata et al., *Phys. Rev. D* **38**, 448 (1988); R.M. Bionta et al., *Phys. Rev. Lett.* **58**, 1494 (1987); C.B. Bratton et al., *Phys. Rev. D* **37**, 3361 (1988); E.N. Alekseev, L.N. Alekseeva V.I. Volchenko and I.V. Krivosheima, *JETP Lett.* **45**,

589 (1987) [*Pisma Zh. Eksp. Teor. Fiz* **45**, 461 (1987)]; E.N. Alekseev, L.N. Alekseeva, I.V. Krivosheina and V.I. Volchenko, *Phys. Lett. B* **205**, 209 (1988).
[14] See, for example, Kaufmann, William J, *Universe*, (3rd Edition, W.H. Freeman, 1991).
[15] S. Eidelman et al. *Phys. Lett. B* **592**, 1 (2004).
[16] J.F. Beacom, R.N. Boyd and A. Mezzacappa, *Phys. Rev. D* **63**, 073011 (2001)
[17] http://snews.bnl.gov/.
[18] For example, C. Lunardini and A.Y. Smirnov, *Nucl. Phys. B* **616**, 307 (2001).

14. Cost Estimate and Schedule

14.1. Introduction

We have developed a cost estimate for a construction project to build the detector described in this proposal. In this chapter we explain briefly the methods used in the cost estimate and contingency analysis. We also discuss some of the important features of the estimates for each of the major elements of the proposal. We present a model for costing operational expenses, both during and after the completion of the construction project. The bottom line is that a construction project would total $ 165 M in FY2004 $, including a 50% contingency. No escalation is included. Additional required R&D is discussed in Chapter 15.

We have developed a schedule for the construction of the NOνA detectors, and that schedule is discussed in this chapter. The bottom line is that a project construction start at the beginning of FY07 leads to a complete detector in July 2011. Data taking with a fraction of the detector begins in October 2009.

14.2. Cost Estimate Methodology

In preparing this cost estimate we have primarily followed the principles used in costing and tracking the MINOS Detector construction project. For each major system we have itemized the materials and services (M&S) that must be procured, fabricated or assembled. Each system is itemized to the lowest level that is realistic for the current state of the system design. For each cost estimate we indicate the source of the estimate as a vendor quote, engineer's estimate or physicist's estimate. These sources are used to distinguish the confidence level in each estimate and hence are used in the contingency determination.

For each system we also itemize the labor tasks associated with the construction of each system. The cost of each task is determined by identifying the type of labor and duration of time required to carry out the task. Each type of labor is assigned a labor rate. For the purposes of this preliminary estimate we have used labor rates based on Fermilab salaries and fringe (SWF) for technicians, designers, drafters, engineers and project management personnel. For staff and installers at the far detector site we have used the labor rates currently applicable at the Soudan Underground Laboratory. Labor estimates have been made by either engineers or physicists based on time and motion studies or recent experience with similar tasks.

For each detector system we have included costs for engineering, design, inspection and administration (EDIA) throughout the life of the construction project. At this stage we have done this by estimating the person-years required based on experience from similar scale projects. We have also included costs for project management and ES&H oversight throughout the life of the construction project.

Our cost summary includes an estimate for institutional overhead based on percentages calculated from the actual costs incurred on the MINOS Detector project, namely 28% for SWF, 9% for M&S procurements under $500k, 1.5% on the first $500k of procurements of $500k or larger, and 0% on the remaining amount of the procurement. Additional overhead on large procurements at collaborating institutions must be negotiated with each institution and we have included contingency funds to cover any such agreements that might not be overhead free.

Contingency is estimated on each item or task based on the confidence level of the estimate, or on an analytical calculation based on a plausible variation of the unit cost or labor estimate. Finally we add an additional allowance to bring the overall contingency on the complete project to 50%. This is discussed in Section 14.4.3.

Table 14.1 summarizes the results of our cost estimate for the construction of this experiment. Our Total Project Cost (TPC) estimate is $ 165 M and that number includes a 50% contingency. The TPC includes the cost for the detectors and for other costs associated with the project. All costs are presented in FY 2004 dollars. At this time the cost estimate is in the form of an Excel Workbook and has not been linked

WBS	Description	Base Cost (K$)	Overhead (K$)	Contingency (K$)	% Contingency	Sub-total (K$)
1.0	**Far Detector**					
1.1	Active Detector					
	1.1.1 PVC Modules + Assembly	19,513	2,184	7,085	33%	28,782
	1.1.2 Liquid Scintillator + handling	24,063	59	6,187	26%	30,309
	1.1.3 Waveshifting Fiber	13,400	8	4,022	30%	17,430
	1.1.4 EDIA	1,680	470	860	40%	3,011
1.2	Electronics, Trigger and DAQ	7,853	803	4,756	55%	13,412
1.3	Shipping & Customs Charges	4,799	960	1,200	21%	6,958
1.4	Installation	7,530	1,963	4,048	43%	13,541
	Far Detector Sub-total	**78,837**	**6,446**	**28,159**	**33%**	**113,442**
2.0	**Near Detector**	**1,678**	**470**	**945**	**44%**	**3,092**
3.0	**Building and Outfitting**					
3.1	Site Work	5,275	158	4,075	75%	9,509
3.2	Building	11,532	346	5,345	45%	17,223
3.3	Outfitting	1,262	38	1,300	100%	2,599
	Building & Outfitting Sub-total	**18,070**	**542**	**10,720**	**58%**	**29,332**
4.0	**Project Management**	**2,985**	**805**	**948**	**25%**	**4,738**
5.0	**Additional Contingency**	**-**	**-**	**14,145**		**14,145**
	due to the early stage of the cost estimate					
TPC	**Total Project Cost**	**101,570**	**8,263**	**54,916**	**50%**	**164,749**

Table 14.1: Work Breakdown Structure and cost estimate for a NOνA construction project in FY04 $.

to project software like Microsoft Project or Open Plan.

14.3. The Detector Cost Estimate

The proposed 30 kiloton NOνA detector is large but uses only a few types of simple components. This simplicity makes the cost estimating exercise straightforward and easy to understand. Most of the mass of the detector is liquid scintillator and the channels are all read out by a single system of electronics. The detector is a monolithic PVC structure assembled from smaller modules constructed in factories at collaborating institutions with small crews in each factory. The detector is assembled in a short time at the far site using a crew of 34 people, about the same size as the crew which assembled the MINOS detector in the Soudan mine.

In this section we briefly discuss each of the major pieces of the estimate.

14.3.1. Liquid Scintillator Active Detector: There are three major components to the liquid scintillator active detector. These are the extruded PVC modules with their endcaps and fiber manifolds, the wavelength shifting fibers, and the liquid scintillator.

The detector requires the assembly of ~24,000 PVC modules with fibers. It is the simplicity of this assembly process that makes the liquid scintillator such a cost effective active detector. The time/motion analysis of the module assembly process indicates that a factory staffed with three assemblers and one supervisor can assemble 10 - 12 modules in one shift. At this rate, three assembly factories can produce the modules at the required rate. The cost of setting up these factories is included in WBS 1.1.1.

The modules are filled with liquid scintillator at the far site. The cost estimate assumes the purchase of pre-mixed liquid scintillator (mineral oil, pseudocumene, and fluors), so there will be no mixing on site. Liquid Scintillator handling is included in WBS 1.1.2 with appropriate storage

tanks and a piping system to move the liquid to the detector assembly front.

14.3.2. Front End Electronics, Trigger and DAQ: The key components in the detector readout are the APD arrays and the custom front-end electronics to read out the APDs. The detector has ~ 762,000 channels to be read out. The custom electronics require the development of two custom ASICs incorporating a pre-amplifier, integrating amplifier, Cockroft-Walton voltage generators, multiplexer and ADC. The current estimate for the overall production cost of the readout is ~$10 per channel.

14.3.3. Shipping: For this design the shipping estimates include shipping (via truck) the empty modules from the three factories to the installation site and mixed scintillator oil (via truck) from Texas to the detector site. There are over 300 truckloads of modules and over 1100 truckloads of scintillator to ship. We deliberately kept the modules less than 53 feet in length so that standard trucks could be used without over-length permit fees. Similarly, no single load will be over the standard road weight limits.

14.3.4. Installation: We have developed an installation procedure that enables us to determine the number of people that will be required to install the detector and how long it will take. 2 people on the day shift will handle the incoming modules and scintillator oil. 25 people split over two shifts a day will construct and install detector planes, cable the electronics, and fill the completed planes with scintillator. There are an additional 7 support staff. We have built into the estimate three phases of the installation: ramp-up while assembling a full crew, steady state, and ramp down.

The installation cost estimate also includes the design and materials costs of the specialized tools and fixtures required for the installation process. This includes vacuum lifting fixtures, the "block raiser" and assembly tables described in Chapter 5, several scissor lifts for working at heights, and 220 tons of epoxy.

14.3.5. Near Detector: The detector described in Chapter 9 is built of identical objects to those in the NOvA Far Detector. The cost estimate assumes the same cost per module or channel for this device as for the Far Detector. Two items are unique to the Near Detector: ~ 5 planes of detector with fast electronics to resolve multiple events occurring in a 500 nsec window, and a steel or aluminum structure which allows installation of the 8-plane modules via the MINOS shaft to the underground enclosure. Cost estimates for these two special items are based on physicist estimates and have a 100% contingency.

14.4. Other Costs

14.4.1. Far Detector Site, Building and Outfitting: The current cost estimate does not include any land acquisition costs. However, the building cost estimate does include general preparation of the site such as clearing and grading. A one-mile access road is also costed. Additional access roadway costs ~$ 0.75 M per mile.

The building cost estimate has been based on a simple industrial style building with no overburden. To estimate costs we are using an algorithm developed by Fermilab Engineering Services Section (FESS), which allows us to specify the detector dimensions, the desired depth below grade of the detector, as well as an installation staging area. The building estimate includes basic utilities such as electrical distribution, fire protection and HVAC but does not include any detector specific structures or outfitting.

Outfitting costs for the detector within the building include additional HVAC and humidity control, detector specific electrical work, and the building bridge crane. The cost of epoxy paint to coat the inside of the containment bathtub is included here as are modest costs to outfit a control room and technician shop.

14.4.2. Project Management: We have estimated the manpower needs and corresponding cost of a project office that would oversee the management and administration of this project. This category of project management includes the Project Manager, a deputy, "Level 1" managers for the detector and the conventional construction, a project scheduler, a budget officer and an administrative assistant. Travel costs for this staff are included here.

14.4.3. Extra Contingency: We are at a very early stage of the design of this experiment. Most designs are only conceptual and still require detailed engineering. Our line by line contingency analysis gives a total contingency in the range of ~35% and we feel this is not sufficient. The detector is composed of a small number of different systems, but the large amounts of single commodi-

ties used in the device do mean that a change in the cost per unit of the commodity will have a large cost effect. A ten cent per gallon increase in the cost of mixed liquid scintillator translates into a $0.75 Million dollar increase in cost. Similarly, an increase of one dollar per channel of electronics would add $0.75 Million dollars. A three cent per meter increase in the cost of wavelength shifting fiber gives a similar cost increase.

As stated above, our cost estimate is in FY04 dollars since many of our vendor quotes are over a year old. We have been told by vendors that the prices of plastic and mineral oil do not follow the price of crude oil, but we have not observed enough market history to verify this fact. In addition, several of our procurements are from foreign countries and the foreign exchange rate can fluctuate during a project timescale of years. Our estimate does not include a funding profile and escalation.

We feel that at this early design stage it is important to allocate contingency in a very conservative manner. For all the reasons outlined above, we have specifically added a line to our cost estimate to reflect an exact 50% contingency of our base estimate plus overhead.

14.5. Operating Costs

We have used experience from the NuMI-MINOS Project to develop a model that costs those expenses incurred during the construction of a project which are not appropriate to be funded by capital equipment funds. These are items such as temporary building rental, utilities in the buildings, telephone and network expenses, etc. During the construction of the MINOS far detector these costs were about $350,000 per year. Upon completion of the construction project, a budget was developed for the annual laboratory operating expenses which is currently ~$1.3M per year to support the laboratory with a crew of 8 persons. At this time it is not obvious how the laboratory for the NOνA Far Detector would have to be staffed, but such expenses should not be in excess of those currently needed for the Soudan Laboratory. These operating costs are not included in Table 14.1.

14.6. Offline Computing

Data rates in the NOνA Far Detector are dominated by ~ 100 Hz of out-of-spill cosmic ray data. As explained in Chapter 7, the event record size is about 100 kB per 30 μsec long data record, so 100 Hz of out-of-spill triggers gives (100 records per sec)(3 x 10^7 sec per year)(100 kB per record) = ~300 TB per year.

The Far Detector in-spill data consists of one event record for every 30 μsec MI spill. The event record consists of the zero-suppressed list of hits with time stamps in 500 nsec slices (see Chapter 7). There are a maximum of 1.1 x 10^7 MI spills to NOνA per year (see Chapter 11), so there are 1.1 x 10^7 event records per year, each 100 kB in size. This results in ~1.1 TB per year. Actual neutrino events in the in-spill data amount to only about 1 GB per year.

The NOνA Near Detector also generates a computing load. Just like the Far Detector, the thirty 500 nsec slices per 10 microsecond spill are read out as one record. Unlike the Far Detector, the record size is much smaller since the Near Detector only has 12,000 channels compared to the Far Detector's 762,000. The Near Detector data is therefore (12/762)(~1.1 TB) = ~ 17 GB per year.

Assuming ~5 GHz-sec/event reconstruction time, reconstruction of Far Detector in-spill (cosmic + beam) data can be accomplished with a few nodes of 3 GHz Linux machines. Reconstruction of the 100Hz triggered cosmic ray background should take less time per event since it is mostly straight line tracking in an unmagnetized medium. Without detailed studies of what is needed for calibration and monitoring one can only guess at the computing requirements, but a rough estimate is ~1 GHz-sec/event, thus requiring 100 GHz of dedicated CPU. This is easily achievable in a cluster of 12 nodes of four 3 GHz CPUs. Given that the NOνA read out is not multiplexed (unlike MINOS), the expansion factor for reconstruction quantities should not be larger than two to four.

We note that additional NOνA Monte Carlo samples would change the conclusions in this section. These operating costs are not included in Table 14.1.

14.7. Schedule

Table 14.2 shows a list of milestones for R&D and construction of the detector referenced to a time t_0 = construction "Project Start" date. This schedule is approximately "technically driven."

Milestone	Date (in months relative to Project Start)	Proposed Calendar Dates	FY
Procure 32-cell test extrusions with final design	t_0 - 12	October-2005	
initiate R&D on APD packaging	t_0 - 12	October-2005	
start advanced conceptual design work on the Far Site	t_0 - 7	March-2006	06
start advanced conceptual design work on the Far Building	t_0 - 6	April-2006	
Site Work advanced conceptual design complete	t_0 - 2	August-2006	
Far Building advanced conceptual design work complete	t_0 - 1	September-2006	
Project Start	**t_0**	**October-2006**	
Order extrusions	t_0 + 1	November-2006	
Order waveshifting fiber	t_0 + 1	November-2006	07
Notice to Proceed on Far Site Work and Building *(linked to advanced conceptual designs above)*	t_0 + 1	November-2006	
R&D prototype Near Detector complete	t_0 + 3	March-2007	
Site work complete	t_0 + 9	July-2007	
Begin receiving packaged APD modules *(linked to R&D start above)*	t_0 + 12	October-2007	
Start Extrusion Module Factories *(linked to available extrusions, manifolds, and electronics)*	t_0 + 12	October-2007	
Start construction of Near Detector	t_0 + 14	December-2007	08
Beneficial Occupancy of Far Building	t_0 + 19	May-2008	
Start Outfitting of Far Building	t_0 + 19	May-2008	
Start operation of Near Detector	t_0 + 21	July-2008	
Order scintillator oil for continuous delivery 6 months later	t_0 + 26	December-2008	
Far Building Outfitting complete	t_0 + 31	May-2009	09
Start construction of Far Detector	t_0 + 31	May-2009	
Start filling Far Detector planes with Scintillator	t_0 + 32	June-2009	
First kiloton (800 modules) operational	**t_0 + 36**	**October-2009**	
5 kilotons (4000 modules) operational	t_0 + 40	February-2010	10
10 kilotons (8000 modules) operational	t_0 + 43	May-2010	
15 kilotons (12,000 modules) operational	t_0 + 47	June-2010	
20 kilotons (16,000 modules) operational	t_0 + 50	October-2010	
25 kilotons (20,000 modules) operational	t_0 + 53	March-2011	11
Full 30 kilotons operational	t_0 + 57	July-2011	

Table 14.2: Proposed NOνA schedule. Dates are shown relative to Project Start at time t_0. Our proposed calendar schedule and the relevant fiscal years are also shown. Most R&D tasks are shown prior to the Project Start time.

We have not started a Microsoft Project or Open Plan exercise to link our cost estimate to a schedule. The main critical path is 1) construction and outfitting of the building, followed by 2) installation of the modules at the far site. Thus the module factories have a well defined time interval in which to produce the 24,000 required modules and we have chosen a production model to match that time interval. Figure 14.1 illustrates how the two assembly tasks interleave. Liquid scintillator filling of the detector begins shortly after the far site module assembly work begins and will follow the solid red curve in Figure 14.1 with a time offset of one month.

A timely start to advanced conceptual design of the Far Site work and Far Detector building during the R&D period is a critical path to ensure that procurements can be placed soon after the project start. The other main critical path is for electronics R&D to begin in time to produce the final electronics packages needed in the module factories. Table 14.2 shows these start times during the R&D period as (t_0 - N month) entries.

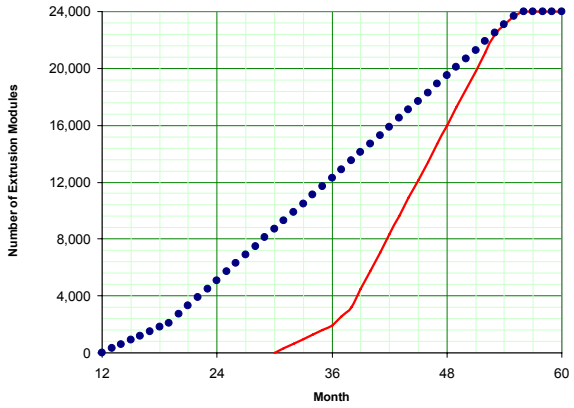

Figure 14.1: Completion schedules for modules produced in the factories (blue dots) and modules assembled into planes in the Far Detector (red line). 4,000 modules are required for each 5 kilotons of detector.

A project start in October 2006 results in NOνA data taking with the first 5 kilotons beginning in February 2010. The full detector is completed by July 2011. Figure 14.2 shows the NOνA 3 σ sensitivity to $\sin^2(2\theta_{13})$ vs. years from the Project Start date.

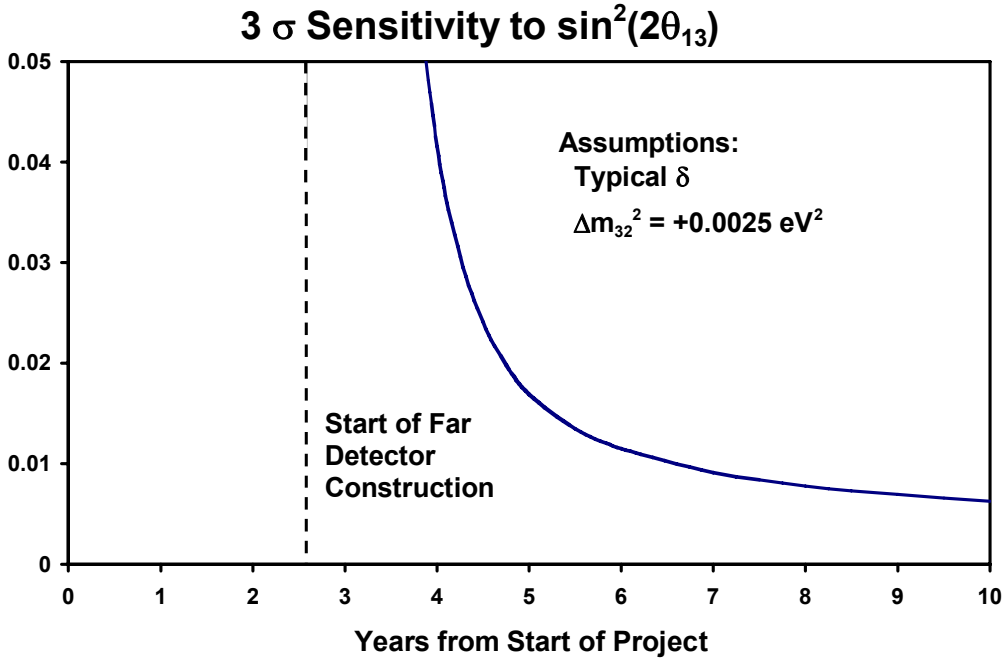

Fig. 14.2: NOνA 3 s sensitivity to $\sin^2(2\theta_{13})$ vs. years from the Project Start date.

15. NOνA R&D Request

15.1. Introduction

This chapter outlines the R&D steps we need to pursue during the next few years, FY05–FY07. Approximately $ 2 M to $ 3 M of R&D funds will be required to advance the design between now and the beginning of the construction project described in Chapter 14. Some of the R&D funds and tasks will overlap the first year of the construction project. In addition we assume contributions of effort from Fermilab and the NOνA collaborating institutions to accomplish this R&D.

The next section outlines particular subsets of the R&D, describing our progress to date and the remaining work to be done. We expect the R&D to conclude with a major effort to build a prototype NOνA Near Detector as described in Chapter 9. The final construction project Near Detector cannot be available until July 2008 (see Chapter 14), but this prototype could be complete in early 2007. The prototype Near Detector will focus our efforts to address many detailed design issues. As outlined in Chapters 9 and 10, we would run this prototype in the Fermilab test beam and in the extreme off-axis NuMI beam available in the MINOS Surface Building.

15.2. Specific R&D tasks

In this section we briefly discuss each of the major R&D tasks.

15.2.1. Extrusions of Rigid PVC: We have obtained about 3,000 feet of a 3-cell rigid PVC extrusion with a cell profile of 2.2 cm deep by 4.2 cm wide, as described in Chapter 6. These extrusions had 1.4 mm thick outer walls and 1.1 mm thick interior webs. Our next step is to repeat this 3-cell exercise with the NOνA design of cells that are 3.87 cm by 6.00 cm with 3 mm outer walls and 2 mm webs. This will give us modest lengths of extrusion with the final profile which can be used for light collection and structural studies.

The final step involves scaling up to a 32-cell extrusion with the NOνA profile. We expect to work with two vendors on these prototypes to sharpen the cost estimate and encourage competitive bidding for the final detector. The prototype 32-cell extrusions would be used in the prototype Near Detector and for structural studies of the Far Detector.

15.2.2. Reflectivity of Rigid PVC loaded with TiO2: The 3,000 feet of 3-cell extrusion discussed above have about 12% TiO_2. In pursuing these we have found that "rigid PVC" is not well defined and can contain variable amounts of acrylic impact modifiers, fillers (usually calcium carbonate), wax lubricants for the extrusion process, and organotin compounds to stabilize the extrusion process by scavenging excess HCl in the melting process.

We have seen rigid PVC products with these additives that have very poor reflectivity at 425 nm, so we need to understand the effect of each component. We want to be able to specify the composition and mechanical properties of the final NOνA rigid PVC procurement and be able to verify the product content and reflectivity.

The next step is to procure small samples from our initial vendor with additives removed one at a time so we can understand the effects, if any. The additives may change the structural properties and the reflectivity of the PVC. At the same time we will explore an increased TiO_2 content for better reflectivity as discussed in Chapter 6.

15.2.3. Bottom Closures and Top Manifolds for the Extrusions: For the design described in Chapter 5 we need to investigate injection molded top manifold parts and machined bottom closure parts. Initial prototypes of each will be custom machined during the R&D period.

15.2.4. Wavelength Shifting Fiber: We plan to investigate controlling the position of the fibers in the cells as discussed in Chapter 6. We will also look at products from other vendors for our large fiber order.

15.2.5. Liquid Scintillator: We have been investigating custom mixtures of mineral oil and fluors and will continue this work to find an optimum price scintillator. We also need to study the effect of PVC, fiber, and epoxies on the scintillator and the effect of the scintillator on the PVC, fiber and epoxies.

15.2.6. APD Packaging: We have been investigating a NOνA-specific APD pixel array and packaging for our thermo-electric coolers. R&D on this subject has to be concluded in time to get

electronics for the final detectors as indicated in Table 14.2.

15.2.7. ASIC Designs: We need two ASICs for NOνA, a low noise preamp chip and a Cockroft-Walton high voltage chip. Both are being designed by the ASIC group at Fermilab. Prototype runs would likely include enough wafers to build the prototype Near Detector discussed below in 15.2.10.

15.2.8. Site and Building Work: We need consultant engineering help with a field inspection of the possible Ash River sites so as to narrow the choices. As noted in Chapter 14, we then need to proceed with advanced conceptual designs for the Site(s) and the Far Detector building.

15.2.9. Structural Analysis and Prototypes of the Far Detector: A great deal of engineering study and finite element analysis has already gone into understanding the PVC structure in Chapter 5. We still plan to hire an outside consulting firm to validate the safety factors and look for failure modes of the structure that our in-house effort may have missed. This is a unique structure and we need to verify the design.

We will continue to build small prototypes of the structure to understand its properties. We have also built a ~ half-scale prototype using a commercial garage door PVC product with a cell size about half the NOνA cell size. A picture of this structure is shown in Figure 15.1. We plan to pursue a similar structure with the "full-size" NOνA extrusions, "full" meaning a few meters wide by as tall as we can fit in an existing building at Fermilab or Argonne.

Fig. 15.1: The "half-size" prototype of NOνA at Argonne National Laboratory. The prototype is ~ 8 meters high and it is made of two layers of extrusions. The planes were assembled on a Unistrut strongback and winched up against the vertical bookend on the right while pivoting about the lower right corner.

15.2.10. Prototype Near Detector: Our final goal for the R&D period is to construct a prototype Near Detector like the one described in Chapter 9. This will test all our designs and our assembly procedures. The resulting device will let us get started understanding our detector response with studies in the Fermilab test beam and in the MINOS Surface Building. The device will also let us check the cosmic ray rates seen by the detector on the surface.

This prototype Near Detector might be done relatively cheaply via a loan [1] of NuTeV liquid scintillator to NOνA and by utilizing existing steel at Fermilab for the muon catcher. The electronics would be based on off-the-shelf APDs and thermo-electric coolers mated with prototype NOνA ASICs. R&D funding restrictions might limit the length of the prototype.

15.3. R&D Cost Estimate

Table 15.1 gives a rough cost estimate for the R&D tasks described in Section 15.2. A 33% contingency is included (mostly for uncertainties in the cost of the prototype Near Detector). The items in Table 15.1 include the costs of consultants and labor at collaborating institutions. Fermilab engineering and technical help would be in addition to this total.

R&D Task	Approximate Materials & Services funding required (K$)
Extrusions of Rigid PVC	325
Refectivity of Rigid PVC	50
Bottom Closures and Top Manifolds	150
Liquid Scintillator studies	50
APD Packaging	275
ASIC Designs	135
Site and Building Designs	150
Structural Analysis and Prototypes	240
Prototype Near Detector	885
Contingency @ ~ 33%	740
Total	3,000

Table 15.1: Estimated cost of remaining R&D.

Chapter 15 References

[1] Janet Conrad, private communication. Approximately 4,000 gallons are in storage at Fermilab.